Universidade de Brasília
Instituto de Geociências
Programa de Pós-graduação em Geologia

Petrography, geochemistry and isotope geochemistry of the basement and impact melt breccias of the Rochechouart impact structure, NW Massif Central, France

DANIELA ALEXANDRA GUERRERO GUTIÉRREZ

Doctorate Thesis N° 215

Supervisor: Prof. Wolf Uwe Reimold

Co-supervisor: Profa. Natalia Hauser

Brasília, DF / February 28 / 2025

Universidade de Brasília
Instituto de Geociências
Programa de Pós-graduação em Geologia

Petrografia, geoquímica e geoquímica isotópica do embasamento e brechas de fusão por impacto da estrutura de impacto de Rochechouart, NW Maciço Central, França

DANIELA ALEXANDRA GUERRERO GUTIÉRREZ

Thesis presented to the Post-Graduate Program in Geology – Geosciences Institute – IG at the University of Brasília – UnB, as a partial prerequisite to obtain the title of Doctor of Philosophy in Geology.

Concentration Area: Regional Geology

Supervisor: Prof. Wolf Uwe Reimold

Comissão Examinadora:

Prof. Dr. Nilson Francisquini Botelho (IG/UnB)
Prof. Dr. Carl Alwmark (Lund University)
Prof. Dr. Roger Gibson (University of the Witwatersrand, Johannesburg)
Prof. Dr. Lutz Hecht (Substitute - Museum für Naturkunde)

Ficha catalográfica elaborada automaticamente,
com os dados fornecidos pelo(a) autor(a)

GG934p

Guerrero Gutierrez, Daniela Alexandra
Petrography, geochemistry and isotope geochemistry of the basement and impact melt breccias of the Rochechouart impact structure, NW Massif Central, France. / Daniela Alexandra Guerrero Gutierrez; orientador Wolf Uwe Reimold; co-orientador Natalia Hauser. Brasília, 2025.
297 p.

Tese(Doutorado em Geologia) Universidade de Brasília, 2025.

1. Rochechouart impact structure. 2. French Massif Central. 3. impact breccia. I. Reimold, Wolf Uwe , orient. II. Hauser, Natalia, co-orient. III. Título.

ACKNOWLEDGMENTS

I express my deepest gratitude to my supervisors, Uwe Reimold and Natalia Hauser. Their support and insightful advice have been essential in shaping this research and guiding me throughout this journey.

I am also profoundly grateful to my family and friends, whose encouragement and support have been a constant source of strength, making even the most difficult moments more manageable.

Additionally, I extend my sincere gratitude to the collaborators at the institutions where data for this research was acquired. Without their contributions, technical assistance, and support, the current thesis would not have been completed.

Finally, I am grateful to everyone who has supported me along this path. Your contributions, whether through scientific discussions, technical assistance, or words of encouragement, have played an essential role during this entire project.

This study was financed in part by the Coordenação de Aperfeiçoamento de Pessoal de Nível Superior – Brasil (CAPES) – Finance Code 001. I also acknowledge for financial support the Conselho Nacional de Desenvolvimento Científico e Tecnológico (CNPq) and the Barringer Family Fund for Meteorite Impact Research, as well as both financial support and hosting during the field campaign to the Center for International Research and Restitution on Impacts and on Rochechouart (CIRIR).

RESUMO

A estrutura de impacto de Rochechouart de 24 km de diâmetro, está localizada na parte NW do embasamento cristalino do Maciço Central Francês (FMC). O nível de erosão da estrutura permite ter acesso ao fundo da cratera e oferece uma grande oportunidade para estudar as rochas do embasamento e uma ampla variedade de depósitos de preenchimento de cratera, entre eles rochas fundidas pelo impacto e suevitos. O FMC foi formado durante a amalgamação da Pangeia na Orogenia Variscana, entre o Siluriano Superior e o Permiano Inferior. Na área da estrutura de impacto, o embasamento inclui gnaisses, anfibolitos, serpentinitos e corpos graníticos, além de intrusões de diques máficos e félsicos. Este projeto está focado em um estudo da relação entre suevitos e rochas fundidas por impacto, com as rochas do embasamento cristalino na área da estrutura de impacto de Rochechouart. O estudo envolve petrografia, geoquímica de rocha total, análise de isótopos de Sr e Nd em rocha total por TIMS, análise U-Pb em zircão por LA-ICP-MS e SIMS, além de uma caracterização detalhada de EBSD em zircão.

Este estudo foi desenvolvido com o objetivo de compreender a dinâmica de formação das impactitas em relação a (1) as principais rochas precursoras dos diferentes tipos de impactitas, (2) a avaliação da idade do evento de impacto, e de possíveis eventos pós-impacto, e (3) o estudo do reequilíbrio do sistema isotópico U-Pb em função das texturas de metamorfismo de choque em zircão. Observações microscópicas indicam que diferentes níveis de alteração hidrotermal são comuns em todas as amostras. Além disso, a maioria das amostras de embasamento coletadas apresenta baixo grau de deformação, enquanto as impactitas contêm misturas de clastos não afetados pelo choque e clastos variavelmente chocados. A caracterização textural detalhada dos zircões das impactitas permitiu a identificação de uma variedade de texturas de deformação de choque, incluindo reidita, zircão granular do tipo “former reidite in granular neoblastic” (FRIGN) e grãos granulares cujos grânulos não apresentam relações sistemáticas de orientação, sugerindo que essas feições são mais difundidas do que se documentava anteriormente na estrutura de impacto de Rochechouart.

O reequilíbrio do sistema isotópico U-Pb em zircão é altamente heterogêneo e parece ser controlado pela intensidade do choque e pelo conteúdo de U e Th no zircão. No entanto, na rocha de fusão de Babaudus, fatores adicionais parecem influenciar o reequilíbrio da idade. As idades registradas nos zircões das impactitas variam do Neoproterozoico ao Jurássico. Embora tenham sido obtidas idades compatíveis com a idade de impacto mais aceita (~203–206 Ma), a similaridade das características dos zircões com idades próximas a esse evento ressalta os desafios em distinguir idades relacionadas ao impacto daquelas associadas a eventos pós-impacto. Idades pós-impacto (~191–196 Ma) foram documentadas em zircões das rochas de fusão de impacto e da suevita de Videix, indicando que um evento térmico/hidrotermal afetou os zircões de mais litologias do que se reconhecia anteriormente.

Múltiplas idades entre o impacto e os estágios finais da evolução do FMC também foram registradas, especialmente em zircões das rochas de fusão de impacto. Isso levou a uma forte correlação de idades com rochas-alvo específicas no estudo de proveniência dos zircões só para as suevitas: com paragnaisses para a suevita de Chassenon e com monzodiorito e leptinitos para a suevita de Videix. A fraca correlação entre as litologias do embasamento e as rochas de fusão de impacto sugere um reequilíbrio incompleto das idades ou a presença de rochas adicionais no embasamento no momento do impacto, que ainda não foram documentadas na área da estrutura de impacto.

A caracterização multidisciplinar das impactitas e das rochas do embasamento mostra que as impactitas apresentam melhor correlação com rochas-alvo de conteúdo intermediário de sílica, enquanto as brechas líticas e os suevitos geralmente se assemelham às litologias das rochas-alvo mais próximas. Os dados isotópicos de Sr e Sm-Nd indicam que a composição de rochas de fusão de impacto amarelas é mais comparável à dos gnaisses do embasamento, enquanto a das vermelhas sugere uma maior contribuição de granodiorito ou monzodiorito. Esses resultados mostram que abordagens alternativas à proveniência de zircões pelo método U-Pb, como a análise isotópica de Sm-Nd, proporcionam uma melhor

correlação com o embasamento e são preferíveis para avaliar os protólitos mais prováveis dessas impactitas.

Os resultados obtidos neste projeto são apresentados em três artigos. O primeiro focado na análise de proveniência, o segundo nos resultados de geocronologia U-Pb de rochas de fusão de impacto e suevites, além de uma caracterização detalhada das texturas de deformação por choque em zircão, e o terceiro compara os resultados completos de geoquímica e proveniência de zircão para as litologias do embasamento e as rochas de fusão de impacto.

Palavras-chave: Estrutura de impacto de Rochechouart, Maciço Central Francês, brechas de impacto.

ABSTRACT

The 24 km diameter Rochechouart impact structure is located in the northwestern part of the crystalline basement of the French Massif Central (FMC). This structure offers a great opportunity to study the crater floor, the shocked target rocks, and a wide variety of crater-fill deposits, including impact melt rocks and suevite. The FMC was formed during the amalgamation of Pangea in the Variscan Orogeny between the Late Silurian and Early Permian. In the area of the impact structure, the basement includes gneisses, amphibolites, serpentinites and granitic bodies, and minor intrusions of mafic and felsic dikes. This project is focused on a comprehensive study of the relationship between impact melt rock (IMR) and suevite samples and the crystalline basement rocks in the area of the Rochechouart impact structure. This involves petrography, whole-rock geochemical analysis, Sr and Nd isotope analysis of whole-rock samples by TIMS, U-Pb analysis on zircon by LA-ICP-MS and SIMS, and some detailed EBSD characterization of zircon.

This work has been developed with the purpose of studying the dynamics of impactite formation in terms of (1) the principal precursor rocks for the different types of impactites, (2) evaluating the age of the impact event as well as potential post-impact events, and (3) understanding the resetting of the U-Pb isotopic system in relation to zircon shock deformation features. Microscopic observations show that some levels of hydrothermal alteration are common for all samples. Furthermore, most of the collected basement samples display low degrees of shock deformation, whereas the impactites have mixtures of unshocked and variably shocked clasts. The detailed textural characterization on zircons from the impactites allowed the identification of a variety of shock deformation textures, including reidite, “former reidite in granular neoblastic” (FRIGN) zircon, and granular grains with granules lacking systematic orientation relationships, which suggests that these shock features are more widespread in the Rochechouart impact structure than previously documented.

The resetting of the U-Pb system in zircon is highly heterogeneous and appears to be controlled by the shock intensity and the zircon U and Th contents. However, in

the Babaudus IMR, additional factors could influence age resetting. The ages recorded by zircon from the impactites range from the Neoproterozoic to the Jurassic. Although ages consistent with the most accepted impact age were obtained (~203–206 Ma), the similarity of zircon characteristics for ages close to this impact age highlights challenges in distinguishing impact-related ages from those associated with post-impact events. Post-impact ages (~191–196 Ma) were documented in zircons from the impact melt rocks and the Videix suevite, indicating that a thermal/hydrothermal event affected zircons from more lithologies than previously recognized.

Multiple ages between the impact and the latest stages of the evolution of the FMC were also registered, especially in zircon from impact melt rocks. This led to a strong age correlation only for the suevites in the zircon provenance study: to paragneisses for the Chassenon suevite and monzodiorite and leptynites for the Videix suevite. The poor correlation between basement lithologies and impact melt rocks suggests incomplete age resetting of target rock zircon or the presence of additional basement rocks at impact time that have not yet been documented within the area of the impact structure.

Multidisciplinary characterization of the impactites and the basement rocks shows that the impactites are better correlated with the target rocks with intermediate silica content, and the lithic breccias and suevites resemble the compositions of the nearest target rock lithologies. The Sr and Sm-Nd isotopic data show that the composition of the yellow IMRs is more comparable with the compositions of basement gneisses, whereas the one of the red IMRs suggests a higher contribution of granodiorite or monzodiorite. These findings show that alternative approaches to U-Pb zircon provenance, such as Sm-Nd isotopic analysis, provide a better correlation with the basement and are preferable for evaluating the most probable protoliths of these impactites.

The results obtained in this project are presented in three articles. The first is focused on provenance analysis, the second on U-Pb geochronology results of additional impact melt rock and suevite samples and on a detailed characterization of zircon

shock deformation textures, and the third one on a comparison of the full geochemical/zircon provenance results for basement lithologies, impact melt rocks, and suevites.

Keywords: Rochechouart impact structure, French Massif Central, impact breccia.

List of Figures

Figure 1.1. (a) Geological map of the French Massif Central, at the scale of 1:1,000,000 (Bureau de Recherches Géologiques et Minières), with the location of the Rochechouart impact structure marked by the white dot. (b) Geological map at the scale of 1:50,000, Sheet Rochechouart (after Chèvremont et al., 1996). The black circle indicates the extent of exposures of crater fill deposits (centered on the black cross). The white cross is the probable center of the initial Rochechouart impact structure, as derived from a shock zoning study and gravity anomaly measurements (Lambert, 1977; Pohl et al., 1978). This map also shows the locations of all samples of this study, divided into three sections: first set of samples (FSS), second set of samples (SSS), and from drill-cores. UGU – Upper Gneiss Unit, LGU – Lower Gneiss Unit. 26
Figure 3.1 Geological map at the scale of 1:50,000, Sheet Rochechouart (after Chèvremont et al., 1996). The white circle indicates the extent of exposures of crater fill deposits (centered on the white cross). The red cross is the probable center of the initial Rochechouart impact structure, as derived from the present exposure pattern (P. Lambert, CIRIR, pers. communication). The locations of the samples of this study are shown with symbols according to their respective lithology. 40
Figure 3.2. Photographs of some of the quarries and samples of this study. (a) Quarry of the leptynitic gneiss from Le Petit Mascureau (C220607-1115) that corresponds to the LGU. The orthogneiss is homogeneous and shows various families of joints. (b) Quarry at Moulin de Laurière (C180825-0930) from the LGU, where a homogeneous paragneiss cut by various families of joints is found. (c) Paragneiss from Saillat Sur Vienne (C220506-0954) from the UGU, which is folded (yellow line) and has quartzofeldspathic lenses. (d) Amphibolite from Exideuil (C180824-1500) with a narrow vein of K-feldspar (black arrow). (e) Monzodiorite sample from La Martinie (C180825-1115) collected from LGU. The sample is partially altered and shows evidence of shock metamorphism in the form of shatter cones (black line). (f) Outcrop of Champagnac pegmatite (C220514-1340) that cuts UGU gneiss. (g) Quarry of Exideuil granodiorite (C220511-1352), cut by two families of joints. 42
Figure 3.3 . Microphotographs of the leptynitic gneisses from (a, b, and c) Champagnac (C180824-1645) and (d, e and f) Le Petit Mascureau (C220607-1115). Images a, c, and d were taken with plane-polarized light, images b, e and f with cross-polarized light. (a) General texture of the rock showing the lineation marked by the prismatic minerals and phyllosilicates. (b) Aggregate of idioblastic mica and amphibole. (c) Biotite partially and completely altered to chlorite, with idioblastic and xenoblastic grains; some regions of the biotite are totally oxidized. (d) K-feldspar with perthitic exsolution in contact with a plagioclase crystal with myrmekitic texture. (e and f) General texture of the rock showing the faint lineation marked by the prismatic minerals and the phyllosilicates. Mineral abbreviations after Whitney and Evans (2010). 43
Figure 3.4. Microphotographs of the paragneisses from (a, b, and c) Moulin de Laurière, from the LGU (C180825-0930), and (d and e) from Saillat Sur Vienne, from the UGU (C220506-0954). Except for image (b), all others were taken with plane-polarized light. (a) General granolepidoblastic texture

with a pervasive orientation of elongated crystals of phyllosilicate and irregular bands with different proportions of quartz and feldspar. (b) Feldspar porphyroblast with pressure shadows of subhedral biotite. (c) Very fractured, post-kinematic garnet. (d) General granolepidoblastic texture of the C220506-0954 sample. (e) Aggregate of subhedral biotite with some adjacent euhedral biotite and muscovite. Mineral abbreviations after Whitney and Evans (2010). 45
Figure 3.5. Microphotographs of the amphibolites from (a and b) St Junien (C180822-1625) and from (c and d) Exideuil (C180824-1500), and the (e and f) serpentinite from Merly (C220522-1749). Except for images a and c which were taken in plane-polarized light, all others were taken with cross-polarized light. (a) General view of the sample showing the lepidoblastic texture of the biotite and the nematoblastic texture of the amphibole. (b) Porphyroblast of plagioclase with inclusions of amphibole. (c and d) A close-up of the inequigranular texture with some phenocrysts of zoned and altered plagioclase (e) Fibrous habit of the serpentine. (f) Inequigranular serpentine with a mesh-texture and cut by a fracture filled with magnetite and secondary phyllosilicates. Mineral abbreviations after Whitney and Evans (2010). 47
Figure 3.6. Microphotographs of the general texture of the (a and b) La Martinie monzodiorite (C180825-1115), (c and d) Champagnac pegmatite (C220514-1340), and (e and f) Chéronnac granite (C220607-1502). Except for image (b) taken in plane polarized light, all others were taken with cross-polarized light. (a) Quartz phenocryst with inclusions of opaques, a faint development of one set of PDFs (red line), and a micro-fault (yellow arrows). (b) Matrix with feldspars, quartz, and micas. Anhedral and euhedral crystals of biotite partially altered to chlorite; the euhedral crystals can show kink bands (red arrows). (c and d) The Champagnac pegmatite is inequigranular, the plagioclase is partially altered to sericite and separated by aggregates of fine-grained crystals of quartz. The clasts are fractured and some of them have veins filled with secondary carbonate and quartz. (e) Plagioclase crystals with poikilitic texture and inclusions of muscovite. (f) Aggregate of fine-grained chlorite between anhedral quartz crystals. Mineral abbreviations after Whitney and Evans (2010). 50
Figure 3.7. Cross-polarized light microphotographs of the granite from (a and b) Champagnac (C180824-1630) and the granodiorites (c and d) from Exideuil (C220511-1352) and (e and f) La Chassagne (C220608-2001). (a) Strong sericite alteration of the plagioclase and subhedral biotite partially altered to chlorite along cleavage. (b) Microcline with a graphic texture with intergrowth of quartz. (c) Strong sericite alteration of plagioclase. (d) A close-up of amphibole with poikilitic texture characterized by inclusions of partially chloritized biotites and opaque phases. (e) Perthitic alkali feldspar with inclusions of biotite and amphibole. (f) Subhedral grains of biotite and plagioclase with strong oscillatory zoning. Mineral abbreviations after Whitney and Evans (2010). 52
Figure 3.8 Field photographs of the outcrops of some of the studied impactites. (a) Recoudert quarry with strongly weathered, clast-poor, yellow impact melt rock (C180824-1900). (b) Montoume quarry, a large deposit of clast-rich, red impact melt (C180823-0955), cut by subvertical joints. (c) Quarry of suevite at Videix (C220510-1745). (d) Quarry of the Chassenon suevite (C220805-1315) showing the rock with apparently cross-bedded stratification. Person for scale 1.7 m tall. 55

Figure 3.9 Geological logs of the drill-cores (from Lambert, 2019), showing the locations of the samples analyzed in this study..... 58
Figure 4.1 (a) Location of the French Massif Central in the territory of France, with the position of the impact structure marked by the red dot. (b) Geological map at the scale of 1:50,000, Sheet Rochechouart (after Chevremont et al., 1996), and (c) the geology along the schematic composite cross section for the profiles NW-SE to N-S marked in (b). The white circle indicates the extent of exposures of crater fill deposits (centered on the white cross). The red cross is the probable center of the initial Rochechouart impact structure, as derived from the present exposure pattern (after Lambert, 2010). The yellow dots indicate sites of samples previously used for constraining the impact age (compare text). The cross section in (c) is modified after Lambert (2010) and Quesnel et al. (2021), and also shows the locations of the 2017 drillings. 70
Figure 4.2 Cathodoluminescence (CL) images showing the different types of zircon found in the samples of this study. Also shown are the locations of the analysis spots, analysis number, and the respective 206Pb/238U apparent ages. (a) Monzodiorite (C180825-1115), (b) paragneiss from Moulin de Lauriere (C180825-0930), (c) amphibolite from Exideuil (C180824-1500), (d) amphibolite from St. Junien (C180822-1625), (e) Recoudert IMR (C180824-1900), and (f) Montoume IMR (C180823-0955). (g,h) Selected CL, backscattered electron (BSE), and secondary electron (SE) images from the Recoudert IMR zircon mounts. BSE images of zircon grains from polished thin sections from (i,j) the Recoudert and (k–m) Montoume IMR samples. 83
Figure 4.3 (a) Wetherill plot for the monzodiorite (C180825-1115). Inset with the weighted average age for the youngest three zircons considered valid. (c) Tera-Wasserburg plot for the paragneiss (C180825-0930). Data not considered as valid are shown with plain red lines. (b, d) Histograms (bin sizes = 20 Ma) for the monzodiorite and the paragneiss data with the age peaks of the probability density plot. Probability density plot in plain blue lines and kernel density plot in pink dashed lines. 88
Figure 4.4 Tera-Wasserburg plots for the data from (a) the amphibolite from Exideuil (C180824-1500) and (b) the amphibolite from St. Junien (C180822-1625). (c) Data used for the estimation of concordia ages (CA) plotted in black, data used for weighted average ages (WA) are plotted in green, and data not used for the determination of any age are plotted in red. (b, d) Histograms (bin sizes = 20 Ma) for the Exideuil and the St. Junien amphibolite data, respectively, with the age peaks of the probability density plot. Probability density plot in blue and kernel density plot in pink dashed lines. 89
Figure 4.5 Tera-Wasserburg plots for zircon data for impact melt rocks from (a) Recoudert (C180824-1900) and (c) Montoume (C180823-0955). Data used for the estimation of concordia ages (CA) plotted with black lines, data used for weighted average ages (WA) with green error ellipses, and good quality analyses not used for the calculation of those ages plotted in red lines (Vermeesch, 2018a). (b, d) Histograms for the Recoudert (bin size = 6 Ma) and Montoume (bin size = 15 Ma) IMR superimposed onto the age peaks of the probability density plot. Probability density plot in plain blue lines and kernel density plot in pink dashed lines. 93

Figure 4.6 Kernel density plot for the results from this study, for Neoproterozoic to Ordovician (lower part) and Silurian to -Jurassic (upper part) times. Only data with 7/5:6/8 discordance less than 10 % have been considered. The upper colored bars refer to major events constrained in the geologic evolution of the French Massif Central (after Lardeaux, 2014). The granitization phase is after Reimold et al. (1987) and lamprophyre formation as discussed in the text. Plot made with Detrital Py v. 1.3 (Sharman et al., 2018). 99
Figure 4.7 Probability density plot for the results from this study for the Montoume and Recoudert IMRs. Only data with 7/ 5:6/8 discordance less than 10 % have been considered. Plot made with Detrital Py v. 1.3 (Sharman et al., 2018). 101
Figure 4.8 Multi-dimensional scaling (MDS) model for the samples of this study. The model was calculated with the Kolmogorov-Smirnov D statistic dissimilarity method (Vermeesch, 2018b). Distances between the sample locations is proportional to the dissimilarity between their U-Pb age distributions (Vermeesch et al., 2018b). The pie plots represent the age distributions obtained for the various samples. The plot was done with the Detrital Py v. 1.3software (Sharman et al., 2018). .. 104
Figure 4.9 (a) Distribution of U-Pb zircon ages for the Montoume and Recoudert impact melt rocks analyzed in this study and the Babaudus impact melt rock analyzed by Rasmussen et al. (2020). Dashed red line at 206.92 + 0.20/-0.32 Ma corresponds to the 40Ar/39Ar age for the impact event by Cohen et al. (2017). The bars in the grayish region are shown in diagrams b, c, and d. (b) TuffZirc age plot (Isoplot v. 4.15; Vermeesch, 2018a) for the youngest ages reported for all the IMRs. Diagrams (a) and (b) categorize the crystals with different zircon textures observed in BSE images, and diagrams (c) and (d) show the zircon classifications based on CL and optical characteristics of the crystals. 108
Figure 5.1 Schematic geological map of the Rochechouart impact structure (modified after Chèvremont et al., 1996, Cohen et al., 2017; Lambert, 2010; Rasmussen et al., 2020). The black circle indicates the extent of exposures of crater fill deposits (centered on the black cross). The red cross is the probable center of the initial Rochechouart impact structure, as derived from the present exposure pattern (after Lambert, 2010). (b) Schematic composite cross section for the profile NW-SE/ N-S marked in (a), modified after Lambert (2010) and Quesnel et al. (2021). 137
Figure 5.2 Bar chart showing the textures on zircon grains recognized by CL images and the associated shock deformation of the zircon grains from the samples of this study, for data with discordance < 10 % on the $^{207}Pb/^{235}U$ - $^{206}Pb/^{238}U$ ages and with errors on the apparent $^{206}Pb/^{238}U$ age < 5 %. Gr = granular; Bdd? = possible baddeleyite. 144
Figure 5.3. Imaging and microstructural characterization of granular zircon from (a) the Babaudus IMR and (b) the Videix suevite with the locations of the spots where SIMS analyses were conducted and the corresponding ages and compositions obtained. The ages in red have a discordance >10 % and/or high errors on the apparent $^{206}Pb/^{238}U$ age. BSE images showing possible zirconia granules of higher mass contrast (red arrows). The location of the BSE images is indicated with red rectangles on the CL images. The only grain displaying a clear igneous zonation texture in CL is shown in (a).

(c and d) The colors and clusters of the {001} and {110} planes in inverse pole figures show three main clusters that indicate three orthogonal orientations indicative of “former reidite in granular neoblastic” (FRIGN) zircon (Cavosie et al., 2018). BSE: Backscattered electron, CL: cathodoluminescence, GS: gran size, IPF: inverse pole figure. 146
Figure 5.4. Imaging and microstructural characterization of granular zircon from (a) the Babaudus IMR, (b) the Chassenon suevite, with the locations of the spots where SIMS analyses were conducted and the corresponding ages and compositions obtained. BSE images showing possible zirconia granules of higher mass contrast (red arrows). Grains #1643-22 and #1315-57 show up to 5 % of reidite. (c and d) The colors and clusters of the {001} and {110} planes in inverse pole figures show three main clusters that indicate three orthogonal orientations indicative of “former reidite in granular neoblastic” (FRIGN) zircon (Cavosie et al., 2018). BSE: Backscattered electron, CL: cathodoluminescence, Ph: phase, IPF: inverse pole figure. 147
Figure 5.5. Imaging and microstructural characterization of granular zircon from (a) the Videix suevite with the locations of the spots where SIMS analyses were conducted and the corresponding ages and compositions obtained. Both ages have a discordance >10 % and/or high errors on the apparent $^{206}Pb/^{238}U$ age. BSE images show possible zirconia granules of higher mass contrast (red arrows). Grain #1745-01 shows 2.5 % of reidite. (b) Scattered and contoured inverse pole figures that show that there is no systematic orientation of the granules. BSE: Backscattered electron, CL: cathodoluminescence, Ph: phase, IPF: inverse pole figure. 148
Figure 5.6. Imaging and microstructural characterization of zircon from the Chassenon suevite with the location of the spot where the SIMS analysis was conducted and the corresponding age and compositions obtained. Grain #1315-29 has an exposed surface of 52 x 38 µm and in the CL image shows an irregular, very low CL intensity core with an overgrowth rim. Furthermore, the grain contains 7.4 % reidite, which is confined to sub-micrometer lamellae sets (L1 and L2) of similar orientation and with spacings between ~ 0.45 and 3 µm. These lamellae are crosscut by a reidite set with a width up to 2 µm and spacings between ~ 2.5 and 5 µm (B1). Host zircon has up to ~ 13° of crystal plastic deformation and reidite up to 7°. Grain boundaries > 70° are located in the reidite domains. Orientation maps and their related pole figure show that B1 and L2 are parallel along all planes and in the plane {110} have a topotaxial relationship with L1. BSE: Backscattered electron, CL: cathodoluminescence, GB: grain boundaries, Ph: phase, GROD: grain reference orientation deviation, IPF: inverse pole figure. 150
Figure 5.7. Imaging and microstructural characterization of zircon of the Chassenon suevite with the locations of the spots where SIMS analyses were conducted and the corresponding ages and compositions obtained. Grain #1315-05 has an exposed surface of 52 x 34 µm and an irregular pattern with very low CL intensity. Up to 4.4 % reidite was indexed, and it is distributed in three sets of sub-micrometer lamellae (L1, L2, and L3). L1 and L2 share the same orientation and seem to cut L3, which shares a similar orientation with the planar fractures located at the center of the grain, and which are delimited by L1 and L2. Plastic deformation of the zircon is up to 13° and of reidite is up to

5°, and almost all grain boundaries are < 10°. Orientation maps and their related pole figure show that L1 and L2 are dispersed and aligned only on one {112} direction, L3 tends to have a topotaxial relationship with L1 and L2, and the $\{110\}_{zircon}$ and $\{001\}_{reidite}$ orientations are parallel. BSE: Backscattered electron, CL: cathodoluminescence, GB: grain boundaries, Ph: phase, GROD: grain reference orientation deviation, IPF: inverse pole figure. 151
Figure 5.8. Histograms for the apparent $^{206}Pb/^{238}U$ ages of the impactites analyzed in this study. Age peaks are for the kernel density estimation plots in both suevites and for the probability density plot for data from the Babaudus IMR. Dashed line at 206.92 + 0.20/- 0.32 Ma corresponds to the $^{40}Ar/^{39}Ar$ age for the impact event by Cohen et al. (2017). The minimum age documented for target rocks is 272 ± 12 Ma (Guerrero et al., 2024). Plots and age peaks calculated with Detrital Py v. 1.3 (Sharman et al., 2018). 152
Figure 5.9 Tera-Wasserburg plots of the impactites analyzed in this study of the Rochechouart impact structure. (a, b, and c) Plots developed with all uncorrected data. (d, e and f) Plots developed selecting grains without fractures, with a discordance <10 % on the 7/5:6/8 ages, and with errors of the apparent $^{206}Pb/^{238}U$ age < 5 %. Colors indicate no shock and shock metamorphic textures (different types). Color convention on (a) is valid for all diagrams. 155
Figure 5.10. Tera-Wasserburg plots of the uncorrected data for grains with $^{206}Pb/^{204}Pb$ > 9000, U < 1000 ppm, and radiogenic Pb > 99 %, following McGregor et al. (2019), for the impactites analyzed in this study. Colors indicate different shock metamorphic textures. Color convention on (a) is valid for all diagrams. 156
Figure 5.11. Tera-Wasserburg plot and (b) TuffZirc age plot (Isoplot v. 4.15; Vermeesch, 2018a) for the youngest ages reported for all the three impactites analyzed in this study. 158
Figure 5.12 Conceptual models illustrating the formation conditions of (a) reidite, found in zircons from both suevites; (b) 'former reidite in granular neoblastic' (FRIGN) zircon, identified in both suevites and the IMR; and (c) granular zircon with neoblasts lacking systematic orientation, observed only in zircon from the Videix suevite. The image includes inverse pole figure (IPF) maps and pole figures, showing examples of these shock deformation features identified in the grains analyzed by EBSD in this study. Models modified from Cavosie et al. (2018). T_D -- temperature of zircon dissociation. . 163
Figure 5.13. Multidimensional scaling plot for the U-Pb geochronological data for impactites of this study and from the previous study by Guerrero et al. (2024). Plot made with the provenance package in R with the Kuiper test (Vermeesch et al., 2016). Each sample is connected to its closest neighbor with a solid line, and to its second-closest neighbor with a dashed line. 167
Figure 5.14. U-Pb geochronological data from this study, represented as probability density plot for the Babaudus impact melt rock and as kernel density estimation plots for the suevites of this study and previous reports for zircon from rocks of the impact area (Guerrero et al., 2024). Plot and age peaks calculated with Detrital Py v. 1.3 (Sharman et al., 2018). 169
Figure 5.15. Distribution of the youngest apparent $^{206}Pb/^{238}U$ zircon ages for the samples of this study showing the optical, shock deformation, and CL textural characteristics of the related zircon grains.

Red line at 206.92 + 0.20/-0.32 Ma corresponds to the $^{40}Ar/^{39}Ar$ age for the impact event by Cohen et al. (2017). The figure shows the diversity of zircons that can record ages close to the impact. Badd. – Baddeleyite. 173
Figure 6.1 (a) Location of the French Massif Central in the territory of France, with the position of the impact structure marked by the red dot. (b) Geological map at the scale of 1:50,000, Sheet Rochechouart (after Chèvremont et al., 1996), and (c) the geology along the schematic composite cross section for the profiles NW-SE to N-S marked in (b). The white circle indicates the extent of exposures of crater fill deposits (centered on the white cross). The red cross is the probable center of the initial Rochechouart impact structure, as derived from the present exposure pattern (after Lambert, 2010). The cross section in (c) is modified after Lambert (2010) and Quesnel et al. (2021), and also shows the locations of the 2017 drillings. PLB - Polymict lithic breccia, IMR – Impact melt rock. 202
Figure 6.2 Photographs of the hand-specimens of the drill-core samples (first two rows) and surface samples (next two rows) of the impactites analyzed in this study. Scale bars at the upper right corner of the surface samples correspond to 1 cm. 215
Figure 6.3 Composition of the impactites determined with the petrographic analysis of main components and types of mineral and lithic clasts. IM- impact melt. 217
Figure 6.4 Microphotographs showing the diversity of clast types found in the impactites. The images (a, b, and f) were taken with plane-polarized light. (a-b) Quartzofeldspathic clasts without banding, likely derived from granitic rocks. (c-d) Clasts mainly composed of quartz and/or feldspar (sometimes altered) with a clear orientation of the minerals, probably derived from leptynitic gneisses. (e-f) Clasts of different proportions of quartz, feldspar, and biotite (sometimes oxidated). The biotite has a lepidoblastic texture that defines the texture of these clasts, which are probably derived from paragneisses. (e) Clasts of quartz aggregates without orientation, these clasts could be derived either from granitic rocks or quartz veins of a gneiss. 220
Figure 6.5 Microphotographs of some of the types of deformation found in mineral and lithic clasts of the impactites. Only images (b and e) were taken with plane-polarized light. (a) Toasted quartz clast with two sets of PDFs. (b) Ballen silica. (c) Recrystallized quartz clast. (d) Quartz clast with two sets of PDFs and PFs. (e) Thermally altered orthoclase. (f) Biotite with kink bands. 221
Figure 6.6 Harker plots of SiO_2 versus major elements for the basement samples of this study. Literature data taken from Bambier et al. (1983), Chèvremont et al. (1996), El Korh et al. (2020), Faucher (2021), Lambert (1977), Reimold et al. (1983), and Reimold and Oskierski (1987). LGU – Lower Gneiss Unit, UGU – Upper Gneiss Unit. 224
Figure 6.7 Harker plots of SiO_2 versus selected major elements, mg#, the ratio K_2O / Na_2O, as well as the abundances for Ni for the impactites analyzed in this study in comparison with literature data (smaller symbols). The colors indicate the lithology and the symbols the location of the samples. The lithic breccia symbol represents the monomict breccias of this study and the monomict and polymict

lithic breccias of the literature. Literature data for the impactites taken from Chèvremont et al. (1996), Faucher (2021), and Tagle et al. (2009). 225
Figure 6.8 (a)$^{147}Sm/^{144}Nd$ vs. $^{143}Nd/^{144}Nd$ and (b) ($^{87}Sr/^{86}Sr$)i vs. εNd(t) diagrams for the samples analyzed in this study recalculated to the impact age (206.92 + 0.20 / - 0.32 Ma; Cohen et al., 2017). Unfilled fields represent literature data for gneisses, while filled fields correspond to literature data for various granitoid types in the Limousin region of the FMC. The granitoid categories include muscovite-bearing peraluminous granitoids (MPG), cordierite-bearing peraluminous granitoids (CPG), K-feldspar porphyritic calc-alkaline granitoids (KCG), and the tonalite line of the Limousin (LTL)formed by amphibole-rich calc-alkaline granitoids. LGU – Lower Gneiss Unit, UGU – Upper Gneiss Unit, IMR – Impact melt rock. Literature data taken from Moyen et al. (2017). 228
Figure 6.9 Tera-Wasserburg plots for the data from the basement rocks analyzed in this study. Data used for the estimation of concordia ages (CA) plotted in black, data used for the estimation of upper and lower intercepts plotted in blue, data not used for the determination of any age plotted in gray, and data with high error and/or high discordance plotted in red. 232
Figure 6.10 Principal component analysis (PCA) of all impactite samples from this study and from literature data taken from Chèvremont et al. (1996) and Faucher (2021). Analyses are made with the (a) major and (b) trace elements separately. PC1 and PC2 explain together 77.72% and 48.1% of the total variance of the data on each diagram. The colors indicate the lithology and the symbols the location of the samples. The lithic breccia symbol represents the monomict breccias of this study and the monomict and polymict lithic breccias of the literature. 236
Figure 6.11 Principal component analysis (PCA) for all the impactites of the Rochechouart impact structure and the basement rocks with compositions considered more similar to them. Immobile major and trace elements were considered only, and PC1 and PC2 explain 64.2% of the total variance of the data. The lithic breccia symbol represents the monomict breccias of this study and the monomict and polymict lithic breccias of the literature. Literature data taken from Bambier et al. (1983), Chèvremont et al. (1996), El Korh et al. (2020), and Faucher (2021). 239
Figure 6.12 Kernel density estimation and probability density plots for the basement results from this study, as well as literature data for rocks on the impact area from Guerrero et al. (2024, 2025 - in review). The upper colored bars refer to major events constrained in the geologic evolution of the French Massif Central (after Lardeaux, 2014). The relatively young granitization phase is after Reimold et al. (1987). Plot and age peaks calculated with Detrital Py v. 1.3 (Sharman et al., 2018). 241
Figure 6.13 Multidimensional scaling (MDS) plots for the U-Pb geochronological data of the basement rocks of this study and previous reports for rocks on the impact area from Guerrero et al. (2024, 2025 - in review). Plot made with the provenance package in R with the Kuiper test (Vermeesch et al., 2016). Each sample is connected to its closest neighbor with a solid line, and to its second-closest neighbor with a dashed line. 243

List of tables

Table 2.1. Radiometric age data reported for the area of the Limousin of the French Massif Central. In plain text are U-Pb on zircon or monazite ages, in bold are U-Th- Pb ages on monazite, in bold and italic are whole rock Rb-Sr, in italic are Ar-Ar ages on hornblende, and in italic and underlined are Ar-Ar ages on micas. 36
Table 3.1. Surface samples and drill-core samples used in this project. LGU – Lower Gneiss Unit, UGU – Upper Gneiss Unti, LTL – Tonalite Line of the Limousin. * Distance to the apparent center of the structure. 41
Table 3.2 Deformation features observed at the thin section scale for the basement rocks of this study. Only the single PDF noted in sample C180825-1115 can be related exclusively as shock deformation. PDFs -- Planar deformation features. 54
Table 3.3 Summary of the details of the analytic conditions and data processing of the LA-ICP-MS analyses developed in this study. 62
Table 6.1 Surface and drill core samples of this study. 207
Table 6.2 Summary of the petrographic lithic clast populations and the basement rocks that exhibit the closest similarities to the impactites in this study in terms of geochemistry, isotopic composition, and U-Pb on zircon provenance analysis. >>> High abundance, >> Intermediate abundance, < low abundance, NA - Not analyzed. 244

Table of contents

1 INTRODUCTION 24
1.1 Objectives 27
1.1.1 General objective 27
1.1.2 Specific objectives 28
1.2 Thesis structure 28
2 GEOLOGICAL BACKGROUND 31
2.1 Rochechouart Impact Structure 31
2.2 The basement to the French Massif Central (FMC) in the area of the impact structure 33
3 METHODOLOGY 39
3.1 Sample Material 39
3.1.1 Basement samples 39
3.1.2 Impactites 54
3.2 Analytical methods 59
3.2.1 Petrography 59
3.2.2 Geochemistry 59
3.2.3 Whole-rock Sr-Nd isotopic analysis 60
3.2.4 Zircon U-Pb isotope analysis 61
4 MANUSCRIPT 1 68
4.1 Introduction 69
4.2 Geological background 72
4.2.1 The Rochechouart impactites and previous constraints on the impact age 72
4.2.2 The FMC basement in the realm of the impact structure 74
4.3 Sample descriptions 76
4.3.1 Basement rocks 76
4.3.2 Impact melt rocks 78
4.4 Analytical methods 80
4.4.1 Sample preparation and imaging 80
4.4.2 U-Pb isotope analysis 80

4.5 Results 82
4.5.1 Zircon textures 82
4.5.2 U-Pb age dating of zircon from basement rocks 85
4.5.3 U-Pb age results for zircon from the impact melt rocks 90
4.5.4 U and Th contents and Th/U ratios. 91
4.6 Discussion 95
4.6.1 U and Th systematics 95
4.6.2 The basement to the Rochechouart impact structure 97
4.6.3 U-Pb on zircon results for the impact melt rocks 101
4.6.4 Provenance analysis (Comparison of zircon ages from impact melt rock and possible protoliths) 103
4.6.5 The age of the Rochechouart impact 106
4.7 Conclusions 108
4.8 Supplementary material 110
5 MANUSCRIPT 2 133
5.1 Introduction 134
5.2 Geological background 136
5.2.1 Prior U-Pb isotope work on the Rochechouart impactites. 138
5.3 Materials and methods 139
5.3.1 Sample Material 139
5.3.2 Sample preparation 140
5.3.3 Zircon imaging 140
5.3.4 U-Pb analyses on zircon 140
5.4 Results 142
5.4.1 Zircon characteristics 142
5.4.2 EBSD analyses 144
5.4.3 U-Pb isotopic systematics 152
5.5 Discussion 158
5.5.1 Significance of the shock deformation textures in the context of the Rochechouart impact 158
5.5.2 Implications of zircon shock deformation textures in the Rochechouart impact context 161

5.5.3 Shock deformation and recorded ages: what are the parameters that control age resetting? *163*
5.5.4 Provenance analysis *167*
5.5.5 Impact and post impact ages *170*
5.6 Conclusions **173**
5.7 Supplementary material **175**
6 MANUSCRIPT 3 ..... **199**
6.1 Introduction **200**
6.2 Geological background **203**
6.2.1 Target rocks *203*
6.2.2 Rochechouart impactites *205*
6.3 Sample material and methodology **207**
6.3.1 Sample material *207*
6.3.2 Methodology *209*
6.4 Results **213**
6.4.1 Petrography *213*
6.4.2 Whole rock geochemistry *222*
6.4.3 Strontium and Sm-Nd isotopic results *226*
6.4.4 U-Pb zircon isotope results *228*
6.5 Discussion **232**
6.5.1 Petrographic evidence for possible precursors lithologies of impact breccias *233*
6.5.2 Geochemistry *234*
6.5.3 Strontium and Sm-Nd isotopes *240*
6.5.4 U-Pb zircon provenance analysis *240*
6.5.5 So what were the protoliths for the Rochechouart impactites? *245*
6.6 Conclusions **247**
6.7 Supplementary material **249**
7 SYNTHESIS AND OVERALL CONCLUSIONS **271**
References **276**

CHAPTER 1

INTRODUCTION

1 INTRODUCTION

Impact structures are the most important feature on the surfaces of basically all solid planetary bodies, from small asteroids to the large planets. The only exception is Earth, where the preservation of these structures is hampered by the highly dynamic processes that affect the Earth's lithosphere (Crósta et al., 2019). The impact cratering process has been fundamental throughout the evolution of the solar system and its bodies. In this process, the collision of two planetary bodies generates a shock wave where extreme physical conditions are achieved within microseconds to minutes over relatively small areas of surface (e.g., French, 1998; Melosh, 1989; Osinski and Pierazzo, 2013). This process is mostly known by its destructive effects, on global and local scales, such as the K-Pg mass extinction that has been recorded at the global scale (e.g., Schulte et al., 2010), or the Tunguska and Chelyabinsk airbursts at varied local scales (e.g., Artemieva and Shuvalov, 2016). The role that the impact process has played in generating new habitats that favor the potential development of microbial life has major implications for astrobiology, either in the understanding of the origin and evolution of life on earth or in the search of life on other planetary bodies (e.g., Osinski et al., 2020). Currently, about 210 hypervelocity impact structures are recognized on Earth (Gottwald et al., 2020; Kenkmann, 2021; Osinski et al., 2022). The well-preserved and exposed crater structures on Earth represent the only natural laboratory in the solar system that can be readily accessed to study this highly dynamic, indeed catastrophic process and its geological and environmental effects in detail.

The Rochechouart impact structure is located at 45°50'N, 0°56'E in the NW part of the French Massif Central (FMC). It is the only impact structure yet discovered in France (cf. Figure 1.1a; Gottwald et al., 2020; Kenkmann, 2021; Osinski et al., 2022). Rochechouart is located in the area of the Limousin, straddling the departments of Haute Vienne and Charente. The structure is a medium-sized impact structure with a widely accepted diameter of 24 km (Lambert, 2010). The structure has been significantly eroded, which erased the original crater morphology but has allowed the study of a great diversity of shock metamorphic/impactite facies, the crater floor, and the transition to the target lithologies (Lambert, 2010; Lambert and Reimold, 2023;

Sapers et al., 2014). These features, along with the good accessibility of the structure, make the Rochechouart impact structure an outstanding site to contribute to the understanding of the impact cratering process (Lambert and CIRIR Consortium, 2020; Lambert and Reimold, 2023).

However, since its confirmation as an impact structure in 1971 (Kraut and French, 1971), this structure was relatively little studied until the last decade. Then the interest in the investigation of this impact structure greatly increased with the formation of entities like the “Reserve Naturelle Nationale Astroblème Rochechouart – Chassenon” in 2008 and the “Centre International de Recherche et Restitution sur les Impacts et sur Rochechouart” (CIRIR) in 2016. These entities are aimed at the preservation and promotion of this structure for research and education purposes, also with activities like the CIRIR Congress-Festival of 2022 and the drilling campaign of 2017-2018 that made available ~540 m of core of crater fill deposits and shocked target rocks (Lambert et al., 2019).

In this context, even though the amount of scientific investigations developed in the Rochechouart impact structure has greatly increased, some doubts remain regarding various aspects, such as the original crater dimensions; the formation dynamics of the impactites (e.g., Lambert, 2010; Sapers et al., 2014); the nature of the projectile (e.g., Tagle et al., 2009); the impact age and its relation with other major events (e.g., Rasmussen et al., 2020; this work); and the different processes that affected the target rocks, the impactites, and the environment, during and after the impact event at a local, regional, or possibly even a global scale (e.g., Lambert, 2010; Lambert and Consortium, 2020; Ramboz et al., 2015; Rasmussen et al., 2020; Schmieder et al., 2010; Simpson et al., 2017).

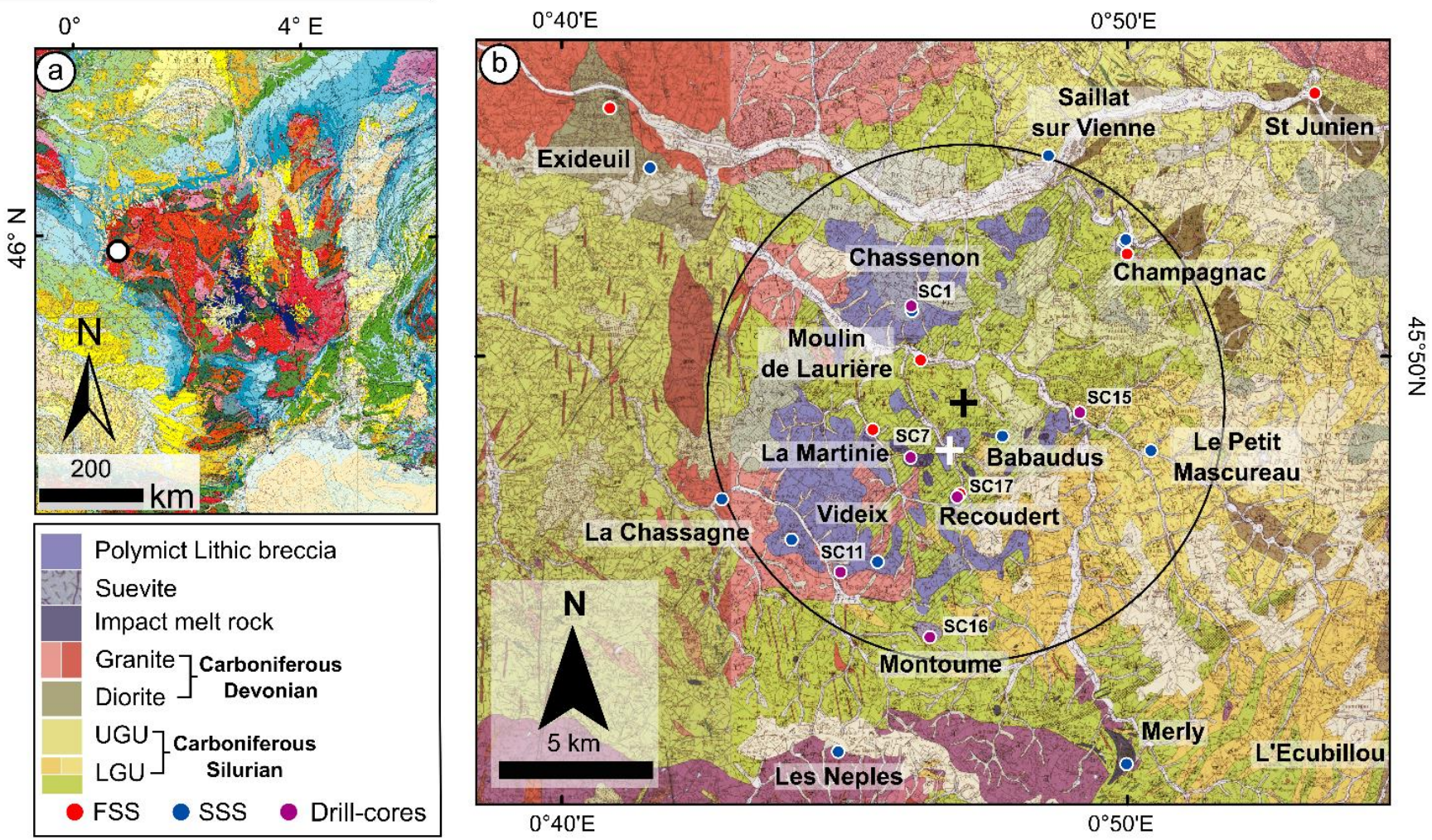


Figure 1.1. (a) Geological map of the French Massif Central, at the scale of 1:1,000,000 (Bureau de Recherches Géologiques et Minières), with the location of the Rochechouart impact structure marked by the white dot. (b) Geological map at the scale of 1:50,000, Sheet Rochechouart (after Chèvremont et al., 1996). The black circle indicates the extent of exposures of crater fill deposits (centered on the black cross). The white cross is the probable center of the initial Rochechouart impact structure, as derived from a shock zoning study and gravity anomaly measurements (Lambert, 1977; Pohl et al., 1978). This map also shows the locations of all samples of this study, divided into three sections: first set of samples (FSS), second set of samples (SSS), and from drill-cores. UGU – Upper Gneiss Unit, LGU – Lower Gneiss Unit.

The FMC represents one of the most extensive exposures of the Variscan Belt, which was mainly created in the course of multiple tectono-metamorphic and magmatic events during the collision of Gondwana against Laurussia from the Late Silurian to the Early Permian (e.g., Faure et al., 2009; Lardeaux, 2014; Regorda et al., 2020; Vanderhaeghe et al., 2020). In the area of the impact structure, the FMC country rocks are well exposed and constitute a great opportunity to study the evolution of this part of the FMC. The local basement at Rochechouart mainly corresponds to the Lower Gneiss Unit (LGU) and the Upper Gneiss Unit (UGU) of the FMC (ibid, and Lambert, 2010; see also Chapter 2, this work). In addition, multiple intrusions of granitic and granodioritic bodies are noted and minor amphibolites, pegmatites, micro-granites, and micro-diorites, are present (Figure 1.1; Lambert, 2010). In the area of the impact structure, these basement rocks have been studied in the past only by a few authors (e.g., Chèvremont et al., 1996; Faucher, 2021; Lambert, 2010, 1977, 1974; Reimold et al., 1983).

This Ph.D. project, developed within the framework of the CIRIR consortium, is aimed at comprehensive characterization of some of the impact breccias and target rocks of the Rochechouart impact structure through detailed petrography, major and trace element whole-rock geochemistry, and Sr and Nd on whole-rock and U-Pb on zircon isotopic analyses. These results will help in the understanding, on the one hand, of the cratering processes related with the dynamics of impactite formation, and, on the other, provide a contribution to FMC basement characterization.

1.1 Objectives

1.1.1 General objective

A multidisciplinary characterization of a suite of surface and borehole samples of impact breccias and target lithologies from the Rochechouart impact structure contributes to the study of several aspects of this impact structure, such as constraining the age of the impact event and possible post-impact processes. This also allows to investigate the dynamics of formation of the impact deposits in terms of protolith (target) rocks for selected impactites from different sectors of the structure.

1.1.2 Specific objectives

The petrographic, geochemical and isotopic characterization (Sr-Nd whole rock), along with the integrated textural analysis and U-Pb isotope study of zircon from some of the more representative impactites and basement rocks of the Rochechouart impact structure, were conducted with the following specific objectives:

- To characterize and compare the shock deformation features, clast populations, and geochemical and isotopic signatures of impactites from different locations in the impact structure.
- To characterize the zircon shock deformation textures and estimate the temperature and pressure conditions achieved during the impact event.
- To investigate the response of the zircon U-Pb isotopic system to varying levels of shock metamorphism, which provides valuable insights into the significance of the geochronologic record of zircon from each impactite sample.
- To compare the age distributions of the impactites and basement lithologies to conduct a provenance study and attempt to determine the most probable precursor lithologies for each impactite type.
- To integrate the petrographic, geochemical, isotopic, and geochronologic information for the impact breccias and the target lithologies to identify the target rocks preferentially involved with the formation of the different types of impact breccia.

1.2 Thesis structure

This thesis is organized as follows: Chapter 1 provides a general introduction to the research topic, outlining the objectives and scope of the thesis; Chapter 2 presents the geological background of the Rochechouart impact structure and the FMC basement; Chapter 3 reviews the methodology employed in this study; and in Chapters 4 to 7 the results of this investigation are presented. Chapter 4 presents the paper titled *"Zircon U-Pb provenance analysis of impact melt and target rocks from the Rochechouart impact structure, France",* published in the journal *Meteoritics*

& Planetary Science on July 29, 2024. The objectives of this paper were to present U-Pb isotope data for impact melt rocks and basement samples, correlate the U-Pb isotopic data with zircon shock deformation, and conduct a first provenance analysis to identify the probable precursor rocks for the analyzed impactites.

Chapter 5 presents the paper *"Shock deformation and U-Pb isotope systematics in zircon from impactites of the Rochechouart impact structure: impact age and zircon provenance"* submitted in February 2025 to the journal *Geochimica et Cosmochimica Acta.* This paper, which is currently in revision, presents a combined study of high-spatial resolution geochronology including SIMS analysis, with detailed textural characterization of zircons from three impactite samples. The objectives of this paper are to better understand the ages obtained and the extent of isotopic resetting in different shock metamorphic textures, as well as to expand the geochronologic dataset of zircons from heterogeneous lithologies.

Chapter 6 presents a preliminary draft of a paper *"What were the protoliths of the Rochechouart impactites? – A multiproxy provenance study"*. This chapter integrates petrographic, geochemical, and whole-rock isotopic (Sr, Sm – Nd) data for multiple impactites and basement rocks, along with geochronologic information of additional basement samples. The objectives of this paper are to characterize the geochemical and isotopic signature of each lithology and use various techniques to identify the most probable precursor rocks for the Rochechouart impactites. For three samples, two granites and a pegmatite, additional U-Pb isotope data need to be collected to improve the statistics of the results. As soon as this has been achieved, this article will be submitted to a suitable journal as well. Chapter 7 provides a comprehensive synthesis and overall conclusions of the principal findings from this investigation.

The complete list of references for all papers is provided in the Reference section (pages 263–285). All supplementary materials for each manuscript are included within their respective chapters.

CHAPTER 2

GEOLOGICAL BACKGROUND

2 GEOLOGICAL BACKGROUND

2.1 Rochechouart Impact Structure

The Rochechouart impact structure is located in the departments of Haute Vienne and Charente, in the region of the Limousin, France. The advanced erosion of this structure challenges the estimation of its original dimensions, for which multiple values have been proposed in the past. The remaining impact deposits are distributed over an area of 15 km diameter (Figure 1.1); however, shock deformation in the basement lithologies extends over a 24 km wide area. This value agrees with the extent of a negative gravity anomaly (Pohl et al., 1978) and consequently has been cited widely as the actual diameter of this impact structure. Lambert (2010), under the assumption that the Rochechouart impact structure is a flat floored readjusted crater, compared the extent of the impact deposits at Rochechouart with those at other, better preserved impact structures and estimated that the original crater diameter, including the collapsed crater wall, could be as wide as 40-50 km. Other authors recently reinterpreted this impact structure as a complex impact crater and calculated an apparent crater diameter of 32 km based on the relationship found for several complex impact structures on Earth between apparent crater diameter and the maximum spatial occurrence of shatter cones (Osinski and Ferrière, 2016).

The impactites of the Rochechouart impact structure occurring below the apparent crater floor, as described in quite some detail by Lambert (2010) and Sapers et al. (2014), include: 1) autochthonous and parautochthonous basement rocks without any macroscopic impact-induced deformation but with shock deformation at the thin section scale; 2) monomict lithic breccias with no or only weak shock metamorphism; and 3) dikes/veins of monomict, polymict and pseudotachylite/pseudotachylitic breccia. Above the crater floor, the allochthonous impactites form a continuum with increasing melt content in the following order: 1) polymict lithic impact breccia (“Rochechouart breccia”), with quartzofeldspathic lithic and mineral clasts of variable shock levels in a fine-grained, clastic matrix; 2) the melt-bearing impact breccia (“Chassenon suevite”), with melt matrix and irregular shaped, variegated glass clasts; 3) the so-called transitional melt-rich impactite (“Vallette-type breccia”), with

a purple quartzo-feldspathic melt matrix, elevated content of glass clasts, and lithic and mineral clasts of varied shock levels; 4) the impact melt rock (“Montoume breccia”), a clast-rich impact melt breccia with mineral, lithic, and glass clasts, and a red to gray-brown, crystalline melt matrix with flow features; and 5) the impact melt rock (“Babaudus melt”), a yellow, clast-free to clast-poor impact melt rock with a quartzofeldspathic homogeneous matrix, rich in vesicles, and with a limited content of quartzofeldspathic lithic clasts. In addition, in the Chassenon quarry occurs a fine-grained, layered deposit, the co-called impactoclastite unit, the origin of which is still poorly understood. It has been suggested that this material may represent resurge deposits formed in a shallow marine target environment (Ormö et al., 2023).

Major element analyses of the different types of impactite and the target rocks from across the impact structure have shown significant variation in the compositions of the different impactites, even within the same units but for samples from different locations. These local variations seem to be controlled by the respective occurrences of basement rocks in the vicinity of melt rock sampling sites (Lambert, 1977, 2010). This author reports that the polymict lithic breccias plot in the compositional field for a mixed granitic and felsic gneiss basement; the composition of the suevite at Chassenon resembles the composition of the locally occurring gneiss; the transitional breccia unit of the southwestern part of the structure has a generally granitic composition; the Montoume impact melt rock matches the composition of the locally present granitoids, gneisses, and leptynites; and the impact melt rock from Babaudus is more felsic and seemingly had a major contribution of locally occurring leptynite.

All these impactites exhibit significant hydrothermal alteration indicative of a widespread post-impact hydrothermal system, marked by a strong K-metasomatism (stronger in the melt-rich phases) and the development of argillic, carbonate, oxide, and sulfide alteration assemblages (Faucher, 2021; Lambert, 2010; Sapers et al., 2014; Simpson et al., 2017).

Most of the geochronological work developed at Rochechouart has been focused on determining the age of the impact event. Several authors used different methods,

principally on the melt-rich units, and a wide variety of ages has been reported (Carporzen and Gilder, 2006; Cohen et al., 2017; Eitel et al., 2014; Horne, 2016; Kraut and French, 1971; Kelley and Spray, 1997; Lambert, 1974; Pohl and Soffel, 1971; Rasmussen et al., 2020; Reimold and Oskierski, 1987; Schmieder et al., 2010; Wagner and Storzer, 1975). Initially, there was an indication – causing great interest – that the age of the Rochechouart impact was close to that of the Triassic-Jurassic boundary (201.3 Ma; Hillebrandt et al., 2013); however, global effects of the Rochechouart impact event are highly unlikely taking into consideration the estimated, restricted crater dimension. Nevertheless, some authors proposed that an association of at least five impact structures dated to the late Triassic may have combined for a potential cause of the extinction at the Triassic-Jurassic boundary (Carporzen and Gilder, 2006; Kelley and Spray, 1997). More recent and precise datation for these impact events has shown that these structures in fact are not coeval (e.g., Cohen et al., 2017; Schmieder et al., 2010).

Currently, the most widely accepted age of the Rochechouart impact event, obtained on Babaudus impact melt rock, is 206.92 + 0.20/- 0.32 Ma ($^{40}Ar/^{39}Ar$; Cohen et al., 2017). Later U-Pb analyses of three former reidite in granular neoblastic (FRIGN) zircon grains from the same sample yielded ages of 194 ± 2.9, 204 ± 2.2, and 207 ± 3.6 Ma (Rasmussen et al., 2020). The youngest age was attributed to possible Pb-loss from a metamict crystal as consequence of an unknown post-impact thermal or hydrothermal event, whereas the two older ages were interpreted as approximating the impact age (ibid). Jurassic ages for zircon (191.6 ± 9.1 Ma) have also been reported for zircons from impact melt rock samples from Montoume and Babaudus (Horne, 2016).

2.2 The basement to the French Massif Central (FMC) in the area of the impact structure

The Rochechouart impact structure is located in the northwestern part of the French Massif Central (FMC). The FMC is made up of Neoproterozoic to Paleozoic igneous, low- to high-grade metamorphic, and low-grade sedimentary units (e.g., Martínez Catalán et al., 2021). This massif represents one of the largest exposures of the

Variscan Belt, which was formed by successive collisions between Laurussia, Gondwana-derived microcontinents, and Gondwana during the amalgamation of Pangea in the widespread Variscan Orogeny, which started in the Devonian and lasted until the Carboniferous (e.g., Franke et al., 2017; Lardeaux, 2014; Martínez Catalán et al., 2021). The FMC, located in the internal part of the orogen, mainly encompasses allochthonous and parautochthonous units, which have been interpreted to represent the ocean-continent transition (OCT) and the outermost continental part of the hyper-extended northern Gondwana margin (e.g., Martínez Catalán et al., 2021).

In the area of the Rochechouart impact structure, the Paleozoic basement of the FMC, as previously described by Lambert (2010), is mainly represented by the allochthonous metamorphic units of the Lower Gneiss Unit (LGU) and the Upper Gneiss Unit (UGU), with a lesser proportion of igneous intrusions with granitic (Chéronnac, St Gervais, and Chabanais) and intermediate/mafic (Tonalite Line of Limousin (LTL)) compositions, and an even lesser proportion of minor bodies of pegmatites, micro-granites, micro-diorites, amphibolites, serpentinites, and lamprophyres that cut the earlier formations (Chèvremont et al., 1996; Lambert, 2010).

The LGU is the most widespread unit (compare Figure 1.1) and is made up of gneisses and metarhyolites represented in the impact structure by occurrences of plagioclase-rich paragneisses and orthogneisses. The UGU is limited to the northeastern part of the impact structure (Figure 1.1) and is represented by a bimodal association of micaceous paragneisses with lenses of leptynites and amphibolites known as the “leptynite-amphibolite complex” (LAC), characteristic of the basal part of this unit. There are mafic and ultramafic lenses of amphibolites intercalated in both units. The paragneisses and orthogneisses of both units are subdivided in the geological map (Figure 1.1; Chèvremont et al., 1996) according to variations in texture, mineralogy, and geochemistry of the rocks.

The protoliths of the LGU and UGU are assumed to have been Ediacaran sedimentary rocks that were intruded by Cambrian plutons that later would constitute

the protoliths for lower Paleozoic sedimentary rocks. These rocks were formed during the southward subduction of the Iapetus Ocean beneath the northern Gondwana margin (e.g., Faure et al., 2009), and subsequently affected by progressive crustal thinning and rifting of the continental margin during the Ordovician, forming the characteristic bimodal suite of the leptynite-amphibolite complex (LAC; Faure et al., 2009; Lardeaux, 2014; Vanderhaeghe et al., 2020).

Throughout the FMC, both gneissic units were affected by the different stages of the Variscan Orogeny. During the Upper Silurian – Devonian, a high-pressure (HP) to ultra-high pressure (UHP) granulite/eclogite facies metamorphism occurred on the UGU (e.g., Do Couto et al., 2016). During the Devonian, retrogression of the HP rocks to granulite facies metamorphic conditions took place, and both LGU and UGU underwent anatexis and synmetamorphic ductile shearing (e.g., Vanderhaeghe et al., 2020). Finally, in the uppermost Devonian-Lower Carboniferous, the period of main continental collision of the Variscan Orogeny, amphibolite facies medium pressure-medium temperature (MP-MT) metamorphism affected both gneisses followed by retrogression to greenschist facies conditions (e.g., Faure et al., 2009; Lardeaux, 2014).

The igneous rocks in the area of the impact structure correspond to the Chéronnac granite to the south, the quartz diorites with hornblende and biotite from the Tonalite Line of Limousin (LTL; Chèvremont et al., 1996), and the gray-pink, calc-alkaline Chabanais granite-granodiorite to the north. In between, the Bouloux and Saint Gervais-Videix granitic bodies occur. The intermediate-mafic, calc-alkaline rocks of the LTL are the oldest magmatic rocks known from the FMC and have been interpreted as intrusions of an andesitic arc above a subduction zone, and also formed during anatexis of the metagraywackes and amphibolite intercalations of the UGU host rock (Chèvremont et al., 1996). The Chéronnac Massif, the calc-alkaline intrusions of Chabanais and St. Gervais, and the micro-granites and micro-granodiorites are attributed to this period of anatexis, too, with ages of 315-305 Ma (Duthou et al., 1984) and are probably derived from metasedimentary or aluminous metagranitic protoliths, and from rocks with a mantellic component for the subalkaline microgranites (Pin, 1989). A summary of the ages reported from the

Limousin for the units present in the impact structure, and their interpretation in the context of the Variscan Orogeny, is presented in Table 2.1.

Table 2.1. Radiometric age data reported for the area of the Limousin of the French Massif Central. In plain text are U-Pb on zircon or monazite ages, in bold are U-Th- Pb ages on monazite, in bold and italic are whole rock Rb-Sr, in italic are Ar-Ar ages on hornblende, and in italic and underlined are Ar-Ar ages on micas.

Unit	Lithology	*Tectonic event*				References
		HP metamorphism	Exhumation	Collision	Extension and collapse of the belt	
UGU	Eclogites, granulites	390 to 430	382 ± 5			1
	Paragneiss	390 to 430				1
	Migmatitic Paragneiss			**362 ± 4**		2
	Migmatite/granulite		383 ± 5, **387 ± 6**	*348.5 ± 4.1*	*334.3 ± 3.1*, *309.2 ± 2.4*	1, 3, 4
	Amphibolites		*380 to 370*, *381 ± 5*, *389 ± 8*, *380 ± 8*, *385 ± 8*			6, 7, 8
LGU	Eclogites	412 ± 10	382 ± 7	*352 ± 7*, 352 ± 2	***332 to 336***, *335 to 337*	1, 9, 10
	Paragneiss			**359 ± 2**		2
	Orthogneiss			**357 ± 4**, **365 ± 5**		2
	Migmatitic gneiss		**378 ± 5, 374 ± 6**		***332***, *337 to 335*, 317 ± 1, 316 ± 2, 315 ± 4	5, 12, 13,14
Granites	Synkinematic Leucogranites (Padrines fault)				313 ± 4	15
	Limousin-type granite (Blond)				*335.9 ± 0.8*, *310.7 ± 0.5*, *315 to 300*, 319 ± 7, 324 ± 4	16, 17, 18, 19
	Guéret granite (Thaurion)			***356 ± 10***, 353 ± 6, 351 ± 5, ***346 ± 14***	324 ± 1	20, 21, 22, 23
	St Sylvestre granite (Thaurion)				*308.3 ± 0.3*	19

UGU = Upper Gneiss Unit, LGU = Lower Gneiss Unit. References: 1 = Bellot and Roig (2007); 2 = Melleton et al. (2009); 3 = Lafon (1986); 4 = Cocherie et al. (2005); 5 = Faure et al. (2008); 6 = Boutin et al. (1991); 7 = Costa and Maluski (1988); 8 = Boutin and Montigny (1993); 9 = Berger et al. (2010); 10 = Santallier (1981); 11 = Faure et al. (2009); 12 = Bellot (2001); 13 = Gébelin et al. (2007); 14 = Gébelin et al. (2009); 15 = Gebelin (2004); 16 = Holliger et al. (1986); 17 = Scaillet et al. (1996); 18 = Alexandrov et al. (2000); 19 = De Veslud et al. (2013); 20 = Berthier et al. (1979); 21 = Duthou (1978); 22 = Cartannaz et al. (2007).

The metamorphic events and magmatic stages recorded for the FMC are part of the major geodynamic evolution of this large block in the context of the Variscan Orogeny, with several major episodes (e.g., Faure et al., 2009; Lardeaux, 2014; compare summary in Table 2.1): 1) Upper Silurian – Lower Devonian subduction of the northern Gondwana passive margin responsible for high-pressure (HP) metamorphism; 2) Middle-Upper Devonian migmatization and exhumation of the HP

rocks and retrogression to amphibolite facies; 3) Upper Devonian formation of the Morvan Arc in the eastern FMC and emplacement of peraluminous plutons; 4) Upper Devonian - Lower Carboniferous continental collision between Gondwana and Laurussia associated with NW-SE dextral strike-slip shear zones, MP-MT metamorphism, and granitoid intrusions; 5) Middle Carboniferous syn-orogenic extension in the north and crustal thickening to the south with late-collisional magmatism throughout the massif; 6) Upper Carboniferous - Lower Permian extensional tectonics with syn-orogenic NW-SE and then post-orogenic NNE-SSW extension, formation of coal basins, exhumation of migmatitic domes, and high-temperature (HT) metamorphism and granitoid intrusions.

CHAPTER 3

METHODOLOGY

3 METHODOLOGY

3.1 Sample Material

Representative samples of the principal basement and melt-bearing impactite units in the study area were collected in two field trips. A first sample set of six basement rocks and two impact melt rocks was obtained by Philippe Lambert and Wolf Uwe Reimold in August 2018 (Table 3.1). A second set of seven basement samples, one impact melt rock, two suevite samples, one impact breccia, and one pseudotachylite were collected in May-June 2022 by Daniela Guerrero and Philippe Lambert (Table 3.1). Additional fourteen samples of impact melt rock and melt-bearing breccia from six drill-cores were collected by Daniela Guerrero and Philippe Lambert in June 2022 (Table 3.1). The locations of all the samples are shown in Figure 3.1.

3.1.1 Basement samples

All modal compositional percentages correspond to vol % and were obtained by counting of ~300 points on each sample. Data from point counting are vol%.

3.1.1.1 Gneisses from LGU and UGU

One orthogneiss and one paragneiss sample each were obtained from the LGU and UGU terranes.

3.1.1.1.1 Leptynitic gneisses

The orthogneiss from the UGU (C180824-1645) sample was collected at Champagnac quarry, 7.5 km to the NE of the center of the impact structure (Figure 3.1). At this locality, the basement shows intense fracturing and is represented by gray micaceous paragneisses cut by diorite intrusions and amphibolitic dikes, and is intersected by felsic gneissic/granitic lenses. Furthermore, along some of the fractures occur hydrothermal deposits with carbonates, quartz, fluorite, and pyrite. The orthogneiss collected at Champagnac is composed of orthoclase (50%), quartz (17%), plagioclase (10%), biotite (7%), microcline (6%), amphibole (3%), accessory phases such as apatite, zircon, epidote, and titanite (3%) and alteration minerals such as sericite (2%) and chlorite (2%).

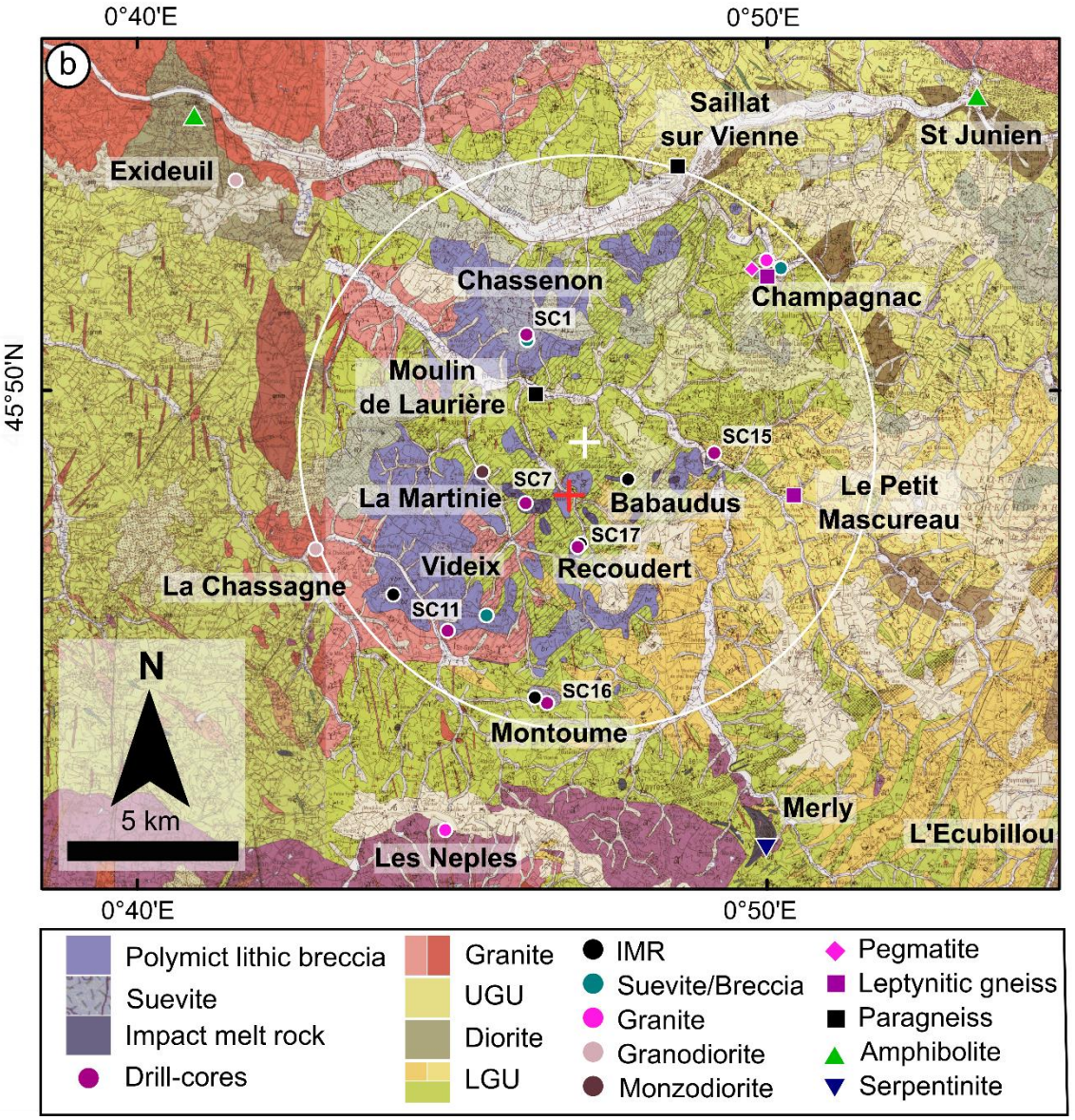


Figure 3.1 Geological map at the scale of 1:50,000, Sheet Rochechouart (after Chèvremont et al., 1996). The white circle indicates the extent of exposures of crater fill deposits (centered on the white cross). The red cross is the probable center of the initial Rochechouart impact structure, as derived from the present exposure pattern (P. Lambert, CIRIR, pers. communication). The locations of the samples of this study are shown with symbols according to their respective lithology.

The orthogneiss from the LGU (C220607-1115) sample was collected at Le Petit Mascureau, at 6.3 km to the east of the center of the impact structure (Figure 3.1). The outcrop is partially covered by vegetation and has multiple sets of fractures, along which the rock is partially oxidized. The sample comprises homogeneous, pink, leptynitic gneiss composed of quartz (43%), orthoclase (30%), plagioclase (12%), microcline (5%), garnet (1%), amphibole (1%) and biotite (2%), as accessory

phases epidote and opaques, and as alteration products, sericite (3%) and chlorite (1%).

*Table 3.1. Surface samples and drill-core samples used in this project. LGU – Lower Gneiss Unit, UGU – Upper Gneiss Unti, LTL – Tonalite Line of the Limousin. * Distance to the apparent center of the structure.*

Code	Unit	Lithology	Location	Coordinates		Distance to the center* (km)
				N	E	
First set of samples						
C180824-1645	UGU	Leptynitic gneiss	Champagnac	45° 51.258'	0° 50.000'	7.5
C180824-1630	UGU	Granite	Champagnac	45° 51.258'	0° 50.000'	7.5
C180824-1500	UGU	Amphibolite	Exideuil Qu	45° 53.052'	0° 40.842'	12.7
C180822-1625	UGU	Amphibolite	St Junien Ceitce	45° 53.238'	0° 53.320'	15.2
C180825-1115	LGU	Monzodiorite	La Martinie	45° 49.092'	0° 45.488'	3.1
C180825-0930	LGU	Paragneiss	Moulin de Laurière	45° 49.949'	0° 46.338'	1.9
C180824-1900	-	Clast-poor, yellow IMR	Recoudert	45°48.349'	0°47.099'	3
C180823-0955	-	Clast-rich, red IMR	Montoume	45° 46.535'	0° 46.488'	7.7
Second set of samples						
C220506-0954	UGU	Paragneiss	Saillat Sur Vienne	45° 52.465'	0° 48.597'	8.4
C220511-1352	LTL	Granodiorite	Exideuil Qu	45° 52.312'	0° 41.554'	12.7
C220514-1340	UGU	Pegmatite	Champagnac	45° 51.258'	0° 49.986'	7.5
C220522-1749	Serpentinized peridotites	Serpentinite	Merly	45° 44.987'	0° 49.977'	12.8
C220607-1115	LGU	Leptynitic gneiss	Le Petit Mascureau	45° 48.850'	0° 50.416'	6.3
C220607-1502	Chéronnac	Granite	Les Neples	45° 45.128'	0° 44.869'	11.9
C220608-2001	La Chassagne	Granodiorite	La Chassagne	45° 48.236'	0° 42.801'	8.4
C220706-1650	UGU	Pseudotachylite	Champagnac	45°51.432'	0° 49.961'	7.5
C220510-1414	-	Clast-poor, red IMR	Videix	45° 47.738'	0° 44.055'	7
C220510-1745	-	Suevite	Videix	45° 47.485'	0° 45.607'	6.4
C220705-1643	-	Clast-poor, yellow IMR	Babaudus	45° 49.013'	0° 47.784'	1.7
C220805-1315	-	Suevite	Chassenon	45°50.579	0°46.357'	3.7

Drill-core samples				Coordinates		Depth relative to surface (m)	
Code	Core ID	Lithology	Location	N	E	Top	Bottom
S1/3/112-125-F1-1 (SC1-3)	SC1	Clast-poor, yellow IMR	Chassenon	45°50' 36.87"	0°46' 10.18"	4.12	4.25
S7/1/25-36-F1-1 (SC7-1)	SC7	Clast-poor, red IMR	Valette	45°48' 45.01"	0°46' 9.24"	0.25	0.36
S7/4/45-48-F1-1 (SC7-4)		Clast-rich, yellow IMR				4.94	4.97
S7/10/122-132-F1-1 (SC7-10)		Melt-rich, red suevite/ IMR				15.25	15.35
S7/15/100-105-F1-1 (SC7-15)		Clast-rich, red IMR				22.97	23.02
S11/5/155-169-F1-1 (SC11-5)	SC11	Clast-rich, red IMR	Videix	45°47' 20.20"	0°44' 55.01"	7.83	7.97
S11/17/132-152-F1-1 (SC11-17)		Clast-rich, red impact breccia				26.87	27.07
S11/25/150-155-F1-1 (SC11-25)		Clast-rich, red impact breccia				40.15	40.2
S15/1/30-40-F1-1 (SC15-1)	SC15	Clast-rich, yellow IMR	Rochechouart	45°49' 18.35"	0°49' 8.92"	0.3	0.4
S16/6/138-150-F1-1 (SC16-6)	SC16	Clast-rich, red IMR	Montoume	45°46' 32.24"	0°46' 30.01"	9.38	9.5
S16/7/124-144-F1-1 (SC16-7)		Clast-rich, red IMR				10.86	11.06
S17/2/144-148-F1-1 (SC17-2)	SC17	Red IMR	Recoudert			3.14	3.18

S17/7/79-122-F1-2 (SC17-7)	Clast-poor, yellow IMR	45°48' 15.98"	0°46' 59.15"	10.5	10.93
S17/13/40-50-F1-2 (SC17-13)	Clast-rich, red IMR			18.4	18.5

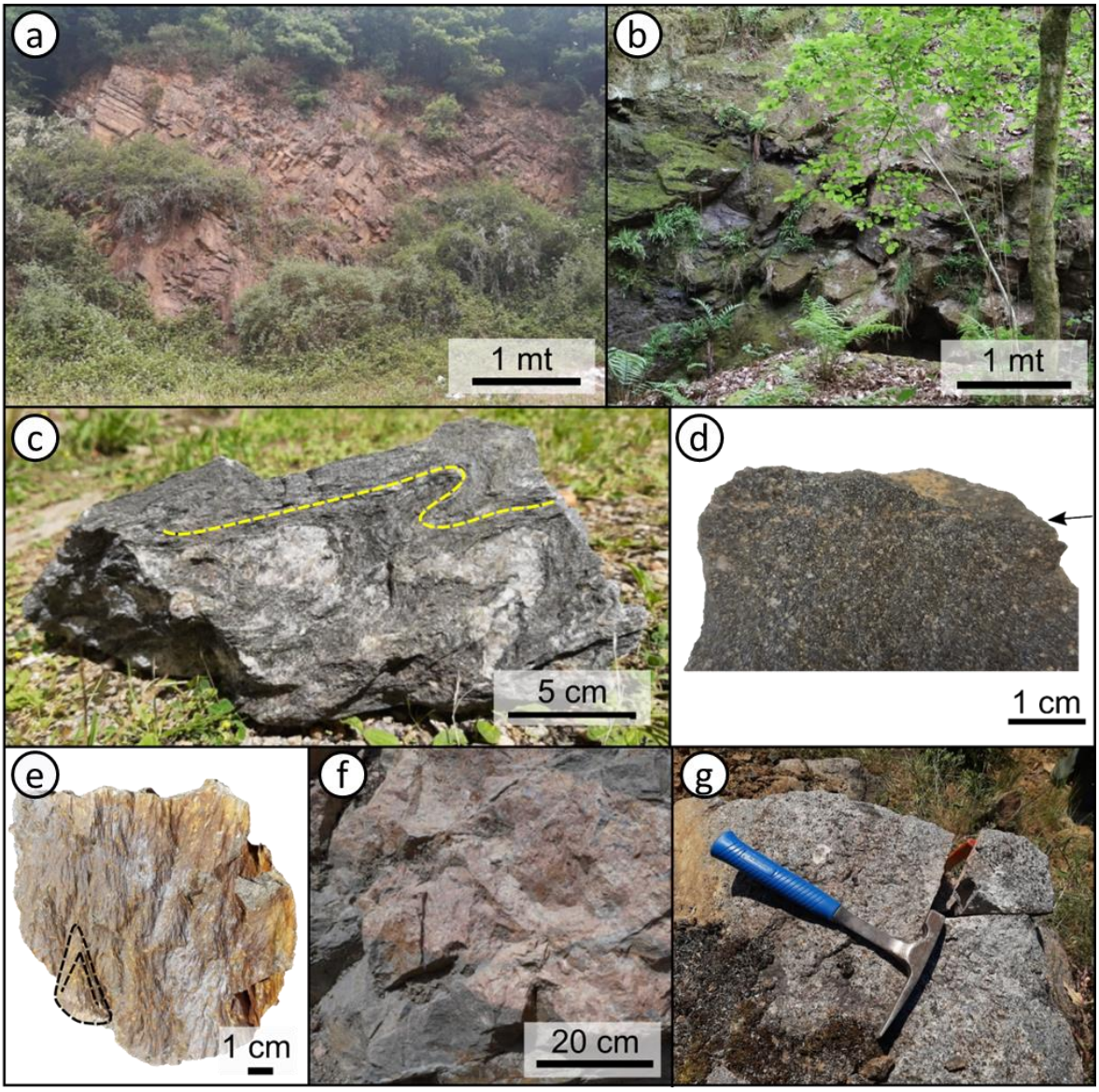


Figure 3.2. Photographs of some of the quarries and samples of this study. (a) Quarry of the leptynitic gneiss from Le Petit Mascureau (C220607-1115) that corresponds to the LGU. The orthogneiss is homogeneous and shows various families of joints. (b) Quarry at Moulin de Laurière (C180825-0930) from the LGU, where a homogeneous paragneiss cut by various families of joints is found. (c) Paragneiss from Saillat Sur Vienne (C220506-0954) from the UGU, which is folded (yellow line) and has quartzofeldspathic lenses. (d) Amphibolite from Exideuil (C180824-1500) with a narrow vein of K-feldspar (black arrow). (e) Monzodiorite sample from La Martinie (C180825-1115) collected from LGU. The sample is partially altered and shows evidence of shock metamorphism in the form of shatter cones (black line). (f) Outcrop of Champagnac pegmatite (C220514-1340) that cuts UGU gneiss. (g) Quarry of Exideuil granodiorite (C220511-1352), cut by two families of joints.

Both samples have fine- to medium-grained crystals and have similar grano-nematoblastic textures (Figure 3.3b and f), with a faint alignment marked by the orientation of the prismatic minerals and by some of the phyllosilicates (Figure 3.3a

and d). The feldspars are partially altered to sericite and can have inclusions of quartz and biotite. Moreover, perthitic K-feldspar is common in both samples, and to a lesser extent intergrowth myrmekitic textures are also present (Figure 3.3d).

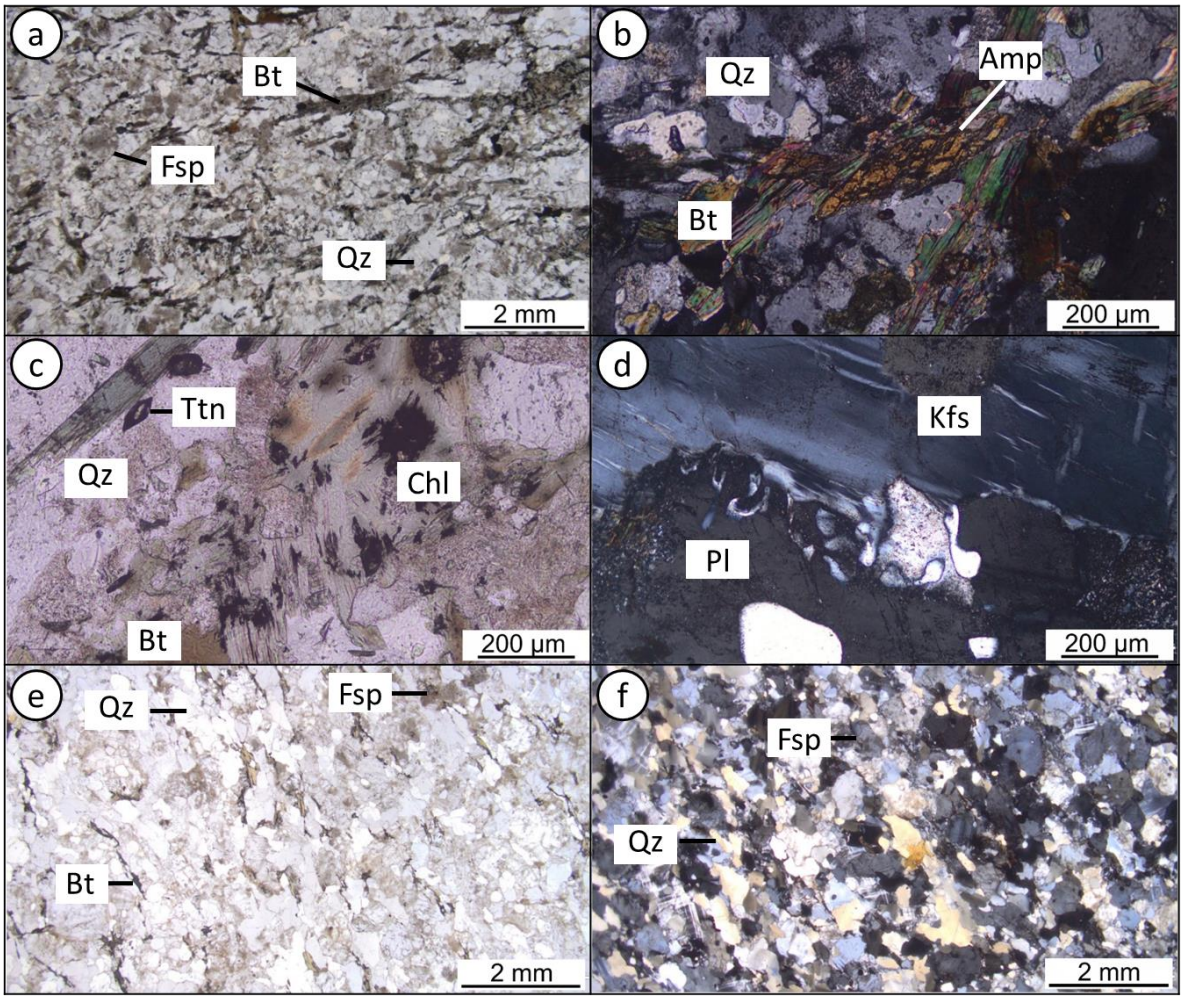


Figure 3.3 . Microphotographs of the leptynitic gneisses from (a, b, and c) Champagnac (C180824-1645) and (d, e and f) Le Petit Mascureau (C220607-1115). Images a, c, and d were taken with plane-polarized light, images b, e and f with cross-polarized light. (a) General texture of the rock showing the lineation marked by the prismatic minerals and phyllosilicates. (b) Aggregate of idioblastic mica and amphibole. (c) Biotite partially and completely altered to chlorite, with idioblastic and xenoblastic grains; some regions of the biotite are totally oxidized. (d) K-feldspar with perthitic exsolution in contact with a plagioclase crystal with myrmekitic texture. (e and f) General texture of the rock showing the faint lineation marked by the prismatic minerals and the phyllosilicates. Mineral abbreviations after Whitney and Evans (2010).

The amphiboles of both gneisses frequently form aggregates and form nematoblastic texture. In the Le Petit Mascureau gneiss, xenoblastic and idioblastic crystals of amphibole are present, whereas the Champagnac sample has idioblastic grains, which can be associated with mica (mostly biotite) (Figure 3.3b). The biotite of both samples forms lepidoblastic texture and is partially to completely altered to

chlorite (Figure 3.3c). In the Le Petit Mascureau gneiss only idioblastic biotite is found, whereas the Champagnac gneiss also has xenoblastic crystals (Figure 3.3c). Some biotite in both samples has inclusions of opaque phases, and in the leptynitic gneiss from Champagnac also of titanite and epidote. Furthermore, in some parts the biotite can be totally oxidized (Figure 3.3c).

In both samples quartz presents undulatory extinction, and in general there is a low level of fractures, with the sample from Champagnac almost not displaying any. No other evidence of deformation, especially of shock deformation, is observed in these samples.

3.1.1.1.2 Paragneiss samples

The paragneiss from the LGU (C180825-0930) sample was collected at Moulin de Laurière. It represents the basement sample from closest to the suspected center of the impact structure, at only 2 km distance (Figure 3.1). The outcropping rock is weathered, covered with vegetation, and comprises meter-sized blocks of relatively homogeneous, foliated, black gneiss with a few millimeter-wide quartz veins and multiple sets of fractures (Figure 3.2b). The sample is composed of plagioclase (35%), biotite (35%), quartz (26%), and minor K-feldspar (2%) and garnet (2%). Accessory minerals are muscovite, apatite, zircon, titanite, opaque phases, and sericite, chlorite, and carbonate as secondary minerals. There are quartzofeldspathic aggregates with a granoblastic texture. These aggregates form irregular bands and lenses with generally larger grain size than elsewhere, and they are poor in mica (Figure 3.4a). They are intercalated with aggregates of biotite that define the lepidoblastic texture, which sometimes forms pressure shadows around the quartzofeldspathic aggregates (Figure 3.4b). Biotite is frequently idioblastic and forms aggregates, sometimes with minor muscovite, that are partially altered to chlorite. In a few cases kink bands were observed in biotite. There is also some xenoblastic biotite that generally follows the same foliation of the rock. Feldspar is generally not affected by alteration. Zircon is found associated mainly with quartz, plagioclase, and biotite of sizes of ~ 50 µm. Some quartz grains display undulatory extinction, but no further shock deformation effects were noted in this sample. Garnet is subhedral, apparently post-kinematic, and commonly very fractured (Figure 3.4c).

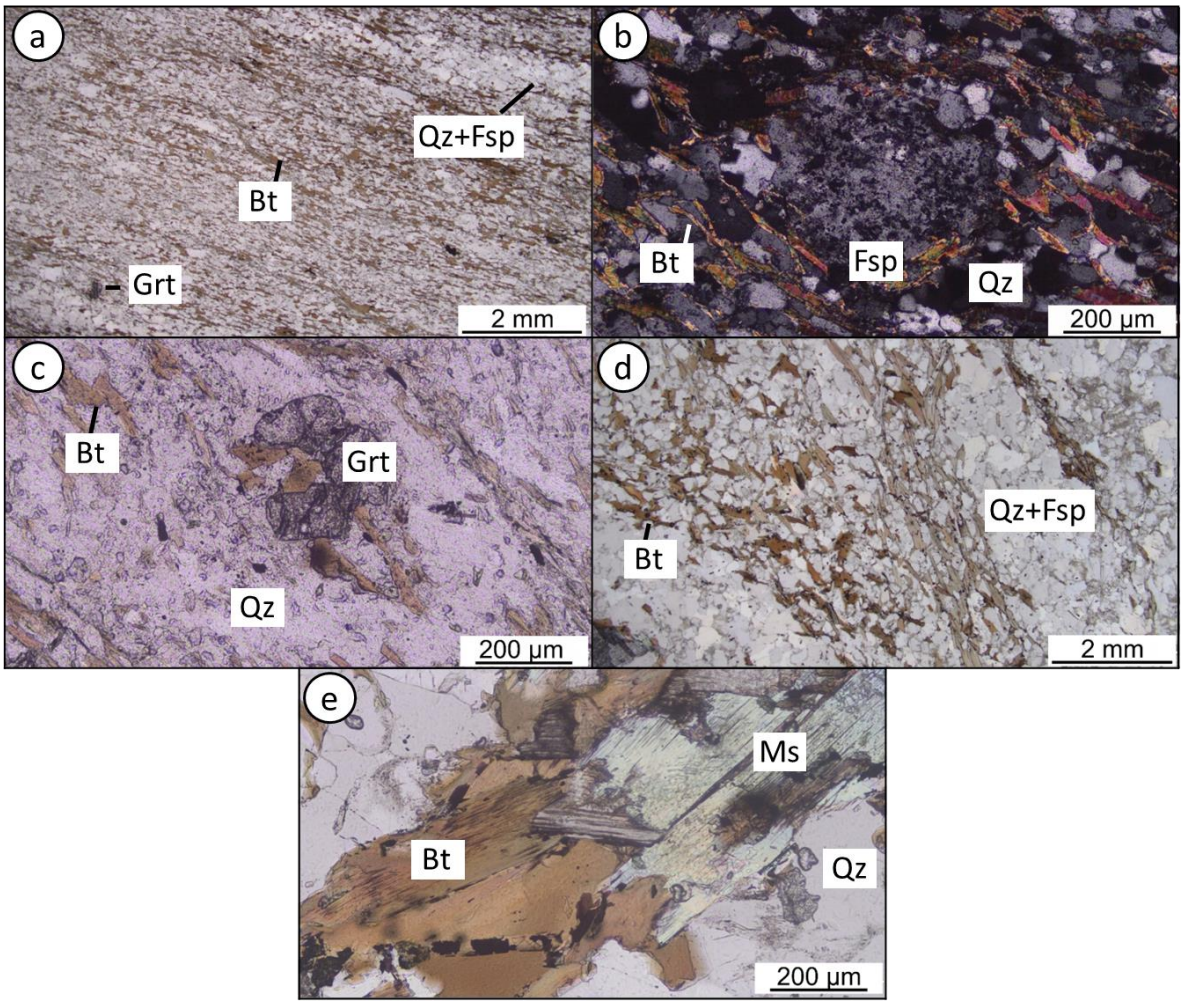


Figure 3.4. Microphotographs of the paragneisses from (a, b, and c) Moulin de Laurière, from the LGU (C180825-0930), and (d and e) from Saillat Sur Vienne, from the UGU (C220506-0954). Except for image (b), all others were taken with plane-polarized light. (a) General granolepidoblastic texture with a pervasive orientation of elongated crystals of phyllosilicate and irregular bands with different proportions of quartz and feldspar. (b) Feldspar porphyroblast with pressure shadows of subhedral biotite. (c) Very fractured, post-kinematic garnet. (d) General granolepidoblastic texture of the C220506-0954 sample. (e) Aggregate of subhedral biotite with some adjacent euhedral biotite and muscovite. Mineral abbreviations after Whitney and Evans (2010).

The paragneiss from the UGU sample (C220506-0954) was collected at Saillat Sur Vienne, 10 m from a road next to the Vienne River, 8.4 km to the NE of the suspected center of the structure (Figure 3.1). In contrast to the paragneiss from the LGU, this sample is transected by numerous faults and strongly folded (Figure 3.2c). In addition, it shows some evidence of partial melting (anatexis) in the form of migmatitic textures. This sample is inequigranular, mostly fine-grained but with a few medium-grained crystals, and has comparatively larger proportions of quartz (46%), K-feldspar (20%), muscovite (5%), and less plagioclase (5%) and biotite (16%) than the paragneiss from Moulin de Laurière. Furthermore, the paragneiss from Saillat

Sur Vienne has a higher content of alteration products such as chlorite (4%) and sericite (2%), besides minor amounts of epidote (2%). In this sample not all the grains of idioblastic biotite follow the same orientation, and the xenoblastic crystals do not adhere to lepidoblastic texture. Muscovite, too, can be found with idioblastic and xenoblastic habits, with only some crystals following the preferred orientation marked by lepidoblastic biotite (Figure 3.4d and e). Biotite and muscovite may have inclusions of opaque phases and can display kink bands. In general, the crystals do not display fractures. Feldspar and quartz have the same texture as in the paragneiss from Moulin de Laurière.

3.1.1.2 Amphibolites

The amphibolite from St Junien (C180822-1625) sample was collected 15.2 km to the NE of the center of the structure, in a low road-cut just below the castle wall, along the main village thoroughfare (Figure 3.1). This amphibolite seems to cut the UGU in a NW-SE direction. At this occurrence, the amphibolite is intersected by a few, several-millimeter-wide veins filled by K-feldspar and epidote. The sample has an overall schistosity marked mainly by the amphiboles and phyllosilicates (Figure 3.5a), and is made of amphibole (30%), plagioclase (30%), K-feldspar (16%), quartz (10%), biotite (7%), and opaque phases (3%). The accessory phases are epidote, apatite, ilmenite, and zircon, and the alteration products are sericite (1%) and chlorite (2%). Amphibole is xenoblastic and frequently has inclusions of quartz, feldspar, biotite, chlorite, epidote, apatite, ilmenite, and zircon. Commonly, biotite is partially altered to chlorite and is found as idioblastic and xenoblastic crystals, of which some of the former have kink bands. Part of the plagioclase has a low degree of alteration to sericite. Feldspars and quartz form granoblastic texture. Rare feldspar crystals have inclusions of amphibole and ilmenite (Figure 3.5b). Locally at the edge of such grains, phyllosilicates form pressure shadows. Zircon is subhedral and can be found as inclusions in the amphibole and feldspars, with sizes of zircon between 40 and 60 μm.

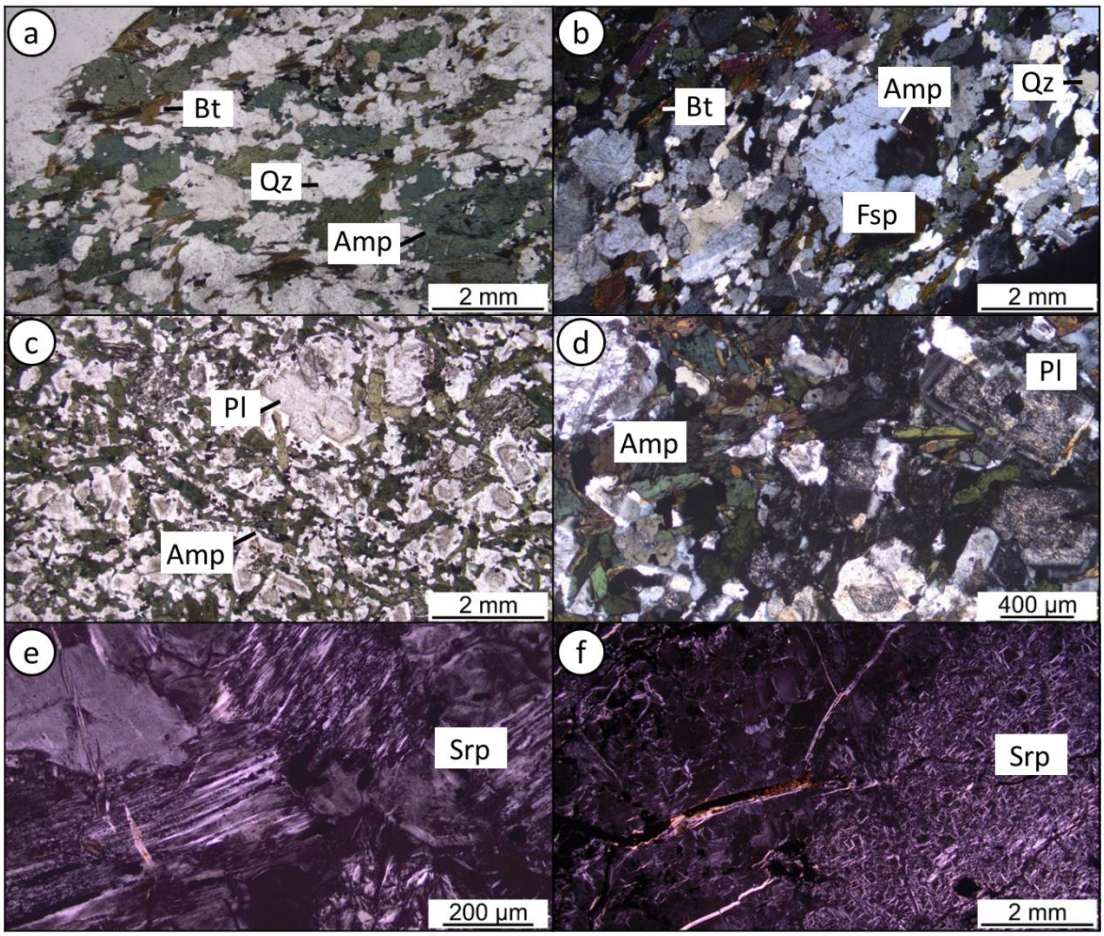


Figure 3.5. Microphotographs of the amphibolites from (a and b) St Junien (C180822-1625) and from (c and d) Exideuil (C180824-1500), and the (e and f) serpentinite from Merly (C220522-1749). Except for images a and c which were taken in plane-polarized light, all others were taken with cross-polarized light. (a) General view of the sample showing the lepidoblastic texture of the biotite and the nematoblastic texture of the amphibole. (b) Porphyroblast of plagioclase with inclusions of amphibole. (c and d) A close-up of the inequigranular texture with some phenocrysts of zoned and altered plagioclase (e) Fibrous habit of the serpentine. (f) Inequigranular serpentine with a mesh-texture and cut by a fracture filled with magnetite and secondary phyllosilicates. Mineral abbreviations after Whitney and Evans (2010).

The Exideuil amphibolite (C180824-1500) sample was collected in the Exideuil quarry, ~13 km to the NW of the center of the impact structure (Figure 3.1). The amphibolite is fine-grained and massive. This rock is in contact with the granodiorites from the Tonalite Line of the Limousin (LTL), which normally intrude the UGU (Chèvremont et al., 1996). This amphibolite is intersected by a few, several-millimeter-wide veins of K-feldspar (Figure 3.2d). The sample has a diablastic texture (Figure 3.5c) and its modal composition is similar to that of the St Junien amphibolite, with amphibole (40%), plagioclase (25%), K-feldspar (10%), quartz (10%), opaque phases (5%), biotite (1%), and accessory apatite, ilmenite, and zircon. As alteration products the sample has chlorite (8%), and minor sericite and epidote (1%). In this

sample, amphibole is mostly xenoblastic and has a poikiloblastic texture with inclusions of chlorite, quartz, apatite, ilmenite, and zircon. Some amphibole is altered to chlorite. Feldspar frequently has poikiloblastic texture as well, and this mineral is partially characterized by an internal zone altered to sericite separated from a clear, unaltered overgrowth (Figure 3.5d). Zircon can be associated with quartz and amphibole, is euhedral, and has sizes from 50 to 100 μm. The opaque phases occur as inclusions in the principal mineral constituents.

The two amphibolite samples show inequigranular texture with crystals of plagioclase of medium grain size embedded in a fine matrix composed of quartz and amphibole. Furthermore, both samples have quartz with undulatory extinction and crystals with irregular microfractures without any preferential orientation; however, the crystals of the sample from St. Junien have a higher density of microfractures than the ones of the Exideuil sample, where microfracturing is generally limited to amphibole.

3.1.1.3 Serpentinite

The serpentinite sample (C220522-1749) was collected at Merly quarry, 13 km to the SE of the center of the impact structure (Figure 3.1). The quarry is located at the base of the LGU (Chèvremont et al., 1996) and consists of massive blocks almost completely composed of finest-grained serpentine with two different textures, fibrous crystals (Figure 3.5e) and crystals with a mesh texture (Figure 3.5f). The sample has some millimeter wide magnetite veins that are randomly oriented (Figure 3.5f).

3.1.1.4 Igneous rocks

The monzodiorite sample (C180825-1115) was collected at La Martinie and was obtained from a dike cutting the LGU, from 3 km to the SW of the center of the impact structure (Figure 3.1).. The outcrop is densely covered by vegetation. The rock is overall homogeneous, composed of a black diorite with an aphanitic matrix and centimeter scale (3-15 cm) shatter cones and a few fractures were observed. The surface of the rock has a more or less homogeneous alteration coating that can have red and slightly purple coloration, probably due to the presence of oxides of Fe or Mn after biotite (Figure 3.2e). The sample has inequigranular porphyritic texture with

medium-grained phenocrysts in a fine- to very fine-grained matrix (Figure 3.6a). Some fractures, sometimes sinuous, are cutting through the sample (Figure 3.6a), and some of them are partially filled by quartz. The sample is composed of plagioclase (47%), K-feldspar (5%), quartz (15%), biotite (20%), opaque phases (3%), as accessory mineral zircon, and as alteration products sericite and chlorite (10%). The phenocrysts are anhedral crystals of quartz and heavily sericitized plagioclase (Figure 3.6a). Some of them are rimmed by chlorite and some have inclusions of quartz, biotite, chlorite, and opaque phases (Figure 3.6a). Inclusions of microgranular quartz are also found in the quartz phenocrysts. One quartz phenocryst has a faint set of PDFs (Figure 3.6a). The matrix is more or less homogeneous and is composed of mostly lath-shaped plagioclase, besides quartz, biotite, chlorite, and opaque phases (Figure 3.6b). These crystals do not follow any orientation. Biotite is found in anhedral and euhedral forms - both types can be found partially and totally altered to chlorite. The euhedral variety may display kink bands (Figure 3.6b). The feldspars in the matrix can be altered to sericite but this alteration is less strong than that observed in the phenocrysts. The opaque phases can be found as inclusions in all the phases but are mainly associated with mica.

The pegmatite sample (C220514-1340) was collected at the Champagnac quarry (Figure 3.1) and corresponds to one of the lenses intruding the gneisses and the diorites from the UGU below the crater floor. The rock is leucocratic, highly fractured, is homogeneous with a pink coloration, and it has some degree of hydrothermal alteration along fracture surfaces (Figure 3.2f). The sample has inequigranular xenomorphic to hypidiomorphic texture of normally very fine- to medium-grained minerals; locally coarse grains with sizes up to 1.5 cm are present. The larger grains are interspersed with aggregates of smaller crystals (Figure 3.6c and d). This sample is composed of quartz (33%), K-feldspar (32%), plagioclase (20%), microcline (3%), carbonate (2%), muscovite (1%), and apatite and opaque phases as accessory minerals. Sericite and chlorite (9%) are found as alteration products of plagioclase and muscovite, respectively. All minerals (except the apatite) may be present as large crystals and in the fine-grained aggregates in between. Furthermore, some of the crystals are fractured, and sometimes the fractures are filled with late-stage

quartz or carbonates (Figure 3.6c and d). Muscovite is partially subhedral in the interspersed aggregates and euhedral as secondary crystals in sericitized K-feldspar. Kink-bands are found in both mica varieties.

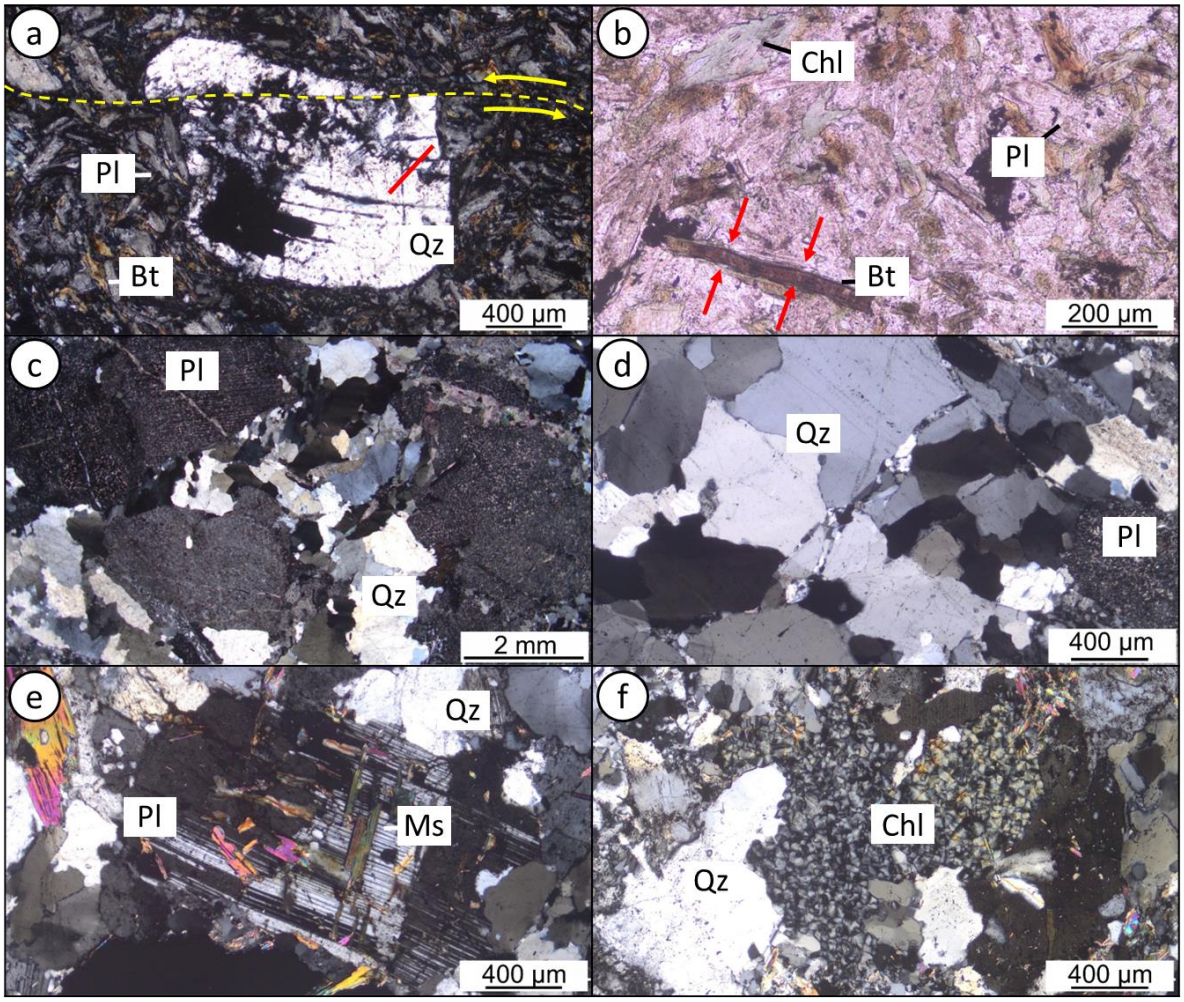


Figure 3.6. Microphotographs of the general texture of the (a and b) La Martinie monzodiorite (C180825-1115), (c and d) Champagnac pegmatite (C220514-1340), and (e and f) Chéronnac granite (C220607-1502). Except for image (b) taken in plane polarized light, all others were taken with cross-polarized light. (a) Quartz phenocryst with inclusions of opaques, a faint development of one set of PDFs (red line), and a micro-fault (yellow arrows). (b) Matrix with feldspars, quartz, and micas. Anhedral and euhedral crystals of biotite partially altered to chlorite; the euhedral crystals can show kink bands (red arrows). (c and d) The Champagnac pegmatite is inequigranular, the plagioclase is partially altered to sericite and separated by aggregates of fine-grained crystals of quartz. The clasts are fractured and some of them have veins filled with secondary carbonate and quartz. (e) Plagioclase crystals with poikilitic texture and inclusions of muscovite. (f) Aggregate of fine-grained chlorite between anhedral quartz crystals. Mineral abbreviations after Whitney and Evans (2010).

The *Chéronnac granite (C220607-1502)* is from outside the impact structure, at 12 km to the SW of the center of the structure (Figure 3.1). The rock occurs as blocks in areas without grass. The granite is part of the Chéronnac body, which intrudes the LGU, and is represented by leucogranites with amphibolite enclaves and pegmatite

intrusions (Chèvremont et al., 1996). The sample is quite strongly weathered and has an inequigranular texture with very fine- to medium-grained crystals (Figure 3.6e). The sample is composed of quartz (42%), K-feldspar (21%), microcline (3%), plagioclase (7%), and muscovite (18%), as well as the accessory minerals apatite, zircon, epidote, and chlorite, and sericite as alteration product (7%). Plagioclase is partially altered to sericite and frequently shows poikilitic texture with inclusions of muscovite and opaque phases (Figure 3.6e). Quartz commonly has undulatory extinction. It also has inclusions of feldspar and muscovite. Muscovite is euhedral or anhedral, and some crystals have kink bands. Chlorite is present as frequently rounded aggregates of radial crystals (Figure 3.6f). In general, just a few crystals of quartz and feldspar display irregular fractures with random orientations.

The Champagnac granite sample (C180824-1630) is the nearest granite to the center of the impact structure from 7.5 km to the NE of the center of the structure (Figure 3.1). This granite corresponds to an intrusion into orthogneiss of the UGU previously described (C180824-1645), is heavily altered, and is transected by multiple fractures. The sample is composed of quartz (37%), plagioclase (13%), orthoclase (6%), microcline (15%), and biotite, with epidote and zircon as accessory minerals.

The sample from the *granodiorite from Exideuil (C220511-1352)* was collected 12.7 to the NW of the center of the structure (Figure 3.1) in an outcrop along the road, from a block cut by multiple fractures, and quite strongly altered and is composed of quartz (29%), plagioclase (20%), orthoclase (10%), amphibole (8%), and microcline (2%), opaque phases (2%) and muscovite (1%), and trace amounts of epidote, titanite, and zircon.

The Champagnac granite and Exideuil granodiorite samples are heavily altered and have large contents of sericite (20-23%) and chlorite (3 - 5%) as alteration products of feldspars and biotite/muscovite, respectively (Figure 3.7 a, b, and c).

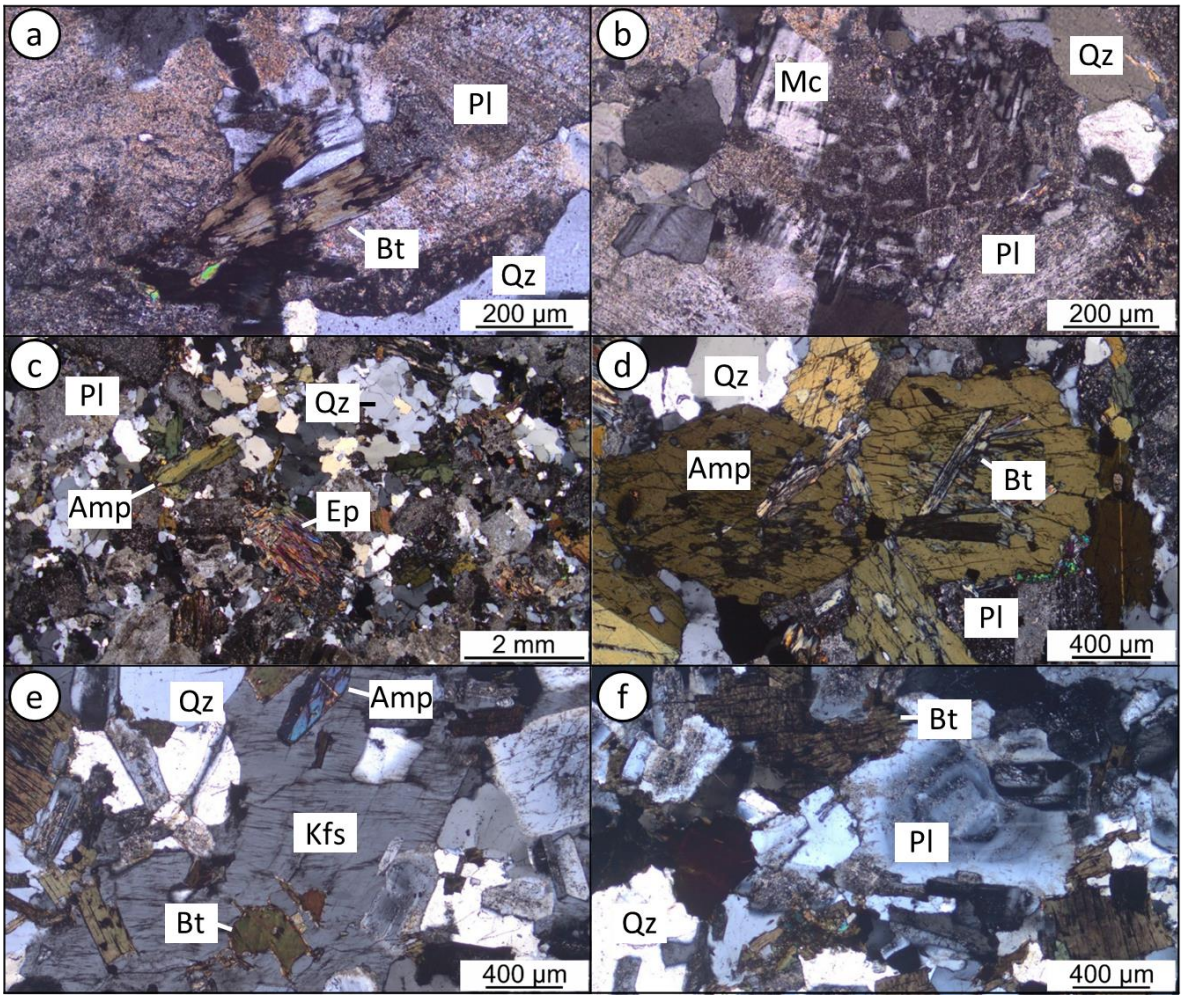


Figure 3.7. Cross-polarized light microphotographs of the granite from (a and b) Champagnac (C180824-1630) and the granodiorites (c and d) from Exideuil (C220511-1352) and (e and f) La Chassagne (C220608-2001). (a) Strong sericite alteration of the plagioclase and subhedral biotite partially altered to chlorite along cleavage. (b) Microcline with a graphic texture with intergrowth of quartz. (c) Strong sericite alteration of plagioclase. (d) A close-up of amphibole with poikilitic texture characterized by inclusions of partially chloritized biotites and opaque phases. (e) Perthitic alkali feldspar with inclusions of biotite and amphibole. (f) Subhedral grains of biotite and plagioclase with strong oscillatory zoning. Mineral abbreviations after Whitney and Evans (2010).

The sample from *the granodiorite of La Chassagne (C220608-2001)* was collected from 8.5 to the SW of the center of the structure (Figure 3.1) in an outcrop at the crater floor; the sample exhibits a pink/brown homogeneous color, without any deformation but with an irregular surface due to partial weathering. This unit is made of medium-grained granodiorite composed of plagioclase (35%), quartz (33%), orthoclase (19%), biotite (12%), amphibole (1%), and trace amounts of zircon and apatite, and sericite and chlorite as alteration products. This sample has a higher density of fractures than the Exideuil granodiorite.

The feldspar in both granodiorites and the Champagnac granite frequently has poikilitic textures with inclusions of quartz, mica, and opaque phases. In the Exideuil and La Chassagne granodiorites there are also inclusions of amphibole (Figure 3.7e). Furthermore, in the Champagnac granite part of the feldspars shows graphic texture (Figure 3.7b), and in the La Chassagne sample some feldspar crystals are perthitic (Figure 3.7e) or have oscillatory zoning (Figure 3.7f). Different types of biotite are found within these samples. In the Champagnac and La Chassagne samples, some biotite has inclusions of opaque phases and occurs as anhedral and euhedral crystals. In some euhedral biotite of the sample from La Chassagne kink bands are found. The Exideuil sample has anhedral biotite, and some aggregates of chlorite and epidote are observed (Figure 3.7c). Finally, some amphibole in the Exideuil sample has a poikilitic texture with inclusions of mica, quartz, and opaques (Figure 3.7d).

3.1.1.5 Deformation/Shock metamorphism

Common deformation features found in the basement rocks of this study include at the microscopic scale, undulatory extinction of especially quartz, kink bands in biotite and muscovite, and fracturing. Fractures are mostly of irregular shape, in general nonplanar, and have subparallel to random orientations. The most common of these features is the undulatory extinction of quartz. The paragneiss from Moulin de Laurière (C180825-0930) is the sample that was collected closest to the apparent center of the impact structure (at a distance of ~ 2 km). This sample only displays the features just described.

The second closest sample to the apparent crater center (~ 3.1 km) is the monzodiorite (C180825-1115). This is the only sample where unequivocal evidence of shock metamorphism has been found, in the form of macroscopic shatter cones and a rare, single set of decorated PDFs in quartz at the micro-scale.

The samples from the Champagnac and Le Petit Mascureau quarries, located ~ 6.3 and ~ 7.5 km from the apparent crater center, respectively, show very little deformation, with only minor development of microfractures, and some quartz shows undulous extinction. Except for the Champagnac pegmatite where few muscovite

has kink bands. The samples from further away (~ 8.4 to ~ 15.2 km from the apparent crater center) show a higher proportion of microfractures and/or phyllosilicate with kink bands. The Merly serpentinite is essentially undeformed.

Table 3.2 Deformation features observed at the thin section scale for the basement rocks of this study. Only the single PDF noted in sample C180825-1115 can be related exclusively as shock deformation. PDFs -- Planar deformation features.

Distance to the apparent center of the structure	Location	Rock	Samle ID	Kink bands		Undulatory exctinction	Micro-fractures	PDFs
				bt	ms			
1.9 km	Moulin de laurière	Paragneiss	C180825-0930	X		X	X	
3.1 km	La Martinie	Monzodiorite	C180825-1115	X				X
6.3 km	Le petit Masc.	Leptynite	C220607-1115			X	some	
7.5 km	Champagnac	Pegmatite	C220514-1340		X			
7.5 km	Champagnac	Granite	C180824-1630			X		
7.5 km	Champagnac	Leptynite	C180824-1645			X		
8.4 km	Saillat sur vienne	Paragneiss	C220506-0954	X	X	X		
8.4 km	La Chassagne	Granodiorite	C220608-2001	X		X		
11.9 km	Les neples	Granite	C220607-1502		X	X	some	
12.7 km	Exideuil	Granodiorite	C220511-1352			X	some	
12.7 km	Exideuil	Amphibolite	C180824-1500			X	X	
12.8 km	Merly	Serpentinite	C220522-1749					
15.2 km	St Junien	Amphibolite	C180822-1625	X		X	X	

3.1.2 Impactites

In total, 21 samples of impactites, 7 from the surface and 14 from drill-cores, were collected (Table 3.1). Detailed descriptions of the impactite samples are provided in the manuscript 3 (Chapter 6).

3.1.2.1 Surface samples

Clast-poor impact melt rocks: The Recoudert sample (C180824-1900) was obtained 3 km to the south of the center of the impact structure. This sample is very similar to samples of the impact melt rock (IMR) from Babaudus (C220705-1643), from a location 1.7 km from the crater center (Figure 3.1). Both samples are clast-poor and have a homogeneous, yellow groundmass. This type of yellow IMR occurs as isolated outcrops in the central part of the impact structure (Figure 3.8a). The sample collected at Videix (C220510-1414), 7 km to the SW of the center of the impact structure (Figure 3.1), corresponds mainly to the matrix of a clast-poor, red/purple

IMR, which is characterized also by millimeter sized disseminated, white mineral inclusions. The sample has a few paragneiss clasts of a purple coloration.

Clast-rich impact melt rock: One sample of reddish, clast-rich IMR was collected at Montoume 7.5 km to the SW of the apparent center of the structure (Figure 3.1). This type of impact melt rock is mainly found at the tops of some hills in the southern part of the structure, including the highest point within the impact structure at Montoume hill, where the impact melt rock forms a massive, 25 m thick deposit with vertical/subvertical jointing (Figure 3.8b). The rock is heterogeneous, on centimeter to decimeter scales, with respect to populations of lithic, mineral, and impact glass clasts. None of these clast types display preferred orientation. The Montoume IMR (C180823-0955) has a matrix with purplish-reddish tones and displays a pronounced fluidal texture. The sample consists of ca. 75 % matrix and 25 % lithic and mineral clasts. The lithic clasts are mainly derived from gneiss with different textures (e.g., oriented grains and/or bands of different compositions) and to a lesser proportion of granitic provenance.

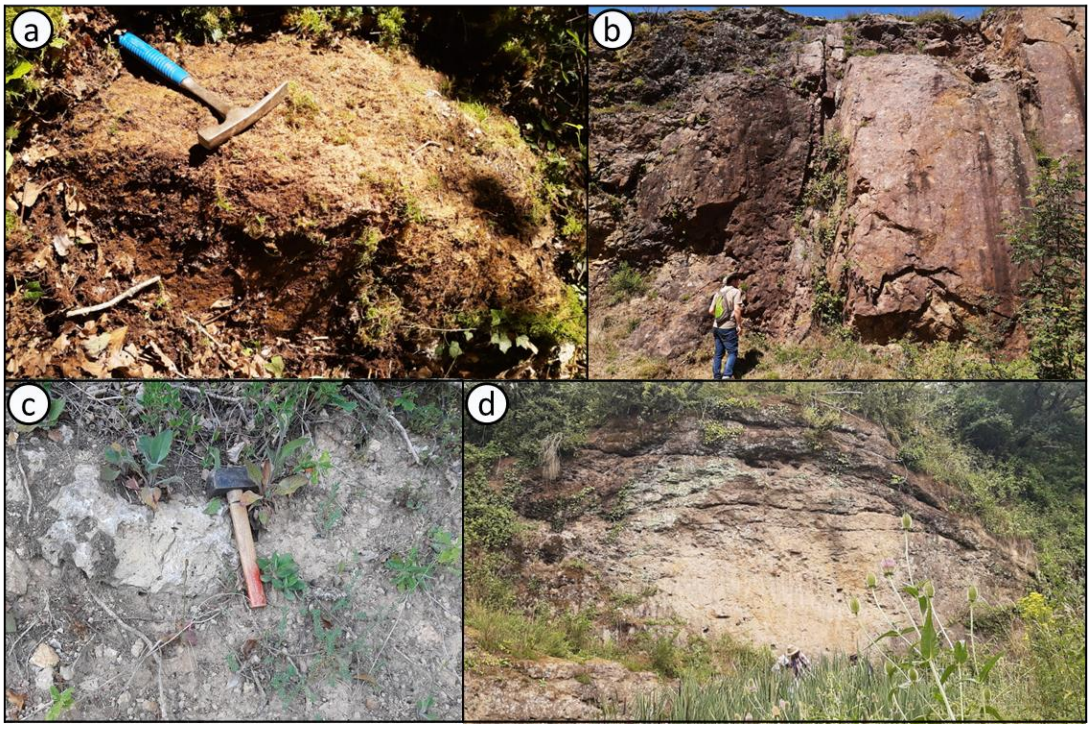


Figure 3.8 Field photographs of the outcrops of some of the studied impactites. (a) Recoudert quarry with strongly weathered, clast-poor, yellow impact melt rock (C180824-1900). (b) Montoume quarry, a large deposit of clast-rich, red impact melt (C180823-0955), cut by subvertical joints. (c) Quarry of suevite at Videix (C220510-1745). (d) Quarry of the Chassenon suevite (C220805-1315) showing the rock with apparently cross-bedded stratification. Person for scale 1.7 m tall.

Suevites: Two suevite samples were collected, one at Videix (C220510-1745) and the other at Chassenon (C220805-1315), 6.4 km to the SW and 3.7 km to the NW of the center of the impact structure, respectively (Figure 3.1). The suevite of Videix was collected in a road-cut partially covered by vegetation (Figure 3.8c). At the locality of Chassenon and intercalated with suevite occurs the so-called impactoclastite unit, a fine-grained deposit with evidence of sedimentary sorting, which is presumed to mark the upper surface of the impact crater fill deposits (Lambert, 2010; Ormö et al., 2023). The suevite sample of this study was collected at the Grosse Pièce quarry, where the suevite displays apparent bedding (Figure 3.8d). The Videix sample is characterized by a yellow matrix, whereas the Chassenon suevite has a gray-green matrix. In both samples, this aphanitic matrix has vesicles and a high proportion of highly heterogeneous mineral and lithic clasts, which can be granitic and gneissic. Both samples have similar proportions of matrix (~81 vol%), melt clasts (3 vol%), and mineral and lithic clast (15 vol%). The melt clasts in both samples have very irregular forms.

The impactites of Rochechouart were widely used in the past for construction, in the case of the suevite from Chassenon since the Gallo-Roman period (Lambert, 2010).

3.1.2.2 Samples of impact breccia from CIRIR drill cores

Overall, the drill cores obtained under the auspices of the CIRIR within the Rochechouart impact structure are heterogeneous, with numerous intercalations of different types of impactites and basement rocks (Lambert et al., 2019). It must be remembered that the impact structure is deeply eroded, so that these materials represent the lowermost crater fill, crater floor, and sub-crater floor basement.

The drill-core samples selected for this study (Table 3.1 and Figure 3.9) represent a wide variety of lithic breccias, suevites, and impact melt rocks. At Chassenon, in the drill-core SC1 obtained from a vertical impactoclastite dike, a sample of clast-poor, yellow IMR was collected (1-3). The drill-core SC2, from the same location, contains a sequence of 39.8 m of melt-rich suevite, followed by 48.2 m of melt-poor suevite, 26 m of brecciated gneiss of the crater floor, and 7.4 m of gneiss basement. At Valette, four samples were collected from drill-core SC7 (7-1, 7-14, 7 10, and 7-15).

This drill-core exhibits a sequence of 16 m of IMR with vesicular clasts, and 48.6 m of a clast-rich impact melt or suevite. From Puy Chiraud, to the southwest, three samples were collected from drill-core SC11 (11-5, 11-17, and 11-25). This core comprises 16 m of red, clast-rich IMR, followed by 16 m of a granite clast-rich IMR, 27 m of a lithology that could correspond to the same IMR but with multi-meter sized blocks or a highly deformed granite with impact breccia injections, and 7.6 m of a polymict lithic breccia. From close to Rochechouart castle, one sample was collected from the SC15 drill-core (15-1). This core contains 1 m of massive, yellow IMR. From the same location, the SC14 drill-core shows a sequence of 1.5 m of polymict breccia, followed by 63.4 m of brecciated gneiss. The SC16 drill-core, obtained at Montoume, shows a sequence of 26 m of a clast-rich, red IMR, from which two samples were selected (16-6 and 16-7), followed by 29 m, and then 10.6 m of two lithologies that could correspond to either a severely deformed granite and gneiss, respectively, or granite and gneiss dominated, clast-rich IMRs. The SC17 drill-core from Recoudert, shows a sequence of 23 m of red IMR with an intercalation of yellow IMR, from which three samples were collected (17-2, 17-7, 17-13), followed by 21.1 m of fractured gneiss, a 2.5 m thick suevite dike, and 18 m of a felsic gneiss.

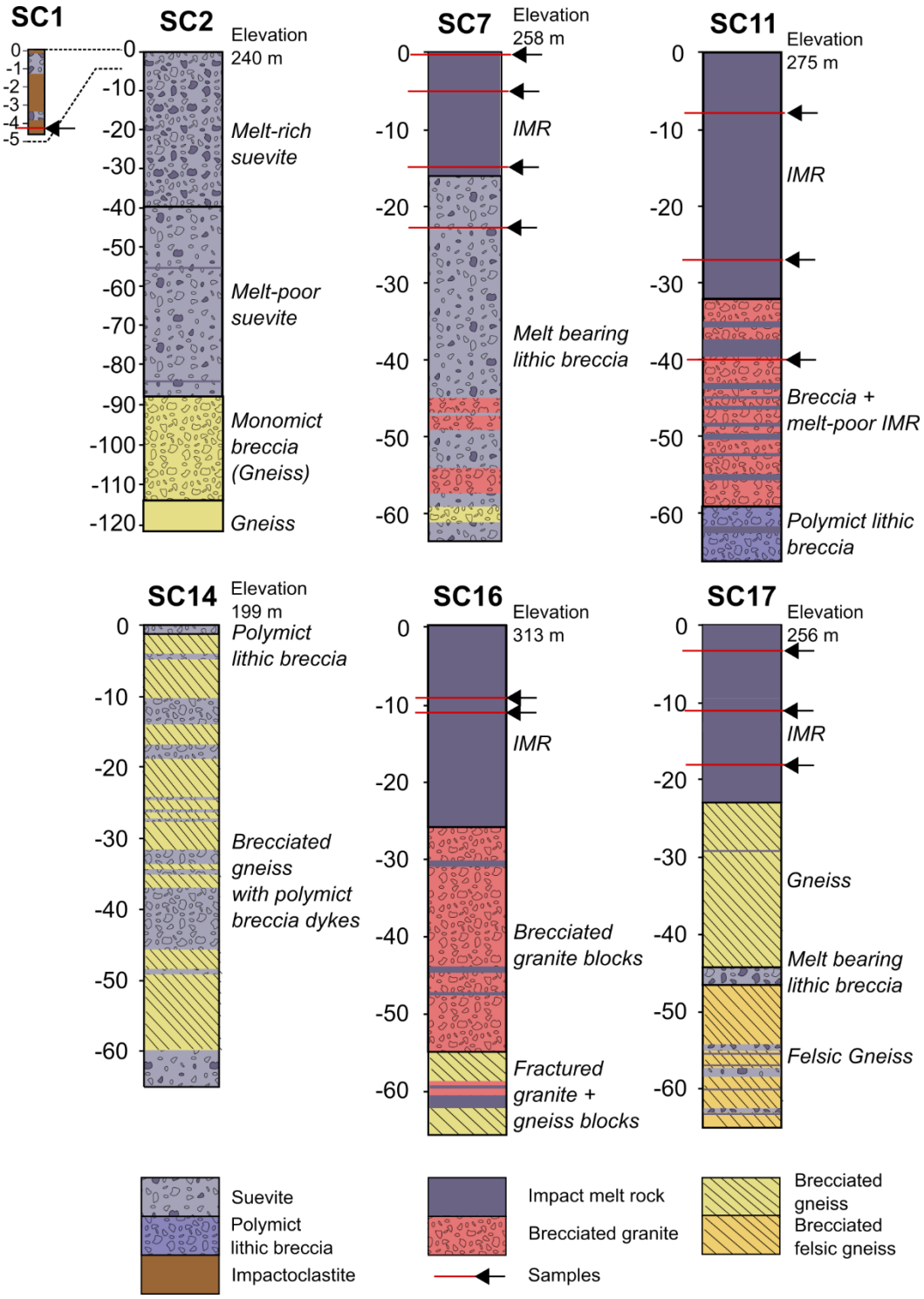


Figure 3.9 Geological logs of the drill-cores (from Lambert, 2019), showing the locations of the samples analyzed in this study.

3.2 Analytical methods

3.2.1 Petrography

Polished thin sections from the first set of samples were prepared at the Naturkunde Museum (MfN) Berlin, Germany. Thin sections from the second set of samples were made in part at MfN and in part at the Naturhistorisches Museum (NHM) of Vienna, Austria.

The thin sections were studied in the Mineralogy Laboratory at the Universidade de Brasília (UnB) with an Olympus BX60F5 microscope, as well as with a Zeiss Axiophot microscope at the Laboratório de Estudos Geodinâmicos, Geocronológicos e Ambientais (LEGGA) at UnB.

3.2.2 Geochemistry

All samples were crushed at LEGGA at UnB to fine powder fractions. The analyses of major and trace elements of six samples from the first set were made through ICP-MS methodology at the Laboratório SGS Geosol in Vespasiano, Minas Gerais, Brazil. The remaining samples from the first set (C180824-1630 and C180825-1115) and all the samples from the second set and from the drill-cores were analyzed at the Vrije Universiteit Brussels. A Herzog puck mill was used to pulverize the samples. Although this milling system can influence the concentrations of certain trace elements (e.g., Cr, Ni, Co, W, Fe, Mn), the results generally do not show anomalous values for these elements.

At SGS Geosol (www.sgsgeosol.com.br), the samples of the first group were analyzed with their method ICP95A. Accuracies for all major elements are of the order of 10 %. For trace element analysis the certified reference materials GRE-03 and GRE-05 were used, and accuracy at 95 % confidence level is quoted at the following levels (in % of the analytical value): Ce ± 2, Dy ± 4, Eu ± 2, Ga ± 4, Gd ± 3.6, Ho ± 0.3, La ± 36, Lu ± 0.1, Nb ± 44, Nd ± 33, Pr ± 9, Sm ± 5, Ta ± 9, Hf ± 7, Tb ± 0.5, Tm ± 0.1, Y ± 6, Yb ± 0.25, Zr ± 47, Sc ± 0.5, Ti ± 0.1 , Th ± 2.4, U ± 1, W ± 0.5. Further details about this method can be found in Reimold et al. (2021).

At the Laboratoire G-Time of the Université Libre de Bruxelles (ULB), major and trace element concentrations were determined by inductively coupled plasma-optical emission spectrometry (ICP-OES). Around 50 mg of powdered samples were weighed and mixed with ~1 g of a 4:1 ultrapure lithium metaborate (Li_2O)-tetraborate ($Li_2B_4O_7$) mixture by hand shaking. The mixtures were fused in graphite crucibles in a muffle furnace at 1000 °C for 10 minutes. After cooling down, the glass beads were dissolved in 50 ml of $2NHNO_3$ using stirring magnets for 5 hours. Following aliquoting, dilution, and addition of yttrium (Y) as internal standard, all major element concentrations were determined by quantification versus external calibration curves constructed using multi-element standard solutions of Si, Mg, Fe, Al, Ca, Na, Ti, K, P, Mn, and Cr on the Thermo Scientific iCAP 7000 Series ICP-OES instrument at ULB. Trace element concentrations were determined on the same sample solutions using an Agilent Technologies 7700 Series ICP-MS. Internal standards (yttrium and indium) were added and corrections for oxide production were applied using standard element solutions of Pr and Nd, Ba, and Ce. Besides samples and replicates, international reference basalt BHVO-2 and andesite AGV-2 of the USGS with certified chemical compositions were used to evaluate the accuracy and precision of the applied procedures. Loss on ignition (LOI) was determined by weighing 0.5 g of sample into a ceramic crucible that was heated to 1000 ˚C in a muffle furnace for 1 hour. After cooling down to room temperature, the samples were weighed again to determine the weight percent (wt%) loss of volatiles.

3.2.3 Whole-rock Sr-Nd isotopic analysis

All basement samples and eight impactite samples from the drill-cores (1-3, 7-1, 7-4, 7-10, 11-17, 15-1, 16-7, 17-7) were selected to determine whole-rock Sr and Sm-Nd isotopic data. The selected samples are representative of the heterogeneity of the sample suite. The Sm-Nd analyses were done at LEGGA at UnB, whereas the $^{87}Sr/^{86}Sr$ analyses were done at the University of Vienna.

The separation procedures and analytical methods used at UnB were described by Gioia and Pimentel (2000). Approximately 50 mg of rock powder were mixed with a $^{149}Sm/^{150}Nd$ spike solution and dissolved in Savillex capsules. All samples were

subjected to cation exchange techniques with Teflon® columns with LN-Spec resin (HDEHP-Di-(2-ethylhexyl) phosphoric acid supported on polytetrafluoroethylene). Analyses were conducted using a Thermo Scientific TRITON™ Plus Thermal Ionization Mass Spectrometer (TIMS) in static multi-collector mode. Mass fractionation was corrected by normalizing the $^{143}Nd/^{144}Nd$ ratio to $^{146}Nd/^{144}Nd = 0.7219$. The Sm-Nd decay constant applied was 6.54×10^{-12} yr^{-1} (Lugmair and Marti, 1978). Over the duration of this study, the average for values of the $^{143}Nd/^{144}Nd$ ratio for the USGS BHVO-2 standard was 0.512981 ± 0.00006 (2σ), consistent with published values (e.g., 0.512979 ± 0.000028; Jochum et al., 2016). Laboratory blanks were approximately 0.25 ng for Nd and 0.04 ng for Sm. The precision of Sm/Nd and $^{143}Nd/^{144}Nd$ measurements was better than ± 0.1 % (2σ) and ± 0.001 % (2σ), respectively, based on repeated analyses of the BHVO-2 and BCR-1 rock standards.

The $^{87}Sr/^{86}Sr$ analyses were conducted at the Department of Lithospheric Research, University of Vienna, Austria. Rock powders (50–100 mg) were digested in tightly sealed Savillex beakers with an ultra-pure 4:1 HF:HNO_3 mixture at 100–120 °C for 2–4 weeks. After acid evaporation, the residues were treated repeatedly with 6M HCl to obtain clear solutions. Strontium was isolated using AG 50W-X8 resin (200–400 mesh) with 2.5 M and 4.0 M HCl as eluants. Procedural blanks for Sr were < 1 ng, negligible for this study. Isolated fractions were analyzed using a Thermo-Finnigan Triton$^+$ TIMS in static mode with mass fractionation corrected to $^{88}Sr/^{86}Sr = 8.3752$. Measurements were performed in one batch, for which a $^{87}Sr/^{86}Sr$ ratio of 0.710260 ± 0.000004 for the NBS 987 standard was also obtained. Uncertainties are quoted as 2σ. The $^{87}Rb/^{86}Sr$ ratios were calculated from Rb/Sr concentrations obtained by XRF analysis. Assigned uncertainties were 1 % for $^{87}Rb/^{86}Sr$ and 1 % and 0.4 % for Rb and Sr determinations, respectively (Mader and Koeberl, 2009; Nagl and Mader, 2019; Son and Koeberl, 2005).

3.2.4 Zircon U-Pb isotope analysis

Zircon separation for isotope analysis was conducted at LEGGA by crushing, grinding, and screening of the samples to different mesh sizes to eventually obtain

the < 125 µm and 125-300 µm grain size fractions. Subsequently, the denser material was concentrated with a pan, and after drying, by magnetic separation with a Frantz magnetic barrier laboratory separator (model LB-1). Then zircon crystals were hand-picked from the final concentrate under a binocular microscope and mounted on one-inch acrylic discs.

Table 3.3 Summary of the details of the analytic conditions and data processing of the LA-ICP-MS analyses developed in this study.

Laboratory	Laboratório de Geoquímica Isotópica - UFOP	Laboratório de Geocronologia e Geoquímica Isotópica, Instituto de Geociências, Universidade de Brasília - UnB		Laboratório de Geologia Isotópica - UFPA
Samples analyzed	First group	First group	Second group	Third group
Laser ablation system				
Make, Model and type	Photon-Machines	Teledyne Analyte Excite	Iridia Excimer	LSX-213 G2 CETAC
Laser wavelength (nm)	193 nm	193 nm	193 nm	213 nm
Fluence (J cm-2)	1-2 J cm-2	4.0 J cm-2	2 J cm-2	4-5 J cm-2
Repetition rate (Hz)	6 Hz	8 Hz	20 Hz	10 Hz
Spot size	30 µm	20 µm	25 µm	25 µm
ICP-MS Instrument				
Make, Model and type	Neptune Pluss Thermo Finnigan, MC-ICP-MS	Thermo-Fischer, NeptuneXT, MC-ICP-MS	Thermo Finnigan Element XR, SC-ICP-MS, triple detection mode (SEM+Faraday)	LA-Q-ICP-MS
Gas blank	20 s	10 s		20 s
Data processing package used / Correction for LIEF	Saturn (Silva, 2020)	Iolite v.4.0 (Paton et al., 2011) & VizualAge (Petrus and Kamber, 2012) with blank subtraction and LIEF correction using exponential plus linear modelling. UComPbine DRS (Chew et al. 2014).		Qtegra and a Microsoft Excel macro (Miranda et al., 2023)
Quality control / Validation	GJ-1, Blue Berry, and Plešovice	GJ-1 zircon, 91500, and Plešovice		GJ-1 and Blue Berry

The samples were analyzed for zircon imaging and U-Pb analysis in three groups. The first group comprised six samples from the first set (C180824-1900, C180823-0955, 180822-1625, C180824-1500, C180825-0930, and C180825-1115), the second group had three impactite samples from the second set (C220705-1643, C220510-1745, and C220805-1315), and the third group corresponds to the remaining samples from the first set (C180824-1630 and C180824-1645) and six basement samples from the second set (C220506-0954, C220607-1115, C220511-1352, C220608-2001, C220607-1502, and C220514-1340). A summary of the

analytical conditions used in the LA-ICP-MS analysis of each group is provided in Table 3.3.

3.2.4.1 Zircon imaging

First group: Cathodoluminescence (CL) images of the zircon mounts were obtained with a scanning electron microscope (SEM) type JEOL 6510 at the Federal University of Ouro Preto (UFOP), Brazil. Backscattered electron (BSE) zircon images of the thin sections and zircon mounts, as well as secondary electron (SE) and CL images of the zircon mounts were obtained with a QUANTA 450—FEIJEOL SEM using 15 kV and a working distance of 10.5 mm at LEGGA. Extra BSE images of polished thin sections were obtained with a JEOL JXA-8500F field emission electron microprobe at the Museum für Naturkunde, Berlin.

Second group: CL, BSE, and SE images of the zircon crystals from each sample were obtained on a FEI Quanta FEG 650 SEM equipped with a Gatan ChromaCL2 system at the NordSIMS laboratory in the Swedish Museum of Natural History, Stockholm. Subsequently, on the same instrument and with an Oxford Instruments Symmetry S3 detector, electron backscatter diffraction (EBSD) images were obtained on eight selected zircon crystals. The grains were indexed for zircon and reidite comparing crystallographic data from Hazen and Finger (1979) and Howard et al. (1988), and with the same analytical conditions and data collection and processing described in Kenny et al. (2022). However, for this work the maps were made using step sizes between 80 and 175 nm. Grain reference orientation deviation (GROD) maps indicate the orientation deviation relative to the average orientation for the grain (e.g., Wright et al., 2016).

Third group: BSE and CL images of the zircon mounts were obtained at the Microanalysis Laboratory of the Geosciences Institute of the Federal University of Pará (UFPA), Brazil, with a MEV Zeiss model LEO-1430 and a MEV Zeiss model SIGMA-VP coupled with a cathodoluminescence Gatan Chroma CL2, respectively. The operation conditions were an acceleration voltage of 20 kV, electron beam current between 80-90 µA, and working distance between 15 and 17 mm.

3.2.4.2 U-Pb isotope analysis

First group: Selected zircon crystals were analyzed by laser ablation–multicollector – inductively coupled plasma–mass spectrometry (LA-MC-ICP-MS) at the Laboratory of Isotope Geochemistry of the UFOP and at LEGGA. The analyses were acquired at UFOP using a Neptune Plus Thermo Finnigan instrument coupled with a Photon-Machines 193 nm laser system. Data were acquired using peak jumping mode with background measurement for 20 s, zircon ablation during 20 s and 30 µm spot size. At LEGGA, zircon crystals were analyzed with a Thermo Finningan Neptune XT high-resolution multi-collector, sector-field ICP-MS coupled to a 193 nm Teledyne Analyte Excite laser ablation system. The laser ablation system is equipped with a HelEx II dual-volume chamber. Each analysis consisted of 10 s of background measurement followed by 20 s of sample data acquisition. Each mass was measured simultaneously using a combination of Faraday, SEM and CDD detectors. Laser conditions included a spot diameter of 20 µm, 8 Hz, and 4.0 J cm-2. The reduction of the U-Pb raw data from UFOP was performed with Saturn Software (Silva, 2020) and for data from LEGGA with Iolite 4.0 (Paton et al., 2011). For LEGGA, individual signal inspection was done with VizualAge (Petrus and Kamber, 2012).

Second group: Initially, U-Pb analyses on zircon were obtained by secondary ion mass spectrometry (SIMS) using a CAMECA ims1280 ion microprobe at the NordSIMS laboratory. Complementary single-collector sector field ICP-MS analyses of these zircons were done at LEGGA. The SIMS analyses were done on selected zircon crystals in two analytical sessions, with spot sizes of 8 µm and 15 µm. For the U-Pb analyses, O_2^- ions were generated using an Oregon Physics Hyperion H201 RF plasma high-brightness oxygen source. The measurements were performed at a mass resolution of ~ 8000 to avoid any possible interferences of extraneous elements in the granular zircon grains. During the analyses a peak switching routine was used with a single ion-counting electron multiplier as detection device and an energy window of 45 eV with energy adjustments made using the $^{90}Zr_2^{16}O$ peak. Precise mass calibration was conducted with an automatic routine in the CAMECA CIPS software.

The LA-ICP-MS analyses were done with a Thermo Finnigan Element XR high-resolution single-collector sector field ICP-MS coupled to a 193 nm Iridia Excimer (ArF) laser ablation system at LEGGA. The laser ablation system is equipped with a Cobalt dual-volume chamber. Each analysis consisted of 10 s of background measurement followed by 20 s of sample data acquisition. Each mass was measured using the triple detection mode (SEM+Faraday) by sweeping the electrostatic sector on each mass. Each sweep took 82 ms, resulting in over 800 scans for each ablation. Laser conditions comprised a spot diameter of 25 µm, repetition rate of 20 Hz, and fluence of 2.0 J cm-2. Raw data were processed as described for the first group.

Third group: The U-Pb analyses were conducted by laser ablation inductively coupled plasma–mass spectrometry with a quadrupole type mass analyzer (LA-Q-ICP-MS) at the Isotopic Geology Laboratory (Pará-Iso) of the UFPA. The analyses were done with a Thermo Fisher iCAP-Q and a 213 nm laser probe LSX-213 G2 CETAC. The laser operation conditions are spot size of 25 µm, a frequency of 10 Hz, and a fluence of 4-5 J/cm2. Each analysis consisted of 20 s of background measurement followed by 40 s of sample ablation. Acquisition and reduction of raw data were done with the software Qtegra and a Microsoft Excel macro (Miranda et al., 2023).

Quality control: For the LA-ICP-MS analyses, the reference material GJ-1 (601.7 ± 1.3 Ma; Jackson et al., 2004) was used as primary standard at UFOP, LEGGA and Pará-Iso. For quality control, the Blue Berry zircon (BB; 560 ± 1.1 Ma; Santos et al., 2017) was used at UFOP and Pará-Iso, Plešovice zircon (337.1 ± 0.37 Ma; Slama et al., 2008) at UFOP and LEGGA, and 91500 (1062.4 0.8 Ma; Wiedenbeck et al., 1995) at LEGGA. For the SIMS analysis, the principal and secondary reference materials used correspond to the zircon standards M257 (561.3 ± 0.3 Ma; Nasdala et al., 2008) and Temora 2 (416.78 ± 0.33 Ma; Black et al., 2004).

Data processing:

All ages are reported at the 95% confidence level (2σ uncertainty) and do not reflect external (systematic) uncertainties. For analyses with values of $f^{206}c$ (which indicate

the fraction of total ^{206}Pb that corresponds to common ^{206}Pb) higher than 2, and ratios $^{206}Pb/^{204}Pb$ lower than 500, data corrected for common Pb were used. The common Pb correction was made using the model Pb composition of Stacey and Kramers (1975).

Data are presented in Wetherill and Tera-Wasserburg plots developed with Isoplot v. 4.15 (Vermeesch, 2018a), and in histograms, probability density plots, and kernel density estimations made with the software DetritalPy v. 1.3 (Sharman et al., 2018). Furthermore, the similarity between the geochronologic data between different samples is quantitatively evaluated with a non-metric multi-dimensional scaling (MDS) method. For this purpose, the software DetritalPy v. 1.3 and the provenance package in R using the Kolmogorov-Smirnov test, which is based on the maximum separation between cumulative distribution functions (Vermeesch et al., 2016), were used. In this method, the plot obtained is unitless and the relative distribution of the samples and the distance between each other are proportional to their dissimilarity.

To determine the most reliable ages, only data with a 10 % discordance threshold, calculated as $^{206}Pb/^{238}U$ age x 100/$^{207}Pb/^{235}U$ age (7/5:6/8 discordance for short), and with errors of the apparent $^{206}Pb/^{238}U$ age < 5 %, have been considered valid. In complex distributions of data, different zircon age populations were determined using the TuffZirc function of the Isoplot program, which eliminates the bias associated with the manual selection of the different populations. This algorithm is useful for populations where at least 30 % of the grains are cogenetic and free of Pb loss. This method selects the largest cluster of analyses with a probability of fit > 0.05 to calculate median ages (Ludwig and Mundil, 2002).

Radiation doses were calculated for each analysis against the respective apparent $^{206}Pb/^{238}U$ ages after Murakami et al. (1991), an updated method originally from Holland and Gottfried (1955), via the equation

$$D = 8\,N_1[exp(a_1 t) - 1] + 7\,N_2[exp(a_2 t) - 1] + 6\,N_3[exp(a_3 t) - 1]$$

Where N_1, N_2, N_3 correspond to ^{238}U, ^{235}U, and ^{232}Th, respectively (atoms/mg); a represents the decay constants for each isotope; and t is the geologic age. ^{235}U was calculated based on the natural abundance of ^{238}U.

CHAPTER 4

Manuscript 1

4 MANUSCRIPT 1

Published on July 29, 2024 in the journal *Meteoritics & Planetary Science*:

Guerrero, D., Reimold, W.U., Hauser, N., Figueiredo, I., Kenni, L., Lambert, P., 2024. Zircon U-Pb provenance analysis of impact melt and target rocks from the Rochechouart impact structure, France. *Meteoritics and Planetary Science* 59(10): 2718-2743.

Zircon U-Pb provenance analysis of impact melt and target rocks from the Rochechouart impact structure, France.

Daniela GUERRERO[1*], Wolf Uwe REIMOLD[1], Natalia HAUSER[1], Igor FIGUEIREDO [2], Lucas KENNI [2], and Philippe LAMBERT[3]

[1]Laboratory of Geochronology, Geosciences Institute, Postgraduate Program in Geology, University of Brasília, Darcy Ribeiro Campus, Asa Norte, CEP 70910-900, Brasília, DF, Brazil

[2]Departament of Geology - Escola de Minas, Federal University of Ouro Preto, CEP 35402 163, Ouro Preto, MG, Brazil

[3]CIRIR - Centre International de Recherche et de Restitution sur les Impacts et sur Rochechouart, 87600 Rochechouart, France.

*Corresponding author. E-mail: daaguerrerogu@gmail.com

Abstract - The Rochechouart impact structure in the northwestern part of the French Massif Central (FMC) has a great diversity of impactites, including monomict impact breccias, suevite, and impact melt rocks. The structure is strongly eroded, which allows the study of impactites of the crater fill, and the transition into the crater floor. The FMC has had a multi-stage geological evolution from the late Neoproterozoic-Ordovician (600 – 450 Ma) until the later stages of the Variscan Orogeny (~300 Ma). Previous geochronological work on Rochechouart has been focused mainly on the impactites and constraining the impact age, and scarce work has been done on the FMC-related target rocks. Here, U-Pb isotope analysis by LA-MC-ICP-MS has been conducted on zircon from two impact melt rocks from the Recoudert and Montoume localities, and from a monzodiorite, a paragneiss, and two amphibolite samples of the basement to the impact structure. Zircon from the target rocks yielded mainly Neoproterozoic to Carboniferous ages (~924 to ~301 Ma) that can mostly be

correlated to different stages of the geological evolution of the FMC. The monzodiorite also yielded a Permian age of 272 ± 12 Ma. Zircon from the impact melt rocks, and specially from the Montoume sample, gave a comparatively higher diversity of Neoproterozoic to Jurassic ages (~552 to ~195 Ma). Provenance analysis for the zircon age populations of the impactites compared to those of the basement rocks shows overall poor correlation between the two age groups. This suggests that other target lithologies were involved in the formation of these impact melts as well. Post-Variscan and pre-impact ages (281 – 226 Ma) obtained for both melt rocks probably reflect a previously unconstrained event in the evolution of the regional geological history. Ages similar to the currently most widely accepted impact age of ~204-206 Ma were obtained from both impact melt rock samples. In addition, the Montoume melt rock yielded several post-204 Ma ages, which might reflect a to date unconstrained, ca. 194 Ma post-impact thermal/hydrothermal event.

Keywords: Rochechouart impact structure, French Massif Central, U-Pb isotope analysis, Zircon, Provenance analysis, Impact melt rock.

4.1 Introduction

The Rochechouart impact structure, located at 45°50'N / 0°56'E in the NW part of the French Massif Central (FMC), is the only impact structure known in France (Figure 4.1a; e.g., Gottwald et al., 2020; Kenkmann, 2021; Osinski et al., 2022). The structure is located in the Limousin region and straddles the departments of Haute Vienne and Charente. The impact origin of the Rochechouart impactites was first related by Kraut et al. (1969), based on the recognition of shatter cones in granites and gneisses and PDFs in quartz. The currently most accepted size of the structure is delimited by the distribution of shock deformation in basement rocks, which extends over a circular area of ~24 km diameter (Lambert, 2010). This value also agrees with the size of a negative gravity anomaly (Pohl et al., 1978). Estimates of the original crater diameter have yielded values up to 40-50 km based on comparisons with other, less eroded impact structures (Lambert, 2010), and up to 32 km based on the spatial extent of occurrence of in situ shatter cones (Osinski & Ferrière, 2016).

The highly eroded impact structure does not retain a crater morphology. Nevertheless, the impact breccia facies and crater floor with transition into shock-metamorphosed basement are well accessible. Five main impactite units overlie the impact-damaged basement, the respective bulk chemical compositions of which seem to be good reflections of the target rocks exposed around different impact breccia localities (e.g., Lambert, 1977a, 2010; Sapers et al., 2014). This has been attributed to the development of heterogeneous impact melts formed from a spatially heterogeneous target, and relatively inefficient mixing of different target rock melts (Faucher, 2021; Lambert, 2010).

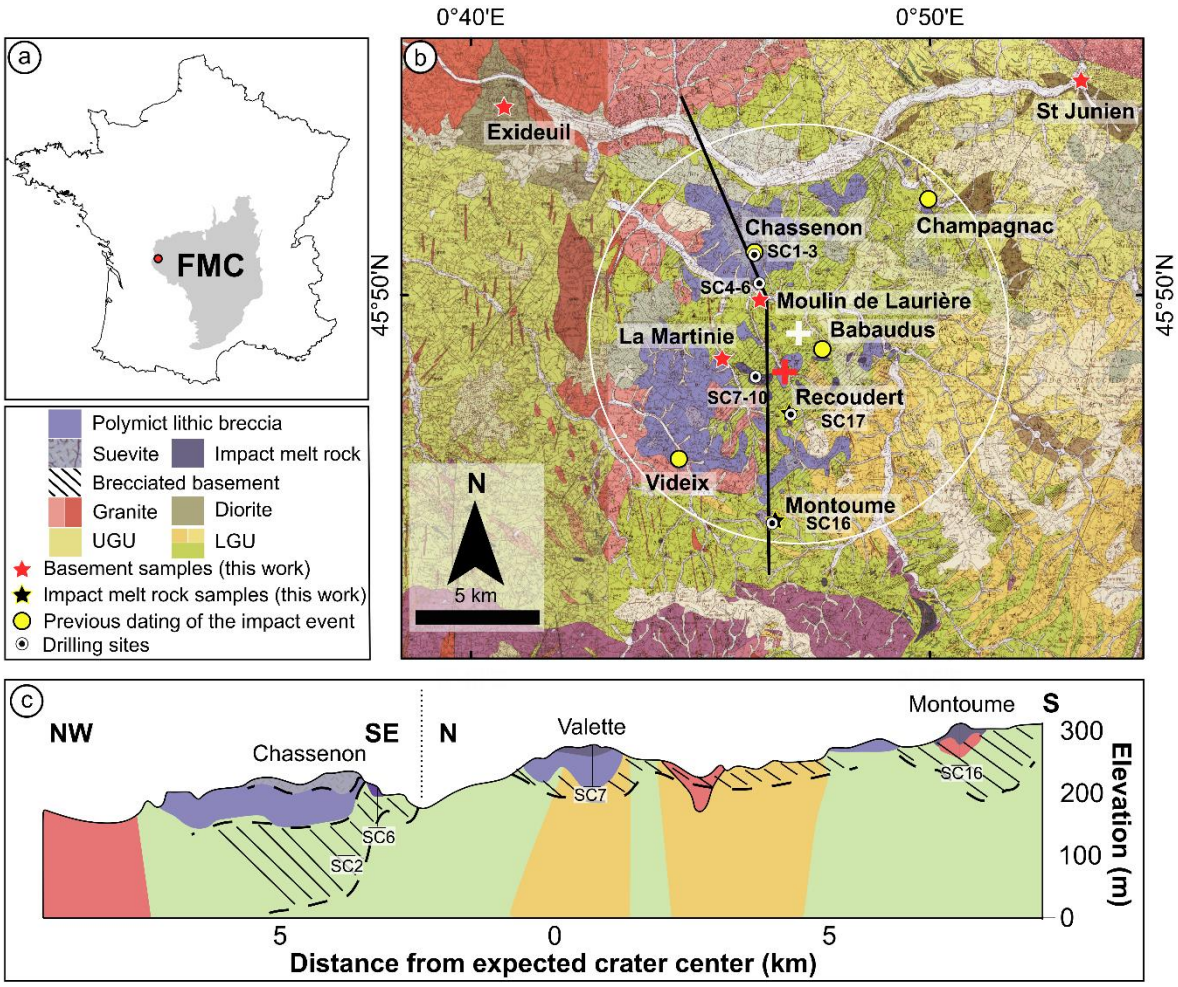


Figure 4.1 (a) Location of the French Massif Central in the territory of France, with the position of the impact structure marked by the red dot. (b) Geological map at the scale of 1:50,000, Sheet Rochechouart (after Chevremont et al., 1996), and (c) the geology along the schematic composite cross section for the profiles NW-SE to N-S marked in (b). The white circle indicates the extent of exposures of crater fill deposits (centered on the white cross). The red cross is the probable center of the initial Rochechouart impact structure, as derived from the present exposure pattern (after Lambert, 2010). The yellow dots indicate sites of samples previously used for constraining the impact age (compare text). The cross section in (c) is modified after Lambert (2010) and Quesnel et al. (2021), and also shows the locations of the 2017 drillings.

The most widespread basement units in the study area are the Silurian-Carboniferous Lower Gneiss Unit (LGU) and Upper Gneiss Unit (UGU) of the FMC (Chèvremont et al., 1996; Lambert, 2010). These units are intruded by multiple granitic and granodioritic bodies and, less abundant, mafic dikes (today amphibolites), pegmatite, microgranite-granodiorite, diorite, and gabbro (Lambert, 2010). All these lithologies are part of the FMC, which represents one of the largest exposures of the Variscan Belt (e.g., Faure et al., 2009; Lardeaux, 2014; Regorda et al., 2020; Vanderhaeghe et al., 2020). The FMC was formed during a series of tectono-metamorphic and magmatic events that started in the Neoproterozoic-early Paleozoic at the hyper-extended northern margin of Gondwana. This was followed by a Silurian-Devonian accretion system and Upper Devonian–lower Carboniferous continental collision during the Variscan Orogeny. This tectonic evolution was completed in the Lower Permian with late-collisional magmatism and extension (ibid).

Geochronological work in the Rochechouart impact structure has so far been focused on determining the age of the impact event. Most of this work was on impact melt-bearing lithologies, and a wide range of results has been reported. The impact age is currently constrained to 206.92 + 0.20/-0.32 Ma ($^{40}Ar/^{39}Ar$ data from Babaudus impact melt rock; Cohen et al., 2017). Only few earlier studies (Lambert, 1974; Reimold et al., 1983; 1987) were focused on geochronological analysis of basement rock, although this information is fundamental for the interpretation of impactite ages. These authors reported Permian to Jurassic ages for gneisses and granitic rocks and Devonian and Neo-Proterozoic ages for amphibolites.

Direct comparison of isotopic results (U-Pb in zircon) for impact lithologies and target rocks could allow the development of provenance analysis, whereby it may be possible to determine the precursor lithologies of individual impact melt rocks (see also Moser et al., 2011; Petrus et al., 2016). The present work is part of a comprehensive zircon U-Pb study of the Rochechouart impact structure. Our objective is to develop provenance analysis that includes basement and impactite lithologies and also evaluates the response of zircon to shock metamorphic conditions. Here, U-Pb isotopic data for zircon from two impact melt rock (IMR)

samples from Recoudert and Montoume, and four basement rock samples, from a monzodiorite dike from La Martinie, a paragneiss from Moulin de Laurière from the LGU, and two amphibolite lenses from Exideuil and St Junien (Figure 4.1b), were acquired with laser ablation-multi collector-inductively coupled plasma-mass spectrometry (LA-MC-ICP-MS). We correlate the response of zircon to different shock-metamorphic degrees and evaluate the currently known, most precise ages for the impact event. Furthermore, provenance analysis is developed by comparing the zircon age distributions for these samples with the well-constrained ages of the evolutionary stages of the FMC.

4.2 Geological background

4.2.1 The Rochechouart impactites and previous constraints on the impact age

The allochthonous impactites of the Rochechouart impact structure have been described in detail by Lambert (1977a, 2010) and Sapers et al. (2014). According to these authors, these rocks form a continuum with increasing melt and decreasing clast contents (description of each unit provided in the Supplementary Material (SM) 1). Furthermore, all these impactites exhibit strong hydrothermal alteration indicative of a widespread post-impact hydrothermal system, with a strong K-metasomatism (higher in the melt-rich phases) and the development of argillic, carbonate, oxide, and sulfide alteration assemblages (Faucher, 2021; Lambert, 2010; Sapers et al., 2014; Simpson et al., 2017). One of the two impact melt rocks analyzed in this study corresponds to a clast-rich impact melt rock, known as “Montoume breccia”, with mineral, lithic, and glass clasts and a red to gray-brown crystalline melt matrix (50 and 70 vol%) with flow features. The second sample is from the Recoudert location. It is very similar to the clast-free to clast-poor melt rock known as “Babaudus melt”, with a yellow quartzofeldspathic homogeneous matrix (up to 99 vol%), rich in vesicles, and with a limited content of quartzofeldspathic lithic and mineral clasts (Fig. 1b; Lambert, 2010).

Major element analyses of the different types of impactites and the target rocks from across the impact structure show a significant spatial variation in composition, with

distinctive Fe-Mg contents (Lambert, 1977a, 2010). According to this author, these local variations appear to be controlled by the respective occurrences of basement rocks in the vicinity of melt rock sampling sites. The Montoume impact melt rock matches the composition of the locally present granitoids, gneisses, and leptynites; and the impact melt rock from Babaudus is more felsic and is thought to have had a major contribution from local leptynite (Lambert, 1977a, 2010). A recent drilling campaign that made available 18 drill-cores throughout the structure allowed a better constraint of the distribution of the different lithologies (Figure 4.1b and c). In the SC16 drill-core, the Montoume IMR extends to 25 m depth, and then is followed by 30 m of brecciated granite, followed by a mixture of fractured gneiss and granite. In the SC17 drill-core from Recoudert, the impact melt rock has a length of 25 m, followed by brecciated gneiss and then by a felsic gneiss intercalated with suevite dykes (Lambert et al., 2019).

Currently, the most precise impact age is 206.92 + 0.20/ -0.32 Ma (Cohen et al., 2017). This age was further supported by a second study on the same sample, where ages of 204 ± 2.2 and 207 ± 3.6 Ma were obtained on two “former reidite in granular neoblastic” (FRIGN) zircon crystals analyzed by U-Pb LA-ICP-MS (Rasmussen et al., 2020). Previous attempts to determine the age of the Rochechouart impact event were also focused on impact melt-bearing lithologies, using different geochronological techniques, but mainly yielded younger ages (e.g., Kraut & French, 1971; Lambert, 1974; Reimold et al., 1987; Reimold & Oskierski, 1987; Schmieder et al., 2010). Some of these ages were of special interest due to their similarity to the 201.3 ± 0.2 Ma age of the Triassic-Jurassic boundary (Carporzen & Gilder, 2006; Hillebrandt et al., 2013; Kelley & Spray, 1997). However, there is no strong evidence for a link between the Rochechouart impact and this extinction event (Cohen et al. 2017; Schmieder et al., 2010). A small group of younger ages around 192-194 Ma was attributed to a possible post-impact thermal/hydrothermal event (Horne, 2016; Rasmussen et al., 2020). Recently, an Early Jurassic age for the impact was suggested based on a paleogeography study were a marine target environment with ~200 m of water depth was interpreted (Ormö et al. 2023).

4.2.2 The FMC basement in the realm of the impact structure

The basement to the Rochechouart impact structure is composed of Paleozoic crystalline rocks of the northwestern part of the FMC. The FMC represents one of the largest exposures of the Variscan Belt, which was consolidated during the Variscan Orogeny in the Devonian – Carboniferous. This was achieved by successive collisions between Laurussia, Gondwana, and Gondwana derived microcontinents during the amalgamation of Pangea (e.g., Franke et al., 2017; Kroner & Romer, 2013; Lardeaux, 2014; Martínez Catalán et al., 2021; Schulmann et al., 2014). The basement rocks exposed in the impact structure and its vicinity belong to some of the principal units distinguished in the tectono-metamorphic and igneous evolution of the Variscan Orogeny in the region of the FMC (Lambert, 2010).

Lower Gneiss Unit (LGU) and Upper Gneiss Unit (UGU)

The most widespread units in the impact area are the allochthonous metamorphic rocks of the Lower Gneiss Unit (LGU) and the Upper Gneiss Unit (UGU) (Chèvremont et al., 1996). The LGU represents intercalations of micaceous paragneisses and orthogneisses (metarhyolites). The UGU corresponds to the “leptynite-amphibolite complex” (LAC), a bimodal magmatic association that comprises mainly micaceous paragneisses, similar to the ones of the LGU, with lenses of fine-grained leptynites and amphibolites. The paragneisses and orthogneisses of both units are estimated to represent ~50 and ~25 %, respectively, of the basement rocks in the crater area (Lambert, 1977b). Within each unit, both gneiss types can vary in terms of texture and composition. The paragneisses at the top of the LGU and the bottom of the UGU are migmatitic. Furthermore, different types of mafic and ultramafic amphibolite lenses are intercalated with gneisses of both units. Locally, serpentinized peridotites occur in the basal part of the LGU. Both gneissic units are interpreted as the Proterozoic-early Paleozoic margin of northern Gondwana. These units evolved from Ediacaran sedimentary rocks that were intruded by Cambrian plutons during the southward subduction of the Iapetus Ocean beneath the northern Gondwana margin (e.g., Faure et al., 2009), and were subsequently affected by Cambro-Ordovician crustal thinning and rifting. This

resulted in the characteristic bimodal suite of the LAC (Faure et al., 2009; Lardeaux, 2014; Vanderhaeghe et al., 2020).

Throughout the entire FMC, the UGU is characterized by high-pressure (HP) granulite/eclogite facies metamorphism dated to the Upper Silurian/Devonian and proposed to be generated by the subduction of the northern Gondwana margin (e.g., Faure et al., 2008; Kroner & Romer, 2013; Lotout et al., 2018; Vanderhaeghe et al., 2020). Thereafter, the HP rocks were exhumed and retrogressed in the Middle-Upper Devonian to amphibolite facies conditions. Subsequently, the LGU and UGU underwent partial melting and synmetamorphic ductile shearing. This phase has been dated to the Upper Devonian in the western part of the FMC (e.g., Faure et al., 2009, 2008; Vanderhaeghe et al., 2020). During the uppermost Devonian-Lower Carboniferous, both gneiss units underwent Barrovian medium pressure-medium temperature (MP-MT) metamorphism attributed to the continental collision between Gondwana and Laurussia in the Variscan Orogeny. Later exhumation stages include a syn-orogenic extensional period at 340 to 335 Ma and a post-orogenic extensional stage at 310 to 305 Ma related to the collapse of the whole belt (Bellot & Roig, 2007; De Veslud et al., 2013). For the area of the Rochechouart impact structure, previous Rb-Sr ages for amphibolite of 397 ± 1.1 and 645 ± 6.4 Ma were reported by Reimold et al. (1983), who suggested that these ages represented the age of Devonian metamorphism and a Precambrian protolith, respectively.

Intrusive Bodies in the FMC

Several types of igneous rocks intrude the metamorphic formations and have been estimated to represent ~25 % of the basement in the area of the impact structure (Lambert, 1977b). The Devonian age intermediate and mafic intrusions of the Tonalite Line of the Limousin (LTL) correspond to the oldest magmatic rocks in the western part of the FMC. They have been interpreted as the mantle component of an andesitic arc above a subduction zone (e.g., Faure et al., 2005, 1997) and as the product of anatexis of metagreywacke and amphibolite intercalations of the UGU (Chenevoy, 1958). This period of anatexis may have lasted until the Carboniferous (ca. 360-295 Ma) with the final stages associated to the formation of the

leucogranites of the Chéronnac Massif, the calc-alkaline intrusions of Chabanais and St Gervais, and the minor intrusions of pegmatites, microgranites-granodiorites, and lamprophyres that cut the previous units (Duthou et al., 1984). These magmatic rocks were probably derived from metasedimentary or aluminous metagranitic protoliths, and from rocks with a mantellic component in the case of the subalkaline micro-granites (Pin, 1989). A summary of the radiometric age data reported for the area of the Limousin and the associated tectonic events is presented in SM 1.

Post Variscan Events

Some chronological work on basement rocks from the Rochechouart area dates back to the 1970s and 1980s, with most of these studies having yielded post-Variscan ages (SM 1). Similar ages have not been reported in other areas of the crystalline basement of the FMC. Post-Variscan rocks occurring close to the impact structure include alluvial deposits of the Vienne River to the north, the oldest of which are of Oligocene age. Then, there is the sedimentary sequence of the Aquitaine Basin, exposed 17 km to the west of the structure. This basin comprises a Triassic-Jurassic evaporitic sequence and Jurassic platform carbonates that were formed during two successive rifting events in the Triassic to lower Cretaceous (Cathelineau et al., 2012). Other post-Variscan events reported in the FMC region include Pb-Zn and U mineralization of the southeastern FMC formed during different pulses from the Permian to the Cretaceous (Cathelineau et al., 1990; Clauer, 2020).

4.3 Sample descriptions

Samples of some of the main lithologies occurring within the wider crater area were collected within and outside of the impact structure.

4.3.1 Basement rocks

Four basement rock samples were analyzed for this study (Figure 4.1b). One monzodiorite and one paragneiss are from near the center of the impact structure, from La Martinie and Moulin de Laurière, respectively. Two amphibolite samples are from the north and outside of the impact structure, one from Exideuil quarry and the

other from St Junien (Figure 4.1b). A more detailed description of the samples and thin section microphotographs are provided in SM 2.

The fine-grained *monzodiorite from La Martinie* (C180825-1115, 45°49.092'N / 0° 45.488'E) is from a dike cutting LGU gneiss. The rock is cut by a few fractures and shows shatter cones of 1 to 15 cm length. The rock is porphyritic, composed of a black, fine- to very fine-grained matrix, and millimeter-sized white plagioclase and quartz phenocrysts (Fig. SM2a). The sample is composed of plagioclase (50 vol%), orthoclase (14 vol%), quartz (3 vol%), biotite (20 vol%), and opaque phases (3 vol%), as well as accessory zircon, and has as alteration products sericite and chlorite (10 vol%). One quartz phenocryst has a single set of decorated planar deformation features (PDFs) that occur in their majority along the edge of the grain (Figs. SM2a and SM2b). The fine-grained matrix is composed of microliths of feldspar, and quartz, biotite, chlorite, and opaques. Biotite can be found partially or totally altered to chlorite. The euhedral biotite grains display kink bands. Phenocrysts of feldspar show stronger sericitization than feldspar of the matrix.

The *paragneiss from Moulin de Laurière* (C180825-0930, 45°49.949'N, 0° 46.338'E) was collected close to the suspected center of the impact structure (Figure 4.1b) and corresponds to the LGU according to the BRGM (Bureau de Recherches Géologiques et Minières) geological map, the most dominant rock type of the basement (Chèvremont et al., 1996). The outcrop comprises meter-sized blocks of relatively homogeneous, foliated gneiss with some quartz veins of several millimeter width. The rock is very fine- to fine-grained and composed by bands rich in plagioclase (35 vol%), quartz (26 vol%) and minor orthoclase (2 vol%) and by dark bands composed by biotite (35 vol%), and garnet (2 vol%). Accessory minerals are muscovite, apatite, zircon, titanite and opaque phases, whereas as secondary phases sericite, chlorite, and carbonate were observed. There are quartzofeldspathic aggregates with granoblastic texture intercalated with biotite in lepidoblastic texture. Biotite is in large part euhedral, occasionally shows kink bands, and forms aggregates that are partially altered to chlorite, sometimes with minor muscovite. Porphyroblastic, subhedral garnet is strongly fractured and appears to be post-kinematic as it is overgrowing the foliation. Zircon crystals of ~ 50 µm size

represent the main accessory mineral. Some quartz grains display undulatory extinction, but no diagnostic shock effects were noted.

The two amphibolite samples were obtained 13-15 km from the apparent center of the impact structure (Figure 4.1b). The *amphibolite from Exideuil* (C180824-1500, 45°53.052'N, 0° 40.842'E) was collected to the NW, where it occurs together with granodiorites of the Tonalite Line of the Limousin, which intrude the UGU. The *amphibolite from St Junien* (C180822-1625, 45°53.238'N, 0° 53.320'E) was collected in a low, NW-SE trending road-cut just below the castle wall, along the village thoroughfare, in UGU. These samples are inequigranular, fine- to medium-grained, and are transected by millimeter-wide veins of orthoclase and/or epidote. The Exideuil sample is not foliated, whereas the St Junien sample has a strong schistosity marked by amphibole and phyllosilicate. Both samples share a similar composition, with amphibole (30–40 vol%), plagioclase (25–30 vol%), orthoclase (10–16 vol%) and quartz (10 vol%) as the main phases. Opaque phases (3–5 vol%), biotite (1–7 vol%), and apatite, ilmenite, and zircon as accessory minerals, together with chlorite, sericite, and epidote (3-8 vol%) as alteration products. In both samples, amphibole is generally anhedral and has inclusions of quartz, apatite, and ilmenite, and in the St Junien amphibolite also orthoclase and biotite. In the Exideuil sample, plagioclase is characterized by crystals with a very sericitized core. In the St Junien sample, orthoclase and quartz form granoblastic aggregates, and some euhedral biotite displays kink bands. In these samples, zircon is subhedral to euhedral and has sizes between 40 and 100 μm.

Neither amphibolite has unequivocal evidence of shock metamorphism. Minerals in the sample from St Junien have a higher density of microfractures than the ones of the Exideuil sample. These fractures, in general, are irregular, nonplanar, and have subparallel to random orientations. Quartz in both amphibolites displays minor undulatory extinction. These features are not shock-diagnostic.

4.3.2 Impact melt rocks

The *clast-poor impact melt rock sample from Recoudert* (C180824-1900, 45° 48.349'N, 0° 47.099'E; Figure 4.1b) is generally similar to samples of the impact melt

rock from Babaudus that were previously analyzed by Cohen et al. (2017) and Rasmussen et al. (2020). The sample has a homogeneous, yellowish groundmass with abundant elongated amygdules filled with quartz and biotite. Clasts are mostly quartz and K-feldspar that indicate quartzofeldspathic precursor lithologies. This type of impact melt rock occurs as isolated outcrops in the central part of the impact structure. The analyzed sample is composed of 85 vol% matrix, 10 vol% lithic and mineral clasts, and 5 vol% amygdules. The matrix is aphanitic to microcrystalline and composed by disseminated Fe-Ti oxides (Figs. SM2c and SM2d). Backscattered electron (BSE) images indicate that the matrix contains feldspar in an interlocking texture. Under the binocular microscope, we identified brownish, toasted quartz clasts and some quartz clasts with one set of PDFs per host crystal. Multiple sets of PDFs have not been observed. Ballen silica of type 4 according to Ferrière et al. (2009) (Fig. SM2c), characterized by heterogeneous extinction between individual ballen, and some clasts that are partially isotropic (Fig. SM2d) are also noted. Feldspar in clasts is devoid of shock deformation.

The *impact melt rock sample from Montoume* (C180823-0955, 45° 46.535'N, 0° 46.488'E) is reddish and clast-rich. This type of impact melt rock is mainly found at the tops of some hills in the southern part of the structure, including at the highest point within the impact structure near Montoume village, 7.5 km south of the apparent center of the structure (Figure 4.1b). Here the impact melt rock forms a massive, 25 m thick deposit. The rock is heterogeneous, on centimeter to decimeter scales, with respect to populations of lithic, mineral, and annealed clasts of former impact glass. Clasts do not show preferred orientation. The sample consists of ca. 75 vol% matrix and 25 vol% of mostly lithic, and mineral clasts. The matrix is purplish-reddish and displays a pronounced flow banding texture. Lithic clasts do not have a preferred orientation, are fine-grained, and have quartzofeldspathic composition, with some of them showing a gneissic foliation. The matrix contains very fine-grained microliths of mostly quartz and K-feldspar, plus some Fe-oxyhydroxides. Some of the quartz clasts are recrystallized. There are toasted quartz clasts, and up to two sets of PDFs with different crystallographic orientations have

been observed in quartz of mineral and lithic clasts (Fig. SM2e). Ballen silica of type 4 after Ferrière et al. (2009) has been observed as well (Fig. SM2f).

In both impact melt rock samples, some zircon crystals with granular texture were identified in thin section. Sometimes spots of higher intensity in backscattered electron (BSE) images, which probably correspond to baddeleyite, are located at the border of the zircon crystals.

4.4 Analytical methods

4.4.1 Sample preparation and imaging

Zircon separation for isotope analysis was conducted at the Laboratório de Estudos Geodinâmicos, Geocronológicos e Ambientais (LEGGA) at the University de Brasília by crushing, grinding, magnetic separation, and hand-picking of the final concentrate under a binocular microscope. Cathodoluminescence (CL) images of the zircon mounts were obtained with a Scanning Electron Microscope (SEM) type JEOL 6510 at the Federal University of Ouro Preto (UFOP), Brazil. Backscattered electron (BSE) images of the thin sections and zircon mounts and secondary electron (SE) and CL images of the zircon mounts were obtained with a QUANTA 450 - FEIJEOL SEM using 15 kV and a working distance of 10.5 mm at LEGGA. Extra BSE images of polished thin sections were obtained with a JEOL JXA-8500F field emission electron microprobe at the Museum für Naturkunde, Berlin.

4.4.2 U-Pb isotope analysis

Selected zircon crystals were analyzed by LA-MC-ICP-MS at the Laboratory of Isotope Geochemistry of the UFOP and at LEGGA, with a total of 447 analyses obtained on 417 crystals from the six samples. For the Recoudert IMR (C180824-1900), Montoume IMR (C180823-0955), and Exideuil amphibolite (C180824-1500), multiple zircon mounts were analyzed. The analyses were acquired at UFOP using a Neptune Plus Thermo Finnigan instrument coupled with a Photon-Machines 193 nm laser system, with an ablation spot size of 30 µm. At LEGGA, zircon crystals were analyzed with a Thermo Finnigan Neptune XT high-resolution multi-collector, sector-field ICP-MS coupled to a 193 nm Teledyne Analyte Excite laser ablation

system, with a spot size of 20 µm. In both laboratories, isotope ratios were calibrated against the zircon GJ-1 (601.7 ± 1.3 Ma; Jackson et al., 2004). For quality control, the Plešovice (337.1 ± 0.37 Ma; Sláma et al., 2008) and the Blue Berry (BB; $^{206}Pb/^{238}U$ age of 560 ± 1.1 Ma; Santos et al., 2017), as well as the 91500 (1062.4 ± 0.8 Ma; Wiedenbeck et al., 1995) reference materials were analyzed. All ages are reported at the 95% confidence level (2σ uncertainty) and do not reflect external (systematic) uncertainties. All the data obtained by both laboratories, the measured values for the standards, and further details of the analytical conditions and data processing are presented in SM 3.

The $f^{206}c$ values, which indicate the fraction of total ^{206}Pb that corresponds to common ^{206}Pb, and the $^{206}Pb/^{204}Pb$ ratio values are lower than 2 and higher than 500, respectively, for most of the analyses. Thus, mainly ratios and ages uncorrected for common Pb were used. For analyses with higher values of $f^{206}c$ (>2) and smaller values of $^{206}Pb/^{204}Pb$ (<500) data corrected for common Pb were used. Data are presented in Wetherill and Tera-Wasserburg plots developed with Isoplot v. 4.15 (Vermeesch, 2018a), and in histograms, probability density plots, and kernel density estimations made with the software DetritalPy v. 1.3 (Sharman et al., 2018). Furthermore, a non-metric multi-dimensional scaling (MDS) method was applied, also using this software, to quantitatively compare the geochronological data of the different samples. In this method, the plot obtained is unitless and the relative distribution of the samples and the distance between each other are proportional to their dissimilarity. In this case the dissimilarities were obtained based on the D value of the Kolmogorov-Smirnov test, where D indicates the greatest separation between the cumulative age distributions of two samples (Vermeesch, 2018b).

To determine the most reliable ages, only data with a 10 % discordance threshold, calculated as $^{206}Pb/^{238}U$ age x 100 / $^{207}Pb/^{235}U$ age (7/5:6/8 discordance for short), and with errors of the apparent $^{206}Pb/^{238}U$ age < 5 % have been considered valid. The ages reported correspond to the most reliable concordant or weighted average ages calculated, depending on the data distribution. They were calculated for presumedly cogenetic zircon populations, using the maximum number of analyses in such groups of data. In complex distributions of data, different zircon age

populations were determined using the TuffZirc function of the Isoplot program, which eliminates the bias associated with the manual selection of the different populations. This algorithm is useful for populations where at least 30 % of the grains are cogenetic and free of Pb loss. This method selects the largest cluster of analyses with a probability of fit > 0.05 to calculate median ages (Ludwig & Mundil, 2002).

For all zircon grains with a 7/5:6/8 discordance lower than 10 % the radiation dose was calculated against the respective apparent $^{206}Pb/^{238}U$ ages after Murakami et al. (1991), an updated method originally from Holland and Gottfried (1955).

4.5 Results

4.5.1 Zircon textures

Monzodiorite, paragneiss, and amphibolites: The zircon crystals from basement samples are generally prismatic, colorless, and transparent to translucent. Most of the zircon from the monzodiorite and paragneiss is equidimensional, euhedral, and smaller than the zircon from amphibolites. Most zircon grains from the monzodiorite and paragneiss have aspect ratios between 1:1 and 3:2, and sizes up to 150-200 µm. In amphibolites, zircon crystals with aspect ratios up to 7:3 are common, and grains with sizes up to 290 µm are also present. The zircon textures observed in CL images are heterogeneous (Figure 4.2 and SM 4), especially for zircon from the paragneiss and the monzodiorite. In most samples the most common texture is oscillatory zoning, represented by bands of different CL intensities (Figure 4.2a, #91 and #96), or by bands with overall strong or weak CL intensities (Figure 4.2b, #72 and #57). Zircon grains with either broad or fine zonation are present in the paragneiss and the monzodiorite (Figure 4.2 a, #96 and #90 and 2b, #57), and a fine zonation is found in some zircon grains from the amphibolites (Figure 4.2c, #18 and #32 and 2d, #114). A faint and irregular zonation is common for the elongated crystals of the amphibolite from Exideuil (Figure 4.2c, #38). Besides oscillatory zoning, homogeneous crystals are also quite common for zircon of the paragneiss, which normally display very weak CL intensities (Figure 4.2b, #91), and zircons with inherited core are also present in the monzodiorite (Figure 4.2a, #168).

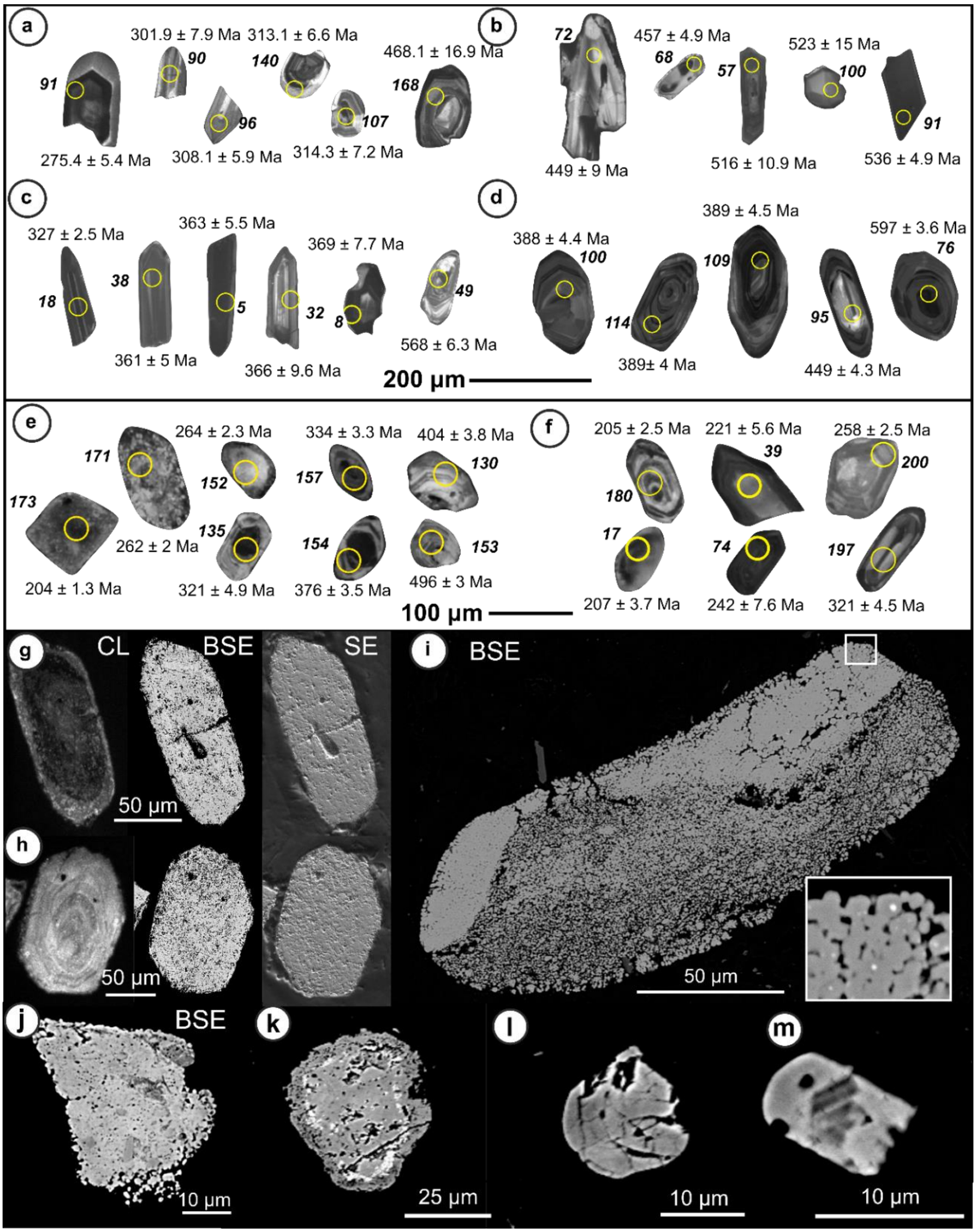


Figure 4.2 Cathodoluminescence (CL) images showing the different types of zircon found in the samples of this study. Also shown are the locations of the analysis spots, analysis number, and the respective 206Pb/238U apparent ages. (a) Monzodiorite (C180825-1115), (b) paragneiss from Moulin de Lauriere (C180825-0930), (c) amphibolite from Exideuil (C180824-1500), (d) amphibolite from St. Junien (C180822-1625), (e) Recoudert IMR (C180824-1900), and (f) Montoume IMR (C180823-0955). (g,h) Selected CL, backscattered electron (BSE), and secondary electron (SE) images from the Recoudert IMR zircon mounts. BSE images of zircon grains from polished thin sections from (i,j) the Recoudert and (k–m) Montoume IMR samples.

The most common features of zircon crystals from the St Junien amphibolite are inherited cores. These crystals normally have a rim with oscillatory zoning and a core

that may display different types of oscillatory zoning with different CL intensities (Figure 4.2d, #109, #76, and #95) or sector zoning (Figure 4.2d, #100). In addition to these textures, zircon crystals with sector zoning (Figure 4.2a, #107, 2b, #100, and 2c, #8), metamorphic overgrowths (Figure 4.2a, #140), and zones with local recrystallization (Figure 4.2b, #68, 2c, #49 and 2d, #109) were found in all these samples.

Impact melt rocks: Zircon crystals from impact melt rock samples are strongly heterogenous and can be broadly divided into two groups by optical characteristics: 1) brownish/reddish but translucent, subhedral to sub-rounded, prismatic crystals, and 2) colorless, transparent to translucent, rounded to sub-rounded, in part prismatic crystals. In both IMR samples, the first group has normally larger crystals than the second, although some brownish and colorless crystals are part of both the small and large fractions. In the Montoume IMR, the brownish population has aspect ratios between 3:2 and 2:1, and most of the grains have sizes between 90 and 180 μm, with some crystals as small as 45 μm. The colorless zircon in this sample has aspect ratios between 3:1 and 1:1, and lengths from 60 to 156 μm. In the Recoudert IMR, both populations have aspect ratios between 3:1 and 1:1 and sizes between 106 and 180 μm. However, the colorless crystals are generally more elongated than the brownish ones and a smaller fraction of mostly transparent, colorless zircon with sizes between 37 and 96 μm is also present.

The zircon textures from the impact melt rock samples are varied. The BSE and SE images show that most of the crystals of the brownish population of both samples are granular (Figure 4.2e, #173 and #171, 2g, and 2h). However, some colorless crystals also show this texture. In the Recoudert IMR, the brownish granular crystals are mostly homogeneous (Figure 4.2e, #173) while in the Montoume sample are more diverse, with irregular or oscillatory zoning (Figure 4.2f, #39), inherited cores, or sector zoning textures (Figure 4.2f, #200). Brownish grains without a granular texture are most common in the Montoume IMR and have mainly a fine oscillatory zoning texture. The colorless population, on the other hand, has heterogeneous textures in both samples, with crystals with oscillatory or irregular zoning (Figure 4.2f, #74), inherited cores (Figure 4.2e, #135), or homogeneous textures. Some

grains also have zones of local recrystallization/resorption. Oscillatory zoning in both samples can involve bands of different CL intensities (Figure 4.2f, #180 and # 39, and 2g), but individual crystals may have bands with an overall weak (Figure 4.2e, #157 and f #74), or overall strong CL intensity (Figure 4.2h).

Zircons observed in the thin sections from both IMR samples also show different degrees of shock deformation. In the Recoudert IMR, most of the grains are granular and some crystals exhibit inclusions as regions of slightly lower grey tones (Figure 4.2i and j). The Montoume IMR has grains with granular texture only along the margin (Figure 4.2k). Furthermore, both samples have some crystals that show brighter zones or spots of higher backscattered electron density (likely baddeleyite) (Figure 4.2i), which in the Montoume IMR can be found between the granular border and the grain core (Figure 4.2k). Other zircon crystals show various types of irregular fractures (Figure 4.2l), and more prismatic euhedral crystals with no shock evidence and different igneous textures (Figure 4.2m).

4.5.2 U-Pb age dating of zircon from basement rocks

U-Pb isotope data for zircon are plotted in Figure 4.3-4.5. Raw data and histograms showing the CL textures of the analyzed zircons are provided in SM 3 and SM 5, respectively. Due to the limitations in the spatial resolution of the ICP-MS technique and the generally narrow width of the bands in zonation of some crystals, some ages have seemingly been obtained in mixed domains. In general, some of the groups of zircon with similar textures in CL images yield a wide distribution of ages, especially for the monzodiorite and the paragneiss. The opposite is also observed: zircon crystals with different textures may record similar ages, which was particularly evident for the amphibolites (SM5).

Monzodiorite: A total of 66 analyses were acquired on 66 crystals. Data from 22 crystals could not be considered. The ages mostly range from 267 to 625 Ma, with just one crystal yielding an older age of 924 Ma. Most of the ages were obtained in cores or in the bands of internal zoning, and younger ages correspond to measurements made in cores or in mixed domains. The ages are distributed along the concordia line (Figure 4.3a), which does not allow to calculate a distinct

concordant age. It is possible to identify 12 different age peaks in the probability density plot (PDP) (Figure 4.3b), which correspond to 481, 457, 438, 411, 391, 375, 334, 328, 308, 301, 275, and 268 Ma. The weighted average age of the 3 youngest zircon crystals corresponds to an age of 272 ± 12 Ma (MSWD of 2).

Paragneiss: Sixty analyses were made on 58 zircon crystals, of which 45 analyses could be validated. The grains yielded apparent $^{206}Pb/^{238}U$ ages ranging from the Neoproterozoic to the Silurian (Figure 4.3c). In the Kernel density plot (KDP), five main age maxima are calculated at 565, 543, 521, 471, and 456 Ma, of which the principal ones are at 543 and 521 Ma. In the probability density plot, nine main ages at 581, 565, 549, 543, 522, 516, 505, 473, and 457 Ma are distinguished (Figure 4.3d). Most of the crystals that gave the youngest ages have oscillatory zoning textures. The zircon populations registering older ages, encompassing the principal age peaks of the sample, are strongly heterogeneous, with zoned, homogeneous, or irregular crystals, or ones with metamorphic overgrowths or resorption zones. The proportions of analyses made in cores and in rim zones are approximately equal (SM 5).

Exideuil amphibolite: One-hundred and twelve analyses were made on 104 crystals, of which 109 analyses were validated. The sample yielded four different weighted average ages. The youngest one corresponds to 328 ± 1 Ma and was obtained from 8 analyses made on 8 zircon crystals. This is followed by an age of 361 ± 1 Ma from 87 analyses made on 76 zircon crystals. Furthermore, two older ages of 448 ± 3 Ma and 567 ± 3 Ma were registered for 3 and 4 zircons, respectively, with one analysis per zircon crystal (Figure 4.4a). The two youngest ages were obtained in elongated zircon crystals, in the cores of zoned or homogeneous zircons, and in a few cases in crystals with inherited cores. The two oldest ages were obtained on the rims of crystals. The 567 ± 3 Ma age stems from small, rounded zircons with patchy zonation, and the 448 ± 3 Ma age was determined in crystals with oscillatory zonation or inherited cores (SM 5).

St Junien amphibolite: A total of 56 analyses were carried out on 45 zircon crystals, of which 51 analyses were of good quality. Two concordia ages were calculated, one

at 388 ± 1 Ma for 26 analyses on 26 crystals and another at 449 ± 3 Ma for 3 analyses in 3 zircon crystals. Three weighted average ages were calculated: the oldest at 597 ± 3 Ma for 5 data from 5 crystals, and the two youngest ones at 351 ± 5 Ma obtained in 3 analyses on 3 crystals and at 371 ± 2 Ma obtained from 6 data from 5 grains. (Figure 4.4c). The two oldest ages are based mainly on inherited cores. The cores of the zircons of 449 ± 3 Ma age are mostly bright with high CL intensities, whereas the cores of crystals that yielded the 597 ± 3 Ma age were mostly patchy or sector zoned. The two youngest ages were also recorded in crystals with inherited cores or sector zoning. The 388 ± 1 Ma age was mainly obtained on the cores of zircons with sector zoning and in rims and cores of zircons with dark and grayish inherited cores (SM 5). Analyses made on the core and rim of the same crystals show that the rim tends to register younger ages than the corresponding core. Multiple crystals with rim ages belonging to the 388 ± 1 Ma age population have cores that are part of the zircon population of 597 ± 3 Ma age.

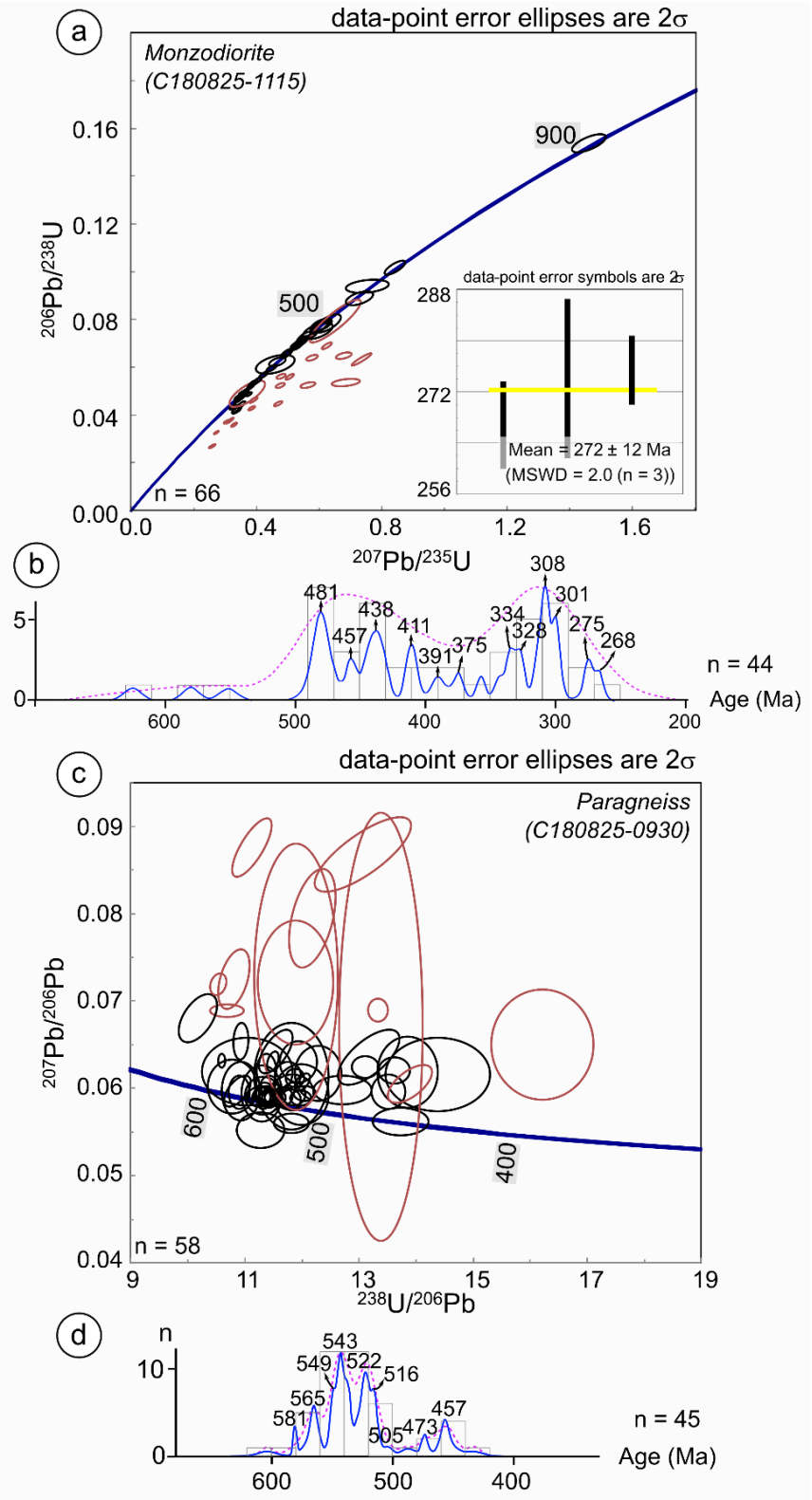


Figure 4.3 (a) Wetherill plot for the monzodiorite (C180825-1115). Inset with the weighted average age for the youngest three zircons considered valid. (c) Tera-Wasserburg plot for the paragneiss (C180825-0930). Data not considered as valid are shown with plain red lines. (b, d) Histograms (bin sizes = 20 Ma) for the monzodiorite and the paragneiss data with the age peaks of the probability density plot. Probability density plot in plain blue lines and kernel density plot in pink dashed lines.

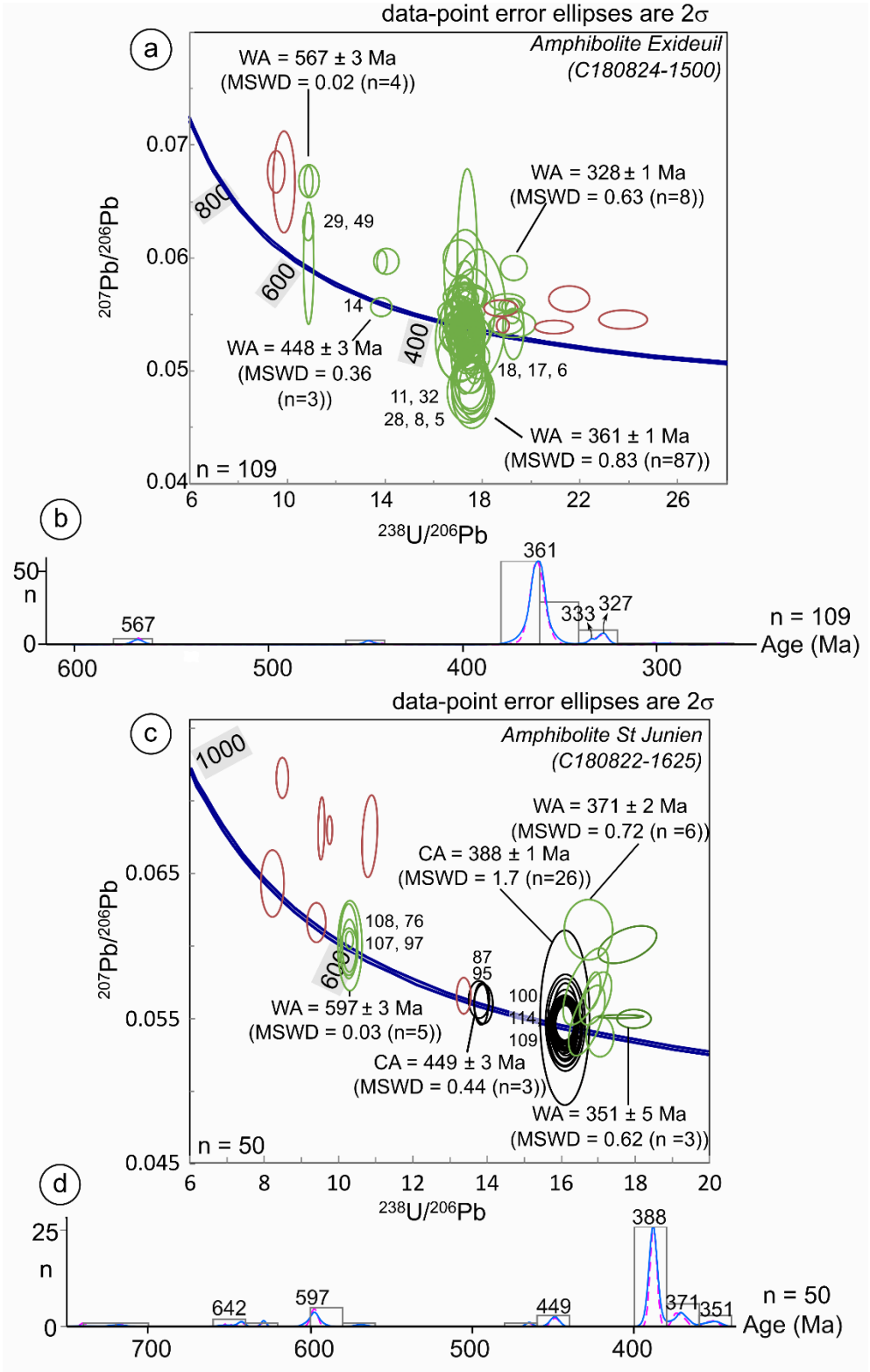


Figure 4.4 Tera-Wasserburg plots for the data from (a) the amphibolite from Exideuil (C180824-1500) and (b) the amphibolite from St. Junien (C180822-1625). (c) Data used for the estimation of concordia ages (CA) plotted in black, data used for weighted average ages (WA) are plotted in green, and data not used for the determination of any age are plotted in red. (b, d) Histograms (bin sizes = 20 Ma) for the Exideuil and the St. Junien amphibolite data, respectively, with the age peaks of the probability density plot. Probability density plot in blue and kernel density plot in pink dashed lines.

4.5.3 U-Pb age results for zircon from the impact melt rocks

Recoudert impact melt rock: Eighty-one analyses were done on 72 zircon crystals, of which 33 analyses could be validated. The analyses are distributed along the concordia line (Figure 4.5a), and the probability density plot shows age peaks at 560, 501, 377, 281, 262, and 203 Ma (Figure 4.5b). The 10 youngest crystals yield a concordia age of 204 ± 1 Ma. All the zircons that record the two youngest ages (204 ± 1 and 262 Ma) and most of the zircons that yield the 281 Ma age belong to the population of large reddish crystals, which show a granular texture in BSE images. All the zircon crystals that gave the youngest age are homogeneous and most of these analyses were made in cores. For the 281 Ma and 262 Ma ages, most of the zircons were zoned and the analyses were made in rim zones. The 377 Ma age was mainly obtained in colorless zircons with inherited cores. Most of the zircons registering older ages are smaller, transparent, and zoned (SM 5).

Montoume impact melt rock: Seventy-two analyses were made, with one analysis per crystal. Nine of these analyses could not be validated. The analyses are distributed along the concordia line (Figure 4.5c). Eleven age peaks were obtained in the probability density plot at 551, 491, 440, 403, 349, 321, 258, 238, 226, 206, and 195 Ma (Figure 4.5d). From 8 younger zircons a concordia age of 196 ± 2 Ma was obtained and a weighted average age of 206 ± 2 Ma was obtained from 5 analyses. All zircons that record the 440 Ma age are colorless and all crystals yielding the 258 Ma age correspond to reddish crystals. The other ages were obtained in zircon from both populations distinguished optically. The zircons that yielded the youngest age are mainly part of the colorless population of crystals. The 491, 403, 321, and 206 ± 2 Ma ages were obtained mostly on grains from the brownish population. The 349 Ma age, along with the other Triassic-Permian ages, were obtained on a mix with a more or less equal proportion of colorless and brownish crystals. All the zircon crystals that yielded the 321 Ma age and most of the zircons that gave the 349 and 491 Ma ages are zoned. The 440 Ma age was obtained on zircons with fine oscillatory zoning and with metamorphic overgrowths, and the 403 Ma age was obtained on zoned crystals, zircons with inherited cores, and grains with metamorphic features. For the younger ages, most of the crystals were zoned

too but there was a higher proportion of homogeneous and metamorphic zircons. All analyses that yielded the 206 ± 2 Ma age and most of the analyses that gave the varied Triassic-Permian ages, as well as the youngest age, were obtained in cores (SM 5).

The reported ages are considered reliable, as for most of them the associated MSWD values are within the accepted range (Spencer et al., 2016). The MSWD values of the ages are > or < 1 (Figure 4.3-4.5), indicating that the uncertainties could have been under- or overestimated. Values > 1 indicate a scattering in the data that could reflect the presence of more than one zircon population. Values < 1 could indicate that the uncertainty of the mean age does not reflect the actual variation in the data (ibid). The 204 ± 1 Ma age calculated for the Recoudert IMR and the 388 ± 1 Ma obtained on the amphibolite from St Junien are the only ages displaying a MSWD outside the accepted limits, with values that are 0.01 lower and 0.1 higher, respectively. If the respective zircon populations are divided to improve the age statistics no significant differences in the calculated ages could be identified for these 2 cases. Therefore, it is preferable to use these ages, calculated considering the maximum quantity of good quality analyses.

4.5.4 U and Th contents and Th/U ratios.

The U and Th contents and the Th/U ratios for the analyzed zircons are, in general, very heterogeneous for individual samples. The composition of crystals with discordant ages of most of the samples is very similar to that of the crystals recording concordant data. Only for the monzodiorite and the Recoudert IMR samples, zircons with discordant data display higher contents of U and Th. Plots showing the relative composition of all zircon crystals with concordant ages with low errors, for each sample, versus their textural characteristics and apparent $^{206}Pb/^{238}U$ ages are provided in SM 6.

The zircons from the St Junien amphibolite register less scattering and the lowest median values of U (133 ppm), Th (47 ppm), and Th/U (0.36) for all basement samples analyzed. The highest median values of U (495 ppm), Th (503 ppm), and Th/U (0.97) and the widest scattering of the latter two parameters are registered for

the zircons from the Exideuil amphibolite. The monzodiorite and the paragneiss zircons display more similar values, which are intermediate between those for the amphibolites. In general, the IMR zircons have U, Th, and Th/U values with similar distributions to those of the basement samples; however, the Montoume IMR shows many outliers with higher concentrations of U and Th. Both IMRs display similar values of Th, whereas the U content is higher in the Montoume IMR zircons. The median U and Th values of both IMRs and the Th/U ratio of the Recoudert IMR are comparable to those of the zircons from monzodiorite and paragneiss. The Th/U values of the Montoume IMR zircons are comparable to the St Junien amphibolite (Fig. SM6a).

The compositions of the grains for each sample are controlled to different degrees by their texture and age. In general, the composition of the zircon grains from the paragneiss and the Recoudert IMR is mainly controlled by the texture of the crystals; in the Exideuil amphibolite, the Montoume IMR, and the monzodiorite, the composition varies principally as a function of the zircon ages; and in the amphibolite from St Junien, the zircon composition is not well related to texture or age.

The variation of the U, Th, and Th/U values in relation to zircon textures

Zircon populations defined by texture can display a wide range of compositions. However, crystals with different textures can also register similar values, and each zircon population can record different relationships between the U, Th, and Th/U values (Fig. SM6b). In general, crystals with strong CL intensities record lower U and Th contents, normally ≤ 250 ppm and ≤100 ppm, respectively. Crystals with a weak CL intensity record more heterogeneous U values, which can be similar, but usually are higher than for the brighter grains. Some of the zircon populations registering the highest values of U are also associated with the lowest values of the Th/U ratio, such as the homogeneous darkish grains of the paragneiss. The opposite is also observed, with crystals that register the lowest contents of U and Th also yielding the highest Th/U ratios, such as the crystals with fine oscillatory zoning from the paragneiss and the monzodiorite. Some zircon populations can register either high or low contents of U, Th, and Th/U are also observed, such as – the high values for

crystals with irregular and broad oscillatory zoning of the monzodiorite and low values for crystals with fine oscillatory zoning of the impact melt samples (Fig. SM6b).

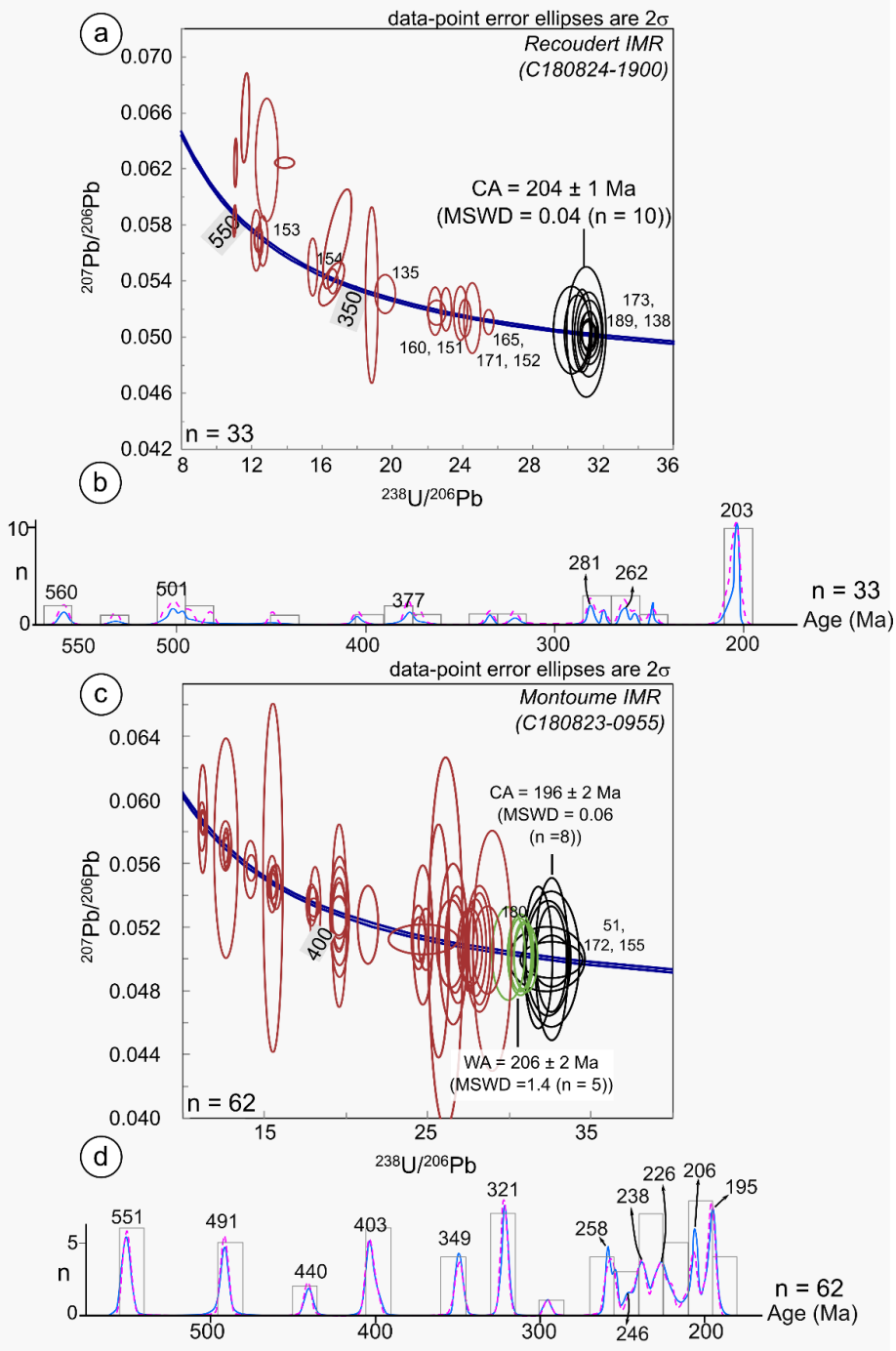


Figure 4.5 Tera-Wasserburg plots for zircon data for impact melt rocks from (a) Recoudert (C180824-1900) and (c) Montoume (C180823-0955). Data used for the estimation of concordia ages (CA) plotted with black lines, data used for weighted average ages (WA) with green error ellipses, and good quality analyses not used for the calculation of those ages plotted in red lines (Vermeesch, 2018a). (b, d) Histograms for the Recoudert (bin size = 6 Ma) and Montoume (bin size = 15 Ma) IMR superimposed onto the age peaks of the probability density plot. Probability density plot in plain blue lines and kernel density plot in pink dashed lines.

The variation of U, Th, and Th/U values in relation to ages

The variation of the U, Th, and Th/U values in relation to ages is characterized by higher contents and stronger scattering of these values in the case of younger zircons (Fig. SM6c). This pattern is observed in the U and Th contents of zircons from the amphibolite from Exideuil, the monzodiorite, and the impact melt rocks, especially the Montoume IMR. While the Th/U ratio shows this pattern only in zircons from the amphibolite from Exideuil and from both impact melt rocks. Zircons with younger ages from the Montoume IMR have the highest contents of U (up to 2244.58 ppm) of all samples. Likewise, zircons that yielded the 361 ± 1 Ma age for the Exideuil amphibolite display the highest contents of Th (up to 1799.78 ppm) and Th/U ratios (2.06) of all grains analyzed. In general, the stronger scattering for zircon of younger age is related to zircon populations with more heterogeneous textures. Zircons with Ordovician or older ages generally are from more homogeneous populations, characterized by lower U and Th abundances. Higher values of U and Th in younger zircons in both IMR are related to zircon populations with homogeneous or faint zonation with very weak intensities in CL images. These ages are also registered in zircons with brighter tones in CL images, with more evident oscillatory zoning, and with lower values of U and Th. In the Exideuil amphibolite, the population of zircons yielding the 361 ± 1 Ma age does not show a systematic variation of the U, Th, or Th/U values depending on the texture of the grains.

Radiation doses were calculated according to Murakami et al. (1991). The values show that all analyzed grains, for all samples, are within the range from 1.93×10^{16} to 2.34×10^{18} α-decay events/g. These values tend to be higher for younger ages in the Exideuil amphibolite sample and in the monzodiorite. For the other samples there is no relationship between radiation dose and age (Fig. SM6c). Furthermore, this range of radiation dose data is below the transition zone of the radiation dose related to transformation of crystalline zircon domains into metamict domains (Ewing et al. 2003).

In addition, the younger zircons of the Montoume IMR and the zircon population yielding the 361 ± 1 Ma age from the Exideuil amphibolite are characterized by higher

values of $f^{206}\%$ than the other zircon age populations of the different samples. However, for both cases, there is a negative correlation between the contents of U and Th and the $f^{206}\%$ value. In contrast, for the Recoudert IMR no systematic variation of the $f^{206}\%$ with zircon age or with the U, Th, and Th/U ratio is observed. This indicates that for none of the samples the higher U, Th, and Th/U values could be related to incorporation of common Pb.

4.6 Discussion

4.6.1 U and Th systematics

4.6.1.1 Possible Metamictization

Loss of radiogenic Pb from zircon can occur under solid-state diffusion at high temperatures (900-1000 °C), by recrystallization, or at lower temperatures, where the effects of radiation damage accumulate. Lead loss may become enhanced in the presence of fluids (e.g., Ewing et al., 2003; Herrmann et al., 2021; Nasdala et al., 2001). Over geologic periods of time, annealing of zircon fission tracks can occur at temperatures as low as 200-250 °C and radiation damage occurs at higher temperatures, generating zircon with higher crystallinity and hampering Pb-loss (e.g., Ginster et al., 2019; Herrmann et al., 2021; Jonckheere et al., 2019). The relationship between younger ages for zircon crystals with higher U and Th contents, as observed for both our IMR samples, has also been observed for zircon from other impact structures (Herrmann et al., 2023; Kenny et al., 2019; Rasmussen et al., 2019; Schwarz et al., 2020; Tartèse et al., 2022). This effect has been associated with comparatively stronger, or even complete, metamictization in such younger zircons. Lead loss is facilitated when such crystals are affected by weathering or hydrothermal alteration. These crystals can display highly discordant U-Pb dates and high contents of common Pb, Y, and REE (e.g., Andersen & Elburg, 2021; Geisler et al., 2003).

To evaluate the possibly metamict character of our analyzed zircon, the values of common Pb and radiation doses are evaluated here against apparent $^{206}Pb/^{238}U$

ages (Fig. SM6c). The low values of common Pb, the absence of any relationship between common Pb and the U and Th contents, and minor lattice damage of all zircons with a 7/5:6/8 discordance lower than 10 % indicate that these crystals have not suffered significant perturbation of the U-Pb system since crystallization. Textural features indicative of impact-induced Pb-loss are found in some zircon with granular texture from the IMRs. A better characterization of these zircons, with a higher spatial resolution, would be needed to identify metamict domains in such crystals. However, with the information available at present, the most probable interpretation is that none of the concordant zircons analyzed so far underwent Pb diffusion at lower P-T conditions due to local metamictization.

4.6.1.2 Significance of the U and Th contents and Th/U ratios

In contrast to the U and Th concentrations in zircon, which can be widely variable, the Th/U ratio may be useful for understanding the growth process of zircon (e.g., Hoskin & Schaltegger, 2003; Kirkland et al., 2015; Rubatto et al., 2017; Wang et al., 2011). Most of our zircon crystals record Th/U values > 0.1, a value normally attributed to igneous zircon and to zircon formed at high to ultrahigh thermal metamorphic conditions (Hoskin & Schaltegger, 2003; Rubatto et al., 2017; Wang et al., 2011). This is consistent with the absence of Th-rich phases in these rocks, which would sequester Th from zircon at low-temperature metamorphism (Kohn et al., 2015; Rubatto et al., 2017). For the monzodiorite and the paragneiss, most of the zircon crystals show oscillatory zoning, besides a low proportion of zircons with overgrowth rims or sector zoning. This, along with the composition of the crystals, suggests that most of these zircons record crystallization ages; either autocrystic, formed from the host melt; inherited, as xenocrysts derived from country rock; or antecrysts, if they were formed during earlier phases of magmatism (e.g., Siégel et al., 2018).

The zircon crystals from the amphibolite from Exideuil show a greater proportion of crystals with an irregular or faint zonation, which could indicate some metamorphic disturbance of the primary texture, which is only partially preserved (Corfu et al., 2003; Hoskin & Schaltegger, 2003). For the St. Junien amphibolite most of the zircons show core-rim textures. These cores and rims display a great variety of

textures and dimensions. Some crystals have regular oscillatory zoning in both core and rim, delimited by resorption borders where the zoning pattern of the core is truncated. Other crystals display more irregular textures, with evidence of recrystallization, convolute zoning, or sector zoning at rims and/or in cores of the crystals. This reflects that the effects of metamorphism in the zircons are heterogenous, with some zircons displaying obvious metamorphic textures and others preserving original igneous textures. Most analyses of cores and rims of crystals with either igneous or metamorphic textures register similar ages and Th/U ratios > 0.1. This may indicate that the isotopic system and the composition of the analyzed zircons were not altered during metamorphism.

Some samples have heterogeneous zircon compositions and different ages within groups of crystals with similar textural characteristics. A similar decoupling of zircon textures from U and Th contents and dates was reported for zircons from granulite facies or ultrahigh temperature metamorphism (e.g., Kunz et al., 2018; Whitehouse et al., 2014). The mechanism causing decoupling of U-Pb ages and trace element geochemistry is not well understood. Effects such as metamictization, hydrothermal alteration, and plastic deformation have been variably discussed as possible causes for such disturbances (Piazolo et al., 2016; Rubatto, 2017). As there is no evidence to support metamictization or fluid alteration, we favor that possible variations of zircon compositions and ages within groups of similar textures could be the result of mixed zone analysis or related to unknown variations in the formation conditions of the crystals.

4.6.2 The basement to the Rochechouart impact structure

The 4 basement rocks of this study from the Rochechouart area gave a great diversity of zircon U-Pb ages, ranging from the Neoproterozoic to the Permian (Figure 4.6).

Paragneiss

The 565 and 522 Ma age peaks obtained in the paragneiss sample can largely be correlated with previous chronological results from samples of LGU and UGU paragneisses derived from ~35 km to the southwest of the structure (Melleton et al.,

2010). Our data and the reported ages of 573 ± 12 Ma and 523 ± 4 Ma (Melleton et al., 2010) are interpreted to represent maximum depositional ages for these lithologies, based on the youngest age detected on detrital zircon to constrain depositional age (e.g., Vermeesch, 2021).

Amphibolites

Our two amphibolite samples gave Neoproterozoic, Ordovician, and Devonian ages, with very similar Neoproterozoic (567 ± 3 and 597 ± 3 Ma) and Ordovician ages (448 ± 3 and 449 ± 3 Ma). Although these ages are based on relatively small numbers of analyses, the zircons share textural characteristics. The Neoproterozoic ages were obtained on zircons with sector or patchy zonation or in inherited cores that also have sector zoning. All these zircon grains register low U, Th, and Th/U values. The Ordovician ages were mostly obtained on zircons with inherited cores. These ages, although poorly constrained by numbers of analyses, seem to correlate with similar Cambrian-Silurian ages for mafic igneous protoliths reported from other areas of the Limousin (Chèvremont et al., 1996).

The Middle Devonian concordia age (388 ± 1 Ma) obtained here for the St Junien amphibolite is within the range of ages for exhumation, retrogression, and migmatization of UGU eclogites from the Limousin at 389-370 Ma (e.g, Berger et al., 2010; Costa, 1992; Duthou et al., 1994; Faure et al., 2008). Most of our zircons that yielded such ages have inherited cores or sector zoning, and highly variable Th contents. The Late Devonian concordia age (361 ± 1 Ma) for the Exideuil amphibolite is similar to the 357 ± 4 Ma and 365 ± 5 Ma for paragneisses and orthogneisses of the LGU, and 362 ± 4 Ma for paragneisses of the UGU, attributed to the major period of continental collision of the Variscan Orogeny, followed by rapid exhumation and cooling between 360 and 350 Ma (Melleton et al., 2009). Furthermore, these ages are coeval with the anatectic episode reported for the region of the Limousin for diatexites from d'Oradour-sur-Gane and a granite from Cieux-Vaulry at 375 ± 6 Ma and 352 ± 12 Ma, respectively (Rb-Sr dating by Duthou, 1977, as cited in Duthou et al., 1984). The 361 ± 1 and 328 ± 1 Ma ages of the Exideuil amphibolite were

recorded mostly on zoned or homogeneous crystals of highly variable U and Th values.

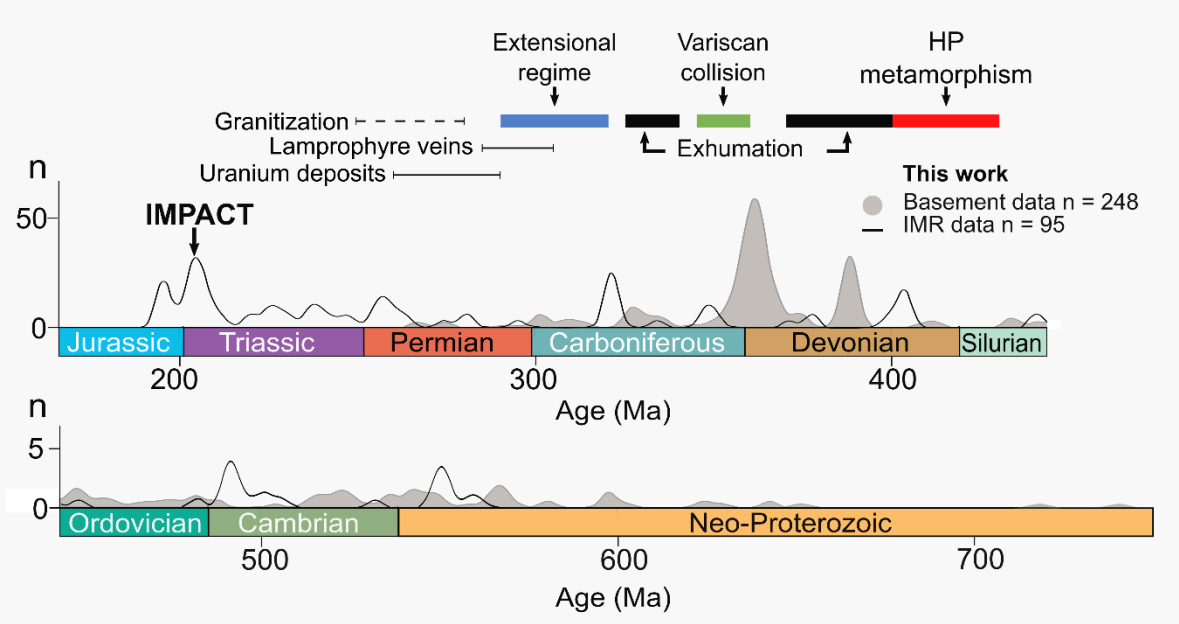


Figure 4.6 Kernel density plot for the results from this study, for Neoproterozoic to Ordovician (lower part) and Silurian to -Jurassic (upper part) times. Only data with 7/5:6/8 discordance less than 10 % have been considered. The upper colored bars refer to major events constrained in the geologic evolution of the French Massif Central (after Lardeaux, 2014). The granitization phase is after Reimold et al. (1987) and lamprophyre formation as discussed in the text. Plot made with Detrital Py v. 1.3 (Sharman et al., 2018).

Monzodiorite

The monzodiorite has Neoproterozoic to Permian zircons. Some of the Neoproterozoic-Silurian ages (481, 457, 438 Ma age peaks) can be compared with ages obtained in the amphibolites (597, 567, 449 Ma age peaks) with also low values of U and Th; however, in the monzodiorite, the related zircons display oscillatory zoning with strong CL intensities. These ages are interpreted as the magmatic crystallization ages of inherited zircons, which are similar to the Precambrian and early Paleozoic protolith ages of the metamorphic rocks analyzed here and in other metamorphic rocks from elsewhere in the Limousin: magmatic emplacement ages of orthogneisses of the LGU, like the Tulle and Aubazine orthogneisses to the south (475-470 ± 11 Ma; Melleton et al., 2010) and the Thaurion orthogneiss to the west (457 ± 23 Ma; Alexandre, 2007) of the impact structure. The younger Carboniferous age peaks were registered in heterogeneously zoned grains. These ages fall between the periods of collisional and post-collisional extension, exhumation, and

magmatism of the FMC, as constrained by U-Pb on zircon and monazite, and $^{40}Ar/^{39}Ar$ analyses on muscovite and biotite from granitoids of the Blond-Vaulry area of the Limousin (De Veslud et al., 2013, and references therein), and U-Pb dating on monazite and zircon of the Guéret and Millevaches massifs (Cartannaz et al., 2007).

The monzodiorite also provided a weighted average age of 272 ± 12 Ma obtained for 3 crystals with oscillatory zoning textures. Even though this is a result for a small number of zircons, this is the only basement rock of this study with zircons yielding ages younger than 300 Ma. Our results provide the first report of post-Variscan U-Pb on zircon ages for basement rocks from the area of the impact structure. Other reports of post-Variscan ages have been made for granites, pegmatites, and microgranites from the basement of the Rochechouart impact structure based on Rb-Sr and K-Ar analyses (Lambert, 1974; Reimold et al., 1983). Reimold et al. (1983) proposed a post-Variscan granitization phase in the Haut-Limousin at 280 to 250 Ma. However, this has not been reported from other parts of the FMC, and the geological evolution of the basement to the impact structure has been generally considered to have been complete by 300 Ma (e.g., Lambert, 2010). However, the results obtained for the monzodiorite might indicate that the magmatic activity of the FMC basement in this region could have lasted longer.

Dating of lamprophyre veins from the St.-Sylvestre leucogranite massif and the St.-Yrieix-la-Perche region yielded ages of 295 ± 10 Ma and 290 ± 5 Ma, respectively (Chalier et al., 1994; Leroy & Sonnet, 1976). The St.-Sylvestre massif also has low-temperature uranium deposits that were dated by U-Pb isotope analysis to 280 Ma (Cathelineau et al., 1990). This deposit is part of a phase of major U deposition at 290-260 Ma in the FMC, associated with late brittle deformation and major shear zone development. The 272 ± 12 Ma age obtained for our sample could be interpreted as the age of crystallization of the monzodiorite in a post-orogenic extensional phase, coeval with these lamprophyre emplacements.

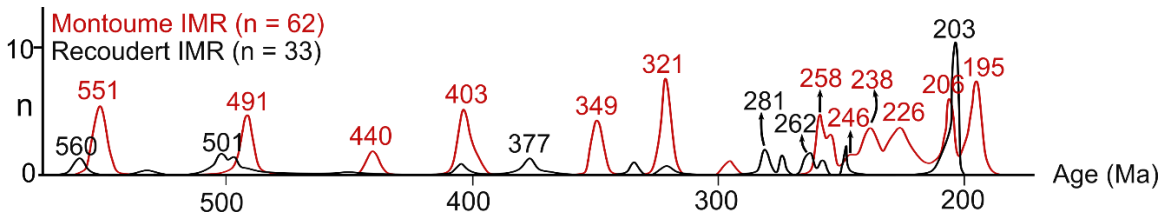


Figure 4.7 Probability density plot for the results from this study for the Montoume and Recoudert IMRs. Only data with 7/ 5:6/8 discordance less than 10 % have been considered. Plot made with Detrital Py v. 1.3 (Sharman et al., 2018).

4.6.3 U-Pb on zircon results for the impact melt rocks

The zircon crystals from the Montoume IMR record a greater diversity of ages than those from the Recoudert IMR. Montoume IMR zircons yield ages from the Neoproterozoic to the Jurassic and lack ages for the Ordovician, whereas the Recoudert IMR zircons give ages from the Neoproterozoic to the Triassic, lacking ages for both the Ordovician and Silurian. Both IMRs gave similar Neoproterozoic (551 Ma and 560 Ma), Cambrian (491 Ma and 501 Ma), Permian (258 Ma and 262 Ma), and Triassic ages (206 Ma and 203 Ma) (Figure 4.7). Overall, correlation between optical and CL characteristics of the zircon populations yielding these similar ages from these two samples is poor (Figure 4.9a and SM 5).

This pattern of similar ages for different types of zircons from both IMRs could be related to different scenarios: 1) Different protoliths yielding the same ages but with different types of zircon that later were collectively included into the impact melt. 2) In the case of zircon with different shock metamorphic textures, common protoliths to both IMRs were affected by different pressure and temperature conditions during the impact event. In this case, the behavior of the U-Pb isotopic system would have been similar for zircons from both samples to still register similar ages. 3) The first and the second process could have occurred together. However, we note that some of these age peaks are based on data from only 2 or 3 zircon grains, so that the age significance should be evaluated with caution.

For the Recoudert sample the larger crystals, and those with granular texture yielded the youngest ages. In the case of the Montoume sample, the larger, reddish crystals showed comparatively more diverse CL characteristics and gave heterogeneous

ages (Figure 4.9). To better interpret the ages recorded by these reddish crystals some BSE images of zircon were obtained (Figure 4.2). A large proportion of the zircons from the Recoudert sample are granular, with homogeneous textures in CL images. Granular zircons can be produced in a wide variety of settings, and for a better characterization of their possible origin, was planned for the future a detailed textural analysis by EBSD (e.g., Cavosie et al., 2018; Kovaleva, 2020; Timms et al., 2017; Wittmann et al., 2006). Furthermore, the bright spots observed for the granular crystals of both impact melt rocks (Figure 4.2i and k) may represent baddeleyite crystals. Baddeleyite crystals could form by dissociation of zircon to ZrO_2 and SiO_2 under high temperatures alone or from shock decompression (Timms et al., 2017).

Recently, textural characterization of zircon with SEM and EBSD analysis from the Chassenon suevite deposit and the Babaudus yellow impact melt rock reported both reidite and FRIGN zircon (Plan et al., 2021; Rasmussen et al., 2020). This indicates shock pressures for such zircon > 30 GPa (Cavosie et al., 2018; Timms et al., 2017). Both types of shocked zircon can display granular textures. In a number of impact structures, FRIGN zircon has been shown to preserve the age of the impact event (Hauser et al., 2019; Kenny et al., 2019; Rasmussen et al., 2020). However, crystals with a less developed granular texture may be associated with radiation damage, and might yield post-impact ages (Rasmussen et al., 2020). Neither the apparently unshocked, nor the shocked granular, crystals (classified with CL and BSE images) show evidence of metamictization, so this process does not seem to apply to our results.

The crystals from the Montoume IMR that have a low level of shock metamorphism as seen in BSE imaging (Figure 4.2), show a great diversity of ages (Neoproterozoic to post-impact). Granular crystals record a wide variety of Devonian / Carboniferous to Jurassic ages. The older ages are obtained in granular crystals with a faint zonation in the CL images, whereas granular homogeneous crystals yielded the age of impact and may correspond to the highest shock level. As the reddish crystals of this sample have very diverse textures in CL, there is at present no clear correlation with the results for reddish grains and the level of shock deformation.

Previously, U-Pb ages ranging from 487 ± 7 to 194 ± 2.9 Ma on an impact melt rock sample from Babaudus (Fig. 9a; Rasmussen et al., 2020) obtained in zircon of different levels of shock deformation (as determined by EBSD) were interpreted (at least some) as possibly reflecting regional tectonics. Guerrero et al. (2024) recently presented preliminary U-Pb on zircon data for a sample from the Babaudus IMR and two suevite samples from Videix and Chassenon. They referred kernel density estimations with age peaks from 538 to 236 Ma. The majority of the ages for the two suevites are pre-Variscan, whereas for the Babaudus IMR most of the zircon ages are closer to the impact age.

The zircons from the two impact melt rocks analyzed here are very different. For the Recoudert sample most of the grains yielding pre-Permian ages apparently do not show evidence of shock deformation and probably reflect pre-impact regional tectonics. However, the zircons from the Montoume sample are more heterogeneous; and both the reddish and colorless crystals register very heterogeneous ages. Therefore, to understand the significance of these ages is challenging. However, it is still possible to relate some age groups to specific, well constrained stages in the evolution of the FMC (Figure 4.6), as discussed in the next section.

4.6.4 Provenance analysis (Comparison of zircon ages from impact melt rock and possible protoliths)

The spectrum of currently available zircon ages for Rochechouart impact melt rock cannot be well correlated with the ages for our basement rocks (Figure 4.6). This is further confirmed with the application of a multi-dimensional scaling (MDS; Figure 4.8) model (Vermeesch, 2018b), where the two impact melt rock samples cluster because of their similar age distributions, but at the same time, these samples are isolated from the basement lithologies. This shows the low level of correlation between the geochronologic results between these IMRs and basement lithologies, where the most important age peaks registered for the basement lithologies are not represented by the two IMRs.

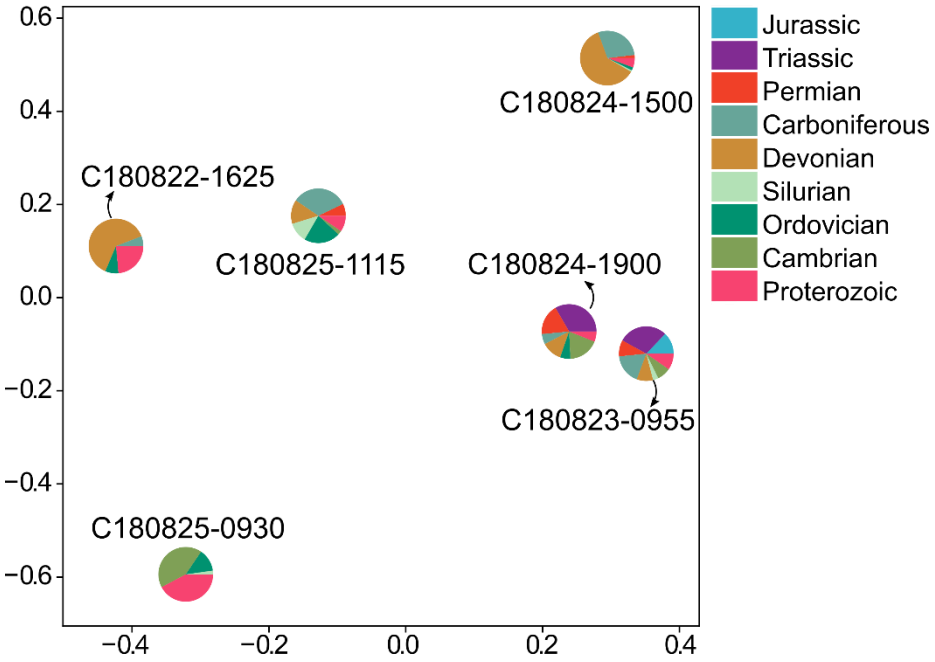


Figure 4.8 Multi-dimensional scaling (MDS) model for the samples of this study. The model was calculated with the Kolmogorov-Smirnov D statistic dissimilarity method (Vermeesch, 2018b). Distances between the sample locations is proportional to the dissimilarity between their U-Pb age distributions (Vermeesch et al., 2018b). The pie plots represent the age distributions obtained for the various samples. The plot was done with the Detrital Py v. 1.3software (Sharman et al., 2018).

The monzodiorite is the only basement sample that registers a few zircon ages also observed for the two IMRs, especially for the Montoume sample. However, the principal age peaks of the IMRs (e.g., 321, 349, 403 Ma) are not represented in the monzodiorite zircon population either, with a common offset of some 10 Ma between the principal ages obtained in these samples. The 438 and 481 Ma age peaks are the only ones older than 300 Ma registered by the monzodiorite that can be directly correlated to ages observed for the IMRs, i.e., the age peaks at 440 Ma for the Montoume IMR and at 487 ± 7 Ma for the Babaudus IMR (Rasmussen et al., 2020). The zircon populations yielding these ages in the monzodiorite are heterogeneous. The crystals that yielded similar ages for the Montoume IMR and the monzodiorite display fine oscillatory zoning textures and weak CL intensities. Most of these crystals have U and Th contents lower than 500 ppm and 200 ppm, respectively, and Th/U ratios lower than 0.6. Therefore, it is possible that these zircon populations represent inherited zircon that shared a similar evolution and could also have come from the same protolith(s). The zircon crystal of 487 ± 7 Ma age of the Babaudus IMR (Rasmussen et al., 2020) was described with irregular zoning in CL and U contents < 170 ppm. In the monzodiorite sample, the crystals that gave the 490 Ma

age display different oscillatory zoning patterns and most of them have U contents < 200 ppm. Overall, with this information available at present it is difficult to establish a relationship between the Babaudus IMR and the monzodiorite.

Most of the post-Variscan ages for zircon from our impact melt rocks and the Babaudus sample of Rasmussen et al. (2020) can be correlated with post-Variscan K-Ar and Rb-Sr ages for granitic rocks of the basement of the impact structure (Lambert, 1974; Reimold et al., 1983; Reimold & Oskierski, 1987). However, these post-Variscan ages for target rocks have been attributed to disturbances in the isotopic systems of local samples, as similar ages have not been reported from elsewhere in the FMC (Lambert, 2010). The rocks analyzed by earlier authors were not studied with other isotopic systems; therefore, the relationship between those lithologies and the impact melt rock data remains to be tested further.

As noted above, the tectonomagmatic evolution of the FMC is thought to have only lasted until about 300 Ma in this region (Kelley & Spray, 1997; Lambert, 2010). Our monzodiorite sample yielded first U-Pb ages younger than 300 Ma for basement of the impact area, suggestive of magmatism in this region until 272 ± 12 Ma. Similar post-Variscan ages have been obtained for our Recoudert IMR (262 to 281 Ma). Most of these zircons have granular texture, and all of them have lower U and Th contents than the post-Variscan zircons from the monzodiorite. Although zircons from both samples record similar ages, the implicated zircon crystals correspond to different textural populations.

The age peaks > 300 Ma for the IMRs could be attributed to zircon from other basement lithologies that so far have not been analyzed yet and might register ages corresponding to other stages in the evolution of the FMC. IMR zircons with Cambrian to Silurian ages could be derived from protoliths that register ages similar to the 495 ± 8 and 451 ± 5 Ma ages for orthogneiss in other areas of the Limousin (U-Pb chronology; Lafon, 1986; Melleton et al., 2010). Similarly, IMR zircon could also be derived from protoliths registering other events documented in the FMC, such as the Devonian HP metamorphic phase or the final Late Carboniferous exhumation period.

A possible explanation for the post-300 Ma ages for zircon from both IMRs is that there is another lithology in the pre-impact basement that may only have minor representation in the currently accessible target rock suite. This has been documented for other impact structures, where age populations not previously identified in the target rocks were attributed to an unknown pre-impact material (e.g., at Sudbury: Petrus et al., 2016). We intend to analyze further target rocks from the Rochechouart area, such as the leptynitic gneisses and paragneisses, part of the UGU, and the granitoids that intrude the metamorphic rocks. In particular, granitic lithologies that are interpreted as part of the anatectic period around 315-305 Ma in other parts of the Limousin (Rb/Sr data; Duthou, 1977, as cited in Duthou et al., 1984), must still be analyzed by U-Pb on zircon chronology for the Rochechouart area.

Furthermore, comparing these geochronologic results with previous geochemical results that suggested that the impactite compositions represented good reflections of the local target rocks (Lambert, 1977a, 2010), the poor level of correlation of the geochronological data between the basement lithologies and the impact melt rocks could imply that the granite and gneisses that are below the IMRs (based on the SC16 and SC17 drill-cores) are not represented in the geochronologic results of the samples of this study or that the correlation with geochemical results is not correct and other lithologies were melted during the formation of the IMRs. For both cases more basement rocks are to be analyzed. Another possibility would be that the ages of zircons from the basement were modified during the impact event and are no longer preserved. However, this seems more unlikely, at least for the zircons with ages >300 Ma, as most of these crystals do not show strong shock metamorphism.

4.6.5 The age of the Rochechouart impact

The youngest age obtained by us for the Recoudert impact melt rock (204 ± 1 Ma) and one of the youngest ages of the Montoume sample (206 ± 2 Ma) are similar to previous U-Pb results for zircon from the Babaudus impact melt rock of 204 ± 2.2 and 207 ± 3.6 Ma (Rasmussen et al., 2020). They are also similar to the currently most widely accepted age for the Rochechouart impact event of 206.92 +0.20 / -0.32

Ma ($^{40}Ar/^{39}Ar$; Cohen et al., 2017). Our results and the data by Rasmussen et al. (2020) were plotted together, as they all result from U-Pb on zircon analysis (Figure 4.9). For the combined data set two TuffZirc ages could be calculated, to 203.83 +2.19/-0.62 Ma and 194.93 +1.19/-0.93 Ma (Figure 4.9b). The former is also very similar to the age for the impact event by Cohen et al. (2017). The zircons from which we obtained our impact ages from both samples are mostly reddish, granular, and with homogeneous or zoned CL textures (Figure 4.9b-d). These grains probably correspond to recrystallized (neoblastic) crystals, the isotopic system of which was fully reset during the impact event.

The Jurassic age of 196 ± 2 Ma for the Montoume IMR was obtained on crystals that mostly are colorless, homogeneous in BSE images, and homogeneous or zoned in CL (Figure 4.9b-d). These crystals may correspond to neoformed zircon crystals or inherited crystals with heterogeneous Pb-loss. This young age is comparable to Rasmussen et al.´s (2020) U-Pb age of 194 ± 2.9 Ma from one zircon from Babaudus IMR, and to the (U-Th)/He age from Horne (2016) of 191.6 ± 9.1 Ma for zircon from Montoume and Babaudus impact melt rocks. This group of relatively young, apparently post-impact ages was interpreted by Rasmussen et al. (2020) as the result of possible Pb-loss from a metamict crystal, which was caused by an unknown post-impact thermal event.

We have shown that none of our analyzed zircons was seemingly affected by significant radiation damage. In the case of zircon with post-impact age from the Montoume sample a post-impact thermal/hydrothermal event with temperatures of at least ~900 °C may have resulted in Pb-loss (Cherniak & Watson, 2001). There are multiple hydrothermal veins cutting the basement rocks of the Rochechouart impact structure, and the impactites are extensively altered. Absolute ages for this vein-forming event are not available but it could be argued that post-impact thermal/hydrothermal processes could have resulted in some Pb loss and age resetting. It is, however, doubtful that temperatures of more or less than 900°C could have affected the area of the impact structure at a time of 10 Ma after impact.

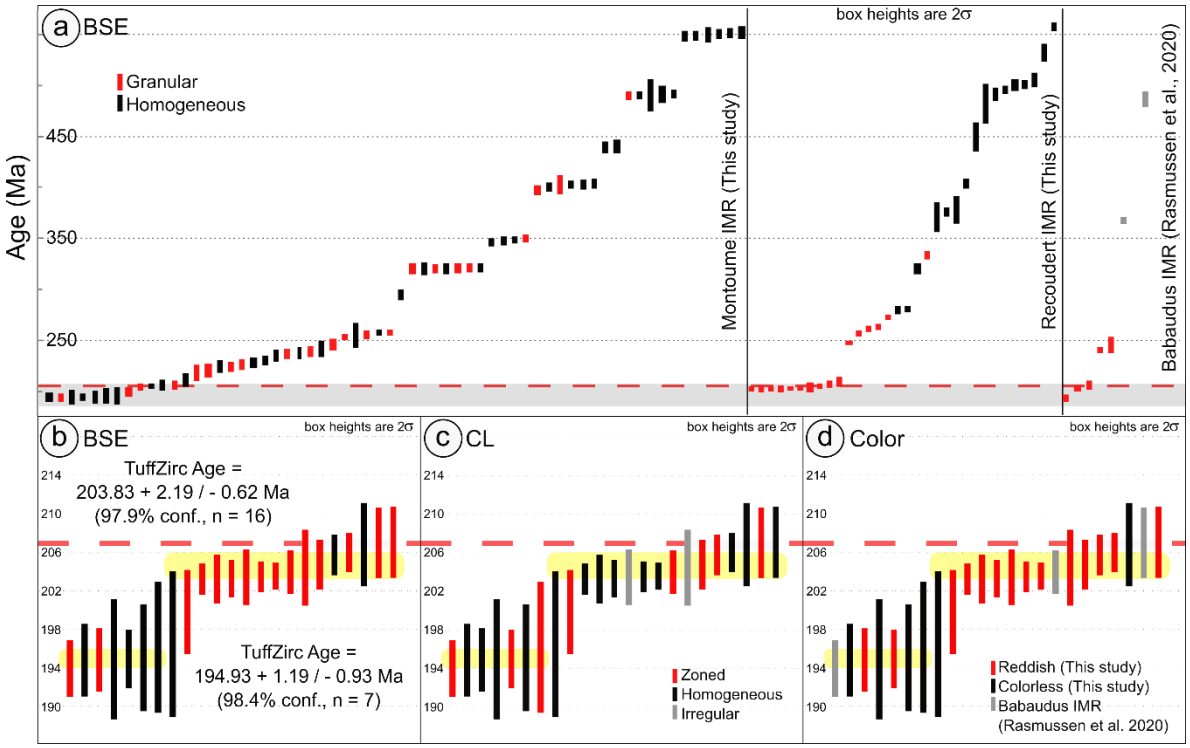


Figure 4.9 (a) Distribution of U-Pb zircon ages for the Montoume and Recoudert impact melt rocks analyzed in this study and the Babaudus impact melt rock analyzed by Rasmussen et al. (2020). Dashed red line at 206.92 + 0.20/-0.32 Ma corresponds to the 40Ar/39Ar age for the impact event by Cohen et al. (2017). The bars in the grayish region are shown in diagrams b, c, and d. (b) TuffZirc age plot (Isoplot v. 4.15; Vermeesch, 2018a) for the youngest ages reported for all the IMRs. Diagrams (a) and (b) categorize the crystals with different zircon textures observed in BSE images, and diagrams (c) and (d) show the zircon classifications based on CL and optical characteristics of the crystals.

4.7 Conclusions

U-Pb isotope analysis by LA-MC-ICP-MS has been conducted on zircon from two impact melt rocks and four basement lithologies from the Rochechouart impact structure. These results represent the first part of a comprehensive U-Pb on zircon isotope study of the most important target lithologies and impactites of this impact structure. Main results achieved so far are:

- The U-Pb zircon ages from a monzodiorite, a paragneiss, and two amphibolite samples from the basement of the French Massif Central in the area of the Rochechouart impact structure can only in part be correlated with results of previous geochronology related to the Variscan geodynamic evolution of the FMC.
- There is poor correlation between the zircon age populations of these basement rocks and zircon ages from two impact melt rock (IMR) samples

from Montoume and Recoudert, and data for another IMR sample from Babaudus (Rasmussen et al., 2020). This indicates the necessity of analyzing more basement lithologies from the Rochechouart area, such as the gneisses of the Upper Gneiss Unit (UGU) and the other granitoids, to eventually obtain a more complete database to better assess the zircon provenance registered in impact melt rock and determine if the previous existence of a basement rock no longer preserved in the impact structure may be possible.

- The geochronologic results presented here can be complemented with other types of analyses (e.g., whole rock geochemistry and Sr, Sm-Nd, and trace elements, REE, and Lu-Hf in zircon) to better track the most probable protoliths for each type of impactite.
- Zircon from the two IMR samples and the monzodiorite register ages younger than 300 Ma, which is widely considered the end of the Variscan evolution of the FMC. The post-300 Ma ages obtained so far cannot be explained by Pb-loss along metamict domains, as all analyzed zircon records low radiation doses. The few < 300 Ma ages obtained may reflect an unconstrained, likely magmatic event that generated zircon not previously analyzed in the impact area.
- Ages that can be correlated with the current best estimate of the impact age are recorded in just a small fraction of zircon grains from the two IMRs. These zircon crystals mostly have a reddish coloration in both IMRs and have variably homogeneous or zoned textures. Most of these crystals have a granular texture, which indicates that the original crystals were converted at high temperature to neoblastic zircon.
- Most of the zircons from the two IMRs record pre-impact ages, clearly supporting what has been noted for other impact structures (e.g., Moser et al., 2011; Petrus et al., 2016). U-Pb systematics of zircon from protoliths to impact melt are preserved through the impact melting process.
- A few zircon crystals from IMR record ages of ~204 and ~206 Ma, which are indistinguishable within errors from the currently favored age of the Rochechouart impact event. Several even younger post-impact ages were

also obtained and may reflect a to date unconstrained post-impact thermal or hydrothermal event.

Acknowledgements -- The authors are grateful to the University of Brasília and to the laboratory teams that helped with data acquisition. Funding for this study has been provided by the Conselho Nacional de Desenvolvimento Científico e Tecnológico (CNPq) through grant No. 140048/2022-7, a grant from the Barringer Family Fund for Meteorite Impact Research, and a CIRIR Career Development Award, all to DG. This study was financed in part by the Coordenação de Aperfeiçoamento de Pessoal de Nível Superior - Brasil (CAPES) - Finance Code 001. The research of Natalia Hauser and Wolf Uwe Reimold has been supported by Bolsa de Produtividade grants (Nos 309878/2019-5 and 305761/2019-6, respectively) from CNPq. The authors also thank Axel Wittmann and Raiza Quintero for their valuable comments, and the associated editor Christian Koeberl for his advice.

4.8 Supplementary material

Table SM1a. Description of the impactites of the Rochechouart impact structure (using information from Lambert, 1977a, 2010; Sapers et al., 2014).

Impactite type	Description	Compositional similarity to basement
Polymict lithic impact breccia ("Rochechouart breccia")	Quartzofeldspathic lithic and mineral clasts of variable shock levels in a fine-grained, clastic matrix – clast – supported.	Granitic gneiss of the basement
Melt-bearing impact breccia ("Chassenon suevite")	~ 50 vol% of clastic matrix; contains irregularly shaped, variegated glass clasts.	Gneiss
Transitional melt-rich impactite ("Vallette-type breccia")	Purple, quartzo-felspathic melt matrix, glass clasts and melt content between < 10 and > 60 vol%; lithic and mineral clasts of varied shock levels.	Granite
Impact melt rock ("Montoume breccia")	Clast-rich impact melt breccia with a red to gray-brown crystalline melt matrix (50 to 70 vol%), with flow features and mineral, lithic, and glass clasts.	Granitoid, gneisses and leptynite
Impact melt rock ("Babaudus melt")	Yellow, clast-free to clast-poor melt rock with a felsic matrix (up to 99 vol%), rich in vesicles; with a limited content of quartzofeldspathic lithic and mineral clasts.	Locally occurring leptynite
Impactoclastite	Fine-grained, reddish, clastic deposit; lithic and mineral clasts of gneiss and granites, and vitreous debris.	Gneiss and granite

Table SM1b. Radiometric age data for the area of the Limousin of the French Massif Central. UGU= Upper Gneiss Unit, LGU= Lower Gneiss Unit. 1 = Bellot and Roig (2007); 2 = Melleton et al. (2009); 3 = Lafon (1986); 4 = Faure et al. (2005); 5 = Faure et al. (2008); 6 = Boutin et al. (1991); 7 = Costa and Maluski (1988); 8 = Boutin and Montigny (1993); 9 = Berger et al. (2010); 10 = Santallier (1981); 11 = Faure et al. (2009); 12 = Bellot (2001); 13 = Gébelin et al. (2007); 14 = Gébelin et al. (2009); 15 = Gebelin (2004); 16 = Holliger et al. (1986); 17 = Scaillet et al. (1996); 18 = Alexandrov et al. (2000); 19 = De Veslud et al. (2013); 20 = Berthier et al. (1979); 21 = Duthou (1978); 22 = Gebauer et al. (1981); 23 = Cartannaz et al. (2007). All ages in Ma.

Unit	Lithology	Tectonic event				References
		HP metamorphism	Exhumation	Collision	Extension and collapse of the belt	
UGU	Eclogites, granulites	390 - 430	382 ± 5			1
	Paragneiss	390 - 430				1
	Migmatitic Paragneiss			362 ± 4		2
	Migmatite/granulite		382 ± 5, 377 - 387	348.5 ± 4.1	334.3 ± 3.1 - 309.2 ± 2.4	1, 3, 4, 5
	Amphibolites		380 - 370, 381 ± 5, 389 ± 8, 383 ± 8, 385 ± 8			6, 7, 8
LGU	Eclogites	390 - 430, 412 ± 10	382 ± 5, 382 ± 7	352 ± 7, 352 ± 2	332 - 336, 335 - 337	1, 9, 10
	Paragneiss			359 ± 2		2
	Orthogneiss			357 ± 4, 365 ± 5		2
	Migmatitic gneiss		378 - 374 ± 5		332 ± 337 - 335, 317 ± 1, 316 ± 2 - 315 ± 4	5, 12, 13
	Migmatite		370 - 385	349 - 359		5, 11, 14
Granites	Synkinematic Leucogranites (Padrines fault)			350	313 ± 4	15
	Limousin-type granite (Blond)				335.9 ± 0.8, 310.7 ± 0.5, 319 ± 7, 315 - 305, 324 ± 4, 315 - 300	16, 17, 18, 19
	Guéret granite (Thaurion)			356 ± 10, 353 ± 6, 351 ± 5, 346 ± 14	324 ± 1	20, 21, 22, 23
	St Sylvestre granite (Thaurion)				308.3 ± 0.3	19

Table SM1c. Post-Variscan age data for the basement rocks of the Rochechouart impact structure. 1 = Lambert (1974); 2 = Reimold et al., (1983); 3 = Reimold et al. (1987). a: feldspar; b: biotite. Ages in Ma.

Lithology	Method	Ages	Reference
Leptynite	K-Ar	246 ± 10[a], 236 ± 10[b]	1
Breccia enclave	K-Ar	149 ± 7[a], 271 ± 10[b]	1
Gneiss	K-Ar	152 ± 8[a], 262 ± 20[b]	1
Microgranites	K-Ar whole rock	246 ± 10	1
Microgranites	K-Ar whole rock	196 ± 10	1
Augen gneiss	Rb-Sr whole rock	249 ± 38	2
Granite-pegmatite	Rb-Sr whole rock	256 ± 38	2
Three microgranties	Rb-Sr whole rock	265 ± 6	3

Supplementary material 2

Basement rocks

The fine-grained monzodiorite from La Martinie (C180825-1115, 45°49.092'N / 0° 45.488''E) is from a dike cutting LGU gneiss. The outcrop is densely covered by vegetation. The rock is overall homogeneous, cut by only a few fractures, and composed of a black, aphanitic to fine-grained matrix and millimeter-sized, white plagioclase and quartz phenocrysts. Altered surfaces can have reddish and slightly purple coloration, probably due to coatings with Fe and Mn oxides. The sampled block pervasively contains shatter cones of 1–15 cm length. The sample has inequigranular porphyritic texture. Some fractures, sometimes sinuous, are cutting the sample, some of which are partially filled by quartz. The sample is composed of plagioclase (50 vol%), orthoclase (14 vol%), quartz (3 vol%), biotite (20 vol%), and opaque phases (3 vol%), and has accessory zircon, and as alteration products, sericite and chlorite (10 vol%). The phenocrysts are subhedral, fine- to medium-grained crystals of quartz and heavily sericitized feldspars. Some of them are rimmed by chlorite and some have inclusions of quartz, biotite, chlorite, and opaque phases. Inclusions of microgranular quartz are also found in the quartz phenocrysts. One quartz phenocryst has a faint set of decorated PDFs. No other shock deformation has been observed. The matrix is composed of fine- to very fine-grained, mostly lath-shaped feldspar, besides quartz, biotite, chlorite, and opaques. Biotite is anhedral or euhedral, both types of which can be found partially or totally altered to chlorite. The euhedral variety in part displays kink bands. The feldspar in the matrix is significantly altered to sericite but this alteration is less strong than that of the phenocrysts. Opaque phases occur as inclusions in all other phases but are mainly associated with mica.

The paragneiss from Moulin de Laurière (C180825-0930, 45°49.949'N, 0° 46.338'E) was obtained close to the assumed center of the impact structure (Lambert, 2010) in LGU gneiss. In outcrop, the rock is weathered, covered with vegetation, and comprises meter-sized blocks of relatively homogeneous, foliated gneiss with some quartz vein intercalations. The outcrops show little deformation (faults or fractures).

In hand-specimen, the analyzed sample is black, homogeneous, and has a few, several millimeter wide quartz veins. The rock is very fine- to fine-grained and composed of plagioclase (35 vol%), biotite (35 vol%), quartz (26 vol%), and minor orthoclase (2 vol%) and garnet (2 vol%). Accessory minerals are muscovite, apatite, zircon, titanite, opaque phases, and secondary sericite, chlorite, and carbonate. There are quartzofeldspathic aggregates with a granoblastic texture that form irregular bands and lenses with generally larger grain size and minor mica. They are intercalated with lepidoblastic biotite, which sometimes forms pressure shadows around quartzofeldspathic aggregates. Biotite is in large part euhedral and forms aggregates that are partially altered to chlorite, sometimes with minor muscovite. A few kink bands were observed in biotite. Some anhedral biotite follows the foliation. Most feldspar is relatively fresh. Zircon at sizes of ~ 50 µm occurs with the main mineral constituents. Some quartz grains display undulatory extinction, but no further shock effects were noted. Garnet is subhedral, apparently post-kinematic, and rather fractured. An explanation for the overall lack of shock deformation could be that this sample was part of a large block that originally resided significantly below the crater floor and then became uplifted in the course of collapse of the central uplift.

The amphibolite from Exideuil (C180824-1500, 45°53.052'N, 0° 40.842'E) was collected in a quarry ~13 km to the NW of the center of the impact structure – i.e., just outside of the impact structure (compare Fig. 1). The amphibolite is fine-grained, not foliated, and mainly composed of amphibole, plagioclase, and quartz. The rock occurs together with granodiorites of the Tonalite Line of the Limousin (LTL), which intrude the UGU gneisses. The sample is fine- to medium-grained and is composed of amphibole (40 vol%), plagioclase (25 vol%), quartz (10 vol%), orthoclase (10 vol%), opaque phases (5 vol%), and biotite (1 vol%), and has accessory apatite, ilmenite, and zircon, and as alteration products chlorite (8 vol%), and minor sericite and epidote (1 vol%). Amphibole is mostly anhedral and has inclusions of chlorite, quartz, apatite, ilmenite, and zircon. Some amphibole is altered to chlorite and to a lesser proportion to epidote. Feldspar is characterized by a sieve texture where an internal zone altered to sericite is separated from a clear, unaltered border. Zircon is

associated with quartz and amphibole, is euhedral, and has sizes between 50 and 100 μm.

The amphibolite from St Junien (C180822-1625, 45°53.238'N, 0° 53.320'E) was collected in a low road-cut just below the castle wall, along the village thoroughfare. The amphibolite presumably occurs in UGU gneiss. The exposure trends in NW-SE direction. The sample is inequigranular, fine- to medium-grained and has a strong schistosity marked by amphibole and phyllosilicate. The mineral composition is similar to that of the Exideuil sample, with amphibole (30 vol%), plagioclase (30 vol%), orthoclase (16 vol%), quartz (10 vol%), biotite (7 vol%), and opaque phases (3 vol%), as well as minor sericite and chlorite (3 vol%) as alteration products, and as accessory phases epidote, apatite, ilmenite, and zircon. Amphibole is generally anhedral and frequently has inclusions of quartz, feldspar, biotite, chlorite, epidote, apatite, ilmenite, and zircon. Biotite is commonly altered to chlorite. Part of the feldspar is altered to sericite. Feldspars and quartz form granoblastic aggregates. Rare feldspar porphyroblasts may have inclusions of amphibole and ilmenite. At the edge of such grains, biotite occasionally forms pressure shadows. Zircon is subhedral and has sizes between 40 and 60 μm.

Both amphibolites are located ~13-15 km from the apparent center of the impact structure and none of them have unequivocal evidence of shock metamorphism. Minerals in the sample from St Junien have a higher density of microfractures than the ones of the Exideuil sample. These fractures, in general, are irregular, nonplanar, and have subparallel to random orientations. Some euhedral biotite crystals display kink bands but bona fide shock effects are lacking. Quartz in both amphibolites displays some undulatory extinction. The noted features are not shock-diagnostic.

Impact melt rocks

The impact melt rock sample from Recoudert (C180824-1900, 45° 48.349'N, 0° 47.099'E) is generally similar to samples of the impact melt rock from Babaudus previously analyzed by Cohen et al. (2017) and Rasmussen et al. (2020). The sample is clast-poor and has a homogeneous, yellowish groundmass with abundant elongated vesicles filled with quartz and biotite. Clasts are mostly quartz and

sanidine. This type of impact melt rock occurs as isolated occurrences in the central part of the impact structure. The analyzed sample is composed of 85 vol% matrix, 10 vol% lithic and mineral clasts, and 5 vol% amydules. The matrix is aphanitic to microcrystalline and is full of disseminated oxides. Backscattered electron (BSE) images indicate that the matrix contains feldspar micro-laths in an interlocking texture. From the quartz and K-feldspar dominated clast population, quartzofeldspathic precursor lithologies can be deduced. There are toasted quartz clasts and some quartz clasts have one set of PDFs. Multiple sets of PDFs have not been observed. Ballen silica of type 4 according to the classification of Ferrière et al. (2009) and some clasts that are partially isotropic are also present. Feldspar in clasts is devoid of shock deformation. The majority of quartzo-feldspathic clasts are recrystallized to aggregates of mosaic micro-crystals.

The impact melt rock sample from Montoume (C180823-0955, 45° 46.535'N, 0° 46.488'E) is, in contrast, clast-rich and reddish. This type of impact melt rock is mainly found at the tops of some hills in the southern part of the structure, including at the highest point within the impact structure, at Montoume hill, 7.5 km south of the apparent center of the structure. Here the impact melt rock forms a massive, 25 m thick deposit. The rock is heterogeneous, on centimeter to decimeter scales, with respect to populations of lithic, mineral, and recrystallized, former impact glass clasts. Clasts do not show preferred orientation. The sample consists of ca. 75 vol% matrix and 25 vol% of mainly lithic and mineral clasts. In thin section, the matrix is purplish-reddish and displays a pronounced fluidal texture. Lithic clasts are fine-grained and have quartzofeldspathic compositions, with some of them having a gneissic foliation. The matrix contains very fine-grained microliths of mostly quartz and K-feldspar, plus some oxide minerals. Some of the quartz clasts are recrystallized. Foliated clasts are altered in part to reddish oxidic material. There are toasted quartz clasts, and up to two sets of PDFs with different crystallographic orientations have been observed in quartz clasts or quartz of lithic clasts. Ballen silica of type 4 after Ferrière et al. (2009) has been found as well.

Figure SM2 Cross- (a - d) and plane-polarized (e and f) light microphotographs of some shock metamorphic features of the samples of this study. (a) Monzodiorite (C180825-1115) with a phenocryst of quartz in a fine-grained matrix largely composed of microliths. The phenocryst is cut by a sinistral micro-fault (dashed yellow line) and has one set of planar deformation features (PDFs) (a zoom of this feature is shown in b). (c) A clast of ballen silica in the Recoudert impact melt rock (C180824-1900) and (d) a partially isotropic clast (delimited by the dashed red line). (e) Montoume impact melt rock (C180823-0955) with two quartz clasts displaying PDFs, and (f) a clast of ballen silica. Qz - quartz, Bt - biotite, and Pl – plagioclase (Whitney & Evans, 2010).

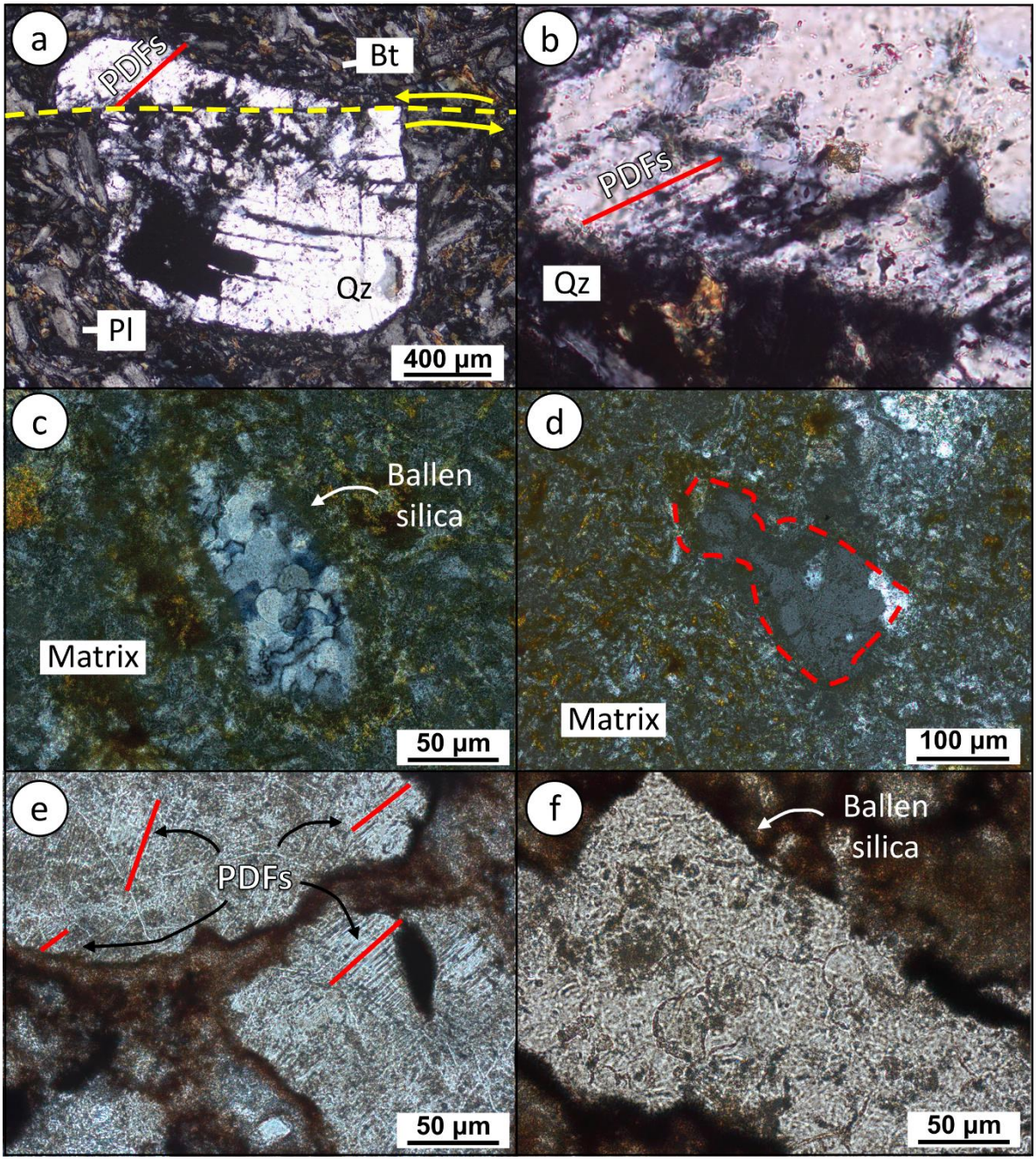


Table SM3 U-Pb on zircon radiogenic data of the samples analyzed in this study.

							Ratios							Dates							
Laboratory	Sample_ID	Analysis_ID	f_{206}	$^{206}Pb/^{204}Pb$	U (ppm)	Th/U	$^{207}Pb/^{206}Pb$	2σ (%)	$^{207}Pb/^{235}U$	2σ (%)	$^{206}Pb/^{238}U$	2σ (%)	Rho	$^{207}Pb/^{235}U$	2σ (abs)	$^{206}Pb/^{238}U$	2σ (abs)	$^{207}Pb/^{206}Pb$	2σ (abs)	Conc.(%)	Corrected for common-Pb
UFOP	C180825-1115	1.sSMPABC148.TXT	0.0	1351	1024	0.4	0.0579	2.4810	0.3376	3.6051	0.0423	2.6157	0.7	295	10	267	7	527	55	90	No
UFOP	C180825-1115	1.sSMPABC108.TXT	0.0	357	741	0.4	0.0575	2.1071	0.3442	5.0970	0.0434	4.6410	0.9	300	14	274	12	510	47	91	No
UFOP	C180825-1115	1.sSMPABC091.TXT	0.0	3873	762	0.3	0.0541	1.6473	0.3259	2.5910	0.0436	1.9999	0.8	286	7	275	5	377	37	96	No
UFOP	C180825-1115	1.sSMPABC112.TXT	0.0	-3841	573	0.2	0.0522	1.7587	0.3424	2.6679	0.0476	2.0061	0.8	299	7	300	6	293	41	100	No
UFOP	C180825-1115	1.sSMPABC119.TXT	0.0	1828	718	0.4	0.0525	2.0956	0.3455	3.1124	0.0477	2.3012	0.7	301	8	301	7	307	48	100	No
UFOP	C180825-1115	1.sSMPABC127.TXT	0.0	700	431	0.6	0.0533	1.9470	0.3516	4.6148	0.0478	4.1839	0.9	306	13	301	12	342	45	98	No
UFOP	C180825-1115	1.sSMPABC090.TXT	0.0	3016	321	0.8	0.0530	2.2424	0.3506	3.5055	0.0479	2.6945	0.8	305	10	302	8	331	52	99	No
UFOP	C180825-1115	1.sSMPABC096.TXT	1.7	311	194	1.3	0.0525	1.9023	0.3545	2.7363	0.0489	1.9668	0.7	308	8	308	6	308	44	100	Yes
UFOP	C180825-1115	1.sSMPABC098.TXT	0.0	2303	1918	0.8	0.0551	8.5330	0.3723	12.5022	0.0490	9.1374	0.7	321	35	308	28	417	203	96	No
UFOP	C180825-1115	1.sSMPABC160.TXT	0.0	2932	527	0.6	0.0525	2.1817	0.3568	2.9978	0.0493	2.0560	0.7	310	8	310	6	307	50	100	No
UFOP	C180825-1115	1.sSMPABC140.TXT	0.0	738	813	0.4	0.0530	1.7901	0.3636	2.8066	0.0498	2.1617	0.8	315	8	313	7	328	41	99	No
UFOP	C180825-1115	1.sSMPABC107.TXT	0.0	1297	337	0.5	0.0532	1.7098	0.3661	2.9078	0.0500	2.3520	0.8	317	8	314	7	335	39	99	No
UFOP	C180825-1115	1.sSMPABC173.TXT	0.0	2161	442	0.7	0.0532	1.5901	0.3816	2.5316	0.0520	1.9700	0.8	328	7	327	6	339	36	100	No
UFOP	C180825-1115	1.sSMPABC113.TXT	0.0	-16710	1017	0.4	0.0531	1.6814	0.3826	2.6333	0.0522	2.0266	0.8	329	8	328	6	333	39	100	No
UFOP	C180825-1115	1.sSMPABC092.TXT	0.0	2444	889	0.5	0.0526	1.5780	0.3864	2.4970	0.0533	1.9352	0.8	332	7	335	6	312	36	101	No
UFOP	C180825-1115	1.sSMPABC117.TXT	0.0	3145	685	0.5	0.0533	1.6332	0.3930	2.5691	0.0534	1.9832	0.8	337	8	336	6	343	37	100	No
UFOP	C180825-1115	1.sSMPABC155.TXT	0.0	3261	629	0.5	0.0537	1.6509	0.4054	2.6466	0.0548	2.0686	0.8	346	8	344	7	356	38	100	No
UFOP	C180825-1115	1.sSMPABC129.TXT	0.0	1156	538	0.6	0.0539	1.6013	0.4241	2.5540	0.0570	1.9897	0.8	359	8	358	7	368	36	100	No
UFOP	C180825-1115	1.sSMPABC118.TXT	0.0	1879	322	0.6	0.0544	1.8101	0.4492	2.7083	0.0599	2.0145	0.7	377	9	375	7	388	41	100	No
UFOP	C180825-1115	1.sSMPABC114.TXT	0.0	59	26	1.2	0.0545	9.5017	0.4609	10.7916	0.0614	5.1163	0.5	385	35	384	19	391	229	100	No
UFOP	C180825-1115	1.sSMPABC149.TXT	0.0	35	28	0.7	0.0542	3.8165	0.4682	4.5438	0.0626	2.4659	0.5	390	15	391	9	381	88	100	No
UFOP	C180825-1115	1.sSMPABC120.TXT	0.0	496	160	1.2	0.0548	1.7283	0.4951	2.6398	0.0655	1.9954	0.8	408	9	409	8	403	39	100	No
UFOP	C180825-1115	1.sSMPABC089.TXT	0.0	576	88	0.8	0.0544	1.8335	0.4946	2.8817	0.0659	2.2232	0.8	408	10	411	9	389	42	101	No
UFOP	C180825-1115	1.sSMPABC159.TXT	0.0	9355	602	0.5	0.0548	1.6189	0.4995	2.5021	0.0661	1.9077	0.8	411	9	413	8	405	37	100	No
UFOP	C180825-1115	1.sSMPABC097.TXT	0.0	541	285	0.8	0.0556	1.6700	0.5330	2.7782	0.0695	2.2202	0.8	434	10	433	9	438	38	100	No
UFOP	C180825-1115	1.sSMPABC139.TXT	0.0	563	195	0.8	0.0552	2.0569	0.5304	3.1221	0.0697	2.3488	0.8	432	11	434	10	421	47	100	No
UFOP	C180825-1115	1.sSMPABC110.TXT	0.0	-3232	125	0.6	0.0557	1.8930	0.5374	2.9400	0.0700	2.2495	0.8	437	11	436	9	439	43	100	No
UFOP	C180825-1115	1.sSMPABC134.TXT	0.0	291	156	0.6	0.0558	1.9526	0.5446	3.0382	0.0708	2.3277	0.8	441	11	441	10	443	44	100	No
UFOP	C180825-1115	1.sSMPABC094.TXT	0.0	185	60	0.7	0.0552	1.8787	0.5394	2.8349	0.0708	2.1231	0.7	438	11	441	9	421	42	101	No
UFOP	C180825-1115	1.sSMPABC147.TXT	0.0	749	358	0.5	0.0554	1.6176	0.5465	2.5632	0.0716	1.9883	0.8	443	10	446	9	428	36	101	No
UFOP	C180825-1115	1.sSMPABC176.TXT	0.0	7719	270	0.9	0.0549	2.1881	0.5524	3.3007	0.0730	2.4711	0.7	447	12	454	11	409	50	102	No
UFOP	C180825-1115	1.sSMPABC168.TXT	0.0	867	518	0.3	0.0575	5.4059	0.5967	6.5708	0.0753	3.7352	0.6	475	26	468	17	509	123	99	No
UFOP	C180825-1115	1.sSMPABC132.TXT	0.0	147	102	0.7	0.0569	2.3228	0.5995	3.5352	0.0764	2.6650	0.8	477	14	475	12	488	52	100	No
UFOP	C180825-1115	1.sSMPABC151.TXT	0.0	201	115	1.0	0.0565	2.8394	0.5995	3.5806	0.0770	2.1814	0.6	477	14	478	10	471	64	100	No
UFOP	C180825-1115	1.sSMPABC174.TXT	0.0	578	370	0.5	0.0573	1.8744	0.6124	3.0867	0.0775	2.4525	0.8	485	12	481	11	502	42	99	No
UFOP	C180825-1115	1.sSMPABC099.TXT	0.0	424	82	1.1	0.0570	2.2680	0.6101	3.0965	0.0776	2.1082	0.7	484	12	482	10	492	51	100	No
UFOP	C180825-1115	1.sSMPABC153.TXT	0.0	492	81	1.0	0.0564	2.9921	0.6038	3.7438	0.0776	2.2503	0.6	480	15	482	10	469	68	100	No
UFOP	C180825-1115	1.sSMPABC135.TXT	0.0	389	186	0.4	0.0565	3.6677	0.6078	4.5141	0.0780	2.6316	0.6	482	18	484	12	473	83	100	No
UFOP	C180825-1115	1.sSMPABC154.TXT	0.0	-1621	168	0.8	0.0580	4.1115	0.6282	5.6032	0.0786	3.8067	0.7	495	23	488	18	529	93	99	No

Table SM3 U-Pb on zircon radiogenic data of the samples analyzed in this study (continuation).

UFOP	C180825-1115	1.sSMPABC116.TXT	0.0	185	54	0.7	0.0594	4.7358	0.6522	10.2649	0.0796	9.1072	0.9	510	42	494	43	583	106	97	No
UFOP	C180825-1115	1.sSMPABC100.TXT	0.0	87	42	1.5	0.0592	4.1553	0.7293	4.9456	0.0893	2.6819	0.5	556	22	551	14	576	93	99	No
UFOP	C180825-1115	1.sSMPABC138.TXT	0.0	17	8	0.8	0.0580	7.1036	0.7538	7.4684	0.0942	2.3057	0.3	570	34	580	13	531	164	102	No
UFOP	C180825-1115	1.sSMPABC093.TXT	0.0	79	38	0.4	0.0601	2.0697	0.8432	3.1376	0.1018	2.3581	0.8	621	15	625	14	606	45	101	No
UFOP	C180825-1115	1.sSMPABC095.TXT	0.0	98	18	1.4	0.0687	2.2285	1.4609	3.0382	0.1542	2.0651	0.7	914	19	924	18	891	47	101	No
UFOP	C180825-1115	1.sSMPABC171.TXT	0.0	477	1054	1.3	0.0769	2.7280	0.2549	6.5986	0.0240	6.0083	0.9	231	14	153	9	1119	55	66	No
UFOP	C180825-1115	1.sSMPABC115.TXT	0.0	572	1005	1.4	0.0695	1.6085	0.2587	3.2086	0.0270	2.7763	0.9	234	7	172	5	914	33	73	No
UFOP	C180825-1115	1.sSMPABC087.TXT	0.0	1051	1176	0.6	0.0603	1.1162	0.2729	2.1932	0.0328	1.8879	0.9	245	5	208	4	614	24	85	No
UFOP	C180825-1115	1.sSMPABC088.TXT	0.0	879	606	1.7	0.0664	1.4945	0.3296	2.3881	0.0360	1.8626	0.8	289	6	228	4	818	32	79	No
UFOP	C180825-1115	1.sSMPABC158.TXT	0.0	775	688	1.0	0.0594	1.1591	0.3048	1.9775	0.0372	1.6022	0.8	270	5	236	4	581	25	87	No
UFOP	C180825-1115	1.sSMPABC128.TXT	0.0	679	377	1.2	0.0606	1.2809	0.3163	2.9815	0.0379	2.6923	0.9	279	8	240	6	623	28	86	No
UFOP	C180825-1115	1.sSMPABC170.TXT	0.0	1246	929	0.5	0.0650	1.3033	0.3858	1.9916	0.0431	1.5059	0.8	331	6	272	4	773	28	82	No
UFOP	C180825-1115	1.sSMPABC133.TXT	0.0	325	117	1.2	0.0760	1.5872	0.4704	2.4465	0.0449	1.8617	0.8	391	8	283	5	1096	32	72	No
UFOP	C180825-1115	1.sSMPABC111.TXT	0.0	1330	1228	1.3	0.0611	1.4796	0.3906	2.6223	0.0463	2.1650	0.8	335	8	292	6	644	32	87	No
UFOP	C180825-1115	1.sSMPABC137.TXT	0.0	-3396	551	0.3	0.0559	1.2461	0.3772	1.9307	0.0489	1.4748	0.8	325	6	308	4	450	28	95	No
UFOP	C180825-1115	1.sSMPABC109.TXT	0.0	2186	323	0.8	0.0658	1.8411	0.4768	2.3663	0.0525	1.4865	0.6	396	8	330	5	802	39	83	No
UFOP	C180825-1115	1.sSMPABC172.TXT	0.0	296	472	0.7	0.0777	2.8247	0.5655	3.3288	0.0528	1.7612	0.5	455	13	332	6	1139	57	73	No
UFOP	C180825-1115	1.sSMPABC136.TXT	0.0	6	8	1.6	0.4739	3.4193	3.4892	7.9633	0.0534	7.1918	0.9	1525	66	335	24	4162	52	22	No
UFOP	C180825-1115	1.sSMPABC131.TXT	0.0	23	17	1.4	0.0924	4.9794	0.6854	5.4173	0.0538	2.1338	0.4	530	23	338	7	1476	98	64	No
UFOP	C180825-1115	1.sSMPABC156.TXT	0.0	-487	163	1.4	0.0652	1.3389	0.5062	2.2007	0.0564	1.7466	0.8	416	8	353	6	779	28	85	No
UFOP	C180825-1115	1.sSMPABC152.TXT	0.0	906	545	0.6	0.0617	1.9895	0.4800	2.5002	0.0564	1.5143	0.6	398	9	354	5	665	43	89	No
UFOP	C180825-1115	1.sSMPABC157.TXT	0.0	420	784	0.1	0.0840	1.1927	0.7355	3.4398	0.0635	3.2264	0.9	560	15	397	12	1292	23	71	No
UFOP	C180825-1115	1.sSMPABC150.TXT	0.0	816	288	0.9	0.0654	2.1174	0.5790	2.6183	0.0643	1.5402	0.6	464	10	401	6	786	45	87	No
UFOP	C180825-1115	1.sSMPABC175.TXT	0.0	401	193	0.8	0.0757	2.5855	0.6796	3.0380	0.0651	1.5952	0.5	527	13	407	6	1088	53	77	No
UFOP	C180825-1115	1.sSMPABC169.TXT	0.0	1601	659	0.2	0.0654	1.2283	0.6245	2.0676	0.0693	1.6632	0.8	493	9	432	7	787	26	88	No
UFOP	C180825-1115	1.sSMPABC132.TXT	0.0	371	201	0.8	0.0571	1.2864	0.5794	1.9621	0.0736	1.4815	0.8	464	8	458	7	495	29	99	No
UFOP	C180825-1115	1.sSMPABC167.TXT	0.0	0	0	-1.0	1.1752	2.0620	18.8446	18.3454	0.1163	18.2292	1.0	3034	197	709	124	5463	29	23	No
UFOP	C180825-0930	1.sSMPABC097.TXT	0.3	566	954	0.1	0.0614	5.6340	0.5885	7.6815	0.0695	5.2214	0.7	469	19	433	15	655	83	92	Yes
UFOP	C180825-0930	1.sSMPABC072.TXT	5.1	37	108	1.0	0.0617	5.3767	0.6139	6.2178	0.0721	3.1227	0.5	486	16	449	9	665	79	92	Yes
UFOP	C180825-0930	1.sSMPABC080.TXT	0.4	495	1024	0.4	0.0561	2.3377	0.5631	3.7347	0.0728	2.9125	0.8	454	14	453	13	457	52	100	No
UFOP	C180825-0930	1.sSMPABC068.TXT	2.3	79	241	0.8	0.0619	2.0334	0.6270	2.6266	0.0734	1.6627	0.6	494	7	457	5	672	29	92	Yes
UFOP	C180825-0930	1.sSMPABC098.TXT	1.6	117	192	0.5	0.0595	2.7324	0.6066	3.2763	0.0739	1.8078	0.6	481	8	460	5	586	40	96	Yes
UFOP	C180825-0930	1.sSMPABC092.TXT	1.7	104	213	0.5	0.0623	1.6937	0.6551	2.2419	0.0762	1.4688	0.7	511	6	474	4	686	24	93	Yes
UFOP	C180825-0930	1.sSMPABC078.TXT	1.7	110	234	0.7	0.0597	2.2809	0.6469	3.9904	0.0786	3.2742	0.8	506	11	488	10	594	33	96	Yes
UFOP	C180825-0930	1.sSMPABC076.TXT	7.6	25	62	0.7	0.0616	4.2387	0.6903	5.0466	0.0813	2.7389	0.5	533	14	504	9	659	62	95	Yes
UFOP	C180825-0930	1.sSMPABC075.TXT	1.1	164	362	0.9	0.0593	1.2044	0.6782	1.7842	0.0829	1.3163	0.7	525	5	513	4	579	18	98	Yes
UFOP	C180825-0930	1.sSMPABC057.TXT	2.4	75	219	0.6	0.0592	4.8118	0.6798	5.8346	0.0833	3.2997	0.6	526	16	516	11	574	71	98	Yes
UFOP	C180825-0930	1.sSMPABC096.TXT	0.8	225	399	0.4	0.0588	1.2636	0.6758	1.7610	0.0834	1.2265	0.7	524	5	517	4	558	18	99	Yes
UFOP	C180825-0930	1.sSMPABC054.TXT	1.2	146	547	0.8	0.0629	3.0572	0.7253	3.8028	0.0837	2.2616	0.6	553	11	518	8	704	44	94	Yes
UFOP	C180825-0930	1.sSMPABC094.TXT	1.5	118	219	0.8	0.0611	1.4346	0.7084	1.8598	0.0841	1.1835	0.6	543	5	521	4	642	21	96	Yes
UFOP	C180825-0930	1.sSMPABC055.TXT	3.8	49	169	0.6	0.0593	1.8253	0.6884	2.2867	0.0842	1.3773	0.6	531	6	521	5	577	27	98	Yes
UFOP	C180825-0930	1.sSMPABC070.TXT	4.4	42	133	0.6	0.0594	2.8492	0.6917	3.7715	0.0844	2.4710	0.7	533	10	522	8	583	42	98	Yes
UFOP	C180825-0930	1.sSMPABC100.TXT	8.2	24	41	0.6	0.0613	8.1470	0.7144	9.3037	0.0846	4.4929	0.5	547	27	523	15	649	121	96	Yes
UFOP	C180825-0930	1.sSMPABC077.TXT	1.4	130	243	0.5	0.0585	1.6333	0.6828	2.0467	0.0846	1.2335	0.6	528	6	524	4	549	24	99	Yes
UFOP	C180825-0930	1.sSMPABC087.TXT	0.3	574	1273	0.1	0.0558	1.6405	0.6508	2.6280	0.0846	2.0530	0.8	509	11	523	10	446	36	103	No
UFOP	C180825-0930	1.sSMPABC099.TXT	1.9	95	157	0.9	0.0614	1.9948	0.7194	2.5394	0.0850	1.5713	0.6	550	7	526	5	653	29	96	Yes
UFOP	C180825-0930	1.sSMPABC052.TXT	1.2	147	519	0.4	0.0590	1.4383	0.6970	1.8971	0.0857	1.2370	0.7	536	5	530	4	567	21	99	Yes
UFOP	C180825-0930	1.sSMPABC060.TXT	1.2	149	394	0.7	0.0589	1.0665	0.7031	1.6732	0.0866	1.2892	0.8	540	5	536	4	562	16	99	Yes
UFOP	C180825-0930	1.sSMPABC091.TXT	0.8	221	462	0.5	0.0588	1.2267	0.7038	1.9040	0.0868	1.4562	0.8	541	5	536	5	561	18	99	Yes
UFOP	C180825-0930	1.sSMPABC089.TXT	1.1	162	300	0.4	0.0595	2.5405	0.7173	2.8357	0.0874	1.2599	0.4	549	8	540	4	586	37	98	Yes

Table SM3 U-Pb on zircon radiogenic data of the samples analyzed in this study (continuation).

UFOP	C180825-0930	1.sSMPABC049.TXT	1.4	133	484	0.4	0.0589	1.4035	0.7128	2.1034	0.0877	1.5666	0.7	546	6	542	5	565	21	99	Yes
UFOP	C180825-0930	1.sSMPABC079.TXT	3.4	54	93	0.8	0.0619	2.5568	0.7495	2.8311	0.0878	1.2158	0.4	567	8	543	4	670	37	96	Yes
UFOP	C180825-0930	1.sSMPABC059.TXT	1.5	117	290	0.4	0.0591	1.4375	0.7157	2.0233	0.0878	1.4238	0.7	548	6	543	5	570	21	99	Yes
UFOP	C180825-0930	1.sSMPABC047.TXT	4.1	45	205	0.5	0.0591	1.9366	*0.7181*	*2.2674*	*0.0881*	*1.1793*	*0.5*	549	6	544	4	571	28	99	Yes
UFOP	C180825-0930	1.sSMPABC048.TXT	14.3	14	61	0.9	0.0590	3.0412	*0.7184*	*3.7808*	*0.0883*	*2.2463*	*0.6*	549	11	546	8	567	45	99	Yes
UFOP	C180825-0930	1.sSMPABC067.TXT	3.0	61	191	0.5	0.0592	4.4236	*0.7227*	*5.1240*	*0.0885*	*2.5860*	*0.5*	552	15	547	9	576	65	99	Yes
UFOP	C180825-0930	1.sSMPABC051.TXT	1.0	183	669	0.9	0.0589	1.5889	*0.7208*	*2.1862*	*0.0888*	*1.5016*	*0.7*	551	6	548	5	562	23	100	Yes
UFOP	C180825-0930	1.sSMPABC088.TXT	0.5	398	882	0.1	0.0551	3.0598	*0.6723*	*4.3163*	*0.0886*	*3.0443*	*0.7*	522	18	547	16	416	68	105	No
UFOP	C180825-0930	1.sSMPABC050.TXT	0.7	265	633	0.3	0.0618	5.1418	0.7701	7.8120	0.0904	5.8812	0.8	579	23	558	21	666	75	96	Yes
UFOP	C180825-0930	1.sSMPABC053.TXT	10.2	19	64	1.0	0.0595	4.6221	0.7498	5.2419	0.0914	2.4726	0.5	568	15	564	9	586	68	99	Yes
UFOP	C180825-0930	1.sSMPABC073.TXT	2.4	75	168	0.8	0.0594	2.5642	0.7514	2.9210	0.0917	1.3990	0.5	569	9	566	5	583	38	99	Yes
UFOP	C180825-0930	1.sSMPABC058.TXT	0.8	230	499	0.5	0.0601	4.1483	0.7678	5.2716	0.0927	3.2529	0.6	578	16	571	12	607	61	99	Yes
UFOP	C180825-0930	1.sSMPABC069.TXT	-	1974	199	0.1	0.0669	29.8833	0.6891	30.2100	0.0747	4.4307	0.1	532	134	464	20	836	790	87	No
UFOP	C180825-0930	1.sSMPABC056.TXT	-	1275	21	6.2	0.2423	24.1377	10.2064	24.5449	0.3056	4.4524	0.2	2454	259	1719	68	3135	448	70	No
UFOP	C180825-0930	1.sSMPABC074.TXT	-	1362	161	0.5	0.0720	8.0273	0.8347	9.2091	0.0841	4.5134	0.5	616	44	520	23	986	173	84	No
UFOP	C180825-0930	1.sSMPABC090.TXT	-	3845	221	0.5	0.0726	17.1694	0.8412	17.8784	0.0840	4.9847	0.3	620	87	520	25	1004	394	84	No
UFOP	C180825-0930	1.sSMPABC093.TXT	-	204	204	0.2	0.0649	8.0327	0.5514	9.2081	0.0616	4.5016	0.5	446	34	386	17	771	179	86	No
LEGGA	C180825-0930	0930_1	4.0	83	194	0.0	0.0594	2.4456	0.7551	2.0048	0.0919	1.8210	0.2	570	9	567	10	565	54	99	No
LEGGA	C180825-0930	0930_2	6.3	136	130	0.2	0.0642	3.2915	0.7646	2.4300	0.0865	2.0508	0.0	575	11	535	11	716	67	93	No
LEGGA	C180825-0930	0930_3	0.2	-319	533	0.0	0.0627	1.5264	0.7545	1.3047	0.0869	0.6952	0.1	570	6	537	4	692	32	94	No
LEGGA	C180825-0930	0930_4	-4.7	55	57	0.1	0.0883	6.0624	0.9143	3.3091	0.0765	5.2283	0.6	657	16	474	24	1354	128	72	No
LEGGA	C180825-0930	0930_5	2.7	355	163	0.0	0.0658	2.9459	0.6482	2.1662	0.0719	2.2907	0.3	506	9	448	10	773	62	88	No
LEGGA	C180825-0930	0930_6	0.9	-320	286	0.0	0.0587	1.7782	0.7109	1.5464	0.0878	1.0354	0.2	547	7	542	5	541	38	99	No
LEGGA	C180825-0930	0930_7	10.0	-7	108	0.0	0.0786	5.1039	0.8975	5.2221	0.0820	2.7346	0.0	644	24	508	13	1108	102	79	No
LEGGA	C180825-0930	0930_8	4.3	21	104	0.0	0.0640	4.1945	0.6636	3.0640	0.0758	3.3348	0.2	515	12	471	15	697	91	91	No
LEGGA	C180825-0930	0930_9	2.0	-7802	422	0.3	0.0585	1.3700	0.7233	1.3132	0.0890	0.6617	0.1	552	6	550	3	541	31	100	No
LEGGA	C180825-0930	0930_10	3.2	-92	155	-0.5	0.0668	2.9523	0.7381	2.0267	0.0806	2.0210	1.0	560	9	500	10	802	63	89	No
LEGGA	C180825-0930	0930_11	0.0	67	272	-2.2	0.0658	2.9612	0.8239	2.6983	0.0915	0.9879	0.3	608	12	564	5	788	59	93	No
LEGGA	C180825-0930	0930_12	0.1	209	127	0.1	0.0690	3.3976	0.8871	2.3936	0.0935	2.2324	0.9	643	11	576	12	861	71	90	No
LEGGA	C180825-0930	0930_13	-1.3	62	151	-0.1	0.0735	4.0457	0.9220	3.4276	0.0924	2.0860	0.1	662	17	569	11	964	82	86	No
LEGGA	C180825-0930	0930_14	0.1	-98	376	0.0	0.0687	2.2297	0.7119	1.8486	0.0750	1.0401	0.6	545	8	466	5	868	45	85	No
LEGGA	C180825-0930	0930_15	-2.3	31	111	0.0	0.0676	3.2256	0.9196	2.9488	0.0981	2.6336	0.3	661	14	603	15	843	71	91	No
LEGGA	C180825-0930	0930_16	1.8	144	409	0.0	0.0604	1.3470	0.6956	1.1641	0.0832	0.9324	0.2	536	5	515	5	610	29	96	No
LEGGA	C180825-0930	0930_17	0.9	281	674	0.0	0.0627	1.2199	0.8196	1.0834	0.0943	0.4798	0.4	607	5	581	3	691	26	96	No
LEGGA	C180825-0930	0930_18	2.3	152	448	0.0	0.0716	1.3212	0.9391	1.5344	0.0949	1.0599	0.5	672	8	584	6	970	26	87	No
LEGGA	C180825-0930	0930_19	-3.0	55	94	0.0	0.0888	3.4421	1.0844	2.0427	0.0899	2.5439	0.1	745	11	555	14	1386	68	74	No
LEGGA	C180825-0930	0930_20	18.0	214	53	0.0	0.1327	7.6907	1.9285	8.9195	0.1104	4.5306	0.5	1078	56	673	29	2028	128	62	No
UFOP	C180824-1500	1.sSMPABC005.TXT	0.5	370	587	0.8	0.0541	1.7922	0.4317	2.9586	0.0579	2.3540	0.8	364	11	363	6	375	27	100	No
UFOP	C180824-1500	1.sSMPABC006.TXT	0.3	577	943	0.6	0.0557	0.8499	0.4021	1.4307	0.0524	1.1509	0.8	343	3	329	2	439	13	96	No
UFOP	C180824-1500	1.sSMPABC007.TXT	0.1	1873	544	0.7	0.0565	1.6335	0.4516	2.4667	0.0579	1.8483	0.7	378	8	363	4	473	24	96	No
UFOP	C180824-1500	1.sSMPABC008.TXT	0.5	383	426	0.4	0.0550	1.1883	0.4394	1.6883	0.0580	1.1994	0.7	369	4	363	3	411	18	98	No
UFOP	C180824-1500	1.sSMPABC009.TXT	0.6	328	450	0.5	0.0542	1.1798	0.4327	3.4017	0.0579	3.1906	0.9	365	16	363	8	378	18	100	No
UFOP	C180824-1500	1.sSMPABC011.TXT	0.4	474	1114	1.2	0.0551	0.9845	0.4404	2.5411	0.0579	2.3426	0.9	370	10	363	6	418	15	98	No
UFOP	C180824-1500	1.sSMPABC012.TXT	0.3	587	515	0.7	0.0545	1.1782	0.4352	2.5071	0.0579	2.2129	0.9	367	9	363	5	391	18	99	No
UFOP	C180824-1500	1.sSMPABC013.TXT	0.6	331	438	0.8	0.0568	1.5218	0.4540	2.1449	0.0580	1.5114	0.7	380	6	363	4	484	23	96	No
UFOP	C180824-1500	1.sSMPABC014.TXT	0.5	332	301	0.9	0.0557	1.2092	0.5534	2.8431	0.0721	2.5731	0.9	447	14	449	7	438	18	100	No
UFOP	C180824-1500	1.sSMPABC015.TXT	0.6	307	328	0.7	0.0548	1.3751	0.4377	1.9168	0.0579	1.3354	0.7	368	5	363	3	405	21	99	No
UFOP	C180824-1500	1.sSMPABC016.TXT	0.6	328	1119	1.2	0.0591	1.5626	0.4228	2.8082	0.0519	2.3333	0.8	358	10	326	5	571	23	91	No
UFOP	C180824-1500	1.sSMPABC017.TXT	0.4	455	746	0.7	0.0558	0.9635	0.4014	2.2854	0.0522	2.0724	0.9	342	7	328	4	443	14	96	No
UFOP	C180824-1500	1.sSMPABC018.TXT	0.3	636	842	0.4	0.0548	1.0236	0.3931	1.5565	0.0520	1.1726	0.8	336	4	327	2	406	15	97	No

Table SM3 U-Pb on zircon radiogenic data of the samples analyzed in this study (continuation).

UFOP	C180824-1500	1.sSMPABC019.TXT	0.4	514	276	0.7	0.0570	1.8851	0.4553	2.9082	0.0580	2.2145	0.8	381	11	363	5	491	28	95	No
UFOP	C180824-1500	1.sSMPABC020.TXT	0.4	518	742	1.0	0.0540	1.1360	0.4317	2.3807	0.0580	2.0922	0.9	364	8	363	5	371	17	100	No
UFOP	C180824-1500	1.sSMPABC025.TXT	0.5	371	1177	0.8	0.0537	4.1160	0.3842	4.5074	0.0519	1.8370	0.4	330	12	326	4	359	13	99	No
UFOP	C180824-1500	1.sSMPABC027.TXT	0.5	352	249	0.5	0.0596	1.3591	0.5920	1.7973	0.0720	1.1760	0.7	472	6	448	3	590	20	95	No
UFOP	C180824-1500	1.sSMPABC028.TXT	0.9	192	112	0.4	0.0595	7.4103	0.7555	7.5720	0.0921	1.5566	0.2	571	27	568	6	586	111	99	No
UFOP	C180824-1500	1.sSMPABC029.TXT	0.7	257	138	0.4	0.0668	1.6349	0.8469	2.1212	0.0919	1.3516	0.6	622	9	567	5	832	23	91	Yes
UFOP	C180824-1500	1.sSMPABC030.TXT	0.4	470	715	1.4	0.0540	1.0137	0.3953	1.4985	0.0531	1.1036	0.7	338	4	333	2	372	15	99	No
UFOP	C180824-1500	1.sSMPABC031.TXT	0.5	368	297	0.7	0.0574	1.2659	0.4583	1.6905	0.0579	1.1203	0.7	383	4	363	3	506	19	95	No
UFOP	C180824-1500	1.sSMPABC032.TXT	0.8	241	251	0.4	0.0585	1.7279	0.4665	2.3729	0.0578	1.6264	0.7	388	8	362	4	548	25	93	No
UFOP	C180824-1500	1.sSMPABC033.TXT	1.0	186	289	0.8	0.0566	1.6811	0.4517	4.4339	0.0579	4.1028	0.9	378	28	363	10	474	25	96	No
UFOP	C180824-1500	1.sSMPABC034.TXT	0.1	1948	85	0.9	0.0667	5.5177	0.9332	6.6429	0.1014	3.6991	0.6	669	49	623	15	830	79	93	No
UFOP	C180824-1500	1.sSMPABC037.TXT	0.4	458	974	1.0	0.0541	1.7566	0.3876	4.3133	0.0519	3.9394	0.9	332	23	326	8	213	27	98	No
UFOP	C180824-1500	1.sSMPABC038.TXT	0.7	280	275	0.8	0.0604	10.2135	0.4788	10.3892	0.0575	1.9025	0.2	397	35	361	7	617	220	91	Yes
UFOP	C180824-1500	1.sSMPABC049.TXT	0.4	415	268	0.5	0.0628	1.6249	0.7966	2.3771	0.0921	1.7350	0.7	594	11	568	6	700	23	96	No
UFOP	C180824-1500	1.sSMPABC052.TXT	0.7	258	375	0.8	0.0539	3.0114	0.4312	4.3815	0.0580	3.1827	0.7	364	20	363	8	368	46	100	No
UFOP	C180824-1500	1.sSMPABC010.TXT	-	9220	258	0.5	0.0540	1.2547	0.3931	3.2584	0.0528	3.0072	0.9	337	10	332	10	372	29	98	No
UFOP	C180824-1500	1.sSMPABC026.TXT	-	8181	235	0.8	0.0552	1.4990	0.4529	3.4481	0.0595	3.1052	0.9	379	11	373	11	419	34	98	No
UFOP	C180824-1500	1.sSMPABC035.TXT	-	5880	251	1.2	0.0552	1.1954	0.4372	3.3672	0.0574	3.1479	0.9	368	11	360	11	422	27	98	No
UFOP	C180824-1500	1.sSMPABC036.TXT	-	7567	55	1.2	0.0539	0.8927	0.3549	3.1681	0.0478	3.0397	1.0	308	9	301	9	365	20	98	No
UFOP	C180824-1500	1.sSMPABC039.TXT	-	5387	208	0.7	0.0564	1.5593	0.4515	3.3893	0.0581	3.0093	0.9	378	11	364	11	467	35	96	No
UFOP	C180824-1500	1.sSMPABC040.TXT	-	9210	222	0.6	0.0555	1.0347	0.4083	3.1688	0.0533	2.9951	0.9	348	10	335	10	434	23	96	No
UFOP	C180824-1500	1.sSMPABC045.TXT	-	6951	433	0.8	0.0565	1.6648	0.4482	4.1158	0.0575	3.7641	0.9	376	13	360	13	474	37	96	No
UFOP	C180824-1500	1.sSMPABC046.TXT	-	30408	95	0.6	0.0565	1.1387	0.4401	3.2009	0.0565	2.9915	0.9	370	10	354	10	472	25	96	No
UFOP	C180824-1500	1.sSMPABC047.TXT	-	8476	242	0.9	0.0676	2.2747	0.9776	3.8529	0.1048	3.1097	0.8	692	20	643	19	857	48	93	No
UFOP	C180824-1500	1.sSMPABC048.TXT	-	6148	202	0.5	0.0597	1.5568	0.5853	3.3899	0.0711	3.0113	0.9	468	13	443	13	593	34	95	No
UFOP	C180824-1500	1.sSMPABC050.TXT	-	3946	156	0.7	0.0561	1.1441	0.4064	3.3372	0.0526	3.1349	0.9	346	10	330	10	454	26	95	No
UFOP	C180824-1500	1.sSMPABC051.TXT	-	10828	157	0.4	0.0668	1.7657	0.8460	3.5252	0.0918	3.0511	0.9	622	17	566	17	832	37	91	No
UFOP	C180824-1500.2	1.sSMPABC007.TXT	0.0	-4203	308	0.8	0.0538	1.8926	0.4331	2.6859	0.0584	1.9058	0.7	365	8	366	7	363	43	100	No
UFOP	C180824-1500.2	1.sSMPABC008.TXT	0.3	611	280	0.8	0.0528	5.7486	0.4268	7.3573	0.0587	4.5917	0.6	361	23	368	16	318	131	102	No
UFOP	C180824-1500.2	1.sSMPABC009.TXT	0.1	1778	397	1.3	0.0538	2.7947	0.4312	4.4306	0.0581	3.4380	0.8	364	14	364	12	364	63	100	No
UFOP	C180824-1500.2	1.sSMPABC010.TXT	0.1	1250	478	1.3	0.0533	4.5276	0.4267	5.2942	0.0581	2.7439	0.5	361	16	364	10	343	102	101	No
UFOP	C180824-1500.2	1.sSMPABC011.TXT	0.1	1351	585	1.1	0.0532	3.2642	0.4192	4.3827	0.0572	2.9246	0.7	355	13	359	10	337	74	101	No
UFOP	C180824-1500.2	1.sSMPABC012.TXT	0.3	684	466	1.2	0.0512	2.3409	0.4005	3.8138	0.0567	3.0109	0.8	342	11	356	10	251	54	104	No
UFOP	C180824-1500.2	1.sSMPABC013.TXT	0.0	6495	495	1.1	0.0540	2.8320	0.4308	4.0234	0.0579	2.8580	0.7	364	12	363	10	372	64	100	No
UFOP	C180824-1500.2	1.sSMPABC014.TXT	0.1	1619	547	0.8	0.0534	2.0826	0.4149	3.2448	0.0564	2.4883	0.8	352	10	354	9	345	47	100	No
UFOP	C180824-1500.2	1.sSMPABC015.TXT	0.0	-282030	985	1.1	0.0541	1.6756	0.4324	2.6408	0.0580	2.0411	0.8	365	8	363	7	375	38	100	No
UFOP	C180824-1500.2	1.sSMPABC016.TXT	0.1	2337	370	1.0	0.0530	2.1582	0.4145	3.0524	0.0567	2.1585	0.7	352	9	356	7	330	49	101	No
UFOP	C180824-1500.2	1.sSMPABC017.TXT	-0.1	-3169	463	0.9	0.0554	5.4827	0.4331	6.9127	0.0568	4.2102	0.6	365	21	356	15	427	122	97	No
UFOP	C180824-1500.2	1.sSMPABC018.TXT	0.2	772	434	0.8	0.0517	4.5198	0.4038	4.9708	0.0566	2.0689	0.4	344	15	355	7	274	104	103	No
UFOP	C180824-1500.2	1.sSMPABC019.TXT	0.0	-22841	389	0.7	0.0538	1.8979	0.4300	2.7449	0.0580	1.9830	0.7	363	8	363	7	364	43	100	No
UFOP	C180824-1500.2	1.sSMPABC020.TXT	0.2	838	468	1.0	0.0516	2.2593	0.4100	3.4380	0.0576	2.5914	0.8	349	10	361	9	268	52	104	No
UFOP	C180824-1500.2	1.sSMPABC027.TXT	-0.1	-2223	390	1.6	0.0534	3.2675	0.4284	5.5995	0.0582	4.5473	0.8	362	17	365	16	346	74	101	No
UFOP	C180824-1500.2	1.sSMPABC028.TXT	5.3	36	653	0.7	0.0538	1.5621	0.4259	2.2695	0.0574	1.6464	0.7	360	5	360	4	362	24	100	Yes
UFOP	C180824-1500.2	1.sSMPABC029.TXT	0.2	1109	628	1.1	0.0523	1.7271	0.4141	2.5923	0.0575	1.9331	0.7	352	8	360	7	297	39	102	No
UFOP	C180824-1500.2	1.sSMPABC030.TXT	0.0	5711	549	2.0	0.0536	2.0141	0.4188	2.7801	0.0567	1.9163	0.7	355	8	355	7	356	45	100	No
UFOP	C180824-1500.2	1.sSMPABC031.TXT	0.2	776	230	0.9	0.0516	5.8052	0.4117	6.3893	0.0579	2.6688	0.4	350	19	363	9	268	133	104	No
UFOP	C180824-1500.2	1.sSMPABC032.TXT	-0.1	-2323	468	1.6	0.0548	2.8152	0.4415	4.6803	0.0585	3.7390	0.8	371	15	367	13	402	63	99	No
UFOP	C180824-1500.2	1.sSMPABC033.TXT	0.0	7612	811	1.5	0.0542	1.8116	0.4314	2.9010	0.0578	2.2659	0.8	364	9	362	8	379	41	99	No
UFOP	C180824-1500.2	1.sSMPABC034.TXT	0.1	1516	819	1.6	0.0525	2.8085	0.4237	3.6220	0.0586	2.2872	0.6	359	11	367	8	307	64	102	No
UFOP	C180824-1500.2	1.sSMPABC035.TXT	0.0	42201	320	1.1	0.0543	1.7855	0.4351	2.5588	0.0582	1.8328	0.7	367	8	365	6	382	40	99	No

Table SM3 U-Pb on zircon radiogenic data of the samples analyzed in this study (continuation).

UFOP	C180824-1500.2	1.sSMPABC036.TXT	0.0	4152	938	1.5	0.0530	1.6909	0.4219	2.5101	0.0578	1.8552	0.7	357	8	362	7	328	38	101	No
UFOP	C180824-1500.2	1.sSMPABC038.TXT	0.0	4169	283	0.9	0.0532	2.3841	0.4225	3.2781	0.0576	2.2500	0.7	358	10	361	8	337	54	101	No
UFOP	C180824-1500.2	1.sSMPABC039.TXT	0.3	665	327	0.9	0.0516	2.9833	0.4103	3.8365	0.0577	2.4122	0.6	349	11	361	8	269	68	104	No
UFOP	C180824-1500.2	1.sSMPABC040.TXT	0.1	2653	255	1.2	0.0541	4.7007	0.4332	5.8577	0.0581	3.4951	0.6	365	18	364	12	374	106	100	No
UFOP	C180824-1500.2	1.sSMPABC047.TXT	0.1	1347	443	0.9	0.0527	2.0620	0.4187	2.9286	0.0577	2.0797	0.7	355	9	362	7	314	47	102	No
UFOP	C180824-1500.2	1.sSMPABC048.TXT	0.1	2034	621	0.9	0.0528	2.9375	0.4184	4.3306	0.0575	3.1820	0.7	355	13	361	11	318	67	102	No
UFOP	C180824-1500.2	1.sSMPABC049.TXT	-0.4	-496	178	0.9	0.0584	5.6683	0.4659	6.9734	0.0578	4.0618	0.6	388	23	362	14	547	124	93	No
UFOP	C180824-1500.2	1.sSMPABC050.TXT	0.2	1195	272	1.6	0.0528	2.4378	0.4176	3.1965	0.0573	2.0675	0.6	354	10	359	7	322	55	101	No
UFOP	C180824-1500.2	1.sSMPABC051.TXT	0.4	438	273	1.0	0.0550	8.5577	0.4247	9.9358	0.0560	5.0484	0.5	359	20	351	12	412	133	98	Yes
UFOP	C180824-1500.2	1.sSMPABC052.TXT	0.1	1311	517	1.0	0.0521	3.1631	0.4103	3.7085	0.0572	1.9357	0.5	349	11	359	7	288	72	103	No
UFOP	C180824-1500.2	1.sSMPABC055.TXT	0.3	687	337	0.9	0.0514	3.5834	0.4145	5.6564	0.0585	4.3765	0.8	352	17	367	16	258	82	104	No
UFOP	C180824-1500.2	1.sSMPABC056.TXT	-0.2	-1154	101	0.4	0.0548	5.5314	0.4404	6.4138	0.0583	3.2466	0.5	371	20	366	12	403	124	99	No
UFOP	C180824-1500.2	1.sSMPABC057.TXT	0.0	4203	549	0.9	0.0532	2.6233	0.4274	4.5283	0.0583	3.6910	0.8	361	14	366	13	335	59	101	No
UFOP	C180824-1500.2	1.sSMPABC058.TXT	0.3	715	451	1.5	0.0519	2.9177	0.4089	3.9524	0.0571	2.6663	0.7	348	12	358	9	282	67	103	No
UFOP	C180824-1500.2	1.sSMPABC060.TXT	0.0	-7057	624	1.6	0.0544	1.8578	0.4266	2.7918	0.0569	2.0839	0.7	361	9	357	7	387	42	99	No
UFOP	C180824-1500.2	1.sSMPABC054.TXT	-	917	80	1.1	0.8543	2.1079	81.6128	6.8756	0.6981	6.5445	1.0	4482	75	3414	175	5015	30	76	Yes
UFOP	C180824-1500.2	1.sSMPABC059.TXT	-	848	88	0.5	0.0599	2.3063	0.4849	3.8875	0.0587	3.1295	0.8	401	13	368	11	602	51	92	No
UFOP	C180824-1500.2	1.sSMPABC037.TXT	-	828	82	1.0	0.0545	1.2499	0.3164	3.6703	0.0421	3.4509	0.9	279	9	266	9	393	28	95	No
UFOP	C180824-1500.2	1.sSMPABC053.TXT	-	841	337	0.4	0.0639	1.6556	0.3606	3.5481	0.0464	3.1381	0.9	313	10	292	8	738	35	93	Yes
UFOP	C180824-1500.3	1.sSMPABC007.TXT	1.1	164	824	1.4	0.0536	1.3678	0.4239	2.2820	0.0573	1.8266	0.8	359	7	359	4	355	8	100	Yes
UFOP	C180824-1500.3	1.sSMPABC008.TXT	0.7	267	1133	1.2	0.0535	1.5110	0.4212	2.0126	0.0571	1.3293	0.7	357	4	358	3	349	23	100	Yes
UFOP	C180824-1500.3	1.sSMPABC009.TXT	1.3	140	573	1.0	0.0535	2.0650	0.4221	2.7477	0.0572	1.8126	0.7	357	9	358	4	352	10	100	Yes
UFOP	C180824-1500.3	1.sSMPABC010.TXT	0.9	199	735	1.0	0.0541	2.2246	0.4291	3.1541	0.0575	2.2360	0.7	362	6	360	5	376	34	100	Yes
UFOP	C180824-1500.3	1.sSMPABC011.TXT	2.8	66	314	0.7	0.0535	4.2325	0.4224	5.1531	0.0572	2.9395	0.6	357	20	359	7	352	21	100	Yes
UFOP	C180824-1500.3	1.sSMPABC012.TXT	1.1	162	732	0.9	0.0532	1.9714	0.4205	2.3966	0.0573	1.3628	0.6	356	5	359	3	338	30	101	Yes
UFOP	C180824-1500.3	1.sSMPABC013.TXT	1.1	161	697	1.0	0.0539	1.4942	0.4287	2.7923	0.0577	2.3589	0.8	362	6	361	6	367	23	100	Yes
UFOP	C180824-1500.3	1.sSMPABC014.TXT	0.7	249	982	0.2	0.0535	1.4765	0.4228	2.4286	0.0573	1.9282	0.8	358	8	359	4	349	9	100	Yes
UFOP	C180824-1500.3	1.sSMPABC015.TXT	1.2	156	446	1.1	0.0532	3.5451	0.4235	4.2036	0.0577	2.2589	0.5	358	8	362	5	338	54	101	Yes
UFOP	C180824-1500.3	1.sSMPABC016.TXT	0.7	277	775	1.5	0.0482	4.3470	0.3770	5.9149	0.0568	4.0113	0.7	325	17	356	14	108	103	110	No
UFOP	C180824-1500.3	1.sSMPABC017.TXT	0.7	274	786	2.1	0.0481	5.3755	0.3771	6.6164	0.0569	3.8576	0.6	325	19	357	13	102	127	110	No
UFOP	C180824-1500.3	1.sSMPABC018.TXT	1.4	131	485	1.0	0.0534	1.5323	0.4224	2.4716	0.0574	1.9393	0.8	357	8	360	5	346	9	101	Yes
UFOP	C180824-1500.3	1.sSMPABC019.TXT	1.3	139	478	1.3	0.0534	2.6149	0.4245	3.2627	0.0576	1.9513	0.6	359	10	361	5	347	11	101	Yes
UFOP	C180824-1500.3	1.sSMPABC020.TXT	2.5	74	204	0.6	0.0538	3.5044	0.4239	4.1268	0.0571	2.1793	0.5	358	8	358	5	364	54	100	Yes
UFOP	C180824-1500.3	1.sSMPABC027.TXT	0.7	247	668	1.5	0.0538	2.4686	0.4279	3.3874	0.0577	2.3196	0.7	361	7	362	5	362	38	100	Yes
UFOP	C180824-1500.3	1.sSMPABC028.TXT	0.5	372	946	1.7	0.0495	2.4227	0.3906	3.4985	0.0572	2.5239	0.7	335	10	359	9	172	57	107	No
UFOP	C180824-1500.3	1.sSMPABC029.TXT	0.8	238	995	1.1	0.0537	2.7387	0.4233	3.6835	0.0572	2.4632	0.7	358	7	359	6	358	42	100	Yes
UFOP	C180824-1500.3	1.sSMPABC030.TXT	1.1	167	502	1.6	0.0534	2.3760	0.4218	3.0706	0.0573	1.9451	0.6	357	6	359	5	345	36	101	Yes
UFOP	C180824-1500.3	1.sSMPABC031.TXT	3.2	59	216	1.0	0.0534	2.3195	0.4274	2.5522	0.0581	1.0648	0.4	361	6	364	3	345	7	101	Yes
UFOP	C180824-1500.3	1.sSMPABC032.TXT	0.7	262	781	1.0	0.0533	1.7410	0.4254	2.5602	0.0579	1.8771	0.7	360	8	363	4	342	9	101	Yes
UFOP	C180824-1500.3	1.sSMPABC033.TXT	0.5	347	923	1.8	0.0493	4.3891	0.3883	5.3720	0.0571	3.0974	0.6	333	15	358	11	162	103	108	No
UFOP	C180824-1500.3	1.sSMPABC034.TXT	0.6	285	671	0.8	0.0481	4.5898	0.3801	6.1390	0.0573	4.0769	0.7	327	17	359	14	104	108	110	No
UFOP	C180824-1500.3	1.sSMPABC035.TXT	0.6	297	689	1.6	0.0490	4.7059	0.3853	5.8760	0.0571	3.5188	0.6	331	17	358	12	146	110	108	No
UFOP	C180824-1500.3	1.sSMPABC036.TXT	0.6	331	849	1.3	0.0490	4.5831	0.3858	5.8876	0.0571	3.6958	0.6	331	17	358	13	148	107	108	No
UFOP	C180824-1500.3	1.sSMPABC037.TXT	0.6	308	588	0.9	0.0484	4.4186	0.3783	5.2079	0.0568	2.7566	0.5	326	15	356	10	117	104	109	No
UFOP	C180824-1500.3	1.sSMPABC038.TXT	0.5	403	884	2.0	0.0495	2.4035	0.3899	3.6083	0.0571	2.6913	0.7	334	10	358	9	173	56	107	No
UFOP	C180824-1500.3	1.sSMPABC039.TXT	2.1	87	368	1.2	0.0533	1.9248	0.4250	2.3182	0.0579	1.2921	0.6	359	6	363	3	340	7	101	Yes
UFOP	C180824-1500.3	1.sSMPABC040.TXT	0.5	361	787	2.0	0.0491	4.4119	0.3851	5.5383	0.0569	3.3479	0.6	331	16	357	12	152	103	108	No
UFOP	C180822-1625	1.sSMPABC079.TXT	0.3	58	331	0.4	0.0538	2.1690	0.4351	2.7834	0.0587	1.7444	0.6	366	12	368	5	362	13	100	No
UFOP	C180822-1625	1.sSMPABC075.TXT	0.1	248	158	0.3	0.0542	2.6185	0.4638	3.0537	0.0620	1.5710	0.5	387	13	388	5	381	14	100	No
UFOP	C180822-1625	1.sSMPABC132.TXT	0.0	487	167	0.5	0.0548	4.0400	0.4686	4.4347	0.0620	1.8288	0.4	390	19	388	6	404	19	100	No

Table SM3 U-Pb on zircon radiogenic data of the samples analyzed in this study (continuation).

UFOP	C180822-1625	1.sSMPABC111.TXT	0.1	334	59	0.4	0.0548	4.9658	0.4683	5.6390	0.0620	2.6719	0.5	390	30	388	8	402	31	100	No
UFOP	C180822-1625	1.sSMPABC113.TXT	0.0	391	48	0.4	0.0547	4.5375	0.4682	5.1080	0.0620	2.3456	0.5	390	25	388	7	401	26	100	No
UFOP	C180822-1625	1.sSMPABC093.TXT	0.1	343	123	0.3	0.0545	3.7128	0.4667	4.2409	0.0621	2.0497	0.5	389	20	388	6	394	21	100	No
UFOP	C180822-1625	1.sSMPABC110.TXT	0.0	544	201	0.3	0.0547	1.9329	0.4680	2.4158	0.0621	1.4492	0.6	389	10	388	5	400	11	100	No
UFOP	C180822-1625	1.sSMPABC094.TXT	0.1	225	174	0.5	0.0546	2.5423	0.4669	2.9977	0.0621	1.5884	0.5	389	13	388	5	394	14	100	No
UFOP	C180822-1625	1.sSMPABC112.TXT	0.0	789	79	0.3	0.0547	2.8391	0.4682	3.3221	0.0621	1.7249	0.5	390	14	388	5	350	15	100	No
UFOP	C180822-1625	1.sSMPABC090.TXT	0.0	1520	90	0.4	0.0542	3.6001	0.4636	4.1952	0.0621	2.1539	0.5	386	20	388	7	378	69	100	No
UFOP	C180822-1625	1.sSMPABC130.TXT	0.1	304	170	0.5	0.0546	2.0974	0.4677	3.2529	0.0621	2.4864	0.8	389	20	388	8	397	21	100	No
UFOP	C180822-1625	1.sSMPABC147.TXT	0.1	281	156	0.5	0.0543	3.0688	0.4650	3.5441	0.0621	1.7729	0.5	387	15	388	6	384	16	100	No
UFOP	C180822-1625	1.sSMPABC119.TXT	0.1	359	146	0.4	0.0548	2.2664	0.4689	2.7234	0.0621	1.5099	0.6	390	11	388	5	403	12	100	No
UFOP	C180822-1625	1.sSMPABC091.TXT	0.1	328	133	0.4	0.0545	2.2052	0.4664	2.5710	0.0621	1.3218	0.5	388	10	388	4	391	11	100	No
UFOP	C180822-1625	1.sSMPABC092.TXT	0.1	201	94	0.4	0.0545	2.4076	0.4666	2.7880	0.0621	1.4058	0.5	388	11	388	4	392	12	100	No
UFOP	C180822-1625	1.sSMPABC117.TXT	0.0	630	121	0.4	0.0547	2.1278	0.4685	2.6544	0.0621	1.5869	0.6	390	11	388	5	401	13	100	No
UFOP	C180822-1625	1.sSMPABC100.TXT	0.1	205	119	0.3	0.0547	2.3004	0.4679	2.6943	0.0621	1.4027	0.5	389	11	388	4	398	12	100	No
UFOP	C180822-1625	1.sSMPABC078.TXT	0.1	268	116	0.4	0.0542	3.6965	0.4639	4.3633	0.0621	2.3183	0.5	387	22	388	7	378	23	100	No
UFOP	C180822-1625	1.sSMPABC118.TXT	0.0	571	147	0.3	0.0547	2.0232	0.4688	2.5460	0.0621	1.5456	0.6	390	11	388	5	402	12	100	No
UFOP	C180822-1625	1.sSMPABC099.TXT	0.0	519	114	0.3	0.0547	2.6569	0.4681	3.0345	0.0621	1.4660	0.5	390	12	388	5	399	13	100	No
UFOP	C180822-1625	1.sSMPABC116.TXT	0.1	266	87	0.3	0.0547	2.6628	0.4686	3.1363	0.0621	1.6570	0.5	390	13	388	5	401	14	100	No
UFOP	C180822-1625	1.sSMPABC098.TXT	0.0	470	119	0.4	0.0546	2.3408	0.4679	2.7570	0.0621	1.4566	0.5	389	11	388	5	397	12	100	No
UFOP	C180822-1625	1.sSMPABC115.TXT	0.1	189	49	0.3	0.0551	8.9118	0.4718	9.5378	0.0621	3.3984	0.4	392	52	389	11	415	53	99	No
UFOP	C180822-1625	1.sSMPABC148.TXT	0.1	232	151	0.5	0.0543	3.2537	0.4649	3.5914	0.0621	1.5206	0.4	387	14	389	5	382	15	100	No
UFOP	C180822-1625	1.sSMPABC114.TXT	0.0	457	174	0.4	0.0548	1.7983	0.4692	2.2037	0.0621	1.2737	0.6	390	9	389	4	402	9	100	No
UFOP	C180822-1625	1.sSMPABC140.TXT	0.0	474	159	0.3	0.0545	2.7576	0.4666	3.3198	0.0621	1.8484	0.6	388	15	389	6	390	16	100	No
UFOP	C180822-1625	1.sSMPABC109.TXT	0.0	732	260	0.3	0.0547	1.8252	0.4689	2.3288	0.0622	1.4464	0.6	390	10	389	5	400	11	100	No
UFOP	C180822-1625	1.sSMPABC087.TXT	0.0	918	402	0.3	0.0560	1.9696	0.5548	2.4585	0.0718	1.4712	0.6	448	11	447	5	453	13	100	No
UFOP	C180822-1625	1.sSMPABC095.TXT	0.0	468	120	0.3	0.0561	2.0882	0.5578	2.4047	0.0722	1.1926	0.5	450	10	449	4	455	11	100	No
UFOP	C180822-1625	1.sSMPABC120.TXT	0.0	1261	403	0.4	0.0563	1.8567	0.5631	2.5178	0.0725	1.7006	0.7	453	13	451	6	465	14	100	No
UFOP	C180822-1625	1.sSMPABC129.TXT	0.0	398	148	0.3	0.0566	1.8048	0.5833	2.1875	0.0748	1.2360	0.6	466	10	465	5	475	11	100	No
UFOP	C180822-1625	1.sSMPABC108.TXT	0.1	301	82	0.5	0.0601	4.2055	0.8032	4.9195	0.0970	2.5525	0.5	598	37	597	12	606	39	100	No
UFOP	C180822-1625	1.sSMPABC107.TXT	0.0	-1777	87	0.4	0.0601	2.4586	0.8036	2.8863	0.0970	1.5120	0.5	598	17	597	7	606	18	100	No
UFOP	C180822-1625	1.sSMPABC076.TXT	0.0	763	192	0.4	0.0604	0.8141	0.8089	1.1144	0.0971	0.7610	0.7	601	5	597	4	619	15	99	No
UFOP	C180822-1625	1.sSMPABC077.TXT	0.0	500	148	0.3	0.0596	2.2104	0.7986	2.8964	0.0971	1.8717	0.6	595	19	598	9	590	21	100	No
UFOP	C180822-1625	1.sSMPABC097.TXT	0.0	447	83	0.3	0.0603	3.4479	0.8098	3.9213	0.0973	1.8677	0.5	602	24	599	9	616	26	99	No
UFOP	C180822-1625	1.sSMPABC133.TXT	0.0	1544	346	0.4	0.0617	1.8119	0.9039	2.8329	0.1063	2.1777	0.8	653	23	651	11	662	26	100	No
UFOP	C180822-1625	1.sSMPABC139.TXT	0.0	1057	29	0.2	0.0643	2.9396	1.0782	4.2283	0.1216	3.0393	0.7	742	48	740	18	752	51	100	No
LEGGA	C180822-1625	1625_1	-10.9	-75	113	0.0	0.0615	4.9879	0.4660	3.1486	0.0562	3.6004	0.9	387	10	352	12	580	111	91	No
LEGGA	C180822-1625	1625_2	0.5	53	286	0.0	0.0568	1.8207	0.4659	1.6740	0.0593	1.0127	0.2	386	5	372	4	473	41	96	No
LEGGA	C180822-1625	1625_3	-0.1	65	148	0.0	0.0569	2.8866	0.4593	2.4381	0.0590	2.1152	0.3	381	8	370	8	451	63	97	No
LEGGA	C180822-1625	1625_4	1.0	-22	258	0.0	0.0682	2.6830	0.9844	2.5481	0.1048	0.7068	0.1	692	12	642	4	852	55	93	No
LEGGA	C180822-1625	1625_5	0.2	-393	131	0.0	0.1406	1.8606	4.0129	2.1567	0.2059	0.8408	0.5	1624	17	1207	9	2223	32	74	No
LEGGA	C180822-1625	1625_6	0.4	-34	96	0.5	0.0716	3.0694	1.1636	2.2115	0.1178	1.5252	0.7	782	12	718	10	956	64	92	No
LEGGA	C180822-1625	1625_7	-5.2	-38	129	-0.1	0.0674	3.4312	0.8593	3.3771	0.0922	1.5380	0.2	627	16	569	8	828	73	91	No
LEGGA	C180822-1625	1625_8	-1.9	-1946	95	0.0	0.0620	5.6189	0.5036	4.2097	0.0597	3.1452	0.7	412	14	374	11	592	121	91	No
LEGGA	C180822-1625	1625_9	-11.6	313	115	-0.9	0.0554	3.1930	0.4220	2.2638	0.0556	2.0705	0.9	355	7	349	7	389	76	98	No
LEGGA	C180822-1625	1625_10	-3.9	-603	185	0.2	0.0657	2.9902	0.5324	3.0067	0.0587	1.5581	0.2	428	9	367	6	762	60	86	No
LEGGA	C180822-1625	1625_11	0.9	-643	166	0.0	0.0657	2.8972	0.5267	2.8432	0.0581	1.5225	0.2	425	9	364	5	768	63	86	No
LEGGA	C180822-1625	1625_12	4.8	-4	110	0.0	0.0577	3.8447	0.4737	2.9770	0.0600	2.9350	0.2	393	10	375	11	478	90	96	No
LEGGA	C180822-1625	1625_13	-1.2	260	320	0.0	0.0677	1.5010	0.9602	1.3451	0.1024	0.5639	0.4	681	7	629	3	849	32	92	No
LEGGA	C180822-1625	1625_14	-1.7	-597	57	0.0	0.1069	1.6329	4.2191	1.4323	0.2852	0.9167	0.1	1668	13	1617	13	1737	30	97	No
LEGGA	C180822-1625	1625_15	-9.1	-403	66	0.0	0.0635	5.2829	0.4936	3.2572	0.0573	4.4204	0.1	406	11	359	15	670	119	88	No

Table SM3 U-Pb on zircon radiogenic data of the samples analyzed in this study (continuation).

LEGGA	C180822-1625	1625_16	-4.6	56	99	0.0	0.0562	4.1001	0.4316	2.7998	0.0567	2.8060	1.0	360	9	356	10	384	93	99	No
LEGGA	C180822-1625	1625_17	-12.4	9	111	0.0	0.0657	4.4410	0.5333	3.3901	0.0592	3.0854	0.0	433	12	371	11	748	96	86	No
LEGGA	C180822-1625	1625_18	-8.4	-213	159	0.0	0.0547	3.5064	0.4533	2.9191	0.0599	2.3661	0.1	379	9	375	9	371	83	99	No
UFOP	C180824-1900	1.sSMPABC139.TXT	0.0	129	277	0.5	0.0504	2.3768	0.2225	2.6513	0.0320	1.1749	0.4	204	4	203	2	213	4	100	No
UFOP	C180824-1900	1.sSMPABC138.TXT	0.0	508	209	0.9	0.0504	3.7384	0.2223	4.1642	0.0320	1.8345	0.4	204	7	203	2	211	8	100	No
UFOP	C180824-1900	1.sSMPABC174.TXT	0.0	126	391	0.4	0.0502	2.6366	0.2217	2.9818	0.0320	1.3928	0.5	203	5	203	2	203	5	100	No
UFOP	C180824-1900	1.sSMPABC185.TXT	0.0	166	121	0.6	0.0502	4.9054	0.2219	5.3353	0.0321	2.0982	0.4	203	10	204	3	203	10	100	No
UFOP	C180824-1900	1.sSMPABC168.TXT	0.0	218	524	0.4	0.0502	1.5533	0.2219	1.9265	0.0321	1.1395	0.6	203	3	204	2	203	3	100	No
UFOP	C180824-1900	1.sSMPABC173.TXT	0.0	126	350	0.3	0.0502	1.7775	0.2221	2.0438	0.0321	1.0086	0.5	204	3	204	1	204	3	100	No
UFOP	C180824-1900	1.sSMPABC189.TXT	0.1	26	64	1.0	0.0504	7.5574	0.2238	8.1009	0.0322	2.9171	0.4	205	16	204	4	213	17	100	No
UFOP	C180824-1900	1.sSMPABC179.TXT	0.0	101	446	0.5	0.0505	4.8054	0.2259	5.0279	0.0325	1.4791	0.3	207	8	206	2	216	8	100	No
UFOP	C180824-1900	1.sSMPABC175.TXT	0.0	155	547	0.4	0.0503	4.4415	0.2271	4.8752	0.0328	2.0100	0.4	208	9	208	3	208	9	100	No
UFOP	C180824-1900	1.sSMPABC155.TXT	0.0	107	259	1.1	0.0505	5.0570	0.2305	5.7774	0.0331	2.7937	0.5	210	13	210	4	218	14	100	No
UFOP	C180824-1900	1.sSMPABC177.TXT	0.0	209	368	0.8	0.0511	1.3941	0.2764	1.6534	0.0393	0.8890	0.5	248	3	248	1	244	3	100	No
UFOP	C180824-1900	1.sSMPABC165.TXT	0.0	801	59	0.6	0.0514	4.0158	0.2885	4.3180	0.0407	1.5868	0.4	257	9	257	3	257	9	100	No
UFOP	C180824-1900	1.sSMPABC171.TXT	0.0	134	167	0.5	0.0513	2.1034	0.2936	2.4169	0.0415	1.1904	0.5	261	5	262	2	256	5	100	No
UFOP	C180824-1900	1.sSMPABC152.TXT	0.0	92	117	1.1	0.0517	3.0306	0.2984	3.3053	0.0418	1.3191	0.4	265	7	264	2	273	7	100	No
UFOP	C180824-1900	1.sSMPABC145.TXT	0.0	119	195	0.5	0.0520	2.4028	0.3109	2.6324	0.0434	1.0753	0.4	275	5	274	2	285	5	100	No
UFOP	C180824-1900	1.sSMPABC160.TXT	0.0	332	492	0.4	0.0518	1.4246	0.3168	2.3612	0.0444	1.8830	0.8	279	6	280	3	275	7	100	No
UFOP	C180824-1900	1.sSMPABC151.TXT	0.0	153	150	0.5	0.0519	2.6767	0.3189	3.0177	0.0446	1.3935	0.5	281	7	281	3	280	7	100	No
UFOP	C180824-1900	1.sSMPABC135.TXT	0.0	170	491	0.7	0.0531	2.1090	0.3733	3.1758	0.0510	2.3744	0.7	322	11	321	5	332	12	100	No
UFOP	C180824-1900	1.sSMPABC157.TXT	0.0	152	198	0.9	0.0530	9.7071	0.3885	9.8227	0.0532	1.5026	0.2	333	21	334	3	329	22	100	No
UFOP	C180824-1900	1.sSMPABC154.TXT	0.0	336	554	0.2	0.0540	1.3439	0.4477	1.9663	0.0602	1.4354	0.7	375	6	377	4	370	7	100	No
UFOP	C180824-1900	1.sSMPABC130.TXT	0.0	156	72	0.5	0.0550	3.0577	0.4908	3.3829	0.0647	1.4472	0.4	405	10	404	4	412	11	100	No
UFOP	C180824-1900	1.sSMPABC134.TXT	0.0	240	173	0.2	0.0569	2.5525	0.6213	3.1719	0.0792	1.8831	0.6	490	13	492	6	487	14	100	No
UFOP	C180824-1900	1.sSMPABC153.TXT	0.0	202	168	0.5	0.0568	1.3581	0.6266	1.6538	0.0801	0.9437	0.6	493	5	496	3	482	6	101	No
UFOP	C180824-1900	1.sSMPABC131.TXT	0.0	234	224	0.7	0.0570	1.3054	0.6344	2.0443	0.0807	1.5732	0.8	498	8	500	5	491	9	100	No
UFOP	C180824-1900	1.sSMPABC137.TXT	0.0	565	179	0.5	0.0570	1.2587	0.6357	1.6877	0.0809	1.1243	0.7	499	6	502	4	491	7	100	No
UFOP	C180824-1900	1.sSMPABC156.TXT	0.0	144	103	0.3	0.0569	3.1370	0.6408	3.6980	0.0817	1.9581	0.5	502	15	506	6	488	16	101	No
UFOP	C180824-1900	1.sSMPABC132.TXT	-	6450	578	0.4	0.0626	5.6974	0.6713	6.9897	0.0777	4.0492	0.6	521	29	482	19	696	126	93	No
UFOP	C180824-1900	1.sSMPABC136.TXT	-	6259	754	0.9	0.2224	29.9049	3.0013	31.7415	0.0979	10.6403	0.3	1408	277	602	61	2998	587	43	No
UFOP	C180824-1900	1.sSMPABC140.TXT	-	5713	1314	0.7	0.1608	2.9566	0.5039	4.2957	0.0227	3.1163	0.7	414	15	145	4	2465	51	35	No
UFOP	C180824-1900	1.sSMPABC146.TXT	-	5673	877	0.6	0.2102	2.3355	0.8552	3.8953	0.0295	3.1175	0.8	628	19	188	6	2907	38	30	No
UFOP	C180824-1900	1.sSMPABC147.TXT	-	5624	956	0.0	0.2228	4.6731	0.2382	17.0271	0.0078	16.3733	1.0	217	34	50	8	3001	77	23	No
UFOP	C180824-1900	1.sSMPABC148.TXT	-	5389	755	0.6	0.1250	2.3382	0.4711	3.7656	0.0273	2.9517	0.8	392	13	174	5	2029	42	44	No
UFOP	C180824-1900	1.sSMPABC149.TXT	-	5279	1180	0.0	0.1609	1.5065	0.6161	3.4139	0.0278	3.0636	0.9	487	14	177	5	2465	26	36	No
UFOP	C180824-1900	1.sSMPABC158.TXT	-	5211	1190	0.6	0.0696	2.6823	0.8772	5.7612	0.0914	5.0987	0.9	639	28	564	28	917	56	88	No
UFOP	C180824-1900	1.sSMPABC159.TXT	-	5278	949	2.1	0.3753	5.1167	0.3874	10.5154	0.0075	9.1865	0.9	332	31	48	4	3813	80	14	No
UFOP	C180824-1900	1.sSMPABC167.TXT	-	5053	950	0.5	0.1779	2.1318	0.6021	3.7707	0.0246	3.1103	0.8	479	15	156	5	2633	36	33	No
UFOP	C180824-1900	1.sSMPABC166.TXT	-	5041	949	0.6	0.1320	3.9558	0.6777	5.2750	0.0372	3.4896	0.7	525	22	236	8	2125	71	45	No
UFOP	C180824-1900	1.sSMPABC169.TXT	-	82792	1024	0.5	0.1638	2.5117	0.5133	3.9133	0.0227	3.0009	0.8	421	14	145	4	2495	43	34	No
UFOP	C180824-1900	1.sSMPABC170.TXT	-	84008	1034	0.5	0.2922	1.8073	0.6330	3.8101	0.0157	3.3542	0.9	498	16	100	3	3429	28	20	No
UFOP	C180824-1900	1.sSMPABC172.TXT	-	82626	947	0.4	0.1252	3.6355	0.5273	4.7404	0.0306	3.0421	0.6	430	17	194	6	2031	66	45	No
UFOP	C180824-1900	1.sSMPABC176.TXT	-	83420	942	0.4	0.2433	2.3436	1.6490	4.1754	0.0491	3.4556	0.8	989	28	309	10	3142	38	31	No
UFOP	C180824-1900	1.sSMPABC178.TXT	-	80880	565	1.2	0.2343	3.9191	1.4021	5.1953	0.0434	3.4106	0.7	890	32	274	9	3082	64	31	No
UFOP	C180824-1900	1.sSMPABC180.TXT	-	81099	754	0.4	0.0863	1.2567	0.4514	3.1374	0.0379	2.8747	0.9	378	10	240	7	1345	24	63	No
UFOP	C180824-1900	1.sSMPABC186.TXT	-	103264	593	0.9	0.2959	2.0548	0.9391	4.8134	0.0230	4.3528	0.9	672	25	147	6	3449	32	22	No
UFOP	C180824-1900	1.sSMPABC187.TXT	-	101644	937	0.6	0.1446	3.5704	0.6140	4.6699	0.0308	3.0100	0.6	486	19	196	6	2283	63	40	No
UFOP	C180824-1900	1.sSMPABC188.TXT	-	91037	1185	0.5	0.1284	2.3216	0.5283	4.2017	0.0298	3.5021	0.8	431	15	190	7	2076	41	44	No
LEGGA	C180824-1900	1900.2_1	8.4	-523	155	0.0	0.0998	203.3220	0.7157	1.7753	0.0704	1.7464	0.1	547	8	439	7	1026	45	80	No

Table SM3 U-Pb on zircon radiogenic data of the samples analyzed in this study (continuation).

LEGGA	C180824-1900	1900.2_2	-0.3	25	128	0.0	0.2958	83.2278	0.7026	1.9530	0.0653	2.2258	0.9	539	8	408	9	1132	59	76	No
LEGGA	C180824-1900	1900.2_3	-6.9	131	131	0.0	0.1456	48.2200	0.4976	2.4353	0.0545	2.8128	0.0	409	8	342	9	797	80	83	No
LEGGA	C180824-1900	1900.2_4	-3.6	-22	54	0.0	0.0369	1400.9440	0.4204	3.8002	0.0455	6.8735	0.6	356	12	286	19	893	205	80	No
LEGGA	C180824-1900	1900.2_5	6.1	416	109	0.0	0.2206	89.8480	0.7416	6.2470	0.0351	5.9964	0.1	559	26	222	13	2330	132	40	No
LEGGA	C180824-1900	1900.2_6	15.0	-979	139	0.0	0.3170	100.5890	2.1046	2.9615	0.0405	4.7007	0.2	1147	21	256	12	3797	78	22	No
LEGGA	C180824-1900	1900.2_7	3.7	10	97	0.0	0.5167	77.9280	0.9715	2.7785	0.0346	6.4138	0.2	687	14	219	14	2882	115	32	No
LEGGA	C180824-1900	1900.2_8	19.9	-16	74	0.0	0.5560	77.6928	1.5359	6.9229	0.0419	7.2098	0.2	929	39	264	19	3289	134	28	No
LEGGA	C180824-1900	1900.2_9	6.6	5	47	-0.3	0.5326	98.1032	0.5739	5.1588	0.0367	13.2740	0.2	457	19	231	30	1863	260	51	No
LEGGA	C180824-1900	1900.2_10	-11.4	4	55	0.0	0.5835	55.0296	0.5397	3.7260	0.0389	8.9211	0.4	436	13	245	22	1618	184	56	No
LEGGA	C180824-1900	1900.2_11	-3.5	-155	79	0.6	0.1084	157.8826	0.6226	3.3358	0.0722	3.3003	1.0	493	14	449	14	677	108	91	No
LEGGA	C180824-1900	1900.2_12	14.6	39	1799	0.0	0.0801	22.8620	0.5776	5.1732	0.0204	1.8104	0.3	465	22	130	2	2839	90	28	No
LEGGA	C180824-1900	1900.2_13	1.3	-1129	624	0.0	0.0495	32.7060	0.7514	2.0533	0.0805	0.8850	0.4	568	9	499	4	832	52	88	No
LEGGA	C180824-1900	1900.2_14	-0.9	-31	145	0.0	-0.0167	########	0.6043	2.3357	0.0663	2.1025	0.9	479	9	413	8	787	69	86	No
LEGGA	C180824-1900	1900.2_15	2.3	479	370	0.0	0.0826	44.2020	0.6093	2.9063	0.0514	1.9440	0.6	482	11	323	6	1319	48	67	No
LEGGA	C180824-1900	1900.2_16	4.6	-19	254	0.0	0.0432	402.5080	0.4569	2.0947	0.0460	1.9281	0.1	382	7	290	5	953	55	76	No
LEGGA	C180824-1900	1900.2_17	9.6	-666	138	0.0	0.1890	86.3732	0.4493	2.6853	0.0386	3.4352	0.8	376	8	244	8	1326	100	65	No
LEGGA	C180824-1900	1900.2_18	20.3	-49	37	0.1	0.0302	2305.0000	0.6031	5.5382	0.0590	10.8896	0.5	475	21	367	39	995	260	77	No
LEGGA	C180824-1900	1900.2_19	-0.3	1272	370	0.1	0.0608	31.8740	0.7787	2.2870	0.0904	0.7409	0.1	584	10	558	4	674	49	96	No
LEGGA	C180824-1900	1900.2_20	17.2	38	110	0.0	0.0377	417.6360	0.5605	2.8310	0.0403	4.9872	0.6	450	10	254	12	1628	120	56	No
LEGGA	C180824-1900	1900.2_21	4.4	2	257	0.0	0.0882	206.8880	0.5621	4.6062	0.0378	3.9015	0.4	449	17	239	9	1731	86	53	No
LEGGA	C180824-1900	1900.2_22	0.6	121	224	0.0	0.2535	59.8474	0.5073	2.9175	0.0491	3.3894	0.5	415	10	309	10	1048	62	74	No
LEGGA	C180824-1900	1900.2_23	-3.2	-220	99	0.0	0.0899	103.1860	0.4486	2.8517	0.0605	3.7211	0.8	377	9	378	14	364	113	100	No
LEGGA	C180824-1900	1900.2_24	1.3	111	157	0.0	0.1748	64.1400	0.7795	3.7231	0.0860	1.6658	0.1	583	17	532	9	778	81	91	No
LEGGA	C180824-1900	1900.2_25	7.7	-216	150	-0.1	0.0521	285.4380	0.5385	2.5342	0.0566	2.5662	0.1	436	9	355	9	873	70	81	No
LEGGA	C180824-1900	1900.2_27	9.6	243	1680	0.2	0.0841	19.2000	0.6324	2.0206	0.0305	3.0103	0.4	497	8	194	6	2348	49	39	No
LEGGA	C180824-1900	1900.2_30	7.8	49	101	0.0	0.0773	326.0480	0.4194	2.8386	0.0467	4.0096	0.7	355	9	294	12	767	107	83	No
LEGGA	C180824-1900	1900.2_31	0.6	257	351	0.0	0.0874	39.3180	0.7300	1.5285	0.0908	0.6582	0.1	556	7	561	4	518	35	101	No
LEGGA	C180824-1900	1900.2_32	2.2	82	88	0.1	0.1991	125.6602	0.4667	3.6189	0.0594	4.0120	0.1	387	12	371	15	445	109	96	No
LEGGA	C180824-1900	1900.2_33	1.0	-5	133	-0.1	0.0386	298.6500	0.6203	3.9694	0.0633	2.5529	0.1	489	16	395	10	913	98	81	No
LEGGA	C180824-1900	1900.2_34	4.8	-537	574	0.0	0.1219	41.2000	0.5196	1.7866	0.0355	1.7766	1.0	424	6	225	4	1717	52	53	No
LEGGA	C180824-1900	1900.2_35	1.1	298	343	0.0	0.0177	289.0800	0.5298	1.9752	0.0517	1.1750	0.6	431	7	325	4	1021	50	75	No
LEGGA	C180824-1900	1900.2_36	8.0	1849	967	0.0	0.1095	26.2600	0.6320	1.4060	0.0311	2.7534	0.3	497	6	197	5	2314	47	40	No
LEGGA	C180824-1900	1900.2_37	5.3	-4	140	0.0	0.1497	137.2450	0.8266	2.8221	0.0489	4.5952	0.1	610	13	308	14	1991	94	50	No
LEGGA	C180824-1900	1900.2_39	4.0	233	538	0.0	0.0587	28.1200	0.8407	4.9789	0.0626	1.4947	0.5	614	21	391	6	1519	69	64	No
UFOP	C180823-0955	1.sSMPABC171.TXT	0.0	546	2241	0.3	0.0499	2.6277	0.2110	3.9233	0.0307	2.9134	0.7	194	10	195	4	188	10	100	No
UFOP	C180823-0955	1.sSMPABC172.TXT	0.3	67	112	0.7	0.0500	8.3097	0.2116	8.6851	0.0307	2.5257	0.3	195	15	195	3	195	15	100	No
UFOP	C180823-0955	1.sSMPABC211.TXT	0.0	406	1471	0.3	0.0499	1.8717	0.2114	5.1681	0.0307	4.8173	0.9	195	21	195	6	193	22	100	No
UFOP	C180823-0955	1.sSMPABC155.TXT	0.1	145	122	0.5	0.0500	5.4132	0.2117	5.8954	0.0307	2.3353	0.4	195	11	195	3	195	11	100	No
UFOP	C180823-0955	1.sSMPABC178.TXT	0.1	161	486	0.4	0.0500	6.9215	0.2118	8.1472	0.0307	4.2976	0.5	195	23	195	6	195	24	100	No
UFOP	C180823-0955	1.sSMPABC212.TXT	0.1	308	1010	0.4	0.0500	3.3099	0.2133	6.7169	0.0310	5.8447	0.9	196	31	197	8	353	32	100	No
UFOP	C180823-0955	1.sSMPABC180.TXT	0.1	362	643	0.5	0.0501	3.4994	0.2227	3.9719	0.0323	1.8790	0.5	204	7	205	3	198	8	100	No
UFOP	C180823-0955	1.sSMPABC154.TXT	0.1	167	348	0.3	0.0502	3.4425	0.2246	3.7630	0.0324	1.5197	0.4	206	6	206	2	205	7	100	No
UFOP	C180823-0955	1.sSMPABC151.TXT	0.1	214	270	0.5	0.0510	4.4221	0.2661	5.1546	0.0379	2.6485	0.5	239	13	240	4	239	14	100	No
UFOP	C180823-0955	1.sSMPABC157.TXT	0.1	209	259	0.4	0.0512	3.0503	0.2837	3.4031	0.0402	1.5090	0.4	253	7	254	3	251	7	100	No
UFOP	C180823-0955	1.sSMPABC207.TXT	0.0	988	2245	0.2	0.0512	1.5054	0.2858	7.2021	0.0404	7.0430	1.0	255	53	256	12	252	55	100	No
UFOP	C180823-0955	1.sSMPABC150.TXT	0.1	130	109	0.4	0.0515	6.9334	0.2877	7.2278	0.0405	2.0418	0.3	256	15	256	3	264	15	100	No
UFOP	C180823-0955	1.sSMPABC188.TXT	0.0	412	374	0.5	0.0512	2.2057	0.2891	2.5896	0.0409	1.3568	0.5	258	5	259	2	251	6	100	No
UFOP	C180823-0955	1.sSMPABC200.TXT	0.1	129	146	0.3	0.0513	3.1657	0.2897	3.4903	0.0409	1.4699	0.4	258	7	259	2	256	7	100	No
UFOP	C180823-0955	1.sSMPABC209.TXT	0.0	561	420	0.3	0.0522	3.8212	0.3373	4.5218	0.0469	2.4177	0.5	295	13	295	5	292	14	100	No
UFOP	C180823-0955	1.sSMPABC194.TXT	-0.1	-170	86	0.6	0.0527	5.8681	0.3704	6.3264	0.0510	2.3640	0.4	320	18	321	5	314	18	100	No

Table SM3 U-Pb on zircon radiogenic data of the samples analyzed in this study (continuation).

UFOP	C180823-0955	1.sSMPABC168.TXT	0.1	169	156	0.6	0.0527	4.7829	0.3707	5.3842	0.0510	2.4725	0.5	320	16	321	5	316	17	100	No
UFOP	C180823-0955	1.sSMPABC179.TXT	0.0	658	123	0.5	0.0527	3.2326	0.3711	3.6411	0.0511	1.6758	0.5	320	9	321	3	316	10	100	No
UFOP	C180823-0955	1.sSMPABC197.TXT	0.0	375	421	0.4	0.0526	2.0367	0.3705	2.9806	0.0511	2.1762	0.7	320	10	321	5	312	11	100	No
UFOP	C180823-0955	1.sSMPABC193.TXT	0.1	141	97	0.9	0.0527	8.9018	0.3716	9.1019	0.0511	1.8977	0.2	321	21	321	4	317	21	100	No
UFOP	C180823-0955	1.sSMPABC191.TXT	0.0	571	774	0.4	0.0527	1.9113	0.3717	2.7175	0.0512	1.9318	0.7	321	8	322	4	316	9	100	No
UFOP	C180823-0955	1.sSMPABC175.TXT	0.1	187	136	0.3	0.0528	3.5668	0.3725	4.0043	0.0512	1.8199	0.5	321	11	322	4	319	11	100	No
UFOP	C180823-0955	1.sSMPABC176.TXT	0.1	208	198	0.4	0.0533	3.8385	0.4060	4.1177	0.0552	1.4906	0.4	346	10	347	3	341	11	100	No
UFOP	C180823-0955	1.sSMPABC187.TXT	0.0	1341	1481	0.2	0.0532	0.8656	0.4076	1.8695	0.0555	1.6570	0.9	347	5	348	4	339	6	100	No
UFOP	C180823-0955	1.sSMPABC153.TXT	0.0	521	370	0.3	0.0535	1.5985	0.4100	2.0981	0.0556	1.3590	0.6	349	6	349	3	348	6	100	No
UFOP	C180823-0955	1.sSMPABC159.TXT	0.0	367	182	0.6	0.0534	2.0108	0.4114	2.4910	0.0559	1.4703	0.6	350	7	351	3	345	8	100	No
UFOP	C180823-0955	1.sSMPABC160.TXT	0.1	355	287	0.4	0.0545	2.1165	0.4785	2.6758	0.0636	1.6372	0.6	397	9	398	4	393	10	100	No
UFOP	C180823-0955	1.sSMPABC152.TXT	0.1	263	158	0.3	0.0546	1.8255	0.4836	2.2734	0.0642	1.3549	0.6	400	7	401	4	397	8	100	No
UFOP	C180823-0955	1.sSMPABC173.TXT	0.1	129	262	0.4	0.0551	16.2717	0.4905	16.5820	0.0645	3.1929	0.2	405	53	403	8	417	53	100	No
UFOP	C180823-0955	1.sSMPABC208.TXT	0.0	639	419	0.2	0.0547	1.3850	0.4872	1.8573	0.0646	1.2374	0.7	403	5	403	3	402	6	100	No
UFOP	C180823-0955	1.sSMPABC158.TXT	0.0	1063	129	0.4	0.0547	2.6613	0.4870	3.1233	0.0646	1.6348	0.5	403	10	404	4	399	11	100	No
UFOP	C180823-0955	1.sSMPABC170.TXT	0.0	1148	1323	0.3	0.0546	1.2286	0.4869	1.9785	0.0647	1.5508	0.8	402	6	404	4	395	7	100	No
UFOP	C180823-0955	1.sSMPABC216.TXT	0.0	902	765	0.2	0.0557	1.1887	0.5423	2.0398	0.0706	1.6577	0.8	440	7	440	5	442	9	100	No
UFOP	C180823-0955	1.sSMPABC156.TXT	0.1	352	392	0.2	0.0556	2.6494	0.5427	3.3948	0.0707	2.1225	0.6	440	14	441	6	438	15	100	No
UFOP	C180823-0955	1.sSMPABC192.TXT	0.1	355	205	0.4	0.0569	1.8967	0.6200	2.2308	0.0790	1.1742	0.5	489	7	490	4	488	8	100	No
UFOP	C180823-0955	1.sSMPABC169.TXT	0.0	455	213	0.5	0.0567	1.3224	0.6184	1.7170	0.0791	1.0952	0.6	488	5	491	3	480	6	100	No
UFOP	C180823-0955	1.sSMPABC149.TXT	0.0	1171	23	0.5	0.0570	9.9207	0.6213	10.9568	0.0791	4.6510	0.4	490	65	491	15	490	67	100	No
UFOP	C180823-0955	1.sSMPABC199.TXT	0.0	461	179	0.3	0.0571	2.2392	0.6243	3.2519	0.0793	2.3581	0.7	492	16	492	7	496	17	100	No
UFOP	C180823-0955	1.sSMPABC215.TXT	0.0	594	305	0.2	0.0570	1.3899	0.6237	1.7702	0.0793	1.0963	0.6	492	6	492	3	492	7	100	No
UFOP	C180823-0955	1.sSMPABC217.TXT	0.0	1481	346	0.1	0.0585	1.0929	0.7175	1.6715	0.0889	1.2647	0.8	549	6	549	4	550	8	100	No
UFOP	C180823-0955	1.sSMPABC219.TXT	0.0	1377	349	0.1	0.0586	1.0982	0.7184	1.6426	0.0889	1.2214	0.7	549	6	549	4	552	7	100	No
UFOP	C180823-0955	1.sSMPABC214.TXT	0.1	292	228	0.7	0.0588	4.7316	0.7220	5.1084	0.0891	1.9256	0.4	551	21	550	7	559	22	100	No
UFOP	C180823-0955	1.sSMPABC220.TXT	0.0	1032	350	0.1	0.0586	0.9520	0.7215	1.4943	0.0892	1.1518	0.8	551	5	551	4	554	7	100	No
UFOP	C180823-0955	1.sSMPABC218.TXT	0.0	775	342	0.1	0.0586	1.0202	0.7223	1.5130	0.0894	1.1173	0.7	552	5	552	4	553	7	100	No
UFOP	C180823-0955	1.sSMPABC167.TXT	0.0	500	223	0.4	0.0583	2.1659	0.7193	2.6620	0.0895	1.5476	0.6	550	11	552	5	542	12	100	No
UFOP	C180823-0955	1.sSMPABC189.TXT	-	1259	192	0.5	0.0796	7.6652	0.6803	8.6986	0.0620	4.1123	0.5	527	37	388	15	1187	159	74	No
UFOP	C180823-0955	1.sSMPABC190.TXT	-	1231	124	0.5	0.0797	9.0983	0.6766	10.0523	0.0616	4.2744	0.4	525	42	385	16	1189	191	73	No
UFOP	C180823-0955	1.sSMPABC195.TXT	-	1124	181	0.7	0.0797	10.5999	0.6695	12.2299	0.0609	6.1002	0.5	520	51	381	23	1190	225	73	No
UFOP	C180823-0955	1.sSMPABC196.TXT	-	1239	7	1.2	0.3285	17.0234	8.3301	17.5050	0.1839	4.0782	0.2	2268	174	1088	41	3610	289	48	No
UFOP	C180823-0955	1.sSMPABC213.TXT	-	1763	420	0.6	0.1056	14.6473	1.2164	15.1812	0.0836	3.9904	0.3	808	89	517	20	1725	296	64	No
UFOP	C180823-0955	1.sSMPABC174.TXT	-	1952	5	-0.3	0.9793	8.1139	9.7350	70.3832	0.0721	69.9140	1.0	2410	1034	449	310	5208	119	19	No
UFOP	C180823-0955	1.sSMPABC177.TXT	-	1562	159	0.7	0.0840	21.6617	0.7976	22.3285	0.0689	5.4162	0.2	595	106	429	23	1293	492	72	No
UFOP	C180823-0955.2	1.sSMPABC051.TXT	0.5	377	1134	0.1	0.0500	5.9003	0.2131	6.8584	0.0309	3.4963	0.5	196	12	196	7	196	143	100	No
UFOP	C180823-0955.2	1.sSMPABC038.TXT	1.5	122	203	0.5	0.0501	7.2641	0.2174	7.5849	0.0315	2.1826	0.3	200	14	200	4	200	178	100	No
UFOP	C180823-0955.2	1.sSMPABC030.TXT	0.9	213	860	1.4	0.0503	4.1325	0.2259	4.6354	0.0326	2.0998	0.5	207	9	207	4	207	99	100	No
UFOP	C180823-0955.2	1.sSMPABC017.TXT	0.5	363	540	0.5	0.0503	3.7416	0.2262	4.1531	0.0326	1.8024	0.4	207	8	207	4	207	89	100	No
UFOP	C180823-0955.2	1.sSMPABC009.TXT	0.7	263	493	0.3	0.0503	33.7535	0.2311	34.4629	0.0333	6.9562	0.2	211	68	211	14	211	1054	100	No
UFOP	C180823-0955.2	1.sSMPABC028.TXT	0.6	315	1151	0.5	0.0504	4.7393	0.2319	5.4769	0.0334	2.7452	0.5	212	11	212	6	212	114	100	No
UFOP	C180823-0955.2	1.sSMPABC067.TXT	1.9	99	132	1.3	0.0505	12.1835	0.2405	12.6310	0.0345	3.3321	0.3	219	25	219	7	219	309	100	No
UFOP	C180823-0955.2	1.sSMPABC039.TXT	0.6	313	335	0.3	0.0506	4.4072	0.2433	5.1035	0.0349	2.5734	0.5	221	10	221	6	221	105	100	No
UFOP	C180823-0955.2	1.sSMPABC035.TXT	0.1	1342	726	0.7	0.0506	6.3769	0.2479	6.8269	0.0355	2.4376	0.4	225	14	225	5	225	155	100	No
UFOP	C180823-0955.2	1.sSMPABC069.TXT	1.1	174	194	0.6	0.0506	5.6788	0.2479	5.9814	0.0355	1.8783	0.3	225	12	225	4	225	137	100	No
UFOP	C180823-0955.2	1.sSMPABC036.TXT	0.2	1030	506	0.5	0.0507	4.8932	0.2505	5.2508	0.0358	1.9046	0.4	227	11	227	4	227	117	100	No
UFOP	C180823-0955.2	1.sSMPABC053.TXT	0.1	2853	879	0.4	0.0507	3.8780	0.2530	4.3526	0.0362	1.9764	0.5	229	9	229	4	229	92	100	No
UFOP	C180823-0955.2	1.sSMPABC015.TXT	0.3	675	1787	0.5	0.0508	3.6643	0.2553	4.0873	0.0365	1.8109	0.4	231	9	231	4	231	87	100	No
UFOP	C180823-0955.2	1.sSMPABC073.TXT	0.9	209	294	0.9	0.0509	5.8539	0.2613	6.2138	0.0372	2.0840	0.3	236	13	236	5	236	141	100	No

Table SM3 U-Pb on zircon radiogenic data of the samples analyzed in this study (continuation).

UFOP	C180823-0955.2	1.sSMPABC068.TXT	-0.1	-2099	560	0.5	0.0509	4.9198	0.2631	5.2653	0.0375	1.8760	0.4	237	11	237	4	237	118	100	No
UFOP	C180823-0955.2	1.sSMPABC052.TXT	0.4	444	907	0.7	0.0509	8.0913	0.2645	8.5299	0.0377	2.7000	0.3	238	18	238	6	238	198	100	No
UFOP	C180823-0955.2	1.sSMPABC074.TXT	1.0	182	174	0.4	0.0510	18.5741	0.2696	18.8467	0.0383	3.1937	0.2	242	42	242	8	242	496	100	No
UFOP	C180823-0955.2	1.sSMPABC012.TXT	0.2	743	275	0.5	0.0511	11.6897	0.2748	11.8662	0.0390	2.0387	0.2	246	27	246	5	246	294	100	No

Figure SM4 Cathodo-luminescence (CL) images showing the different types of zircon found in the samples of this study, as well as the locations of the analysis spots, analysis number, and the 206Pb/238U apparent ages. (a) Monzodiorite (C180825-1115), (b) paragneiss from Moulin de Laurière (C180825-0930), (c) amphibolite from Exideuil (C180824-1500), (d) amphibolite from St Junien (C180822-1625), (e) Recoudert impact melt rock (C180824-1900), and (f) Montoume impact melt rock (C180823-0955). (g) Selected CL, backscattered electron (BSE), and secondary electron (SE) images from the Recoudert and Montoume IMR zircon mounts.

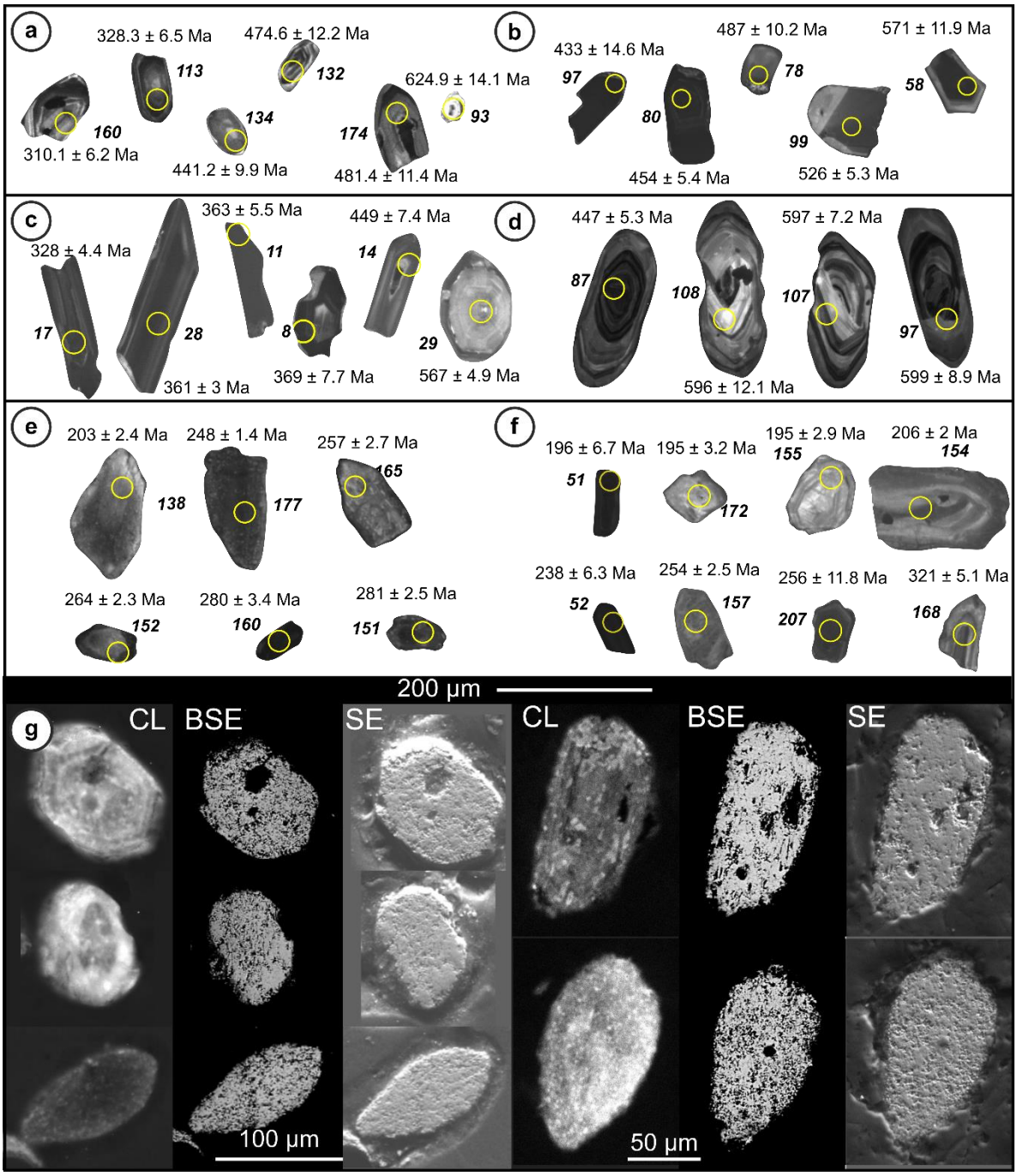


Figure SM5 Histograms for the age distributions of the different samples, considering the different zircon textures from CL imaging and the respective locations of the analysis spots. On the left are the histograms of the basement rocks: Amphibolite from St Junien (C180822-1625), amphibolite from Exideuil (C180824-1500), paragneiss from Moulin de Laurière (C180825-0930), and monzodiorite (C180825-1115). On the right are the diagrams for Recoudert (C180824-1900) and Montoume (C180823-0955) impact melt rocks.

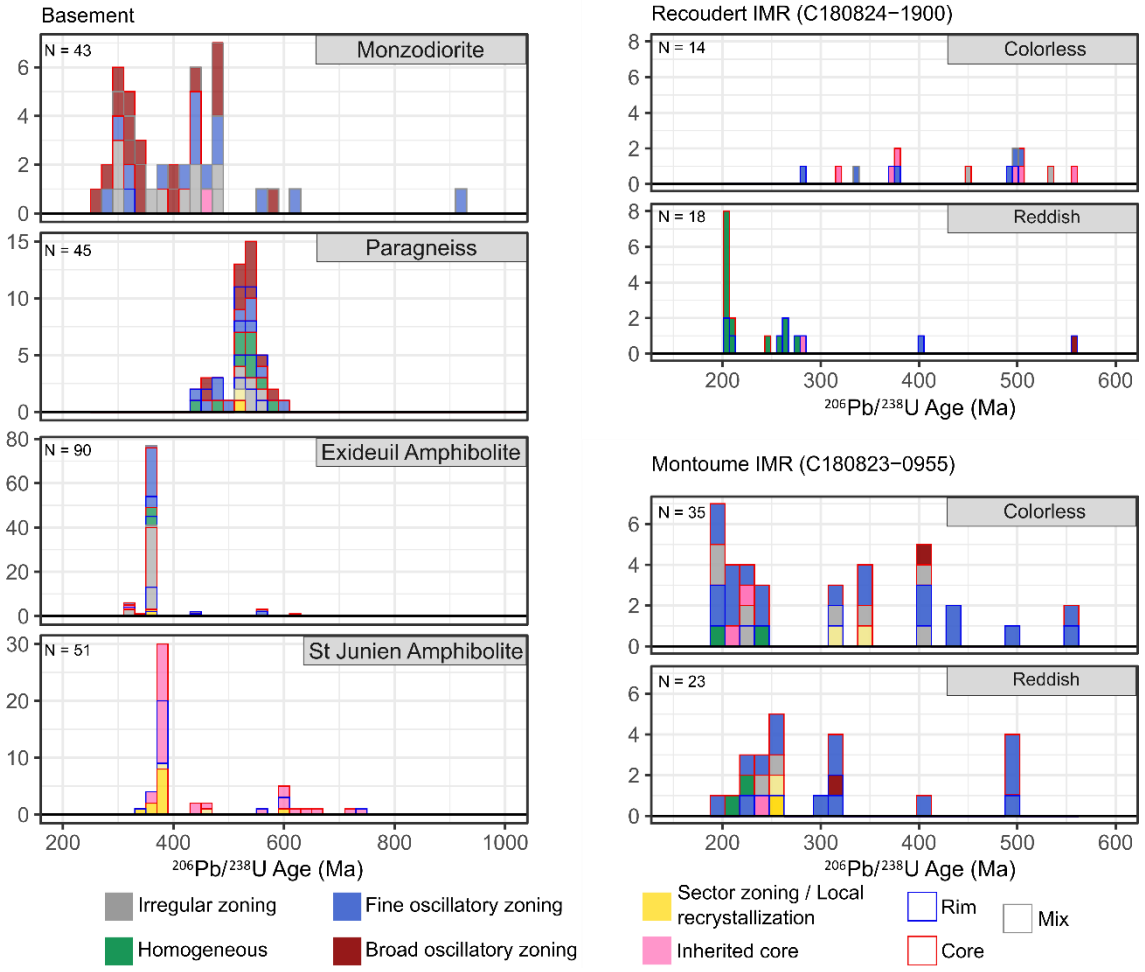


Figure SM6a. Box plots for U and Th contents and Th/U ratios of all zircon grains with a 7/5 : 6/8 concordance within the 90-110 % limit.

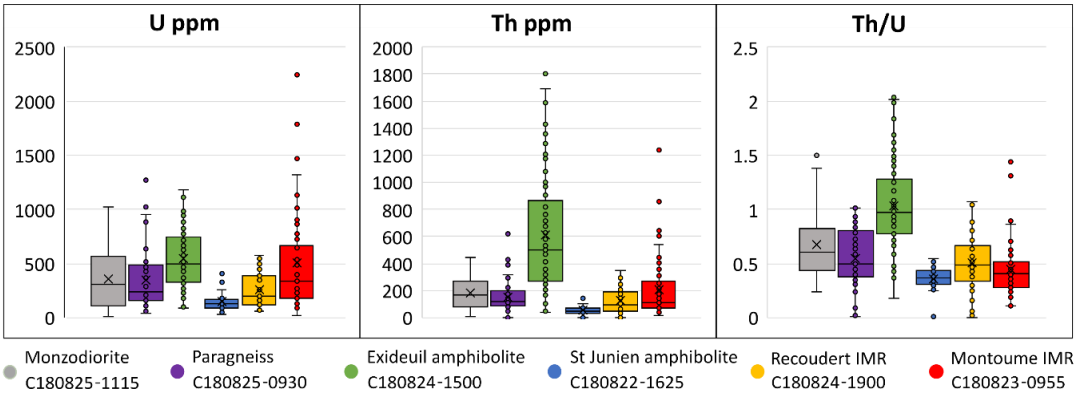


Figure SM6b. Box plots of the U and Th contents and Th/U ratio of the different zircon populations of each sample classified according to the textural characteristics and CL response.

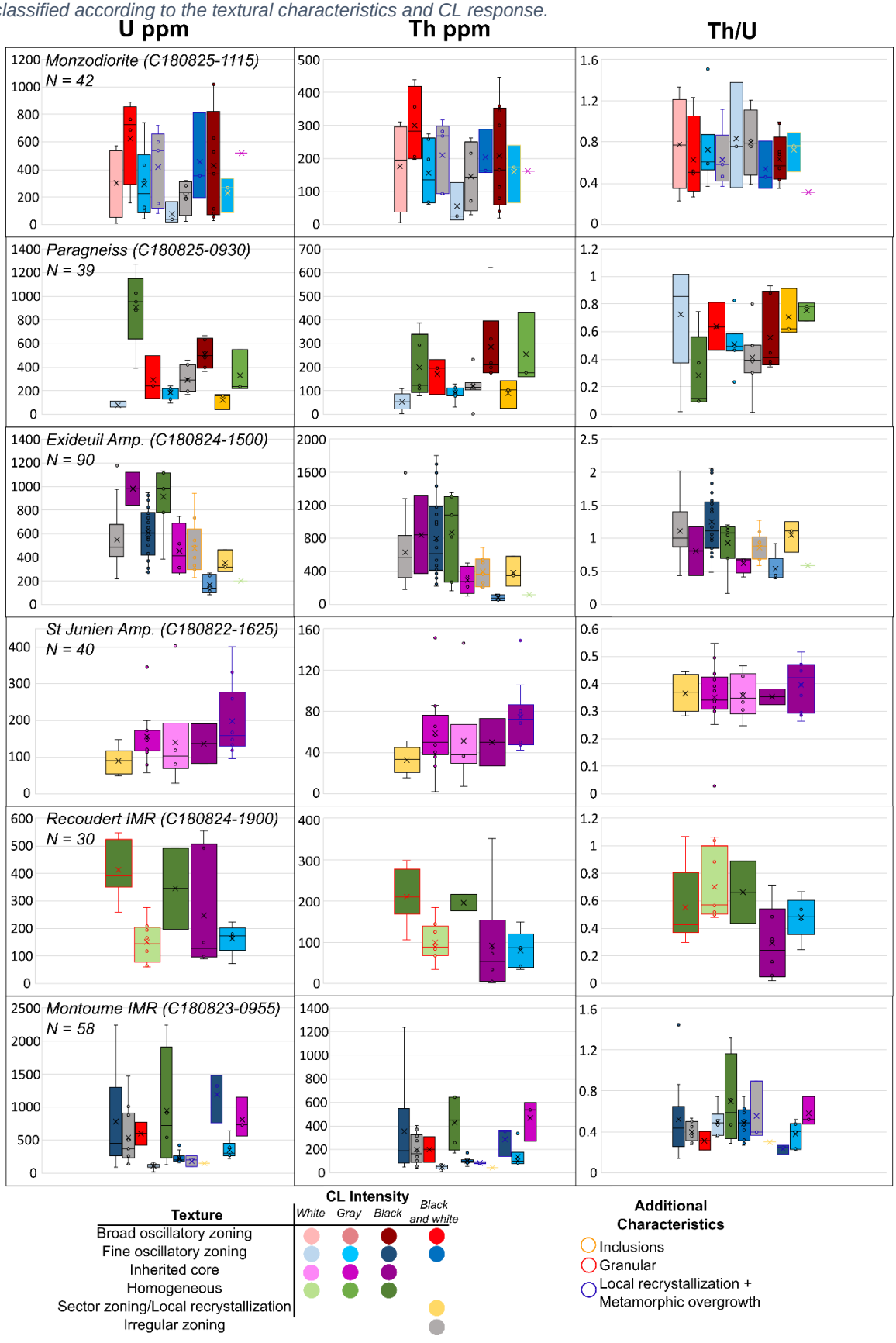


Figure SM6c. Contents of (a) U and (b) Th, and (c) Th/U ratios, as well as (d) radiation dose plotted versus the apparent $^{206}Pb/^{238}U$ ages for all zircon grains with a 7/5 : 6/8 concordance within the 90-110 % limit. (d) Radiation doses calculated according to Murakami et al. (1991) and transition zone between crystalline and metamict zircon domains at 3.5 to 8.0 x 10^{18} α/g taken from Ewing et al. (2003).

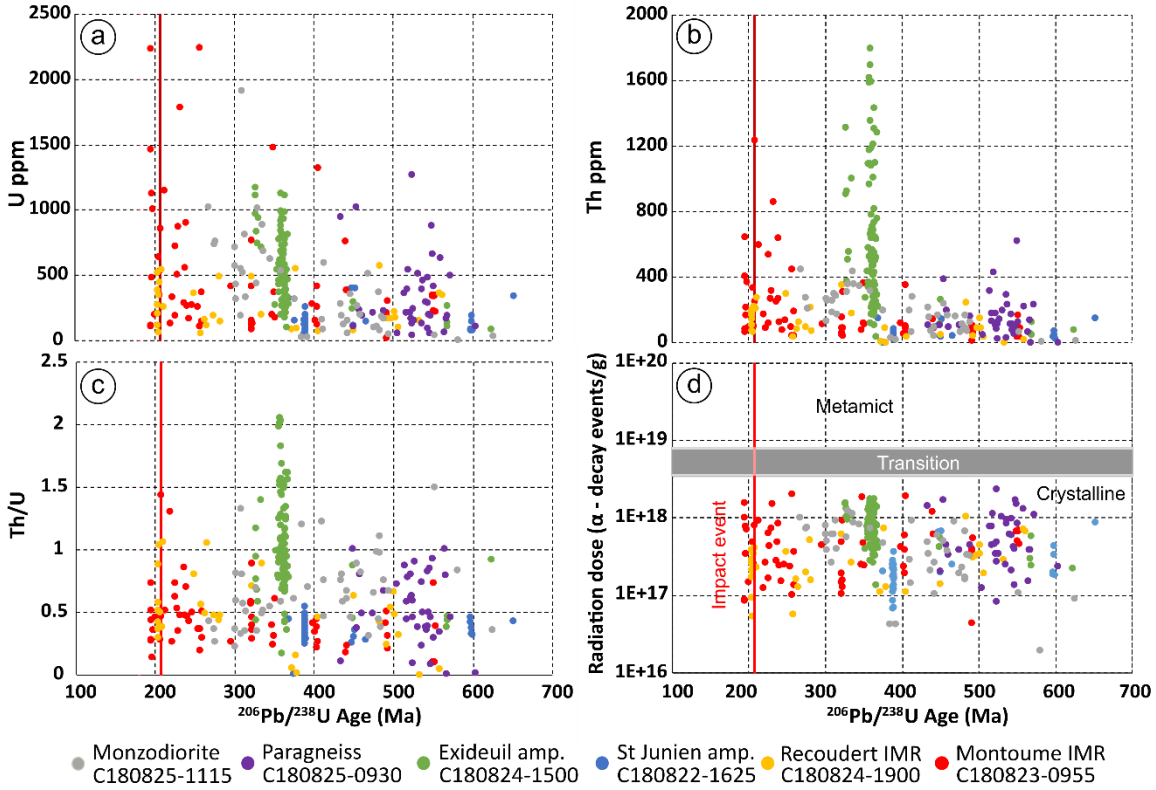


Table SM7. Zircon characteristics, CL textures, composition, and ages for the six samples analyzed in this study.

Sample ID	Lithology	Location	Zircon characteristics	Zircon CL textures	Zircon composition	Calculated Ages
C180825-1115	Monzodiorite	La Martinie 45° 49.092' N 0° 45.488' E	Prismatic, colorless to grayish, transparent to translucent, rounded to sub-rounded AR = 1:1 - 7:2, size = 40 - 200 µm	Oscillatory zonation, metamorphic overgrowths, local recrystallization	U = 8 - 1024 ppm Th = 7 - 446 ppm Th/U = 0.2 - 1.5	PDP age peaks: 481, 457, 438, 411, 391, 375, 334,328, 308, 301, 275, 268 Ma
C180825-0930	Paragneiss	Moulin de Laurière 45° 49.949' N 0° 46.338' E	Prismatic, colorless, transparent to translucent, subhedral to sub-rounded AR = 2:1 - 1:1, size = 60 - 275 µm	Homogeneous, oscillatory or sector zonation, inherited cores, metamorphic overgrowths, local recrystallization	U = 41 - 1273 ppm Th = 24 - 622 ppm Th/U = 0.1 - 1.0	PDP age peaks: 581, 565, 549, 543, 522, 516, 505, 473, 457 Ma
C180824-1500	Amphibolite	Exideuil Qu 45° 53.052' N 0° 40.842' E	Type 1 and 2: Prismatic, colorless, transparent to translucent, euhedral to subhedral Type 1 - AR = 6:1–7:3, size = 88 - 270 µm Type 2 - AR = 3:2–5:2, size = 90 - 173 µm	Type 1= Homogeneous, oscillatory zonation, inherited cores, metamorphic overgrowths Type 2 = Oscillatory or sector zonation, local recrystallization, metamorphic overgrowths	U = 55 - 1177 ppm Th = 37 - 1800 ppm Th/U = 0.2 - 2.1	WA = 567 ± 3 (MSWD = 0.02; n = 4), 448 ± 3 (MSWD = 0.36; n = 3), 361 ± 1 (MSWD = 0.83; n = 87), 328 ± 1 (MSWD= 0.63; n= 8)
C180822-1625	Amphibolite	St Junien Ceitce 45° 53.238' N 0° 53.320' E	Prismatic, colorless, transparent, euhedral to sub-rounded AR = 4:1–3:2, size = 145 - 290 µm	Inherited cores, sector or oscillatory zonation, metamorphic overgrowths, local recrystallization	U = 29 - 403 ppm Th = 7 - 151 ppm Th/U = 0.2 - 0.5	WA = 597 ± 3 (MSWD = 0.03; n = 5), 371 ± 2 (MSWD = 0.72; n = 6), 351 ± 5 (MSWD = 0.62; n = 3); CA = 449 ± 3 (MSWD = 0.44; n = 3), 388 ± 1 (MSWD = 1.7; n = 26)
C180824-1900	Yellow impact melt rock	Recoudert 45°48.349' N 0°47.099' E	Type 1 = Reddish, translucent, subhedral to sub-rounded, prismatic Type 2 = Colorless, transparent to translucent, rounded to sub-rounded, prismatic Type 1 and 2 - AR = 3:1–1:1, size = 37 - 180 µm	Type 1= Homogeneous, in part granular, oscillatory zonation, inherited cores. Type 2= Oscillatory zonation, inherited cores	U = 59 - 578 ppm Th = 33 - 351 ppm Th/U = 0.2 - 1.1	PDP age peaks: 560, 501, 377, 281, 262, 203 Ma
C180823-0955	Red impact melt	Montoume 45° 46.535' N 0° 46.488' E	Type 1 = Reddish, translucent, subhedral to sub-rounded, prismatic Type 2 = Colorless, transparent to translucent, rounded to sub-rounded, prismatic Type 1- AR = 3:2–2:1, size = 45 - 180 µm Type 2 - AR = 3:1–1:1, size = 60 - 156 µm	Type 1 and 2= Oscillatory or sector zonation, homogeneous, inherited cores, metamorphic overgrowths, local recrystallization	U = 238 - 2241 ppm Th = 12 - 1236 ppm Th/U = 0.1 - 1.4	PDP age peaks: 551, 491, 440, 403, 349, 321, 258, 238, 226, 206, 195 Ma

Qu = quarry; AR = aspect ratio; PDP = probability density plot; WA = weighted average age; CA = concordia

CHAPTER 5

Manuscript 2

5 MANUSCRIPT 2

This version of the manuscript has been submitted to the journal *Geochimica et Cosmochimica Acta* on February 16, 2025. At the present time of revision of the thesis, the manuscript is in revision based on the reviews received from the journal.

Shock deformation and U-Pb isotope systematics in zircon from impactites of the Rochechouart impact structure: impact age and zircon provenance.

Daniela Guerrero [a, *], Wolf Uwe Reimold [a], Natalia Hauser [a], Gavin Kenny [b], Martin Whitehouse [b], Philippe Lambert [c]

[a] *Postgraduate Program in Geology, Laboratory of Geochronology, Geosciences Institute, University of Brasília, 70910-900 Brasília, DF, Brazil.*

[b] *Department of Geosciences, Swedish Museum of Natural History, SE-104 05 Stockholm, Sweden.*

[c] *CIRIR - Centre International de Recherche et de Restitution sur les Impacts et sur Rochechouart, 87600 Rochechouart, France.*

*Corresponding author. E-mail: daaguerrerogu@gmail.com

ABSTRACT

The > 23 km diameter, ~207 Ma old Rochechouart impact structure is located in the NW part of the Paleozoic basement of the French Massif Central. Despite significant erosion, this impact structure preserves a heterogeneous suite of impactites and the transition between the crater floor and the basement. U-Pb isotopes in zircon from impactites and basement lithologies of this structure have shown a wide variety of shock deformation textures and age distributions. In this study, we present a comprehensive analysis combining a detailed textural characterization (CL, BSE, EBSD) and U-Pb geochronological analyses at different spatial resolutions (SIMS and LA-ICP-MS) of zircon from two melt-bearing breccias (suevites) from Chassenon and Videix, and one impact melt rock (IMR) from Babaudus. The analyzed crystals display a variety of shock deformation textures, and the identification of FRIGN zircon and grains with high proportions of reidite in the Videix

suevite indicates that these types of shock deformation are more widespread than previously reported. In the Chassenon suevite, U-Pb age resetting increases with shock intensity, while in the Videix suevite, higher U and/or Th contents also appear to control resetting. In the Babaudus IMR, the similar ages between shocked granular zircons and some unshocked grains suggests that additional factors, beyond shock deformation and composition, influence age resetting. The best estimate of the impact age obtained from this study is 203 ± 4 Ma (2σ, MSWD = 3.4, probability = 0.065) for SIMS analyses of two granular grains from the Babaudus IMR and one granular crystal from the Videix suevite. Zircons with youngest ages - but close to the widely accepted age for the impact at 207 Ma - show similar characteristics, highlighting the challenge of distinguishing between grains and separating ages related to the impact from possible post-impact events (e.g., hydrothermal alteration). Finally, the geochronological results for the Videix and the Chassenon suevites show a clear correlation with provenance results for granitic and gneissic target lithologies, respectively. In contrast, the Babaudus IMR has an age distribution comparable with other impact melt rocks, Montoume and Recoudert, but not from an identified target lithologies.

Keywords: Rochechouart impact structure, U-Pb in zircon, Shock metamorphism, EBSD, suevites, impact melt rock.

5.1 Introduction

The > 23 km Rochechouart impact structure is currently the only impact structure identified in France. It is located in the NW part of the Paleozoic crystalline basement of the French Massif Central (FMC) (cf. Figure 5.1a; e.g., Gottwald et al., 2020; Kenkmann, 2021; Osinski et al., 2022; Schmieder and Kring, 2020). The impact origin of Rochechouart was first described by Kraut et al. (1969) through recognition of shatter cones and planar deformation features (PDFs) in quartz. The allochthonous impactites of the Rochechouart impact structure form a continuum with increasing melt and decreasing clast content, from polymict lithic impact breccia to suevite, and to clast-free to clast-poor impact melt rock (Lambert, 2010; Sapers et al., 2014). Furthermore, all impactites exhibit strong overprint from hydrothermal

alteration, indicative of a widespread post-impact hydrothermal system, with a strong K-metasomatism (particularly in the melt-rich phases) and the development of argillic, carbonate, oxide, and sulfide alteration assemblages (Lambert, 2010; Sapers et al., 2014; Simpson et al., 2017).

Combined detailed textural characterization and geochronologic analysis on zircon have been conducted in numerous impact structures in the last ten years (e.g., Cavosie et al., 2015; Crow et al., 2017; Erickson et al., 2021; Hauser et al., 2019; Herrmann et al., 2023; Kenny et al., 2017, 2019; McGregor et al., 2019, 2021; Moser et al., 2011; Rasmussen et al., 2019, 2020; Schmieder et al., 2015; Schwarz et al., 2020). These investigations have shown that zircons with similar shock deformation features can record a wide range of ages, and in consequence, their interpretation can be very complex. Furthermore, methodologies applied play a crucial role in obtaining accurate data and ensuring reliable age interpretations.

Previous geochronological studies in the Rochechouart impact structure have been mainly focused on determining the age of the impact event, which is currently widely considered as constrained to 206.92 + 0.20 / -0.32 Ma (Cohen et al., 2017). Comprehensive U-Pb geochronologic analyses have been conducted by laser ablation inductively coupled plasma mass spectrometry (LA-ICP-MS) in zircons from impact melt rocks (Guerrero et al., 2024; Horne, 2016; Rasmussen et al., 2020). These studies document four types of ages: 1) compatible with the impact event, 2) post-impact ages, 3) ages concordant with pre-impact regional geological events, and 4) ages that suggest incomplete resetting of the isotopic system. Detailed textural characterization of zircons from the Chassenon suevite and the Babaudus impact melt rock (Figure 5.1) has revealed a great variety of shock-metamorphic features, including ‘‘former reidite in granular neoblastic” (FRIGN) zircon and multiple variants of reidite, the high-pressure polymorph of zircon (Plan et al., 2021; Rasmussen et al., 2020). The highly heterogeneous zircon shock deformation and age distributions provide a good opportunity to investigate the response of the zircon U-Pb isotopic system to variable shock metamorphic conditions.

Here, we present a detailed analysis of impact-generated microtextures in zircon and high-spatial resolution geochronology with secondary ion mass spectrometry (SIMS) and LA-ICP-MS. This approach allowed the analysis of discrete domains of zircons from two suevites from Chassenon and Videix, and a further impact melt rock from Babaudus, with a total of 320 zircons analyzed (Figure 5.1). This represents the first comprehensive U-Pb geochronologic study for impactites from the Rochechouart impact structure beyond the impact melt rocks. This expanded dataset for zircon of varied levels of shock deformation, from impactite samples from diverse localities allows to evaluate the pressure and temperature conditions associated with the observed shock deformation textures, the relation of shock textures with recorded ages, and the significance of the multiple age distributions previously documented only for impact melt rocks. Furthermore, the relationships between the geochronologic age distributions of the impactites and the target rocks (Guerrero et al., 2024) are explored to identify the most probable precursor lithologies for each sample. Additionally, the comparison of the results obtained by different geochronologic methodologies allows to evaluate their possible limitations and influence on the obtained ages.

5.2 Geological background

The basement of the French Massif Central (FMC) represents one of the largest exposures of the Variscan Belt, consolidated during the Devonian – Carboniferous Variscan Orogeny through successive collisions between Laurussia, Gondwana-derived microcontinents, and Gondwana, during the amalgamation of Pangea (e.g., Franke et al., 2017; Kroner and Romer, 2013; Lardeaux, 2014; Martínez Catalán et al., 2021; Schulmann et al., 2014). The most widespread basement units in the area of the Rochechouart impact structure are the paragneisses and leptynites with amphibolite lenses of the allochthonous Lower and Upper Gneiss units (LGU, UGU; Chèvremont et al., 1996; Lambert, 2010). These units are interpreted to be derived from Ediacaran sedimentary rocks of the northern Gondwana margin intruded by Cambrian to Early Ordovician alkaline granitic rocks. These lithologies underwent multiple phases of metamorphism and retrogression from the Late Silurian to the

uppermost Devonian / lower Carboniferous, during the main continental collision of the Variscan Orogeny (e.g., Lardeaux, 2014).

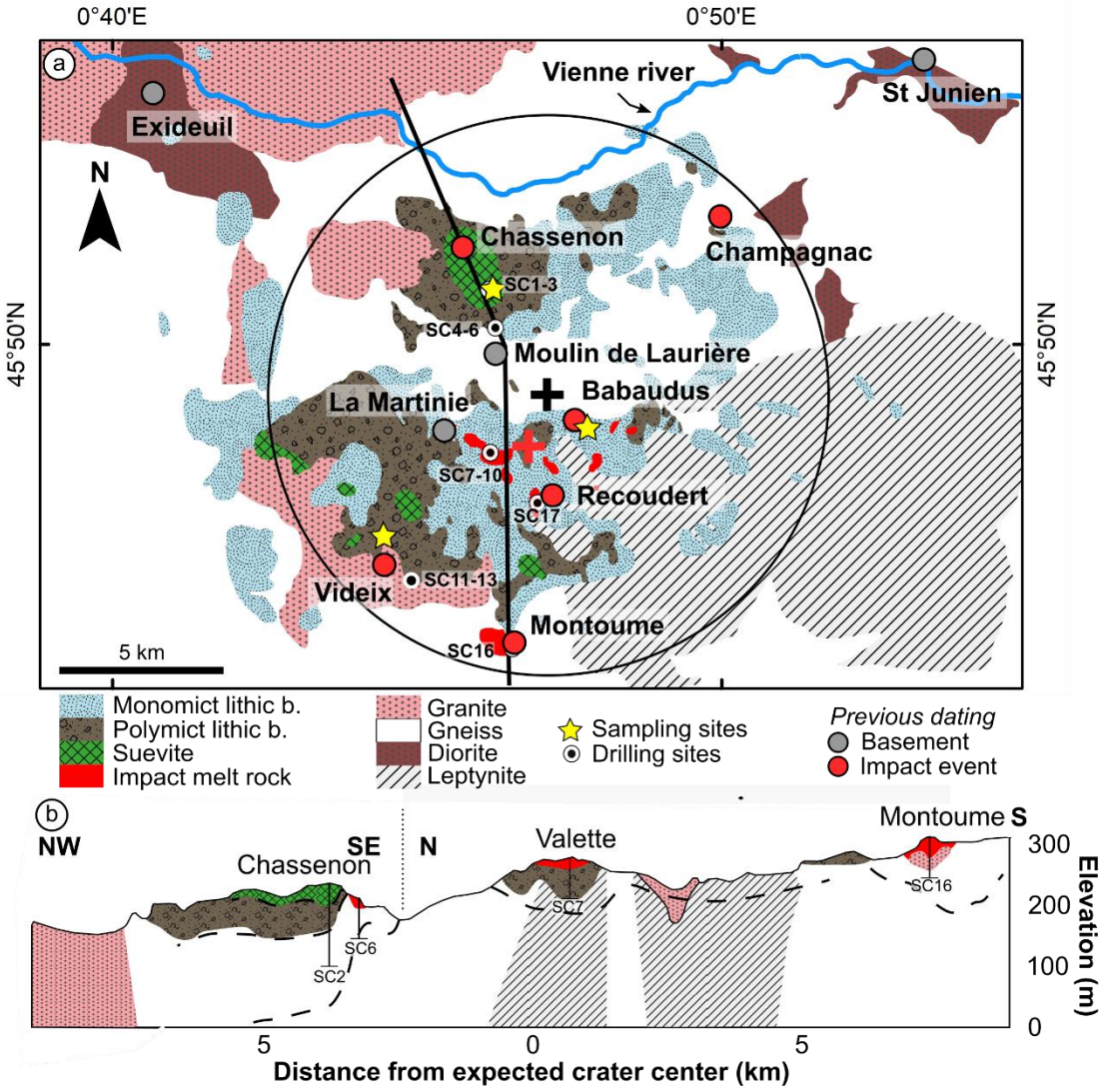


Figure 5.1 Schematic geological map of the Rochechouart impact structure (modified after Chèvremont et al., 1996, Cohen et al., 2017; Lambert, 2010; Rasmussen et al., 2020). The black circle indicates the extent of exposures of crater fill deposits (centered on the black cross). The red cross is the probable center of the initial Rochechouart impact structure, as derived from the present exposure pattern (after Lambert, 2010). (b) Schematic composite cross section for the profile NW-SE/ N-S marked in (a), modified after Lambert (2010) and Quesnel et al. (2021).

Additionally, these rocks are intruded by multiple calc-alkaline intrusions and multiple N-S-oriented fine-grained dikes of micro-granite and –granodiorite, and lamprophyres (diorites / gabbros), associated with a final phase of orogenic anatexis that may have lasted until the Carboniferous (~360–295 Ma) (Chèvremont et al., 1996; Lambert, 2010). Post-Variscan events in the FMC region include a

hydrothermal episode during the Upper Permian which has been documented in the gneisses from the eastern part of the Massif Central (Velay dome). This event was tentatively related to the closure of the Paleo-Tethys (Faure et al., 2024). There are also Pb-Zn and U mineralizations in the southeastern FMC, which were emplaced in several pulses from the Permian to the Cretaceous (Clauer, 2020), and Ba-F-Fe–rich and F-Ba-(Pb)–rich veins in the northern FMC emplaced during the lower Jurassic (Sizaret et al., 2004).

The Rochechouart impact structure (45°50'N / 0°46'E) is located in the northwestern part of the FMC. The structure is significantly eroded and does not feature a crater morphology anymore. Its currently accepted size, delimited by the recognized distribution of shock deformation in basement rocks, extends over a circular area with a 23 km diameter (Lambert, 2010). Estimations of the original crater diameter range from 32 km (Osinski and Ferrière, 2016) to 40-50 km (Lambert, 2010). Previous analyses have shown a significant geochemical variation in the Rochechouart impactites, even within the same units and between samples from different locations (Lambert, 2010). This author surmised that these variations could be controlled by the respective occurrences of basement rocks in the vicinity of specific sampling sites of impact melt rock.

5.2.1 Prior U-Pb isotope work on the Rochechouart impactites.

Most of the previous geochronological work developed on the Rochechouart impact structure has been focused on determining the age of the impact event obtained through $^{40}Ar/^{39}Ar$ dating of an impact melt rock sample from Babaudus (206.92 + 0.20/ -0.32 Ma; Cohen et al., 2017). Recent studies have focused on analyzing the textures of shocked zircon grains and the different age populations recorded by shocked and pristine grains. Reidite has been described by electron backscatter diffraction (EBSD) analysis in zircons from the Chassenon suevitic breccia (Plan et al., 2021). Furthermore, FRIGN zircon has been reported in Chassenon suevite and the Babaudus impact melt rock (Plan et al., 2021; Rasmussen et al., 2020).

LA-ICP-MS U-Pb zircon analyses were previously conducted on zircon crystals from impact melt rock from Babaudus, Montoume, and Recoudert (Guerrero et al., 2024;

Horne, 2016; Rasmussen et al., 2020). These studies documented ages ranging from the Neoproterozoic to the Jurassic. Ages between 204 and 207 Ma were obtained in two FRIGN zircons (Rasmussen et al., 2020) and in granular neoblastic grains that were not characterized by EBSD (Guerrero et al., 2024). These ages were interpreted as representing the age of the impact event. Ages around 192-195 Ma were obtained from a heterogeneous zircon population, including possible metamict granular grains, as well as apparently unshocked grains (Guerrero et al., 2024; Horne, 2016; Rasmussen et al., 2020). This age range is too young to be considered as part of the impact-generated hydrothermal system and has instead been attributed to a possible post-impact thermal/hydrothermal event, which has not yet been reported in basement lithologies (Guerrero et al., 2024; Rasmussen et al., 2020). Pre-impact ages falling into the apparent gap between the accepted impact age and the youngest phase of geologic evolution of the FMC basement (272 ± 12 Ma; Guerrero et al., 2024), were also documented in zircons with heterogeneous textures. These ages have been attributed to zircon reflecting incomplete resetting of target rock ages, or zircon derived from target rocks that have not yet been represented in the regional geochronologic record and that may no longer be preserved in the impact area (Guerrero et al., 2024).

Furthermore, a previous provenance study revealed a weak correlation between the age distributions of the impact melt rocks and the U-Pb isotopic data for zircon from basement rocks sampled in the area of the impact structure (Guerrero et al., 2024).

5.3 Materials and methods

5.3.1 Sample Material

Two suevite samples were collected at Videix (C220510-1745, 45°47.485'N/0°45.607'E) and Chassenon (C220805-1315, 45°50.579'N/0°46.357'E), 6.4 km SW and 3.7 km NW of the apparent center of the impact structure, respectively (Figure 5.1a). One impact melt rock (IMR) was collected at Babaudus (C220705-1643, 45°49.013'N/0°47.784'E), 1.7 km from the crater center (Figure 5.1a). The deformation features of clasts of both suevites include kink bands in micas, toasted quartz, and quartz with up to two sets of PDFs

(Fig. S1). In the IMR, up to two sets of PDFs have been identified in quartz, along with recrystallized or toasted crystals and ballen silica (Fig. S1) (Ferrière et al., 2009). A detailed petrographic description of all these samples is provided in S1.

5.3.2 Sample preparation

Zircon separation for isotope analysis was conducted by crushing, grinding (<125 and 125-300 µm grain size fractions), magnetic separation, and finally hand-picking of the pre-concentrate under a binocular microscope at the Laboratório de Estudos Geodinâmicos, Geocronológicos e Ambientais (LEGGA) at the Universidade de Brasília, Brazil.

5.3.3 Zircon imaging

Cathodoluminescence (CL), backscattered electron (BSE), and secondary electron (SE) images of the zircon crystals from each sample were obtained on a FEI Quanta FEG 650 Scanning Electron Microscope (SEM) equipped with a Gatan ChromaCL2 system at the NordSIMS laboratory in the Swedish Museum of Natural History, Stockholm. Subsequently, the Oxford Instruments Symmetry S4 detector on this SEM was used to collect electron backscatter diffraction (EBSD) maps of eight selected zircon crystals. The grains were indexed for zircon and reidite comparing crystallographic data from Hazen and Finger (1979) and Howard et al. (1988) and with the same analytical conditions and data collection and processing described in Kenny et al. (2022). The maps were made using step sizes between 80 and 175 nm. Grain reference orientation deviation (GROD) maps indicate the deviations relative to the average orientation for the grain (e.g., Wright et al., 2016). Inverse pole figure (IPFz) maps were generated, in which the color coding represents crystallographic orientations relative to the z-axis of the polished sample. Zircon pole figures are equal area upper hemisphere plots and with the same color code of the IPFz maps.

5.3.4 U-Pb analyses on zircon

The grains selected for U-Pb analyses were intended to represent all zircon populations observed in the CL images, as well as all shock deformation features identified by EBSD in each sample. Additionally, multiple grains were analyzed on

both the core and rim to ensure a more comprehensive characterization of the ages of each domain. For grains exhibiting shock deformation, this approach was also applied to areas with contrasting deformation features.

Initially, U-Pb analyses on zircon were measured by secondary ion mass spectrometry (SIMS) using a CAMECA ims1280 ion microprobe at the NordSIMS laboratory. Complementary single-collector sector field inductively coupled plasma mass spectrometry (LA-ICP-MS) analyses were done at LEGGA. The SIMS analyses were done on selected zircon crystals in two analytical sessions, with spot sizes of 8 µm and 15 µm. The principal and secondary reference materials used correspond to the zircon standards M257 (561.3 ± 0.3 Ma; Nasdala et al., 2008) and Temora 2 (416.78 ± 0.33 Ma; Black et al., 2004). The decay constants of Steiger and Jäger (1977) were used.

The LA-ICP-MS analyses were done with a Thermo Finnigan Element XR high-resolution single-collector sector field ICP-MS coupled to a 193 nm Iridia Excimer (ArF) laser ablation system at LEGGA. Laser conditions included a spot diameter of 25 µm, a frequency of 20 Hz, and a fluence of 2.0 J/cm^2. Raw data were processed on Iolite 4.0 (Paton et al., 2011) as a time-resolved signal, and an individual signal inspection was done with the assistance of VizualAge (Petrus and Kamber, 2012). Data were normalized to values from the GJ-1 zircon (601.7 ± 1.3 Ma; Jackson et al., 2004), and as quality control the 91500 (1062.4 ± 0.8 Ma; Wiedenbeck et al., 1995) and Plešovice (337.1 ± 0.37 Ma; Sláma et al., 2008) reference materials were used. All the data obtained by both laboratories, the measured values for the standards, and additional information on the methodology used for the U-Pb analyses, are provided in S2.

The proportion of common Pb (f_{206}%), which refers to the percentage of total Pb that corresponds to common ^{206}Pb, is interpreted to be modern and introduced into crevices in granular grains during the preparation of the zircon mounts. These values were estimated based on the measured ^{204}Pb assuming the present-day Pb isotopic composition of Stacey and Kramers (1975). If some of the common Pb is ancient, the age of the impact may be likely underestimated by less than ca. 0.5 Ma, as

indicated in previous U-Pb studies of shocked zircon (e.g., Kenny et al., 2019; 2022). Corrected values for common Pb were used for crystals with high values of f_{206}% (> ~0.15).

All ages are reported at the 95 % confidence level (2σ uncertainty) and do not reflect external (systematic) uncertainties. Additionally, to determine the most reliable ages, data with errors of the apparent $^{206}Pb/^{238}U$ age < 5 % and with ± 10% discordance in the $^{206}Pb/^{238}U$ and $^{207}Pb/^{235}U$ ages (7/5:6/8 discordance, for short), are considered valid. Data are presented in Tera-Wasserburg plots developed with Isoplot v. 4.15 (Vermeesch, 2018a) and in histograms, probability density plots, and kernel density estimations made with the software DetritalPy v. 1.3 (Sharman et al., 2018). Additionally, the TuffZirc function in Isoplot was used for complex data distributions to minimize bias associated with the manual selection of populations (Ludwig and Mundil, 2002). The similarity between the geochronologic data is quantitatively evaluated with a non-metric multi-dimensional scaling method. For this purpose, the Kolmogorov-Smirnov test was used in the provenance package in R (Vermeesch et al., 2016). In this plot the distance between the samples is proportional to their dissimilarity.

For all zircon grains the radiation dose was calculated against the respective apparent $^{206}Pb/^{238}U$ ages after Murakami et al. (1991), an updated method originally provided by Holland and Gottfried (1955).

5.4 Results

5.4.1 Zircon characteristics

In the three selected samples, zircon grains range from transparent to opaque. Most analyzed grains in both suevite samples are colorless and those in the IMR are mainly reddish when viewed under a binocular microscope. Inclusions of apatite, K-feldspar, quartz, and micas are present in the zircon crystals from all samples, and inclusions of Fe-oxides and amphibole were observed only in the IMR zircons (EDS). There are zircons with oscillatory zoning, irregular zoning, or sector zoning textures (CL images); moreover, the former is the most common zircon texture in all the

impactites (Figure 5.2 and S3). The oscillatory zoning texture in zircons in both suevites shows different patterns and can be associated with metamorphic overgrowths, resorption borders, or local recrystallization. Besides these textures, both suevites have grains with inherited cores, and in the Chassenon suevite, there are also grains with sector zoning. Grains from the Videix suevite have very weak CL intensities in comparison with zircon from the Chassenon sample. The IMR, in contrast, has homogeneous grains, grains with sector zoning, and grains with local recrystallization, sometimes associated with convolute zoning. Additionally, some zircons from the Chassenon suevite and the IMR also display very faint oscillatory zoning. A compilation of typical zircon CL textures is provided in Figure S3.

The most common shock metamorphic textures observed in BSE and SE images correspond to granular grains, granular grains with spots of higher backscattered electron intensity (tentatively considered as possible baddeleyite or another zirconia polymorph; e.g., Timms et al., 2017), and grains with planar parallel lamellae (Figure 5.2 and S4). The Babaudus IMR is the only sample without grains showing the lamellae texture. Some grains with lamellae in the suevites and the granular grains in all three samples have oscillatory or irregular zoning (Figure 5.3-5.7 and S4-5). Besides this texture, a few homogeneous grains, grains with sector zoning, or grains with inherited cores also display granular textures. The granular grains associated with higher electron intensity spots are more common in the IMR and are present in only very few zircons of the suevites (Figure 5.3-5.5). Furthermore, in a few grains a porous texture is visible (Fig. S4a; e.g., Herrmann, et al., 2023; Plan et al., 2021). These textures are observed only for reddish grains in the IMR and the Videix suevite, and in transparent and reddish grains in the Chassenon suevite.

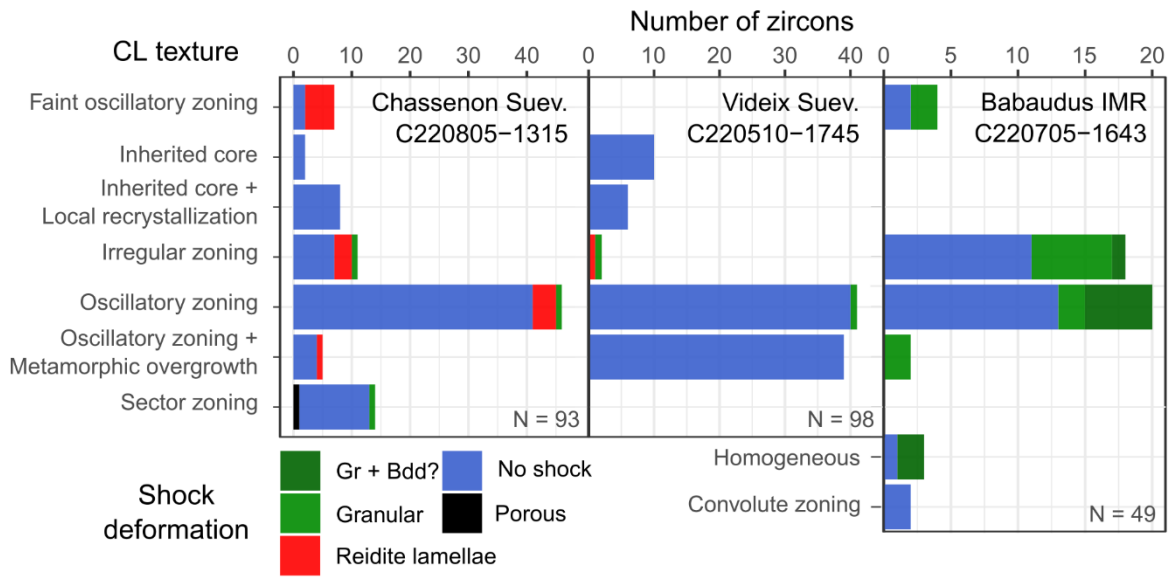


Figure 5.2 Bar chart showing the textures on zircon grains recognized by CL images and the associated shock deformation of the zircon grains from the samples of this study, for data with discordance < 10 % on the $^{207}Pb/^{235}U$ - $^{206}Pb/^{238}U$ ages and with errors on the apparent $^{206}Pb/^{238}U$ age < 5 %. Gr = granular; Bdd? = possible baddeleyite.

5.4.2 EBSD analyses

EBSD maps and IPF were produced for eight zircon grains that exhibit the variety of shock metamorphic features observed in the three samples (Figure 5.3- 5.7, and S5). Granular reddish zircons from all samples were analyzed. These grains display mostly irregular zonation with a weak CL response, with the exception of grain #1643-01, which shows a clear oscillatory zoning texture (Figure 5.3a) and grain #1315-57, which has a strong CL response (Figure 5.4b). Granular zircons show neoblasts with sizes from ~ 0.1 to 13.7 µm. The size of the neoblasts varies in most grains, from tiny neoblasts in the grain core to more coherent regions at the rim (Figure 5.3a and 5.5), or they can be heterogeneously distributed throughout the grains (Figure 5.3b and 5.4b). An exception is grain #1643-22 (Figure 5.4a) that shows a uniform grain size for the neoblasts. The oscillatory zoning texture of grain #1643-01 is preserved only in the finer grained portion of the grain (Figure 5.3a).

Adjacent granules, in some cases, can show consistent crystallographic orientations (Figure 5.3b and 5.4b). Four of the granular grains analyzed by EBSD have neoblasts that display three principal orientations that are misoriented at ~90° with <110> directions. This constitutes crystallographic evidence of the presence of

FRIGN zircon (Cavosie et al., 2018). This type of grain is present in all samples(#1315-57, #1745-12, #1643-01, #1643-22). In the cases of the IMR and the Videix suevite, such grains contain spots of higher BSE intensity at their margins (Figure 5.3 and 5.4a). Grain #1745-01 of the Videix suevite is the only one analyzed here by EBSD where the granules do not show these crystallographic orientation relationships (Figure 5.5). Furthermore, it was possible to index very fine-grained granules of reidite (0.5 - 1 μm) that occur at proportions up to 5 % in grains #1643-22, #1315-57, and #1745-01 (Figure 5.4 and 5.5). In grain #1643-22, the orientation of granular reidite is quite scattered, but a broad coincidence of the reidite {001} plane with the zircon planes {001} and {110} is observed (Figure 5.4c). In grain #1315-57, the plane $\{100\}_{reidite}$ aligns with two orientations of the plane $\{110\}_{zircon}$, and $\{001\}_{reidite}$ aligns with the remaining $\{110\}_{zircon}$ and with one $\{001\}_{zircon}$ orientations (Figure 5.4d). In grain #1745-01, the crystallographic orientation relationships of the indexed granular reidite are scattered and deviate from the typical misorientation of ~90° with <110> directions (Figure 5.5b).

The pixels indexed as reidite (#1315-57, #1643-22, and #1745-01) often only partially cover the granules. Verification of these zones using BSE and SE imaging revealed significant contrast only for the grain #1745-01. However, only zircon and the spots of higher electron intensity described previously, were identified. Attempts to verify the presence of this phase by Raman spectroscopy were inconclusive due to its extremely fine grain size and scattered distribution throughout the grains. Based on currently available information, the perceived reidite granules could represent a product of EBSD local mis-indexing.

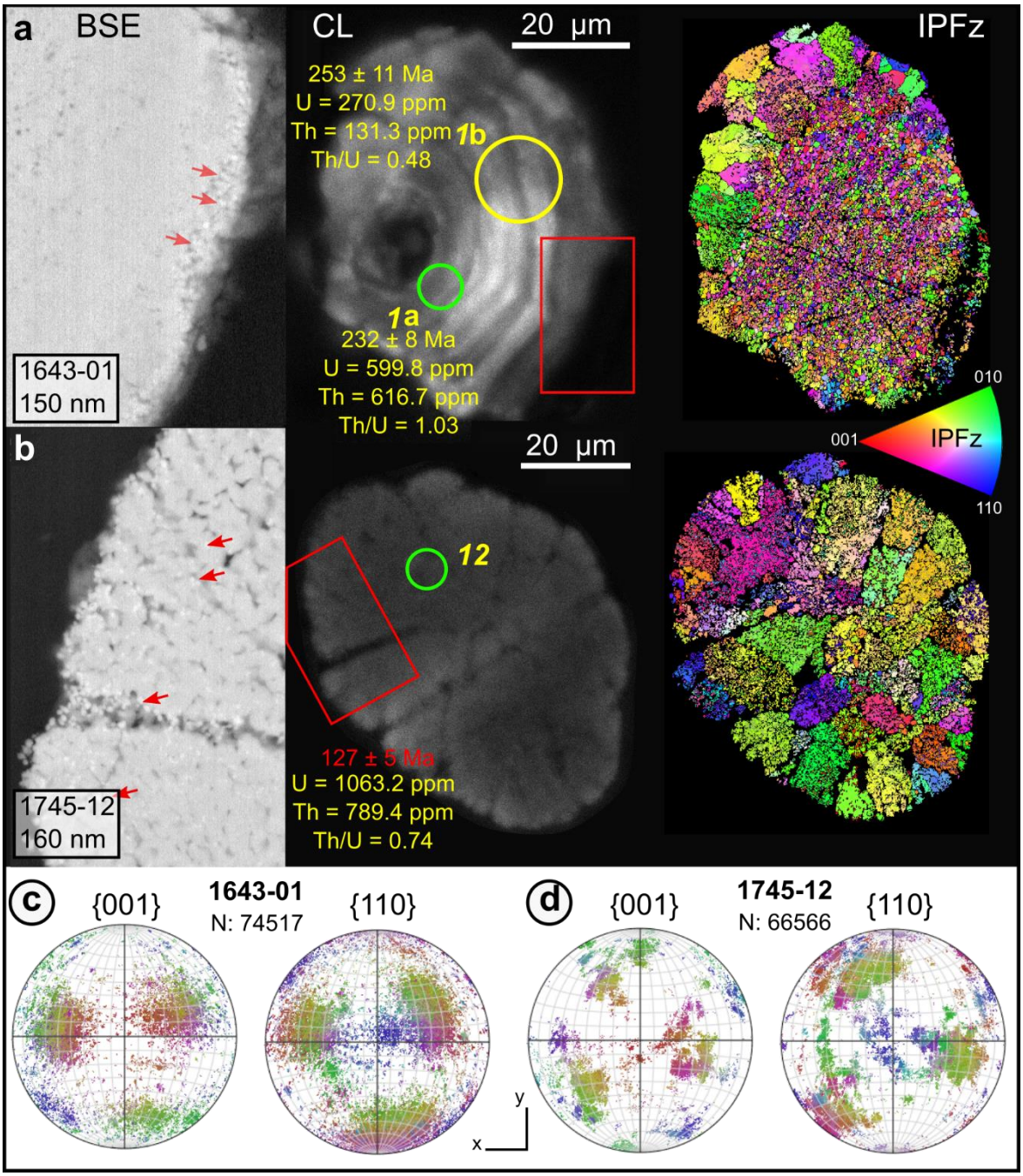


Figure 5.3. Imaging and microstructural characterization of granular zircon from (a) the Babaudus IMR and (b) the Videix suevite with the locations of the spots where SIMS analyses were conducted and the corresponding ages and compositions obtained. The ages in red have a discordance >10 % and/or high errors on the apparent $^{206}Pb/^{238}U$ age. BSE images showing possible zirconia granules of higher mass contrast (red arrows). The location of the BSE images is indicated with red rectangles on the CL images. The only grain displaying a clear igneous zonation texture in CL is shown in (a). (c and d) The colors and clusters of the {001} and {110} planes in inverse pole figures show three main clusters that indicate three orthogonal orientations indicative of "former reidite in granular neoblastic" (FRIGN) zircon (Cavosie et al., 2018). BSE: Backscattered electron, CL: cathodoluminescence, GS: gran size, IPF: inverse pole figure.

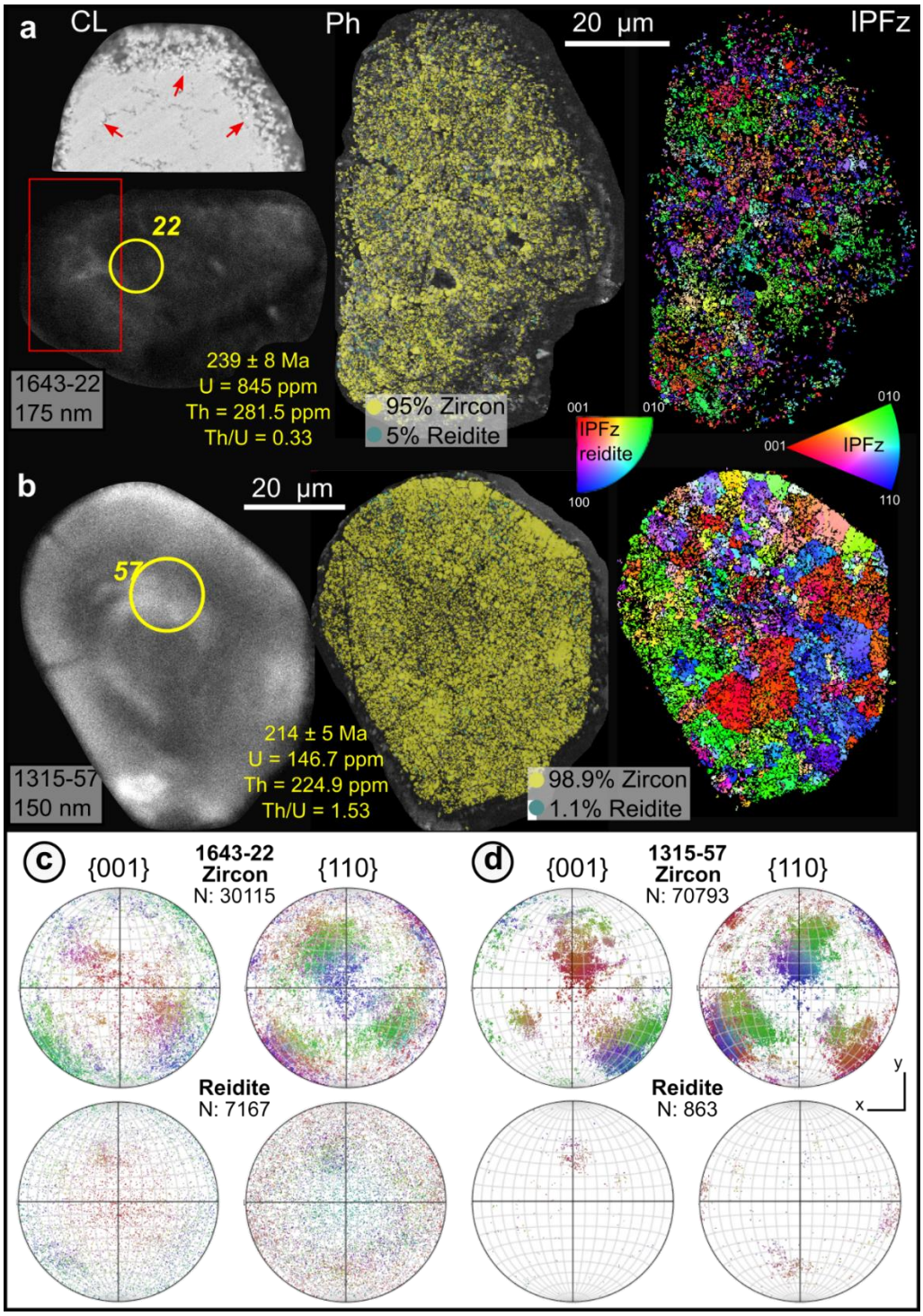


Figure 5.4. Imaging and microstructural characterization of granular zircon from (a) the Babaudus IMR, (b) the Chassenon suevite, with the locations of the spots where SIMS analyses were conducted and the corresponding ages and compositions obtained. BSE images showing possible zirconia granules of higher mass contrast (red arrows). Grains #1643-22 and #1315-57 show up to 5 % of reidite. (c and d) The colors and clusters of the {001} and {110} planes in inverse pole figures show three main clusters that indicate three orthogonal orientations indicative of "former reidite in granular neoblastic" (FRIGN) zircon (Cavosie et al., 2018). BSE: Backscattered electron, CL: cathodoluminescence, Ph: phase, IPF: inverse pole figure.

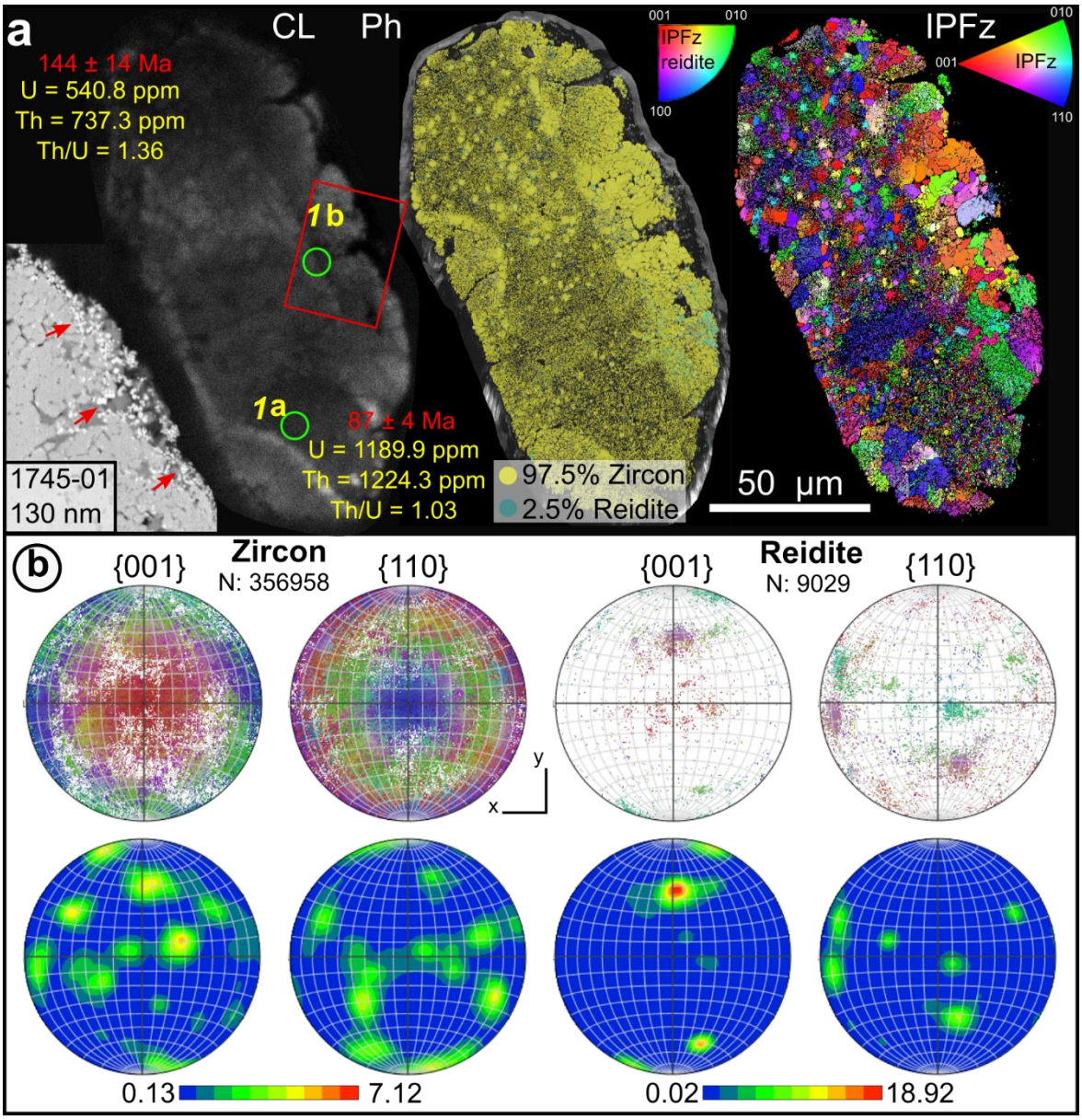


Figure 5.5. Imaging and microstructural characterization of granular zircon from (a) the Videix suevite with the locations of the spots where SIMS analyses were conducted and the corresponding ages and compositions obtained. Both ages have a discordance >10 % and/or high errors on the apparent $^{206}Pb/^{238}U$ age. BSE images show possible zirconia granules of higher mass contrast (red arrows). Grain #1745-01 shows 2.5 % of reidite. (b) Scattered and contoured inverse pole figures that show that there is no systematic orientation of the granules. BSE: Backscattered electron, CL: cathodoluminescence, Ph: phase, IPF: inverse pole figure.

Sets of parallel lamellae were observed in zircon from both suevites, mainly on transparent zircon grains with mostly oscillatory zoning and more rarely, irregular textures in the CL images (Figure 5.2 and S4). Three of these grains were analyzed by EBSD and the lamellae were identified as reidite in all three cases, at proportions up to 7.4 % (Figure 5.6, 5.7, and S5). These lamellae are brighter in BSE than surrounding zircon, dark in CL, and they crosscut the primary zoning patterns of the

grains. The analyzed grains have up to three orientations of reidite lamellae, whereby orientations can vary between the grains. Lamellae have sub-micrometer width, and spacings between ~ 0.45 and 5 μm. In grain #1315-29, a set of reidite lamellae with a width up to 2 μm and spacings between ~ 2.5 and 5 μm is seen (B1, Figure 5.6). The host zircon grains have plastic deformation up to 13° in both crystals, and in the reidite domains up to 7° (Figure 5.6 and 5.7). The most common grain boundary angles are < 10°. A minor proportion of boundary angles > 10° is mainly found in the reidite domains (Figure 5.6, 5.7, and S5). In grains #1315-29 and #1315-05, some high angle grain boundaries have a systematic orientation of <101> 90°, and in grain #1315-05, boundaries at <210> 65°, <112> 90°, and <111> 65° orientations are also present, and are located mainly in the reidite domains. No twins are recorded in either of the grains (Figure 5.6 and 5.7).

Furthermore, crosscutting relationships between the reidite lamellae are observed in grains #1315-29 and #1315-05. In the former, reidite sets L1 and L2, which share the same orientation, are intercepted by B1 (Figure 5.6). In grain #1315-05, some planar fractures are crosscut by the lamellae sets L1 and L2, which also seem to intercept L3 (Figure 5.7).

The pole figures show that in these grains, reidite granules have a broad coincidence between two of the $\{112\}_{reidite}$ orientations, with the $\{112\}_{zircon}$ and the other two with the $\{100\}_{zircon}$. Furthermore, one $\{110\}_{zircon}$ aligns with $\{110\}_{reidite}$ and the other is subparallel to $\{001\}_{reidite}$ (Figure 5.6, 5.7, and S5). The dispersion of reidite sets with heterogeneous widths (Figure 5.6) is higher than observed for the sub-micrometer reidite lamellae alone (Figure 5.7 and S5), and in the latter, the misorientation in relation with the parent zircon tends to be higher.

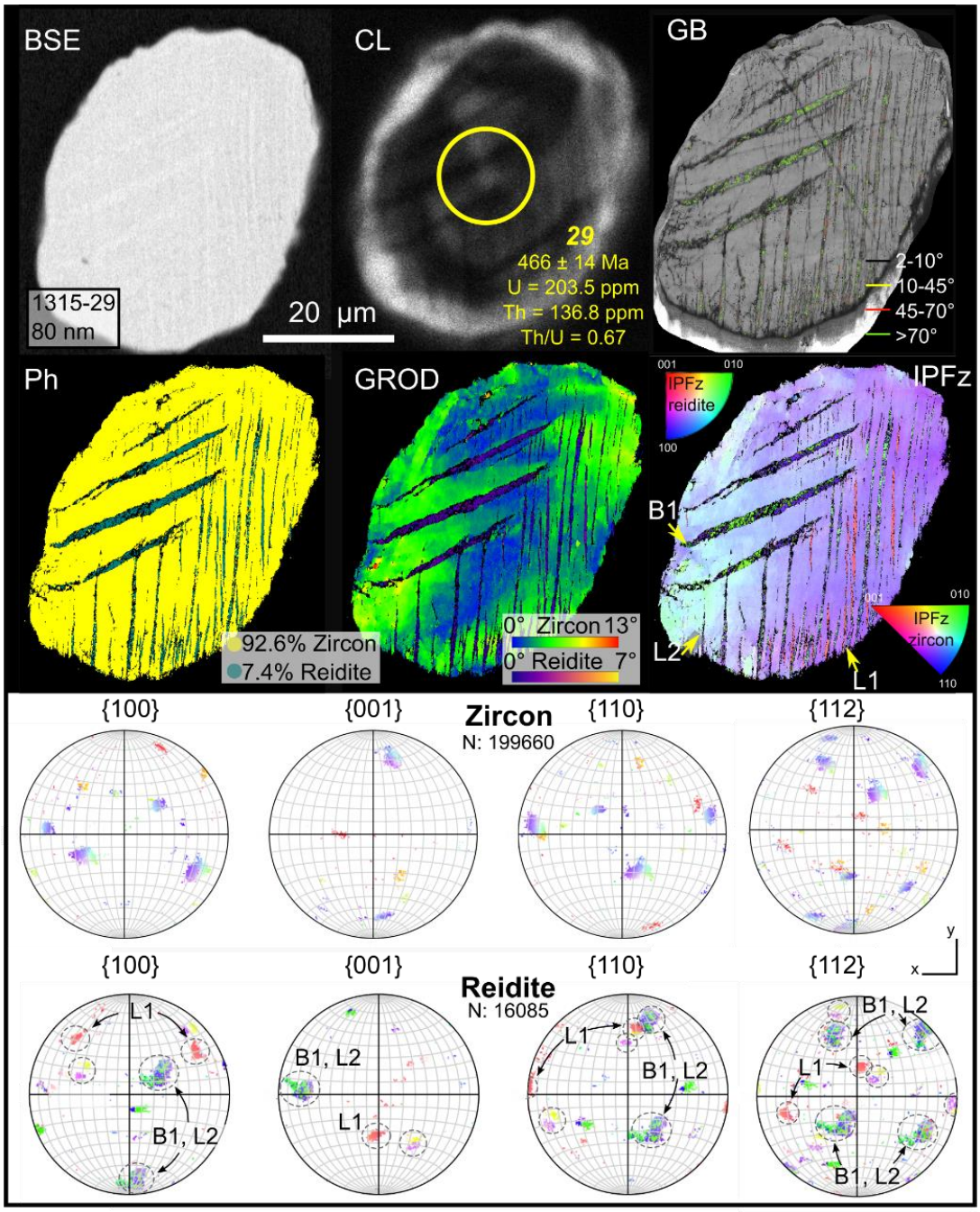


Figure 5.6. Imaging and microstructural characterization of zircon from the Chassenon suevite with the location of the spot where the SIMS analysis was conducted and the corresponding age and compositions obtained. Grain #1315-29 has an exposed surface of 52 x 38 µm and in the CL image shows an irregular, very low CL intensity core with an overgrowth rim. Furthermore, the grain contains 7.4 % reidite, which is confined to sub-micrometer lamellae sets (L1 and L2) of similar orientation and with spacings between ~0.45 and 3 µm. These lamellae are crosscut by a reidite set with a width up to 2 µm and spacings between ~2.5 and 5 µm (B1). Host zircon has up to ~ 13° of crystal plastic deformation and reidite up to 7°. Grain boundaries > 70° are located in the reidite domains. Orientation maps and their related pole figure show that B1 and L2 are parallel along all planes and in the plane {110} have a topotaxial relationship with L1. BSE: Backscattered electron, CL: cathodoluminescence, GB: grain boundaries, Ph: phase, GROD: grain reference orientation deviation, IPF: inverse pole figure.

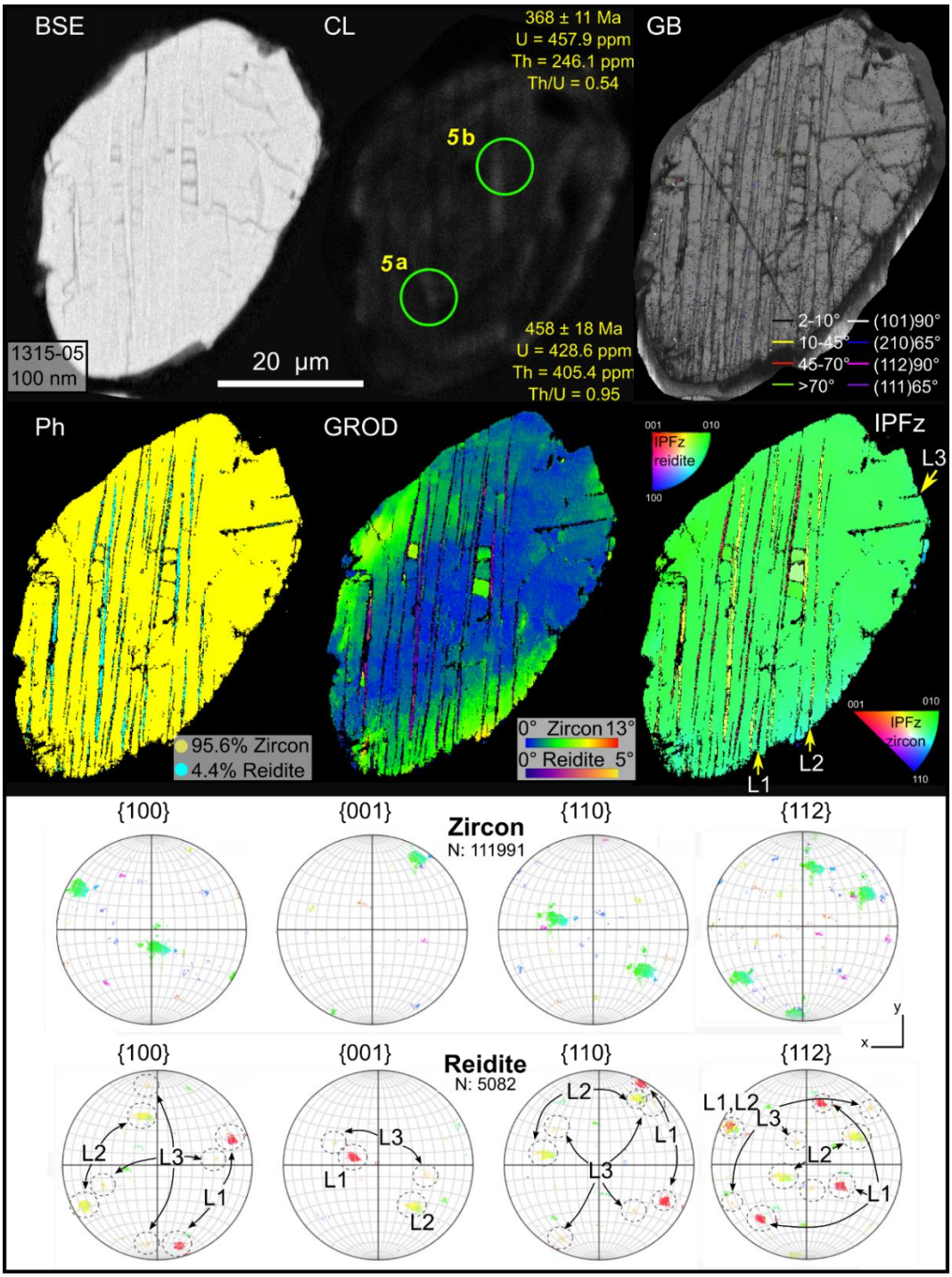


Figure 5.7. Imaging and microstructural characterization of zircon of the Chassenon suevite with the locations of the spots where SIMS analyses were conducted and the corresponding ages and compositions obtained. Grain #1315-05 has an exposed surface of 52 x 34 µm and an irregular pattern with very low CL intensity. Up to 4.4 % reidite was indexed, and it is distributed in three sets of sub-micrometer lamellae (L1, L2, and L3). L1 and L2 share the same orientation and seem to cut L3, which shares a similar orientation with the planar fractures located at the center of the grain, and which are delimited by L1 and L2. Plastic deformation of the zircon is up to 13° and of reidite is up to 5°, and almost all grain boundaries are < 10°. Orientation maps and their related pole figure show that L1 and L2 are dispersed and aligned only on one {112} direction, L3 tends to have a topotaxial relationship with L1 and L2, and the $\{110\}_{zircon}$ and $\{001\}_{reidite}$ orientations are parallel. BSE: Backscattered electron, CL: cathodoluminescence, GB: grain boundaries, Ph: phase, GROD: grain reference orientation deviation, IPF: inverse pole figure.

5.4.3 U-Pb isotopic systematics

The data of the U-Pb isotope analyses obtained by SIMS and LA-ICP-MS have very similar characteristics. Unshocked grains with older ages normally have lower errors and overall show a better concordance. High discordance and/or high errors are associated mainly with shocked grains from the Chassenon suevite and the Babaudus IMR, and this is also seen in unshocked or shocked zircons from the Videix suevite (Figure 5.9). Moreover, grains with reidite lamellae show higher values of discordance and common Pb (f_{206}%) than those with granular texture. Histograms showing the characteristics of the analyzed grains in comparison to their apparent $^{206}Pb/^{238}U$ ages, and plots of the apparent $^{206}Pb/^{238}U$ ages of grains where the rim and the core were analyzed are provided in Figs. S6 and S7, respectively.

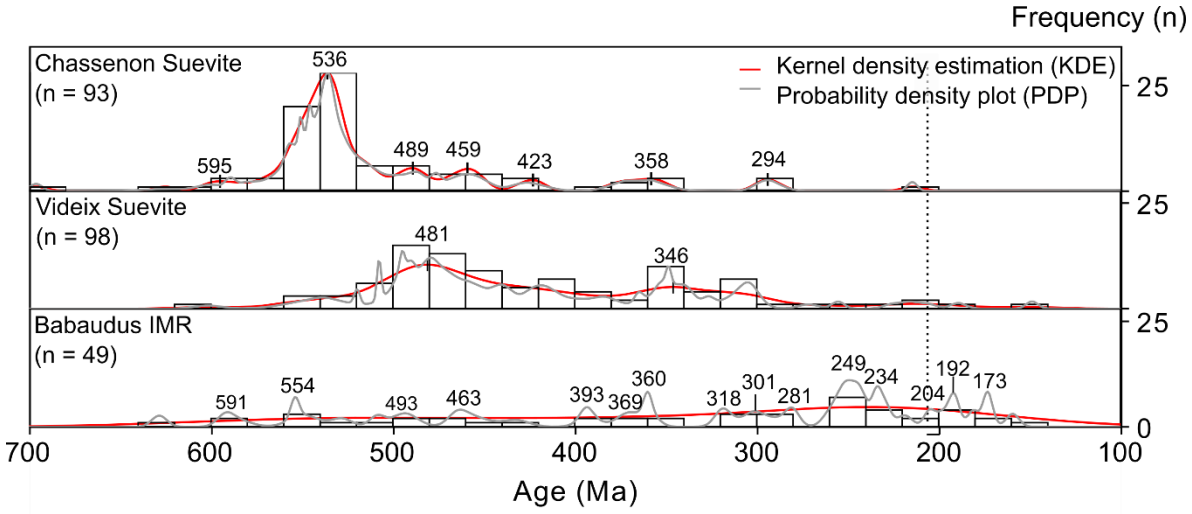


Figure 5.8. Histograms for the apparent $^{206}Pb/^{238}U$ ages of the impactites analyzed in this study. Age peaks are for the kernel density estimation plots in both suevites and for the probability density plot for data from the Babaudus IMR. Dashed line at 206.92 + 0.20/- 0.32 Ma corresponds to the $^{40}Ar/^{39}Ar$ age for the impact event by Cohen et al. (2017). The minimum age documented for target rocks is 272 ± 12 Ma (Guerrero et al., 2024). Plots and age peaks calculated with Detrital Py v. 1.3 (Sharman et al., 2018).

The Chassenon suevite (C220805-1315): a total of 149 analyses on 126 zircon grains were acquired, of which only 93 analyses made on 82 grains have low errors and discordances < 10 %. Most of the analyses were performed in cores of the grains. The ages registered in this sample range mainly from 289 ± 13 to 726 ± 21 Ma, with two older grains at 1274 ± 23 and 3061 ± 10 Ma and one younger grain at 214 ± 5 Ma. The kernel density estimation plot shows a main age peak at 536 Ma, and secondary age peaks at 294, 358, 423, 459, 489 and 595 Ma (Figure 5.8). The main peak and the older ages are obtained mainly in colorless grains with oscillatory

zoning or sector zoning textures, as well as a few crystals displaying inherited cores or irregular zoning. The younger ages are obtained mainly in grains with oscillatory zoning and a lower proportion of grains with irregular or sector zoning textures (Fig. S6). Furthermore, the granular grains yielded ages between 214 ± 5 (FRIGN zircon #1315-57) and 350 ± 15 Ma. The grains that show reidite lamellae record ages ranging from 297 ± 13 to 514 ± 15 Ma, and the unshocked grains have ages that range from 295 ± 11 to 3061 ± 10 Ma (Fig. S6). Most grains have older ages for the cores than for the rims (Fig. S7).

In this suevite, zircons have median U and Th contents of 248 and 115 ppm, respectively. Positive outliers are recorded in granular grains, with values of U of 3169 and Th of 2173 ppm. Besides these outliers, shocked and unshocked zircons have similar U contents, whereas comparatively higher Th (>1000 ppm) and slightly higher Th/U (> 2) values are recorded in shocked grains. For these grains low-quality ages were recorded. Moreover, there is no clear pattern in the variation of the composition of the zircons with ages recorded, and all data fall within the crystalline domain of the radiation dose calculation. (Fig. S9).

The Videix suevite (C220510-1745): A total of 178 analyses in 140 grains were made for this sample. Of these, 98 analyses on 71 crystals have a discordance < 10% and an error < 5% on the apparent $^{206}Pb/^{238}U$ ages, and only three correspond to grains with shock deformation. Most of the ages range from 189 ± 9 Ma to 601 ± 15 Ma, with only two grains outside these limits (149 ± 6 and 2156 ± 67 Ma). Two main age peaks are obtained in the kernel density estimation plot, at 481 and 346 Ma (Figure 5.8). The age of 481 Ma was obtained in reddish and colorless crystals with mainly oscillatory zoning textures or inherited cores. The two ages outside the normal age distribution correspond to transparent grains with oscillatory zoning (Fig. S6). For most of the grains analyzed, the cores are older than the rims (Fig. S7). In this sample, the three shocked zircons with good quality data record ages of 206 ± 10, 225 ± 10 Ma, and 401 ± 17 Ma (Fig. S9). All the grains where FRIGN zircon and reidite were identified by EBSD gave discordant ages and yielded apparent post-impact $^{206}Pb/^{238}U$ ages.

Zircons from this suevite have median U and Th concentrations of 457 ppm and 151 ppm, respectively. Positive outliers reach up to 5332 ppm for U and 7517 ppm for Th. Elevated U concentrations (>1000 ppm) are primarily observed in unshocked crystals, whereas high Th and Th/U ratios (>500 ppm and >1) are recorded in both shocked and unshocked grains (Fig. S9). Most of these crystals yield discordant or high error ages. Among the unshocked zircons with high U contents, only four have low error and low discordance ages and range from 189 ± 8 to 365 ± 5 Ma. Zircons with lower U and Th contents and Th/U normally record ages > 250 Ma (Fig. S9). Moreover, one grain falls into the transition zone towards the domain for metamict crystals. This grain is discordant, is unshocked, and registers very high U and Th contents.

The Babaudus IMR (C220705-1643): A total of 73 analyses were acquired in 54 zircon grains, of which only 49 analyses on 38 crystals have low errors and acceptable discordance. The ages obtained range from 159 ± 7 Ma to 628 ± 8 Ma, with three older ages of 1096 ± 12, 1176 ± 14, and 1676 ± 13 Ma. Only two peaks are obtained in the kernel density estimation plot, at 239 and 500 Ma, whereas the probability density plot identifies 15 different age peaks, showing a better representation of the diverse age population recorded in this sample (Figure 5.8). The principal probability density plot age peaks are at 360, 249, 234, 192, and 173 Ma. Older ages were obtained mainly in colorless grains with irregular or oscillatory zoning texture and without shock deformation. The youngest ages are obtained mostly in reddish granular grains, sometimes where the high-electron density spots occur. These grains have oscillatory zoning and to a lesser proportion irregular zoning or homogeneous textures. FRIGN zircon grains also record ages close to the peaks at 234 and 249 Ma. The crystals with ages younger than the impact event correspond to granular reddish grains with irregular zoning (Fig. S6). In this sample, most zircon grains yielded older ages at the rims of the crystals than in the cores (Fig. S7).

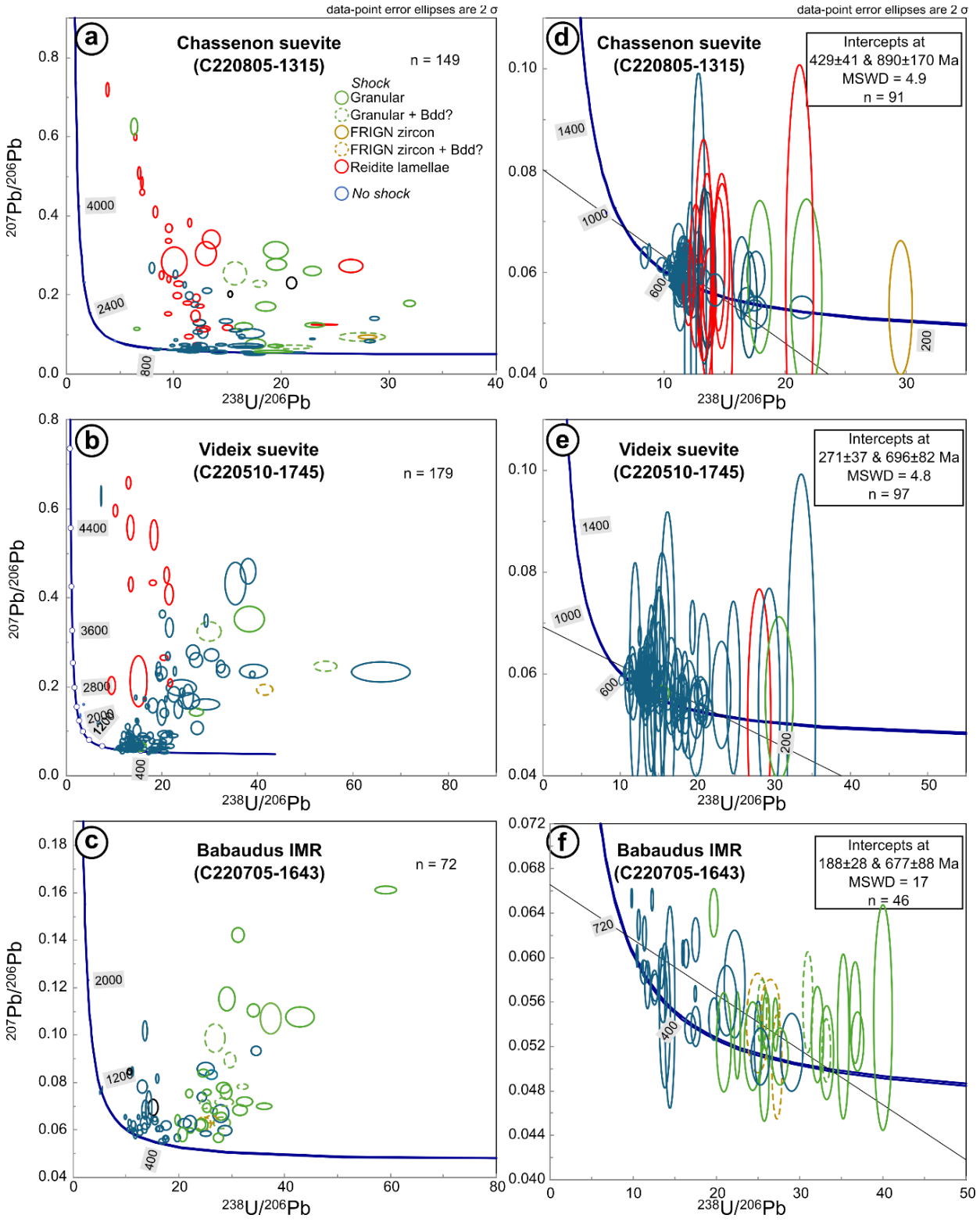


Figure 5.9 Tera-Wasserburg plots of the impactites analyzed in this study of the Rochechouart impact structure. (a, b, and c) Plots developed with all uncorrected data. (d, e and f) Plots developed selecting grains without fractures, with a discordance <10 % on the 7/5:6/8 ages, and with errors of the apparent $^{206}Pb/^{238}U$ age < 5 %. Colors indicate no shock and shock metamorphic textures (different types). Color convention on (a) is valid for all diagrams.

The median values of the U and Th contents of the zircons are 355 and 152 ppm, respectively. Positive outliers are up to 3418 ppm for U and 7496 ppm for Th, both recorded for a granular grain. Besides this outlier, the U contents of shocked and unshocked zircon is comparable. In contrast, higher Th contents (>500 ppm) and Th/U (>1) values are principally recorded in shocked zircons (Fig. S9). Moreover, the zircons with Th/U >1 mainly yield low quality ages. Among the zircons with reliable ages, higher Th contents are recorded in grains with younger apparent $^{206}Pb/^{238}U$ ages (Fig. S9). Furthermore, all data fall into the crystalline domain of the radiation dose calculation.

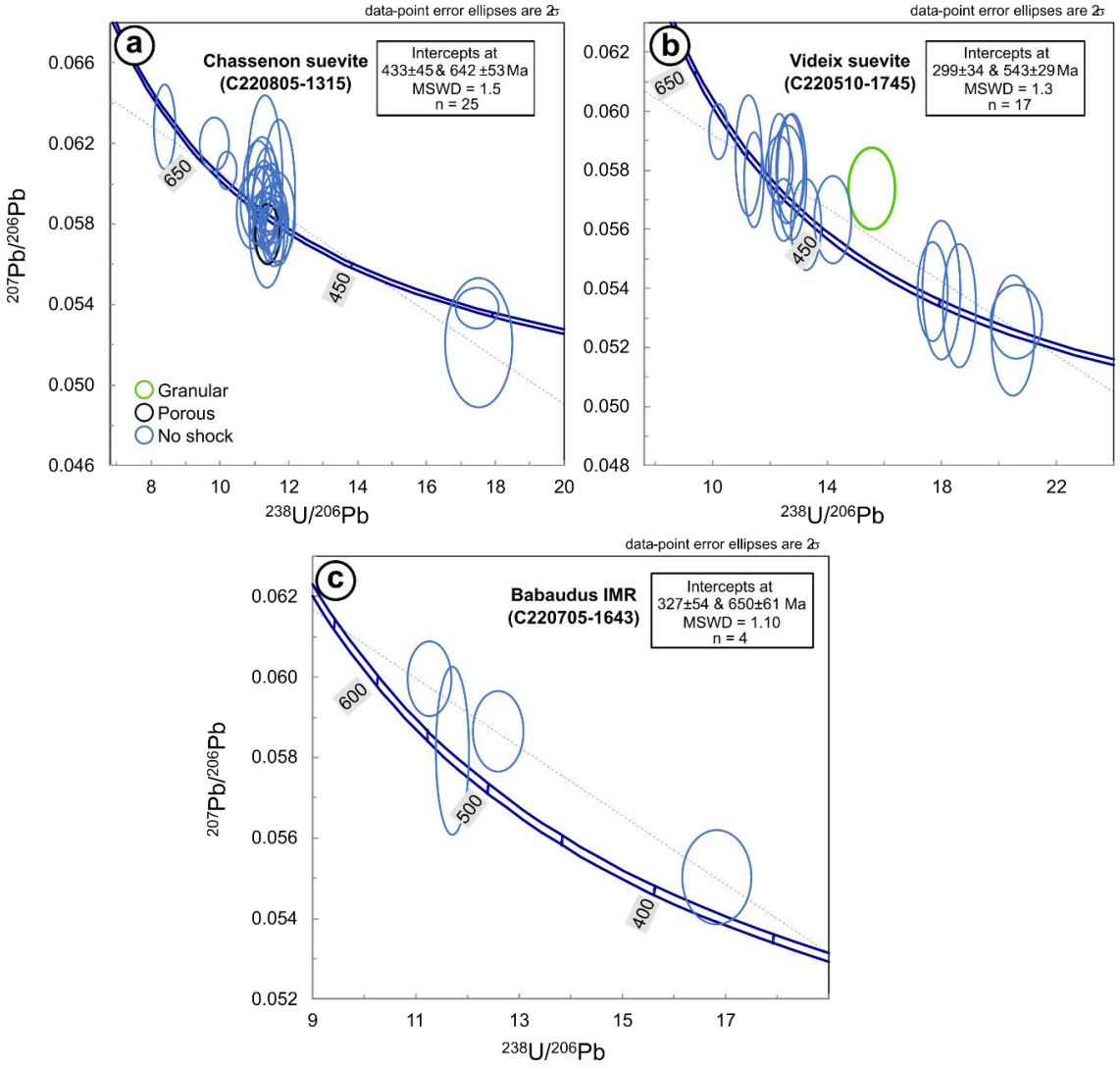


Figure 5.10. Tera-Wasserburg plots of the uncorrected data for grains with $^{206}Pb/^{204}Pb$ > 9000, U < 1000 ppm, and radiogenic Pb > 99 %, following McGregor et al. (2019), for the impactites analyzed in this study. Colors indicate different shock metamorphic textures. Color convention on (a) is valid for all diagrams.

Tera-Wasserburg plots for analyses uncorrected for common Pb did not yield reliable intercepts (Figure 5.9a-5.9c). Moreover, when a combination of uncorrected common Pb data with acceptable concordance and low errors, alongside high-quality common Pb-corrected analyses were selected, the calculated intercept ages exhibited MSWD values exceeding the acceptable threshold for the number of analyses (Figure 5.9d-5.9f).

To improve the statistics, diagrams were generated for grains with $^{206}Pb/^{204}Pb$ > 9000, U < 1000 ppm, and radiogenic Pb > 99 % (McGregor et al., 2019) (Figure 5.10). In these plots, 25 unshocked grains from the Chassenon suevite yielded upper and lower intercepts of 433 ± 45 Ma and 642 ± 53 Ma (MSWD = 1.5, n = 25), 16 unshocked grains and one granular grain from the Videix suevite produced intercepts at 299 ± 34 Ma and 543 ± 29 Ma (MSWD = 1.3, n = 17), and four unshocked grains from the IMR yielded lower and upper intercepts at 327 ± 54 Ma and 650 ± 61 Ma (MSWD = 1.1, n = 4). Despite the acceptable MSWD values, the associated errors remain high.

For the youngest zircons with low discordance and acceptable errors from the combined dataset, three concordia ages were calculated (Figure 5.11). Data for two granular zircons from the Babaudus IMR and one unshocked grain from the Videix suevite yielded a concordia age of 191 ± 4 Ma (MSWD = 0.78, probability = 0.38); two granular grains from the Babaudus IMR and one granular grain of the Videix suevite gave an age of 203 ± 4 Ma (MSWD = 3.4, probability = 0.06); and one FRIGN zircon from the Chassenon suevite and two unshocked zircons for the Videix suevite and Babaudus IMR yielded a concordia age of 216 ± 4 Ma (MSWD = 0.75, probability = 0.39) (Figure 5.11a). Using the TuffZirc function of Isoplot, two ages were determined from the apparent $^{206}Pb/^{238}U$ ages in the combined dataset: 191.3 + 6.5/-2.2 Ma, calculated for four grains, and 215.7 + 9.2/-9.4 Ma, calculated from five grains (Figure 5.11b). The first age is consistent with the youngest concordia age calculated, whereas the second age, due to its significant uncertainties, is within the error margin of the two older concordia ages.

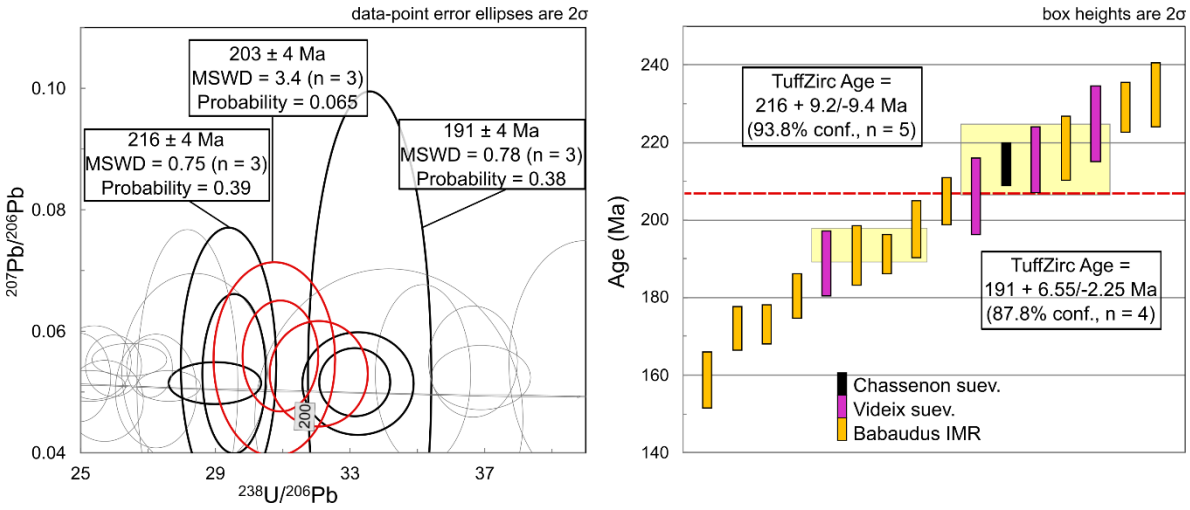


Figure 5.11. Tera-Wasserburg plot and (b) TuffZirc age plot (Isoplot v. 4.15; Vermeesch, 2018a) for the youngest ages reported for all the three impactites analyzed in this study.

5.5 Discussion

In the following, the textural characterization and U-Pb geochronological analyses in zircon crystals from the Chassenon and Videix suevites and the Babaudus IMR are evaluated in relation with: 1) the pressure and temperature conditions associated with the observed shock deformation textures of zircon, 2) the relation of shock textures with recorded ages, and 3) the significance of the age distribution recorded for zircons from these samples in terms of its relationship with chronological data for basement lithologies and the age of the impact event.

5.5.1 Significance of the shock deformation textures in the context of the Rochechouart impact

Zircon from the Chassenon suevite exhibits the highest diversity of shock deformation textures, followed by the zircons from the Videix suevite and the Babaudus IMR (Figure 5.2). EBSD imaging of eight representative grains with different textures revealed that all three samples have granular grains with zircon neoblasts that conform to the crystallographic orientation relationships for FRIGN zircon (Cavosie et al., 2018), the Videix suevite has a granular zircon where the neoblasts lack systematic orientation, and both suevites have zircon crystals with reidite in lamellar and/or blade habits (Erickson et al., 2017; Plan et al., 2021).

5.5.1.1 FRIGN zircon

In the Rochechouart impact structure, FRIGN zircon has been previously reported in zircon from the Chassenon suevite (Plan et al., 2021) and the Babaudus IMR (Rasmussen et al., 2020). In this work four granular grains analyzed by EBSD correspond to FRIGN zircon (1315-57, #1745-12, #1643-01, and #1643-22).

Reidite is a high-pressure polymorph of zircon that begins to form at ~ 20 GPa, with the transformation from zircon to reidite being complete at ~ 53 GPa (Figure 5.12a; Kusaba et al. 1985; Leroux et al. 1999). The most common habits of this phase, lamellae and granular reidite, are thought to form via displacive deviatoric and reconstructive transformations, respectively (e.g., Erickson et al., 2017). Under ambient pressure and temperatures > 1200 °C, reidite becomes unstable and reverts to zircon (Figure 5.12b; Kusaba et al. 1985). The zircon formed by these solid-state phase transformations is known as FRIGN zircon, characterized by neoblasts with three orthogonal orientations of {001} and {110} planes. This orientation relationship that allows the inference of previous phases is known as phase heritage (Cavosie et al., 2018; Timms et al., 2017). At temperatures above ~ 1673 °C, zircon dissociates into silica and zirconium dioxide (Figure 5.12b and 5.12c; Timms et al., 2017).

Associations of FRIGN zircon with granular reidite, as well as with both reidite and baddeleyite, have been documented for crystals from Rochechouart (Plan et al., 2021) and other impact structures (Timms et al., 2017; Tolometti et al., 2022; Zhao et al., 2024; Zhou et al., 2024). The authors interpreted zircon granules that have sharp contact with reidite, as zircon neoblasts reverted from reidite in specific crystal zones that probably underwent higher temperatures, producing annealing in some parts of the grains (Plan et al., 2021; Tolometti et al., 2022; Zhou et al., 2024).

5.5.1.2 Zircon neoblasts with random orientations

Grain #1745-01 (Videix suevite), also analyzed by EBSD, contains zircon granules that lack a systematic orientation relationship in the pole figures, and shows larger granules at the grain border. Furthermore, high BSE electron-intensity granules are observed predominantly along the crystal's border. Zircon neoblasts with random

orientations have been documented in samples from many other impact structures (e.g., Cavosie et al., 2015; Kenny et al., 2017; Kovaleva et al., 2021).

The larger zircon granules at the grain border may indicate that these regions experienced relatively slower cooling and stayed at elevated temperatures for a prolonged period after impact (e.g., Crow et al., 2017; Kenny et al., 2017). In contrast, the fine zircon granules in the central part of the grain were likely subjected to a faster, possibly incomplete, recrystallization at comparatively lower temperatures.

5.5.1.3 Lamellar and blade-shaped reidite

Multiple sets of reidite in lamellar habit have been observed in zircon crystals from the suevites from Chassenon and Videix, three of which were analyzed by EBSD (#1315-29, #1315-05, #1745-26). Reidite from Rochechouart has been reported to date exclusively from samples of Chassenon suevite (Plan et al., 2021). These authors documented crystals with reidite proportions from 4 to 91 % and described five different habits of this phase (granular, lamellar, bladed, wedge-shaped, and relatively massive).

In this study, two zircon grains with reidite lamellae indicate reidite proportions of 4.4 and 7.4 %. Grain #1315-29 (Chassenon suevite) has reidite in lamellar habit, as well as a reidite set (B1) that resembles the bladed habit described by Plan et al., (2021) (Figure 5.6). These sets are distributed in different orientations throughout the grains and are CL-dark.

It has been suggested that lamellar reidite forms through a displacive deviatoric transformation controlled by pre-existing zircon microstructures (Erickson et al., 2017), whereas bladed reidite forms also by displacive shearing, through tensional tearing during shock pressure release (Plan et al., 2021). Lamellar reidite has been reported within crystalline zircon domains and not in dark-CL, possibly metamict zones, where high radiation doses do not allow to accommodate stresses required for the martensitic transformation (e.g., Erickson et al., 2017; Plan et al., 2021; Nan et al., 2024). In the present study, although zircon grains #1315-29 and #1315-05 display weak CL responses (Figure 5.6 and 5.7), their U and Th contents are

relatively low (< 460 ppm) and radiation dose calculations (Fig. S9) indicate that the grains are crystalline and did not undergo significant radiation damage, which might have favored the formation of reidite lamellae.

5.5.2 Implications of zircon shock deformation textures in the Rochechouart impact context

Proportions of reidite of ~ 90 % have been previously reported for zircon from Rochechouart (Plan et al., 2021), Chesapeake Bay (Cavosie et al., 2021), and Ries Crater (Zhou et al., 2024). From Rochechouart, such grains were from a suevitic breccia from the Chassenon locality (in the NW of the impact structure). Here, the suevite is interbedded with the very fine-grained deposits of the impactoclastite unit, suggesting that the complete section of the crater fill deposits is preserved. This preservation has been attributed to rapid burial by a sedimentary cover that is no longer present (Lambert, 2010). Furthermore, sedimentological studies in the SC2 drill-core from near Chassenon proposed that the graded suevites, which have a thickness of 88 m, resemble deposits formed by high-energy water resurge, indicating a shallow marine target environment for the impact (Ormö et al., 2023). This indicates that the Chassenon suevitic breccia likely underwent rapid quenching and cooling influenced by seawater, followed by rapid burial. Plan et al. (2021) attributed the preservation of grains with reidite contents > 90 % to this rapid cooling in the upper section of the impactite sequence, where temperatures were not high enough (i.e., they were < 1200 °C) for full reversion of reidite to zircon.

In the present study, grains with different proportions of lamellae were identified in both suevites from Videix and Chassenon. EBSD analysis of three grains confirmed these lamellae as reidite, with reidite proportions up to 7.4 % in two grains. However, the results of CL, BSE, and SE imaging suggest that other zircons from both samples may contain significantly higher proportions of reidite (Figs. S4 and S5). The preservation of high reidite proportions in several zircon grains from the Videix suevite implies that these grains also underwent rapid cooling and temperatures never exceeded 1200 °C, similar to grains from the Chassenon suevite (Plan et al., 2021). The original position of the Videix suevite within the crater fill deposits is not

well constrained, and the suevite may well have been deposited near the top of the crater-fill sequence in order to have been cooled rapidly. The SC11 drill-core from near the Videix locality has a sequence of 32 m of IMR at the top, followed by 34.6 m of two lithologies that could represent either IMR with multi-meter sized blocks of a polymict breccia, or highly deformed basement granite with breccia intercalations (Lambert et al., 2019). This suggests that the drill core intercepted 66.6 m of crater fill deposits without reaching the basement or that the thickness of the crater fill deposits is limited to 32 m. The presence of significant reidite proportions in zircon from the Videix suevite may indicate that the sample originates from somewhere near the top of the sequence and experienced rapid cooling. However, it is recommended to perform further extensive EBSD analysis of these reidite-bearing zircons to better understand reidite proportions, reidite habits, and their implications for reidite formation and retention conditions.

No grains with reidite lamellae were identified in the Babaudus IMR, which indicates that the thermal insulation that allowed the preservation of high proportions of reidite in the suevites was not possible in the IMR. This is consistent with the reports of reidite mainly made in impactites that underwent shock stages II and III (e.g., Erickson et al., 2017; Plan et al., 2021; Tolometti et al., 2022; Zhou et al., 2024), characterized by pressures below 60 GPa and temperatures below 1500 °C (Stöffler et al., 2018).

In addition to reidite, both suevites display granular grains with evidence of FRIGN zircon, and in the Videix suevite, we also identified a grain with zircon neoblasts lacking systematic orientation. These observations indicate that the temperature and pressure conditions experienced by zircon crystals in both suevites were highly heterogeneous. In contrast, the Babaudus IMR contains only granular grains, some of them classified as FRIGN zircon by EBSD, and apparently unshocked crystals (Figure 5.12). Figure 5.12 presents illustrative models showing the general pressure–temperature conditions required for each phase to form. However, we cannot draw conclusions about the specific P–T path of the grains analyzed by EBSD.

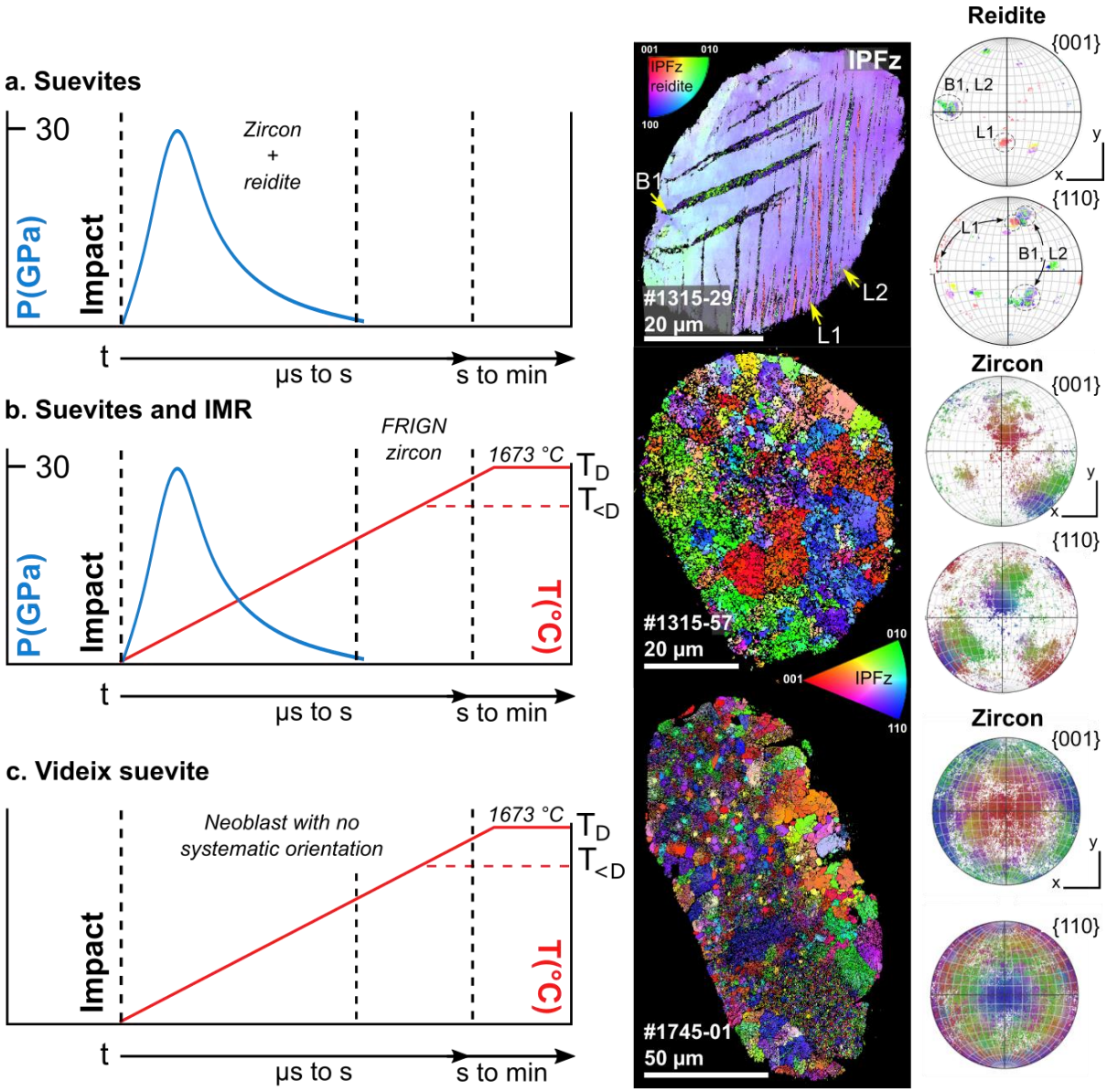


Figure 5.12 Conceptual models illustrating the formation conditions of (a) reidite, found in zircons from both suevites; (b) 'former reidite in granular neoblastic' (FRIGN) zircon, identified in both suevites and the IMR; and (c) granular zircon with neoblasts lacking systematic orientation, observed only in zircon from the Videix suevite. The image includes inverse pole figure (IPF) maps and pole figures, showing examples of these shock deformation features identified in the grains analyzed by EBSD in this study. Models modified from Cavosie et al. (2018). T_D -- temperature of zircon dissociation.

5.5.3 Shock deformation and recorded ages: what are the parameters that control age resetting?

In all samples, the level of discordance on the Tera-Wasserburg plots is closely related to the different types of shock deformation and composition of the grains (Figure 5.9). However, analytical spot size (i.e., SIMS versus LA-ICP-MS) also shows a limited influence (Fig. S8). Younger grains exhibit higher common Pb

content, which is related to larger errors on ages and/or increased discordance compared to unshocked older grains (Figure 5.9a and 5.9c). Consequently, the correction for common Pb was fundamental for accurate age determinations for younger grains. Most of the SIMS analyses used for interpretation were corrected for common Pb. In contrast, most LA-ICP-MS results, even after correcting for common Pb, yielded ages with significant discordances and/or high errors. This is likely due to the larger spot size and deeper ablation crater, which increases the probabilities of sampling mixed or altered zircon domains with high common Pb (Hauser et al., 2019). Therefore, almost all results used for further interpretation of the younger ages, within the acceptable error and discordance ranges, correspond to SIMS analyses corrected for common Pb (Figs. S8d- S8f).

Estimation of reliable upper and lower intercept ages, whether for data corrected or uncorrected for common Pb, for grains selected based on different parameters or for all available analyses from a given sample is challenging (Figure 5.9 and 5.10). None of our data yielded lower intercept ages close to the currently accepted age of the Rochechouart impact event. This is likely a result of relatively large errors on the $^{207}Pb/^{206}Pb$ ratios for some analyses in the Tera-Wasserburg plots, combined with the small age difference between the impact event and youngest basement lithologies (minimum: 272 ± 12 Ma, for a monzodiorite; Guerrero et al., 2024). Consequently, grains with significant inherited radiogenic Pb contributions may plot close to or even on the concordia line. Additionally, most of the calculated ages for all samples exhibit MSWD values higher than the acceptable limit for the given number of analyses, suggesting the presence of more than one zircon population among the data group (Spencer et al., 2016). This is associated with the diversity of zircon textures within each impactite sample, which are potentially derived from different lithologies (Guerrero et al., 2024). Thus, any interpretation of U-Pb systematics of zircons from impactites should be made with great caution, particularly in cases with highly diverse zircon populations and a relatively small age difference between the impact event and the ages of target rocks.

5.5.3.1 Shock deformation and recorded ages

The U–Pb isotopic system of inherited zircon grains affected by varying levels of shock deformation and possible post-shock thermal overprint can exhibit different degrees of resetting, recording post-impact ages, the age of the impact event, or pre-impact ages. A complete reset is typically associated with granular grains (e.g., Hauser et al., 2019; Herrmann et al., 2023; Kamo et al., 1996; Kenny et al., 2017, 2019; Krogh et al., 1993; Moser, 1997; Rasmussen et al., 2020; Schwarz et al., 2020), where neoformed zircon neoblasts are subjected to higher shock temperatures and, in some cases, also retain evidence of higher shock pressures (e.g., Cavosie et al., 2018; Timms et al., 2017; Wittmann et al., 2006). Additionally, some studies have proposed that similar degrees of Pb loss by impact can occur in zircons with different shock metamorphic textures related to metamict domains (Herrmann et al., 2023; Rasmussen et al., 2019; Schmieder et al., 2019; Schwarz et al., 2020). These authors suggest that metamict domains represent “weaknesses” in the zircon lattice, more susceptible to Pb loss due to zircon recrystallization and/or the attack from hydrothermal fluids, leading to possibly even a complete reset of the U-Pb isotopic system during the impact event.

In contrast, reidite-bearing grains in other impact structures have been documented to preserve their primary crystallization ages (Shteynman and Sharp, 2023; Szumila et al., 2023; Zhao et al., 2025). The lack of age resetting suggests that the formation process of reidite does not facilitate age modification. High common Pb concentrations in reidite-bearing grains have been reported in the literature (Shteynman and Sharp, 2023; Zhao et al., 2025). Moreover, local enrichment of trace elements (U, Ti, Th, Pb, Y, Al, Ca, Mg, etc.), have also been reported along fractures, reidite-zircon boundaries, and grain boundaries (e.g., Montalvo et al., 2019; Zhao et al., 2025). These enrichments have been interpreted as resulting from interface migration of the elements during reidite formation (Montalvo et al., 2019) or from the incorporation of these elements from external sources (hydrothermal fluids or impact melt - Zhao et al., 2025).

A general pattern of younger apparent ages mostly recorded in granular grains, and older ages in unshocked grains is observed in zircons from the Babaudus IMR (Fig.

S9). This pattern aligns with the different degrees of resetting of the U-Pb isotopic system: older unshocked grains exhibit minimal (if any) disturbance and likely preserve the ages of protoliths, whereas younger granular zircons reflect strong, possibly complete, age resetting. However, some unshocked zircons with good quality ages have ages comparable to the granular grains. These unshocked grains show similar compositions to the older grains. Only a few crystals show slightly higher U (>1200 ppm) and Th (>500 ppm) contents. This suggests that another factor, besides the degree of shock deformation and the composition of the grains, may control the age resetting in this sample.

In the Chassenon suevite, granular zircons with low error and low discordance ages range from 214 ± 5 to 350 ± 15 Ma, whereas zircons with reidite lamellae and unshocked zircons yield ages greater than ~ 300 Ma. Reidite bearing grains can yield ages up to 515 Ma, while some unshocked zircons can record ages up to 3061 ± 10 Ma. The overlapping age range between grains with reidite lamellae and unshocked grains suggests that the reidite-bearing grains may preserve the primary crystallization age. However, the absence of older ages in these crystals may indicate that the analyzed grains or domains do not capture the full age spectrum, and older ages may exist in reidite-bearing grains, or that some degree of Pb loss is present in the older grains that experience high pressure conditions.

In the Videix suevite, only two granular grains and one zircon with reidite lamellae yielded low discordance and low error ages (206 ± 10, 225 ± 10 Ma, and 401 ± 17 Ma), comparable with the youngest unshocked zircons (189 ± 8 to 255 ± 7 Ma). Shocked and unshocked grains with these younger ages have Th contents > 500 ppm, and the unshocked zircons also U contents > 1000 ppm, which are comparatively higher than those registered for older grains. Even though the radiation dose calculations indicate that most of them are within crystalline zircon domains (Fig. S9), the age resetting of these grains is potentially associated with comparatively higher levels of radiation damage. This suggests that age resetting in this sample was influenced by both the level of shock deformation and the composition of the grains.

The grain with reidite lamellae (225 ± 10 Ma) could indicate age resetting potentially linked to reidite formation. However, it is important to note that reidite was identified solely in BSE images, and the proportion of reidite present in the analyzed spot is unknown. Consequently, it cannot be determined whether the observed age resetting is directly associated with the reidite formation process or rather represents an effect of the composition of the grains.

5.5.4 Provenance analysis

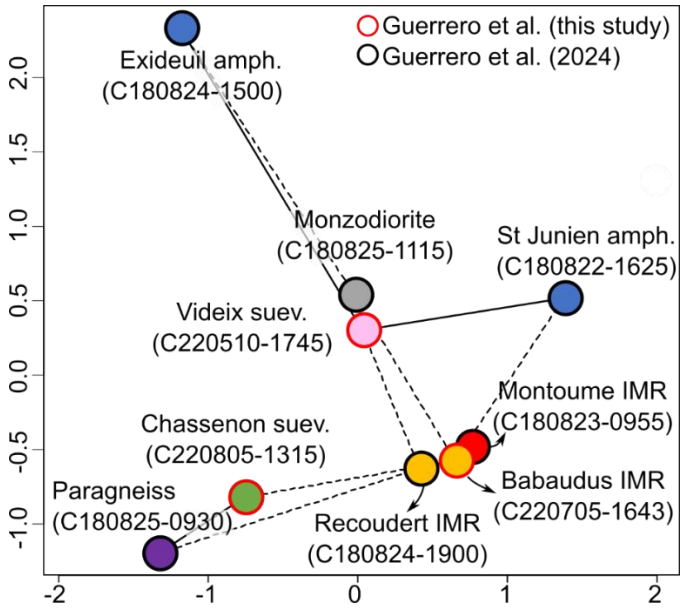


Figure 5.13. Multidimensional scaling plot for the U-Pb geochronological data for impactites of this study and from the previous study by Guerrero et al. (2024). Plot made with the provenance package in R with the Kuiper test (Vermeesch et al., 2016). Each sample is connected to its closest neighbor with a solid line, and to its second-closest neighbor with a dashed line.

The chronologic results of the present study are compared with U-Pb on zircon age data previously reported for impactites from the Rochechouart impact structure, especially with the results by Guerrero et al. (2024) (Figure 5.13 and 5.14). The multi-dimensional scaling plot allows a quantitative comparison between the geochronologic results of the samples of the present study with literature reports (Figure 5.13). It is observed that for the Chassenon suevite the “closest neighbor”, in terms of zircon age statistics, corresponds to the paragneiss from Moulin de Laurière, whereas samples with the closest age provenance to that of the Videix suevite are the monzodiorite from La Martinie, and to a lesser extent, the amphibolites from St. Junien and Exideuil (Guerrero et al., 2024). The Babaudus

IMR plots close to the other IMRs previously analyzed by these authors, and this cluster is not closely related to any basement rock, and exhibits only a partial correlation with the suevites, the paragneiss, and the amphibolite from St. Junien.

These results can be further investigated by comparing the kernel density estimation plots of the suevites and the probability density plot of the Babaudus IMR from this study with data from the literature (Figure 5.14). The Videix suevite has zircon with Silurian to Carboniferous ages similar to those registered for the monzodiorite, although the principal age peaks in the kernel density estimation plots differ. The age distribution of the Chassenon suevite closely resembles that of the paragneiss, with principal age peaks in the Neoproterozoic – Cambrian interval. Additionally, this suevite partially correlates with the ages of other target rocks. The 595 Ma peak is close to the 598 Ma age reported for an amphibolite at St. Junien, the 459 Ma peak matches the 458 Ma age for the monzodiorite from La Martinie, and the 358 Ma peak is comparable to the 362 Ma age for an amphibolite from Exideuil (Guerrero et al., 2024). These peaks are also recorded by zircon from the Babaudus IMR at 591, 463, and 360 Ma. Furthermore, the 489 Ma and 493 Ma peaks for zircon from the Chassenon suevite and Babaudus IMR align with the 491 Ma peak reported for the Montoume IMR (Guerrero et al., 2024) and the 487 ± 7 Ma age reported for the Babaudus IMR (Rasmussen et al., 2020). Besides these ages, the Babaudus, Montoume, and Recoudert impact melt rocks all yielded a significant proportion of Permian, Triassic, and Jurassic ages, which are less represented in the suevites. Some of these ages likely reflect incomplete resetting of the isotopic system; however, the possibility of other basement rocks undergoing post-Variscan events, not yet documented within the area of the impact structure, cannot be ruled out (see also Guerrero et al., 2024).

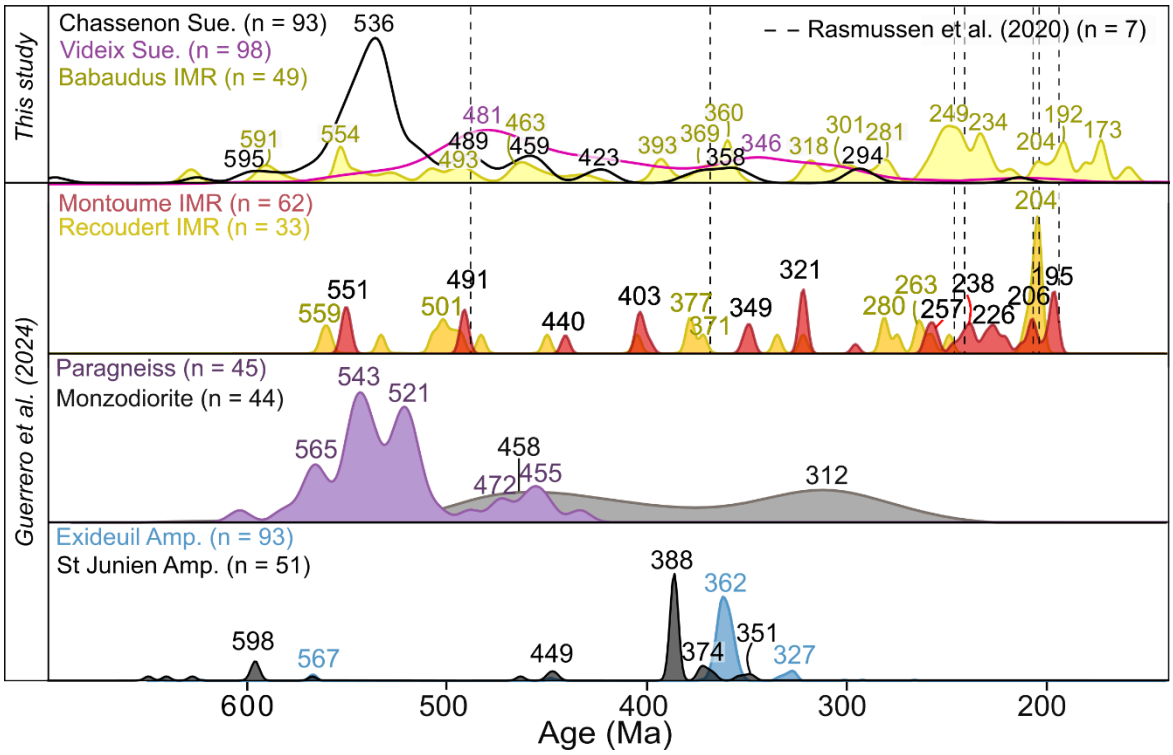


Figure 5.14. U-Pb geochronological data from this study, represented as probability density plot for the Babaudus impact melt rock and as kernel density estimation plots for the suevites of this study and previous reports for zircon from rocks of the impact area (Guerrero et al., 2024). Plot and age peaks calculated with Detrital Py v. 1.3 (Sharman et al., 2018).

The similar age distributions for zircon from the Chassenon suevite and the paragneiss, as well as zircon from the Videix suevite and the monzodiorite, are consistent with some of the nearest target lithologies observed in drill-cores. Furthermore, there is an overall strong correlation when considering the composition of zircons that record ages comparable to those of the basement. In this sense, these target rocks are assumed to be the most probable precursor lithologies for each impactite. However, the age peaks that correlate with the age distributions of other basement rocks suggest that those target rocks likely represent a minor contribution in the formation of these impact breccias.

These results reinforce what was found in previous analyses on other impact melt lithologies from Rochechouart by Guerrero et al. (2024), where it was not possible to establish a clear correlation between the age distributions of the IMRs with those for the basement lithologies. These authors recommended complementing the geochronologic database of the basement lithologies with additional provenance analyses of further regionally occurring lithologies, to better understand the age

distributions for the impactites (Guerrero et al., 2024). In contrast, the results for both suevites allowed a strong correlation with different target rocks. This is likely due to preservation of a significant proportion of unshocked zircons, thereby preserving the ages of the involved target rocks.

5.5.5 Impact and post impact ages

Previous studies have highlighted the potential of granular zircon to record impact ages, including FRIGN zircon and non-FRIGN domains (e.g., Hauser et al., 2019; Herrmann et al., 2023; Kenny et al., 2017, 2019; Rasmussen et al., 2020; Schwarz et al., 2020). Additionally, other shock textures, such as microporous domains and pre-impact metamict domains, have also been useful for this purpose (Herrmann et al., 2023; Rasmussen et al., 2019; Schmieder et al., 2019; Schwarz et al., 2020). However, post-impact metamictization can lead to anomalously young apparent ages (e.g., Rasmussen et al., 2020; Schmieder et al., 2015).

Here, granular grains in three impactite samples register highly heterogeneous ages, with relatively more grains from the two suevite samples showing high discordance and/or large errors compared to those from the Babaudus IMR. These grains are interpreted as crystals with heterogeneous Pb-loss and ages without geological meaning. Granular grains with concordant and low error ages predominantly yielded ages close to the impact and exhibited very similar CL and BSE textures, as well as generally comparable U and Th contents (Figure 5.15 and S9). Furthermore, although higher Th contents and Th/U ratios were registered in shocked grains compared to older unshocked zircons in the Videix suevite and Babaudus IMR, none of these grains show significant radiation damage (Fig. S9).

These similar characteristics of the granular grains with concordant and low error ages complicate the distinction between zircons recording the impact age from those that might register pre-impact ages, potentially due to incomplete isotopic resetting, or post-impact ages that may be associated with metamict domains prone to Pb-loss or overprint from a post-impact thermal/hydrothermal event.

Detailed textural characterization of zircon neoblasts using EBSD was conducted on five granular grains. Of these, three grains yielded ages with reasonable error and

concordance, all of which correspond to FRIGN zircon grains with pre-impact ages (214 ± 5 Ma to 253 ± 11 Ma). Grains with post-impact ages or ages within the error limit of the currently accepted impact age have not been analyzed with EBSD to date, which could have provided valuable insights into which type(s) of grains yielded the different ranges of pre-, syn-, and post-impact ages.

The most precise impact age reported in the literature, 206.92 ± 0.32 Ma ($^{40}Ar/^{39}Ar$; Cohen et al., 2017), falls within the error range of the TuffZirc age of 216 ± 9 Ma and the concordia age of 203 ± 4 Ma obtained in this study. Among these, the concordia age, with its lower uncertainty, is considered the most reliable estimate of the impact age from the present study. This age also aligns with the U-Pb zircon ages reported by previous authors, ranging from 204 to 207 Ma (Guerrero et al., 2024; Rasmussen et al., 2020). These studies also emphasize that zircons exhibiting similar shock-deformation features can record multiple ages. Rasmussen et al. (2020) conducted LA-ICP-MS depth-profiling and EBSD analyses on granular grains, finding that FRIGN zircons yielding impact or post-impact ages can also record pre-impact ages (R-B-2: 207 ± 3.6 and 241 ± 2 Ma; R-B-4: 194 ± 2.9 and 246 ± 7.3 Ma). They attributed a more complete age resetting to better developed granules, likely resulting from more pervasive recrystallization. However, these authors also highlight that the multiple ages recorded in highly shocked FRIGN zircon grains complicate the identification of the most representative age for an impact event based only on this information.

The duration of the widespread hydrothermal alteration documented in the Rochechouart impact structure is not constrained. Multiple K-Ar, Rb-Sr, and apatite fission track ages younger than the currently accepted impact age have been reported in the literature (Kraut and French, 1971; Lambert, 1974; Reimold and Oskierski, 1987; Wagner and Storzer, 1975); however, many of these ages have large errors or are assumed to suffer from significant Ar loss (see discussion in Cohen et al., 2017). A combined $^{40}Ar/^{39}Ar$ age of 201.2 ± 2 Ma for primary and secondary K-feldspars from a shocked gneiss from near Videix was reported by Schmieder et al. (2010; recalculated to 202.7 ± 2.2 Ma by Jourdan et al., 2012). However, it has been argued that this age would hardly represent hydrothermal

overprint of the basement, as this relatively young age would imply a minimum duration of 1.7 Ma for the system (Cohen et al., 2017; Rasmussen et al., 2020). This duration is comparable to numerical estimates for much larger impact structures, such as Chicxulub (180 km diameter) (Abramov and Kring, 2007).

The 203 ± 4 Ma age obtained in the present study could also be correlated with the younger, tentative age for hydrothermal overprint. However, its precision, as well as that of similar U-Pb zircon ages from the Rochechouart impact structure reported in previous works (Guerrero et al., 2024; Horne, 2016; Rasmussen et al., 2020), does not provide sufficient resolution to determine the longevity of such a hydrothermal system (as discussed by Rasmussen et al., 2020).

The youngest concordia age of 191 ± 4 Ma obtained in this study is comparable to the ~195 Ma ages reported in the literature from (U-Th)/He and U-Pb dating of zircon (Guerrero et al., 2024; Horne, 2016; Rasmussen et al., 2020). Here, this age was calculated for two granular grains with irregular CL textures from the Babaudus IMR (#1643-15: 191 ± 8 Ma and #1643-12: 192 ± 5 Ma), and one unshocked crystal with oscillatory zoning texture from the Videix suevite (#1745-57: 189 ± 8 Ma). Previous reports of similar ages were obtained in texturally heterogeneous zircons, including mainly colorless, apparently unshocked grains from the Montoume IMR (Guerrero et al., 2024), a metamict FRIGN zircon grain from the Babaudus IMR (Rasmussen et al., 2020), and 39 grains from the Babaudus and Montoume IMRs (Horne, 2016). These authors attributed this age to a post-impact thermal event not generated by the impact, such as the multiple Pb-Zn and U mineralizations or the Ba-F-Fe–rich and F-Ba-(Pb)–rich veins reported elsewhere in the FMC (Clauer, 2020; Sizaret et al., 2004).

The youngest ages recorded in the present study correspond to four analyses of zircons from the Babaudus IMR, with post-impact ages ranging from 159 ± 7 to 181 ±6 Ma. Notably, these ages exhibit the largest errors on $^{207}Pb/^{206}Pb$ ratios from all analyses of zircon from this sample. The wide range of late, post-impact ages makes it exceedingly unlikely that this period represents a distinct geological event.

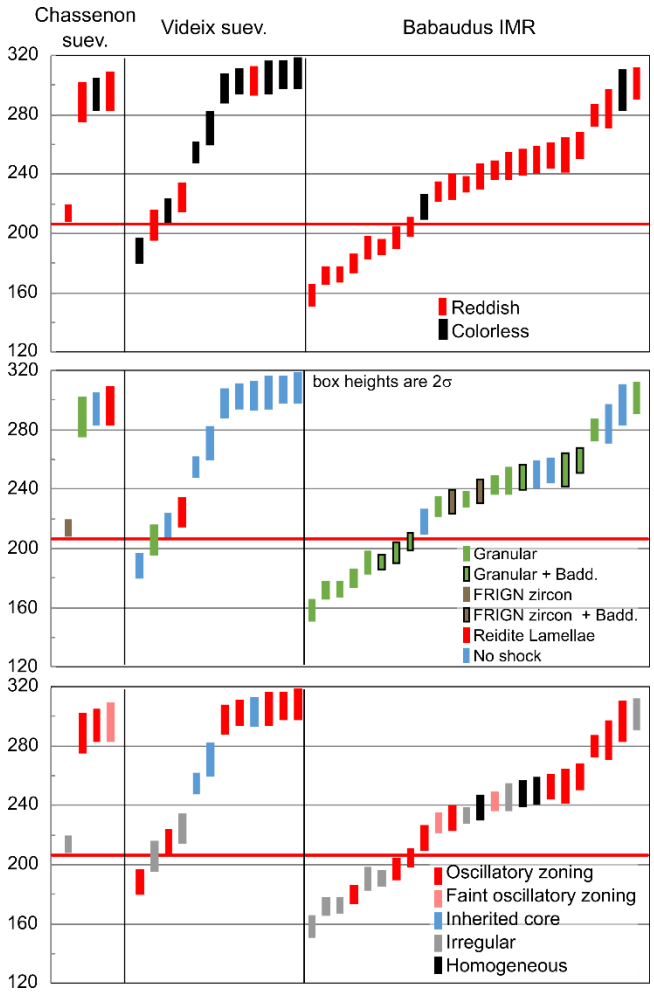


Figure 5.15. Distribution of the youngest apparent $^{206}Pb/^{238}U$ zircon ages for the samples of this study showing the optical, shock deformation, and CL textural characteristics of the related zircon grains. Red line at 206.92 + 0.20/-0.32 Ma corresponds to the $^{40}Ar/^{39}Ar$ age for the impact event by Cohen et al. (2017). The figure shows the diversity of zircons that can record ages close to the impact. Badd. – Baddeleyite.

5.6 Conclusions

We conducted a combined textural characterization and U-Pb geochronological analyses by SIMS and LA-ICP-MS on zircon crystals from the Chassenon and Videix suevites and the Babaudus impact melt rock. The main conclusions that can be drawn from this investigation are:

- The shock metamorphic textures identified in the Videix suevite extend previous reports of FRIGN zircon and/or high proportions of reidite from Chassenon and Babaudus to another locality of the Rochechouart impact structure. The presence of reidite in the Videix suevite has implications for the cooling rates of this lithology and its position within the crater-fill deposits.

- The degree of shock deformation and composition of the zircons influence age resetting. Granular grains that experienced ultrahigh shock temperatures generally record younger ages, and shocked and unshocked zircons with high U and/or Th contents can yield comparable younger ages. However, the presence of unshocked grains with similar ages to those of shocked granular grains, and with compositions comparable to older unshocked grains, suggest an additional process controlling the isotopic resetting.
- The age distribution for zircons from both suevites can be closely related to distinct basement rocks, a paragneiss for the Chassenon suevite and a monzodiorite for the Videix sample. In contrast, the Babaudus IMR age distribution does not match known target lithologies but is similar to other Rochechouart IMRs. This highlights the need for further analysis of other basement rocks and alternative methods to enhance provenance determination.
- The similar characteristics of zircons with ages close to the impact event, with our best estimate being 203 ± 4 Ma and previous studies reporting ages between 204 and 207 Ma, make it challenging to determine the most accurate approximation of the impact age. Only pre-impact ages were recorded in granular grains confirmed as FRIGN zircon.

CRediT authorship contribution statement

Daniela Guerrero: Conceptualization, Writing – original draft & editing, Funding acquisition. **Wolf Uwe Reimold:** Conceptualization, Writing – review & editing, Funding acquisition. **Natalia Hauser:** Conceptualization, Writing – review & editing, Funding acquisition. **Gavin Kenny:** Data curation, Writing – review & editing, Methodology. **Martin Whitehouse:** Data curation and Facility support. **Philippe Lambert:** Editing, Validation.

Acknowledgments

Funding for this study has been provided by the Conselho Nacional de Desenvolvimento Cientıfico e Tecnologico (CNPq) through grants no. 140048/2022-7 and 444320/2020-2, a grant from the Barringer Family Fund for Meteorite Impact

Research, and a CIRIR Career Development Award, all to DG. We acknowledge the CIRIR for hosting DG and for their logistical support during her field campaign. This study was financed in part by the Coordenacão de Aperfeiçoamento de Pessoal de Nıvel Superior—Brasil (CAPES)—Finance Code 001. The research of Natalia Hauser and Wolf Uwe Reimold has been supported by Bolsa de Produtividade grants (Nos. 309878/2019-5, 305761/2019-6, and 307109/2023-2) from CNPq. This is NordSIMS contribution no. XXX (to be filled after manuscript accepted for publication).

5.7 Supplementary material

S1. Sample material

Suevite samples: Two suevite samples were collected for this study at Videix (C220510-1745) and at Chassenon (C220805-1315). The suevite of Videix was collected in a road-cut partially covered by vegetation and the suevite from Chassenon at the Grosse Pièce quarry, where the suevite displays bedding. At the Chassenon locality, and intercalated with suevites, occurs the so-called impactoclastite unit. This is a fine-grained deposit with evidence of sedimentary sorting, which is presumed to mark, at the surface, the top of the impact crater fill deposits (Lambert, 2010; Ormö et al., 2023).

The Videix sample is characterized by a yellow matrix, whereas the Chassenon suevite has a gray-green matrix. In both samples, a high proportion of very heterogeneous mineral and lithic clasts, which seem to be derived from both granitic and gneissic precursors. Both samples have similar proportions of matrix (~58 vol%), melt clasts (6-10 vol%), and mineral and lithic clasts (27-30 vol%); however, there is a higher proportion of vesicles in the Chassenon suevite (8.5 vol%) than in the Videix sample (2.6 vol%). The melt clasts in both samples have irregular forms, are partially associated with opaque phases, and in part are recrystallized to very fine-grained microliths. In the Videix sample the melt is colorless, whereas in the Chassenon sample it has black/gray and green colorations. Both samples have clasts with heterogeneous deformation, including kink bands in micas and diagnostic shock

features like toasted quartz and quartz with up to two sets of PDFs (Fig. S1) (Lambert, 2010; Plan et al., 2021; Sapers et al., 2014).

Both suevite samples were collected close to where two different drill-cores were recovered: Chassenon suevite close to the SC1-3 cores and the Videix suevite in the vicinity of the SC11-13 coring site (Fig. 1a). The SC2 hole yielded a sequence of 39.8 m of a melt-rich suevite intercalated with impactoclastite, followed by 48.2 m of a melt-poor suevite and 26 m of breccia gneiss blocks (Fig. 1b). The SC11 core shows a sequence of 32 m of clast-rich red impact melt, with dominant granite clasts, followed by 27 m of granite blocks that could represent melt-poor lithic breccia, and then 7.6 m of polymict lithic breccia (Lambert et al., 2019).

The impact melt rock sample: The impact melt rock (IMR) from Babaudus (C220705-1643, 45°49.013'N/0°47.784'E) was collected 1.7 km from the crater center (Fig. 1a). This lithology was previously analyzed by Cohen et al. (2017) and Rasmussen et al. (2020). The sample is characterized by a homogeneous, yellow, aphanitic matrix (84 vol%) with a low proportion of vesicles (6.5 vol%), which are elongated preferentially, indicating the flow direction of the melt and in part are filled by quartz or phyllosilicate phases. The sample has a low proportion of mineral (1 vol%) and lithic (8 vol%) clasts, which mostly correspond to quartz grains or aggregates of quartz, biotite, and/or feldspar, with biotite in lepidoblastic texture and sometimes oxidized. These types of clasts are derived from a quartzofeldspathic, likely gneissic target lithology. Furthermore, up to two sets of PDFs have been identified in quartz, and as previously reported, some quartz crystals are recrystallized or toasted (Fig. S1) (Lambert, 2010; Sapers et al., 2014). Additionally, ballen silica has also been reported from this melt rock (Ferrière et al., 2009; Sapers et al., 2014). The matrix displays an interlocking, extremely fine-grained mosaic texture indicative of devitrification and/or /crystallization (Sapers et al., 2014). This type of yellow impact melt rock occurs as isolated outcrops in the central part of the impact structure. The SC17 drill-core from Recoudert, where a very similar yellow, clast-poor IMR crops out at the surface, contains - from the top – a 23 m thick intercalation of red and yellow impact melt rock, followed by 21.1 m of fractured gneiss, a 2.5 m thick suevitic breccia dike, and 18.5 m of felsic gneiss (Lambert et al., 2019).

Fig. S1. Cross- (a, c, d, and f) and plane-polarized (b and e) light microphotographs of the (a and b) Chassenon suevite, (c and d) Videix suevite, and (e and f) Babaudus impact melt rock. (a, c, and e) Diversity of quartzofeldspathic clasts found in the samples (b) Clast of partially melted gneiss with greenish coloration. (d and f) Multiple sets of planar deformation features (PDFs) in quartz within lithic clasts. Red lines indicate crystallographic orientations of PDFs.

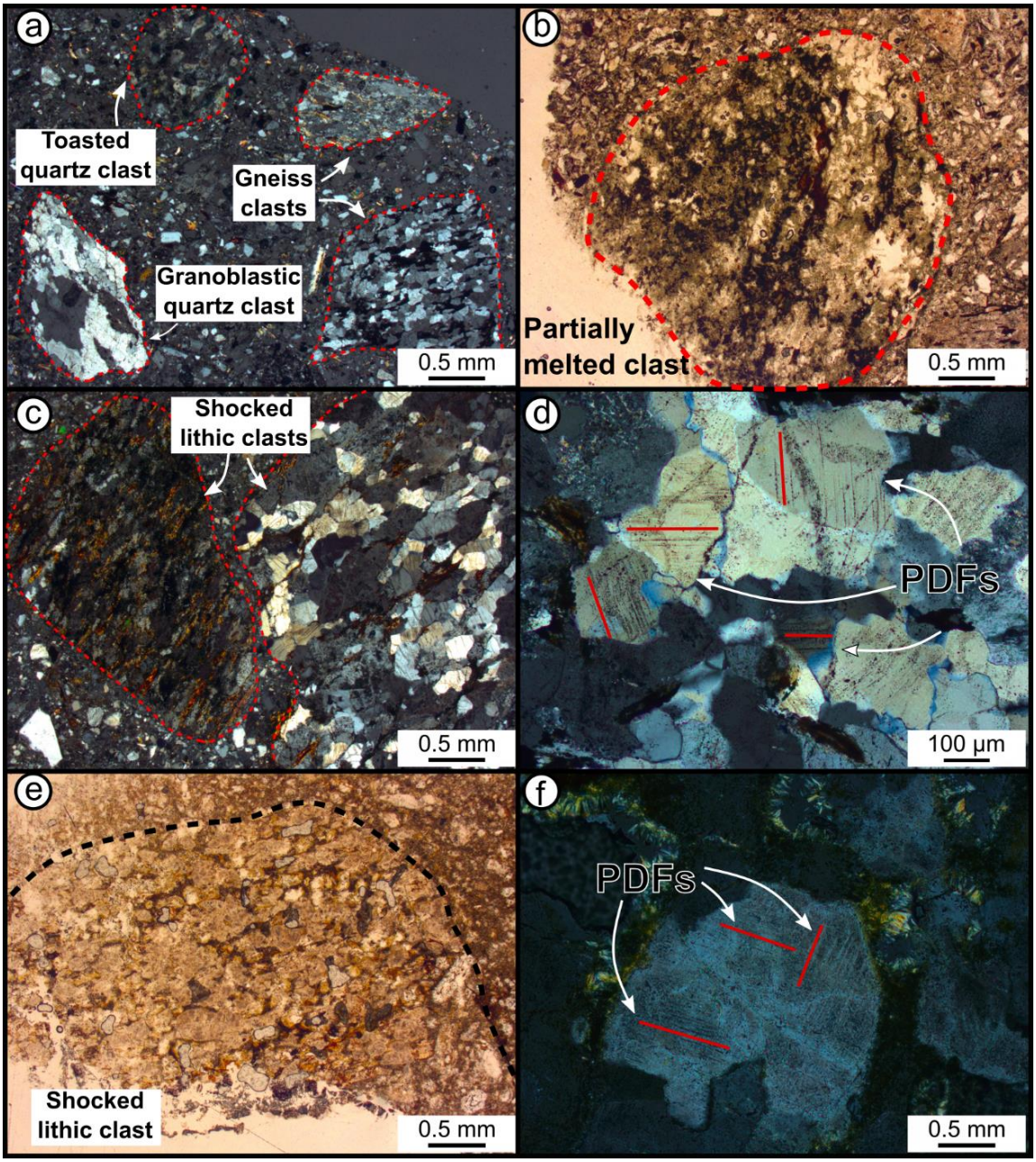


Table S2. U-Pb on zircon radiogenic data of the samples analyzed in this study.

Measured zircon standars

SIMS (Temora 2: 416.78 ± 0.33 Ma; Black et al., 2004)

*Session 1: 414 ± 5.6 Ma (MSWD = 0.98, probability = 0.45, n = 5)

*Session 2: 416 ± 5.5 Ma (MSWD = 0.90, probability = 0.52, n = 5)

LA-ICP-MS

*GJ-1 602.9 ± 1.5 Ma (MSWD = 4.2, probability = 0.04, n = 24)

*91500 1056.7 ± 4.8 Ma (MSWD = 6.5, probability = 0.01, n = 23)

* Plešovice 338.2 ± 1.3 Ma (MSWD = 0.00035, probability = 0.99, n = 19)

									Ratios				Ages							
Laboratory	Sample_ID	Grain_ID	Analysis_ID	Spot Size	f206c	$^{206}Pb/^{204}Pb$	Th/U	U (μg g^{-1})^{a}	$^{238}U/^{206}Pb$	1σ (%)	$^{207}Pb/^{206}Pb$	1σ (%)	$^{207}Pb/^{235}U$	2σ (abs)	$^{206}Pb/^{238}U$	2σ (abs)	$^{207}Pb/^{206}Pb$	2σ (abs)	Conc	Corrected for common-Pb
NordSIMS	C220510-1745	Z1745-01	n6657_1745_@01a	8 um	3E+01	72	1.03	1190	73.2746	2.3176	no data	no data	no data		87	4	no data			Yes
LEGGA	C220510-1745	Z1745.2-001	1745.2_1	25 um	2E+08	0	0.01	484	19.4594	0.6772	0.0693	3.1074	304	63	323	4	867	122	106	No
LEGGA	C220510-1745	Z1745.2-010	1745.2_10	25 um	2E+08	0	0.07	273	13.9082	0.6014	0.0748	1.6192	566	13	448	5	1049	72	79	No
LEGGA	C220510-1745	Z1745.2-011	1745.2_11	25 um	2E+08	0	-0.04	339	13.8391	0.5200	0.0678	1.5969	523	11	450	5	826	69	86	No
LEGGA	C220510-1745	Z1745.2-012	1745.2_12	25 um	2E+08	0	-0.01	374	13.7556	0.6596	0.0718	1.4555	553	12	451	6	966	64	82	No
LEGGA	C220510-1745	Z1745.2-013	1745.2_13	25 um	9E+08	0	-0.01	552	24.2531	0.9821	0.1874	2.1928	737	24	261	5	2696	75	35	No
LEGGA	C220510-1745	Z1745.2-014	1745.2_14	25 um	3E+07	0	0.05	232	3.7516	1.2524	0.1908	1.3611	2117	32	1534	33	2745	44	72	No
LEGGA	C220510-1745	Z1745.2-015	1745.2_15	25 um	2E+08	0	-0.84	306	12.9733	0.7539	0.0567	2.3178	478	18	479	7	491	77	100	No
LEGGA	C220510-1745	Z1745.2-016	1745.2_16	25 um	4E+08	0	-0.01	371	14.7078	0.5067	0.1258	1.5117	790	16	425	4	2014	54	54	No
LEGGA	C220510-1745	Z1745.2-017	1745.2_17	25 um	3E+08	0	0.03	232	14.3617	0.5977	0.0685	1.3862	515	9	435	5	861	57	85	No
LEGGA	C220510-1745	Z1745.2-018	1745.2_18	25 um	8E+08	0	-0.02	848	19.3613	1.0153	0.0546	6.5450	311	41	326	6	994	170	105	Yes
LEGGA	C220510-1745	Z1745.2-019	1745.2_19	25 um	-5E+06	0	0.01	286	13.5427	0.4744	0.0737	1.5215	567	12	459	4	994	63	81	No
LEGGA	C220510-1745	Z1745.2-002	1745.2_2	25 um	1E+08	0	-0.05	239	12.1841	0.6688	0.0730	1.8064	610	15	509	7	974	76	83	No
LEGGA	C220510-1745	Z1745.2-020	1745.2_20	25 um	-7E+07	0	-0.02	478	12.5328	0.2829	0.0578	1.0985	501	9	495	3	500	49	99	No
LEGGA	C220510-1745	Z1745.2-021	1745.2_21	25 um	2E+08	0	0.00	362	14.1485	0.6160	0.0789	1.3218	579	10	442	5	1143	51	76	No
LEGGA	C220510-1745	Z1745.2-022	1745.2_22	25 um	1E+08	0	0.00	589	11.9080	0.3134	0.0591	1.1382	531	9	520	3	556	51	98	No
LEGGA	C220510-1745	Z1745.2-023	1745.2_23	25 um	9E+07	0	0.01	512	12.2113	0.2476	0.0591	1.0523	520	8	507	2	550	47	98	No
LEGGA	C220510-1745	Z1745.2-024	1745.2_24	25 um	2E+08	0	0.01	294	12.6808	0.4485	0.0605	1.2078	514	9	490	4	602	53	95	No
LEGGA	C220510-1745	Z1745.2-025	1745.2_25	25 um	2E+08	0	0.00	304	12.9142	2.5956	0.0467	43.6230	484	132	482	20	1870	307	100	Yes
LEGGA	C220510-1745	Z1745.2-026	1745.2_26	25 um	2E+08	0	-0.15	257	6.8074	2.0284	0.1204	1.1622	1275	35	917	31	1944	42	72	No
LEGGA	C220510-1745	Z1745.2-027	1745.2_27	25 um	7E+08	0	0.00	726	14.5294	0.5547	0.1764	1.2685	1000	16	430	5	2607	43	43	No
LEGGA	C220510-1745	Z1745.2-028	1745.2_28	25 um	2E+09	0	0.01	405	21.0370	1.0335	0.4514	1.5796	1398	21	301	6	4074	48	22	No
LEGGA	C220510-1745	Z1745.2-029	1745.2_29	25 um	7E+08	0	0.01	527	16.9231	0.9158	0.1574	1.5183	839	12	373	7	2406	53	44	No
LEGGA	C220510-1745	Z1745.2-003	1745.2_3	25 um	2E+08	0	0.27	290	13.5492	0.7307	0.0661	1.2762	524	10	461	7	789	56	88	No
LEGGA	C220510-1745	Z1745.2-030	1745.2_30	25 um	1E+09	0	0.00	1683	29.2192	0.6318	0.3491	1.6458	992	23	217	3	3683	48	22	No
LEGGA	C220510-1745	Z1745.2-031	1745.2_31	25 um	1E+09	0	0.00	579	21.2515	0.8005	0.2702	1.4398	1027	15	298	5	3285	45	29	No
LEGGA	C220510-1745	Z1745.2-032	1745.2_32	25 um	1E+07	0	0.00	204	13.2198	1.5209	0.0861	1.8829	654	10	481	13	1301	71	74	No
LEGGA	C220510-1745	Z1745.2-033	1745.2_33	25 um	9E+08	0	0.00	515	22.7357	0.6533	0.2360	1.7781	903	20	278	4	3077	56	31	No
LEGGA	C220510-1745	Z1745.2-034	1745.2_34	25 um	5E+08	0	0.02	570	14.7914	0.7269	0.1252	1.5574	783	14	423	6	2000	56	54	No
LEGGA	C220510-1745	Z1745.2-035	1745.2_35	25 um	1E+08	0	0.00	336	13.0150	0.9636	0.0620	1.5489	516	15	480	9	646	68	93	No
LEGGA	C220510-1745	Z1745.2-036	1745.2_36	25 um	9E+08	0	0.00	915	32.2873	1.1291	0.2458	2.3745	728	18	198	5	3129	76	27	No
LEGGA	C220510-1745	Z1745.2-037	1745.2_37	25 um	9E+08	0	0.00	2242	38.9328	0.5600	0.2281	1.2259	602	9	164	2	3022	39	27	No
LEGGA	C220510-1745	Z1745.2-038	1745.2_38	25 um	5E+07	0	0.05	390	12.5350	0.6492	0.0609	1.7316	522	14	496	6	609	78	95	No
LEGGA	C220510-1745	Z1745.2-039	1745.2_39	25 um	-2E+07	0	0.01	275	12.6185	0.8285	0.0631	1.4148	534	11	494	8	693	58	92	No
LEGGA	C220510-1745	Z1745.2-004	1745.2_4	25 um	2E+07	0	0.01	671	17.9843	0.4267	0.0543	1.2214	355	7	348	3	366	55	98	No
LEGGA	C220510-1745	Z1745.2-040	1745.2_40	25 um	1E+08	0	-0.01	155					650	11	540	8	1030	56	83	No
LEGGA	C220510-1745	Z1745.2-041	1745.2_41	25 um	6E+07	0	-0.10	229	21.5341	1.2909	0.0975	2.0301	494	11	295	7	1538	75	60	No
LEGGA	C220510-1745	Z1745.2-042	1745.2_42	25 um	2E+09	0	0.01	319	7.3220	0.6929	0.6295	1.4485	2597	27	827	10	4571	41	32	No
LEGGA	C220510-1745	Z1745.2-043	1745.2_43	25 um	3E+08	0	0.01	198	14.1817	0.9250	0.0773	1.6266	576	14	442	8	1121	74	77	No
LEGGA	C220510-1745	Z1745.2-044	1745.2_44	25 um	8E+08	0	-0.01	356	21.7573	0.9240	0.2096	1.7915	858	21	290	6	2884	60	34	No

Table S2. U-Pb on zircon radiogenic data of the samples analyzed in this study (continuation).

LEGGA	C220510-1745	Z1745.2-045	1745.2_45	25 um	4E+08	0	0.00	374	20.4517	1.7544	0.1414	3.0063	675	17	314	10	2178	105	46	No
LEGGA	C220510-1745	Z1745.2-046	1745.2_46	25 um	3E+08	0	0.01	605	14.9924	0.5500	0.1231	1.5697	769	16	417	4	1985	56	54	No
LEGGA	C220510-1745	Z1745.2-047	1745.2_47	25 um	1E+09	0	0.01	510	19.3230	0.8812	0.2408	2.5761	1016	40	326	6	3092	80	32	No
LEGGA	C220510-1745	Z1745.2-048	1745.2_48	25 um	2E+08	0	0.33	274	15.4228	0.8097	0.0787	1.7759	540	12	408	6	1113	74	75	No
LEGGA	C220510-1745	Z1745.2-049	1745.2_49	25 um	-2E+06	0	0.01	1735	17.2140	0.6724	0.0515	1.6841	352	10	365	5	224	84	104	No
LEGGA	C220510-1745	Z1745.2-005	1745.2_5	25 um	2E+08	0	0.01	1033	13.0274	0.4387	0.0959	1.2656	713	14	477	4	1530	49	67	No
LEGGA	C220510-1745	Z1745.2-050	1745.2_50	25 um	2E+08	0	-0.01	404	13.9816	0.5534	0.0890	1.5485	641	15	446	5	1375	61	70	No
LEGGA	C220510-1745	Z1745.2-006	1745.2_6	25 um	1E+08	0	-0.02	391	13.0466	0.5060	0.0695	1.3499	560	11	477	5	910	51	85	No
LEGGA	C220510-1745	Z1745.2-007	1745.2_7	25 um	3E+08	0	-0.03	341	13.6497	0.7269	0.0885	1.7798	649	15	457	6	1370	70	70	No
LEGGA	C220510-1745	Z1745.2-008	1745.2_8	25 um	7E+08	0	-0.02	587	20.8060	0.4486	0.1733	1.7682	775	17	303	3	2561	61	39	No
LEGGA	C220510-1745	Z1745.2-009	1745.2_9	25 um	4E+07	0	0.02	818	12.1925	0.2096	0.0599	1.1926	526	9	508	2	582	53	97	No
LEGGA	C220510-1745	Z1745-001	1745_1	25 um			1.76	302	21.4792	1.5612	0.4083	2.2922	1309	27	295	9	3921	69	23	No
LEGGA	C220510-1745	Z1745-010	1745_10	25 um			1.78	48	2.9244	1.7729	0.1353	1.9089	2032	30	1904	60	2156	67	94	No
LEGGA	C220510-1745	Z1745-011	1745_11	25 um			1.08	357	14.6393	1.5730	0.0808	3.2573	575	22	427	13	1178	127	74	No
LEGGA	C220510-1745	Z1745-012	1745_12	25 um			0.42	745	20.8973	1.5688	0.0608	7.4641	336	55	303	9	903	179	90	Yes
LEGGA	C220510-1745	Z1745-013	1745_13	25 um			0.88	304	13.7848	1.9400	0.0636	2.7182	502	15	456	18	690	115	91	No
LEGGA	C220510-1745	Z1745-014	1745_14	25 um			0.95	523	17.5667	1.4924	0.0907	3.6459	545	24	357	11	1408	147	66	No
LEGGA	C220510-1745	Z1745-10	1745_15a	25 um			0.62	3208	30.3844	2.0220	0.2724	2.1520	821	26	211	8	3307	65	26	No
LEGGA	C220510-1745	Z1745-10	1745_15b	25 um			0.57	1399	24.0499	5.2677	0.1987	3.6539	787	82	268	27	2804	115	34	No
LEGGA	C220510-1745	Z1745-016	1745_16	25 um			0.52	288	14.0168	3.0193	0.0588	3.5933	465	21	440	19	510	167	95	No
LEGGA	C220510-1745	Z1745-017	1745_17	25 um			1.21	395	21.6299	1.6347	0.0679	3.2954	366	17	292	9	830	132	80	No
LEGGA	C220510-1745	Z1745-018	1745_18	25 um			0.64	198	12.6744	1.2709	0.0570	2.3102	491	13	492	12	450	103	100	No
LEGGA	C220510-1745	Z1745-019	1745_19	25 um			0.61	294	13.7722	1.4184	0.0626	2.3118	495	15	454	12	658	98	92	No
LEGGA	C220510-1745	Z1745-20	1745_2	25 um			1.00	314	14.7115	1.3710	0.0676	1.9149	501	12	427	11	826	78	85	No
LEGGA	C220510-1745	Z1745-020	1745_20	25 um			0.45	440	12.1077	1.6297	0.0907	4.1830	719	49	513	16	1432	143	71	No
LEGGA	C220510-1745	Z1745-021	1745_21	25 um			0.83	1466	22.5127	2.2450	0.1835	3.8706	763	35	282	13	2657	128	37	No
LEGGA	C220510-1745	Z1745-56	1745_22	25 um			0.77	736	20.4953	1.6515	0.0563	2.3529	328	11	308	10	440	109	94	No
LEGGA	C220510-1745	Z1745-023	1745_23a	25 um			1.01	2193	27.1270	2.0713	0.2608	2.5673	861	35	235	9	3237	86	27	No
LEGGA	C220510-1745	Z1745-023	1745_23b	25 um			0.89	766	18.0847	2.2342	0.1582	4.3222	806	51	348	15	2409	135	43	No
LEGGA	C220510-1745	Z1745-024	1745_24	25 um			0.65	350	12.7838	1.9598	0.0578	2.5847	492	17	489	19	530	138	99	No
LEGGA	C220510-1745	Z1745-025	1745_25	25 um			0.79	795	14.3261	1.5683	0.0637	4.8100	482	30	440	14	888	157	91	Yes
LEGGA	C220510-1745	Z1745-08	1745_26	25 um			1.66	804	12.8149	1.6202	0.1117	2.5480	801	22	487	15	1801	98	61	No
LEGGA	C220510-1745	Z1745-07	1745_27	25 um			0.97	403	13.8864	1.1907	0.0655	3.8315	508	27	448	10	757	152	88	No
LEGGA	C220510-1745	Z1745-57	1745_28	25 um			0.74	933	19.9156	1.9145	0.1432	8.2263	692	88	316	11	2190	282	46	No
LEGGA	C220510-1745	Z1745-029	1745_29	25 um			0.83	379	15.1632	1.6798	0.0518	20.2010	380	112	415	15	964	509	109	Yes
LEGGA	C220510-1745	Z1745-003	1745_3	25 um			0.78	376	13.3278	1.2420	0.0602	1.8592	495	12	468	11	586	80	95	No
LEGGA	C220510-1745	Z1745-030	1745_30	25 um			0.17	251	16.2208	2.5180	0.0606	21.2131	403	173	390	19	1084	425	97	Yes
LEGGA	C220510-1745	Z1745-06	1745_31	25 um			0.82	1021	23.4058	1.5908	0.1512	5.5100	627	42	273	9	2179	192	43	No
LEGGA	C220510-1745	Z1745-63	1745_32	25 um			0.51	471	15.0583	2.8427	0.0577	13.3901	445	94	418	19	1084	384	94	Yes
LEGGA	C220510-1745	Z1745-033	1745_33	25 um			0.90	446	13.0714	2.2645	0.0809	8.6720	617	80	479	21	1174	304	78	No
LEGGA	C220510-1745	Z1745-034	1745_34a	25 um			0.66	404	13.3572	2.2346	0.0750	7.5149	577	54	467	20	973	268	81	No
LEGGA	C220510-1745	Z1745-035	1745_35	25 um			0.58	237	15.5282	2.3962	0.0687	9.0328	451	48	409	19	875	286	91	Yes
LEGGA	C220510-1745	Z1745-05	1745_36	25 um			2.20	642	18.3983	1.7857	0.5420	2.5317	1638	36	339	13	4346	70	21	No
LEGGA	C220510-1745	Z1745-037	1745_37	25 um			0.68	457	14.8189	2.1839	0.1024	5.6014	675	46	424	18	1591	195	63	No
LEGGA	C220510-1745	Z1745-038	1745_38a	25 um			1.63	4502	38.0258	1.7396	0.4597	2.5518	998	26	168	6	4106	76	17	No
LEGGA	C220510-1745	Z1745-038	1745_38b	25 um			1.20	1670	26.4918	2.0728	0.2776	2.4120	912	24	239	10	3342	73	26	No
LEGGA	C220510-1745	Z1745-039	1745_39	25 um			0.88	440	15.0413	1.8109	0.0596	7.4058	434	62	418	15	855	123	96	Yes
LEGGA	C220510-1745	Z1745-18	1745_4	25 um			0.81	991	18.1190	1.3499	0.0568	2.5502	365	10	347	9	446	115	95	No
LEGGA	C220510-1745	Z1745-60	1745_40	25 um			1.11	485	20.5356	2.7116	0.0942	3.3725	500	21	309	17	1490	125	62	No
LEGGA	C220510-1745	Z1745-005	1745_5	25 um			0.35	233	12.0294	2.3651	0.0599	15.0999	519	199	515	21	1454	291	99	Yes
LEGGA	C220510-1745	Z1745-37	1745_6	25 um			0.74	58	11.7522	1.8372	0.0576	4.6246	521	36	529	18	405	228	102	No
LEGGA	C220510-1745	Z1745-11	1745_7	25 um			0.55	313	13.1293	1.8655	0.0613	2.7345	506	16	477	17	611	119	94	No
LEGGA	C220510-1745	Z1745-13	1745_8	25 um			0.93	323	11.6726	1.5818	0.0618	2.4628	554	17	533	16	634	104	96	No
LEGGA	C220510-1745	Z1745-32	1745_9a	25 um			1.20	708	25.5806	3.5161	0.1690	4.3625	659	21	250	18	2526	146	38	No
LEGGA	C220510-1745	Z1745-32	1745_9b	25 um			1.50	364	19.9240	2.5456	0.2308	2.6401	977	42	317	16	3049	86	32	No
NordSIMS	C220510-1745	Z1745-01	n6657_1745_@01b	8 um	3.26E+01	57	1.36	541	44.3729	4.9919	0.0789	28.7105	223	120	144	14	1170	1191	65	Yes
NordSIMS	C220510-1745	Z1745-02	n6657_1745_@02a	8 um	2.55E+01	73	0.97	138	52.5197	3.9465	no data	no data	no data		122	10	no data			Yes
NordSIMS	C220510-1745	Z1745-02	n6657_1745_@02b	8 um	3.92E+01	48	0.17	3286	33.0188	1.8779	0.0586	15.7555	222	64	192	7	551	698	87	Yes
NordSIMS	C220510-1745	Z1745-03	n6657_1745_@03a	8 um	2.13E+01	88	0.10	2255	24.7601	1.3447	0.0574	12.0862	282	61	255	7	508	536	91	Yes

Table S2. U-Pb on zircon radiogenic data of the samples analyzed in this study (continuation).

NordSIMS	C220510-1745	Z1745-03	n6657_1745_@03b	8 um	4.51E+00	415	0.59	392	23.2356	2.0966	0.0560	7.6868	292	41	272	11	454	342	93	Yes
NordSIMS	C220510-1745	Z1745-04	n6657_1745_@04a	8 um	4.81E+01	39	1.15	880	34.8854	2.6738	0.0613	25.2388	220	103	182	10	651	1126	83	Yes
NordSIMS	C220510-1745	Z1745-04	n6657_1745_@04b	8 um	4.78E+01	39	1.41	1384	25.8641	2.6491	0.0594	32.9809	279	168	245	13	583	1535	88	Yes
NordSIMS	C220510-1745	Z1745-05	n6657_1745_@05	8 um	7.78E+01	24	1.31	881	58.6219	5.9671	no data	no data	no data		109	13	no data			Yes
NordSIMS	C220510-1745	Z1745-06	n6657_1745_@06	8 um	6.89E+00	271	0.28	1835	29.3923	1.9735	0.0545	16.8805	231	72	216	8	392	771	93	Yes
NordSIMS	C220510-1745	Z1745-07	n6657_1745_@07	8 um	4.64E+00	403	0.67	330	16.7056	2.1117	0.0578	6.7482	396	47	375	15	521	297	95	Yes
NordSIMS	C220510-1745	Z1745-08	n6657_1745_@08	8 um	9.60E-01	1951	0.30	336	11.2615	1.9707	0.0581	4.0244	545	38	548	21	532	176	101	Yes
NordSIMS	C220510-1745	Z1745-09	n6657_1745_@09a	8 um	3.60E-01	5149	0.38	784	12.8179	1.0949	0.0561	1.5658	480	15	484	10	458	69	101	Yes
NordSIMS	C220510-1745	Z1745-09	n6657_1745_@09b	8 um	1.40E+00	1335	0.62	972	13.1667	2.1677	0.0579	4.8276	481	41	472	20	526	212	98	Yes
NordSIMS	C220510-1745	Z1745-10	n6657_1745_@10	8 um	4.60E-01	4068	0.15	1202	18.5482	1.5618	0.0532	3.7981	339	24	339	10	339	172	100	Yes
NordSIMS	C220510-1745	Z1745-11	n6657_1745_@11	8 um	1.47E+01	127	0.59	431	34.1505	4.7590	0.0456	22.1036	172	73	186	17	-24	1107	108	Yes
NordSIMS	C220510-1745	Z1745-12	n6657_1745_@12	8 um	1.77E+01	106	0.74	1063	50.4075	1.9480	0.0564	16.6568	146	46	127	5	467	751	87	Yes
NordSIMS	C220510-1745	Z1745-13	n6657_1745_@13	8 um	2.83E+00	660	0.94	272	13.9674	2.8967	0.0529	7.2359	427	55	446	25	326	330	104	Yes
NordSIMS	C220510-1745	Z1745-15	n6657_1745_@15	8 um	4.64E+01	40	0.28	5332	66.0019	4.6139	0.0832	55.8481	163	176	97	9	1275	2669	60	Yes
NordSIMS	C220510-1745	Z1745-15	n6657_1745_@15b	15 um	4.20E+00	446	0.51	540	17.4673	1.6169	0.0550	3.1309	366	22	359	11	411	140	98	Yes
NordSIMS	C220510-1745	Z1745-16	n6657_1745_@16	8 um	3.48E+00	538	0.20	233	19.8947	2.0731	0.0499	8.0439	302	44	316	13	189	376	105	Yes
NordSIMS	C220510-1745	Z1745-17	n6657_1745_@17	8 um	8.00E-02	24454	0.22	767	20.5005	1.4916	0.0524	1.5965	307	12	307	9	303	73	100	No
NordSIMS	C220510-1745	Z1745-18	n6657_1745_@18	8 um	1.46E+00	1280	0.28	523	19.9601	1.7586	0.0530	4.2513	317	25	315	11	327	193	100	Yes
NordSIMS	C220510-1745	Z1745-19	n6657_1745_@19	8 um	0.00E+00	391152	0.02	1007	17.6765	1.2214	0.0539	1.2760	356	11	355	8	367	58	100	No
NordSIMS	C220510-1745	Z1745-19	n6657_1745_@19b	15 um	1.65E+00	1131	0.39	592	13.1428	1.4662	0.0590	2.1523	489	20	473	13	568	94	97	Yes
NordSIMS	C220510-1745	Z1745-20	n6657_1745_@20	8 um	4.70E-01	4019	0.28	355	13.5552	1.2607	0.0576	2.4849	469	21	459	11	516	109	98	Yes
NordSIMS	C220510-1745	Z1745-21	n6657_1745_@21	8 um	0.00E+00	597027	0.25	961	11.4655	1.2125	0.0577	1.1452	535	14	539	13	517	50	101	No
NordSIMS	C220510-1745	Z1745-21	n6657_1745_@21b	15 um	7.00E-02	26267	0.27	170	11.2763	1.6548	0.0585	1.4220	548	19	548	17	549	62	100	No
NordSIMS	C220510-1745	Z1745-22	n6657_1745_@22	8 um	1.42E+01	131	1.11	458	11.1095	3.8887	0.0990	13.8870	814	168	556	41	1606	523	68	Yes
NordSIMS	C220510-1745	Z1745-23	n6657_1745_@23	8 um	6.71E+01	28	1.26	994	31.3944	5.0633	0.1064	26.1266	389	180	202	20	1739	991	52	Yes
NordSIMS	C220510-1745	Z1745-24	n6657_1745_@24	8 um	1.14E+01	164	1.22	747	30.7530	2.3899	0.0554	11.7784	225	49	206	10	429	530	92	Yes
NordSIMS	C220510-1745	Z1745-25	n6657_1745_@25a	8 um	1.58E+00	1181	0.75	58	15.2987	4.4115	0.0570	9.1040	421	71	408	35	490	404	97	Yes
NordSIMS	C220510-1745	Z1745-25	n6657_1745_@25b	8 um	4.11E+01	46	1.92	484	64.8909	5.6147	no data	no data	no data		99	11	no data			Yes
NordSIMS	C220510-1745	Z1745-26	n6657_1745_@26	8 um	6.24E+01	30	1.26	457	35.6308	5.0220	0.0982	39.9245	327	238	178	18	1590	1628	55	Yes
NordSIMS	C220510-1745	Z1745-27	n6657_1745_@27	15 um	1.30E-01	14236	0.69	482	15.5877	2.1552	0.0564	1.1214	411	16	401	17	467	50	98	Yes
NordSIMS	C220510-1745	Z1745-28	n6657_1745_@28	15 um	1.71E+01	110	0.86	952	30.7068	2.1996	no data	no data	no data		207	9	no data			Yes
NordSIMS	C220510-1745	Z1745-29	n6657_1745_@29	15 um	2.74E+01	68	0.88	1034	28.1670	2.1725	0.0512	20.3460	227	85	225	10	251	962	99	Yes
NordSIMS	C220510-1745	Z1745-30	n6657_1745_@30	15 um	2.19E+01	85	0.96	157	19.4002	6.0719	no data	no data	no data		324	38	no data			Yes
NordSIMS	C220510-1745	Z1745-31	n6657_1745_@31a	15 um	8.00E-01	2341	0.39	259	15.1087	1.2926	0.0553	2.2663	415	18	413	10	424	101	100	Yes
NordSIMS	C220510-1745	Z1745-31	n6657_1745_@31b	15 um	6.00E-02	29840	0.30	435	12.6271	1.9176	0.0574	1.2141	494	18	491	18	506	53	99	Yes
NordSIMS	C220510-1745	Z1745-32	n6657_1745_@32	15 um	4.10E-01	4571	0.40	377	13.0478	1.1375	0.0565	1.7186	475	16	476	10	470	76	100	Yes
NordSIMS	C220510-1745	Z1745-33	n6657_1745_@33	15 um	2.25E+00	830	0.43	379	16.3106	1.3824	0.0547	3.2711	386	23	384	10	402	147	99	Yes
NordSIMS	C220510-1745	Z1745-34	n6657_1745_@34a	15 um	2.60E-01	7299	0.31	425	13.1912	1.5594	0.0590	1.2661	488	16	471	14	565	55	97	Yes
NordSIMS	C220510-1745	Z1745-34	n6657_1745_@34b	15 um	5.11E+00	366	0.47	1135	13.9141	2.3060	0.0535	11.5241	432	84	447	20	350	525	104	Yes
NordSIMS	C220510-1745	Z1745-35	n6657_1745_@35a	15 um	5.00E-01	3773	0.31	475	13.0918	1.5188	0.0568	1.4814	476	16	475	14	485	65	100	Yes
NordSIMS	C220510-1745	Z1745-35	n6657_1745_@35b	15 um	1.43E+00	1309	0.27	225	19.0365	2.3986	0.0531	7.4091	330	44	330	15	332	337	100	Yes
NordSIMS	C220510-1745	Z1745-36	n6657_1745_@36a	15 um	6.00E-02	30109	0.20	229	12.7731	1.6395	0.0578	1.5083	492	17	486	15	521	66	99	No
NordSIMS	C220510-1745	Z1745-36	n6657_1745_@36b	15 um	2.42E+00	774	0.56	1008	14.1007	1.7723	0.0573	11.7418	452	88	442	15	502	521	98	Yes
NordSIMS	C220510-1745	Z1745-37	n6657_1745_@37	15 um	3.74E+00	500	0.94	88	17.4886	2.0557	0.0552	7.3751	367	48	359	14	422	330	98	Yes
NordSIMS	C220510-1745	Z1745-38	n6657_1745_@38	15 um	2.51E+00	746	0.34	571	20.7798	1.3527	0.0554	2.7831	318	17	303	8	427	124	95	Yes
NordSIMS	C220510-1745	Z1745-39	n6657_1745_@39a	15 um	3.08E+00	607	0.25	494	18.4663	1.2368	0.0545	7.5289	347	45	340	8	393	339	98	Yes
NordSIMS	C220510-1745	Z1745-39	n6657_1745_@39b	15 um	1.10E-01	17717	0.22	390	14.2222	1.8581	0.0555	1.1892	437	16	438	16	433	53	100	Yes
NordSIMS	C220510-1745	Z1745-40	n6657_1745_@40	15 um	2.90E-01	6468	0.53	378	13.2434	1.4174	0.0573	1.2807	475	15	469	13	502	56	99	Yes
NordSIMS	C220510-1745	Z1745-41	n6657_1745_@41	15 um	2.70E-01	6912	0.21	353	12.9541	1.2940	0.0556	1.5525	472	15	479	12	436	69	102	Yes
NordSIMS	C220510-1745	Z1745-42	n6657_1745_@42	15 um	2.35E+00	796	0.88	262	14.1546	1.2155	0.0598	2.9128	466	24	440	10	597	126	94	Yes
NordSIMS	C220510-1745	Z1745-43	n6657_1745_@43a	15 um	9.00E-02	20437	0.13	260	18.6182	1.2393	0.0534	1.5888	338	12	337	8	346	72	100	No
NordSIMS	C220510-1745	Z1745-43	n6657_1745_@43b	15 um	3.30E-01	5696	0.41	296	13.0878	1.6482	0.0567	1.4910	476	17	475	15	480	66	100	Yes
NordSIMS	C220510-1745	Z1745-44	n6657_1745_@44a	15 um	4.90E-01	3835	0.47	308	11.0487	2.0852	0.0603	1.3336	570	22	559	22	614	58	98	Yes
NordSIMS	C220510-1745	Z1745-44	n6657_1745_@44b	15 um	5.00E-02	35255	0.48	706	10.2311	1.2957	0.0589	0.6784	593	13	601	15	563	30	101	Yes
NordSIMS	C220510-1745	Z1745-45	n6657_1745_@45	15 um	3.70E-01	5054	0.28	815	18.2358	1.7871	0.0538	1.0844	347	12	344	12	363	49	99	Yes
NordSIMS	C220510-1745	Z1745-46	n6657_1745_@46	15 um	0.00E+00	462038	0.22	637	12.4906	1.2942	0.0567	0.7589	493	12	497	12	478	34	101	No
NordSIMS	C220510-1745	Z1745-47	n6657_1745_@47a	15 um	3.94E+00	475	0.12	500	21.8381	2.5897	0.0538	15.1488	297	81	289	15	364	693	97	Yes
NordSIMS	C220510-1745	Z1745-47	n6657_1745_@47b	15 um	1.00E+00	1870	0.25	303	18.1366	1.4568	0.0567	2.2874	364	17	346	10	479	101	95	Yes
NordSIMS	C220510-1745	Z1745-48	n6657_1745_@48a	15 um	6.50E-01	2859	0.47	544	12.7913	1.2296	0.0577	1.5166	491	15	485	12	520	67	99	Yes

Table S2. U-Pb on zircon radiogenic data of the samples analyzed in this study (continuation).

NordSIMS	C220510-1745	Z1745-48	n6657_1745_@48b	15 um	1.60E-01	12034	0.29	350	12.3539	1.2706	0.0572	1.2231	501	14	502	12	498	54	100	Yes
NordSIMS	C220510-1745	Z1745-49	n6657_1745_@49	15 um	1.80E+00	1040	0.07	1406	3.6830	3.0276	0.1481	0.9729	1907	55	1548	84	2324	33	81	Yes
NordSIMS	C220510-1745	Z1745-50	n6657_1745_@50a	15 um	1.05E+00	1779	0.45	595	13.3920	1.3707	0.0549	3.6726	455	29	464	12	408	164	102	Yes
NordSIMS	C220510-1745	Z1745-50	n6657_1745_@50b	15 um	6.00E-02	31477	0.46	615	12.3514	1.5627	0.0576	0.8329	504	14	502	15	514	37	100	Yes
NordSIMS	C220510-1745	Z1745-51	n6657_1745_@51	15 um	3.85E+00	486	0.56	973	15.6863	2.1286	0.0578	2.8254	417	24	398	16	521	124	96	Yes
NordSIMS	C220510-1745	Z1745-52	n6657_1745_@52	15 um	8.50E-01	2207	0.54	655	14.7095	1.1766	0.0561	1.3578	429	13	424	10	457	60	99	Yes
NordSIMS	C220510-1745	Z1745-53	n6657_1745_@53	15 um	6.00E-02	31565	0.31	337	13.2730	1.5973	0.0562	1.1193	467	15	468	14	459	50	100	No
NordSIMS	C220510-1745	Z1745-54	n6657_1745_@54a	15 um	1.01E+00	1850	0.07	973	17.7993	0.9103	0.0538	3.8958	354	24	352	6	361	176	100	Yes
NordSIMS	C220510-1745	Z1745-54	n6657_1745_@54b	15 um	8.20E-01	2267	0.48	842	12.5612	1.4734	0.0567	1.1966	492	15	494	14	481	53	100	Yes
NordSIMS	C220510-1745	Z1745-55	n6657_1745_@55	15 um	1.90E-01	9780	0.49	387	12.7207	1.5317	0.0566	1.4638	486	16	488	14	475	65	100	Yes
NordSIMS	C220510-1745	Z1745-56	n6657_1745_@56	15 um	1.00E-02	181168	0.42	798	20.6136	1.7696	0.0529	0.9709	308	11	305	11	324	44	99	No
NordSIMS	C220510-1745	Z1745-57	n6657_1745_@57	15 um	3.58E+01	52	0.67	2153	33.5857	2.2269	0.0524	36.6770	198	137	189	8	304	1834	96	Yes
NordSIMS	C220510-1745	Z1745-58	n6657_1745_@58	15 um	1.08E+00	1739	0.71	466	14.7193	1.3748	0.0560	1.7628	428	16	424	11	452	78	99	Yes
NordSIMS	C220510-1745	Z1745-59	n6657_1745_@59	15 um	5.50E-01	3414	0.32	371	13.6717	1.2841	0.0556	2.7758	452	22	455	11	437	124	101	Yes
NordSIMS	C220510-1745	Z1745-60	n6657_1745_@60	15 um	2.49E+00	751	0.60	287	16.2680	2.2300	0.0577	3.2792	405	27	385	17	520	144	95	Yes
NordSIMS	C220510-1745	Z1745-61	n6657_1745_@61	15 um	1.19E+00	1576	0.47	320	14.1727	1.2201	0.0558	2.1821	440	18	440	10	444	97	100	Yes
NordSIMS	C220510-1745	Z1745-62	n6657_1745_@62	15 um	8.10E-01	2314	0.43	569	13.6486	1.3860	0.0578	1.3804	467	15	456	12	522	61	98	Yes
NordSIMS	C220510-1745	Z1745-63	n6657_1745_@63	15 um	1.40E-01	13362	0.02	177	17.9858	1.4839	0.0539	1.7737	351	14	349	10	368	80	99	No
NordSIMS	C220510-1745	Z1745-64	n6657_1745_@64	15 um	1.27E+00	1468	0.48	222	14.9207	1.2596	0.0592	2.4682	443	20	418	10	573	107	94	Yes
NordSIMS	C220510-1745	Z1745-65	n6657_1745_@65	15 um	1.41E+00	1330	0.28	893	21.1132	1.6512	0.0528	2.4865	301	16	298	10	319	113	99	Yes
NordSIMS	C220705-1643	Z1643-08	n6659_1643_@08b	15 um	1.34E+01	139	2.19	3418	68.3009	1.5547	0.0568	5.2078	110	11	94	3	484	230	85	No
LEGGA	C220705-1643	Z1643.2-001	1643.2_1	25 um	1.20E+00	25	-0.01	507	34.5540	1.0508	0.0934	1.6308	327	9	185	4	1501	73	56	No
LEGGA	C220705-1643	Z1643.2-010	1643.2_10	25 um	5.94E+00	6	0.38	157	15.3494	1.1194	0.0646	1.5795	461	10	411	9	722	68	89	No
LEGGA	C220705-1643	Z1643.2-011	1643.2_11	25 um	-5.06E-01	-433	0.04	324	11.1422	0.4151	0.0591	0.9495	558	7	554	5	555	42	99	No
LEGGA	C220705-1643	Z1643.2-012	1643.2_12	25 um	8.53E-01	200	0.22	138	15.3550	1.6154	0.0637	2.0325	460	12	413	13	690	89	90	No
LEGGA	C220705-1643	Z1643.2-014	1643.2_14	25 um	-1.69E+00	-1187	0.03	185	15.9612	0.8919	0.0604	1.5450	428	8	394	7	606	66	92	No
LEGGA	C220705-1643	Z1643.2-015	1643.2_15	25 um	-3.14E+00	104	-0.30	95	17.5052	2.0661	0.0616	2.5964	401	10	368	14	595	112	92	No
LEGGA	C220705-1643	Z1643.2-016	1643.2_16	25 um	1.24E+00	87	0.03	286	16.3167	1.7349	0.0603	1.7165	423	13	392	14	583	79	92	No
LEGGA	C220705-1643	Z1643.2-017	1643.2_17	25 um	7.17E-01	2	0.22	89	3.3696	0.4537	0.1069	0.8850	1712	13	1677	13	1742	34	98	No
LEGGA	C220705-1643	Z1643.2-002	1643.2_2	25 um	3.44E+00	96	-0.06	180	10.4298	0.8064	0.0601	1.3680	593	10	592	9	580	59	100	No
LEGGA	C220705-1643	Z1643.2-020	1643.2_20	25 um	2.04E+00	62	0.02	285	17.4372	0.6520	0.0568	1.0297	378	5	360	4	479	43	95	No
LEGGA	C220705-1643	Z1643.2-021	1643.2_21	25 um	3.52E+00	172	0.04	194	11.0880	0.6158	0.0845	1.8050	726	15	557	7	1264	69	77	No
LEGGA	C220705-1643	Z1643.2-022	1643.2_22	25 um	5.47E-01	1530	-0.03	133	13.5072	1.4687	0.1017	3.4294	715	26	467	13	1572	107	65	No
LEGGA	C220705-1643	Z1643.2-023	1643.2_23	25 um	-1.94E-01	-74	0.01	143	12.2670	0.8938	0.0652	1.2368	562	10	508	9	772	55	90	No
LEGGA	C220705-1643	Z1643.2-025	1643.2_25	25 um	3.90E-01	-58	0.04	194	22.0965	1.0595	0.0598	1.5202	325	9	287	6	587	72	88	No
LEGGA	C220705-1643	Z1643.2-025	1643.2_26	25 um	-4.96E-02	72915	0.00	457	19.6468	1.0989	0.0640	1.3956	345	91	315	12	1191	190	92	Yes
LEGGA	C220705-1643	Z1643.2-003	1643.2_3	25 um	9.92E+00	-647	1.78	83	11.3393	1.4997	0.0621	2.0379	573	12	550	16	646	88	96	No
LEGGA	C220705-1643	Z1643.2-030	1643.2_30	25 um	1.36E+01	-41	0.01	103	10.6091	1.3101	0.0629	1.8134	609	10	585	15	656	77	96	No
LEGGA	C220705-1643	Z1643.2-004	1643.2_4	25 um	6.86E+00	88	-0.01	181	15.8216	0.8698	0.0816	1.9909	544	14	397	7	1194	80	73	No
LEGGA	C220705-1643	Z1643.2-005	1643.2_5	25 um	-5.41E-01	-6	-0.02	108	5.4000	0.5937	0.0773	1.2863	1117	17	1096	12	1126	55	98	No
LEGGA	C220705-1643	Z1643.2-005	1643.2_6	25 um	-2.85E-02	-68	0.13	78	5.0028	0.6933	0.0758	1.1271	1145	14	1176	14	1071	45	103	No
LEGGA	C220705-1643	Z1643.2-009	1643.2_9	25 um	1.52E+00	45262	-0.02	306	9.7868	0.6960	0.0653	1.0937	663	9	628	8	773	46	95	No
LEGGA	C220705-1643	Z1643-15	1643_1	25 um	1.26E+00	-616	1.30	96	24.2164	2.1092	0.0619	3.7252	306	523	261	1182	591	171	86	No
LEGGA	C220705-1643	Z1643-002	1643_2	25 um	1.32E+00	-880	0.69	355	28.0983	2.2908	0.0629	3.0636	274	454	227	1342	671	166	83	No
LEGGA	C220705-1643	Z1643-003	1643_3	25 um	3.07E+00	-559	0.62	158	13.0411	3.0069	0.0781	2.9200	620	984	492	2192	1096	159	79	No
LEGGA	C220705-1643	Z1643-004	1643_4	25 um	2.31E+00	-844	0.81	137	24.9946	2.5644	0.0856	2.6304	397	518	259	2582	1291	131	65	No
LEGGA	C220705-1643	Z1643-11	1643_5	25 um	2.06E+00	-228	1.25	537	28.9209	1.5167	0.0758	3.4346	313	440	220	2093	1047	140	70	No
LEGGA	C220705-1643	Z1643-04	1643_6	25 um	2.60E+00	-853	1.23	710	27.8035	2.2777	0.0667	4.5261	290	457	229	1578	789	158	79	No
LEGGA	C220705-1643	Z1643-007	1643_7	25 um	7.22E+00	-166	1.06	186	42.8252	2.5449	0.1075	3.2595	311	301	151	3537	1769	97	49	No
LEGGA	C220705-1643	Z1643-008	1643_8	25 um	2.45E+00	-531	1.35	275	27.9261	1.5942	0.0657	2.1097	288	458	229	1527	763	159	79	No
LEGGA	C220705-1643	Z1643-008	1643_9	25 um	2.16E+00	-1772	1.38	465	25.2057	1.2580	0.0691	2.3210	327	503	252	1743	871	154	77	No
NordSIMS	C220705-1643	Z1643-01	n6659_1643_@01	7 um	4.20E+00	446	1.03	600	27.2538	1.8127	0.0502	7.6069	230	32	232	8	202	370	101	Yes
NordSIMS	C220705-1643	Z1643-01	n6659_1643_@01b	15 um	1.05E+00	1777	0.48	271	24.9383	2.2505	0.0541	3.3775	266	19	253	11	376	152	95	Yes
NordSIMS	C220705-1643	Z1643-02	n6659_1643_@02a	7 um	7.08E+00	264	1.40	1222	31.2027	2.3639	0.0603	9.9080	240	44	203	9	615	430	85	No
NordSIMS	C220705-1643	Z1643-02	n6659_1643_@02b	7 um	1.14E+01	164	1.38	851	35.1663	1.6411	0.0529	11.4778	191	41	181	6	325	526	94	Yes
NordSIMS	C220705-1643	Z1643-03	n6659_1643_@03	7 um	5.10E-01	3668	1.10	325	13.6042	2.8046	0.0589	2.5920	475	29	457	25	564	113	96	No
NordSIMS	C220705-1643	Z1643-04	n6659_1643_@04	7 um	2.72E+00	687	0.64	571	24.9628	1.5543	0.0524	5.7152	258	27	253	8	304	261	98	Yes
NordSIMS	C220705-1643	Z1643-05	n6659_1643_@05a	7 um	1.94E+00	963	0.76	350	32.0823	1.8578	0.0531	6.6845	209	26	198	7	331	304	95	Yes
NordSIMS	C220705-1643	Z1643-05	n6659_1643_@05b	7 um	1.27E+00	1469	1.87	1010	24.3095	1.6922	0.0520	3.1086	263	16	260	9	287	142	99	Yes

Table S2. U-Pb on zircon radiogenic data of the samples analyzed in this study (continuation).

NordSIMS	C220705-1643	Z1643-06	n6659_1643_@06	7 um	2.04E+00	919	0.48	835	25.4192	1.7626	0.0550	4.5062	265	23	249	9	411	202	94	Yes
NordSIMS	C220705-1643	Z1643-07	n6659_1643_@07	7 um	6.50E-01	2895	0.59	386	22.1432	2.3128	0.0576	3.4217	311	22	285	13	515	150	91	Yes
NordSIMS	C220705-1643	Z1643-08	n6659_1643_@08	7 um	2.84E+00	658	0.86	422	22.5039	1.2985	0.0530	6.0321	285	31	280	7	328	274	98	Yes
NordSIMS	C220705-1643	Z1643-09	n6659_1643_@09a	15 um	8.60E-01	2163	0.56	843	21.1865	2.3109	0.0561	2.3006	316	18	297	13	456	102	94	Yes
NordSIMS	C220705-1643	Z1643-09	n6659_1643_@09b	15 um	1.05E+00	1790	0.37	483	28.9990	1.9254	0.0515	2.7548	222	13	219	8	262	127	98	Yes
NordSIMS	C220705-1643	Z1643-10	n6659_1643_@10a	15 um	9.30E-01	2022	0.50	633	13.3709	1.0975	0.0590	1.2525	482	13	465	10	566	55	96	Yes
NordSIMS	C220705-1643	Z1643-10	n6659_1643_@10b	15 um	1.60E-01	11493	0.43	773	11.2865	1.5601	0.0587	0.7352	549	15	547	16	556	32	100	Yes
NordSIMS	C220705-1643	Z1643-11	n6659_1643_@11	15 um	2.73E+00	686	0.63	696	25.9868	1.2934	0.0543	3.8118	257	18	243	6	384	171	95	Yes
NordSIMS	C220705-1643	Z1643-12	n6659_1643_@12	15 um	3.39E+00	552	0.60	505	33.1420	1.3109	0.0517	4.4626	198	17	192	5	270	205	97	Yes
NordSIMS	C220705-1643	Z1643-13	n6659_1643_@13a	15 um	5.00E-01	3704	0.33	399	13.5163	1.5211	0.0568	1.8478	464	18	460	14	482	82	99	Yes
NordSIMS	C220705-1643	Z1643-13	n6659_1643_@13b	15 um	1.80E-01	10540	0.24	959	12.6201	1.6042	0.0573	0.8649	493	14	492	15	502	38	100	Yes
NordSIMS	C220705-1643	Z1643-14	n6659_1643_@14	15 um	2.23E+00	841	0.45	429	36.8968	1.6308	0.0524	4.1355	182	15	172	6	304	189	95	Yes
NordSIMS	C220705-1643	Z1643-15	n6659_1643_@15	15 um	2.61E+00	716	0.38	170	33.2396	2.0361	0.0514	6.7328	196	25	191	8	261	310	97	Yes
NordSIMS	C220705-1643	Z1643-16	n6659_1643_@16a	15 um	2.80E-01	6602	1.01	493	17.5034	1.3452	0.0538	1.3495	359	12	358	9	362	61	100	Yes
NordSIMS	C220705-1643	Z1643-16	n6659_1643_@16b	15 um	1.80E-01	10500	0.04	729	16.8605	1.6176	0.0536	1.0314	369	12	371	12	356	47	101	Yes
NordSIMS	C220705-1643	Z1643-17	n6659_1643_@17a	15 um	2.10E-01	8983	0.10	475	10.6231	1.5205	0.0829	0.7816	742	18	580	17	1267	31	78	No
NordSIMS	C220705-1643	Z1643-17	n6659_1643_@17b	15 um	6.20E-01	2993	0.07	916	15.0763	2.6318	0.0646	2.2289	472	26	414	21	763	94	88	No
NordSIMS	C220705-1643	Z1643-18	n6659_1643_@18	15 um	2.80E-01	6722	0.46	663	19.7087	1.2867	0.0545	1.4232	328	11	319	8	391	64	97	Yes
NordSIMS	C220705-1643	Z1643-19	n6659_1643_@19a	15 um	4.27E+00	438	0.78	411	30.9390	1.5010	0.0560	6.6299	226	28	205	6	452	295	91	Yes
NordSIMS	C220705-1643	Z1643-19	n6659_1643_@19b	15 um	2.34E+00	801	0.39	167	29.1288	2.5757	0.0534	5.9078	229	27	218	11	346	268	95	No
NordSIMS	C220705-1643	Z1643-20	n6659_1643_@20	15 um	6.68E+00	280	0.48	441	39.9675	2.2859	0.0546	15.1745	175	50	159	7	396	705	91	Yes
NordSIMS	C220705-1643	Z1643-21	n6659_1643_@21a	15 um	8.00E-02	22949	0.37	237	11.7167	1.1286	0.0575	1.5405	525	16	528	11	512	68	101	Yes
NordSIMS	C220705-1643	Z1643-21	n6659_1643_@21b	15 um	4.50E-01	4135	0.50	637	12.5480	1.2821	0.0573	1.1080	496	13	494	12	504	49	100	Yes
NordSIMS	C220705-1643	Z1643-22	n6659_1643_@22	15 um	1.15E+00	1628	0.33	845	26.4545	1.7295	0.0554	1.9548	257	12	239	8	427	87	93	Yes
NordSIMS	C220705-1643	Z1643-23	n6659_1643_@23	15 um	1.79E+00	1045	0.47	322	27.0464	1.0394	0.0540	3.6280	247	17	234	5	369	164	95	Yes
NordSIMS	C220705-1643	Z1643-24	n6659_1643_@24a	15 um	1.76E+00	1064	0.74	85	14.4303	1.7029	0.0556	6.6991	432	49	432	14	435	299	100	Yes
NordSIMS	C220705-1643	Z1643-24	n6659_1643_@24b	15 um	1.75E+00	1072	0.68	121	13.7974	1.8771	0.0548	4.8548	443	38	451	16	403	218	102	Yes
NordSIMS	C220705-1643	Z1643-25	n6659_1643_@25a	15 um	4.49E+00	416	0.42	427	25.7218	1.8155	0.0486	5.5671	235	25	246	9	128	263	105	Yes
NordSIMS	C220705-1643	Z1643-25	n6659_1643_@25b	15 um	7.09E+00	264	0.66	715	36.6532	1.4730	0.0550	6.7738	191	24	174	5	414	304	91	Yes
NordSIMS	C220705-1643	Z1643-26	n6659_1643_@26	15 um	5.79E+00	323	0.60	186	28.4009	3.1134	0.0534	12.4581	234	54	223	14	344	569	95	No
NordSIMS	C220705-1643	Z1643-27	n6659_1643_@27	15 um	2.30E+00	814	0.59	264	29.1002	1.9149	0.0598	4.6147	253	23	218	8	596	200	86	No
NordSIMS	C220705-1643	Z1643-28	n6659_1643_@28	15 um	9.40E-01	1992	0.53	1260	25.2627	1.7626	0.0511	2.0325	250	12	250	9	245	94	100	Yes
NordSIMS	C220705-1643	Z1643-29	n6659_1643_@29	15 um	7.10E-01	2641	0.62	790	27.6312	1.3987	0.0511	2.0459	231	10	229	6	244	94	99	Yes
NordSIMS	C220705-1643	Z1643-30	n6659_1643_@30	15 um	7.10E-01	2620	0.50	132	20.8450	1.7347	0.0524	3.4813	302	20	302	10	303	159	100	Yes
LEGGA	C220805-1315	Z1315.2-001	1315.2_1	25 um	2.77E+08	0	0.00	561	28.2077	0.7467	0.0843	1.9823	351	11	225	3	1267	79	64	No
LEGGA	C220805-1315	Z1315.2-004	1315.2_4	25 um	4.26E+08	0	0.00	814	28.6717	0.6016	0.1411	1.3097	528	12	221	3	2225	47	42	No
LEGGA	C220805-1315	Z1315.2-005	1315.2_5	25 um	6.85E+08	0	0.00	330	13.1278	1.3434	0.2110	1.2453	1192	22	478	13	2913	38	40	No
LEGGA	C220805-1315	Z1315.2-006	1315.2_6	25 um	1.80E+09	0	-0.01	172	7.0388	0.7885	0.4842	1.1842	2383	26	855	13	4183	36	36	No
LEGGA	C220805-1315	Z1315.2-007	1315.2_7	25 um	9.75E+08	0	-0.04	110	8.8695	0.9080	0.2502	1.8449	1604	22	692	12	3154	58	43	No
LEGGA	C220805-1315	Z1315.2-008	1315.2_8	25 um	1.38E+09	0	0.01	254	11.4918	0.5435	0.3838	1.1290	1752	20	538	6	3840	35	31	No
LEGGA	C220805-1315	Z1315.2-009	1315.2_9	25 um	7.92E+08	0	0.00	321	20.9253	0.8843	0.2308	2.6223	927	32	302	5	2985	83	33	No
LEGGA	C220805-1315	Z1315.2-010	1315.2_10	25 um	1.71E+08	0	-0.05	231	23.0949	1.5775	0.1247	2.1438	563	13	277	8	1980	78	49	No
LEGGA	C220805-1315	Z1315.2-011	1315.2_11	25 um	1.53E+09	0	-0.01	248	8.3053	1.1788	0.4106	1.5257	2090	36	739	17	3934	46	35	No
LEGGA	C220805-1315	Z1315.2-013	1315.2_13	25 um	4.85E+08	0	-0.02	516	31.9118	0.6527	0.1796	1.6806	583	12	200	2	2624	58	34	No
LEGGA	C220805-1315	Z1315.2-014	1315.2_14	25 um	1.19E+09	0	0.33	48	13.4980	2.5634	0.3416	2.8397	1530	20	482	24	3625	93	31	No
LEGGA	C220805-1315	Z1315.2-015	1315.2_15	25 um	1.19E+09	0	0.07	50	12.9800	3.0589	0.3051	3.9191	1453	35	502	26	3409	122	35	No
LEGGA	C220805-1315	Z1315.2-016	1315.2_16	25 um	1.32E+09	0	0.01	244	26.4772	1.6974	0.2740	2.5862	903	41	242	8	3310	81	27	No
LEGGA	C220805-1315	Z1315.2-018	1315.2_18	25 um	1.05E+09	0	0.01	141	22.8863	1.4845	0.2608	1.8819	966	18	281	8	3228	62	29	No
LEGGA	C220805-1315	Z1315.2-019	1315.2_19	25 um	5.00E+08	0	-0.23	255	16.3257	0.6907	0.0959	2.5266	601	24	383	5	1483	97	64	No
LEGGA	C220805-1315	Z1315.2-020	1315.2_20	25 um	1.93E+09	0	0.04	245	6.7782	0.7907	0.5086	1.2470	2463	24	889	13	4252	38	36	No
LEGGA	C220805-1315	Z1315.2-021	1315.2_21	25 um	3.35E+07	0	-0.02	297	11.5699	0.3519	0.0618	1.1057	560	9	534	4	649	48	95	No
LEGGA	C220805-1315	Z1315.2-023	1315.2_23	25 um	1.51E+09	0	0.44	65	19.4884	2.4467	0.3135	2.7378	1183	19	337	15	3474	86	28	No
LEGGA	C220805-1315	Z1315.2-025	1315.2_25	25 um	-1.07E+08	0	-0.10	90	14.3992	1.4850	0.0743	1.7235	551	11	440	12	1011	72	80	No
LEGGA	C220805-1315	Z1315.2-026	1315.2_26	25 um	2.29E+09	0	0.07	169	3.8577	1.3283	0.7195	0.9425	3345	27	1509	35	4744	25	45	No
LEGGA	C220805-1315	Z1315.2-028	1315.2_28	25 um	7.75E+05	0	0.08	291	11.0782	0.3751	0.0594	1.1086	562	9	557	4	557	50	99	No
LEGGA	C220805-1315	Z1315.2-029	1315.2_29	25 um	4.29E+08	0	0.17	85	14.2105	2.1239	0.0565	2.3117	453	12	453	18	419	113	100	No
LEGGA	C220805-1315	Z1315.2-030	1315.2_30	25 um	1.20E+09	0	0.82	103	7.9667	1.1647	0.2691	1.9311	1755	33	773	17	3263	59	44	No
LEGGA	C220805-1315	Z1315.2-031	1315.2_31	25 um	3.34E+08	0	0.03	166	12.2583	0.8250	0.0736	1.3654	614	11	506	8	1012	58	82	No
LEGGA	C220805-1315	Z1315.2-032	1315.2_32	25 um	1.72E+07	0	-0.01	289	11.5125	0.3541	0.0595	1.2371	547	10	537	4	559	53	98	No

Table S2. U-Pb on zircon radiogenic data of the samples analyzed in this study (continuation).

LEGGA	C220805-1315	Z1315.2-033	1315.2_33	25 um	2.48E+08	0	0.06	115	10.6897	0.9124	0.0589	1.5060	574	11	581	10	522	66	101	No
LEGGA	C220805-1315	Z1315.2-034	1315.2_34	25 um	7.00E+07	0	0.02	855	11.2031	0.1987	0.0646	0.8012	596	7	551	2	753	34	92	No
LEGGA	C220805-1315	Z1315.2-035	1315.2_35	25 um	7.94E+08	0	0.01	357	15.2537	0.5668	0.2026	1.5594	1058	21	410	4	2827	52	39	No
LEGGA	C220805-1315	Z1315.2-037	1315.2_37	25 um	-2.85E+07	0	0.00	713	11.3120	0.2015	0.0584	1.0508	547	9	546	2	528	47	100	No
LEGGA	C220805-1315	Z1315.2-038	1315.2_38	25 um	9.09E+08	0	0.02	340	11.0081	0.5620	0.2261	1.2889	1365	17	561	6	3013	41	41	No
LEGGA	C220805-1315	Z1315.2-040	1315.2_40	25 um	9.07E+07	0	0.01	268	13.0747	0.5428	0.0596	1.4326	496	10	476	5	552	65	96	No
LEGGA	C220805-1315	Z1315.2-041	1315.2_41	25 um	2.61E+08	0	0.00	791	22.8638	0.4577	0.0898	1.0342	442	7	276	2	1410	39	63	No
LEGGA	C220805-1315	Z1315.2-042	1315.2_42	25 um	1.09E+09	0	0.01	182	11.4515	1.2069	0.1991	1.8984	1240	26	542	13	2797	61	44	No
LEGGA	C220805-1315	Z1315.2-043	1315.2_43	25 um	2.14E+08	0	-0.01	146	11.5192	0.7523	0.0625	1.1538	571	7	538	8	684	50	94	No
LEGGA	C220805-1315	Z1315.2-044	1315.2_44	25 um	-2.47E+08	0	-0.01	152	11.5790	0.6784	0.0623	1.3466	565	10	535	7	658	60	95	No
LEGGA	C220805-1315	Z1315.2-045	1315.2_45	25 um	3.20E+07	0	0.01	654	11.8053	0.2714	0.0698	1.2282	607	11	524	3	904	51	86	No
LEGGA	C220805-1315	Z1315.2-047	1315.2_47	25 um	-3.56E+08	0	-0.05	111	11.6477	1.1238	0.0641	1.7521	573	13	533	12	700	78	93	No
LEGGA	C220805-1315	Z1315.2-048	1315.2_48	25 um	7.87E+08	0	-0.04	148	9.5727	0.7291	0.2412	1.4211	1520	19	641	9	3119	45	42	No
LEGGA	C220805-1315	Z1315.2-049	1315.2_49	25 um	-5.94E+07	0	-0.04	164	11.5880	0.6060	0.0606	1.2515	551	9	535	6	595	55	97	No
LEGGA	C220805-1315	Z1315.2-050	1315.2_50	25 um	-1.66E+08	0	-0.07	237	10.4624	0.4761	0.0617	1.1176	606	10	589	5	649	48	97	No
LEGGA	C220805-1315	Z1315.2-051	1315.2_51	25 um	-7.21E+06	0	0.03	390	8.7887	0.5268	0.0640	1.0635	708	12	696	7	720	46	98	No
LEGGA	C220805-1315	Z1315.2-052	1315.2_52	25 um	-4.70E+08	0	1.80	93	12.0735	1.1774	0.0694	1.7216	593	13	514	12	872	76	87	No
LEGGA	C220805-1315	Z1315.2-053	1315.2_53	25 um	1.52E+08	0	0.01	215	10.2033	0.6934	0.0866	1.4648	786	13	604	8	1327	58	77	No
LEGGA	C220805-1315	Z1315.2-054	1315.2_54	25 um	2.86E+07	0	-0.05	83	12.2670	1.4489	0.1064	2.2250	803	23	513	15	1687	81	64	No
LEGGA	C220805-1315	Z1315.2-055	1315.2_55	25 um	1.09E+08	0	-0.02	304	11.5845	0.5468	0.0677	1.4661	602	13	534	6	839	63	89	No
LEGGA	C220805-1315	Z1315.2-056	1315.2_56	25 um	4.78E+07	0	-0.11	107	11.5997	1.1289	0.0624	1.7504	566	11	534	11	642	79	94	No
LEGGA	C220805-1315	Z1315.2-057	1315.2_57	25 um	1.51E+08	0	-0.04	521	12.1871	1.6739	0.0431	29.2950	532	103	513	13	1221	311	96	Yes
LEGGA	C220805-1315	Z1315.2-058	1315.2_58	25 um	1.01E+09	0	-0.01	455	10.1403	0.8464	0.2526	1.7021	1514	33	609	9	3181	55	40	No
LEGGA	C220805-1315	Z1315.2-059	1315.2_59	25 um	1.56E+08	0	0.03	134	9.8876	0.9088	0.0729	1.6133	713	13	624	11	976	64	87	No
LEGGA	C220805-1315	Z1315.2-060	1315.2_60	25 um	2.13E+08	0	-0.23	207	6.5665	1.8942	0.1150	1.5565	1261	17	946	32	1856	57	75	No
LEGGA	C220805-1315	Z1315-001	1315_1	25 um	1.85E+00	6369	1.17	334	17.6097	2.1077	0.0778	6.7266	478	50	358	16	1156	295	75	No
LEGGA	C220805-1315	Z1315-002	1315_2	25 um	1.92E+00	3995	1.78	179	11.6150	1.9884	0.0592	2.9631	546	21	539	20	544	137	99	No
LEGGA	C220805-1315	Z1315-003	1315_3	25 um	2.97E-01	1496	1.90	97	12.8707	1.3629	0.0640	2.5788	530	18	484	13	729	119	91	No
LEGGA	C220805-1315	Z1315-004	1315_4	25 um	5.70E+00	2281	2.61	510	12.7454	1.9798	0.1144	2.7053	821	32	493	18	1834	98	60	No
LEGGA	C220805-1315	Z1315-007	1315_7	25 um	1.87E-01	1119	2.03	180	10.8754	1.6906	0.0610	2.0982	584	16	571	18	612	90	98	No
LEGGA	C220805-1315	Z1315-008	1315_8	25 um	1.62E+00	1681	1.38	313	11.7441	1.3750	0.0619	2.4256	555	19	528	14	644	99	95	No
LEGGA	C220805-1315	Z1315-009	1315_9	25 um	9.75E-01	1117	0.96	298	11.1100	1.0704	0.0596	1.8857	563	14	556	11	572	81	99	No
NordSIMS	C220805-1315	Z1315-01	n6658_1315_@01a	8 um	2.00E-02	116218	0.39	151	11.7102	1.6438	0.0596	2.4801	539	25	528	17	587	108	98	No
NordSIMS	C220805-1315	Z1315-01	n6658_1315_@01b	8 um	9.00E-02	21448	1.56	454	11.2241	1.5474	0.0596	1.4800	558	18	550	16	588	64	99	Yes
LEGGA	C220805-1315	Z1315-010	1315_10	25 um	5.52E-01	479	0.81	233	17.6097	1.6455	0.0596	3.0882	532	21	520	18	555	130	98	No
LEGGA	C220805-1315	Z1315-011	1315_11	25 um	7.59E+00	250	2.17	997	27.4506	3.2169	0.0945	4.5125	396	22	233	14	1488	161	59	No
LEGGA	C220805-1315	Z1315-013	1315_13	25 um	1.10E+00	382	1.46	206	11.1832	1.8694	0.0655	2.5089	603	18	558	19	751	103	93	No
LEGGA	C220805-1315	Z1315-016	1315_16	25 um	2.58E-01	797	1.56	319	11.6333	1.9068	0.0615	2.7950	556	17	534	20	629	122	96	No
NordSIMS	C220805-1315	Z1315-02	n6658_1315_@02a	8 um	1.32E+00	1417	0.72	271	12.1131	1.6607	0.0568	3.8174	506	33	511	16	485	169	101	Yes
NordSIMS	C220805-1315	Z1315-02	n6658_1315_@02b	8 um	5.20E-01	3589	1.30	771	12.1284	1.5179	0.0589	2.4000	521	23	511	15	565	105	98	Yes
NordSIMS	C220805-1315	Z1315-03	n6658_1315_@03	8 um	6.00E-01	3119	1.76	97	11.8631	1.8852	0.0592	4.3844	531	40	522	19	573	191	98	Yes
NordSIMS	C220805-1315	Z1315-04	n6658_1315_@04a	8 um	2.16E+01	87	0.86	781	22.9318	1.7101	0.0619	13.4502	321	76	275	9	669	582	86	Yes
NordSIMS	C220805-1315	Z1315-04	n6658_1315_@04b	8 um	2.41E+01	77	0.79	462	20.6517	3.7009	0.0712	33.1271	395	231	305	22	965	1443	77	Yes
NordSIMS	C220805-1315	Z1315-05	n6658_1315_@05a	8 um	9.01E+00	207	0.95	429	13.5872	2.0382	0.0604	10.4454	485	84	458	18	617	454	94	Yes
NordSIMS	C220805-1315	Z1315-05	n6658_1315_@05b	8 um	7.29E+00	257	0.54	458	17.0221	1.6011	0.0536	7.9047	366	50	368	11	356	358	100	Yes
NordSIMS	C220805-1315	Z1315-06	n6658_1315_@06	8 um	3.00E-02	69007	0.94	115	11.3031	1.8119	0.0602	2.8020	559	29	546	19	612	121	98	No
NordSIMS	C220805-1315	Z1315-08	n6658_1315_@08	8 um	4.09E+01	46	1.48	380	16.1458	2.0006	0.0474	31.1802	345	192	387	15	69	1589	112	Yes
LEGGA	C220805-1315	Z1315-09	1315_6	25 um	5.62E-01	2012	1.13	323	12.7378	0.7656	0.0606	1.8534	512	14	486	8	636	96	95	No
NordSIMS	C220805-1315	Z1315-09	n6658_1315_@09a	8 um	1.47E+00	1268	0.65	197	13.4860	1.8561	0.0533	5.5275	442	42	461	17	341	251	104	Yes
NordSIMS	C220805-1315	Z1315-10	n6658_1315_@10	8 um	4.70E-01	3977	0.54	568	19.3493	3.7643	0.0543	2.7349	332	27	325	24	385	123	98	Yes
NordSIMS	C220805-1315	Z1315-11	n6658_1315_@11b	15 um	2.05E+00	911	1.00	431	17.1804	3.3074	0.0542	2.9857	367	28	365	23	380	134	99	Yes
NordSIMS	C220805-1315	Z1315-11	n6658_1315_@11a	8 um	2.40E-01	7711	0.81	645	16.8176	1.4914	0.0545	1.8350	375	15	372	11	392	82	99	Yes
NordSIMS	C220805-1315	Z1315-12	n6658_1315_@12	8 um	1.00E-02	269357	0.40	327	11.3603	1.4498	0.0593	1.7057	551	19	544	15	579	74	99	No
NordSIMS	C220805-1315	Z1315-13	n6658_1315_@13	8 um	3.70E-01	5055	1.04	239	11.2047	1.5806	0.0575	3.0539	544	29	551	17	512	134	101	Yes
NordSIMS	C220805-1315	Z1315-14	n6658_1315_@14	8 um	0.00E+00	410002	0.52	357	8.3853	1.4956	0.0628	1.3687	721	21	726	21	703	58	101	No
NordSIMS	C220805-1315	Z1315-15	n6658_1315_@15a	15 um	2.50E-01	7425	0.59	73	11.6158	2.1852	0.0575	2.5595	528	28	532	22	511	113	101	Yes
NordSIMS	C220805-1315	Z1315-15	n6658_1315_@15b	15 um	2.68E+00	698	0.64	123	11.3273	1.8454	0.0546	4.5235	517	40	545	19	395	203	105	Yes
NordSIMS	C220805-1315	Z1315-16	n6658_1315_@16a	15 um	6.00E-01	3114	0.74	195	11.6121	1.4694	0.0589	1.9086	539	20	533	15	565	83	99	Yes
NordSIMS	C220805-1315	Z1315-16	n6658_1315_@16b	15 um	3.00E-02	58917	0.55	132	11.2708	1.2164	0.0589	1.5334	551	17	548	13	565	67	99	No

Table S2. U-Pb on zircon radiogenic data of the samples analyzed in this study (continuation).

NordSIMS	C220805-1315	Z1315-17	n6658_1315_@17a	15 um	3.55E+01	53	1.39	444	14.7892	1.7894	0.0622	11.2654	464	87	422	15	682	485	91	Yes
NordSIMS	C220805-1315	Z1315-18	n6658_1315_@18	15 um	1.44E+01	130	2.15	189	14.5007	1.4528	0.0616	8.6556	468	67	430	12	660	373	92	Yes
NordSIMS	C220805-1315	Z1315-19	n6658_1315_@19	15 um	1.49E+01	126	1.69	314	21.7980	2.3606	0.0550	14.4150	303	78	289	13	413	653	95	Yes
NordSIMS	C220805-1315	Z1315-20	n6658_1315_@20	15 um	6.50E-01	2896	0.45	70	11.9568	1.6985	0.0577	3.7878	518	34	518	17	519	166	100	Yes
NordSIMS	C220805-1315	Z1315-21	n6658_1315_@21	15 um	1.30E-01	14883	0.30	72	11.3680	1.8387	0.0579	2.1523	540	24	543	19	526	94	101	No
NordSIMS	C220805-1315	Z1315-22	n6658_1315_@22a	15 um	3.90E-01	4761	0.73	69	11.5244	2.4936	0.0574	2.9336	531	32	536	26	506	129	101	Yes
NordSIMS	C220805-1315	Z1315-22	n6658_1315_@22b	15 um	3.10E-01	6016	0.66	97	11.5702	1.6046	0.0586	2.3463	538	24	534	16	551	102	99	Yes
NordSIMS	C220805-1315	Z1315-23	n6658_1315_@23	15 um	0.00E+00	844598	0.10	300	1.7617	1.2404	0.2313	0.3163	2995	25	2898	58	3061	10	97	No
NordSIMS	C220805-1315	Z1315-24	n6658_1315_@24	15 um	6.40E-01	2907	0.76	667	12.6070	1.5868	0.0591	1.6421	507	18	492	15	573	71	97	Yes
NordSIMS	C220805-1315	Z1315-25	n6658_1315_@25	15 um	2.13E+01	88	0.73	257	13.2691	2.0073	0.0643	13.8634	520	117	468	18	752	592	90	Yes
NordSIMS	C220805-1315	Z1315-26	n6658_1315_@26	15 um	1.70E-01	11084	1.70	566	11.4448	1.3951	0.0574	0.8904	534	14	540	14	508	39	101	Yes
NordSIMS	C220805-1315	Z1315-27	n6658_1315_@27	15 um	4.50E-01	4171	0.66	299	11.6300	1.4028	0.0578	1.4798	530	17	532	14	523	65	100	Yes
NordSIMS	C220805-1315	Z1315-28	n6658_1315_@28a	15 um	3.00E-01	6246	1.58	227	10.3195	1.5500	0.0604	1.3957	600	19	596	18	616	60	99	Yes
NordSIMS	C220805-1315	Z1315-28	n6658_1315_@28b	15 um	7.00E-02	26468	1.08	405	9.8298	1.7634	0.0614	0.9355	631	19	625	21	654	40	99	Yes
NordSIMS	C220805-1315	Z1315-29	n6658_1315_@29	15 um	1.56E+01	120	0.67	203	13.3478	1.6079	0.0592	11.9626	485	95	466	14	576	525	96	Yes
NordSIMS	C220805-1315	Z1315-30	n6658_1315_@30	15 um	8.00E-02	24098	0.20	293	11.3951	1.2630	0.0569	1.1434	532	14	542	13	486	50	102	Yes
NordSIMS	C220805-1315	Z1315-31	n6658_1315_@31	15 um	2.00E-02	83887	0.24	283	4.5283	1.5908	0.0832	0.5860	1282	25	1286	37	1274	23	100	No
NordSIMS	C220805-1315	Z1315-32	n6658_1315_@32	15 um	1.70E-01	10966	1.58	131	11.6874	1.8535	0.0570	1.8457	522	21	529	19	493	81	101	Yes
NordSIMS	C220805-1315	Z1315-33	n6658_1315_@33	15 um	3.20E-01	5863	0.52	109	11.4775	1.5182	0.0570	2.2173	530	22	539	16	492	98	102	Yes
NordSIMS	C220805-1315	Z1315-35	n6658_1315_@35	15 um	1.00E-01	18527	0.38	90	17.5271	2.2733	0.0521	2.5088	349	20	358	16	290	115	103	No
NordSIMS	C220805-1315	Z1315-36	n6658_1315_@36	15 um	6.00E-02	29570	0.32	375	11.3933	1.4572	0.0572	1.1694	534	16	542	15	498	52	102	Yes
NordSIMS	C220805-1315	Z1315-37	n6658_1315_@37b	15 um	4.00E-02	47595	0.52	257	10.9293	1.6391	0.0586	1.2807	562	18	564	18	553	56	100	No
NordSIMS	C220805-1315	Z1315-38	n6658_1315_@38	15 um	7.00E-02	27600	0.66	166	11.1033	1.5331	0.0601	1.3760	566	18	556	16	607	60	98	No
NordSIMS	C220805-1315	Z1315-39	n6658_1315_@39	15 um	5.00E-02	37134	0.45	422	11.2700	1.5156	0.0579	0.9157	544	15	548	16	526	40	101	Yes
NordSIMS	C220805-1315	Z1315-40	n6658_1315_@40a	15 um	9.78E+00	191	0.95	977	16.4563	1.7456	0.0589	5.6242	407	40	380	13	563	246	93	Yes
NordSIMS	C220805-1315	Z1315-41	n6658_1315_@41	15 um	1.60E-01	11745	1.06	153	11.2168	2.1409	0.0577	1.6125	544	23	551	23	518	71	101	Yes
NordSIMS	C220805-1315	Z1315-42	n6658_1315_@42a	15 um	5.00E-02	41476	0.20	985	11.5983	1.1579	0.0579	0.6099	532	11	533	12	527	27	100	Yes
NordSIMS	C220805-1315	Z1315-42	n6658_1315_@42b	15 um	6.00E-02	29748	0.30	1324	10.8290	1.7014	0.0575	0.5278	558	15	569	19	512	23	102	Yes
NordSIMS	C220805-1315	Z1315-43	n6658_1315_@43	15 um	9.00E-02	19799	0.60	477	11.1494	1.2893	0.0589	0.8820	556	13	554	14	564	38	100	Yes
NordSIMS	C220805-1315	Z1315-44	n6658_1315_@44	15 um	1.36E+00	1378	0.95	96	12.3816	1.7816	0.0564	3.7859	495	33	501	17	466	168	101	Yes
NordSIMS	C220805-1315	Z1315-47	n6658_1315_@47	15 um	4.00E-02	50833	0.32	158	11.5665	1.4545	0.0580	1.4571	534	17	535	15	529	64	100	No
NordSIMS	C220805-1315	Z1315-48	n6658_1315_@48	15 um	4.00E-02	47699	0.45	679	10.2206	1.1335	0.0604	0.6709	605	12	602	13	616	29	99	Yes
LEGGA	C220805-1315	Z1315-49	1315_12	25 um	2.58E+00	381	1.93	178	12.8758	1.9909	0.0496	40.9419	515	179	488	23	1536	778	95	Yes
NordSIMS	C220805-1315	Z1315-49	n6658_1315_@49a	15 um	1.90E-01	9626	0.46	135	11.5316	1.1074	0.0572	1.8718	529	18	536	11	501	82	101	Yes
NordSIMS	C220805-1315	Z1315-50	n6658_1315_@50	15 um	0.00E+00	405694	0.49	492	11.5661	1.3601	0.0582	0.8213	535	13	535	14	538	36	100	No
NordSIMS	C220805-1315	Z1315-51	n6658_1315_@51	15 um	1.10E-01	16623	0.79	604	11.3737	1.3471	0.0576	0.8343	538	13	543	14	516	37	101	Yes
LEGGA	C220805-1315	Z1315-53	1315.2_22	25 um	3.88E+08	0	-15.14	112	19.4837	1.4764	0.0715	2.1929	415	12	327	10	943	99	79	No
NordSIMS	C220805-1315	Z1315-53	n6658_1315_@53	15 um	7.93E+00	236	0.99	169	17.9232	2.2174	0.0591	10.3179	381	68	350	15	572	452	92	Yes
NordSIMS	C220805-1315	Z1315-54	n6658_1315_@54a	15 um	2.10E-01	8845	0.45	144	11.7892	1.5126	0.0570	1.9494	519	20	525	15	492	86	101	Yes
NordSIMS	C220805-1315	Z1315-54	n6658_1315_@54b	15 um	2.10E-01	8980	0.80	296	11.3519	1.8840	0.0587	1.2956	547	19	544	20	557	57	100	Yes
NordSIMS	C220805-1315	Z1315-55	n6658_1315_@55	15 um	3.00E-01	6324	0.39	379	21.3786	1.8443	0.0531	1.6684	299	13	295	11	334	76	98	Yes
NordSIMS	C220805-1315	Z1315-56	n6658_1315_@56a	15 um	1.14E+01	164	0.99	389	13.5735	1.7177	0.0590	14.1774	477	112	458	15	568	625	96	Yes
NordSIMS	C220805-1315	Z1315-56	n6658_1315_@56b	15 um	4.95E+00	378	0.76	720	12.0304	1.5181	0.0579	5.8874	517	50	515	15	524	259	100	Yes
NordSIMS	C220805-1315	Z1315-57	n6658_1315_@57	15 um	5.22E+00	358	1.53	147	29.5574	1.2951	0.0530	10.1170	224	42	214	5	330	462	96	Yes
NordSIMS	C220805-1315	Z1315-59	n6658_1315_@59	15 um	6.98E+01	27	0.90	503	21.2346	2.2158	0.0574	30.9574	322	179	297	13	506	1448	92	Yes
NordSIMS	C220805-1315	Z1315-60	n6658_1315_@60	15 um	5.22E+01	36	1.43	416	14.8087	2.4475	0.0496	22.9254	385	153	421	20	174	1108	109	Yes
NordSIMS	C220805-1315	Z1315-61	n6658_1315_@61	15 um	2.30E-01	8181	0.97	91	11.6734	2.1690	0.0583	2.2055	532	26	530	22	542	96	100	Yes
NordSIMS	C220805-1315	Z1315-62	n6658_1315_@62	15 um	4.00E-02	45946	0.75	891	17.4869	1.4521	0.0535	0.8107	357	10	358	10	351	37	100	Yes
NordSIMS	C220805-1315	Z1315-63	n6658_1315_@63b	15 um	7.31E+00	256	1.05	210	13.7827	1.5257	0.0555	6.8180	448	51	452	13	431	305	101	Yes
NordSIMS	C220805-1315	Z1315-64	n6658_1315_@64	15 um	2.31E+00	808	0.89	410	12.4680	1.1975	0.0592	2.7583	511	24	497	11	575	120	97	Yes
NordSIMS	C220805-1315	Z1315-65	n6658_1315_@65	15 um	2.70E-01	6929	0.55	78	11.6114	1.8674	0.0638	2.1659	573	25	533	19	735	92	93	No
NordSIMS	C220805-1315	Z1315-66	n6658_1315_@66a	15 um	1.80E+01	104	0.88	283	12.6348	1.7809	0.0593	9.7471	506	81	491	17	577	426	97	Yes
LEGGA	C220805-1315	Z1315-17	1315_5	25 um	6.69E+00	917	1.05	891	14.9964	1.2542	0.1175	2.2638	742	17	419	10	1883	84	56	No
NordSIMS	C220805-1315	Z1315-17	n6658_1315_@17b	15 um	8.17E+00	229	0.37	3170	26.0958	2.2331	0.0625	2.2718	290	16	242	11	691	97	84	Yes
NordSIMS	C220805-1315	Z1315-34	n6658_1315_@34	15 um	7.59E+01	25	2.44	117	26.3465	8.0691	no data	no data	no data		240	38	no data			Yes
NordSIMS	C220805-1315	Z1315-37	n6658_1315_@37a	15 um	{0.50}	3756	0.91	41	13.3786	1.9126	0.0653	2.7111	523	27	465	17	785	114	89	Yes
NordSIMS	C220805-1315	Z1315-40	n6658_1315_@40b	15 um	1.46E+01	128	0.48	139	14.0001	1.4374	0.0646	11.2476	500	92	445	12	763	478	89	Yes
NordSIMS	C220805-1315	Z1315-45	n6658_1315_@45	15 um	1.10E+01	170	0.85	135	10.6462	1.6205	0.0687	8.0662	646	80	579	18	890	334	90	Yes
LEGGA	C220805-1315	Z1315-46	1315_14	25 um	8.61E+00	226	0.86	114	17.1273	3.0358	0.1028	4.6362	611	33	370	22	1632	168	61	No

Table S2. U-Pb on zircon radiogenic data of the samples analyzed in this study (continuation).

NordSIMS	C220805-1315	Z1315-46	n6658_1315_@46	15 um	4.96E+00	377	0.44	126	13.3435	1.5515	0.0673	10.2077	536	88	466	14	848	427	87	Yes
NordSIMS	C220805-1315	Z1315-52	n6658_1315_@52	15 um	3.12E+01	60	1.40	207	28.4345	2.7666	no data	no data	no data		223	12	no data			Yes
NordSIMS	C220805-1315	Z1315-58	n6658_1315_@58	15 um	1.99E+00	941	0.86	487	21.4286	3.6441	0.0538	5.5105	302	35	294	21	362	249	97	Yes
NordSIMS	C220805-1315	Z1315-63	n6658_1315_@63a	15 um	2.84E+01	66	0.83	187	14.0364	6.5638	0.0657	44.4066	506	393	444	56	796	2117	88	Yes
LEGGA	C220805-1315	Z1315-66	1315_15	25 um	1.24E+01	359	2.11	286	12.1098	1.2116	0.1932	2.0027	1171	21	512	12	2759	64	44	No

Fig. S3. Cathodoluminescence (CL) images showing the locations of the analysis spots, analysis number, and the respective $^{206}Pb/^{238}U$ apparent ages. The spots in blue were obtained by LA-ICP-MS and in yellow by SIMS.

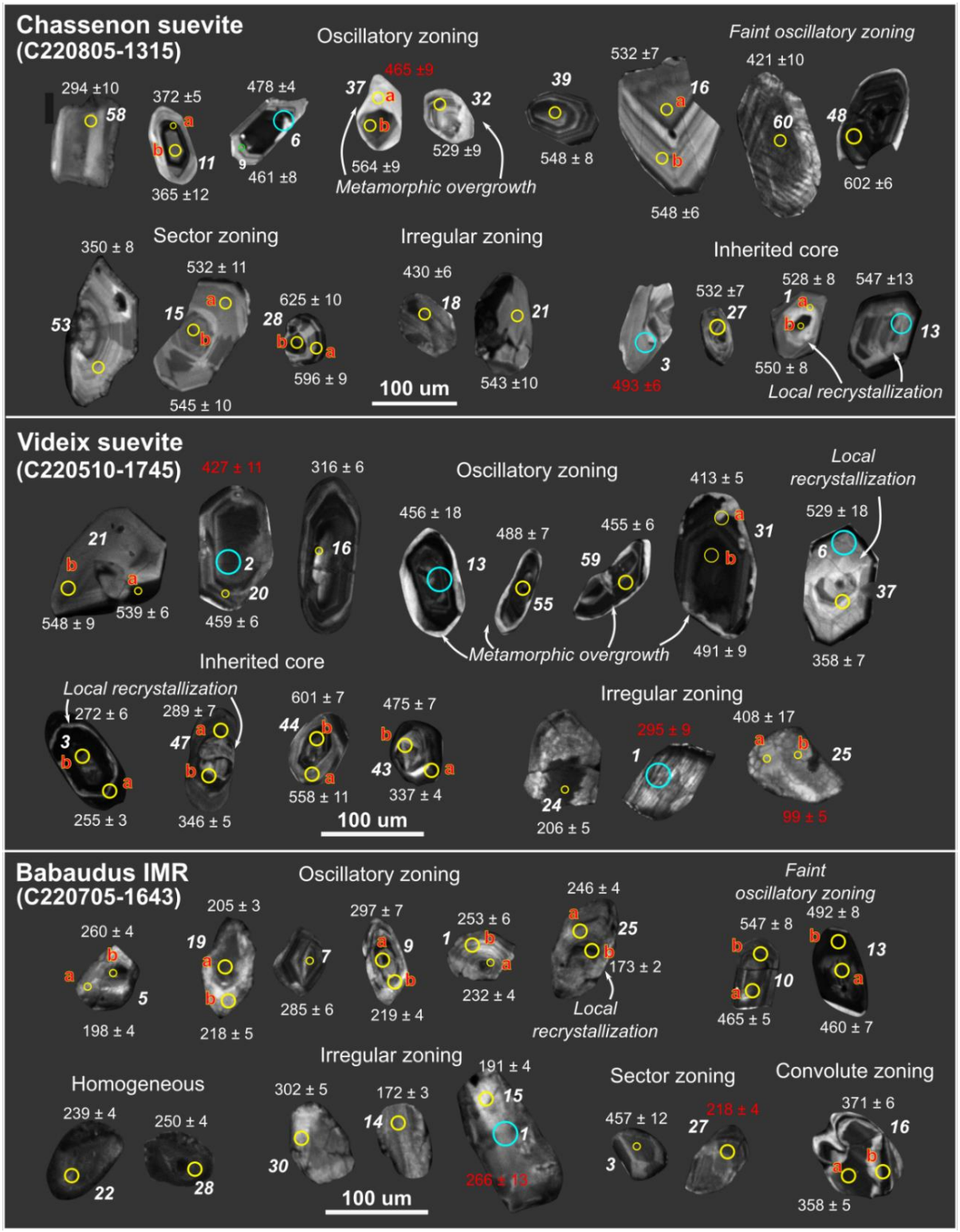


Fig. S4. Selected cathodoluminescence (CL), backscattered electron (BSE), and secondary electron (SE) images that show the shock metamorphic textures of the crystals from (a) the Babaudus IMR, (b-d) the Videix suevite, and (e) the Chassenon suevite. (a and b) Granular grains, (a) zoom into a section showing a porous texture. (c and e) Multiple sets of reidite lamella crosscutting the primary zonation of the grains.

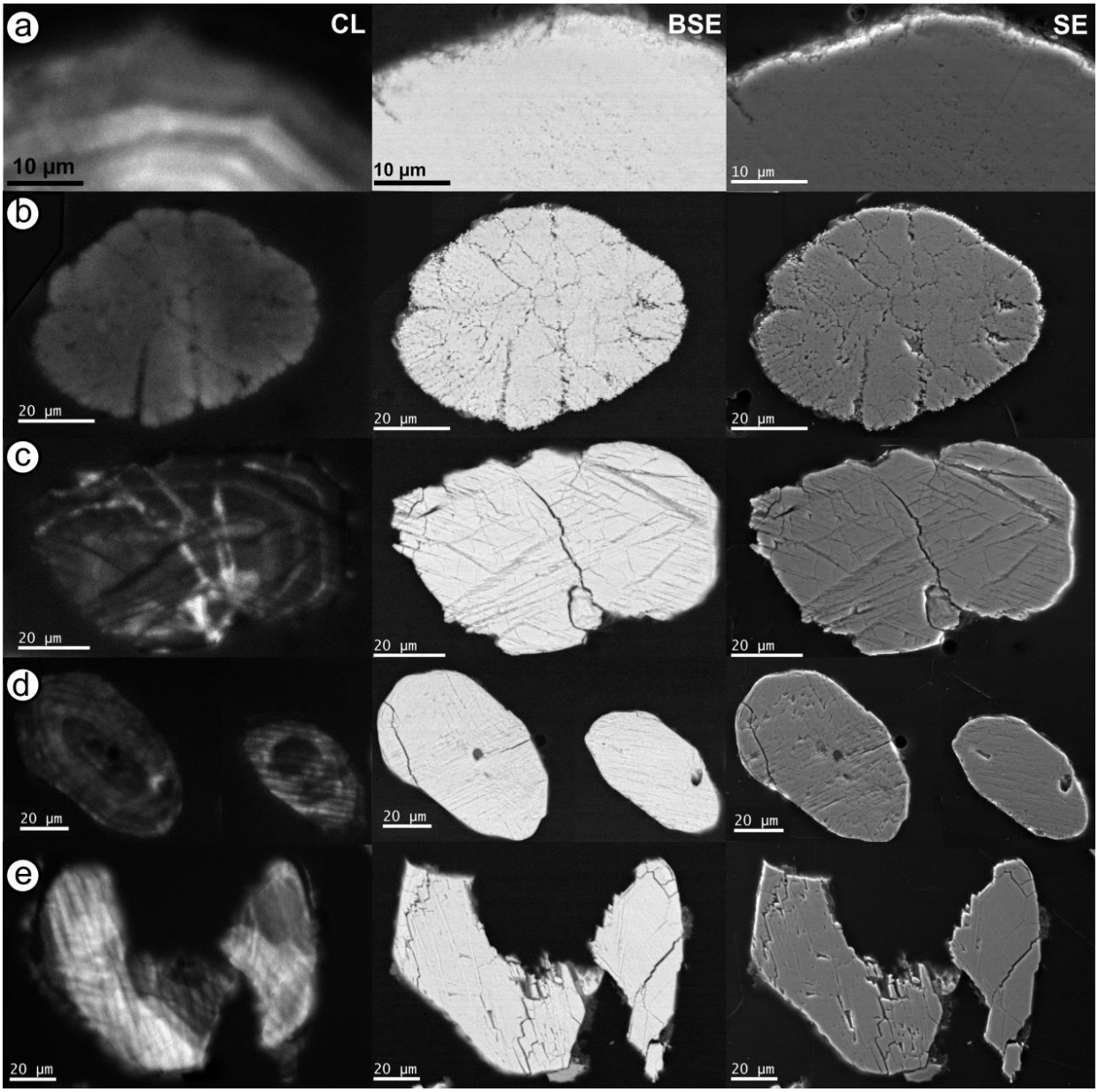


Fig. S5. Imaging and structural characterization of selected zircon of the Videix suevite with the location of the spot where SIMS analysis was conducted and the corresponding age and compositions obtained. The grain 1745-26 has an exposed surface of 109 x 73 µm. In the CL image the grain has an oscillatory zoning texture, which is cut by multiple sets of reidite lamellae that have dark tones. EBSD imaging was done on a portion of the grain and confirmed that the lamellae correspond to reidite. Furthermore, high angle grain boundaries (>70°) are located in the reidite domains. The pole figures are consistent with the crystallographic relationship for reidite lamellae, with a broad coincidence between one of the {112} $_{reidite}$ *with the {112}* $_{zircon}$ *and the other two with the {100}* $_{zircon}$*. Furthermore, one {110}* $_{zircon}$ *aligns with {110}* $_{reidite}$ *and the other is subparallel to {001}* $_{reidite}$*.*

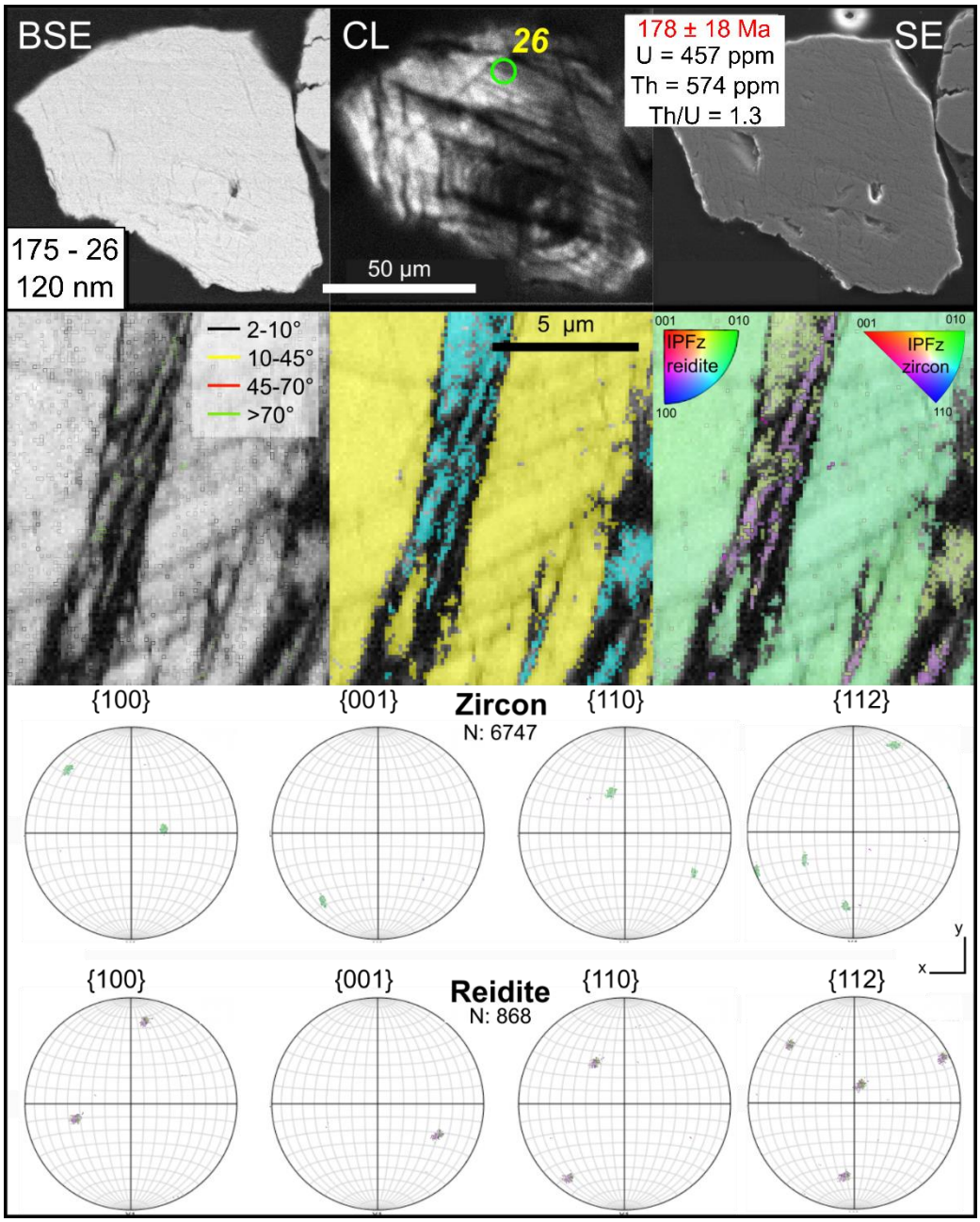
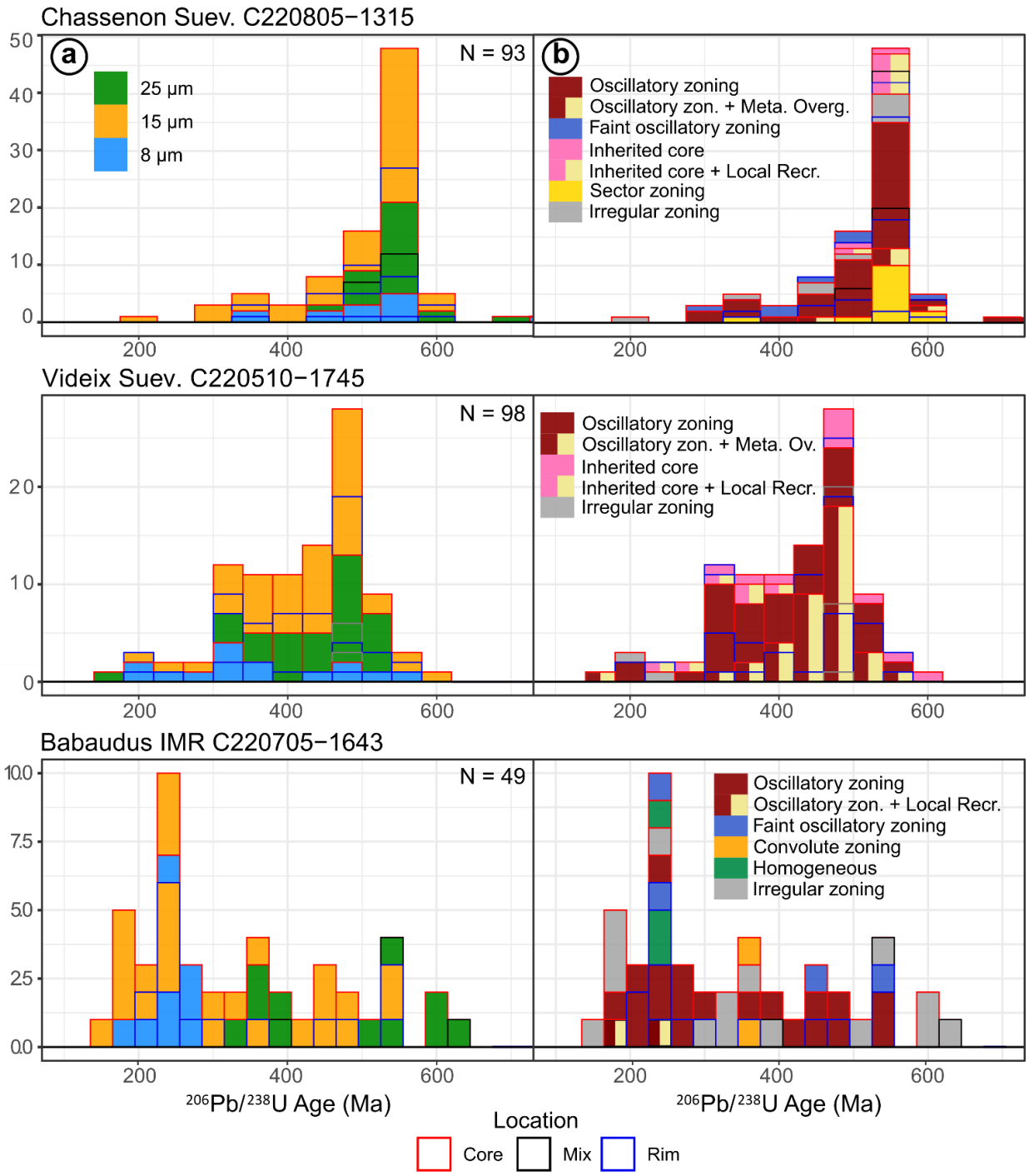
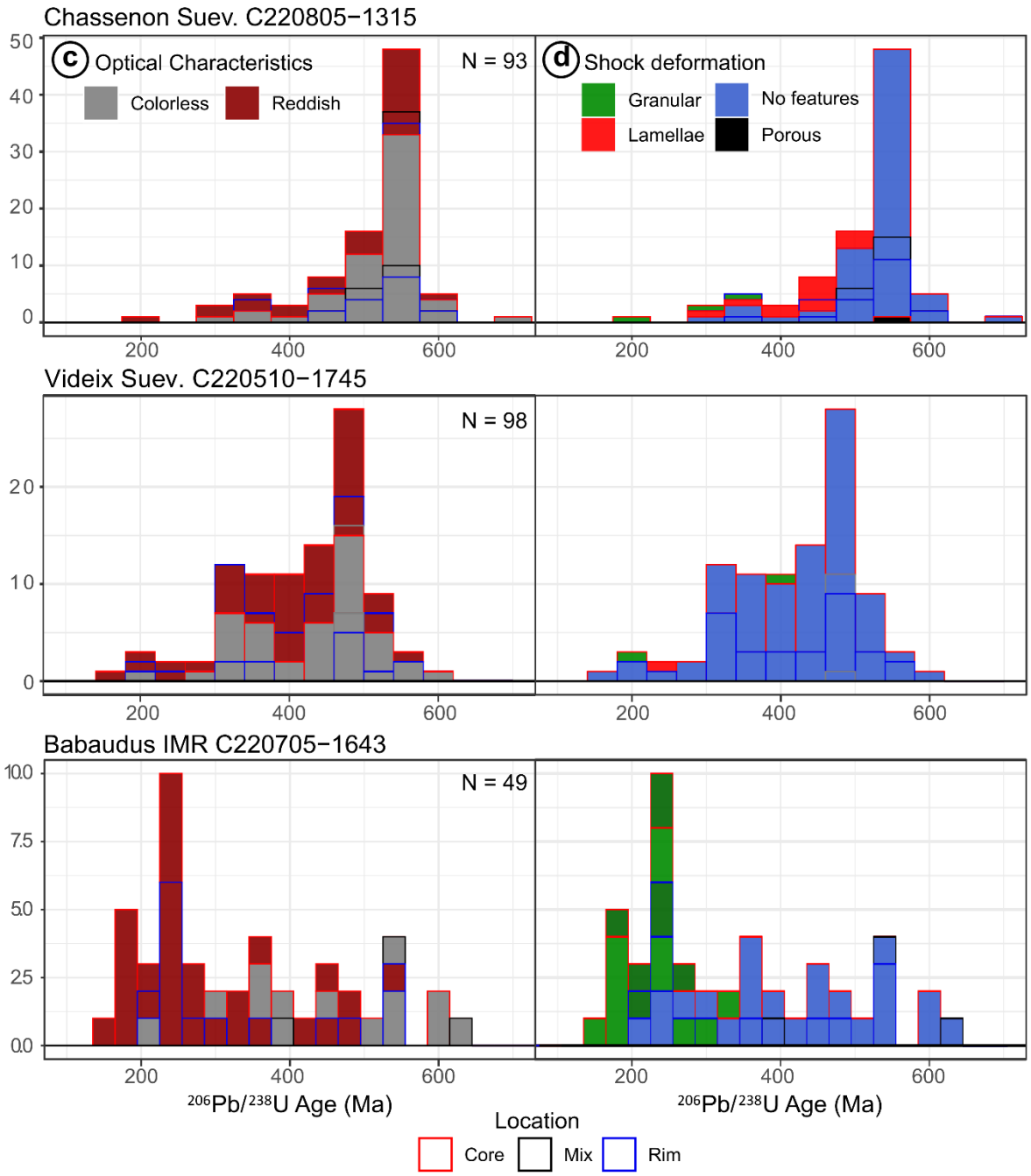


Fig. S6. Histograms for the apparent $^{206}Pb/^{238}U$ age distributions of the samples of this study, in function of (a) the spot size of the analyses, (b) the CL textures of the zircons, (c) the characteristics of the zircons under a binocular microscope, (d) the shock deformation of the grains, and (e) the location of the spots analyzed.




Chassenon Suev. C220805−1315
c Optical Characteristics
Colorless
Reddish
N = 93
d Shock deformation
Granular
No features
Lamellae
Porous
Videix Suev. C220510−1745
N = 98
Babaudus IMR C220705−1643
N = 49
206Pb/238U Age (Ma)
206Pb/238U Age (Ma)
Location
Core
Mix
Rim

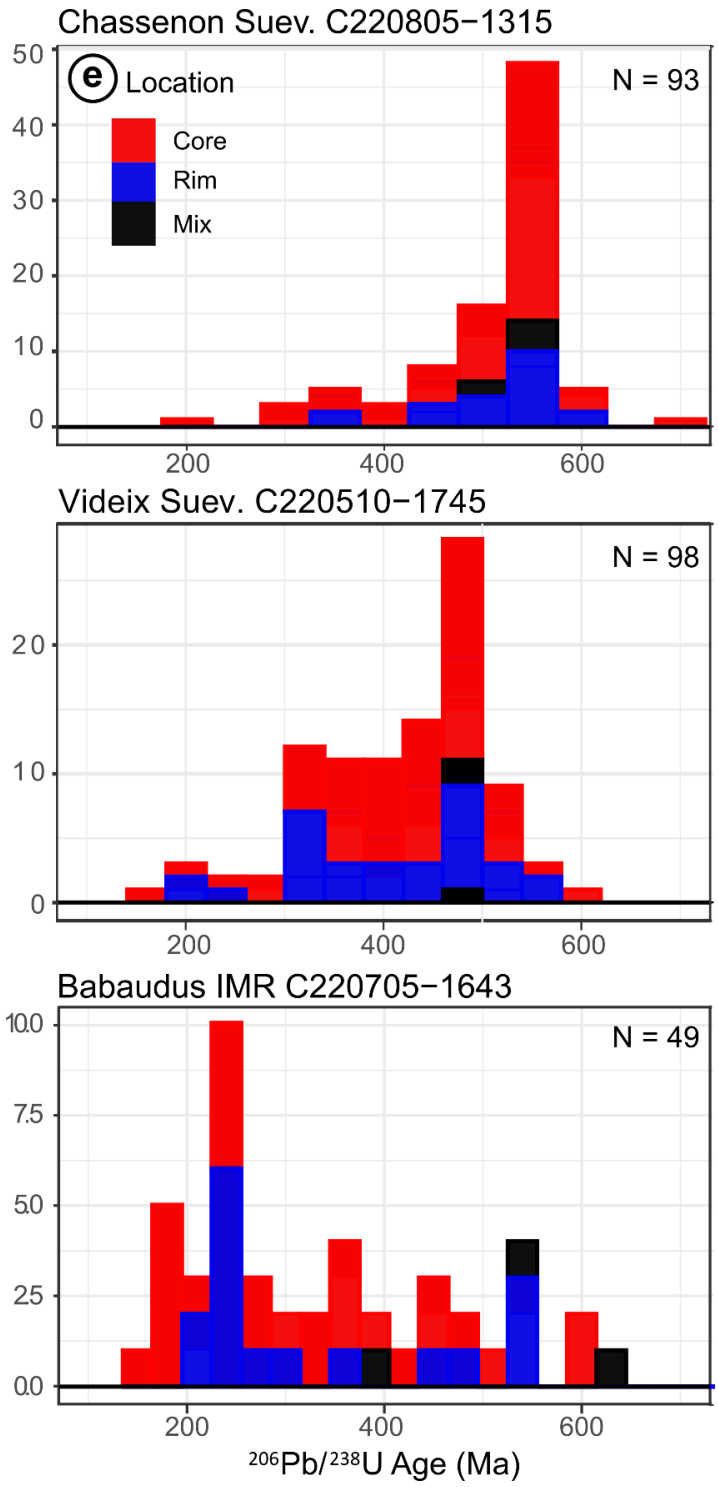

Chassenon Suev. C220805−1315
e
Location
Core
Rim
Mix
N = 93
50
40
30
20
10
0
200
400
600
Videix Suev. C220510−1745
N = 98
20
10
0
200
400
600
Babaudus IMR C220705−1643
N = 49
10.0
7.5
5.0
2.5
0.0
200
400
600
206Pb/238U Age (Ma)

Fig. S7. Plot of the core versus rim apparent $^{206}Pb/^{238}U$ ages for the grains where both locations were analyzed, in relation to the (a) shock deformation and (b) lithology. (c) Probability density plots and age peaks for the ages obtained on each domain (rim or core).

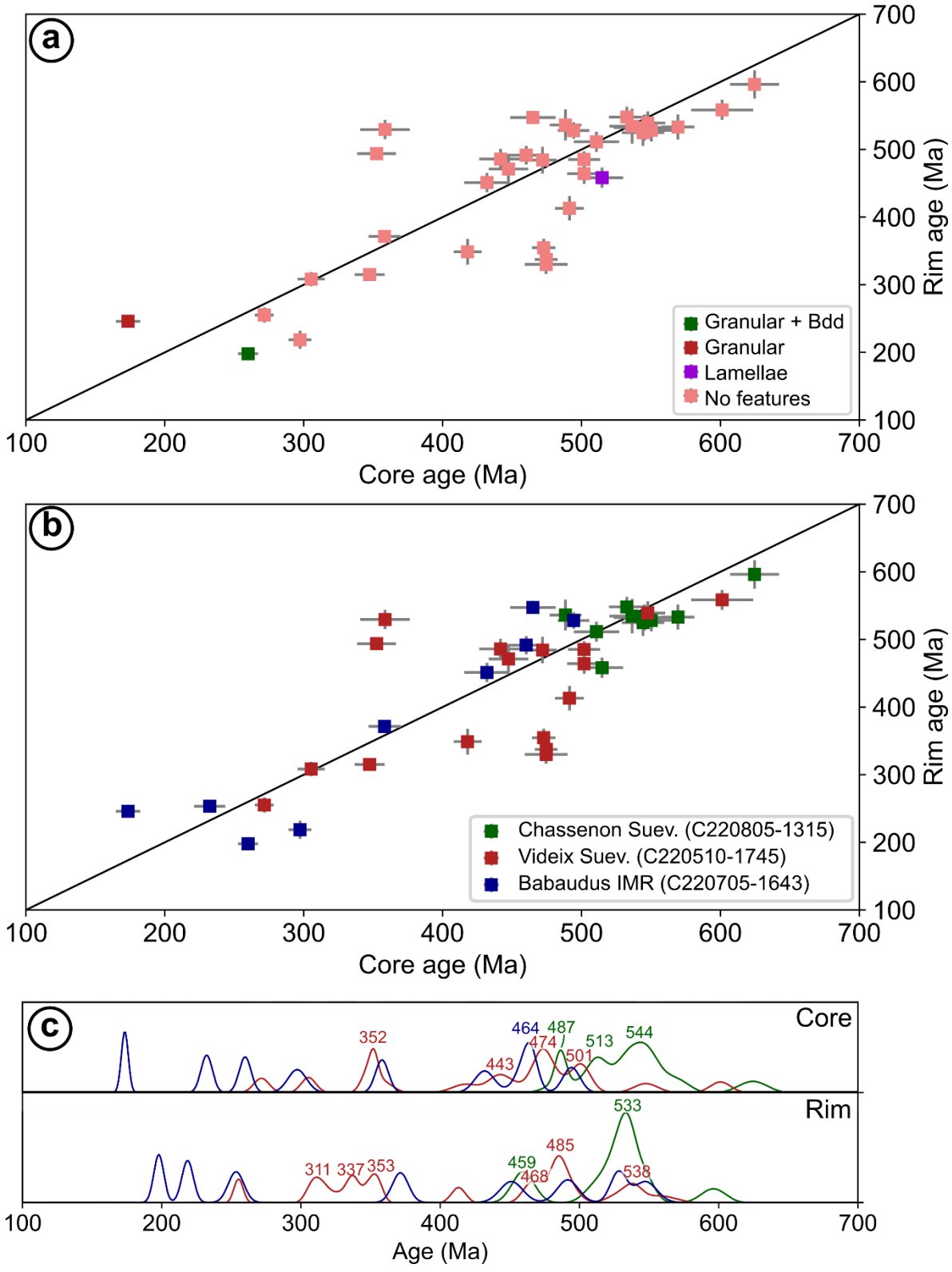
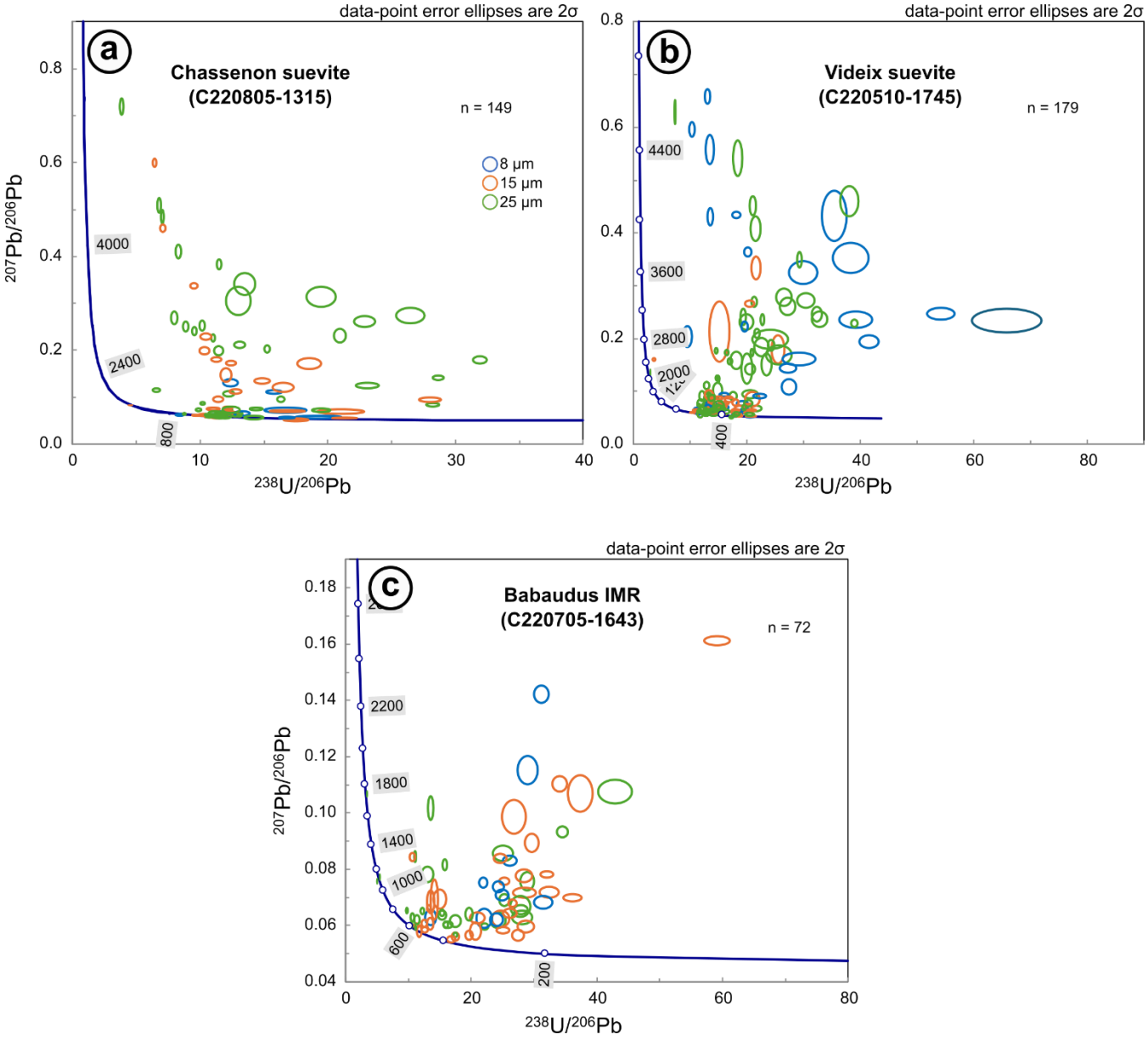


Fig. S8. Tera-Wasserburg plots for the data of the impactites analyzed in this study, in function of the spot diameter of the analyses. (a, b, and c) Plots for uncorrected data. (d, e and f) Plots for concordant data from grains without fractures, with a discordance <10 % on the 7/5:6/8 ages, and with errors on the apparent $^{206}Pb/^{238}U$ age < 5 %. Colors indicate different diameters of the analyzed spots. Color convention on (a) is valid for all diagrams.



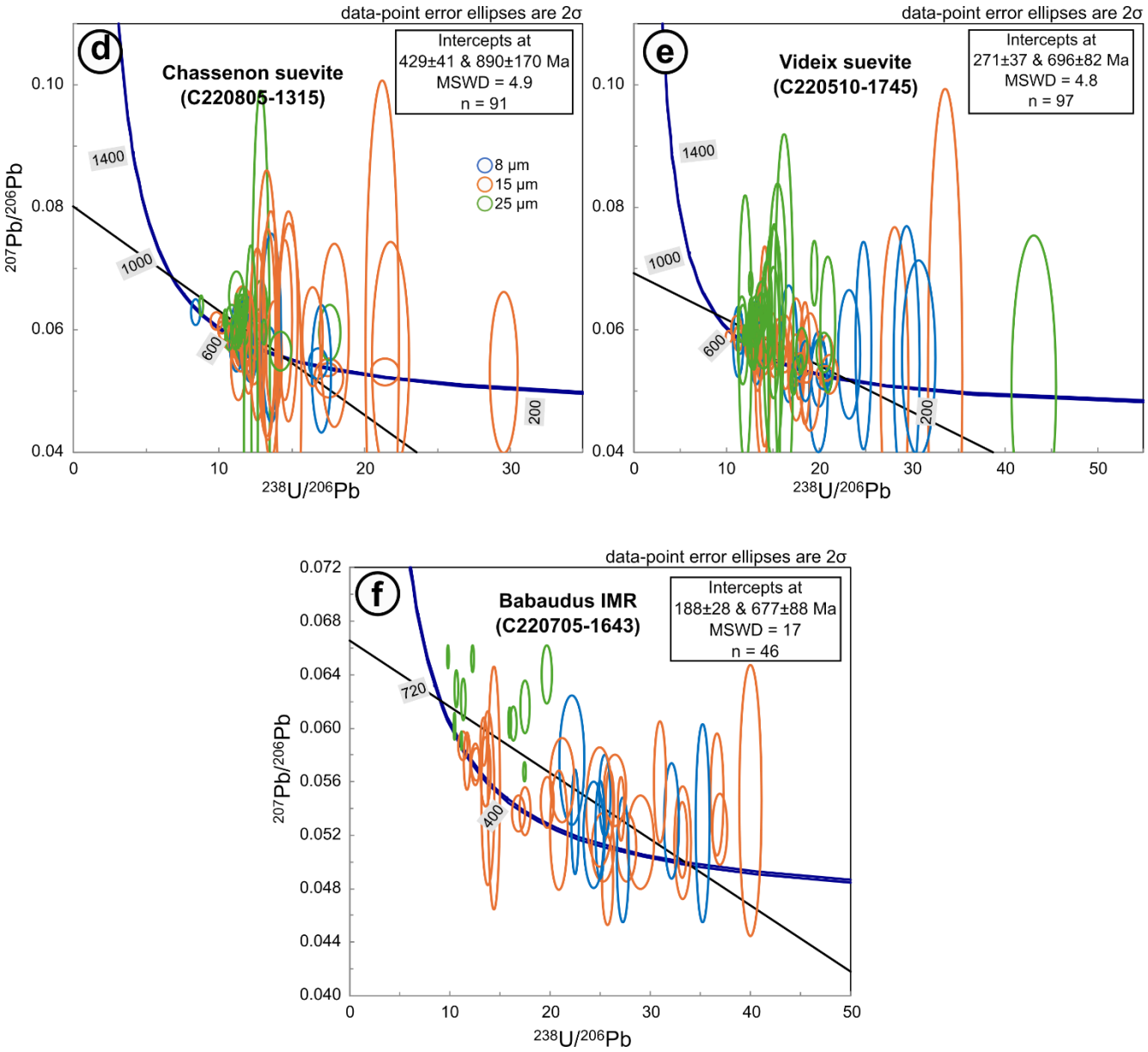
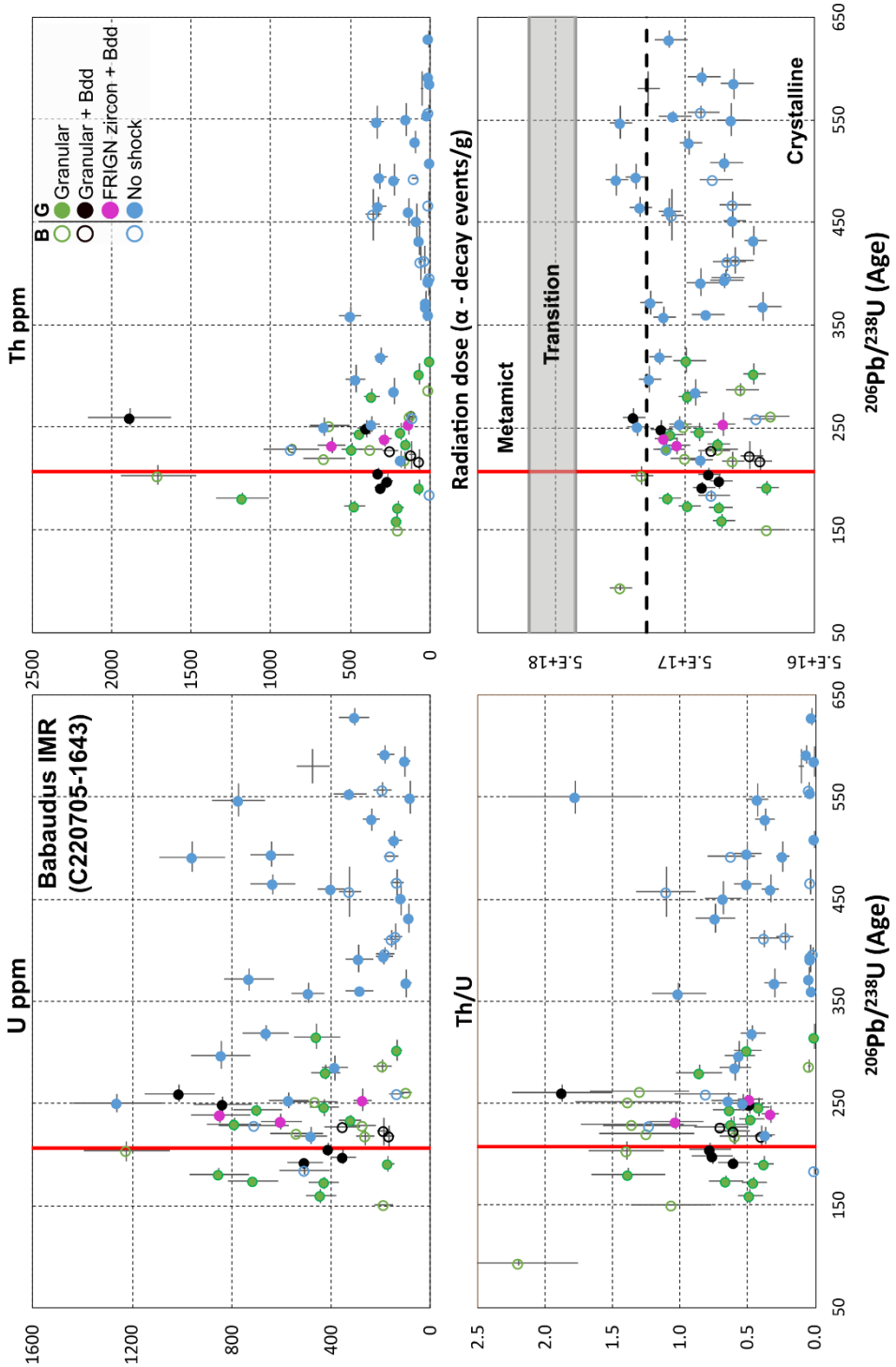
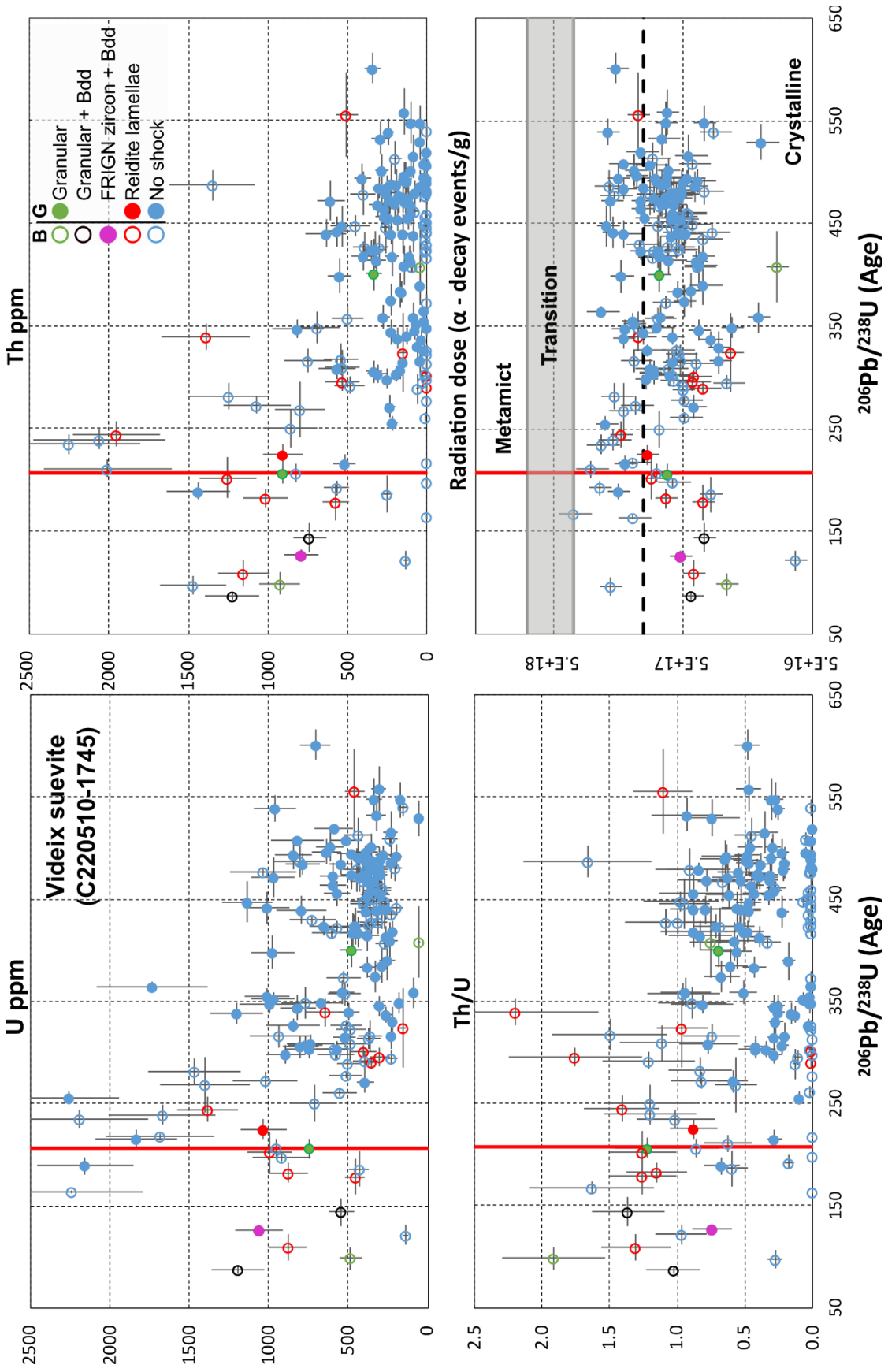
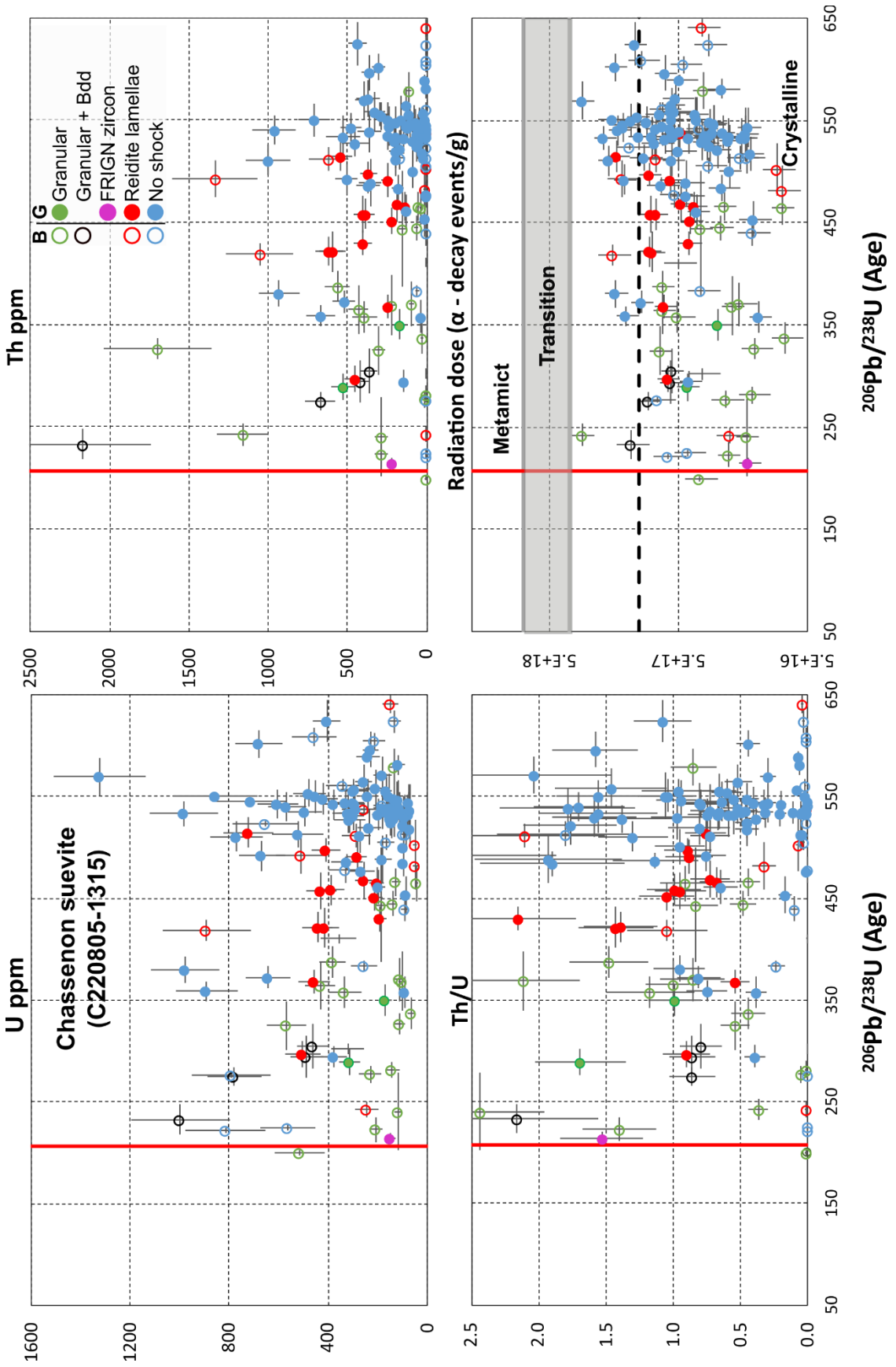

data-point error ellipses are 2σ
d
Chassenon suevite
(C220805-1315)
Intercepts at
429±41 & 890±170 Ma
MSWD = 4.9
n = 91
8 µm
15 µm
25 µm
1400
1000
600
200
0.10
0.08
0.06
0.04
0
10
20
30
207Pb/206Pb
238U/206Pb
data-point error ellipses are 2σ
e
Videix suevite
(C220510-1745)
Intercepts at
271±37 & 696±82 Ma
MSWD = 4.8
n = 97
1400
1000
600
200
0.10
0.08
0.06
0.04
0
10
20
30
40
50
238U/206Pb
data-point error ellipses are 2σ
f
Babaudus IMR
(C220705-1643)
Intercepts at
188±28 & 677±88 Ma
MSWD = 17
n = 46
720
400
0.072
0.068
0.064
0.060
0.056
0.052
0.048
0.044
0.040
0
10
20
30
40
50
207Pb/206Pb
238U/206Pb

Fig. S9. Contents of U and Th, and Th/U ratios, as well as radiation dose plotted versus the apparent $^{206}Pb/^{238}U$ ages for all analyzed zircon grains. Transition zone between crystalline and metamict zircon domains at 3.5 to 8.0 × 10^{18} α/g taken from Ewing et al. (2003). The red line in all diagrams is placed at the preferred age of the impact event (206.92 + 0.20/-0.32 Ma; Cohen et al., 2017). Symbols indicate the shock metamorphic features. "G" are grains with ages with 7/5 : 6/8 discordance <10 % and with errors of the apparent $^{206}Pb/^{238}U$ age < 5 %, "B" do not meet these characteristics.




Videix suevite
(C220510-1745)
U ppm
Th ppm
Th/U
Radiation dose (α - decay events/g)
Metamict
Transition
Crystalline
$^{206}Pb/^{238}U$ (Age)
B G
Granular
Granular + Bdd
FRIGN zircon + Bdd
Reidite lamellae
No shock


Th ppm
B G
Granular
Granular + Bdd
FRIGN zircon
Reidite lamellae
No shock
Radiation dose (α - decay events/g)
Metamict
Transition
Crystalline
U ppm
Chassenon suevite
(C220805-1315)
Th/U
206Pb/238U (Age)
206Pb/238U (Age)

CHAPTER 6

Manuscript 3

6 MANUSCRIPT 3

This is a preliminary version of a manuscript intended for submission to the journal *Geological Society of America Bulletin*. To complete this work, additional U-Pb zircon analyses are needed for the following samples: granites from Chéronnac (C220607-1502) and Champagnac (C180824-1630), and pegmatite from Champagnac (C220514-1340), in order to improve the result statistics.

What were the protoliths of the Rochechouart impactites? – A multiproxy provenance study

Daniela Guerrero [a, *], Wolf Uwe Reimold [a], Natalia Hauser [a], Moacir José Buenano Macambira [b], Steven Goderis [c], Vinciane Grimard [c], Christian Koeberl [d], Toni Schulz [d], Ansgar Greshake [e], Felix Kaufmann [e], Gavin Kenny [f], Philippe Lambert [g].

[a] *Postgraduate Program in Geology, Laboratory of Geochronology, Geosciences Institute, University of Brasília, 70910-900, Brasília, DF, Brazil.*
[b] *Universidade Federal do Pará, Programa de Pós-Graduação em Geologia e Geoquímica, 66075-110, Belém, Pará, Brazil.*
[c] *Archaeology, Environmental changes, and Geo-Chemistry (AMGC), Vrije Universiteit Brussel, Belgium.*
[d] *Department of Lithospheric Research, University of Vienna, Vienna 1090, Austria*
[e] *Museum für Naturkunde Berlin, 10115, Berlin, Germany.*
[f] *Department of Geosciences, Swedish Museum of Natural History, SE-104 05 Stockholm, Sweden.*
[g] *CIRIR - Centre International de Recherche et de Restitution sur les Impacts et sur Rochechouart, 87600 Rochechouart, France.*

*Corresponding author. E-mail: daaguerrerogu@gmail.com

Abstract - The ~207 Ma Rochechouart impact structure is located in the NW region of the Paleozoic crystalline basement of the French Massif Central (FMC). The structure preserves a heterogeneous suite of impactites, including impactites at the transition between the crater floor, and the basement. This study is part of a comprehensive investigation where the relationship between some impactites and basement rocks are analyzed in order to identify the most probable precursor lithologies for each impactite type. Previous U-Pb zircon provenance analyses showed a weak correlation between the zircon age distributions of impact melt rocks (IMRs) and certain basement lithologies, whereas the suevites exhibited a

reasonable correlation with specific target rocks. In this study, we further explore these relationships with a detailed petrographic, whole-rock geochemical, and isotopic characterization (Sr and Sm-Nd on whole rock) of representative impactites and basement lithologies. We also present complementary U-Pb on zircon analyses for previously not analyzed basement rocks. Our results indicate that, although multiple basement lithologies share similar geochemical or isotopic signatures, the impactites correlate more closely with target rocks of intermediate silica content (paragneisses, granodiorites, and some leptynites). Monomict lithic breccias and suevites have compositions very similar to those of the basement lithologies occurring in their vicinity. Although the IMRs likely represent mixtures of various lithologies, Sm-Nd isotopes indicate that the yellow IMRs exhibit a relatively stronger gneiss affinity, whereas the red IMRs show a greater contribution from the granodiorite from La Chassagne or the monzodiorite from La Martinie. It is recommended to still further expand the database, particularly with additional data for major and immobile trace elements and Sm-Nd isotopes, as well as samples from more localities, to better characterize the compositional signatures of the basement rocks and impactites and evaluate the broader applicability of the identified patterns.

Keywords: Rochechouart impact structure, suevites, impact melt rock, provenance, geochemistry, Sr-Nd isotopes.

6.1 Introduction

The ~ 207 Ma Rochechouart impact structure, centered at 45°50’N / 0°46’E, is located in the northwestern region of the Paleozoic crystalline basement of the French Massif Central (FMC) (Figure 6.1a). It is the only confirmed impact structure in France (e.g., Gottwald et al., 2020; Kenkmann, 2021; Osinski et al., 2022). The impact origin of Rochechouart was first identified by Kraut et al. (1969) through the observation of planar deformation features (PDFs) in quartz and shatter cones in granites and gneisses of the crater floor. The structure is deeply eroded (see, e.g., Osinski et al., 2022). The current crater diameter is constrained to ~ 23 km based on the distribution of shock deformation levels of the target rocks (Lambert et al., 1977, 2010). However, larger estimates of the original crater diameter range from 32

km (Osinski & Ferriere, 2016) to 40-50 km (Lambert, 2010). The level of erosion of the structure provides access to partially shocked basement rocks, the crater floor, and remnants of the crater-fill impact breccia deposits. In 2017, a drilling campaign made 544 m of crater fill deposits and basement rocks available, from 18 drill cores at eight locations along two traverses (N-S and NE-SW) through the impact structure (Lambert et al., 2019).

The allochthonous impactites within the Rochechouart structure range from polymict lithic breccias to clast-free or clast-poor impact melt rocks (Lambert, 2010; Sapers et al., 2014). These rocks are highly heterogeneous and all show effects of significant hydrothermal alteration (e.g., Lambert, 2010; Sapers et al., 2014; Simpson et al., 2017). Initial geochemical studies of the impactites and the target rocks indicated that the compositions of the impactites are largely controlled by the target lithologies present at each location, reflecting inefficient mixing and homogenization of a wide impact melt sheet (Lambert, 1977a, 2010; Faucher, 2021).

The crystalline basement of the impact structure is part of the French Massif Central (FMC), one of the largest exposed segments of the Central European Variscan Belt (e.g., Faure et al., 2009; Lardeaux, 2014; Regorda et al., 2020; Vanderhaeghe et al., 2020). The basement in the area of the impact structure is represented by the metamorphic rocks of the Silurian–Carboniferous Lower Gneiss Unit (LGU) and Upper Gneiss Unit (UGU) (Chèvremont et al., 1996; Lambert, 2010). These gneissic units are intruded by granitic and granodioritic bodies. There are also some amphibolite, pegmatite, micro-granite, granodiorite, diorite, and gabbro dikes (Lambert, 2010). Locally, remnants of oceanic crust in the form of serpentinite occurrences are found (Chèvremont et al., 1996).

The present work is part of a comprehensive study of the principal impactite and basement lithologies of the Rochechouart impact structure. They are analyzed with multidisciplinary techniques to constrain the main target rock components involved in the formation of the impactites. Especially isotope techniques are used to identify the most likely precursor lithologies. Geochronological results (Guerrero et al., 2024, 2025 - in review), i.e., U-Pb zircon age provenance analysis, for two suevites from

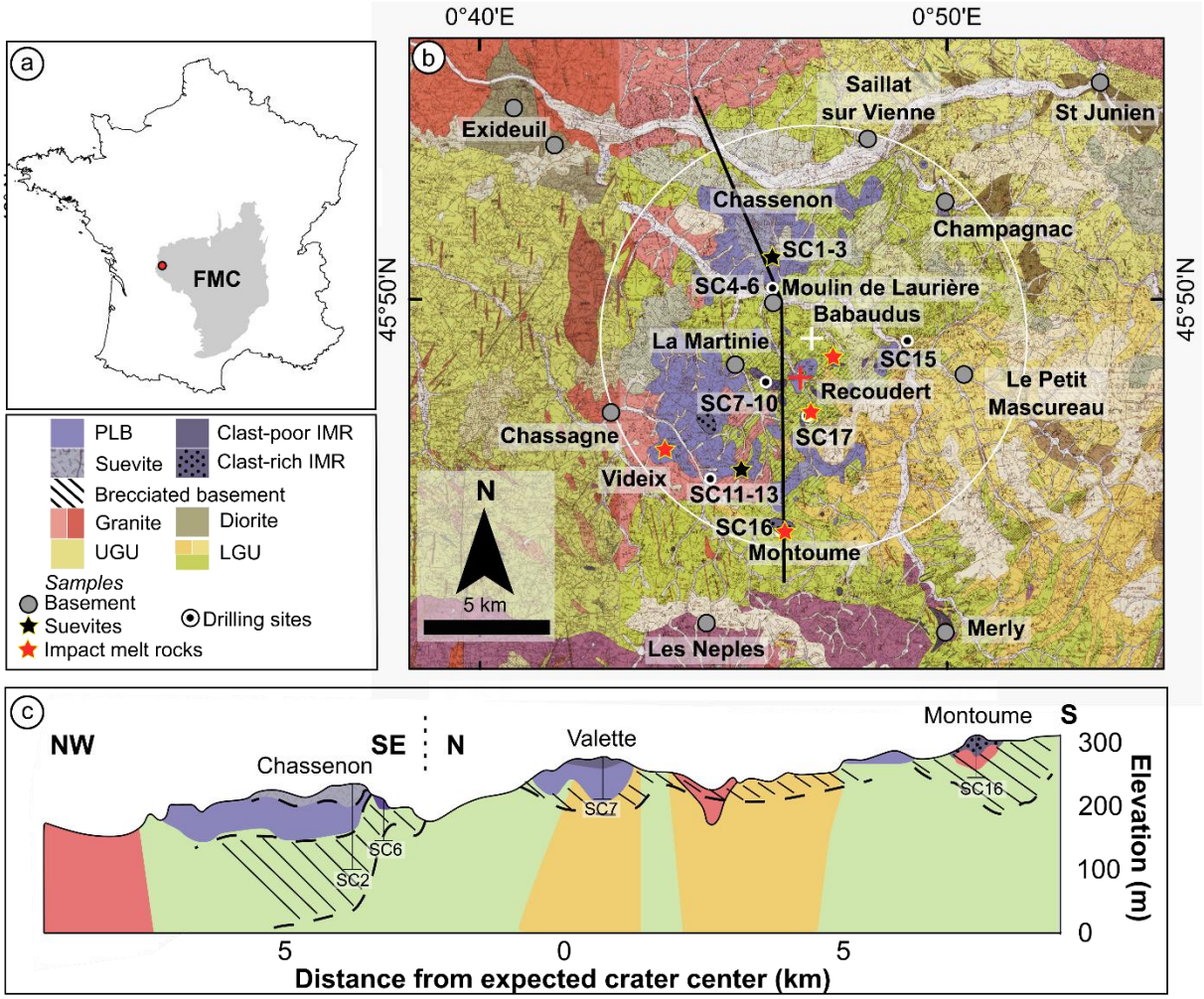


Figure 6.1 (a) Location of the French Massif Central in the territory of France, with the position of the impact structure marked by the red dot. (b) Geological map at the scale of 1:50,000, Sheet Rochechouart (after Chèvremont et al., 1996), and (c) the geology along the schematic composite cross section for the profiles NW-SE to N-S marked in (b). The white circle indicates the extent of exposures of crater fill deposits (centered on the white cross). The red cross is the probable center of the initial Rochechouart impact structure, as derived from the present exposure pattern (after Lambert, 2010). The cross section in (c) is modified after Lambert (2010) and Quesnel et al. (2021), and also shows the locations of the 2017 drillings. PLB - Polymict lithic breccia, IMR – Impact melt rock.

Chassenon and Videix, three impact melt rocks (Babaudus, Recoudert, and Montoume), and four basement samples (paragneiss, two amphibolites, and monzodiorite) (Figure 6.1) have already been presented. These studies showed highly heterogeneous zircon populations in the impactites, with a wide variety of shock deformation textures and U-Pb zircon ages. Ages include post-impact ages ranging from 192 to 195 Ma, ages within the error margins of the impact event, i.e., between 203 and 207 Ma, and pre-impact ages from the Triassic to the Neoproterozoic. The age distributions of the suevites showed a strong correlation with the target lithologies sampled nearby. In contrast, the age distributions of the

impact melt rocks displayed weak correlations with basement lithologies. These zircon populations contain significant proportions of ages from the impact event to the late stages of Variscan evolution (272 ±12 Ma; Guerrero et al., 2024). These previous findings have highlighted the need for further extension of the zircon geochronological database for the Rochechouart basement, to refine the provenance analysis.

Here, the previous results are complemented with a detailed petrographic, whole-rock geochemical, and isotopic (Sr and Sm-Nd on whole rock) characterization of representative impactite lithologies and all basement units currently exposed in the impact structure. The combined provenance dataset includes the results of the previous geochronologic studies (Guerrero et al., 2024, 2025 - in review), as well as new results for additional samples. In total, 13 basement lithologies and 20 impactite samples have now been analyzed. This investigation shows that the impactites can be better correlated with the target rocks with intermediate silica contents, and the geochemical compositions of monomict lithic breccias and suevites tend to resemble the compositions of the closest target rock lithologies. The yellow IMRs have an isotopic affinity more comparable with the gneisses, whereas the red IMRs show a larger contribution of granodiorite and/or monzodiorite from La Chassagne and La Martinie.

6.2 Geological background

6.2.1 Target rocks

The predominant units of the FMC, in the area of the Rochechouart impact structure, are the metamorphic basement rocks of the Lower Gneiss Unit (LGU) and the Upper Gneiss Unit (UGU) (Chèvremont et al., 1996). The LGU, the principal basement rock, corresponds to micaceous paragneisses and orthogneisses (metarhyolites) that are intruded by porphyritic alkaline granitic rocks of Cambrian to Early Ordovician ages. The latter are now transformed into augen orthogneiss (e.g., Faure et al., 2005, 2009). The UGU, which is only present in the northeastern part of the structure, is made up of micaceous paragneisses, similar to the ones of the LGU, and a bimodal

magmatic association known as the “leptynite-amphibolite complex” (LAC), which includes lenses of these lithologies (Chèvremont et al., 1996). The paragneisses and orthogneisses of both units can display variations in texture and composition. It has been estimated that they represent 50% and 25%, respectively, of the basement rocks in the crater area (Lambert, 1977a). Furthermore, amphibolite lenses are intercalated with gneisses of both units, and serpentinized peridotites occur in the basal part of the LGU in the Limousin area (Chèvremont et al., 1996).

These units are interpreted to be derived from mostly Ediacaran sedimentary rocks of the northern Gondwana margin. These rocks were intruded by Cambrian plutons during the southward subduction of the Iapetus Ocean beneath Gondwana and were affected by Cambro-Ordovician crustal thinning and rifting (Faure et al., 2009; Lardeaux, 2014; Vanderhaeghe et al., 2020). During the upper Silurian to Devonian, the UGU unit underwent HP to UHP granulite/eclogite facies metamorphism, followed by partial melting under amphibolite facies conditions in the middle-upper Devonian (Do Couto et al., 2016; Faure et al., 2008; Lotout et al., 2018). Subsequently, during the main continental collision of the Variscan Orogeny in the uppermost Devonian / lower Carboniferous, the LGU and UGU underwent Barrovian-type metamorphism in the entire FMC (e.g., Faure et al., 2009; Lardeaux, 2014).

Igneous rocks intrude the metamorphic formations, comprising approximately 25% of the basement in the impact area (Lambert, 1977a). Outside the impact structure, to the north and the south, occur the calc-alkaline intrusions of Chabanais and the leucogranites of Chéronnac, respectively. Within the western half of the impact structure occur the calc-alkaline Bouloux and Saint Gervais-Videix plutonic bodies. Additionally, multiple N-S-oriented dikes of micro-granites and –granodiorites and lamprophyres (diorites / gabbros) intrude all other units (Duthou et al., 1984). These intrusions have been associated with a final phase of anatexis that may have lasted until the Carboniferous, the last stage of the Variscan Orogeny (approximately 360–295 Ma; e.g., Chèvremont et al., 1996; Lardeaux, 2014).

6.2.2 Rochechouart impactites

The autochthonous and parauthochthonous impactites of the Rochechouart impact structure include shocked target rocks, granitic and gneissic monomict, as well as polymict, lithic impact breccias, and dikes of monomict or polymict impact breccias. There are also local occurrences of pseudotachylite and pseudotachylite-like breccias (Kenkmann et al., 2000; Lambert, 1977a, 2010; Reimold et al., 1983). The allochthonous impactites, described in detail by Lambert (1977a, 2010) and Sapers et al. (2014), include: 1) polymict lithic impact breccia ("Rochechouart breccia"), with quartzofeldspathic lithic and mineral clasts of variable shock levels in more or less fine-grained, clastic matrix of the same materials; 2) melt-bearing impact breccia ("Chassenon suevite"), with an ~ 50 % matrix content and irregularly shaped, variegated glass clasts; 3) melt-rich impactite ("Vallette-type breccia"), with a purple quartzo-feldspathic melt matrix and glass clast content that varies between < 10 and > 60 %, and lithic and mineral clasts of varied shock levels; 4) impact melt rock ("Montoume breccia"), which is a clast-rich impact melt rock with a red to gray-brown crystalline melt matrix (50 to 70 vol%) with flow features and mineral, lithic, and glass clasts; and 5) impact melt rock ("Babaudus melt"), a yellow, clast-free to clast-poor melt rock with voluminous quartzofeldspathic homogeneous matrix (up to 99 vol%), rich in vesicles, and with a limited content of quartzofeldspathic lithic and mineral clasts. Additionally, a fine-grained, layered deposit, the so-called "impactoclastite" unit (Lambert, 2010), occurs in the Chassenon quarry. This unit has evidence of sedimentary sorting and is presumed to mark the top of the within-crater impact deposits (ibid; Ormö et al., 2023).

On surface, some stratigraphic relationships between these units are locally preserved (Lambert, 1977a, 2010; Sapers et al., 2014). Polymict lithic breccia is locally in direct contact with the basement. These breccias form the most widespread impactite type of the structure and may have represented a continuous sheet overlain by suevite. Lenses of suevite occur at the periphery of the structure. The melt-rich suevite lies directly above the shocked basement lithologies and is present at the margins of the structure. This material is overlain by impact melt rocks in the southwestern part of the structure. The impact melt lithologies are also in direct

contact with shocked basement and are found as isolated patches principally in the central part and in the southern area of the structure (Figure 6.1b and c).

Major element analyses of the different types of impactites and the target rocks from across the impact structure have shown a significant spatial variation in composition. The local variations appear to be controlled by the respective occurrences of different basement rocks in the vicinity of melt rock sampling sites (Lambert, 1977a, 2010). According to this author, the polymict lithic breccias from Rochechouart plot in the compositional field of a mixed granitic and gneissic basement. The composition of the suevite at Chassenon resembles the composition of locally occurring gneiss. The melt-rich suevite of the SW part of the structure has a generally granitic composition. All impact melt rock units show an overall granitic signature but with slight differences. The Babaudus melt rock is more felsic and is thought to have a major contribution from locally occurring leptynite. The yellow and the red impact melt rocks from Valette and Montoume, respectively, have similar chemical composition, with a mixed granitic and gneissic signature. The impactoclastite unit has a composition that falls between the granite and the gneiss, similar to an average target composition for this structure (Lambert, 1977a, 2010; Faucher, 2021).

All these impactites exhibit strong hydrothermal alteration, characterized by a strong K-metasomatism (higher in the melt-rich phases) and the development of argillic, carbonate, oxide, and sulfide alteration assemblages (Faucher, 2021; Lambert, 2010; Sapers et al., 2014; Simpson et al., 2017).

Our recent provenance analysis supports that the suevite at Chassenon correlates well with the paragneiss of the LGU, whereas the suevite from Videix (SW) has an age distribution very similar to the granitic lithologies sampled near the center of the structure (Guerrero et al., 2025 - in review). In contrast, the impact melt rocks from Recoudert, Montoume, and Babaudus have a poor correlation with the recorded ages for basement rocks (Guerrero et al., 2024, 2025 - in review).

6.3 Sample material and methodology

6.3.1 Sample material

Thirteen target rock and six impactite surface samples, as well as 14 impactite samples from six drill-cores of the 2017 CIRIR drilling project were analyzed (Table 6.1). The surface samples were collected in two field campaigns in August 2018 and in May-July 2022. The drill-core samples were provided by the CIRIR in 2022. The philosophy behind this sampling was to investigate the most representative lithologies of the basement and the impactites of the Rochechouart impact structure.

Table 6.1 Surface and drill core samples of this study.

Surface samples				
Code	Lithology	Location	N	E
C220506-0954	Paragneiss	Saillat Sur Vienne	45° 52.465'	0° 48.597'
C180825-0930	Paragneiss	Moulin de Laurière	45° 49.949'	0° 46.338'
C180824-1645	Leptynitic gneiss	Champagnac	45° 51.258'	0° 50.000'
C220607-1115	Leptynitic gneiss	Le Petit Mascureau	45° 48.850'	0° 50.416'
C180824-1500	Amphibolite	Exideuil Qu	45° 53.052'	0° 40.842'
C180822-1625	Amphibolite	St Junien Ceitce	45° 53.238'	0° 53.320'
C220522-1749	Serpentinite	Merly	45° 44.987'	0° 49.977'
C220514-1340	Pegmatite	Champagnac	45° 51.258'	0° 49.986'
C180824-1630	Granite	Champagnac	45° 51.258'	0° 50.000'
C220607-1502	Granite	Les Neples	45° 45.128'	0° 44.869'
C220608-2001	Granodiorite	La Chassagne	45° 48.236'	0° 42.801'
C220511-1352	Granodiorite	Exideuil Qu	45° 52.312'	0° 41.554'
C180825-1115	Monzodiorite	La Martinie	45° 49.092'	0° 45.488'
C180824-1900	Clast-poor yellow IMR	Recoudert	45°48'17.3707"	0°47'0.2296"
C180823-0955	Clast-rich red IMR	Montoume	45° 46.535'	0° 46.488'
C220510-1414	Clast-poor red IMR	Videix	45° 47.738'	0° 44.055'
C220510-1745	Suevite	Videix	45° 47.485'	0° 45.607'
C220705-1643	Clast-poor yellow IMR	Babaudus	45° 49.013'	0° 47.784'
C220805-1315	Suevite	Chassenon	45°50.579	0°46.357'

Drill-core samples							
Core ID	Code (Abbreviation)	Lithology	Location	N	E	Top (m)	Bottom (m)
SC1	S1/3/112-125-F1-1 (1-3)	Clast-poo,r yellow IMR	Chassenon	45°50'36.87"	0°46'10.18"	4.12	4.25
SC7	S7/1/25-36-F1-1 (7-1)	Clast-poor, red IMR	Valette	45°48'45.01"	0°46'9.24"	0.25	0.36
	S7/4/45-48-F1-1 (7-4)	Clast-rich, yellow IMR				4.94	4.97
	S7/10/122-132-F1-1 (7-10)	Melt-rich, red suevite/IMR				15.25	15.35
	S7/15/100-105-F1-1 (7-15)	Clast-rich, red IMR				22.97	23.02
SC11	S11/5/155-169-F1-1 (11-5)	Clast-rich, red IMR	Puy Chiraud (Videix)	45°47'20.20"	0°44'55.01"	7.83	7.97
	S11/17/132-152-F1-1 (11-17)	Lithic impact breccia				26.87	27.07
	S11/25/150-155-F1-1 (11-25)	Lithic impact breccia				40.15	40.2
SC15	S15/1/30-40-F1-1 (15-1)	Clast-rich, yellow IMR	Rochechouart	45°49'18.35"	0°49'8.92"	0.3	0.4
SC16	S16/6/138-150-F1-1 (16-6)	Clast-rich, red IMR	Montoume	45°46'32.24"	0°46'30.01"	9.38	9.5
	S16/7/124-144-F1-1 (16-7)	Clast-rich, red IMR				10.86	11.06
SC17	S17/2/144-148-F1-1 (17-2)	Red IMR	Recoudert	45°48'15.98"	0°46'59.15"	3.14	3.18
	S17/7/79-122-F1-2 (17-7)	Clast-poor, yellow IMR				10.5	10.93
	S17/13/40-50-F1-2 (17-13)	Clast-rich, red IMR				18.4	18.5

6.3.1.1 Basement samples

The basement samples include paragneisses and orthogneisses from the LGU from the area of the structure (sites at Moulin de Laurière and Le Petit Mascureau, compare Figure 6.1b), paragneisses and orthogneisses from the UGU at the northeastern margin of the structure (Champagnac and Saillat sur Vienne), two amphibolite dikes intruding the UGU in the northern part just outside of the structure (at Exideuil and St. Junien), a serpentinite from the south (Merly), and the principal igneous rocks intruding the metamorphic units, such as the granite from Chéronnac to the south (Les Neples), the granodiorites from the west (La Chassagne) and northwest (Chabanais - Exideuil) of the structure, the monzodiorite from La Martinie from close to the suspected center of the structure, and the granite and pegmatite from Champagnac to the NE (Figure 6.1b).

6.3.1.2 Impactite samples

The impactite samples are from some of the best described sites in the literature for Rochechouart, and in many cases the surface samples were obtained close to or at drilling sites. The drill-cores selected to obtain samples show a wide variety of lithologies and most of them also show the target rocks beneath the impactites (Lambert et al., 2019). The impactite samples represent three main lithologies: impact melt rocks, suevites, and monomict impact breccia.

Close to the center of the structure, two surface samples of clast-poor, yellow IMR were collected at isolated outcrops at the localities of Babaudus and Recoudert. The SC17 drill-core, also located at Recoudert, shows a sequence of 23 m of red IMR with an intercalation of yellow IMR, from which three samples were collected (17-2, 17-7, 17-13), followed by basement of 21.1 m of fractured gneiss, 2.5 m of a dike of suevite, and 18 m of a felsic gneiss. Furthermore, from close to the center of the structure, four samples were collected from drill core SC7 from Valette (7-1, 7-14, 7-10, and 7-15). This drill-core shows a sequence of 16 m of impact melt rock with vesicular clasts (Figure S1f), and 48.6 m of a clast-rich impact melt or suevite.

The red clast-rich IMRs from Montoume are part of a unit principally located at the top of some hills in the southern part of the structure. The sample was collected near

Montoume village, 7.5 km south of the center of the structure, where a massive, 25 m thick deposit with vertical/subvertical jointing occurs. From the same location, drill-core SC16 shows a sequence of 26 m of a similar lithology, from which two samples were selected (16-6 and 16-7), followed by 29 m, and then 10.6 m of two lithologies that could correspond to either a severely deformed granite and gneiss, respectively, or granite and gneiss dominated, clast-rich IMRs.

The suevite from Chassenon was collected at the Grosse Pièce quarry, where this lithology forms a 20-30 m thick deposit that has intercalations of the impactoclastite unit. At this locality, drill-cores SC1, SC2, and SC3 were obtained. Core SC2 contains a sequence of 39.8 m of melt-rich suevite, followed by 48.2 m of melt-poor suevite, 26 m of brecciated gneiss of the crater floor, and 7.4 m of gneiss basement. In the drill-core SC1 that was obtained from a vertical impactoclastite dike, a sample of clast-poor, yellow IMR was collected (1-3).

To the southwest, two samples were collected at Videix, a suevite and a clast-poor red IMR. The Videix suevite and the red IMR were obtained at isolated outcrops partially covered by vegetation, at a road-cut. This site is close to the drilling sites SC11 - SC13 at Puy Chiraud. Drill-core SC11, from which three samples were collected (11-5, 11-17, and 11-25), comprises 16 m of red, clast-rich IMR, followed by 16 m of a granite clast rich IMR, 27 m of a lithology that could correspond to the same IMR but with multi-meter sized blocks or a highly deformed granite with impact breccia layers, and 7.6 m of a polymict lithic breccia.

One sample was collected from SC15 drill-core (15-1), which was pulled close to Rochechouart castle. This core contains 1 m of massive, yellow IMR. From the same location, the SC14 drill-core shows a sequence of 1.5 m of polymict breccia, followed by 63.4 m of brecciated gneiss.

6.3.2 Methodology

6.3.2.1 Petrography

Polished thin sections of the surface samples were prepared at the Museum für Naturkunde (MfN) in Berlin, Germany. For the drill-core samples, thin sections were made in part at MfN and in part at the Naturhistorisches Museum (NHM) of Vienna,

Austria. The thin sections were studied in the Mineralogy Laboratory at the Universidade de Brasília (UnB) with an Olympus BX60F5 microscope, as well as with a Zeiss Axiophot microscope at the Laboratório de Estudos Geodinâmicos, Geocronológicos e Ambientais (LEGGA) of the UnB. The modal compositions of the rocks were determined by point counting of approximately 600 points per thin section (Table S2).

6.3.2.2 Geochemistry

All samples were crushed at LEGGA to obtain fine powder fractions. The analysis of major and trace elements of the samples C180825-0930, C180824-1500, C180822-1625, C180824-1645, C180824-1900, C180823-0955 was done at SGS Geosol in Vesperiano, Minas Gerais, Brazil. The remaining samples were analyzed at the Université Libre de Bruxelles (ULB).

At SGS Geosol, the samples were analyzed through ICP-MS using their method ICP95A. Accuracies for all major elements are given at 10 %. For trace element analysis the certified reference materials GRE-03 and GRE-05 were used, and accuracy at 95 % confidence level is quoted at the following levels (in % of the analytical value): Ce ± 2, Dy ± 4, Eu ± 2, Ga ± 4, Gd ± 3.6, Ho ± 0.3, La ± 36, Lu ± 0.1, Nb ± 44, Nd ± 33, Pr ± 9, Sm ± 5, Ta ± 9, Hf ± 7, Tb ± 0.5, Tm ± 0.1, Y ± 6, Yb ± 0.25, Zr ± 47, Sc ± 0.5, Ti ± 0.1 , Th ± 2.4, U ± 1, W ± 0.5. Further detail, especially about the accuracies of this method, is provided in Reimold et al. (2021).

At the Laboratoire G-Time of the Université Libre de Bruxelles (ULB) the samples were analyzed by inductively coupled plasma - optical emission spectrometry (ICP-OES). Approximately 50 mg of powdered sample were mixed with ~1 g of a 4:1 ultrapure lithium metaborate (Li_2O) and tetraborate ($Li_2B_4O_7$) mixture. The mixtures were fused in graphite crucibles at 1000 °C for 10 minutes in a muffle furnace. After cooling, the resulting glass beads were dissolved in 50 ml of 2N HNO_3 using magnetic stirring for 5 hours. Major element concentrations were determined by quantification via external calibration curves using multi-element standard solutions (Si, Mg, Fe, Al, Ca, Na, Ti, K, P, Mn, Cr) on a Thermo Scientific iCAP series ICP-OES. Trace element concentrations were determined on the same sample solutions

using an Agilent Technologies 7700 Series ICP-MS. Internal standards (yttrium and indium) were added and corrections for oxide production (using Pr, Nd, Ba, and Ce standard element solutions) were applied. Accuracy and precision were verified using sample replicates and the international reference materials BHVO-2 (basalt) and AGV-2 (andesite) of the U.S.G.S. Loss on ignition (LOI) was measured with weight loss after heating 0.5 g of sample in a ceramic crucible at 1000 °C for 1 hour and cooling down to room temperature. Chemical analyses are compiled in the Supplementary Material in Table S4.

All data have been recalculated to a volatile free basis to avoid the effects of the loss on ignition (see Figure 6.6 and 6.7).

6.3.2.3 Strontium and Samarium-Neodymium isotopes

All basement samples and eight impactite samples from the drill-cores (samples 1-3, 7-1, 7-4, 7-10, 11-17, 15-1, 16-7, 17-7) were selected to determine whole-rock Sr and Sm-Nd isotopic data. These samples are representative of the heterogeneity of the sampled lithologies. The Sm-Nd analyses were done at LEGGA, whereas the $^{87}Sr/^{86}Sr$ analyses were done at the University of Vienna.

The separation procedures and analytical methods used at UnB were described by Gioia and Pimentel (2000). Approximately 50 mg of rock powder were mixed with a $^{149}Sm/^{150}Nd$ spike solution and dissolved in Savillex capsules. All samples were subjected to cation exchange techniques with Teflon® columns with LN-Spec resin (HDEHP-Di-(2-ethylhexyl) phosphoric acid supported on polytetrafluoroethylene). Analyses were conducted using a Thermo Scientific TRITON™ Plus Thermal Ionization Mass Spectrometer (TIMS) in static multi-collector mode. Mass fractionation was corrected by normalizing the $^{143}Nd/^{144}Nd$ ratio to $^{146}Nd/^{144}Nd = 0.7219$. The Sm-Nd decay constant applied was $6.54 \times 10^{-12}\ yr^{-1}$ (Lugmair and Marti, 1978). Over the duration of this study, the average for values of the $^{143}Nd/^{144}Nd$ ratio for the USGS BHVO-2 standard was 0.512981 ± 0.00006 (2σ), consistent with published values (e.g., 0.512979 ± 0.000028; Jochum et al., 2016). Laboratory blanks were approximately 0.25 ng for Nd and 0.04 ng for Sm.

The $^{87}Sr/^{86}Sr$ analyses were conducted at the Department of Lithospheric Research, University of Vienna, Austria. Rock powders (50–100 mg) were digested in tightly sealed Savillex beakers with an ultra-pure 4:1 HF:HNO_3 mixture at 100–120 °C for 2–4 weeks. After acid evaporation, the residues were treated repeatedly with 6M HCl to obtain clear solutions. Strontium was isolated using AG 50W-X8 resin (200–400 mesh) with 2.5 M and 4.0 M HCl as eluants. Procedural blanks for Sr were <1 ng, negligible for this study. Isolated fractions were analyzed using a Thermo-Finnigan Triton$^+$ TIMS in static mode with mass fractionation corrected to $^{88}Sr/^{86}Sr$ = 8.3752. Measurements were performed in one batch, for which a $^{87}Sr/^{86}Sr$ ratio of 0.710260 ± 0.000004 for the NBS 987 standard was also obtained. Uncertainties are quoted as 2σ. $^{87}Rb/^{86}Sr$ ratios were calculated from Rb/Sr concentrations obtained by XRF analysis. Assigned uncertainties were 1 % for $^{87}Rb/^{86}Sr$ and 1 % and 0.4 % for Rb and Sr determinations, respectively (Mader and Koeberl, 2009; Nagl and Mader, 2019; Son and Koeberl, 2005). All these isotope results are compiled in Table S5.

6.3.2.4 U-Pb isotopy

In addition to the results for four basement rocks and five impactite samples already obtained by Guerrero (2024, 2025 - in review), eight further basement samples (C220506-0954, C180824-1645, C220607-1115, C220511-1352, C220608-2001, C180824-1630, C220607-1502, and C220514-1340) were selected for U-Pb isotopy on zircon for this present analytical study. Sample preparation was done at LEGGA by crushing, grinding, magnetic separation, and handpicking of zircon. Backscattered electron (BSE) and cathodoluminescence (CL) images of the zircon mounts were obtained at the Microanalysis Laboratory of the Geosciences Institute of the Federal University of Pará (UFPA) with a MEV Zeiss model LEO-1430 and a MEV Zeiss model SIGMA-VP coupled with a cathodoluminescence Gatan Chroma CL2, respectively. The operation conditions were an acceleration voltage of 20 kV, electron beam current between 80-90 µA, and working distance between 15-17 mm.

The U-Pb analyses were conducted by laser ablation inductively coupled plasma–mass spectrometry with a quadrupole type mass analyzer (LA-Q-ICP-MS) at the Isotopic Geology Laboratory (Pará-Iso) of the UFPA. The analyses were done with

a Thermo Fisher iCAP-Q and a 213 nm laser probe LSX-213 G2 CETAC. The laser operation conditions are spot size of 25 µm, a frequency of 10 Hz, and a fluence of 4-5 J cm^{-2}. Each analysis consisted of 20 s of background measurement followed by 40 s of sample ablation. The acquisition and reduction of raw data were done with the software Qtegra and a Microsoft Excel macro (Miranda et al., 2023). The mass-bias fractionation correction was done by normalizing to the GJ-1 zircon reference material (601.7 ± 1.3 Ma; Jackson et al., 2004), and the BlueBerry reference material (BB; $^{206}Pb/^{238}U$ age of 560 ± 1.1 Ma; Santos et al., 2017) was measured as secondary standard. The correction for common Pb was done using the model Pb composition of Stacey and Kramers (1975). All ages are reported at the 95 % confidence level (2σ uncertainty) and do not reflect external (systematic) uncertainties.

The f_{206} values, which indicate the non-radiogenic fraction of ^{206}Pb, are estimated as $f_{206}=[^{206}Pb/^{204}Pb]_{common}$ / $[^{206}Pb/^{204}Pb]_{sample}$. The discordance is calculated as $^{206}Pb/^{238}U$ age x 100 / $^{207}Pb/^{235}U$ age (7/5:6/8 discordance for short). Data with discordance > 10 % and with errors of the apparent $^{206}Pb/^{238}U$ age > 5 % were not used. The results are presented in Tera-Wasserburg plots developed with Isoplot v. 4.15 (Vermeesch, 2018a), and in histograms, probability density plots, and kernel density estimations made with the software DetritalPy v. 1.3 (Sharman et al., 2018). Furthermore, nonmetric multidimensional scaling (MDS) models are developed with the provenance package in R using the Kolmogorov-Smirnov test, which is based on the maximum separation between cumulative distribution functions (Vermeesch et al., 2016). See Table S6 for the results.

6.4 Results

6.4.1 Petrography

The selected impactites were classified as monomict lithic impact breccia, suevites, and impact melt rocks (Table 6.1). These samples contain heterogeneous clast populations of lithic and mineral clasts derived from mainly gneissic and granitic

protoliths (Figure 6.2-6.4, and S1). Any fragments smaller than 200 μm are considered part of the matrix. The petrographic classification of these clasts is based on their textures, mineral compositions, and the correlation with observations made on hand specimens (Figure 6.2). The most common lithic clasts in the analyzed samples display minerals with lepidoblastic or nematoblastic textures, or bands of different compositions, and are assumed to be derived from gneissic protoliths. Within this group, the proportions of feldspar, biotite, and opaque phases were used to further classify these clasts as para- or orthogneiss clasts. Lithic clasts with minor or no biotite or opaque phases, and rich in feldspar are interpreted as likely being derived from a leptynitic protolith. In contrast, clasts with a higher proportion of phyllosilicates and opaque phases are assumed to be derived from paragneisses. Another, less abundant, type of lithic clasts are the ones derived from granites or granodiorites, where the minerals lack any preferred orientation. These clasts can display different textures and grain sizes but were grouped together to facilitate comparisons between different samples. Additionally, clasts of quartz aggregates not oriented, with a jigsaw texture, are very common. These clasts may have originated from the numerous quartz veins intersecting the metamorphic rocks or could represent remnants of igneous lithologies. The modal composition of the samples and the proportion of shock deformation features in different minerals are provided in Tables S2 and S3.

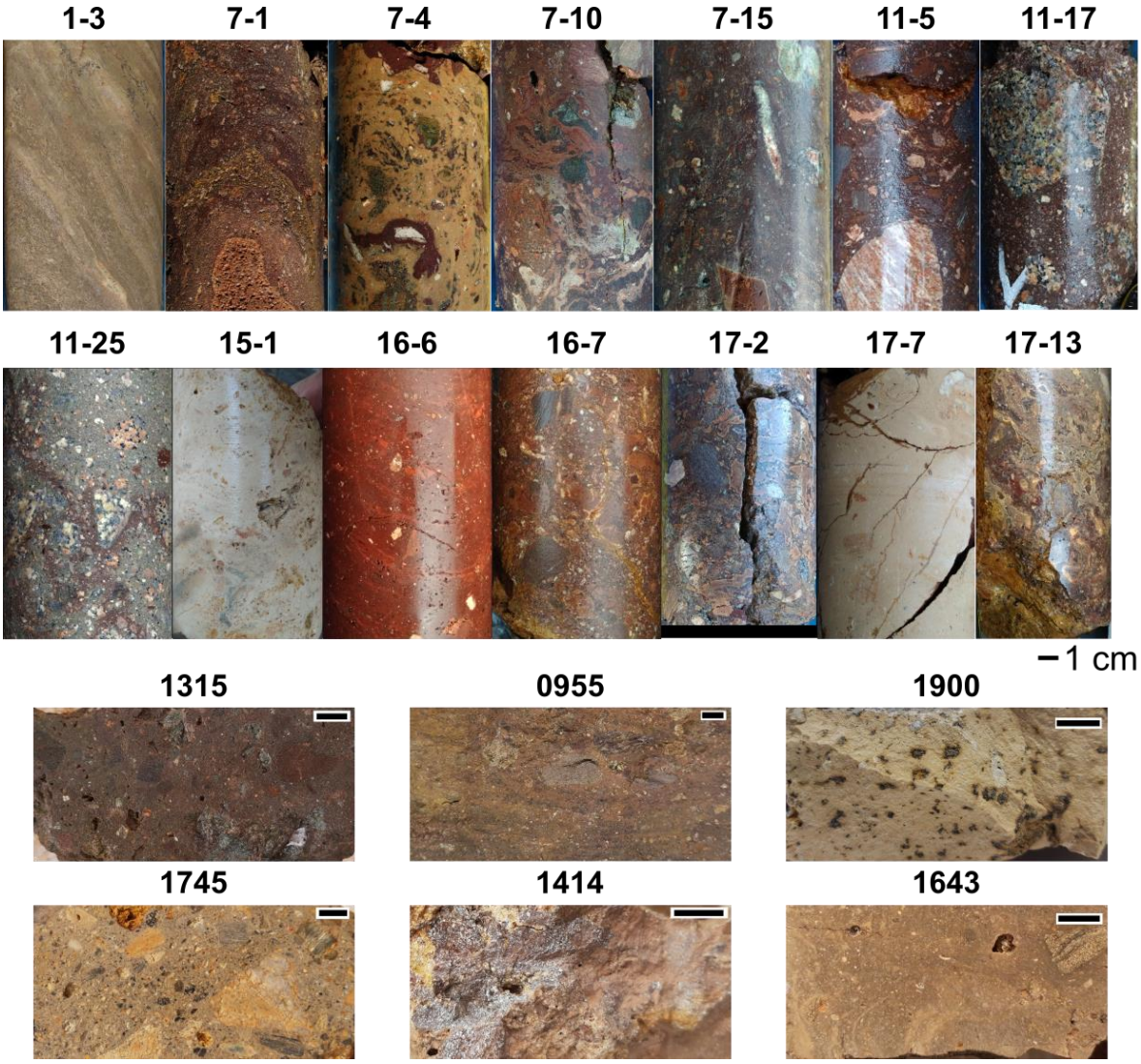


Figure 6.2 Photographs of the hand-specimens of the drill-core samples (first two rows) and surface samples (next two rows) of the impactites analyzed in this study. Scale bars at the upper right corner of the surface samples correspond to 1 cm.

6.4.1.1 Monomict lithic breccias

Both lithic impact breccia samples (11-17 and 11-25) are very similar, with a fine-grained matrix with reddish and greenish coloration with subhedral mineral debris and lithic clasts, which are poorly sorted, and of granitic composition (Figure 6.2). The petrographic analysis of the samples shows a fine-grained clastic matrix with some regions with oxide or oxyhydroxide staining (25.3-42.2 vol%), with vesicles (4.9-0.8 vol%), and lithic (44.1-60.5 vol%) and mineral clasts (9.4-13 vol%) (Figure 6.3). The lithic and mineral clasts have sizes that are generally < 500 μm but can be up to 9 mm and 2.1 mm, respectively.

In both samples, the lithic clasts are made of quartz aggregates or different proportions of quartz, plagioclase, orthoclase, and minor biotite (Figure 6.4a). Some clasts show fractures filled by secondary carbonate. None of these clasts show minerals with a preferred orientation. In sample 11-25 a carbonate clast was identified, the only one found in all the rocks analyzed. Mineral clasts correspond to the same phases present in lithic clasts. Some plagioclase is altered to sericite.

The clasts in these samples are unshocked or have a very low level of shock metamorphism. The only deformation styles observed are biotite with reduced birefringence or kink bands (Figure 6.5f), and toasted quartz grains, quartz with mosaicism, planar fractures with multiple orientations (PFs).

6.4.1.2 Suevites

All suevite samples have an aphanitic, essentially clastic matrix (51-58.8 vol%) with different proportions of vesicles (0.3-8.5 vol%), very heterogeneous lithic (2.2-11.1 vol%) and mineral clast (22.8-32.3 vol%) populations, and melted and partially recrystallized (annealed) debris (5.2-10.6 vol%) (Figure 6.3). The Valette sample (7-10) has a higher proportion of clasts and corresponding lower proportion of matrix and vesicles than the other two samples. In the Chassenon sample (C220805-1315), the matrix is gray-green, in the Videix suevite (C220510-1745) it is yellow, and in the Valette sample it has a reddish coloration (Figure 6.2). The melt clasts in the three samples have irregular forms and can be found recrystallized to very fine-grained microliths. In the Chassenon sample these clasts are mostly gray and black, in the Videix sample colorless, and in the Valette sample they are yellowish and reddish (Fig. S2b).

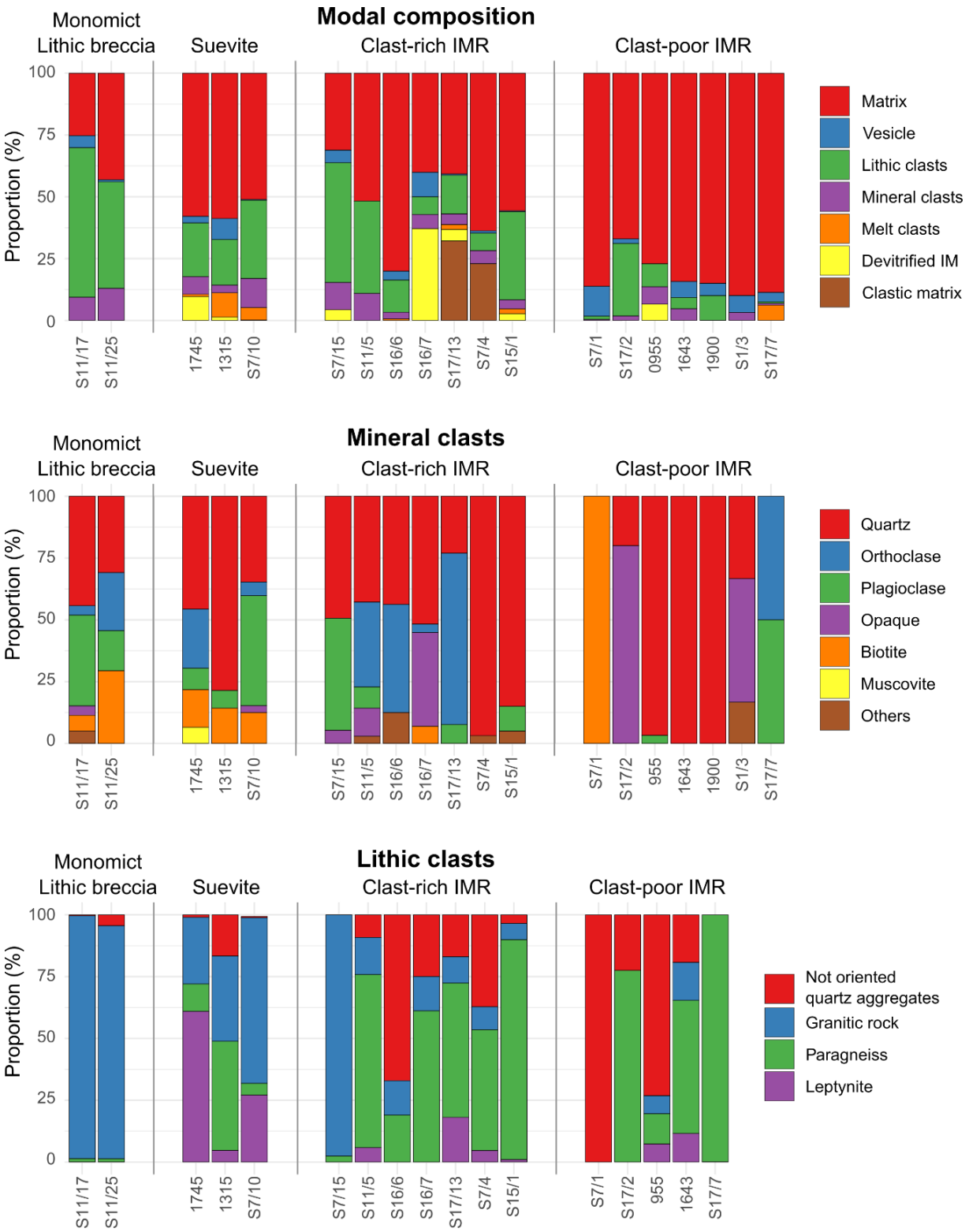


Figure 6.3 Composition of the impactites determined with the petrographic analysis of main components and types of mineral and lithic clasts. IM- impact melt.

The lithic clasts in these three samples are heterogeneous. In hand-sample, the Valette suevite shows the highest diversity of lithic clasts, which includes gneisses with different coloration and granites (Table S1). In thin sections, most of the clasts are quartzofeldspathic aggregates with minor biotite – likely derived from a granitic protolith, and to a lesser proportion, clasts may have a gneissic protolith (with the same mineral composition but where the mineral phases have a preferred orientation) (Figure 6.3). The mineral clasts are derived from the same precursors, and principally are plagioclase and quartz. The hand-samples from Chassenon and Videix show lithic clasts derived from gneisses, and most of the clasts observed in thin-section are probably derived from this lithology as well (Figure 6.4c and e). In the Chassenon suevite the clasts mainly come from paragneisses, whereas in the Videix suevite they are mostly from orthogneisses. Furthermore, there are also some lithic clasts with phases without any preferred orientation that are presumed to be derived from a granitic protolith. In these samples the principal mineral clasts are quartz and biotite, and in the Videix sample also orthoclase. All these clasts show heterogeneous levels of shock deformation or shock-related part-melting, including recrystallized quartz, toasted quartz, quartz with PFs and up to two sets of PDFs, feldspar with checkerboard texture, and kink bands in micas (Figure 6.5).

6.4.1.3 *Impact melt rocks*

The matrix of these samples can be yellow or red, and is very fine-grained, microcrystalline, or hypohyaline with tiny microliths. Almost all samples show fluidal textures, marked by melts with different colorations, and in some samples by varied proportions of clasts (Figs. S3d and S3e). A red oxide or oxyhydroxide staining is also common (Fig. S3b). The matrices are commonly vesicular, and vesicles (0.3-12.13 vol%) are in part filled by secondary quartz, feldspar, or phyllosilicate phases (Sapers et al., 2014). The content of lithic and mineral clasts in these impact melt rocks is varied, and the samples can be classified as clast-poor (< 10 vol%) and clast-rich lithologies (12.32-48.3 vol%) (Figure 6.3). In general, these clasts are poorly-sorted in most of the samples. The lithic clast populations are similar to the ones described in previous lithologies, with clast sizes mostly up to 2 mm, but up to 5.2 mm in clast-rich types. The mineral clasts are quartz, feldspars, opaques, and

micas, and can also have sizes up to 3.5 mm, but mostly they are < 500 µm. Plagioclase in clasts is frequently sericitized, mica is partially oxidized, and sometimes quartz shows graphic texture.

For most of the clast-poor IMRs, the hand-samples only indicate lithic clasts derived from gneisses. Only sample 7-1 also has clasts without a preferred orientation (Figure 6.2 and S1). In thin sections, the most common clasts in all these samples are recrystallized quartz. Besides this, clasts are probably derived from paragneisses in the form of quartzofeldspathic aggregates with oxidized biotites in lepidoblastic texture or with bands of different compositions. There are also quartzofeldspathic aggregates with minor proportions of biotite or opaque phases that can in part have a preferred orientation (Figure 6.4d). This probably indicates leptynitic protoliths. Some of these quartzofeldspathic clasts show strong thermal alteration.

The clast-rich impact melt rocks have more heterogeneous clast assemblages. Clasts from gneissic or granitic protoliths are seen in all hand-samples. However, in thin section most clasts have gneissic origin. The only exceptions are samples 16-6 and 0955, where the majority of clasts are quartz aggregates without mineral orientation. Sample 11-5 has the highest diversity of clasts and is the only sample where a paragneiss clast has an overgrowth of a phase cutting the original lepidoblastic texture. This phase is strongly altered to mixtures of phyllosilicate and Fe- and Mn- rich secondary phases (oxides or oxyhydroxides) (Figure 6.4f). Furthermore, in this sample and in samples 16-7 and 17-13, very fine-grained quartzofeldspathic clasts with opaque phases are also observed, which are devoid of a preferred orientation. Sample 7-15 shows a high proportion of recrystallized quartzofeldspathic clasts with granophyric texture.

Clasts of glass/melt are also observed. These clasts have irregular forms, are isotropic and can be reddish, yellowish or brownish in plane polarized light. They sometimes are vesicular and may show chemical alteration haloes (Fig. S2).

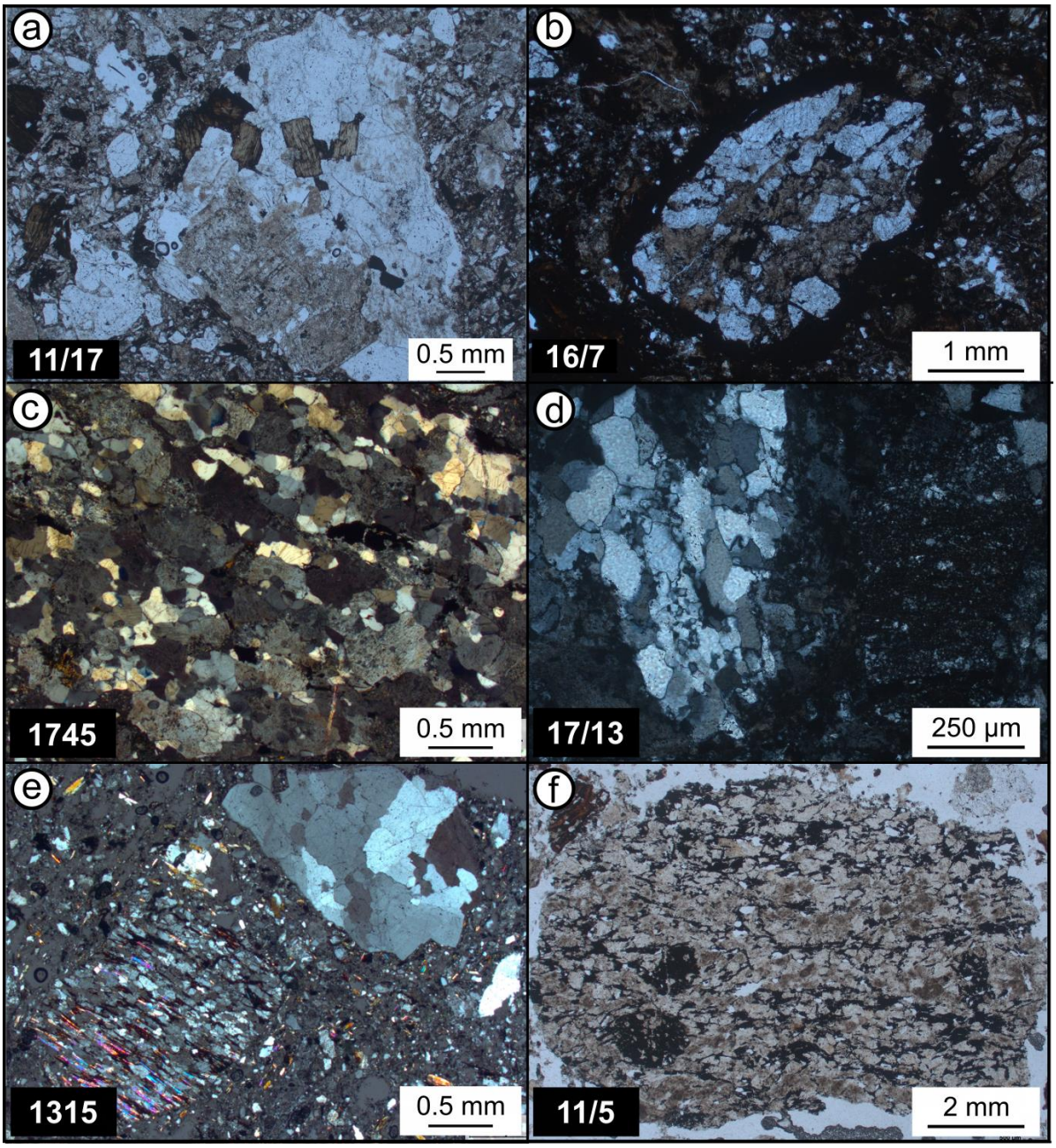


Figure 6.4 Microphotographs showing the diversity of clast types found in the impactites. The images (a, b, and f) were taken with plane-polarized light. (a-b) Quartzofeldspathic clasts without banding, likely derived from granitic rocks. (c-d) Clasts mainly composed of quartz and/or feldspar (sometimes altered) with a clear orientation of the minerals, probably derived from leptynitic gneisses. (e-f) Clasts of different proportions of quartz, feldspar, and biotite (sometimes oxidated). The biotite has a lepidoblastic texture that defines the texture of these clasts, which are probably derived from paragneisses. (e) Clasts of quartz aggregates without orientation, these clasts could be derived either from granitic rocks or quartz veins of a gneiss.

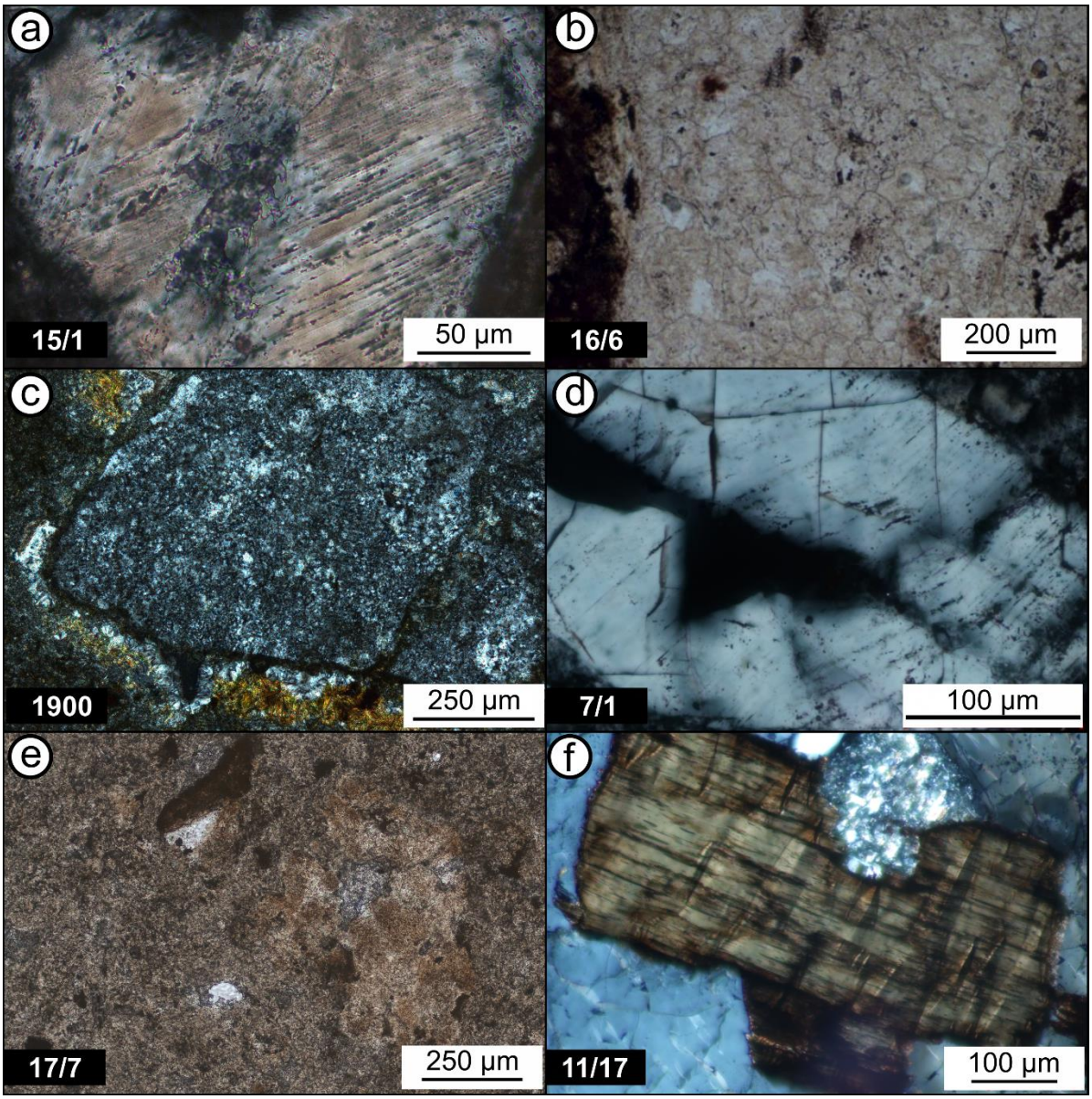


Figure 6.5 Microphotographs of some of the types of deformation found in mineral and lithic clasts of the impactites. Only images (b and e) were taken with plane-polarized light. (a) Toasted quartz clast with two sets of PDFs. (b) Ballen silica. (c) Recrystallized quartz clast. (d) Quartz clast with two sets of PDFs and PFs. (e) Thermally altered orthoclase. (f) Biotite with kink bands.

The deformation of the clasts is also diverse, especially in the clast-rich IMRs, and includes kink bands in mica; quartz with undulous extinction, PFs, FFs, and/or PDFs; clasts of quartz, feldspar, or mica that are partially melted or exhibit reduced birefringence; toasted quartz; recrystallized quartz with a very fine-grained mosaic texture; and ballen quartz. (Figure 6.5). Toasted quartz is very abundant. Quartz clasts with multiple sets of PDFs are seen in samples 7-10, 7-15, 11-5, and 15-1 (Figure 6.5), and four samples (1900, 7-14, 16-6, and 17-2) have rare ballen quartz

clasts that can be classified into types 3, 4 and 5 (individual ballen with homogeneous or heterogeneous extinction, respectively, or completely recrystallized), according to Ferrière et al. (2009) (Figure 6.5b).

6.4.2 Whole rock geochemistry

Major, minor, and trace element geochemical data for the basement rocks and the impactites are provided in Table S4. The data from basement and impactite samples are presented in Harker diagrams (Figure 6.6 - 6.7, and S4 - S5) and multielement spider plots (Figs. S6 - S8). The geochemical data available from the literature are plotted for comparison in each diagram.

6.4.2.1 Basement rocks

The basement rocks of the Rochechouart impact structure are very heterogeneous in composition, and four main subdivisions can be made based on the silica content (Figure 6.6). The serpentinite has the lowest values of SiO_2 (39.03 wt%), followed by the amphibolites (~52 wt%), rocks with intermediate silica content, including granodiorites, diorite, paragneisses, and UGU leptynitic gneiss (59.97- 67.35 wt%), and the group with the highest contents of silica, which includes the granites, the pegmatite, and the LGU leptynitic gneiss (75.58-78.4 wt%). The SiO_2 is positively correlated with K_2O and has a general negative correlation with the other major elements. The serpentinite has the most contrasting composition of all samples, with the lowest contents of Al_2O_3 (4.51 wt%), Na_2O (0.11 wt%), K_2O (0.01 wt%), and the highest contents of TiO_2 (1.59 wt%) and MgO (33.1 wt%). The amphibolite samples have similar compositions, with the Exideuil sample being slightly more mafic. The serpentinite and the amphibolites show the highest MnO content (0.19-0.22 wt%). The group with an intermediate silica content is more heterogeneous, with strong scattering in the contents of Al_2O_3 (13.73-16.94 wt%), Fe_2O_3 (2.52-7.14 wt%), and MgO (1.4-5.15 wt%). Furthermore, this group, along with the samples with the highest contents of silica, are characterized by very heterogeneous values of CaO (0.27-3.94 wt%), Na_2O (2.08-5.75 wt%), K_2O (1.68-5.20 wt%), and P_2O_5 (0.04-0.22 wt%), which do not follow a clear correlation with the content of SiO_2. Finally, the most felsic group is characterized by very limited variations and the lowest values of

Fe_2O_3 (0.57-1.22 wt%), MgO (0.31-0.68 wt%), and TiO_2 (0.02-0.04 wt%). The amphibolites and the granodiorite from Exideuil are the only metaluminous rocks from the basement, whereas the other basement samples are calc-alkaline.

In the multielement, primitive mantle normalized plot (Fig. S8), it is observed that except for the concentrations of serpentinite, the trace element contents have a negative correlation with SiO_2. All lithologies exhibit positive anomalies of U, Ta, and Pb, whereas the amphibolites and intermediate silica rocks also show a positive Nd anomaly. Negative Nb and Ti anomalies are present in all samples except for the serpentinite. Additionally, the serpentinite is enriched in Cr and Ni. The amphibolites and the rocks with an intermediate silica content are within similar ranges (ΣREE = 110.45), whereas the serpentinite and the more felsic rocks have lower values (ΣREE = 12.10-35.15). Furthermore, except for the serpentinite, the granite from Champagnac, and the diorite, most samples show a negative Eu anomaly. This anomaly is more pronounced in the felsic rocks (Eu/Eu* = 0.51-0.72) than in the intermediate silica group and the amphibolites (Eu/Eu* = 0.63-0.91).

6.4.2.2 Impactites

Harker diagrams (Figure 6.7 and S5) show that the IMRs are characterized by a rather wide range of SiO_2 content (60.84 to 70.3 wt%), with a suevite and a yellow IMR as positive outliers and a yellow IMR as a negative outlier. The suevites and monomict lithic breccias have a slightly more restricted range of SiO_2 content (between 66.45 and 73.41 wt%). Similarly, Al_2O_3 content varies significantly in the IMRs (13.84 to 18.53 wt%), whereas the monomict lithic breccias and suevites show a more limited range (13.93 to 15.40 wt%). The highest TiO_2 value was determined for the IMR (0.58 to 0.96 wt%), followed by the suevites (0.54 – 0.69 wt%), and the monomict lithic breccias (0.36 - 0.43 wt%). Fe_2O_3 is generally higher in the red IMRs from Montoume (6.23 – 6.68 wt %), and the lowest values were determined for yellow IMRs and the Videix suevite (0.49-3.28 wt%). The MgO content in the IMRs varies from 0.26 to 2.85 wt%, with higher values in samples from Chassenon and Valette, and lower values for the samples from Recoudert and Montoume. The Chassenon suevite has the highest value (3.18 wt%), and the other

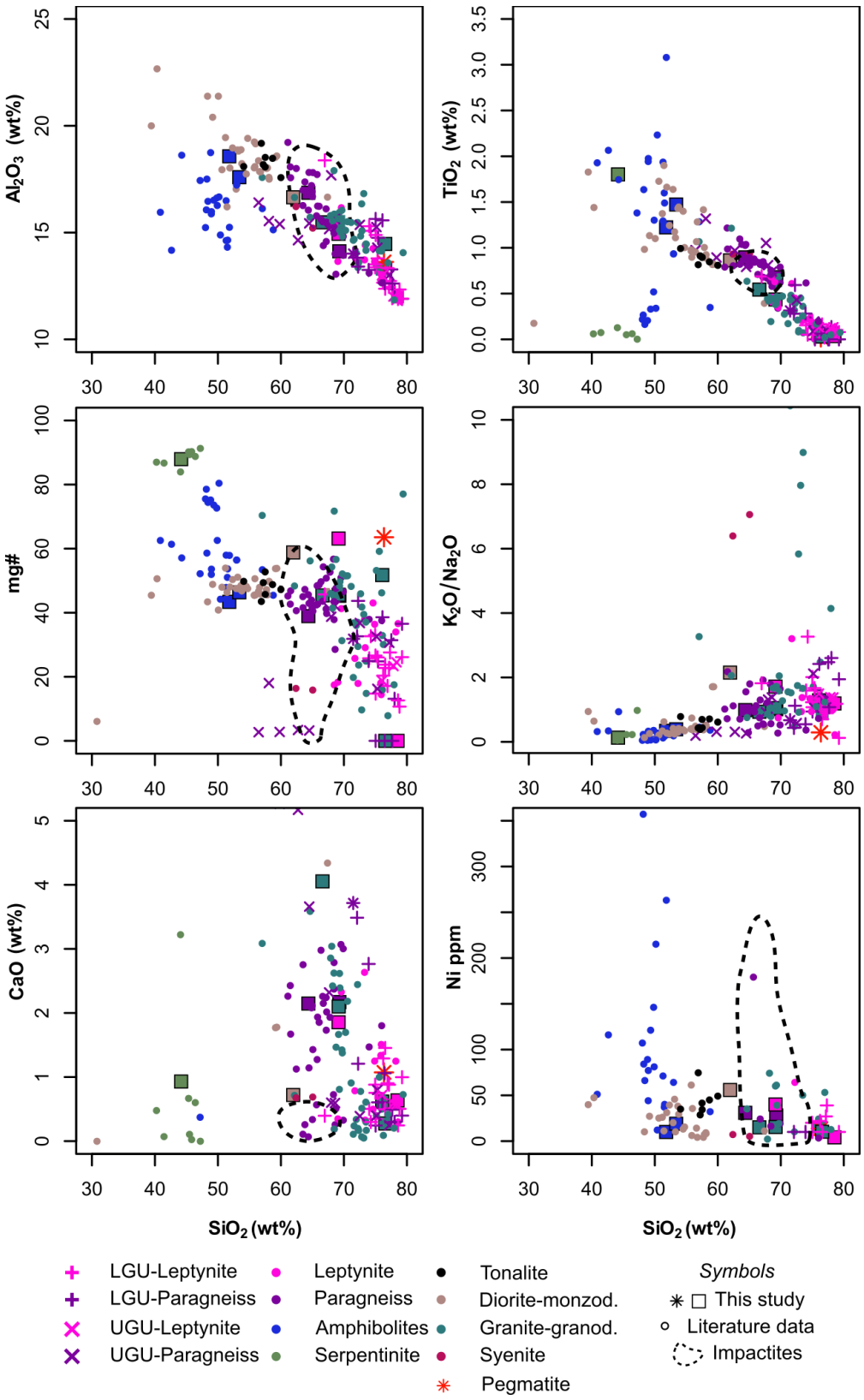


Figure 6.6 Harker plots of SiO_2 versus major elements for the basement samples of this study. Literature data taken from Bambier et al. (1983), Chèvremont et al. (1996), El Korh et al. (2020), Faucher (2021), Lambert (1977), Reimold et al. (1983), and Reimold and Oskierski (1987). LGU – Lower Gneiss Unit, UGU – Upper Gneiss Unit.

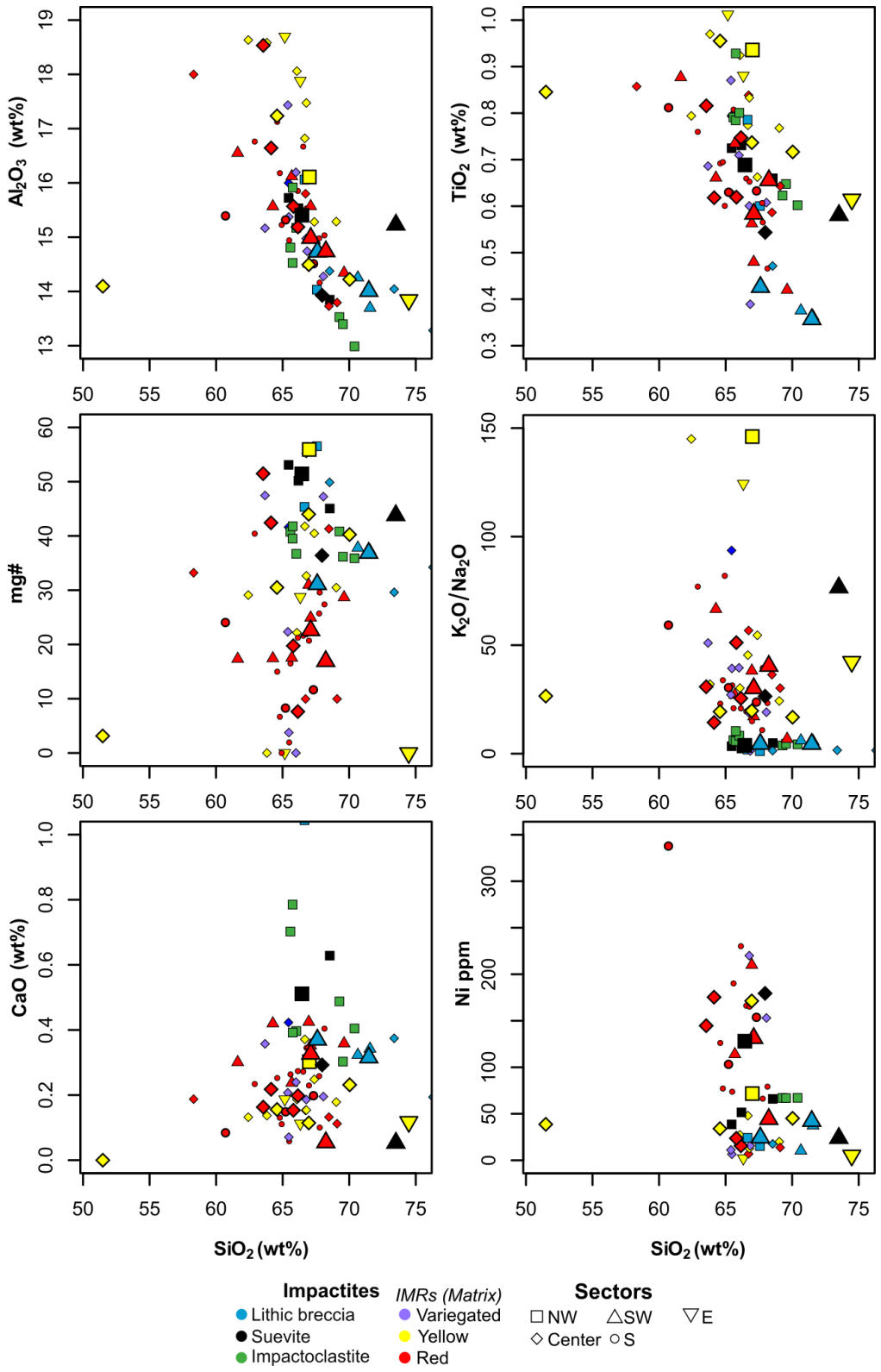


Figure 6.7 Harker plots of SiO_2 versus selected major elements, mg#, the ratio K_2O / Na_2O, as well as the abundances for Ni for the impactites analyzed in this study in comparison with literature data (smaller symbols). The colors indicate the lithology and the symbols the location of the samples. The lithic breccia symbol represents the monomict breccias of this study and the monomict and polymict lithic breccias of the literature. Literature data for the impactites taken from Chèvremont et al. (1996), Faucher (2021), and Tagle et al. (2009).

suevites and lithic breccias range from 0.62 to 1.62 wt%. The mg# value is generally lower for the red IMRs than for the other impactites. (Figure 6.7).

In general, higher CaO and Na_2O values and lower K_2O contents are recorded for the breccias and the suevites (Figure 6.7 and S5). The CaO content of the breccias and suevites ranges from 0.29 to 0.51 wt%, whereas in the IMRs it ranges from 0 to 0.23 wt%. For Na_2O, the highest values are observed in the breccias and Chassenon suevite (1.59 – 1.64 wt%), whereas the other suevites and IMRs fall into a similar range (0.05 – 0.77 wt%). The lowest concentrations of K_2O are in the breccias and Chassenon suevite (6.0 – 7.3 wt%), followed by the other suevites (8.2 – 9.4 wt%) and the IMRs (7.4 – 12.2 wt%). This trend is more clearly observed in the K_2O / Na_2O ratios (Figure 6.7).

The highest Ni values are recorded for red IMRs (100-339 ppm). Both types of IMRs have comparable values and quite high contents of V, Ga, Sc, some HSFE (Zr, Hf, Nb), and REE compared to the other impactites (Figs. S6-S7). Strontium, Cr, Ta, and Th contents are higher in the monomict lithic breccias than in the other impactites. The Rb contents of the IMRs show a strong scattering and generally higher values than observed for the other lithologies.

In the multielement, primitive mantle normalized, plot (Fig. S7), all lithologies have negative Nb, Sr, and Ti and positive U, Pb, and Nd anomalies, with Ta and P scattering significantly. In the chondrite normalized REE plot (Fig. S6), all samples follow a similar pattern very close to the one of the upper continental crust (e.g., Best, 2003). The red IMRs have the widest range and the highest LREE enrichment (ΣLREE = 62.7 - 222.9), followed by the yellow IMRs (ΣREE = 80.7 - 227.3), and the suevites and lithic breccias (ΣLREE = 86.7 - 112). The IMRs and the suevites have a similar enrichment of LREE relative to HREE (median $(La/Yb)_N$ = 7.7 - 8.9). This enrichment is lower than that of the monomict breccias ($(La/Yb)_N$ = 13.5). All impactites have a negative Eu anomaly. This anomaly is smaller for the yellow IMRs (Eu/Eu* = 0.67 - 0.85), and larger for the monomict breccias (Eu/Eu* = 0.57 - 0.58).

6.4.3 Strontium and Sm-Nd isotopic results

The isotopic results are provided in Table S5 and are plotted in Figure 6.8.

6.4.3.1 Basement rocks

The $^{147}Sm/^{144}Nd$ vs. $^{143}Nd/^{144}Nd$ plot (Figure 6.8a) shows that the $^{147}Sm/^{144}Nd$ ratios of most basement rocks are within the range from 0.0917 to 0.1403. However, the pegmatite and the serpentinite are two positive outliers, with values of 0.2024 and 0.2597, respectively. Most lithologies have $^{143}Nd/^{144}Nd$ ratios in the range from 0.512292 to 0.512574. Slightly higher values are registered for the amphibolites, paragneisses, and the granodiorite from Exideuil, whereas the other granitic rocks and the UGU leptynitic gneiss have lower values. Outside this range lie the serpentinite (0.512764 ± 26) and the two negative outliers, the LGU leptynitic gneiss and the granite from Les Neples – Chéronnac. Using the age of the impact event at 206.92 + 0.20 / - 0.32 Ma (Cohen et al., 2017), the εNd(t) values range mainly from -6.5 to 0.8, and the LGU leptynitic gneiss and the granite from Les Neples – Chéronnac also represent negative outliers, with values of -12.71 and -12.37. Calculated T_{DM} values mainly range from 1.53 to 0.92 Ga. The $(^{87}Sr/^{86}Sr)t$ ratios are more homogeneous, with most of the samples falling into the range from 0.7050 to 0.7121, with the same outliers as for the $^{143}Nd/^{144}Nd$ ratio and the εNd(t). The granite has the highest value of 0.7208, and the LGU leptynitic gneiss the lowest at 0.701098 (Figure 6.8b).

6.4.3.2 Impactites

The impactites have $^{147}Sm/^{144}Nd$ ratios ranging from 0.1011 to 0.1369, $^{143}Nd/^{144}Nd$ ratios mostly between 0.512268 and 0.512489, and εNd(t) values, calculated to the impact age, between -4.83 and -1.09 (Figure 6.8). A trend is observed, in which the monomict lithic breccia and the suevite from the SW have the lowest values for these three parameters, whereas the Chassenon suevite shows some of the highest values. The IMRs fall in between, and the yellow variety shows higher values than the red (Figure 6.8). T_{DM} values range from 1.3 to 0.98 Ga. The $(^{87}Sr/^{86}Sr)t$ ratios of the impactites, calculated to the impact age, range from 0.6915 to 0.7166. The highest value is registered for the suevite from the SW and the lowest in the yellow IMR from Chassenon. The IMRs show more scattered ratios compared to the other impactites.

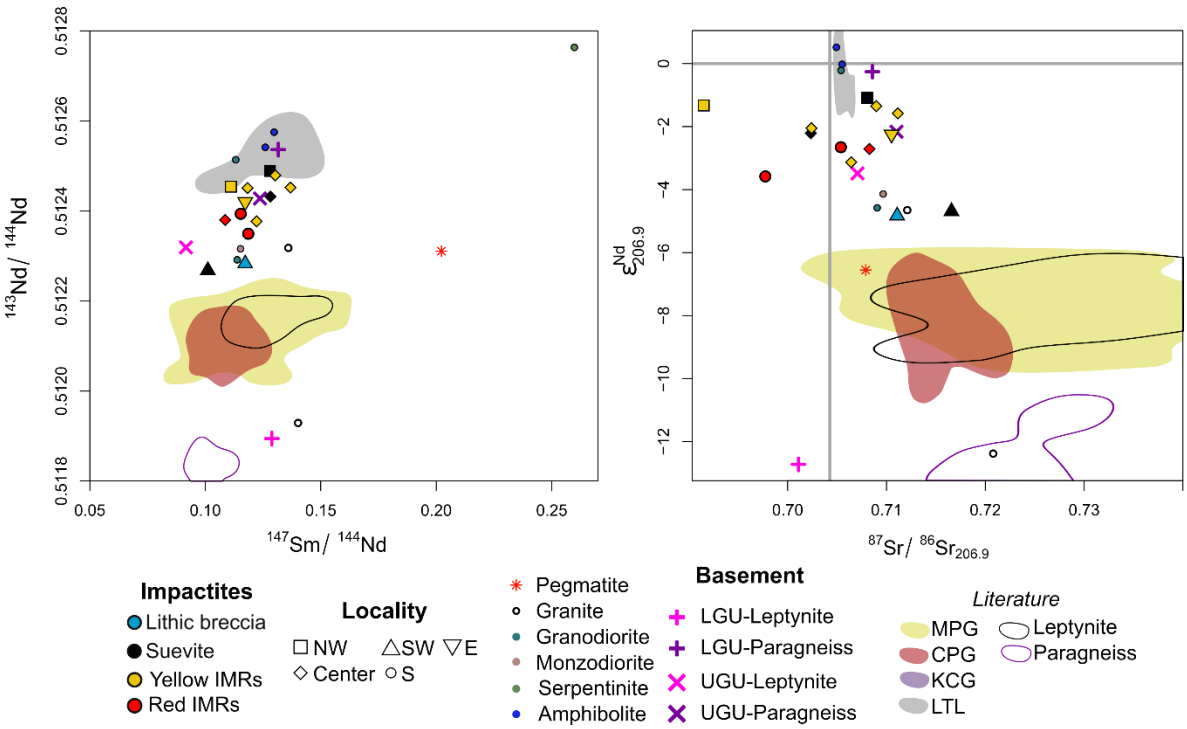


Figure 6.8 (a)$^{147}Sm/^{144}Nd$ vs. $^{143}Nd/^{144}Nd$ and (b) ($^{87}Sr/^{86}Sr$)i vs. εNd(t) diagrams for the samples analyzed in this study recalculated to the impact age (206.92 + 0.20 / - 0.32 Ma; Cohen et al., 2017). Unfilled fields represent literature data for gneisses, while filled fields correspond to literature data for various granitoid types in the Limousin region of the FMC. The granitoid categories include muscovite-bearing peraluminous granitoids (MPG), cordierite-bearing peraluminous granitoids (CPG), K-feldspar porphyritic calc-alkaline granitoids (KCG), and the tonalite line of the Limousin (LTL) formed by amphibole-rich calc-alkaline granitoids. LGU – Lower Gneiss Unit, UGU – Upper Gneiss Unit, IMR – Impact melt rock. Literature data taken from Moyen et al. (2017).

6.4.4 U-Pb zircon isotope results

The U-Pb zircon geochronologic results are provided in Table S6 and are plotted in Tera-Wasserburg plots (Figure 6.9) and probability density plots (PDP) and kernel density estimations (KDE) for the apparent $^{206}Pb/^{238}U$ ages of the basement rocks analyzed in this study (Fig. S9).

UGU paragneiss (C220506-0954): Seventy-two analyses from 72 grains were obtained. Of these, 60 analyses yielded low error and low discordant ages. The data are scattered along the concordia line and are mainly between 451 ± 14 and 741 ± 16 Ma (Figure 6.9a). Three grains yielded older ages (1199 ± 55 to 1457 ± 56 Ma). The KDE plot shows two age peaks, the principal one at 533 and a secondary one at 458 Ma (Fig. S9). A large proportion of the data extends to the Neoproterozoic. Most of these ages were recorded in grains with oscillatory zoning texture, some

with local recrystallization or metamorphic overgrowth, and a smaller proportion in grains with irregular zoning. The principal peak at 533 Ma is related to grains with homogeneous texture and a few grains with sector zoning.

UGU leptynite (C180824-1645): Thirty-two analyses were obtained in 32 zircons. Of these, 20 were validated. The ages mainly range from 342 ± 13 to 509 ± 11 Ma, with only one grain yielding an older age of 2704 ± 24 Ma. In the KDE plot, two age peaks are obtained at 481 and 354 Ma (Fig. S9). In the Tera-Wasserburg plot, a concordia age of 353 ± 5 Ma was determined for data from four grains of homogeneous texture in the CL images (Figure 6.9b). The other analyses are distributed along the concordia line, which makes it difficult to calculate a reliable concordia age. Most of these grains have an oscillatory zoning texture, some with local recrystallization or metamorphic overgrowth. The older ages were measured in the inherited cores of analyzed zircon.

LGU leptynite (C220607-1115): In this sample, 34 spots were analyzed in 33 zircon crystals. Of these, 18 analyses made on 18 grains had good statistics. The ages range from 358 ± 10 to 506 ± 10 Ma. In the Tera-Wasserburg plot, a concordia age of 482 ± 3 Ma was determined for data from 10 grains that mostly have homogeneous texture with local recrystallization or metamorphic overgrowth (Figure 6.9c).

Exideuil granodiorite (C220511-1352): Thirty-seven analyses were done in 37 grains. Only one analysis was discordant with high errors. The ages range from 347 ± 9 Ma to 385 ± 9 Ma. Two zircons yielded older ages at 410 ± 10 and 440 ± 10 Ma. Two age peaks are obtained in the KDE, the principal one at 356 and a minor one at 385 Ma (Fig. S9). In the Tera-Wasserburg plot, a concordia age of 360 ± 2 Ma was determined for data from 32 grains (Figure 6.9d). Most of these grains have oscillatory zoning texture, some with local recrystallization or metamorphic overgrowth, and very few have inherited cores.

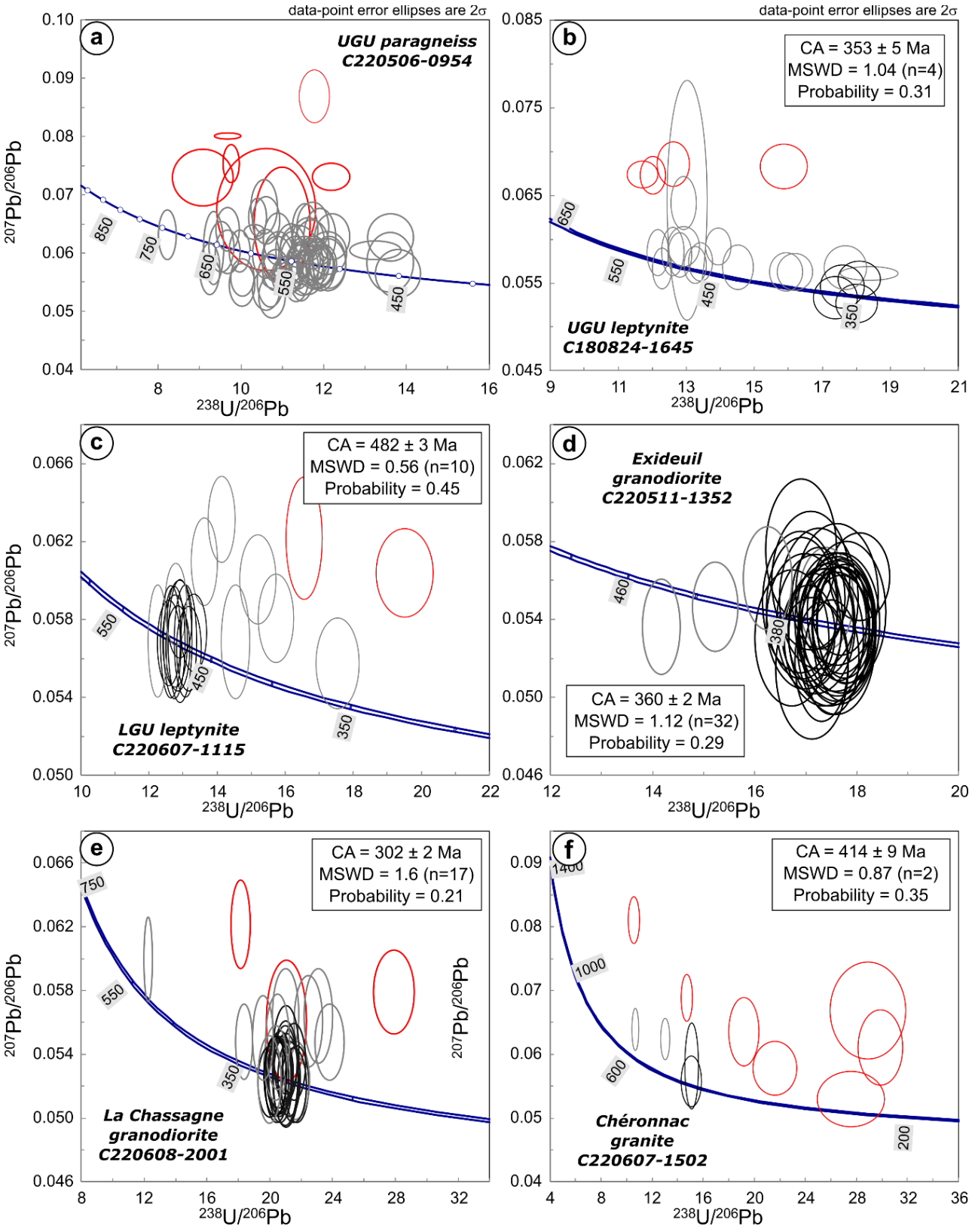
La Chassagne granodiorite (C220608-2001): Thirty-nine spots were analyzed on 38 zircon grains. Thirty analyses on 30 zircons yielded concordant and low error ages, which range mainly from 265 ± 8 to 342 ± 8 Ma, with three grains yielding older ages

(506 ± 9, 984 ± 11, and 1853 ± 35 Ma). A concordia age of 302 ± 2 Ma was obtained for data from 17 grains (Figure 6.9e), all with oscillatory zoning texture, some with local recrystallization, and a few with inherited core.

Chéronnac granite (C220607-1502): In this sample 21 analyses were made in 21 crystals. Only four analyses yielded low error and low discordance ages. The ages are between 413 ± 12 and 576 ± 12 Ma. The two grains with the youngest ages yielded a concordia age of 414 ± 9 Ma (Figure 6.9f). These grains have oscillatory texture.

Champagnac granite (C180824-1630): Twenty-nine analyses on 29 zircon crystals were made. Of these, 13 analyses yielded good statistics. The ages are mainly between 261 ± 11 and 534 ± 17 Ma, with only one grain outside of this range (2058 ± 40 Ma). Two age peaks are obtained in the PDP, the principal one at 349 and another with fewer grains at 381 Ma (Fig. S9). In the Tera-Wasserburg plot, a discordia line calculated with seven grains has a lower intercept at 350 ± 12 Ma and an upper intercept at 1050 ± 70 Ma (Figure 6.9g). Most of these grains have oscillatory zoning texture, and some are homogeneous.

Champagnac pegmatite (C220514-1340): Twenty-three spots were analyzed in this sample on 22 zircons. Of these, only 11, made on 11 grains, could be validated. The ages range from 311 ± 14 to 563 ± 17 Ma, and one grain yielded an age of 3268 ± 18 Ma. In the PDP two ages are obtained, the principal one at 348 and a minor one at 393 Ma (Fig. S9). Most grains show oscillatory zoning textures. The few crystals with homogeneous textures yielded younger ages, and crystals with metamorphic overgrowth or irregular textures yielded older ages. The analyses are distributed along the concordia line in the Tera-Wasserburg plot and a concordia age of 484 ± 10 Ma was calculated for two grains (Figure 6.9h) with irregular and oscillatory zoning textures.


data-point error ellipses are 2σ
a
UGU paragneiss
C220506-0954
b
CA = 353 ± 5 Ma
MSWD = 1.04 (n=4)
Probability = 0.31
UGU leptynite
C180824-1645
c
CA = 482 ± 3 Ma
MSWD = 0.56 (n=10)
Probability = 0.45
LGU leptynite
C220607-1115
d
Exideuil
granodiorite
C220511-1352
CA = 360 ± 2 Ma
MSWD = 1.12 (n=32)
Probability = 0.29
e
CA = 302 ± 2 Ma
MSWD = 1.6 (n=17)
Probability = 0.21
La Chassagne
granodiorite
C220608-2001
f
CA = 414 ± 9 Ma
MSWD = 0.87 (n=2)
Probability = 0.35
Chéronnac
granite
C220607-1502
207Pb/206Pb
238U/206Pb

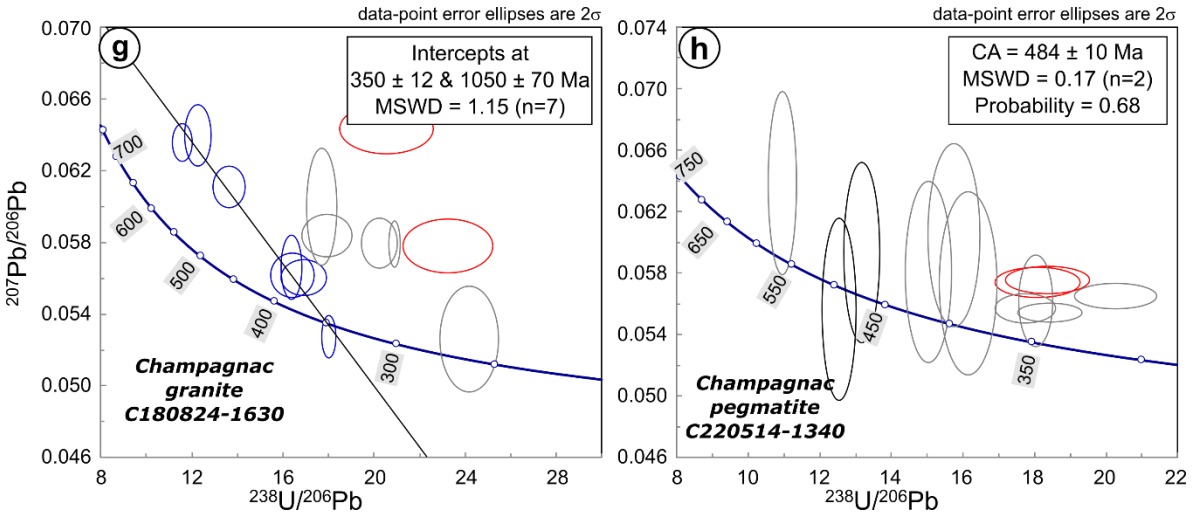


Figure 6.9 Tera-Wasserburg plots for the data from the basement rocks analyzed in this study. Data used for the estimation of concordia ages (CA) plotted in black, data used for the estimation of upper and lower intercepts plotted in blue, data not used for the determination of any age plotted in gray, and data with high error and/or high discordance plotted in red.

A small number of analyses with a discordance <10 % on the 7/5:6/8 ages and with errors of the apparent $^{206}Pb/^{238}U$ age < 5 % were obtained in the granites from Chéronnac (C220607-1502) and Champagnac (C180824-1630), as well as the pegmatite from Champagnac (C220514-1340). This limitation indicates that the zircon age distribution of these lithologies is probably not fully represented, and the ages obtained and calculated should be considered with caution. It is recommended to acquire additional data to more accurately represent the geochronologic information of these units. Nevertheless, preliminary provenance analysis has been carried out based on the available data for these three lithologies.

6.5 Discussion

In order to better understand the relationship between the impactites and the basement rocks of the Rochechouart impact structure, the results of this study are compared with existing geochemical, isotopic, and geochronological data from the literature. By integrating these findings, we aim to identify the most probable precursor rocks of the impactites.

6.5.1 Petrographic evidence for possible precursors lithologies of impact breccias

The petrographic classification of the clast populations into potential precursor lithologies is particularly challenging for clasts with a high level of shock deformation or significant weathering. In some cases, the primary texture of clasts that underwent partial or complete recrystallization may have been modified by the impact, and it is probable that some of the clasts containing minerals without any preferred orientation may have had a primary texture that is no longer preserved, leading to a potential overestimation of clasts derived from granitic rocks. Moreover, hydrothermal alteration is very common and principally affects the feldspars, which are in some cases significantly sericitized or completely replaced by fine-grained secondary phases. Consequently, this classification should be considered as an approximation towards the most likely precursor lithologies for such clasts.

In monomict lithic breccia 11-25, a single carbonate clast was identified, the only one among all analyzed samples. A previous finding of a carbonate clast in a polymict lithic breccia was reported by Sapers et al. (2009). They attributed it to a thin carbonate layer over the crystalline basement at the time of the impact (see also Lambert et al., 2019). Furthermore, sedimentary analysis of the suevites from the SC2 drill-core from Chassenon found evidence for reworking by high-energy water resurge into the crater in the first 39.8 m of melt-rich suevite, and accordingly, a shallow marine target environment was proposed (Ormö et al., 2023). However, the sedimentary cover would not have been significant and maybe restricted to the NW area of the structure (Sapers et al., 2009; Lambert, 2010; Lambert et al., 2019).

The modal analyses presented here (Table S2) show that the lithic clasts in most of our samples are of gneissic origin. The Chassenon suevite, along with the IMRs from Rochechouart, Babaudus, and Recoudert, contain lithic clasts derived from paragneisses. Only minor proportions of leptynite and granitic precursors are found in some samples (17-13 and 1643). Similarly, the Montoume impactites, apart from the clasts composed of quartz aggregates, are dominated by paragneiss clasts, followed by granitic clasts, with a minor presence of leptynite in one sample (955).

This is consistent with the most widespread LGU paragneiss unit at surface and the gneissic basement rocks in the drill-cores from Chassenon and Rochechouart, as well as the basement paragneisses and leptynites in the Recoudert drill-core and granitic rock and paragneisses in the Montoume drill-core.

In contrast, the Valette samples, from close to the center of the structure, show highly heterogeneous clasts populations. In the shallowest sample (7-1), only quartz aggregate clasts were identified. In the next sample (7-4) paragneiss clasts predominate, although leptynitic and granitic clasts are also present. In the lowermost samples the principal lithic clasts are granitic (7-10 and 7-15). This pattern is also reflected in the hand-sample characteristics, where the yellowish 7-4 sample has a predominance of paragneiss clasts, whereas the other reddish samples are dominated by granitic clasts. The closest basement rock to this sampling site is LGU paragneiss, although this location is also very near to the granodiorite from La Chassagne. This suggests that these two lithologies could have been the main precursor rocks for the impactites at this location.

The samples from Videix are also highly heterogeneous. The surface suevite has primarily leptynitic lithic clasts. The surface IMR sample (1414) and the uppermost IMR from the drill-core (11-5) have a predominance of paragneiss clasts. In contrast, the lowermost monomict lithic breccias (11-17 and 11-25) have only granitic clasts. The closest target rock at surface is the granodiorite from La Chassagne, and the basement of the drill-core is also composed of granitic rock.

6.5.2 Geochemistry

6.5.2.1 Nature of the basement

The geochemical data of the basement rocks of this study combined with the literature data for the FMC basement in the Limousin region (Bambier et al., 1983; Chèvremont et al., 1996; El Korh et al., 2020; Lambert, 1977; Reimold et al., 1983) show that the basement of the Rochechouart impact structure comprises lithologies with very heterogeneous silica contents, ranging from ultramafic to mafic rocks like serpentinites and amphibolites to more felsic rocks such as leptynites, granites, and

pegmatites. The serpentinites have a distinct composition compared to the other lithologies for most major and trace elements. For the remaining lithologies, SiO_2 has a strong negative correlation with FeO_t, TiO_2, and CaO, and a positive correlation with K_2O. In contrast, there is a weak negative correlation with MgO and Al_2O_3 and there is no clear correlation with Na_2O and P_2O_5 (Figure 6.7). This means that for these elements, most of the lithologies exhibit compositions that fall within similar ranges. For the trace elements, apart from the serpentinites, all basement lithologies show similar patterns in spider plots (Fig. S8). Moreover, the more mafic rocks contain higher concentrations of most trace elements, except for Cs, Rb, Ba, Th, and U, which are more enriched in the felsic rocks. However, there is also a significant overlap in the trace element compositions among the different lithologies. The similar abundances of some elements across most of the basement lithologies make it difficult to use them to distinguish specific protoliths for each impactite.

6.5.2.2 Nature of the impactites

Using data from this study and the literature (Chèvremont et al., 1996; Faucher 2021; Tagle et al., 2009), the geochemical character of the impactites and its spatial variation throughout the crater have been analyzed. For this purpose, principal component analysis (PCA) was conducted using major and trace elements (Figure 6.10). It should be cautioned, however, that geochemical data from some areas (especially IMRs from Belair, Rochechouart, and Chassenon) are rather limited in number.

In the PCA plot with major elements (Figure 6.10a), the first and the second component explain 50 % and 22.7 % of the total variance of the data, respectively. PC1 is primarily controlled by K_2O, Al_2O_3 and TiO_2 on the negative axis and by CaO and Na_2O on the positive axis. PC2 is mainly influenced by Fe_2O_3 on the positive axis and SiO_2 on the negative. The whole dataset shows that the suevites and breccias have higher CaO and Na_2O than the other impactites; the IMRs have higher Al_2O_3 and K_2O; and the lithic breccias, suevites, and impactoclastites from Chassenon and the red IMRs have higher Fe_2O_3 than the other sample types.

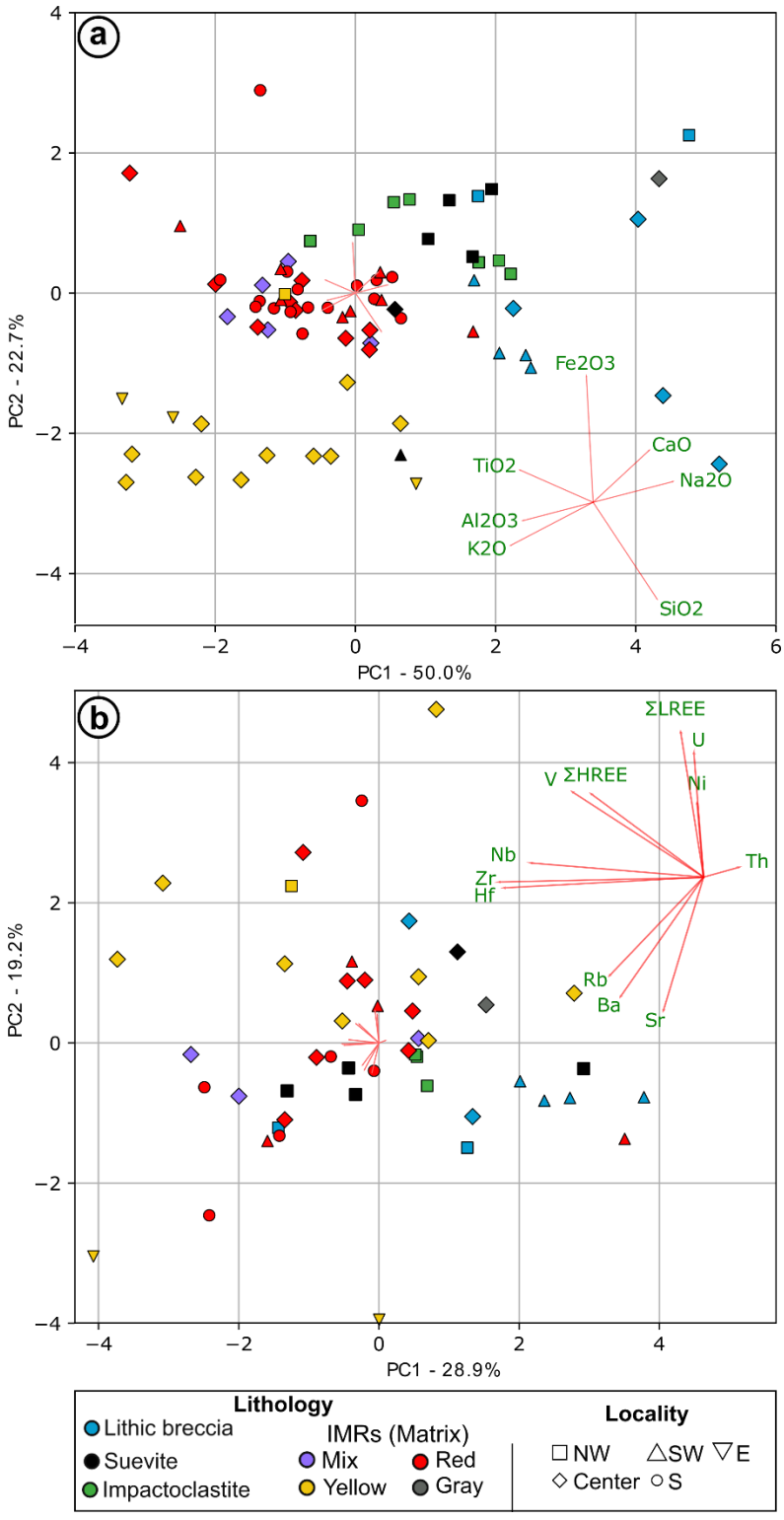


Figure 6.10 Principal component analysis (PCA) of all impactite samples from this study and from literature data taken from Chèvremont et al. (1996) and Faucher (2021). Analyses are made with the (a) major and (b) trace elements separately. PC1 and PC2 explain together 77.72% and 48.1% of the total variance of the data on each diagram. The colors indicate the lithology and the symbols the location of the samples. The lithic breccia symbol represents the monomict breccias of this study and the monomict and polymict lithic breccias of the literature.

Distinct geochemical trends are observed across the sampled locations. Lithic breccias from Valette exhibit the highest silica and the lowest Fe_2O_3 and MgO contents, followed by those from Videix, and finally by the samples from Chassenon and Recoudert. The Videix suevite has a composition more comparable with the yellow IMRs. Suevites and impactoclastites from Chassenon show comparable major element compositions to the monomict lithic breccias from the same area. The yellow and red IMRs form their own distinct clusters, and within each cluster, overall, the samples from different locations are scattered. Moreover, the yellow IMRs exhibit greater geochemical variability and the yellow IMR from Chassenon plots within the cluster of the red IMRs.

The PCA plot based on trace elements has a PC1 and PC2 that explain 28.9% and 19.2% of the total variance of the data, respectively (Figure 6.10b). PC1 is mostly defined by the immobile elements Zr, Nb, and Hf on the negative axis and Th on the positive. PC2 is defined on the positive axis by the moderately mobile elements LREE, Ni, and U and on the negative axis by the mobile elements Rb, Ba, and Sr.

In this plot, most of the monomict and polymict (Faucher, 2021) lithic breccias, primarily from Videix and to a lesser extent from Chassenon and Valette, form a cluster characterized by relatively low concentrations of immobile elements (Zr, Nb, and REE). The suevites and the IMRs have more diverse compositions. In general, the IMRs show higher concentrations of the immobile and moderately immobile elements compared with the other impactites.

6.5.2.3 Comparison with basement

With the geochemical data available, next we compare the composition of the Rochechouart impactites with that of the target rocks from the FMC basement in the Limousin region. Overall, the impactites have SiO_2 and TiO_2 contents that are better correlated with the target rocks with intermediate silica from the basement (paragneisses, granodiorites, and few leptynites) (Figure 6.7). The MgO and FeO_t contents are mostly similar to those of intermediate and felsic target rocks. For Al_2O_3 and P_2O_5, the impactites show compositions that overlap for all target rocks except

for the serpentinites. The CaO, Na_2O, and K_2O contents of the impactites can be compared with very few target rocks such as the serpentinites and/or some paragneisses, leptynites, and granites. Regarding the trace elements, the concentrations of immobile elements (e.g., Y, Zr, Cr, and V) in the impactites are more similar with the group of rocks with intermediate silica, whereas some REE (Ba, La, and Ce) align with both intermediate silica rocks and amphibolites. Moreover, some impactite samples have higher values of incompatible elements (eg., Cs, Ta, La, Nd) compared to all basement lithologies (Fig. S8).

The depletion of mobile elements such as CaO and Na_2O, and the enrichment of K_2O and incompatible trace elements -especially in the IMRs (Figure 6.7 and 6.10)- can be attributed to remobilization processes during the extensive hydrothermal alteration documented in this impact structure (e.g., Faucher, 2021; Lambert, 2010; Sapers et al., 2014; Simpson et al., 2017). Mobile elements were preferentially leached out, while incompatible elements were likely enriched through interaction with external fluids.

To further evaluate the regional geochemical database, a PCA analysis was conducted using immobile major and trace elements, which were likely less affected by secondary processes. In a first PCA diagram with all lithologies, most of the serpentinites, amphibolites, diorites, and tonalites do not plot near the locations of the impactites (Figure S10). To refine the analysis, a second PCA diagram was calculated focusing on basement lithologies with a closer geochemical relationship to the impactites, such as the granitic-granodioritic rocks, and the paragneisses and orthogneisses of the LGU and UGU (Figure 6.11). In this diagram, the first two principal components (PC1 and PC2) explain 64.2% of the total variance. PC1 is characterized by SiO_2 contents on the negative axis and TiO_2, Al_2O_3, and Fe_2O_3 contents on the positive axis. PC2 is defined by the concentrations of Zr, Nb, and ΣLREE on the positive axis, and by Hf, Y, and ΣHREE on the negative axis. The basement rocks predominantly plot along the negative axis of PC1, with granitic rocks plotting on the positive axis of PC2 and paragneisses and most of the leptynites on the negative axis.

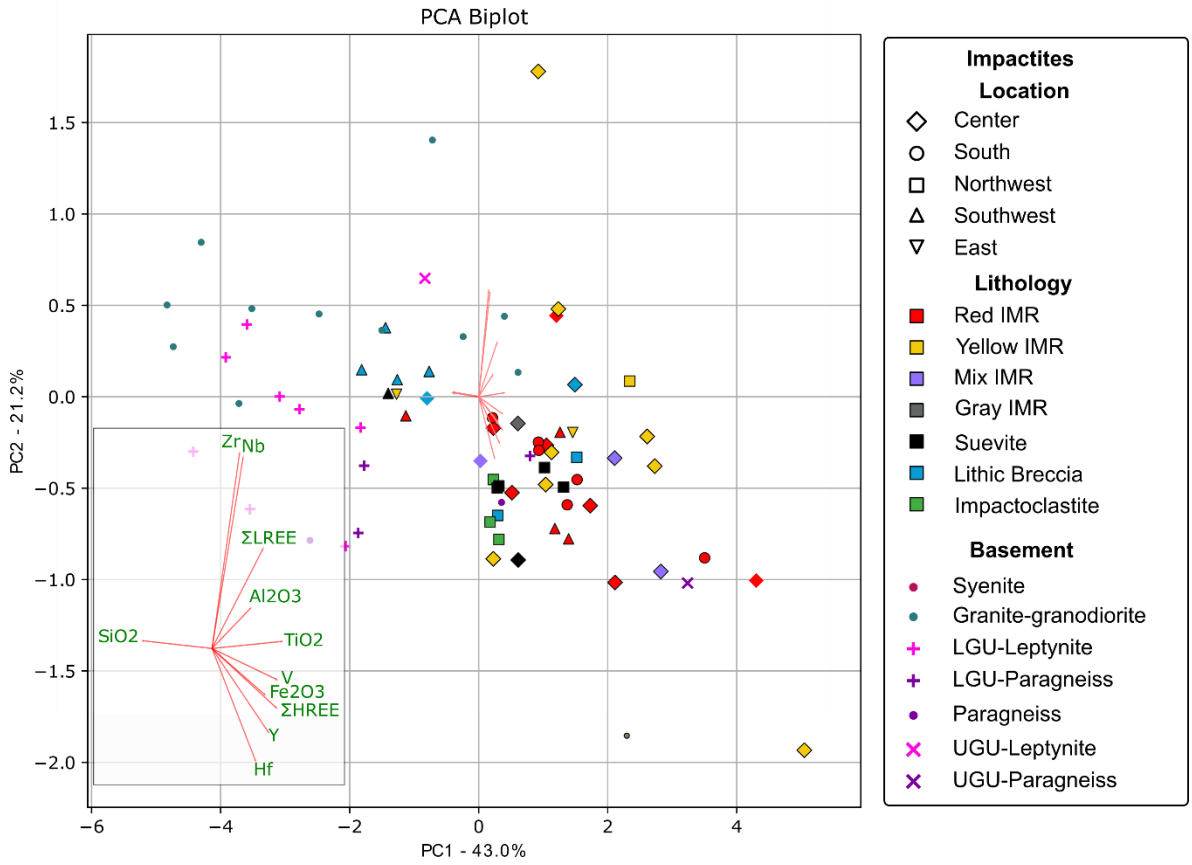


Figure 6.11 Principal component analysis (PCA) for all the impactites of the Rochechouart impact structure and the basement rocks with compositions considered more similar to them. Immobile major and trace elements were considered only, and PC1 and PC2 explain 64.2% of the total variance of the data. The lithic breccia symbol represents the monomict breccias of this study and the monomict and polymict lithic breccias of the literature. Literature data taken from Bambier et al. (1983), Chèvremont et al. (1996), El Korh et al. (2020), and Faucher (2021).

The lithic breccias and the suevite from Videix, as well as a lithic breccia from Valette plot into the same area as the granitic rocks and leptynitic gneisses from the basement. Another lithic breccia from Valette, two yellow IMRs from Babaudus, and one from Chassenon also plot in the positive axis of the PC2. The rest of the impactites plot on the positive axis of PC1 and the negative axis of PC2, negative correlated with SiO_2 and positive with Hf, Y, V, and ΣHREE. Among the few basement rocks that overlap with this field, the paragneisses from the LGU are seemingly closer to the impactites than those from the UGU. The suevites, lithic breccias, and impactoclastites from Chassenon form a distinct cluster in this region. For the IMRs, although the yellow variety shows a more scattered distribution than the red, both lithologies significantly overlap, suggesting that they could have been derived from common protoliths.

However, the low number of analyses including the immobile elements used available for some lithologies to construct the PCA is a limitation to identify clear trends, especially for the IMRs.

6.5.3 Strontium and Sm-Nd isotopes

The basement lithologies can be divided into two groups according to the Sr and Sm-Nd isotopic data: 1) amphibolites, paragneisses, and the Exideuil granodiorite, which have comparatively higher $^{143}Nd/^{144}Nd$ ratios and εNd(t) values, and lower $(^{87}Sr/^{86}Sr)t$; 2) and the remaining granitic rocks and the UGU leptynitic gneiss, which display opposite character, with lower $^{143}Nd/^{144}Nd$ and εNd(t) values, and in general higher $(^{87}Sr/^{86}Sr)t$ (Figure 6.8). The Chassenon suevite and impact melt rock have an isotopic signature very close to the paragneisses from the first group, whereas the Videix samples align with the second group, particularly close to the granodiorites and diorites from La Chassagne and La Martinie. The IMRs fall between these two groups, with the yellow IMRs registering values closer to the Chassenon samples and the paragneisses, whereas the red IMRs present values intermediate between the Chassenon and Videix samples.

In the $(^{87}Sr/^{86}Sr)t$ vs εNd diagram (Figure 6.8b), some impactites yield anomalously low $(^{87}Sr/^{86}Sr)t$ ratios that cannot be directly correlated with basement rocks. However, the overall trend remains consistent, with the Chassenon suevite and most yellow IMRs plotting near the paragneisses, whereas the Videix samples align with the granodiorites and diorites from La Chassagne and La Martinie. Furthermore, in this plot a yellow IMR from Recoudert plots very close to the UGU leptynite.

6.5.4 U-Pb zircon provenance analysis

The zircon geochronologic information from the impactites and basement rocks of the Rochechouart impact structure obtained in this study and in Guerrero (2024, 2025 - in review) were compiled into Kernel density estimation and probability density plots, and multidimensional scaling models calculated to have an overview of all the ages registered in these units (Figure 6.12 - 6.13). PDP is used in samples

with a limited number of analyses to provide a more accurate representation of the age distribution.

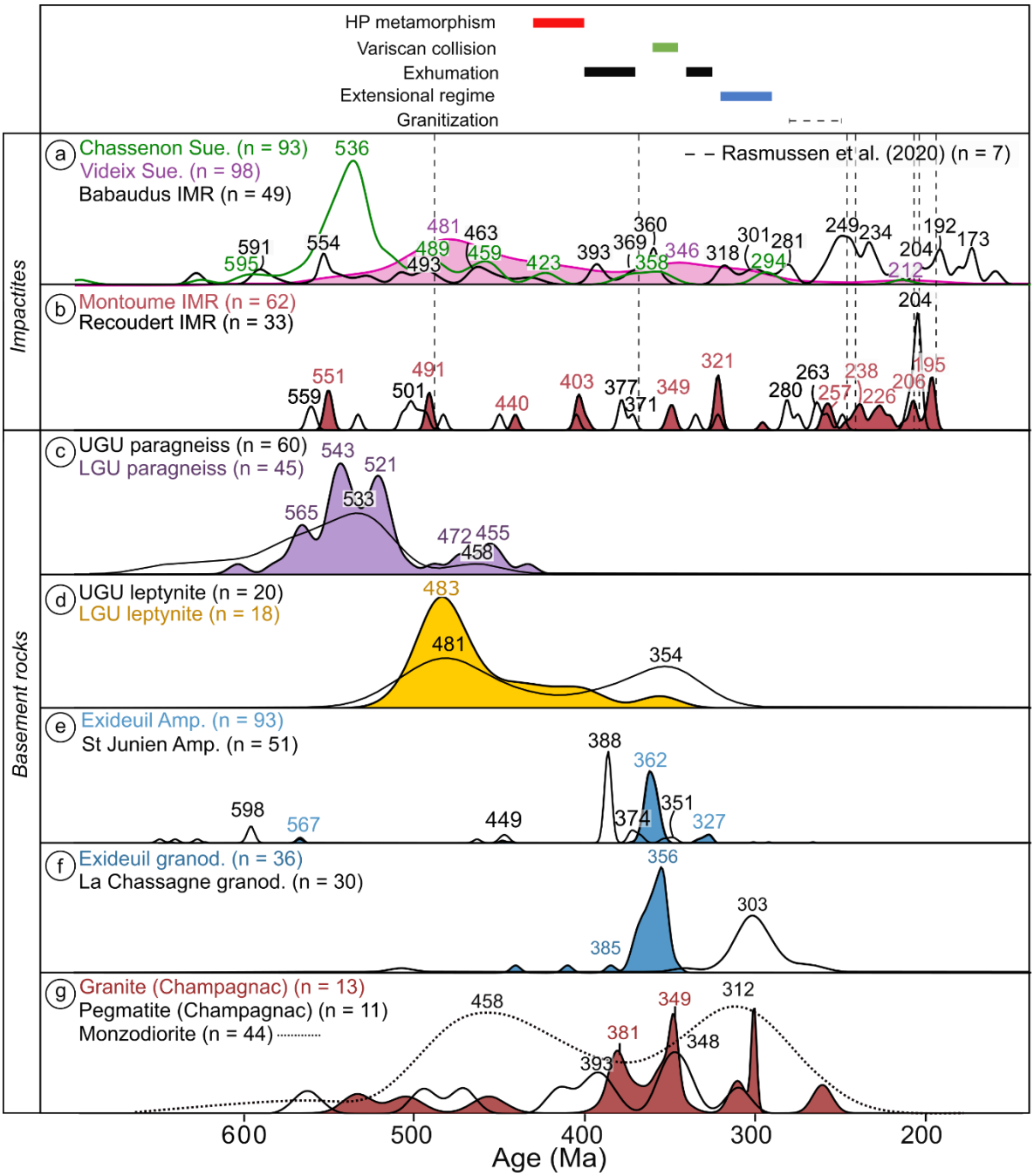


Figure 6.12 Kernel density estimation and probability density plots for the basement results from this study, as well as literature data for rocks on the impact area from Guerrero et al. (2024, 2025 - in review). The upper colored bars refer to major events constrained in the geologic evolution of the French Massif Central (after Lardeaux, 2014). The relatively young granitization phase is after Reimold et al. (1987). Plot and age peaks calculated with Detrital Py v. 1.3 (Sharman et al., 2018).

Overall, the basement of the impact structure is characterized by distinct age patterns (Figure 6.12). The paragneisses of the LGU and UGU show a similar age

distribution, and in both units the principal age peaks are in the Upper Neoproterozoic to Lower Cambrian, with minor peaks at the Ordovician (Figure 6.12b). The ages recorded in zircon from the LGU and UGU leptynites also display a similar distribution and have similar age ranges. Both lithologies have a peak at ~482 Ma, and the UGU has an additional peak at 354 Ma (Figure 6.12d).

The age distribution of the amphibolites and granodiorites from different localities is more varied (Figure 6.12e and f). The St. Junien amphibolite has a main peak at 388 Ma, whereas zircons from the amphibolite and granodiorite from Exideuil show main peaks at 362 and 356 Ma, respectively. The granodiorite from La Chassagne, instead, shows a single peak at 303 Ma. The other granitic rocks contain zircons with ages ranging from the Cambrian to the Carboniferous - Lower Permian, although their main age peaks differ between units (Figure 6.12g). The monzodiorite zircons record KDE peaks at 458 and 312 Ma, whereas the zircons from the Champagnac granitic rocks have PDP peaks in the Devonian (381 and 393 Ma) and Lower Carboniferous (348-349 Ma). The scarce few ages that could be obtained for the Chéronnac granite are highly variable and no age peaks were obtained.

Notably, the granodiorite from La Chassagne, the granite from Champagnac, and the monzodiorite from La Martinie are the only target rocks with zircons yielding post-Variscan ages, ranging from 261 ± 11 to 281 ± 10 Ma. Reimold et al. (1987) already suggested a young granitization phase of similar age (280–250 Ma) for this region.

Overall, the age distributions of the paragneisses from different units strongly overlap, and the leptynites also show internal overlap (Figure 6.12c and d). The monzodiorite and the more felsic granitic rocks also exhibit a similar age distribution, with zircons spanning a wide range of ages (Figure 6.12g). In contrast, the zircons from granodiorites and amphibolites from different localities display more distinct age distributions (Figure 6.12e and f).

A MDS model was made to quantitatively compare the geochronological data of the different basement lithologies and the impactites (Figure 6.13). The plot shows that – in terms of age population - the Chassenon suevite is very similar to the paragneisses, located slightly closer to the one from the LGU. In contrast, the Videix

suevite, although it plots close to the Champagnac granitic rocks, is only directly connected to the monzodiorite and the leptynites, especially the one from the UGU. The three IMRs form a cluster and are only connected with the granodiorite from La Chassagne, probably because it is the sample with a higher proportion of post-Variscan zircons, which are also well represented in the geochronologic record of the IMRs. The samples from Exideuil and Chéronnac are not connected to any impactite.

An additional MDS model was constructed using only ages greater than 300 Ma (Figure 6.13b). This approach reduces the isolation of the IMRs generated by the presence of many post-Variscan ages in these rocks that are poorly represented in the basement. The rationale for this second MDS experiment is that it is not clear whether all post-300 Ma ages obtained can be considered protolith related. They could also represent a fraction of zircon that was partially reset by the impact event. Presumably this may not apply to weakly shocked basement rocks, but it would certainly be a factor in the age statistics for at least partially strongly tempered zircon from IMRs. Further complexity is presented by the polymetamorphic history of the FMC basement.

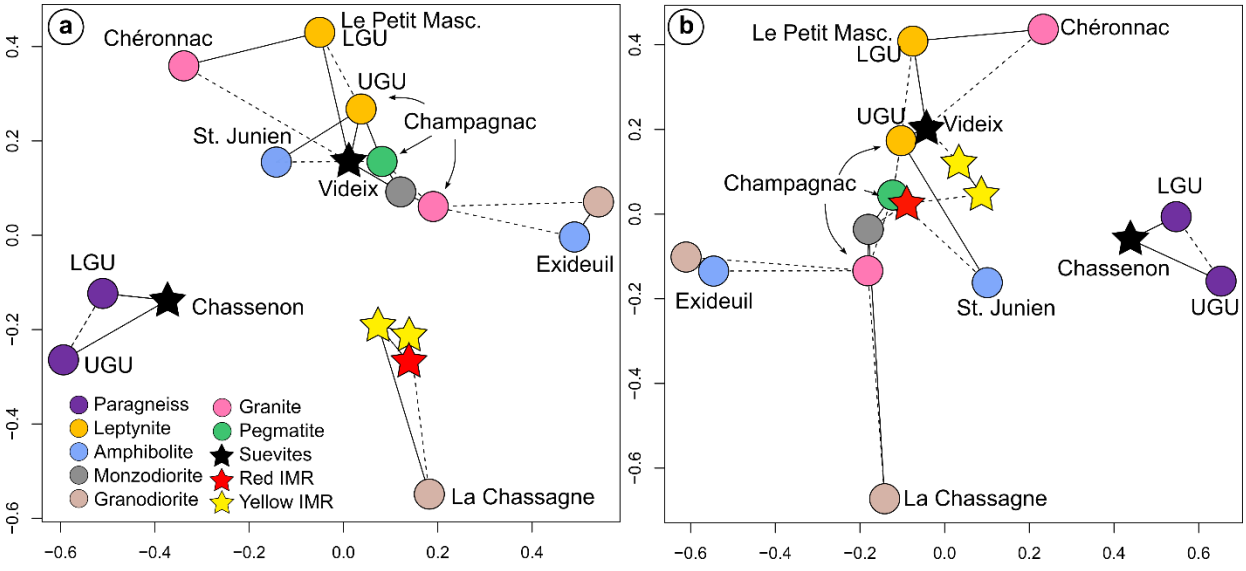


Figure 6.13 Multidimensional scaling (MDS) plots for the U-Pb geochronological data of the basement rocks of this study and previous reports for rocks on the impact area from Guerrero et al. (2024, 2025 - in review). Plot made with the provenance package in R with the Kuiper test (Vermeesch et al., 2016). Each sample is connected to its closest neighbor with a solid line, and to its second-closest neighbor with a dashed line.

Location	ID	Lithology	Lithic clast populations	Geochemistry PCA	Sm - Nd	Sr	U-Pb on zircon
Chassenon	1315	Suevite	> Paragneiss, > granitic rock, and < quartz aggregates	Paragneisses	Paragneisses	Paragneisses	Paragneisses
	1-3	Clast-poor, yellow IMR	-	Not correlated	Paragneisses	Not correlated	NA
Valette	7-1	Clast-poor, red IMR	Quartz aggregate	Paragneisses	Between the paragneisses and the granitoids	UGU leptynite	NA
	7-4	Clast-rich, yellow IMR	>> Paragneiss, > quartz aggregate, < granitic rock, and < leptynite	Paragneisses	Between the paragneisses and the granitoids	UGU leptynite	NA
	7-10	Melt-rich, red suevite / IMR	>> Granitic rock, > leptynite, and < paragneiss	Paragneisses	Paragneisses	Not correlated	NA
	7-15	Clast-rich, red IMR	>>> Granitic rock and < paragneiss	Paragneisses	NA	NA	NA
Videix	1414	Clast-poor, red IMR	-	Paragneisses	NA	NA	NA
	1745	Suevite	>> Leptynite, > granitic rock, and < paragneiss	Granitoids and leptynites	La Chassagne granodiorite, La Martinie monzodiorite, and UGU leptynite	La Chassagne granodiorite, La Martinie monzodiorite, and Champagnac granite	La Martinie monzodiorite and leptynites
	11-5	Clast-rich, red IMR	>>> Paragneiss, < granitic rock, < quartz aggregate, and < leptynite	Paragneisses	NA	NA	NA
	11-17	Lithic impact breccia	Granitic rock	Granitoids and leptynites	La Chassagne granodiorite and La Martinie monzodiorite	La Chassagne granodiorite, La Martinie monzodiorite, and Champagnac granite	NA
	11-25	Lithic impact breccia	Granitic rock	Granitoids and leptynites	NA	NA	NA
Rochechouart	15-1	Clast-rich, yellow IMR	>> Paragneiss, < granitic rock, and < quartz aggregate	Paragneisses	UGU Paragneiss	UGU Paragneiss	NA
Montoume	955	Clast-rich, red IMR	>>> Quartz aggregate, < paragneiss, < leptynite, and < granitic rock	Paragneisses	Between the paragneisses and the granitoids	UGU leptynite	La Chassagne granodiorite
	16-6	Clast-rich, red IMR	>> Quartz aggregate, < paragneiss, and < granitic rock	Paragneisses	NA	NA	NA
	16-7	Clast-rich, red IMR	>> Paragneiss, < quartz aggregate, and < granitic rock	Paragneisses	Between the paragneisses and the granitoids	Not correlated	NA
Recoudert	1900	Clast-poor, yellow IMR	-	Paragneisses	Paragneisses	Paragneisses	La Chassagne granodiorite
	17-2	Clast-poor, red IMR	>>> Paragneiss and < quartz aggregate	Paragneisses	NA	NA	NA
	17-7	Clast-poor, yellow IMR	Paragneiss	Paragneisses	Paragneisses	Not correlated	NA
	17-13	Clast-rich, red IMR	>> Paragneiss, < leptynite, < quartz aggregate, and < granitic rock	Paragneisses	NA	NA	NA
Babaudus	1643	Clast-poor, yellow IMR	>> Paragneiss, < quartz aggregate, < granitic rock, and < leptynite	Not correlated	Paragneisses	Paragneisses	La Chassagne granodiorite

Table 6.2 Summary of the petrographic lithic clast populations and the basement rocks that exhibit the closest similarities to the impactites in this study in terms of geochemistry, isotopic composition, and U-Pb on zircon provenance analysis. >>> High abundance, >> Intermediate abundance, < low abundance, NA - Not analyzed.

In this plot (Figure 6.13b), the Chassenon suevite remains connected to the paragneisses. The Videix suevite is now only connected with the leptynites, especially the one of the UGU. The IMRs plot close to the Champagnac samples and the UGU leptynite. The red IMR plots are very close to the pegmatite, whereas the yellow IMRs are slightly farther apart and are only connected to the Videix suevite and the red IMR sample.

6.5.5 So what were the protoliths for the Rochechouart impactites?

In Table 6.2 the results obtained by different methods regarding the basement rocks that exhibit the closest similarities to each impactite in this study are summarized.

6.5.5.1 Monomict lithic breccias and suevites

The petrographic analysis of the monomict lithic breccia samples from Puy Chiraud (11-17, 11-25) indicates that they originated from granitic precursor rocks. Furthermore, the immobile major and trace element compositions of these samples are comparable with the granitic rocks and leptynites from the basement, and the Sr, Sm-Nd, isotopic data show that the rocks have compositions similar to those of the granodiorites and diorites from La Chassagne and La Martinie, which form the main basement components in the SW area of the structure.

The three suevites analyzed here exhibit significant heterogeneity in lithic clast composition, major and trace element geochemistry, and isotopic signatures. The Valette sample has a larger proportion of granitic clasts, and minor proportions from gneissic lithologies, whereas the Chassenon and the Videix suevites indicate a larger proportion from gneissic lithologies. However, the suevites from Chassenon and Valette have more similar geochemical and isotopic composition in comparison with the suevite from Videix. The geochemistry of the suevite from Videix is closer to the most felsic granitic rocks analyzed, whereas the other two samples are more comparable with the samples with intermediate silica content. The Sm - Nd isotopic data indicate that the Videix suevite has an intermediate composition between the lithic breccia from the same location and the UGU leptynitic gneiss, whereas the Chassenon and Valette suevites have a Sm-Nd isotopic signature closer to that of the paragneisses.

Provenance analysis shows that the Chassenon sample has an age distribution very similar to that of the paragneisses, especially the one from the LGU. This strongly suggests that the paragneisses are the primary basement rocks contributing to the formation of this sample and likely also to the Valette suevite. The paragneisses are the dominant basement lithologies at the sampling sites of these impactites.

In contrast, the zircons from the Videix suevite have a geochronologic record that is not comparable to that of the La Chassagne granodiorite, the most proximal target rock to the sampling site. Instead, the impactite has an age distribution consistent with the monzodiorite from La Martinie and the leptynites, which most probably represent the main contributors for its formation.

6.5.5.2 Impact melt rocks

The modal analyses (Figure 6.3) show that paragneisses represent the most common lithic clasts of almost all analyzed IMRs, with minor proportions from leptynite or granitic rocks also present. This distribution can be correlated with the most widespread target lithology of the impact structure, the LGU paragneisses. This lithology is also present in the basal parts of the drill-cores that reached the basement, in some cases intercalated with leptynites or granites.

At Videix, the closest target lithology is the granodiorite from La Chassagne. However, the IMRs still show a predominance of paragneiss clasts. Valette is the only locality with IMRs where the predominant lithic clast population can be either paragneisses or granitic rocks. The closest basement rock is the LGU paragneiss; however, the main precursor rocks for the impactites at this location would also require a granitic rock.

The geochemical results indicate that the abundances of the immobile major and trace elements (SiO_2, Al_2O_3, TiO_2, Fe_2O_3, REE, Zr, Nb, V, Y, Hf) of the red IMRs are comparatively more similar between different sampling sites than the yellow IMRs, which show greater variability, especially in the samples from the center of the structure (Figure 6.11). However, the overall composition of these elements in both types of IMRs can be well correlated and can be better compared with the basement rocks with intermediate silica content. The isotopic results also show that the

intermediate silica target rocks are closer to the isotopic signature of the impactites. Furthermore, the yellow IMRs have more affinity with the slightly more mafic lithologies (paragneisses), whereas the red IMRs are closer to granodiorite and monzodiorite from La Chassagne and La Martinie.

The multidimensional scaling plot made for only a comparison of the ages that are more represented in the basement, shows that the IMRs are close to the age distributions of the leptynites, the granitic rocks from Champagnac, and the monzodiorite from La Martinie. However, integrating the Sr and Sm-Nd isotopic data, the IMRs show a closer affinity to the UGU leptynite and the monozodiorite form La Martinie. Consequently, the granitic rocks from Champagnac and the LGU leptynite, which are some of the more felsic lithologies, probably did not contribute to the formation of this type of impactite.

In the MDS model, the yellow IMRs are not connected to any basement lithology. This lack of correlation may be an effect of the relatively lower preservation of unshocked zircons with basement ages and may not necessarily imply that the target rocks analyzed so far could not be the precursor rocks for the IMRs. In this sense, other methods that show a better correlation with the basement, such as Sm-Nd isotopy, are preferred to evaluate the most probable protolith rocks of this lithology.

To further strengthen the findings of this study, it is recommended to expand the database—particularly for major and immobile trace elements and Sm-Nd isotopes—to more accurately represent the compositional signatures of the basement rocks and impactites. Additionally, analyzing samples from more localities would help determine whether the patterns observed in this study can be generalized across the entire extent of the impact structure.

6.6 Conclusions

A detailed petrographic, whole-rock geochemical, and isotopic characterization (Sr and Sm-Nd isotope analysis on whole rock and U-Pb on zircon) of representative impactites and basement lithologies of the Rochechouart impact structure was conducted to identify the most probable precursor lithologies for each impactite type. The main conclusions derived from this study are:

- Overall, the impactites can be better correlated with the target rocks with intermediate silica contents (60-68 wt%), and the monomict lithic breccias and suevites mostly resemble the compositions of the target rocks observed in closest outcrops and/or in the basal part of drill-cores.
- Although the IMRs likely represent a mixture of different proportions of various lithologies, the Sm-Nd isotopes show a more gneissic affinity for the yellow IMRs, whereas a larger contribution from granodiorite and/or monzodiorite from La Chassagne and La Martinie is seen for the red IMRs.
- The high proportion of pre-impact ages younger than the final phase of regional basement evolution (ca. 272) led to a poor correlation between the IMRs and the basement in the zircon provenance study. Other methods that show a better correlation with the basement, such as Sm-Nd isotopy, are preferred to evaluate the most probable protolith rocks of impact melt rocks.

Acknowledgments

Funding for this study has been provided by the Conselho Nacional de Desenvolvimento Cientıfico e Tecnologico (CNPq) through grants no. 140048/2022-7 and 444320/2020-2, a grant from the Barringer Family Fund for Meteorite Impact Research, and a CIRIR Career Development Award, all to DG. This study was financed in part by the Coordenacão de Aperfeiçoamento de Pessoal de Nivel Superior—Brasil (CAPES)—Finance Code 001. The research of Natalia Hauser and Wolf Uwe Reimold has been supported by Bolsa de Produtividade grants (Nos. 309878/2019-5, 305761/2019-6, and 307109/2023-2) from CNPq.

6.7 Supplementary material

Table S1. Clast composition of the hand specimens of impactites analyzed in this study.

Sample ID	S11/17	S11/25	1745	1315	S7/10	S7/15	S11/5	S16/6	S16/7	S17/13	S7/4	S15/1	S7/1	S17/2	955	1414	1643	1900	S1/3	S17/7
Clasts (>1cm) (%)																				
Paragneiss (Foliated, sharp contacts)																				
Black		1	6	1.3					4			5	1	4						
Red/purple				3.3	1		21	3	1	1	10		3	3	1.5	2				10
Green					1					1	1	15	2							
Mixture of red and green					4					2	4		3							
White with black spots		3		3			1	10	1	2				7	3		5		1	
Leptynite																				
Quartzo-feldspathic oriented with qtz veins				2																
Granitoid																				
Pink/white, vesicular								3	1	3		2	17	1						
Pink granites (irregular or sharp border)	30	45			3		1	1	3	3	3		2	3					1	3
Leptynite or granitoid																				
Pink fine grained					7	2						5	4	7	2					
Others																				
White (elongated or irregular)		1	10		1	1	2		2		3		3	4						4
Green euhedral		5																		
Melt clasts																				
Red				1			1	1			2									
Green			1	7		2	1				1		0.5							
Black								0.5	0.5											
Yellow			2																	
Mineral clasts in the matrix (<1cm)																				
White	10	4	3	0.7	3		5	2	1	2	1	0	2	4	3		5			3
Pink fine grained	10	4		0.7	2	2.5	2	3	3	3	1		1	6						
Green and red IM						0.5					3	0.5								
Purple gneiss							2	1	2	1				5						
Black	5	2	1							2				1						
Brown												0.5								
Vesicles				1													1	5		
Matrix	70	45	81	81.3	83	95	73	81.5	87.5	88	76	73	64.5	71	93.5	98	94	95	98	83
Purple						X		X		X										
Yellow			X								X	X					X	X	X	X
Green	X	X									X		X						X	
Reddish	X	X			X		X		X	X			X	X	X	X				
Gray				X																

Table S2. Modal compositions of the thin sections analyzed in this study.

Sample ID	S11/17	S11/25	1745	1315	S7/10	S7/15	S11/5	S16/6	S16/7	S17/13	S7/4	S15/1	S7/1	S17/2	955	1643	1900	S1/3	S17/7
Modal compositions																			
Matrix	25.3	43.1	57.9	58.8	51.1	31.2	51.7	80.1	40.1	40.8	63.7	55.7	86.2	67.0	77.1	84.3	85.0	90.0	88.7
Vesicles	4.9	0.8	2.6	8.6	0.3	5.0		3.6	9.9	0.5	1.0	0.4	12.1	1.8		6.5	5.0	6.8	3.8
Melt			0.9	9.9	5.1			0.7		2.0		2.0							6.2
Devitrified melt			9.6	1.3	0.2	4.3			37.2	4.7		2.7			6.6				
Clastic matrix										32.1	23.0								
Mineral clasts																			
Quartz	4.2	4.0	3.3	2.4	4.1	5.5	4.7	1.2	3.0	1.0	5.1	3.1		0.4	6.8	4.7	10.0	1.1	
Ortoclase	0.4	3.1	1.7		0.7		3.7	1.2	0.2	3.0									0.3
Plagioclase	3.4	2.1	0.6	0.2	5.2	5.0	0.9			0.3		0.4			0.2				0.3
Opaque	0.4				0.3	0.6	1.2		2.2					1.5				1.8	
Biotite	0.6	3.8	1.1	0.4	1.5				0.4				0.4						
Muscovite			0.5																
Isotropic clast	0.5						0.3	0.3			0.2	0.2						0.4	
Lithic clasts																			
Quartz aggregate	0.2	1.9	0.2	3.1	0.2		3.4	8.7	1.8	2.7	2.6	1.3	1.3	6.6	6.8	0.9			
Granitoid	59.4	40.6	5.9	6.4	21.2	47.3	5.6	1.8	1.0	1.7	0.7	2.3			0.7	0.7			
Paragneiss	0.8	0.6	2.4	8.1	1.5	1.2	26.2	2.5	4.3	8.5	3.4	31.7		22.7	1.1	2.4			0.7
Leptynite			13.3	0.9	8.6		2.2			2.8	0.3	0.4			0.7	0.5			

Table S3. Proportions of shock deformation features observed on quartz, feldspar, and biotite, in the mineral and lithic clasts of the samples analyzed in this study. PDFs: Planar deformation features.

Sample ID	S11/17	S11/25	1745	1315	S7/10	S7/15	S11/5	S16/6	S16/7	S17/13	S7/4	S15/1	S7/1	S17/2	955	1643	1900	S1/3	S17/7
Mineral clasts																			
Quartz																			
Unshocked	97.1	100	47.6	63.6	16	48.6	80	42.9	86.7	50	67.7	58.8		100	23.3	18.5			
Recrystallized	2.9		47.6	36.4	84	45.9		42.9	6.7	16.7	9.7				63.3	81.5		100	
Toasted								14.3	6.7	33.3	19.4	35.3			13.3				
One set of PDFs						2.7	13.3				3.2	5.9							
Two sets of PDFs						2.7	6.7												
Ballen qtz								x			x			x			x		
Feldspar																			
Unshocked	100	100	100	100	52.8	47.1	100	100	100	100		100			100				50
Thermally altered					47.2	52.9													50
Biotite																			
Unshocked	40	50.5	71.4	100	100								100						
Kink bands	60	50.5	28.6						100										
Lithic clasts																			
Quartz																			
Unshocked	99.2	100	78.7	63.9	45.9		66.7	6.3	29.4	56.3	31	67.9		68.8	34.2	43.8			
Recrystallized	0.8		17.3	33.3	42.9	99.4	6.1	82.8	58.8		10.3	1.9		31.3	60.5	25			
Toasted				2.8		0.3	12.1	6.3	5.9	37.5	55.2	13.2	33.3		5.3	31.3			
One set of PDFs			4		8.2		15.2	4.7	5.9	6.3	3.4	17	66.7						
Two sets of PDFs					2														
Three sets of PDFs					1														
Feldspar																			
Unshocked	97.7		33.3		97.4		85.7		20			92							
Thermally altered	2.3		66.7		2.6		14.3		80		100	8							
Biotite																			
Unshocked	40	54.5							87.5										
Kink bands	60	45.5							12.5										

Table S4. The major and trace element composition for the samples of this study. Bd - bellow detection limit, IMR – Impact melt rock.

Laboratory	Bruxelles	SGS	SGS	Bruxelles	SGS	SGS	Bruxelles	Bruxelles	Bruxelles	Bruxelles	Bruxelles
ID	C220522-1749	C180824-1500	C180822-1625	C220506-0954	C180825-0930	C180824-1645	C220607-1115	C180825-1115	C220511-1352	C220608-2001	C180824-1630
Sample	Serpentinite	Amphibolite	Amphibolite	Paragneiss	Paragneiss	Leptynitic gneiss	Leptynitic gneiss	Monzodiorite	Granodiorite	Granodiorite	Granite
Major elements (wt%)											
SiO_2	39.0	51.7	52.2	64.6	67.4	66.7	78.4	60.0	64.7	67.3	75.6
TiO_2	1.59	1.22	1.44	0.90	0.66	0.42	0.04	0.84	0.53	0.62	0.04
Al_2O_3	4.51	18.5	17.2	16.9	13.7	14.4	12.0	16.1	15.0	15.1	13.2
Fe_2O_3	9.01	10.8	10.2	6.66	5.29	2.52	1.22	7.14	4.50	3.31	0.57
MnO	0.19	0.21	0.19	0.10	0.09	0.05	0.07	0.13	0.10	0.11	0.01
MgO	33.10	4.17	4.45	2.14	2.21	2.18	bd	5.15	1.89	1.40	0.31
CaO	0.82	7.99	6.85	2.16	2.11	1.79	0.63	0.70	3.94	2.04	0.61
Na_2O	0.11	3.53	3.54	3.41	2.81	3.03	3.43	2.08	3.27	3.55	3.94
K_2O	0.01	1.20	1.38	3.36	2.85	5.20	4.10	4.47	3.05	3.71	5.08
P_2O_5	bd	0.45	0.32	0.13	0.12	0.16	bd	0.22	0.13	0.16	bd
LOI	13.60	1.56	1.40	2.03	1.53	2.71	0.55	3.89	0.95	1.43	1.39
Total	101.98	101.29	99.17	102.48	98.75	99.22	100.40	100.69	98.04	98.79	100.74
Trace elements (ppm)											
V	238	228	217	100	90	45	0.1	96	95	46	3.7
Co	89	19	21	15	13	52	0.6	18	8.7	7.0	1.1
Ni	1261	10	19	31	28	40	4.1	56	15	15	15
Cu	164	40	24	60	6.0	2.5	7.8	160	21	16	26
Zn	44	120	109	116	66	38	46	42	74	41	20
Ga	4.5	27	25	26	19	21	7.0	23	20	22	17
Rb	0.8	35	38	101	81	172	47	219	51	134	188
Sr	bd	910	611	218	197	1025	13	154	449	244	152
Y	9.4	41	30	34	23	12	11	14	21	16	2.8
Zr	17	340	240	212	201	182	35	144	115	144	19
Nb	1.0	12	9.8	6.7	9.0	9.6	2.2	8.0	9.3	8.2	4.0
Ba	17	637	525	534	539	1683	378	527	1072	601	364
La	0.1	27	20	35	20	32	6.0	27	25	33	5.1
Ce	1.6	60	48	71	44	58	13	49	54	53	9.5
Pr	0.3	7.8	6.2	8.5	5.1	6.2	1.5	6.0	6.3	7.0	1.0
Nd	1.8	34	27	33	22	22	5.6	22	23	25	3.5
Sm	0.9	7.4	6.3	6.7	4.3	3.3	1.1	4.3	4.3	5.0	0.8
Eu	0.3	2.1	1.7	1.4	1.1	0.8	0.2	1.2	1.2	0.9	0.2
Gd	1.4	7.0	6.0	6.4	4.1	2.4	1.1	3.6	4.0	4.0	0.7
Tb	0.3	1.1	0.9	1.0	0.6	0.4	0.2	0.5	0.6	0.5	0.1
Dy	1.8	6.6	5.4	6.1	3.7	2.1	1.4	2.7	3.4	2.9	0.6
Ho	0.4	1.3	1.0	1.2	0.7	0.4	0.4	0.5	0.8	0.5	0.1
Er	1.3	4.1	3.1	3.6	2.2	1.2	1.5	1.5	2.2	1.5	0.3
Tm	0.2	0.6	0.4	0.6	0.4	0.2	0.3	0.2	0.4	0.2	0.0
Yb	1.4	4.0	2.8	3.6	2.4	1.1	2.4	1.4	2.3	1.4	0.2
Lu	0.2	0.7	0.4	0.5	0.4	0.2	0.4	0.2	0.3	0.2	0.0
Hf	0.6	7.0	5.5	5.6	4.8	4.7	1.3	3.9	3.3	4.1	0.8
Ta	2.1	0.7	0.7	0.3	0.6	0.8	4.9	2.0	2.6	1.2	bd
Th	0.0	6.0	2.5	9.5	7.3	16	3.9	11	9.1	16	5.2
U	0.0	2.2	1.1	3.1	2.3	7.3	0.7	3.6	2.1	4.5	25
Cr	1437	68	68	411	68	68	547	bd	411	bd	479
Sc	37			17			2.0	15	11	7.6	1.8
Pb	0.2			18			8.7	3.7	12	14	31

Table S4. The major and trace element composition for the samples of this study. Bd - bellow detection limit, IMR – Impact melt rock (continuation).

Laboratory	Bruxelles	Bruxelles	SGS	SGS	Bruxelles	Bruxelles	Bruxelles	Bruxelles	Bruxelles	Bruxelles	Bruxelles
ID	C220607-1502	C220514-1340	C180824-1900	C180823-0955	C220510-1414	C220805-1315	C220510-1745	C220705-1643	S1/3	S7/1	S7/4
Sample	Granite	Pegmatite	Yellow IMR	Red IMR	Red IMR	Suevite	Suevite	Yellow IMR	Yellow IMR	Red IMR	Yellow IMR
Major elements (wt%)											
SiO_2	76.2	76.7	62.2	66.9	65.8	64.2	71.8	67.1	61.2	60.9	64.8
TiO_2	0.03	0.02	0.92	0.63	0.63	0.67	0.57	0.69	0.85	0.59	0.71
Al_2O_3	14.4	13.7	16.6	14.4	14.2	14.9	14.9	13.6	14.7	15.8	14.0
Fe_2O_3	0.98	0.77	3.16	6.62	5.67	5.75	1.55	4.83	4.07	4.40	5.90
MnO	0.05	0.03	0.01	0.01	0.01	0.03	0.00	0.01	0.14	0.05	0.11
MgO	bd	0.68	0.70	0.45	0.58	3.07	0.61	1.64	2.61	1.64	2.34
CaO	0.27	1.08	0.15	0.20	0.05	0.49	0.05	0.22	0.28	0.21	0.11
Na_2O	3.96	5.75	0.61	0.39	0.23	1.53	0.11	0.43	0.05	0.73	0.42
K_2O	3.45	1.68	11.80	9.49	9.21	5.86	8.07	7.14	7.24	10.5	8.21
P_2O_5	0.19	0.04	0.17	0.08	0.03	0.13	0.04	0.13	0.18	0.11	0.15
LOI	1.72	2.04	3.50	1.97	2.63	4.42	3.26	4.45	7.02	3.56	3.63
Total	101.21	102.43	99.82	101.13	99.01	101.05	100.88	100.28	98.33	98.45	100.43
Trace elements (ppm)											
V	4.3	4.9	111	121	62	66	45	74	92	67	79
Co	1.6	1.3	4.2	11	7.6	17	3.6	7.8	24	23	15
Ni	10	14	34	155	44	128	24	45	72	175	171
Cu	20	22	100	67	16	23	44	14	28	48	82
Zn	36	31	51	43	15	75	24	17	66	175	151
Ga	17	18	21	20	14	19	17	17	20	25	19
Rb	185	63	445	284	465	148	179	162	188	206	186
Sr	24	186	42	110	55	94	35	58	28	61	70
Y	4.6	5.4	30	19	10	22	18	29	24	16	22
Zr	34	8.3	215	186	94	102	82	96	171	156	162
Nb	7.8	3.1	10.6	9.7	4.4	4.8	4.1	4.5	8.2	7.9	7.4
Ba	37	61	423	704	492	461	512	669	376	716	650
La	2.8	2.4	28	16	17	20	32	18	55	51	27
Ce	5.4	5.2	49	34	29	41	43	37	104	98	53
Pr	0.7	0.7	5.9	3.9	3.2	5.1	6.3	4.1	12	11	6.4
Nd	2.0	2.9	23	15	11	20	24	17	45	41	24
Sm	0.5	1.0	4.5	3.0	2.3	4.4	4.0	3.8	8.2	7.4	4.9
Eu	0.1	0.2	1.2	0.7	0.5	1.0	0.8	0.9	2.0	1.5	1.0
Gd	0.4	1.2	4.6	2.7	1.5	3.6	2.7	3.4	6.8	5.4	4.5
Tb	0.1	0.2	0.7	0.5	0.3	0.6	0.5	0.7	0.9	0.6	0.7
Dy	0.6	1.0	5.0	3.1	1.8	3.9	3.1	4.7	4.8	3.7	4.0
Ho	0.1	0.2	1.0	0.6	0.4	0.8	0.6	1.0	0.9	0.7	0.8
Er	0.5	0.5	3.0	2.1	1.0	2.2	1.8	2.9	2.7	1.9	2.4
Tm	0.1	0.1	0.5	0.3	0.1	0.3	0.3	0.4	0.4	0.3	0.3
Yb	1.0	0.4	2.9	2.1	1.0	2.3	1.6	2.7	2.7	1.7	2.3
Lu	0.1	0.1	0.5	0.3	0.2	0.3	0.3	0.4	0.4	0.2	0.3
Hf	1.5	0.5	5.4	4.6	2.6	2.7	2.3	2.6	4.7	4.4	4.6
Ta	4.3	1.1	0.8	0.8	0.4	0.4	0.4	0.4	3.6	2.1	0.4
Th	1.0	2.9	8.7	8.4	6.3	7.1	7.9	6.6	7.5	13	9.3
U	7.9	7.3	6.5	2.8	3.2	2.5	2.1	10.7	2.7	3.7	3.7
Cr	616	479	68	137	889	2326	2258	958	bd	342	bd
Sc	2.5	1.5			11	13	13	14	15	14	12
Pb	37	9.6			20	12	16	8.4	8.3	24	19

Table S4. The major and trace element composition for the samples of this study. Bd - bellow detection limit, IMR – Impact melt rock (continuation).

Laboratory	Bruxelles	Bruxelles	Bruxelles	Bruxelles	Bruxelles	Bruxelles	Bruxelles	Bruxelles	Bruxelles	Bruxelles	Bruxelles
ID	S7/10	S7/15	S11/5	S11/17	S11/25	S15/1	S16/6	S16/7	S17/2	S17/7	S17/13
Sample	Suevite	Red IMR	Red IMR	Monomict bre.	Monomict bre.	Yellow IMR	Red IMR	Red IMR	Red IMR	Yellow IMR	Red IMR
Major elements (wt%)											
SiO_2	65.1	59.8	64.4	69.3	61.6	72.2	62.2	54.9	62.6	49.6	62.9
TiO_2	0.52	0.77	0.56	0.35	0.39	0.60	0.60	0.73	0.71	0.81	0.59
Al_2O_3	13.3	17.4	14.4	13.6	13.4	13.4	14.6	13.9	14.4	13.6	14.9
Fe_2O_3	5.37	4.44	5.14	3.70	5.54	0.47	5.94	11.43	5.93	22.0	5.26
MnO	0.03	0.09	0.02	0.07	0.23	0.01	0.01	0.08	0.02	0.29	0.03
MgO	1.55	2.38	0.76	1.09	1.26	bd	0.28	1.85	0.25	0.36	0.65
CaO	0.28	0.15	0.31	0.31	0.34	0.11	0.14	0.08	0.19	0.00	0.15
Na_2O	0.34	0.28	0.33	1.55	1.49	0.23	0.35	0.11	0.40	0.34	0.21
K_2O	9.06	8.60	9.94	6.90	6.69	9.90	11.0	6.86	10.1	8.94	10.9
P_2O_5	0.17	0.15	0.12	0.12	0.14	bd	0.09	0.27	0.09	0.42	0.04
LOI	3.58	6.36	3.71	2.47	5.90	1.71	2.27	8.43	4.07	5.52	2.92
Total	99.30	100.40	99.64	99.47	96.99	98.66	97.41	98.60	98.77	101.80	98.46
Trace elements (ppm)											
V	87	64	74	33	43	53	90	87	86	121	77
Co	26	14	15	12	8.7	5.4	5.4	15	5.7	12	4.0
Ni	179	145	131	42	24	5.2	104	339	16	39	24
Cu	259	69	42	16	22	13	41	179	48	769	56
Zn	95	139	52	96	75	98	53	109	55	109	41
Ga	17	22	19	16	19	15	16	24	18	18	18
Rb	182	261	246	180	223	692	346	202	328	191	228
Sr	38	44	73	68	91	130	69	39	73	46	43
Y	26	56	33	13	13	17	26	31	29	32	39
Zr	140	152	148	91	105	131	149	141	156	159	152
Nb	5.1	7.9	6.9	6.3	6.9	6.3	7.2	7.1	7.6	6.8	7.3
Ba	486	511	521	440	514	1272	780	390	619	762	518
La	26	56	32	21	27	26	29	44	38	25	33
Ce	51	101	60	41	50	44	53	92	58	56	62
Pr	6.0	12	7.1	4.7	5.6	5.2	6.1	11	7.3	6.5	7.1
Nd	23	44	27	16	20	20	24	42	27	26	26
Sm	5.2	9.1	5.7	3.3	3.8	4.0	4.7	8.3	5.1	6.2	5.2
Eu	1.1	2.1	1.4	0.6	0.7	1.0	1.1	1.8	1.2	1.7	1.1
Gd	4.9	9.1	5.8	2.7	3.1	3.5	4.6	7.3	5.0	6.1	5.3
Tb	0.7	1.4	0.8	0.4	0.4	0.5	0.7	1.0	0.7	1.0	0.8
Dy	4.3	9.0	5.1	2.3	2.7	3.1	4.2	5.9	4.7	6.2	5.9
Ho	0.9	1.8	1.1	0.5	0.5	0.6	0.8	1.2	0.9	1.2	1.2
Er	2.7	5.3	3.1	1.3	1.6	1.8	2.7	3.5	2.7	3.7	4.1
Tm	0.3	0.7	0.4	0.2	0.2	0.3	0.4	0.5	0.4	0.5	0.6
Yb	2.3	4.4	2.8	1.2	1.4	1.8	2.7	3.5	2.6	3.5	4.0
Lu	0.3	0.6	0.4	0.2	0.2	0.3	0.5	0.5	0.4	0.5	0.6
Hf	3.9	4.3	4.1	2.8	3.1	3.6	4.3	4.1	4.5	4.3	4.5
Ta	0.4	0.1	0.7	5.0	3.7	3.2	0.5	12	2.0	3.2	1.2
Th	8.7	10	8.1	13	14	5.9	8.2	8.2	7.5	6.9	8.7
U	4.5	6.3	3.3	3.7	5.1	3.3	3.8	7.0	2.7	4.9	3.6
Cr	411	bd	342	479	547	342	411	bd	342	bd	411
Sc	11	13	14	5.7	7.9	13	15	13	14	21	14
Pb	23	21	26	20	32	3.3	27	29	44	28	39

Table S5. Sm-Nd whole-rock isotope data for the samples of this study. IMR – Impact melt rock.

ID	Sample	Sm (ppm)	Nd (ppm)	$^{147}Sm/^{144}Nd$	$^{143}Nd/^{144}Nd$ ± 2SE	$\varepsilon_{Nd\ (0)}$	T_{DM} (Ga)	$^{87}Sr/^{86}Sr$	2SD	$^{87}Sr/^{86}Sr_{(206.9)}$	$^{143}Nd/^{144}Nd_{(206.9)}$	$\varepsilon_{Nd\ (206.9)}$	$TDM_{(206.9)}$
C220522-1749	Serpentinite	0.873	2.032	0.2597	0.512764+/-26	3.25	-1.11	0.70586	0.00001		0.512412	0.8	-1.462
C180824-1500	Amphibolite	10.178	47.347	0.1299	0.512574+/-5	-1.25	0.86	0.70528	5E-06	0.704954	0.512398	0.52	0.987
C180822-1625	Amphibolite	8.499	40.776	0.1260	0.512542+/-5	-1.87	0.87	0.70604	8E-06	0.705511	0.512371	-0.01	0.998
C220506-0954	Paragneiss	7.446	36.405	0.1236	0.512428+/-9	-4.10	1.04	0.71494	4E-06	0.711014	0.512261	-2.17	1.155
C180825-0930	Paragneiss	2.612	11.997	0.1316	0.512536+/-4	-1.99	0.94	0.71212	5E-06	0.708636	0.512358	-0.27	1.072
C180824-1645	Leptynite	4.386	28.897	0.0917	0.512318+/-4	-6.25	0.91	0.70852	5E-06	0.707088	0.512194	-3.47	0.997
C220607-1115	Leptynite	3.136	14.708	0.1289	0.511895+/-16	-14.86	2.08	0.73206	4E-06	0.701098	0.51172	-12.71	2.117
C180825-1115	Monzodiorite	5.523	28.947	0.1153	0.512316+/-12	-6.28	1.12	0.72183	5E-06	0.709702	0.51216	-4.13	1.226
C220511-1352	Granodiorite	3.314	17.688	0.1132	0.512514+/-11	-2.42	0.81	0.7064	5E-06	0.70543	0.512361	-0.21	0.918
C220608-2001	Granodiorite	5.045	26.769	0.1139	0.512292+/-14	-6.75	1.14	0.71379	5E-06	0.709112	0.512138	-4.57	1.245
C180824-1630	Granite	0.918	4.079	0.1360	0.512318+/-17	-6.24	1.41	0.72263	6E-06	0.712123	0.512134	-4.64	1.527
C220607-1502	Granite	0.591	2.546	0.1403	0.511928+/-29	-15.49	2.48	0.78702	5E-06	0.7208	0.511738	-12.37	2.356
C220514-1340	Pegmatite	1.215	3.629	0.2024	0.51231+/-14	-6.28	199.66	0.71078	5E-06	0.707888	0.512036	-6.55	7.541
S11/17	Monomict bre.	4.151	21.397	0.1173	0.512283+/-12	-6.93	1.19	0.73367	3E-06	0.711079	0.512124	-4.83	1.299
C220510-1745	Suevite	4.235	25.322	0.1011	0.512268+/-11	-7.22	1.05	0.75992	7E-06	0.716577	0.512131	-4.69	1.141
C220805-1315	Suevite	4.462	21.078	0.1280	0.512489+/-8	-2.91	0.98	0.72145	6E-06	0.708056	0.512316	-1.09	1.108
S7/10	Suevite	5.391	25.422	0.1282	0.512432+/-10	-4.01	1.08	0.74287	5E-06	0.702344	0.512258	-2.21	1.206
C180823-0955	Red IMR	4.200	21.880	0.1160	0.512395+/-6	-4.74	1.01	0.72759	8E-06	0.705532	0.512238	-2.61	1.118
S7/1	Red IMR	8.066	44.897	0.1086	0.512380+/-11	-5.03	0.96	0.73697	3E-06	0.708273	0.512233	-2.71	1.064
S16/7	Red IMR	8.928	45.254	0.1193	0.512351+/-10	-5.61	1.11	0.74207	4E-06	0.697881	0.51219	-3.55	1.222
C180824-1900	Yellow IMR	6.264	31.996	0.1183	0.512451+/-8	-3.65	0.95	0.80215	5E-06	0.711147	0.512291	-1.58	1.059
C220705-1643	Yellow IMR	4.046	18.771	0.1303	0.512479+/-6	-3.11	1.03	0.7327	6E-06	0.708966	0.512303	-1.35	1.154
S1/3	Yellow IMR	8.702	47.361	0.1111	0.512454+/-9	-3.59	0.88	0.74948	6E-06	0.69151	0.512304	-1.33	0.984
S7/4	Yellow IMR	5.107	25.261	0.1222	0.512377+/-11	-5.10	1.10	0.72905	4E-06	0.706427	0.512212	-3.13	1.218
S15/1	Yellow IMR	4.314	22.247	0.1172	0.512411+/-6	-4.42	1.00	0.75604	4E-06	0.710517	0.512252	-2.33	1.108
S17/7	Yellow IMR	6.258	27.635	0.1369	0.512452+/-7	-3.63	1.16	0.73813	6E-06	0.702411	0.512267	-2.05	1.296

Table S6. U-Pb on zircon radiogenic data of the samples analyzed in this study.

[a] Fraction of the non-radiogenic ^{206}Pb in the analyzed zircon spot, where $f_{206}=[^{206}Pb/^{204}Pb]c/[^{206}Pb/^{204}Pb]s$ (c=common; s=sample)

[b] Th/U ratios and amount of Pb, Th and U (in pmm) are calculated relative to GJ-1 reference zircon

[c] Corrected for background and within-run Pb/U fractionation and normalised to reference zircon GJ-1 (ID-TIMS values/measured value); $^{207}Pb/^{235}U$ calculated using $(^{207}Pb/^{206}Pb)*(^{206}Pb/^{238}U)*(137.88)$

[d] Rho is the error correlation defined as the quotient of the propagated errors of the $^{206}Pb/^{238}U$ and the $^{207}/^{235}U$ ratio

[e] Corrected for mass-bias by normalising to GJ-1 reference zircon and common Pb using the model Pb composition of Stacey and Kramers (1975)

[f] Degree of concordance, 6/8-7/5= ($^{206}Pb/^{238}U$ age * 100) / ($^{207}Pb/^{235}U$ age), according to Horstwood et al., 2016.

							Isotope ratios[c]							Ages (Ma)						
Sample_ID	Analysis_ID	f_{206}[a]	Pb (ppm)	Th (ppm)	U (ppm)	Th/U[b]	$^{207}Pb/^{235}U$	1σ (%)	$^{206}Pb/^{238}U$	1σ (%)	Rho[d]	$^{207}Pb/^{206}Pb$	1σ (%)	$^{206}Pb/^{238}U$	1σ (abs)	$^{207}Pb/^{235}U$	1σ (abs)	$^{207}Pb/^{206}Pb$	1σ (abs)	Conc.[f](%)
C220506-0954	0954 36	6.2226	0	0	0	0.19	40.38	9.47	0.31	6.15	0.65	0.93	7.20	1761.6	108.3	3780.2	357.9	5138.3	369.9	46.60
C220506-0954	0954.2 9	0.0033	4	6	57	0.10	1.11	4.28	0.11	3.31	0.77	0.07	2.73	674	22	758	32	1014	28	88.94
C220506-0954	0954.2 16	0.0035	2	8	14	0.56	0.88	7.83	0.09	4.57	0.58	0.07	6.36	581	27	639	50	852	54	90.83
C220506-0954	0954.2 14	0.0034	5	24	23	1.05	0.81	6.64	0.09	2.50	0.38	0.06	6.15	561	14	605	40	773	48	92.74
C220506-0954	0954 52	0.0458	17	85	373	0.23	0.30	4.51	0.04	2.98	0.66	0.05	3.38	258	8	268	12	360	12	96.12
C220506-0954	0954 29	0.6535	0	0	-1	0.44	9.17	14.33	0.11	2.04	0.14	0.61	14.18	663.8	13.5	2354.8	337.4	4539.0	643.8	28.19
C220506-0954	0954.2 13	0.0193	7	9	24	0.37	1.02	2.50	0.08	1.28	0.51	0.09	2.14	526	7	713	18	1358	29	73.75
C220506-0954	0954.2 2	0.0039	8	7	50	0.13	1.25	17.17	0.10	2.18	0.13	0.09	17.03	630	14	823	141	1385	236	76.64
C220506-0954	0954.2 18	0.0035	3	15	21	0.72	1.14	1.41	0.10	1.39	0.98	0.08	0.28	634	9	773	11	1200	3	81.99
C220506-0954	0954.2 15	0.0039	8	14	72	0.19	0.83	2.00	0.08	1.52	0.76	0.07	1.30	509	8	612	12	1015	13	83.14
C220506-0954	0954.2 7	0.0080	14	13	228	0.06	1.06	1.91	0.10	0.80	0.42	0.08	1.73	629	5	736	14	1078	19	85.43
C220506-0954	0954 15	0.0126	11	18	125	0.15	0.56	3.37	0.07	1.60	0.47	0.06	2.97	451.0	7.2	454.3	15.3	470.8	14.0	99.28
C220506-0954	0954 17	0.0142	8	31	72	0.43	0.63	3.16	0.07	1.68	0.53	0.06	2.68	456.7	7.6	498.8	15.8	696.7	18.7	91.57
C220506-0954	0954 55	0.0120	19	193	205	0.95	0.59	3.95	0.07	1.70	0.43	0.06	3.57	457	8	472	19	545	19	96.84
C220506-0954	0954.2 17	0.0046	5	12	38	0.32	0.63	2.21	0.08	1.93	0.87	0.06	1.07	469	9	495	11	619	7	94.68
C220506-0954	0954 19	0.0370	64	540	690	0.79	0.71	2.93	0.08	1.42	0.49	0.06	2.56	508	7	544	16	702	18	93.23
C220506-0954	0954 39	0.0270	6	26	57	0.47	0.66	3.41	0.08	1.37	0.40	0.06	3.13	510	7	517	18	545	17	98.78
C220506-0954	0954 14	0.0113	12	70	109	0.65	0.66	3.46	0.08	1.44	0.42	0.06	3.15	512	7	515	18	528	17	99.40
C220506-0954	0954 26	0.0096	17	43	141	0.31	0.68	2.94	0.08	1.53	0.52	0.06	2.51	512	8	529	16	602	15	96.81
C220506-0954	0954 5	0.0055	22	142	237	0.60	0.67	2.71	0.08	1.18	0.43	0.06	2.44	517	6	520	14	534	13	99.41
C220506-0954	0954 6	0.0157	7	16	77	0.22	0.66	2.99	0.08	1.17	0.39	0.06	2.75	519	6	517	15	506	14	100.48
C220506-0954	0954 34	0.0240	3	11	29	0.37	0.73	3.45	0.08	1.34	0.39	0.06	3.18	520	7	555	19	700	22	93.73
C220506-0954	0954 21	0.0069	28	128	280	0.46	0.68	3.09	0.08	1.42	0.46	0.06	2.75	523	7	524	16	529	15	99.81
C220506-0954	0954 51	0.0103	12	48	116	0.42	0.67	3.09	0.08	1.57	0.51	0.06	2.66	524	8	522	16	511	14	100.47
C220506-0954	0954 8	0.0056	25	66	270	0.25	0.68	2.68	0.08	1.15	0.43	0.06	2.42	525	6	524	14	523	13	100.04
C220506-0954	0954 45	0.0454	34	57	310	0.19	0.69	2.81	0.08	1.31	0.47	0.06	2.49	525	7	533	15	563	14	98.66
C220506-0954	0954 10	0.0137	15	67	142	0.48	0.69	2.84	0.09	1.20	0.42	0.06	2.58	526	6	535	15	570	15	98.45
C220506-0954	0954 20	0.0228	12	56	131	0.43	0.76	3.00	0.09	1.35	0.45	0.06	2.68	527	7	572	17	757	20	92.07
C220506-0954	0954 30	0.0156	8	33	73	0.46	0.72	3.13	0.09	1.47	0.47	0.06	2.77	528	8	553	17	657	18	95.50
C220506-0954	0954 11	0.0133	9	35	104	0.34	0.69	2.84	0.09	1.11	0.39	0.06	2.62	530	6	532	15	544	14	99.51
C220506-0954	0954 42	0.0167	11	65	104	0.63	0.74	2.82	0.09	1.37	0.48	0.06	2.47	532.1	7.3	562.2	15.9	685.9	16.9	94.65
C220506-0954	0954 50	0.0186	5	15	53	0.29	0.67	3.15	0.09	1.37	0.43	0.06	2.83	532	7	524	16	485	14	101.69
C220506-0954	0954 7	0.0218	9	28	92	0.31	0.76	3.04	0.09	1.11	0.36	0.06	2.83	535.3	5.9	576.4	17.5	742.0	21.0	92.87
C220506-0954	0954 13	0.0096	15	56	153	0.37	0.70	3.18	0.09	1.33	0.42	0.06	2.88	535.5	7.1	539.6	17.1	557.0	16.1	99.24
C220506-0954	0954.2 6	0.0061	10	17	64	0.27	0.73	1.12	0.09	0.96	0.86	0.06	0.58	538	5	558	6	643	4	96.30
C220506-0954	0954 49	0.0294	5	17	47	0.37	0.69	3.54	0.09	1.36	0.38	0.06	3.27	538	7	532	19	506	17	101.15
C220506-0954	0954.2 5	0.0090	6	8	37	0.22	0.68	3.67	0.09	1.06	0.29	0.06	3.52	539	6	528	19	479	17	102.13
C220506-0954	0954 25	0.0035	46	83	453	0.18	0.74	2.88	0.09	1.53	0.53	0.06	2.43	542.7	8.3	562.6	16.2	644.1	15.7	96.46
C220506-0954	0954 3	0.0164	8	34	74	0.46	0.70	2.90	0.09	1.11	0.38	0.06	2.68	543	6	538	16	515	14	101.00
C220506-0954	0954 1	0.0157	9	42	89	0.47	0.68	3.12	0.09	1.10	0.35	0.06	2.92	545.1	6.0	525.0	16.4	438.8	12.8	103.82

Table S6. U-Pb on zircon radiogenic data of the samples analyzed in this study (continuation).

C220506-0954	0954 41	0.0187	5	29	43	0.67	0.72	3.04	0.09	1.24	0.41	0.06	2.77	546.3	6.8	549.1	16.7	560.9	15.6	99.48
C220506-0954	0954 2	0.0142	10	73	81	0.90	0.73	3.20	0.09	1.15	0.36	0.06	2.99	549.9	6.3	555.9	17.8	580.7	17.4	98.91
C220506-0954	0954 16	0.0113	11	52	102	0.51	0.74	3.25	0.09	1.31	0.40	0.06	2.98	550.8	7.2	565.2	18.4	623.8	18.6	97.44
C220506-0954	0954 40	0.0088	10	42	102	0.42	0.70	2.71	0.09	1.27	0.47	0.06	2.39	553.3	7.0	536.2	14.5	464.3	11.1	103.18
C220506-0954	0954 37	0.0088	14	50	139	0.36	0.70	2.73	0.09	1.25	0.46	0.06	2.43	556.3	7.0	537.3	14.7	457.3	11.1	103.54
C220506-0954	0954.2 3	0.0046	6	12	48	0.26	0.69	2.19	0.09	1.79	0.82	0.06	1.25	561	10	535	12	425	5	104.85
C220506-0954	0954.2 4	0.0033	12	44	81	0.55	0.70	1.41	0.09	1.12	0.79	0.06	0.87	561	6	541	8	461	4	103.58
C220506-0954	0954 23	0.0099	11	41	111	0.37	0.75	3.08	0.09	1.38	0.45	0.06	2.75	565.6	7.8	570.3	17.6	589.3	16.2	99.17
C220506-0954	0954 43	0.0162	3	14	27	0.51	0.79	3.23	0.09	1.31	0.40	0.06	2.96	566.6	7.4	591.6	19.1	688.5	20.3	95.78
C220506-0954	0954 33	0.0120	10	44	110	0.40	0.75	3.05	0.09	1.39	0.46	0.06	2.71	567	8	567	17	565	15	100.08
C220506-0954	0954 38	0.0142	5	22	51	0.45	0.73	2.81	0.09	1.21	0.43	0.06	2.53	569	7	554	16	493	12	102.68
C220506-0954	0954 35	0.0120	9	56	82	0.69	0.67	3.10	0.09	1.22	0.39	0.05	2.85	573.7	7.0	522.9	16.2	306.8	8.7	109.71
C220506-0954	0954 44	0.0267	3	28	24	1.17	0.71	3.57	0.09	1.22	0.34	0.06	3.36	575.7	7.0	545.5	19.5	421.0	14.1	105.55
C220506-0954	0954 48	0.0203	18	114	181	0.63	0.70	2.96	0.09	1.29	0.44	0.05	2.67	581	8	537	16	357	10	108.07
C220506-0954	0954 12	0.0161	10	46	93	0.50	0.85	2.84	0.09	1.25	0.44	0.07	2.56	580.8	7.2	626.2	17.8	793.9	20.3	92.75
C220506-0954	0954 22	0.0081	19	112	168	0.67	0.78	3.11	0.09	1.26	0.40	0.06	2.84	581.3	7.3	584.9	18.2	598.9	17.0	99.39
C220506-0954	0954 18	0.0281	5	27	40	0.70	0.89	3.06	0.09	1.25	0.41	0.07	2.79	583.2	7.3	645.0	19.7	867.8	24.2	90.42
C220506-0954	0954.2 11	0.0070	9	22	47	0.46	0.88	2.17	0.10	0.83	0.38	0.07	2.00	592	5	639	14	810	16	92.58
C220506-0954	0954.2 8	0.0116	20	30	81	0.37	0.85	1.30	0.10	1.03	0.79	0.06	0.79	596	6	624	8	729	6	95.43
C220506-0954	0954 47	0.0115	11	52	94	0.55	0.77	2.61	0.10	1.15	0.44	0.06	2.35	612	7	577	15	442	10	106.05
C220506-0954	0954 54	0.0121	7	28	62	0.45	0.75	2.99	0.10	1.25	0.42	0.05	2.71	613	8	568	17	393	11	107.88
C220506-0954	0954 9	0.0045	17	56	148	0.38	0.84	2.66	0.10	1.06	0.40	0.06	2.44	616	7	616	16	617	15	99.96
C220506-0954	0954 27	0.0105	14	50	118	0.43	0.91	2.67	0.10	1.23	0.46	0.06	2.37	634	8	659	18	744	18	96.24
C220506-0954	0954 24	0.0093	27	132	221	0.60	0.86	2.85	0.10	1.26	0.44	0.06	2.55	634	8	629	18	611	16	100.82
C220506-0954	0954 32	0.0134	8	30	63	0.48	0.88	3.18	0.11	1.30	0.41	0.06	2.91	643.9	8.4	643.1	20.5	640.0	18.6	100.13
C220506-0954	0954.2 12	0.0050	13	46	85	0.54	0.90	4.32	0.11	1.07	0.25	0.06	4.19	656	7	651	28	634	27	100.73
C220506-0954	0954 53	0.0238	6	19	50	0.38	0.85	3.29	0.11	1.06	0.32	0.06	3.12	662	7	627	21	501	16	105.67
C220506-0954	0954 28	0.0196	2	8	16	0.49	1.06	2.97	0.12	1.09	0.37	0.06	2.76	740.6	8.0	734.0	21.8	713.8	19.7	100.91
C220506-0954	0954 4	0.0163	7	9	32	0.28	2.03	2.39	0.18	0.62	0.26	0.08	2.31	1090.0	6.7	1126.9	26.9	1198.6	27.7	96.73
C220506-0954	0954.2 10	0.0030	7	7	23	0.29	2.56	2.20	0.23	2.19	0.99	0.08	0.25	1321	29	1290	28	1239	3	102.40
C220506-0954	0954 31	0.0142	13	19	50	0.39	2.88	2.03	0.23	0.64	0.32	0.09	1.93	1326.1	8.5	1376.9	28.0	1456.6	28.1	96.31
C220608-2001	055 2001 1.cs	0.0213	31	345	557	0.62	0.34	2.69	0.04	1.61	0.60	0.06	2.16	273.0	4.4	294.5	7.9	468.3	10.1	92.71
C220608-2001	056 2001 2.cs	0.0096	12	80	107	0.76	0.67	2.02	0.08	0.88	0.44	0.06	1.82	505.9	4.5	523.6	10.6	601.6	10.9	96.62
C220608-2001	057 2001 3.cs	0.0088	20	142	311	0.46	0.33	2.37	0.05	1.44	0.60	0.05	1.89	290.1	4.2	290.1	6.9	290.1	5.5	100.00
C220608-2001	058 2001 4.cs	0.0097	40	114	508	0.23	0.41	2.14	0.05	1.21	0.57	0.05	1.76	341.7	4.1	349.8	7.5	403.8	7.1	97.69
C220608-2001	059 2001 5.cs	0.0162	21	147	534	0.28	0.29	2.68	0.04	1.92	0.72	0.06	1.86	227.0	4.4	255.5	6.8	525.9	9.8	88.85
C220608-2001	060 2001 6.cs	0.0072	26	166	497	0.34	0.34	2.32	0.05	1.40	0.61	0.05	1.84	292.5	4.1	299.2	6.9	351.4	6.5	97.78
C220608-2001	061 2001 7.cs	0.0073	20	123	383	0.32	0.34	2.30	0.05	1.39	0.60	0.05	1.84	296.6	4.1	297.8	6.9	306.7	5.6	99.62
C220608-2001	062 2001 8.cs	0.0126	11	51	190	0.27	0.35	2.39	0.05	1.39	0.58	0.05	1.94	299.7	4.2	305.8	7.3	352.6	6.8	98.01
C220608-2001	063 2001 9.cs	0.0101	23	244	716	0.34	0.32	2.39	0.04	1.58	0.66	0.05	1.79	265.2	4.2	279.6	6.7	401.9	7.2	94.85
C220608-2001	064 2001 10.c	0.0057	27	106	419	0.26	0.33	2.38	0.05	1.50	0.63	0.05	1.85	292.7	4.4	292.2	7.0	288.0	5.3	100.18
C220608-2001	068 2001 11.c	0.0266	25	146	493	0.30	0.34	2.68	0.04	1.67	0.62	0.06	2.09	280.9	4.7	300.3	8.0	454.5	9.5	93.52
C220608-2001	069 2001 12.c	0.0034	34	184	608	0.30	0.36	2.63	0.05	1.60	0.61	0.05	2.08	299.4	4.8	309.0	8.1	382.3	8.0	96.88
C220608-2001	070 2001 13.c	0.0078	25	152	464	0.33	0.34	2.77	0.05	1.56	0.57	0.05	2.28	299.4	4.7	299.7	8.3	301.9	6.9	99.90
C220608-2001	071 2001 14.c	0.7139	1	0	1	0.26	20.89	9.95	0.19	8.89	0.89	0.79	4.48	1125.9	100.0	3133.7	311.8	4911.1	220.1	35.93
C220608-2001	072 2001 15.c	0.0075	8	60	146	0.42	0.35	2.91	0.05	1.58	0.54	0.05	2.44	299.9	4.7	301.5	8.8	314.2	7.7	99.46
C220608-2001	073 2001 16.c	0.0057	20	139	370	0.38	0.35	2.73	0.05	1.57	0.58	0.05	2.23	304.4	4.8	305.1	8.3	310.3	6.9	99.78
C220608-2001	074 2001 17.c	0.0073	13	62	247	0.25	0.37	2.71	0.05	1.54	0.57	0.05	2.23	307.3	4.7	318.7	8.6	403.0	9.0	96.42
C220608-2001	075 2001 18.c	0.0021	28	240	483	0.50	0.35	2.63	0.05	1.55	0.59	0.05	2.13	307.8	4.8	307.5	8.1	305.3	6.5	100.10
C220608-2001	076 2001 19.c	0.0043	18	7	515	0.01	0.47	2.28	0.06	1.38	0.61	0.06	1.81	345.6	4.8	392.5	8.9	679.3	12.3	88.04
C220608-2001	077 2001 20.c	0.0043	22	163	385	0.43	0.36	2.61	0.05	1.48	0.57	0.05	2.15	315.0	4.7	313.6	8.2	303.2	6.5	100.45
C220608-2001	081 2001 21.c	0.0000	0	0	0	0.13	50.60	108.89	0.19	106.36	0.98	1.92	23.35	1125.4	1197.0	4004.1	4360.3	6141.6	1434.3	28.11
C220608-2001	082 2001 22.c	0.0202	12	106	182	0.59	0.37	2.61	0.05	1.63	0.63	0.06	2.03	299.7	4.9	320.5	8.4	474.0	9.6	93.53
C220608-2001	083 2001 23.c	0.0067	11	17	27	0.64	5.20	1.04	0.33	0.44	0.42	0.11	0.94	1853.1	8.1	1853.1	19.2	1853.1	17.5	100.00
C220608-2001	084 2001 24.c	0.2029	0	0	0	0.25	74.24	11.64	1.05	7.97	0.68	0.51	8.48	4629.9	369.0	4387.2	510.6	4277.4	362.8	105.53

Table S6. U-Pb on zircon radiogenic data of the samples analyzed in this study (continuation).

C220608-2001	085 2001 25.d	0.0054	10	25	54	0.46	1.63	1.60	0.17	0.54	0.34	0.07	1.51	984.5	5.3	981.9	15.7	976.2	14.7	100.26
C220608-2001	086 2001 26.d	0.0087	6	36	95	0.38	0.39	2.40	0.05	1.38	0.58	0.06	1.97	321.4	4.4	332.8	8.0	413.2	8.1	96.58
C220608-2001	087 2001 27.d	0.0531	0	0	1	0.13	4.85	6.70	0.05	3.28	0.49	0.64	5.84	344.8	11.3	1793.9	120.1	4602.4	268.7	19.22
C220608-2001	088 2001 28.d	0.0064	8	54	152	0.36	0.35	2.39	0.05	1.43	0.60	0.05	1.91	305.1	4.4	305.7	7.3	310.4	5.9	99.80
C220608-2001	089 2001 29.d	0.0062	7	49	152	0.32	0.36	2.41	0.05	1.42	0.59	0.05	1.95	309.5	4.4	309.7	7.5	311.2	6.1	99.94
C220608-2001	090 2001 30.d	0.0054	14	58	245	0.24	0.36	2.31	0.05	1.48	0.64	0.05	1.78	309.0	4.6	313.6	7.3	347.9	6.2	98.53
C220608-2001	094 2001 31.d	0.0250	12	135	196	0.69	0.37	3.75	0.05	2.52	0.67	0.06	2.79	299.1	7.5	317.6	11.9	455.8	12.7	94.17
C220608-2001	095 2001 32.d	0.0038	17	88	335	0.26	0.35	2.27	0.05	1.61	0.71	0.05	1.60	305.9	4.9	307.0	7.0	315.5	5.0	99.64
C220608-2001	096 2001 33.d	0.0075	12	59	201	0.29	0.36	2.33	0.05	1.56	0.67	0.05	1.73	314.1	4.9	312.2	7.3	297.5	5.2	100.63
C220608-2001	097 2001 34.d	0.0056	15	128	277	0.46	0.35	2.42	0.05	1.65	0.68	0.05	1.78	305.3	5.0	305.9	7.4	311.1	5.5	99.78
C220608-2001	098 2001 35.d	0.0070	12	63	243	0.26	0.35	2.44	0.05	1.63	0.67	0.05	1.82	304.2	5.0	305.7	7.5	317.8	5.8	99.48
C220608-2001	099 2001 36.d	0.0095	18	167	337	0.50	0.33	2.56	0.05	1.71	0.67	0.05	1.90	291.5	5.0	292.6	7.5	301.6	5.7	99.62
C220608-2001	100 2001 37.d	0.0066	13	70	248	0.28	0.35	2.39	0.05	1.62	0.68	0.05	1.75	304.8	4.9	305.2	7.3	307.9	5.4	99.88
C220608-2001	101 2001 38.d	0.4127	1	1	1	0.41	2.17	10.79	0.03	9.87	0.91	0.45	4.37	219.2	21.6	1171.0	126.4	4100.4	179.1	18.72
C220608-2001	102 2001 39.d	0.2129	0	0	1	0.05	14.09	8.49	0.20	3.44	0.41	0.52	7.77	1150.3	39.6	2755.9	234.1	4307.9	334.5	41.74
C220511-1352	003 1352 1.cs	0.0098	7	45	97	0.47	0.48	2.26	0.06	1.19	0.53	0.06	1.92	384.9	4.6	395.4	8.9	457.1	8.8	97.35
C220511-1352	004 1352 2.cs	0.0113	8	66	105	0.64	0.52	2.15	0.07	1.08	0.50	0.05	1.86	439.6	4.8	426.3	9.2	354.8	6.6	103.13
C220511-1352	005 1352 3.cs	0.0044	11	93	155	0.61	0.43	2.11	0.06	1.33	0.63	0.06	1.64	347.5	4.6	362.5	7.7	459.5	7.5	95.86
C220511-1352	006 1352 4.cs	0.0070	13	126	172	0.74	0.43	2.26	0.06	1.24	0.55	0.05	1.89	367.4	4.6	363.9	8.2	341.8	6.5	100.96
C220511-1352	007 1352 5.cs	0.0064	9	56	132	0.43	0.42	2.32	0.06	1.30	0.56	0.05	1.92	354.4	4.6	355.1	8.2	359.6	6.9	99.81
C220511-1352	008 1352 6.cs	0.0082	9	65	135	0.48	0.44	2.30	0.06	1.23	0.54	0.06	1.94	363.4	4.5	370.6	8.5	415.9	8.1	98.06
C220511-1352	009 1352 7.cs	0.0054	8	57	127	0.45	0.42	2.14	0.06	1.28	0.60	0.05	1.71	354.6	4.5	359.3	7.7	389.1	6.7	98.72
C220511-1352	010 1352 8.cs	0.0072	13	111	156	0.72	0.49	2.09	0.07	1.21	0.58	0.05	1.70	410.0	4.9	408.2	8.5	397.8	6.8	100.45
C220511-1352	011 1352 9.cs	0.0115	6	49	92	0.54	0.43	2.42	0.06	1.26	0.52	0.05	2.07	360.4	4.5	361.2	8.8	366.2	7.6	99.78
C220511-1352	012 1352 10.c	0.0127	10	77	134	0.58	0.44	2.31	0.06	1.26	0.54	0.06	1.93	360.2	4.5	367.6	8.5	414.9	8.0	97.97
C220511-1352	016 1352 11.c	0.0079	15	105	211	0.50	0.42	3.36	0.06	1.86	0.55	0.05	2.80	359.1	6.7	356.2	12.0	337.6	9.4	100.81
C220511-1352	017 1352 12.c	0.0066	12	81	174	0.47	0.42	3.27	0.06	1.85	0.57	0.05	2.70	356.6	6.6	357.7	11.7	364.6	9.8	99.70
C220511-1352	018 1352 13.c	0.0044	14	104	216	0.49	0.44	3.24	0.06	1.83	0.57	0.06	2.67	363.2	6.6	370.3	12.0	414.9	11.1	98.09
C220511-1352	019 1352 14.c	0.0048	16	129	294	0.44	0.43	3.27	0.06	1.87	0.57	0.06	2.68	355.9	6.6	365.1	11.9	423.7	11.4	97.49
C220511-1352	020 1352 15.c	0.0055	17	155	249	0.63	0.45	3.17	0.06	1.82	0.57	0.06	2.59	366.5	6.7	378.3	12.0	451.6	11.7	96.87
C220511-1352	021 1352 16.c	0.0050	21	191	283	0.68	0.44	3.22	0.06	1.77	0.55	0.05	2.69	374.2	6.6	368.3	11.9	331.6	8.9	101.59
C220511-1352	022 1352 17.c	0.0049	20	170	273	0.63	0.44	3.19	0.06	1.79	0.56	0.05	2.64	368.9	6.6	368.6	11.7	367.1	9.7	100.07
C220511-1352	023 1352 18.c	0.0051	11	67	156	0.43	0.45	3.23	0.06	1.79	0.55	0.05	2.70	370.8	6.6	375.9	12.2	407.3	11.0	98.65
C220511-1352	024 1352 19.c	0.0080	10	66	156	0.43	0.43	3.27	0.06	1.83	0.56	0.05	2.71	364.4	6.7	364.0	11.9	361.4	9.8	100.11
C220511-1352	025 1352 20.c	0.0059	12	89	179	0.50	0.42	3.26	0.06	1.83	0.56	0.05	2.70	361.3	6.6	357.4	11.7	332.2	9.0	101.09
C220511-1352	029 1352 21.c	0.0045	58	644	893	0.73	0.42	3.22	0.06	1.73	0.54	0.05	2.72	355.8	6.1	353.2	11.4	336.0	9.1	100.74
C220511-1352	030 1352 22.c	0.0081	28	366	375	0.98	0.42	3.29	0.06	1.76	0.54	0.05	2.78	356.0	6.3	354.7	11.7	346.2	9.6	100.37
C220511-1352	031 1352 23.c	1.3185	1	0	0	1.13	528.50	15.32	4.67	14.72	0.96	0.82	4.22	11187.1	1647.3	6368.4	975.5	4957.9	209.4	175.67
C220511-1352	032 1352 24.c	0.0042	14	101	221	0.46	0.42	3.25	0.06	1.76	0.54	0.05	2.73	352.4	6.2	356.8	11.6	386.1	10.6	98.74
C220511-1352	033 1352 25.c	0.0085	14	105	206	0.51	0.47	3.07	0.06	1.68	0.55	0.06	2.57	370.4	6.2	390.8	12.0	513.7	13.2	94.77
C220511-1352	034 1352 26.c	0.0070	17	135	241	0.56	0.41	3.34	0.06	1.70	0.51	0.05	2.88	365.9	6.2	352.3	11.8	263.5	7.6	103.87
C220511-1352	035 1352 27.c	0.0055	19	184	270	0.69	0.42	3.24	0.06	1.75	0.54	0.05	2.73	354.6	6.2	355.7	11.5	363.2	9.9	99.68
C220511-1352	036 1352 28.c	0.0049	19	156	275	0.57	0.41	3.33	0.06	1.76	0.53	0.05	2.82	356.4	6.3	351.4	11.7	318.9	9.0	101.41
C220511-1352	037 1352 29.c	0.0045	25	261	348	0.75	0.44	3.20	0.06	1.68	0.53	0.05	2.72	370.1	6.2	373.6	11.9	395.0	10.7	99.08
C220511-1352	038 1352 30.c	0.0030	23	209	337	0.63	0.42	3.23	0.06	1.75	0.54	0.05	2.71	355.9	6.2	355.9	11.5	356.3	9.7	99.98
C220511-1352	043 1352 32	0.0079	8	75	128	0.59	0.42	2.55	0.06	1.26	0.49	0.05	2.22	353.1	4.4	354.9	9.1	366.4	8.1	99.50
C220511-1352	044 1352 33.c	0.0054	10	72	148	0.49	0.42	2.65	0.06	1.27	0.48	0.05	2.32	352.8	4.5	353.8	9.4	360.6	8.4	99.71
C220511-1352	045 1352 34.c	0.0173	9	59	130	0.46	0.42	3.05	0.06	1.26	0.41	0.05	2.78	354.5	4.5	353.6	10.8	348.1	9.7	100.24
C220511-1352	046 1352 35.c	0.0087	9	63	142	0.45	0.42	2.53	0.06	1.24	0.49	0.05	2.21	355.2	4.4	356.0	9.0	361.2	8.0	99.77
C220511-1352	047 1352 36.c	0.0085	9	76	136	0.56	0.41	2.70	0.06	1.24	0.46	0.05	2.40	362.1	4.5	351.0	9.5	277.8	6.7	103.18
C220511-1352	048 1352 37.c	0.0041	13	127	191	0.67	0.43	2.54	0.06	1.23	0.48	0.05	2.22	364.8	4.5	362.6	9.2	348.1	7.7	100.62
C220511-1352	049 1352 38.c	0.0049	9	65	140	0.47	0.41	2.63	0.06	1.27	0.48	0.05	2.30	358.1	4.5	348.9	9.2	288.0	6.6	102.64
C220511-1352	050 BB 07.csv	0.0068	6	12	65	0.19	0.74	2.22	0.09	0.87	0.39	0.06	2.04	560.5	4.9	562.1	12.5	568.6	11.6	99.72
C220511-1352	051 BB 08.csv	0.0055	14	28	143	0.19	0.75	2.19	0.09	0.80	0.37	0.06	2.04	566.2	4.5	566.3	12.4	566.8	11.6	99.98
C220607-1115	071 1115 01.cs	0.0168	27.9	191.2	553.8	0.35	0.37	2.32	0.04	1.86	0.80	0.06	1.39	271.0	5.1	321.2	7.5	703.4	9.7	84.37

Table S6. U-Pb on zircon radiogenic data of the samples analyzed in this study (continuation).

C220607-1115	072 1115 02.cs	0.0525	35.3	505.5	437.2	1.16	0.44	2.25	0.06	1.46	0.65	0.06	1.71	357.4	5.2	368.9	8.3	441.8	7.6	96.89
C220607-1115	073 1115 03.cs	0.0136	11.1	33.4	160.5	0.21	0.61	2.06	0.06	1.26	0.61	0.07	1.63	394.2	5.0	481.8	9.9	923.6	15.1	81.82
C220607-1115	074 1115 04.cs	0.0116	12.7	87.4	211.8	0.42	0.45	2.17	0.05	1.58	0.73	0.07	1.48	310.3	4.9	379.3	8.2	825.6	12.2	81.81
C220607-1115	075 1115 05.cs	0.0137	20.5	88.8	143.8	0.62	0.62	1.84	0.07	1.15	0.63	0.06	1.43	440.7	5.1	487.2	9.0	712.5	10.2	90.45
C220607-1115	076 1115 06.cs	0.0107	10.3	44.3	121.5	0.37	0.62	1.88	0.07	1.14	0.60	0.06	1.50	456.5	5.2	487.9	9.2	638.0	9.5	93.57
C220607-1115	077 1115 07.cs	0.0087	28.0	221.6	279.2	0.80	0.63	1.77	0.08	1.00	0.57	0.06	1.46	485.7	4.9	498.7	8.8	558.8	8.2	97.39
C220607-1115	081 1115 08.cs	0.0214	40.4	902.6	671.5	1.35	0.43	2.33	0.05	1.74	0.75	0.06	1.54	322.2	5.6	360.8	8.4	617.7	9.5	89.28
C220607-1115	082 1115 09.cs	0.0085	5.6	14.4	54.2	0.27	0.91	1.96	0.09	0.94	0.48	0.07	1.72	580.2	5.5	657.8	12.9	934.0	16.1	88.20
C220607-1115	083 1115 10.cs	0.0049	20.7	73.8	262.9	0.28	0.59	1.95	0.08	1.15	0.59	0.06	1.57	471.7	5.4	471.8	9.2	472.3	7.4	99.98
C220607-1115	084 1115 11.cs	0.0099	20.8	291.2	474.8	0.62	0.31	2.87	0.03	2.46	0.86	0.06	1.49	221.7	5.4	273.8	7.9	747.2	11.1	80.96
C220607-1115	085 1115 12.cs	0.0023	54.7	274.3	718.5	0.38	0.61	1.93	0.08	1.12	0.58	0.06	1.57	483.6	5.4	481.7	9.3	472.7	7.4	100.40
C220607-1115	086 1115 13.cs	0.0071	22.7	97.8	275.8	0.36	0.62	1.92	0.08	1.09	0.57	0.06	1.58	492.8	5.4	491.1	9.4	483.0	7.6	100.35
C220607-1115	087 1115 14.cs	0.0142	15.2	102.9	318.3	0.33	0.44	2.53	0.05	2.07	0.82	0.07	1.47	289.8	6.0	371.2	9.4	917.5	13.4	78.05
C220607-1115	088 1115 15.cs	0.0311	13.4	120.3	306.8	0.40	0.30	3.52	0.03	3.20	0.91	0.08	1.47	170.0	5.4	267.7	9.4	1242.5	18.3	63.51
C220607-1115	089 1115 16.cs	0.0076	11.8	95.8	343.8	0.28	0.61	2.06	0.08	1.15	0.56	0.06	1.71	486.2	5.6	486.3	10.0	487.1	8.3	99.97
C220607-1115	090 1115 17.cs	0.0523	18.1	96.6	320.8	0.30	0.33	2.94	0.04	2.30	0.78	0.06	1.83	260.2	6.0	290.6	8.5	543.5	9.9	89.51
C220607-1115	094 1115 18.cs	0.0056	22.1	65.1	271.0	0.24	0.64	2.27	0.08	0.95	0.42	0.06	2.06	505.8	4.8	502.5	11.4	487.6	10.1	100.65
C220607-1115	095 1115 19.cs	0.0067	12.9	45.9	164.3	0.28	0.62	2.32	0.08	1.03	0.44	0.06	2.08	487.3	5.0	486.8	11.3	484.4	10.1	100.10
C220607-1115	096 1115 20.cs	0.0087	15.3	59.9	231.3	0.26	0.60	2.30	0.08	1.03	0.45	0.06	2.06	475.2	4.9	477.3	11.0	487.4	10.0	99.56
C220607-1115	097 1115 21.cs	0.0143	6.6	71.3	129.5	0.55	0.39	2.77	0.05	1.79	0.65	0.06	2.11	287.6	5.1	335.3	9.3	680.9	14.4	85.78
C220607-1115	098 1115 22.cs	0.0079	3.9	19.4	45.6	0.43	0.71	2.30	0.08	1.40	0.61	0.07	1.82	468.3	6.6	547.2	12.6	891.2	16.3	85.57
C220607-1115	099 1115 23.cs	0.0052	18.8	60.5	205.9	0.30	0.62	2.30	0.08	1.00	0.44	0.06	2.07	490.9	4.9	489.9	11.3	485.5	10.1	100.19
C220607-1115	100 1115 24.cs	0.0066	8.1	30.2	111.0	0.27	0.54	2.40	0.07	1.17	0.49	0.06	2.10	428.7	5.0	437.9	10.5	486.4	10.2	97.91
C220607-1115	101 1115 25.cs	0.0196	8.1	41.4	91.2	0.46	0.61	2.53	0.08	1.12	0.44	0.06	2.28	481.1	5.4	482.2	12.2	487.5	11.1	99.77
C220607-1115	102 1115 26.cs	0.0131	9.0	71.4	138.0	0.52	0.52	2.45	0.06	1.32	0.54	0.06	2.06	378.1	5.0	423.7	10.4	680.1	14.0	89.24
C220607-1115	103 1115 27.cs	0.0028	4.6	14.4	55.8	0.26	0.64	2.34	0.07	1.29	0.55	0.07	1.96	430.8	5.6	503.3	11.8	848.0	16.6	85.60
C220607-1115	107 1115 28.cs	0.0141	22.2	178.9	454.3	0.40	0.38	2.43	0.04	2.04	0.84	0.07	1.32	263.2	5.4	329.5	8.0	829.1	11.0	79.87
C220607-1115	108 1115 29.cs	0.0075	52.6	295.3	586.2	0.51	0.62	1.82	0.08	1.15	0.63	0.06	1.41	481.0	5.5	489.7	8.9	530.6	7.5	98.23
C220607-1115	109 1115 30.cs	0.0057	57.5	281.0	724.1	0.39	0.59	1.83	0.08	1.14	0.62	0.06	1.43	467.0	5.3	473.2	8.6	503.3	7.2	98.69
C220607-1115	110 1115 31.cs	0.0232	21.9	176.6	584.8	0.30	0.24	3.78	0.03	3.49	0.92	0.07	1.45	160.7	5.6	218.6	8.3	899.5	13.1	73.51
C220607-1115	111 1115 32.cs	0.0129	12.1	110.5	172.8	0.64	0.54	2.12	0.07	1.43	0.67	0.06	1.56	410.7	5.9	441.5	9.3	605.7	9.5	93.01
C220607-1115	112 1115 33.cs	0.0511	18.1	84.9	277.8	0.31	0.50	2.48	0.05	1.72	0.69	0.07	1.79	310.0	5.3	411.5	10.2	1029.7	18.5	75.33
C220607-1115	113 1115 34.cs	0.0060	18.6	139.3	256.6	0.55	0.51	2.10	0.06	1.35	0.65	0.06	1.60	397.2	5.4	417.6	8.8	531.9	8.5	95.12
C220607-1502	114 1502 01.cs	0.3879	30.9	17.0	309.2	0.06	0.29	5.27	0.02	3.96	0.75	0.10	3.48	140.5	5.6	257.9	13.6	1531.0	53.2	54.50
C220607-1502	115 1502 02.cs	0.0464	49.4	189.4	369.2	0.52	0.53	4.98	0.07	1.43	0.29	0.06	4.77	413.5	5.9	432.6	21.5	535.7	25.5	95.58
C220607-1502	116 1502 03.cs	0.0694	2.9	4.7	25.7	0.19	1.24	2.45	0.08	1.22	0.50	0.11	2.13	484.1	5.9	816.7	20.0	1877.8	40.0	59.28
C220607-1502	117 1502 23.cs	0.3347	28.0	233.7	526.5	0.45	0.14	7.28	0.01	6.24	0.86	0.07	3.75	85.8	5.4	128.7	9.4	1018.3	38.2	66.66
C220607-1502	119 BB 19.csv	0.0050	16.1	30.6	165.2	0.19	0.75	1.90	0.09	0.86	0.45	0.06	1.69	570.4	4.9	569.5	10.8	565.5	9.6	100.17
C220607-1502	120 1502 04.cs	0.0171	5.1	44.2	50.4	0.88	0.66	2.41	0.08	1.14	0.47	0.06	2.12	476.7	5.4	515.0	12.4	688.8	14.6	92.56
C220607-1502	121 1502 05.cs	0.0423	10.4	104.2	235.8	0.45	0.28	3.86	0.03	3.11	0.81	0.07	2.29	179.1	5.6	247.6	9.6	960.1	22.0	72.33
C220607-1502	122 1502 06.cs	0.4038	50.3	398.1	887.9	0.45	0.08	12.13	0.01	10.94	0.90	0.07	5.24	48.1	5.3	73.9	9.0	1017.8	53.3	65.06
C220607-1502	123 1502 07.cs	0.0116	14.7	12.5	132.5	0.09	1.06	2.52	0.09	1.74	0.69	0.08	1.83	584.0	10.1	733.7	18.5	1223.0	22.4	79.59
C220607-1502	124 1502 08.cs	0.1003	15.5	73.4	314.8	0.23	0.25	3.66	0.03	2.79	0.76	0.06	2.36	183.3	5.1	228.7	8.4	725.8	17.1	80.15
C220607-1502	125 1502 09.cs	0.0115	11.5	93.0	77.4	1.21	0.82	2.33	0.09	1.03	0.44	0.06	2.09	575.6	5.9	609.6	14.2	738.1	15.4	94.42
C220607-1502	126 1502 10.cs	0.0186	13.0	44.5	202.7	0.22	0.65	2.49	0.07	1.22	0.49	0.07	2.17	424.0	5.2	505.6	12.6	894.0	19.4	83.86
C220607-1502	127 1502 11.cs	0.4929	48.2	20.5	726.8	0.03	0.14	8.86	0.01	7.43	0.84	0.10	4.81	67.9	5.0	133.0	11.8	1546.0	74.4	51.03
C220607-1502	128 1502 12.cs	0.1080	9.5	23.0	190.9	0.12	0.28	4.63	0.03	2.39	0.52	0.06	3.97	212.4	5.1	252.3	11.7	642.3	25.5	84.17
C220607-1502	129 1502 13.cs	0.1363	23.1	85.5	400.7	0.22	0.46	4.29	0.05	2.55	0.60	0.06	3.44	327.7	8.4	382.3	16.4	727.4	25.0	85.73
C220607-1502	130 BB 20.csv	0.0032	16.3	31.9	173.0	0.19	0.73	1.91	0.09	0.89	0.47	0.06	1.69	556.0	4.9	554.5	10.6	548.2	9.2	100.27
C220607-1502	132 BB 21.csv	0.0033	21.2	49.0	210.9	0.23	0.75	3.03	0.09	1.53	0.50	0.06	2.62	571.2	8.7	570.4	17.3	567.3	14.9	100.14
C220607-1502	133 1502 14.cs	0.0394	49.2	51.5	819.3	0.06	0.41	3.99	0.05	2.72	0.68	0.06	2.92	333.7	9.1	348.5	13.9	448.0	13.1	95.77
C220607-1502	134 1502 15.cs	0.2355	28.1	21.1	660.6	0.03	0.12	13.49	0.01	12.81	0.95	0.08	4.25	73.2	9.4	115.8	15.6	1111.8	47.3	63.28
C220607-1502	135 1502 16.cs	0.0340	17.9	11.0	284.9	0.04	0.37	4.41	0.05	3.22	0.73	0.06	3.02	291.6	9.4	318.7	14.1	522.0	15.8	91.49
C220607-1502	136 1502 17.cs	0.0382	18.3	19.5	442.6	0.04	0.26	5.15	0.04	3.92	0.76	0.05	3.35	229.6	9.0	238.4	12.3	326.4	10.9	96.29
C220607-1502	137 1502 18.cs	0.0081	14.9	18.8	212.4	0.09	0.51	3.60	0.07	2.14	0.59	0.06	2.89	414.6	8.9	418.7	15.1	441.6	12.8	99.01

Table S6. U-Pb on zircon radiogenic data of the samples analyzed in this study (continuation).

C220607-1502	38 1502 19.cs	0.1564	12.4	73.6	169.9	0.44	0.32	6.27	0.03	4.19	0.67	0.07	4.67	219.3	9.2	281.1	17.6	832.8	38.9	78.03
C220607-1502	40 1502 21.cs	0.0670	17.5	72.7	219.0	0.33	0.31	5.68	0.04	3.96	0.70	0.06	4.08	243.0	9.6	271.5	15.4	524.8	21.4	89.51
C180824-1645	5	0.12	100	2653	164	0.04	0.4209	1.95	0.0544	1.88	0.96	0.0561	0.55	342	6	357	7	456	2	95.76
C180824-1645	A17 *	0.47	43	293	15	0.15	0.4229	2.08	0.0553	1.40	0.67	0.0554	1.54	347	5	358	7	430	7	96.93
C180824-1645	A14 *	0.59	55	227	14	0.24	0.4034	2.19	0.0555	1.39	0.63	0.0527	1.69	348	5	344	8	315	5	101.27
C180824-1645	A18 *	7.72	28	226	16	0.12	0.4429	2.28	0.0566	1.42	0.62	0.0568	1.78	355	5	372	8	483	9	95.29
C180824-1645	A7 *	0.33	120	1057	52	0.11	0.4280	2.35	0.0569	1.50	0.64	0.0546	1.81	356	5	362	9	396	7	98.52
C180824-1645	A8 *	0.22	34	684	46	0.05	0.4228	2.39	0.0575	1.53	0.64	0.0533	1.84	360	6	358	9	342	6	100.69
C180824-1645	7	0.32	39	134	13	0.29	0.6314	2.16	0.0774	1.48	0.69	0.0592	1.57	480	7	497	11	574	9	96.65
C180824-1645	A13	0.40	161	530	22	0.31	0.5855	1.82	0.0718	1.10	0.61	0.0592	1.45	447	5	468	9	573	8	95.47
C180824-1645	A4	0.50	20	42	4	0.48	0.6410	2.21	0.0793	1.08	0.49	0.0586	1.93	492	5	503	11	552	11	97.85
C180824-1645	A1	0.80	32	123	11	0.26	0.6629	2.09	0.0822	1.04	0.50	0.0585	1.82	509	5	516	11	548	10	98.63
C180824-1645	A2	0.64	35	131	11	0.27	0.6264	2.10	0.0781	1.10	0.53	0.0582	1.78	485	5	494	10	536	10	98.15
C180824-1645	A11	0.83	158	226	14	0.70	0.5902	1.88	0.0745	1.05	0.56	0.0574	1.56	463	5	471	9	508	8	98.38
C180824-1645	A10	0.42	99	203	17	0.49	0.5935	1.84	0.0754	1.04	0.57	0.0571	1.51	469	5	473	9	495	7	99.06
C180824-1645	A3	0.91	106	321	20	0.33	0.5396	2.23	0.0689	1.27	0.57	0.0568	1.84	429	5	438	10	484	9	98.01
C180824-1645	A9	0.65	40	126	12	0.32	0.6354	1.93	0.0814	0.96	0.50	0.0566	1.67	504	5	499	10	478	8	100.95
C180824-1645	A16	0.39	13	143	9	0.09	0.4872	2.04	0.0628	1.26	0.62	0.0563	1.60	392	5	403	8	464	7	97.38
C180824-1645	A15	1.33	33	623	40	0.05	0.4794	2.01	0.0618	1.31	0.65	0.0563	1.52	386	5	398	8	463	7	97.18
C180824-1645	2	0.14	14	102	70	0.14	11.8320	0.79	0.4622	0.65	0.83	0.1857	0.44	2449	16	2591	20	2704	12	94.53
C180824-1645	10	0.31	76	182	25	0.42	2.0330	2.56	0.0997	2.46	0.96	0.1479	0.70	612	15	1127	29	2322	16	54.36
C180824-1645	6	0.43	59	49	9	1.21	1.1162	2.93	0.0909	1.22	0.42	0.0891	2.66	561	7	761	22	1406	37	73.66
C180824-1645	11	0.33	26	62	8	0.43	0.7933	1.81	0.0854	1.55	0.86	0.0674	0.93	528	8	593	11	849	8	89.08
C180824-1645	1	0.24	49	160	18	0.31	0.7720	1.82	0.0832	1.29	0.71	0.0673	1.28	515	7	581	11	847	11	88.68
C180824-1645	4	0.94	64	169	30	0.38	0.7490	2.15	0.0793	1.53	0.71	0.0685	1.51	492	8	568	12	885	13	86.61
C180824-1645	A5	0.25	9	28	3	0.33	0.6836	2.27	0.0773	1.18	0.52	0.0641	1.94	480	6	529	12	746	14	90.77
C180824-1645	3	0.39	76	413	83	0.19	0.6818	8.87	0.0767	1.84	0.21	0.0644	8.68	477	9	528	47	756	66	90.28
C180824-1645	8	0.44	28	80	5	0.36	0.5937	2.34	0.0630	1.78	0.76	0.0683	1.52	394	7	473	11	879	13	83.23
C180824-1645	A6	1.23	35	118	9	0.30	0.6685	2.09	0.0571	1.50	0.72	0.0850	1.46	358	5	520	11	1314	19	68.83
C180824-1645	9	0.37	81	198	18	0.41	0.7556	3.22	0.0560	2.53	0.79	0.0979	1.99	351	9	571	18	1584	31	61.44
C180824-1645	13	0.50	26	115	7	0.23	0.6426	12.68	0.0436	2.80	0.22	0.1069	12.37	275	8	504	64	1748	216	54.58
C180824-1645	A19	0.59	59	219	10	0.27	0.3559	2.08	0.0408	1.49	0.72	0.0633	1.45	258	4	309	6	717	10	83.38
C180824-1645	A20	0.45	12	45	2	0.26	0.2310	2.84	0.0291	2.02	0.71	0.0575	2.00	185	4	211	6	512	10	87.68
C180824-1645	A12	0.69	45	855	21	0.05	0.2049	3.69	0.0229	3.42	0.93	0.0650	1.39	146	5	189	7	776	11	76.95
C220514-1340	5	0.21	32	598	40	0.05	0.4329	2.07	0.0563	1.95	0.94	0.0557	0.69	353	7	365	8	441	3	96.75
C220514-1340	A4	0.68	56	330	20	0.17	0.4298	2.40	0.0555	1.08	0.45	0.0562	4.30	348	7	363	8	460	4	95.86
C220514-1340	15	0.45	403	5422	366	0.07	0.4377	2.75	0.0553	2.66	0.97	0.0574	0.70	347	9	369	10	507	4	94.12
C220514-1340	21	0.63	250	3242	181	0.08	0.4322	2.70	0.0545	2.62	0.97	0.0575	0.62	342	9	365	10	513	3	93.74
C220514-1340	9	0.34	196	2584	198	0.08	0.4148	2.05	0.0543	2.00	0.98	0.0554	0.44	341	7	352	7	429	2	96.71
C220514-1340	2	0.17	561	2587	154	0.22	0.3511	2.60	0.0462	2.53	0.97	0.0552	0.62	291	7	306	8	419	3	95.20
C220514-1340	A5	0.68	399	6060	285	0.07	0.3433	5.11	0.0455	2.62	0.51	0.0547	4.39	287	8	300	8	401	3	95.73
C220514-1340	12	7.88	416	4568	2477	0.09	0.3157	4.56	0.0397	4.21	0.92	0.0577	1.76	251	11	279	13	518	9	90.07
C220514-1340	4	1.04	461	599	21	0.78	0.1552	7.18	0.0166	6.89	0.96	0.0677	2.00	106	7	147	11	859	17	72.57
C220514-1340	A10	0.85	4	17	13	0.22	21.0338	0.99	0.5790	0.31	0.31	0.2635	0.94	2945	9	3140	13	3268	9	93.78
C220514-1340	A1	1.30	20	58	15	0.35	3.8440	2.08	0.2073	0.98	0.47	0.1345	1.84	1215	12	1602	18	2157	11	75.82
C220514-1340	A9	0.93	62	177	15	0.35	0.8031	4.09	0.0912	1.47	0.36	0.0638	3.82	563	8	599	10	737	7	94.02
C220514-1340	A8	0.60	71	227	20	0.32	0.6121	4.60	0.0798	1.53	0.33	0.0557	4.34	495	8	485	8	439	4	102.03
C220514-1340	A3	0.21	757	1473	129	0.52	0.6208	4.34	0.0759	1.57	0.36	0.0593	4.04	472	7	490	8	579	4	96.18
C220514-1340	A2	0.44	251	1020	74	0.25	0.5325	4.51	0.0665	1.79	0.40	0.0581	4.14	415	7	433	8	532	4	95.76
C220514-1340	A7	0.98	114	389	28	0.30	0.5291	4.44	0.0635	1.90	0.43	0.0605	4.02	397	8	431	9	620	5	92.01
C220514-1340	A6	0.76	161	427	26	0.38	0.4899	4.70	0.0620	2.03	0.43	0.0573	4.24	388	8	405	9	505	5	95.72
C220514-1340	8	0.45	88	2216	211	0.04	0.3845	2.40	0.0494	2.33	0.97	0.0565	0.60	311	7	330	8	473	3	94.00
C220514-1340	A11	0.32	18	77	5	0.24	0.4197	1.59	0.0450	0.65	0.41	0.0677	1.46	283	2	356	6	860	13	79.66
C220514-1340	10	1.23	520	2009	157	0.26	0.3429	2.78	0.0423	2.71	0.97	0.0588	0.64	267	7	299	8	560	4	89.20
C220514-1340	16	0.78	374	330	20	1.14	0.3573	6.16	0.0322	5.94	0.96	0.0804	1.62	204	12	310	19	1207	20	65.91

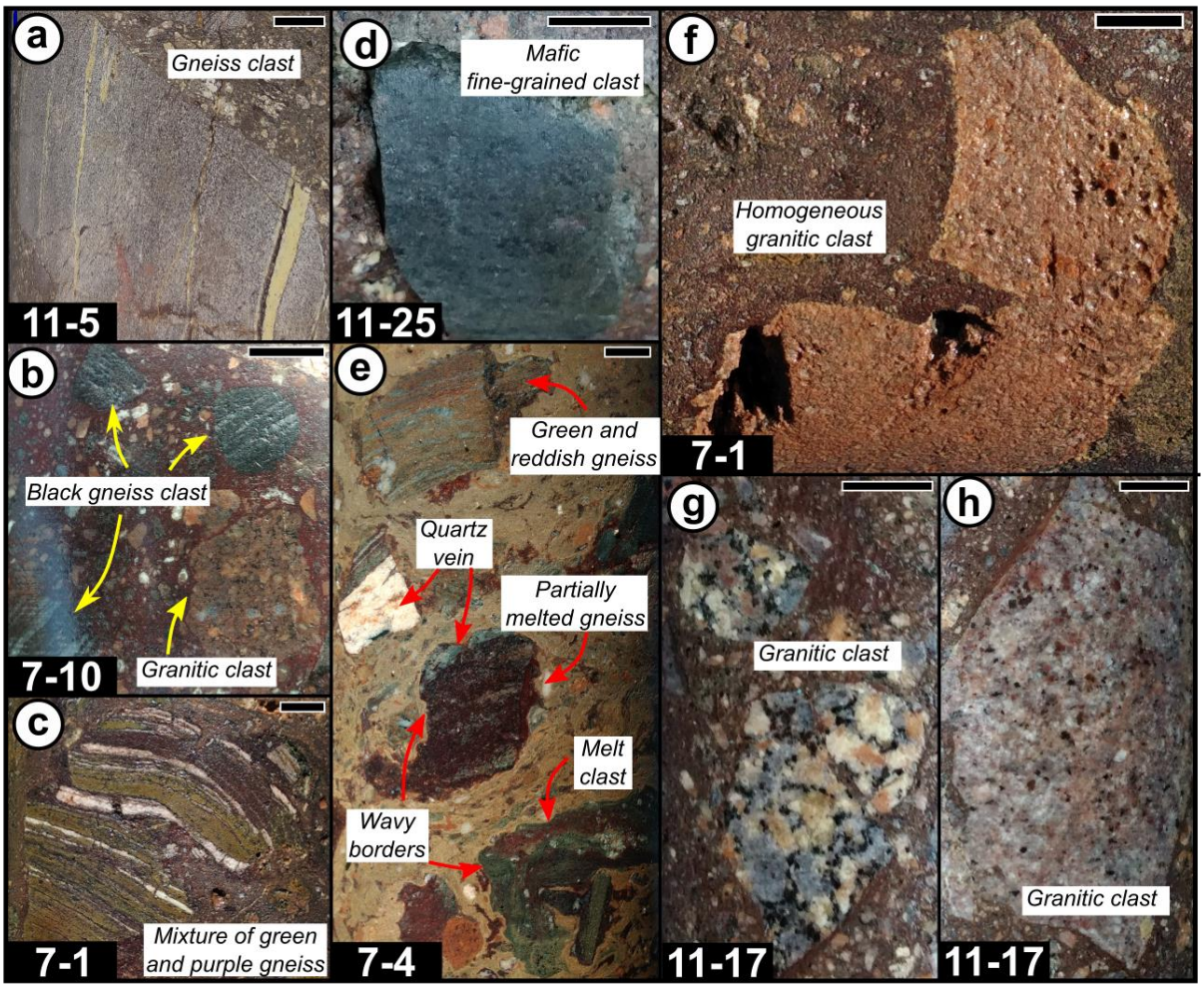


Figure S1. Photographs showing details of the various types of clasts present in the impactite samples analyzed in this study. The black scale bars in the upper right corners correspond to 1 cm. (a, b, c, and e) Clasts derived from paragneisses can appear black, purple, greenish, reddish, or multicolored. They may contain quartz veins and exhibit wavy or sharp borders (7-10, 11-5, 7-1, and 7-4). (f, g, and h) Clasts derived from granitic rocks display diverse textures and mineral compositions and may also contain quartz veins. (d) A few fine-grained, homogeneous greenish clasts, likely originating from a more mafic lithology, are present but scarce (11-25). The matrix contains mineral clasts with compositions similar to those of the lithic clasts.

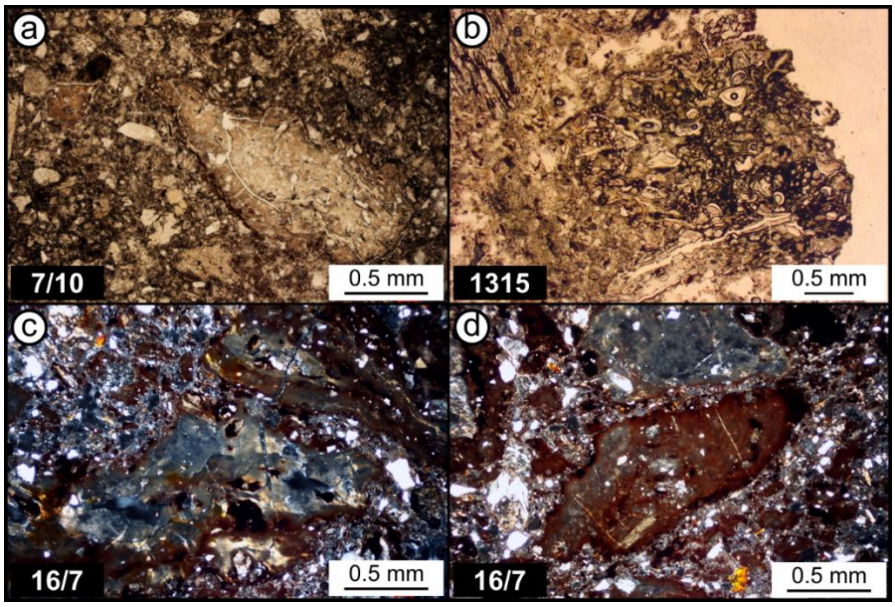


Figure S2. Microphotographs of some of the different types of impact melts, showing their different colorations, irregular forms, and isotropic nature. Images (c and d) were taken with cross-polarized light. Vesicles, fractures, and reddish oxidation borders are common.

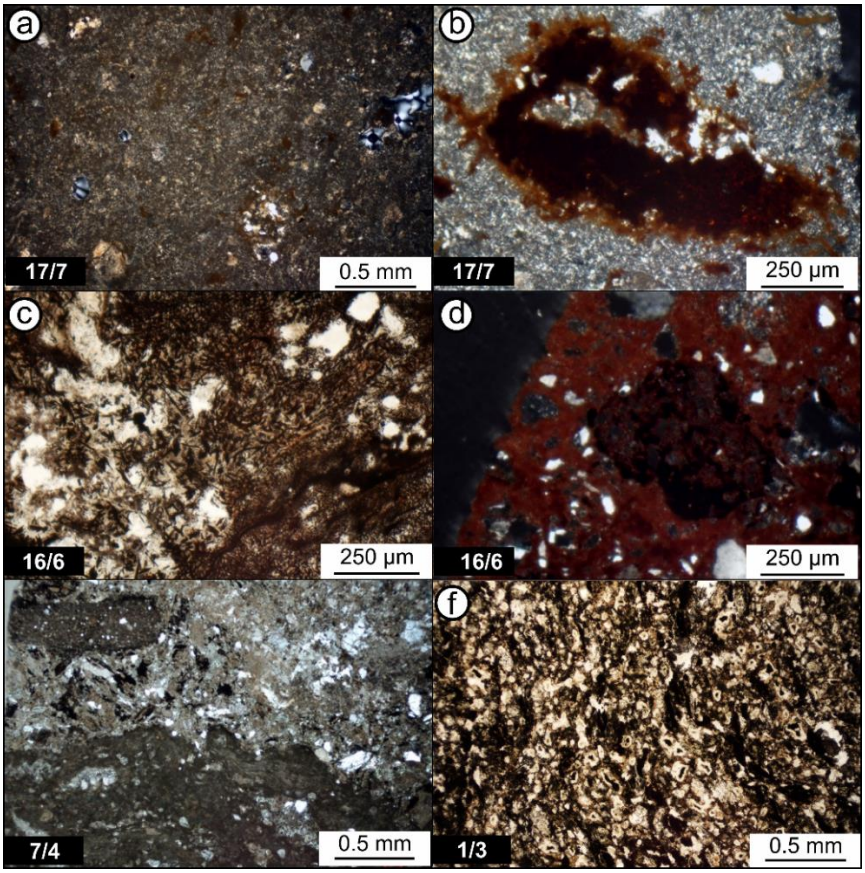


Figure S3. Microphotographs of the matrix of the impact melt rocks. Except for image (c) all were taken with cross-polarized light. (a and b) Homogeneous, fine-grained yellow matrix with some patches of red staining, with tiny crystals of iron oxides. (c and d) Matrix of the red IMRs with (c) tiny iron oxide crystallites and (d) different types of red melt. (e) Matrix with flow banding textures and with clast rich and clast poor zones in a yellow IMR. (f) Matrix of a more heterogeneous yellow IMR that has more vesicles.

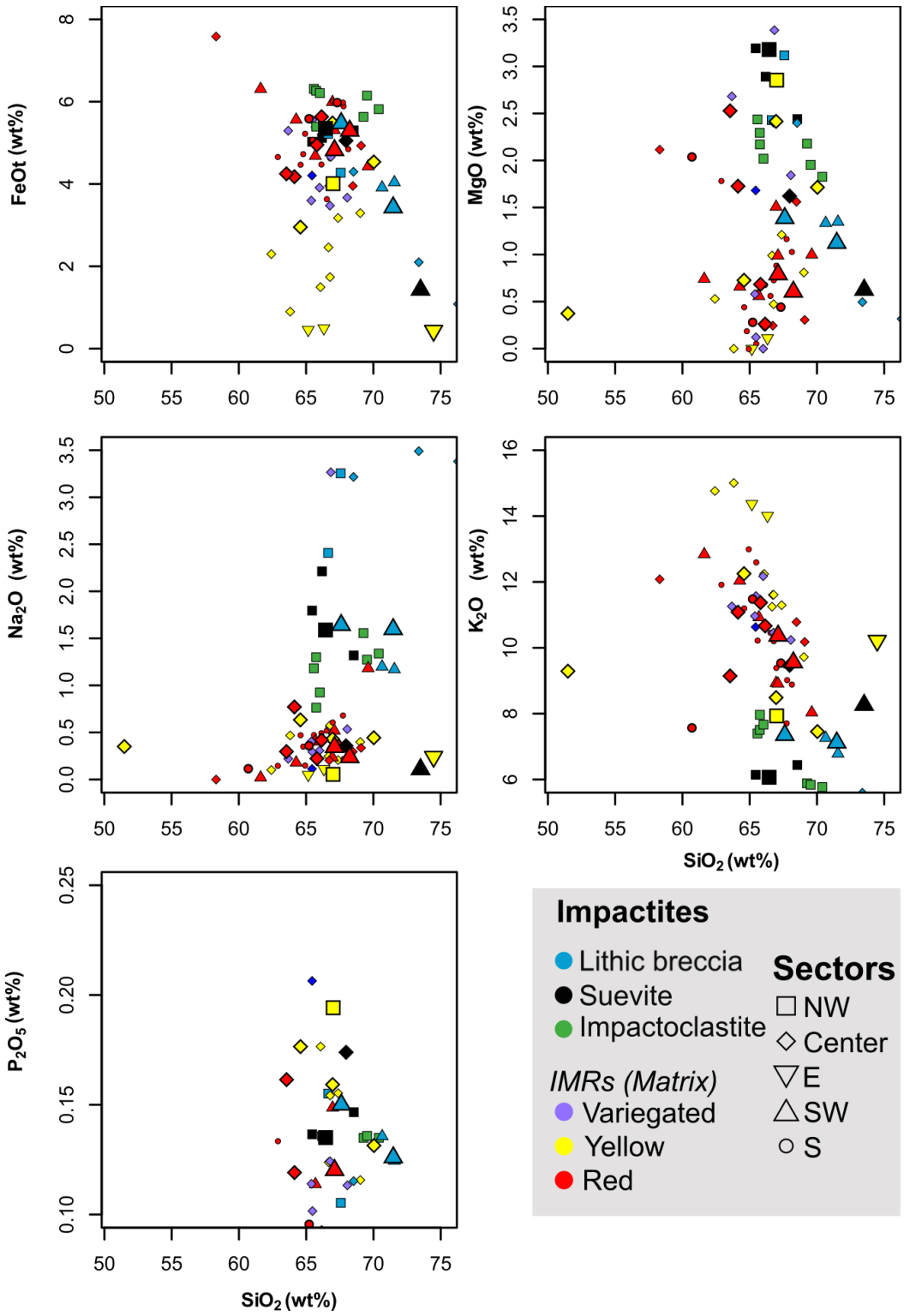


Figure S4. Harker plots of SiO_2 versus major elements for the impactites analyzed in this study in comparison with literature data (smaller symbols). The colors indicate the lithology and the symbols the location of the samples. The lithic breccia symbol represents the monomict breccias of this study and the monomict and polymict lithic breccias of the literature. The term 'Matrix' refers to a visual classification based on the overall coloration of the impact melt rocks (IMRs). Literature data for the impactites taken from Chèvremont et al. (1996), Faucher (2021), and Tagle et al. (2009).

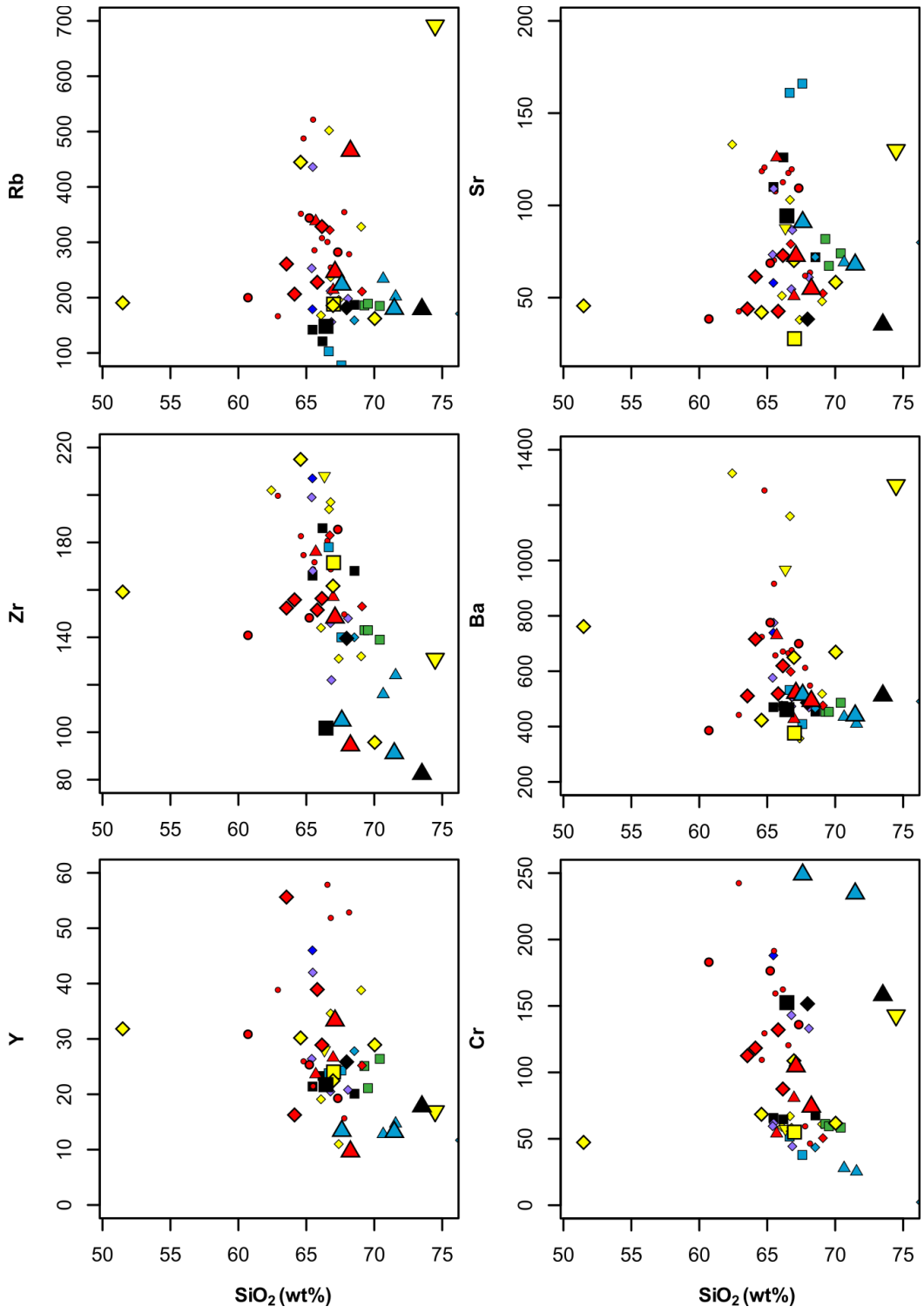


Figure S5. Harker plots of SiO_2 versus selected trace elements of the impactites analyzed in this study in comparison with literature data (smaller symbols). The lithic breccia symbol represents the monomict breccias of this study and the monomict and polymict lithic breccias of the literature. Legend is the same as given for Figure S3. Literature data for the impactites taken from Chèvremont et al. (1996), Faucher (2021), and Tagle et al. (2009).

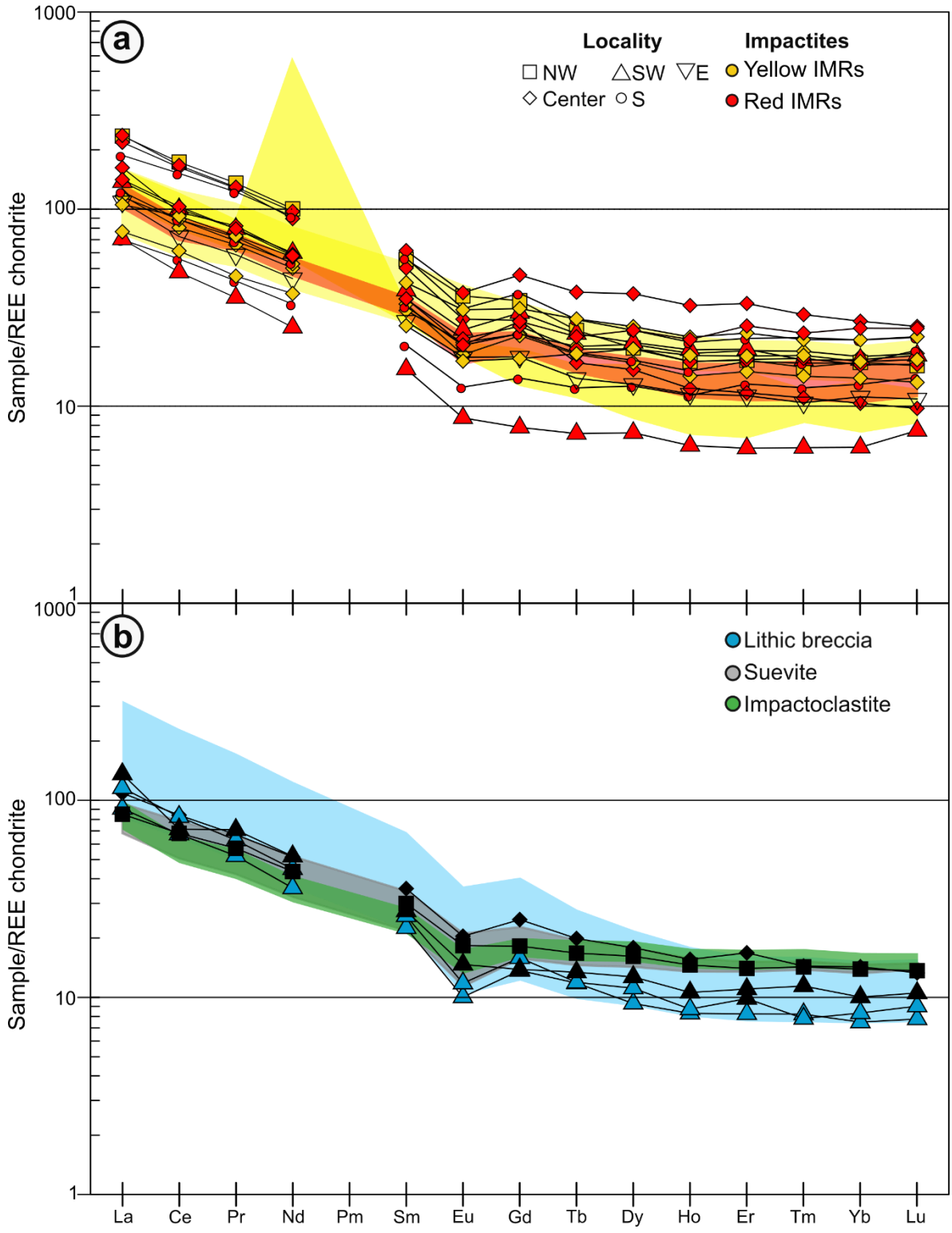


Figure S6. Chondrite normalized rare earth element patterns (normalization factors from Anders and Grevesse, 1989) of the (a) impact melt rocks and (b) lithic breccias, suevites, and impactoclastites of this study compared with other impactites taken from Chèvremont et al. (1996) and Faucher (2021). The lithic breccia represents the monomict breccias of this study and the monomict and polymict lithic breccias of the literature. The impactites of this study are shown with symbols corresponding to their sampling locations, and literature data is represented as background fields. The colors indicate the lithology in both cases.

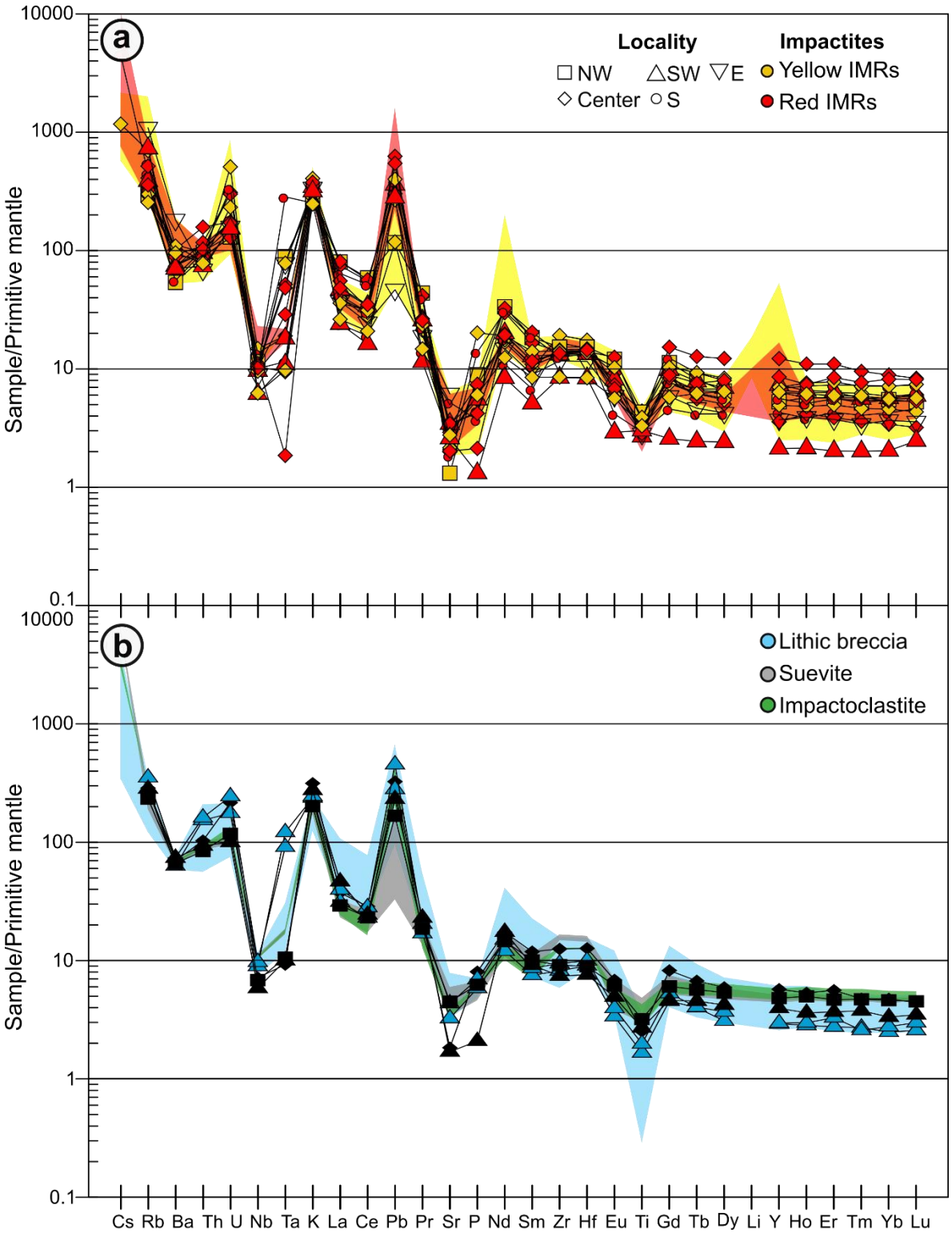


Figure S7. Primitive mantle normalized trace element patterns (normalization factors from Sun and McDonough, 1989) (a) impact melt rocks and (b) lithic breccias, suevites, and impactoclastites of this study compared with other impactites taken from Chèvremont et al. (1996) and Faucher (2021). The impactites of this study are shown with symbols corresponding to their sampling locations, and literature data is represented as background fields. The colors indicate the lithology in both cases.

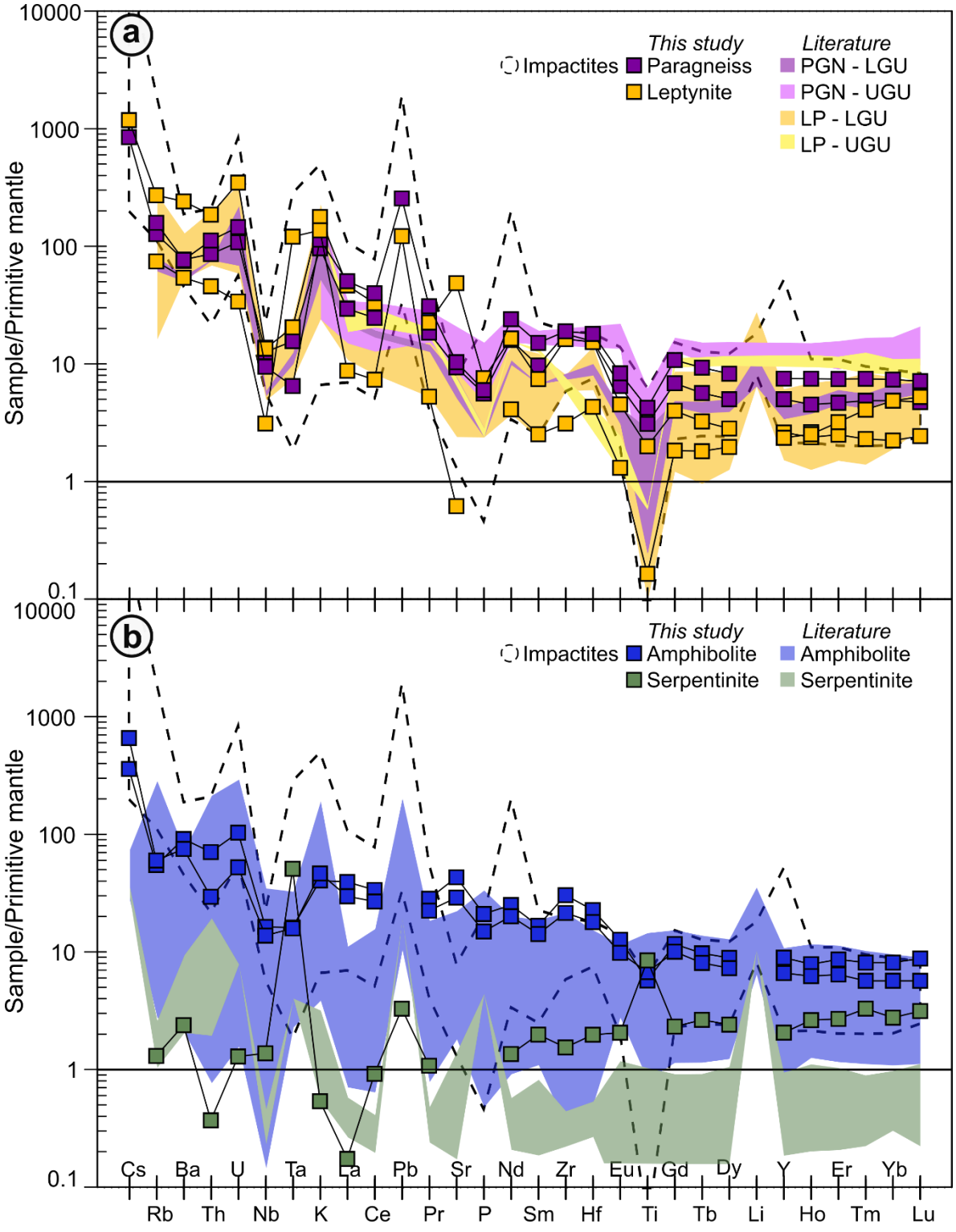


Figure S8. Primitive mantle normalized (normalization factors from Sun and McDonough, 1989) multi-element spider diagrams for the (a and b) metamorphic and (c) igneous basement rocks of the area of the Rochechouart impact structure. Samples of this study (squares) is compared to literature data (fields) reported in Bambier et al. (1983), Chèvremont et al. (1996), and El Korh et al. (2020). The colors indicate the lithology. LP – Leptynite, PGN – Paragneiss, LGU – Lower Gneiss Unit, UGU – Upper Gneiss Unit.

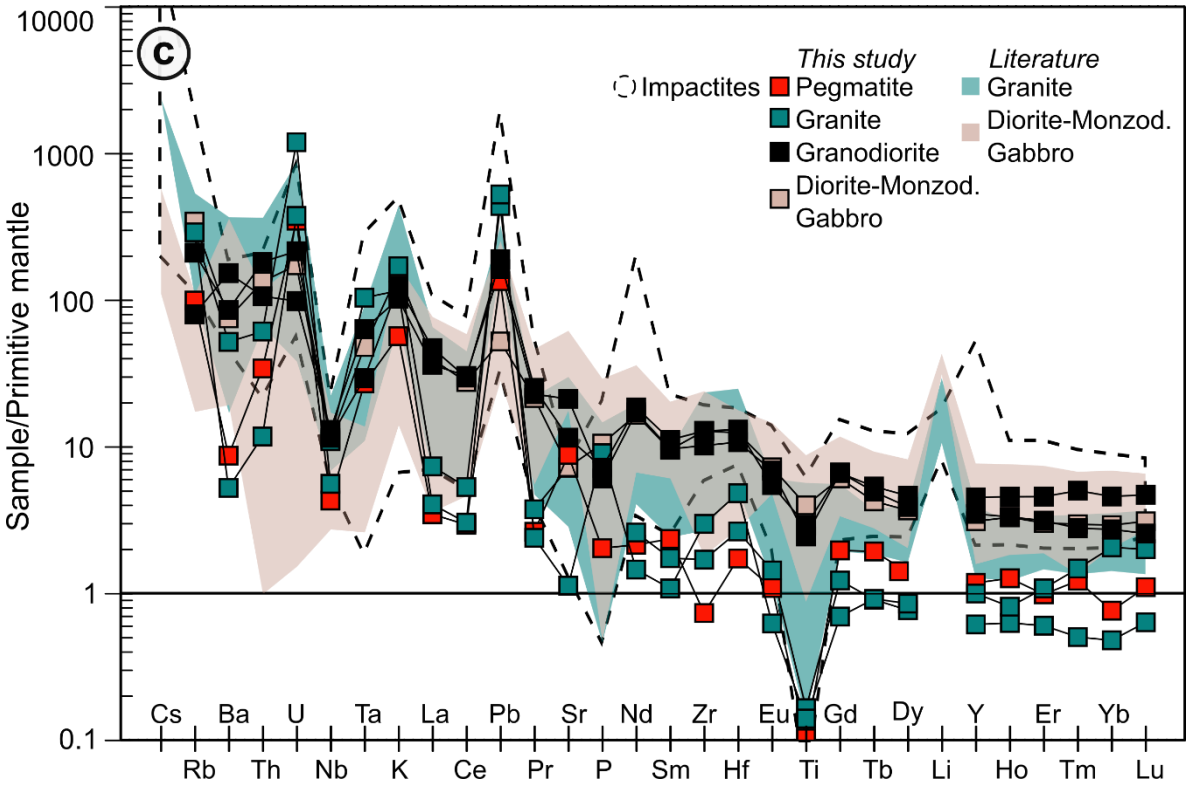


Figure S8. Primitive mantle normalized (normalization factors from Sun and McDonough, 1989) multi-element spider diagrams for the (a and b) metamorphic and (c) igneous basement rocks of the area of the Rochechouart impact structure. Samples of this study (squares) is compared to literature data (fields) reported in Bambier et al. (1983), Chèvremont et al. (1996), and El Korh et al. (2020). The colors indicate the lithology (Continuation).

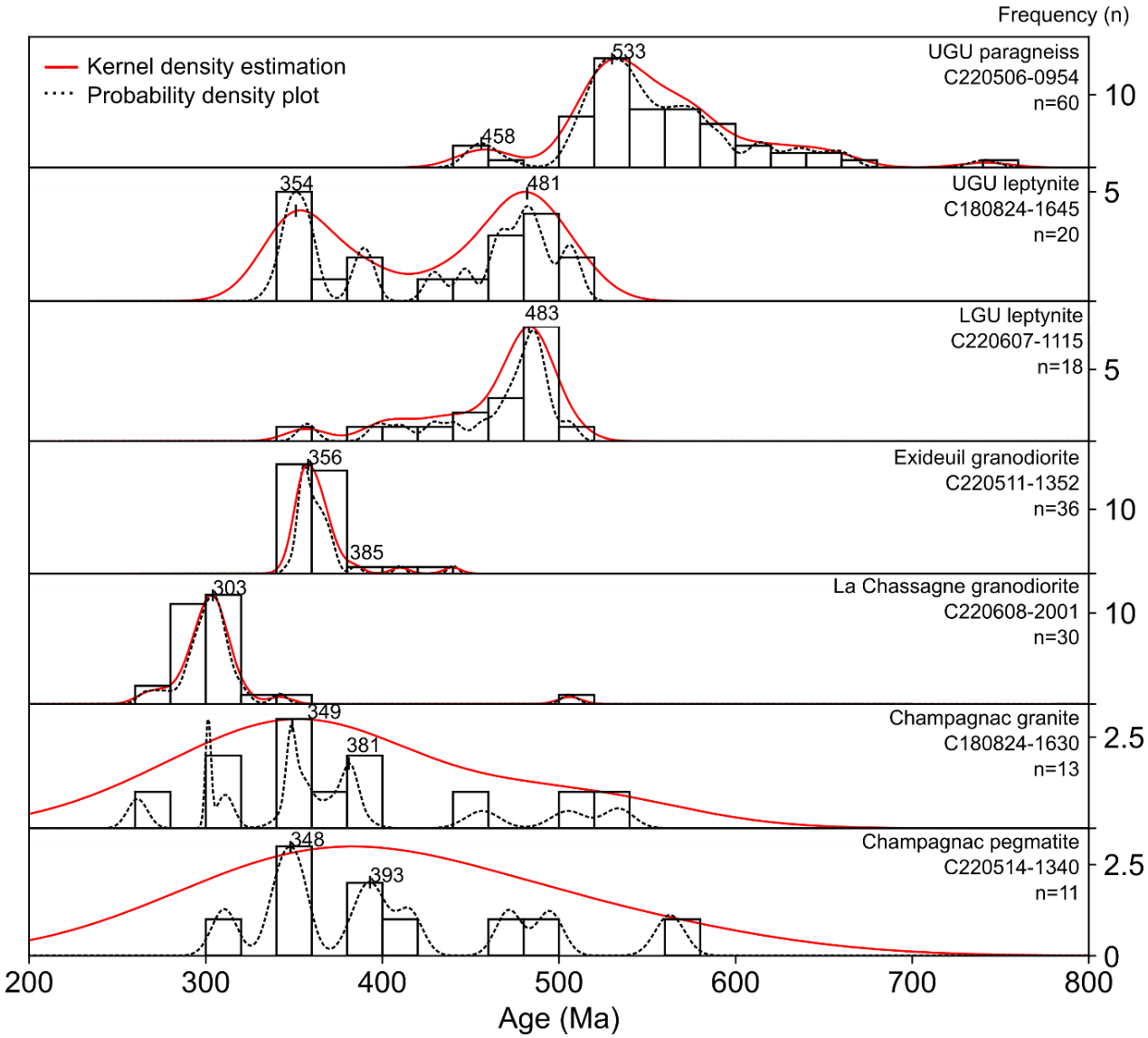


Figure S9. Histograms for the apparent $^{206}Pb/^{238}U$ ages of the zircon in the basement rocks analyzed in this study. Probability density plot (PDP) in gray lines and kernel density plot (KDE) in red lines. Age peaks are from the kernel density plot for all samples except for the Champagnac granite and pegmatite, where age peaks are from the PDP. Plot and age peaks calculated with Detrital Py v. 1.3 (Sharman et al., 2018).

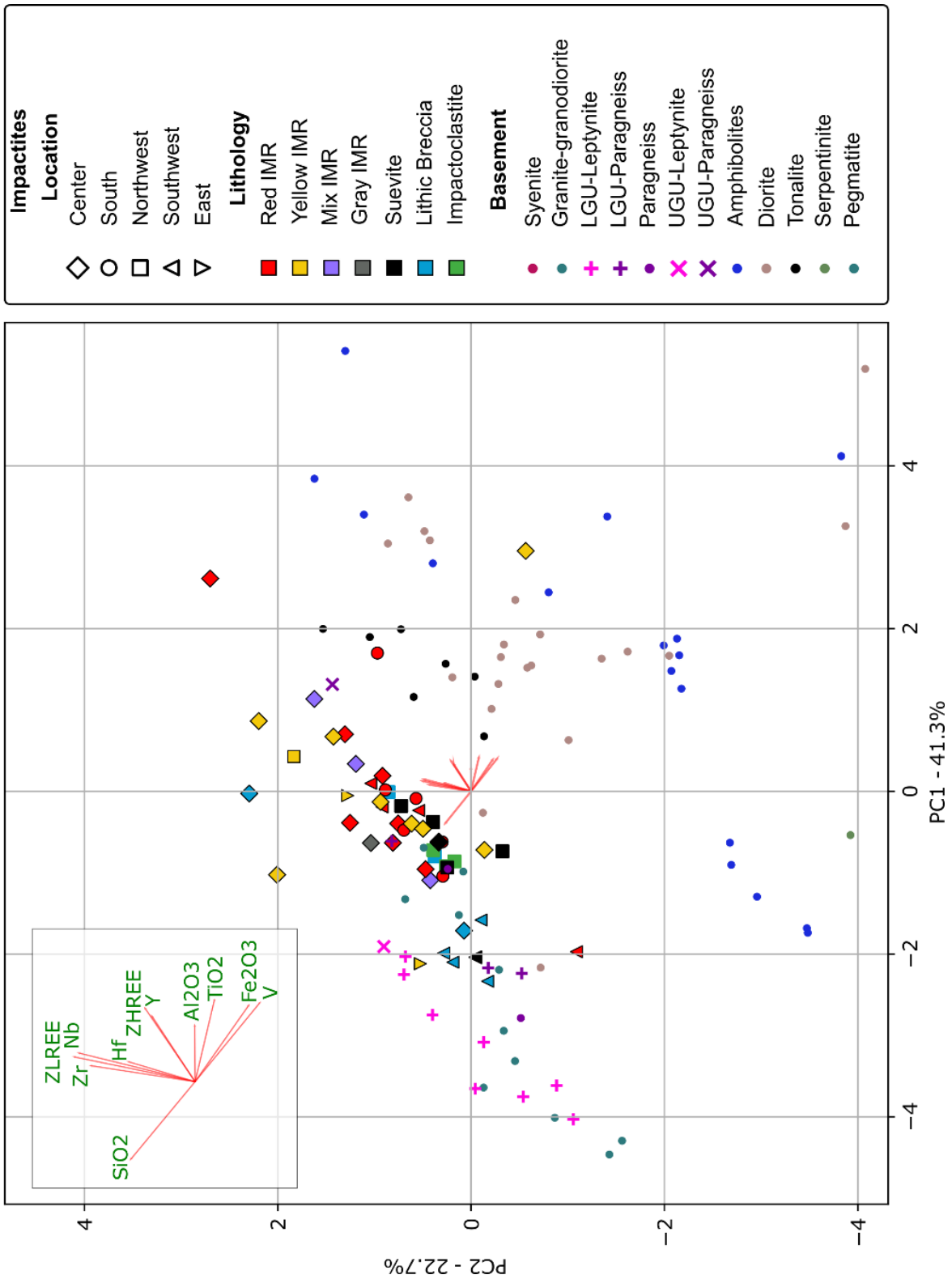


Figure S10. Principal component analysis (PCA) for all the impactites of the Rochechouart impact structure and the basement rocks from this study and literature. Immobile major and trace elements were considered and the PC1 and PC2 explain 64 % of the total variance of the data. The lithic breccia symbol represents both monomict and polymict lithic breccias. Literature data taken from Bambier et al. (1983), Chèvremont et al. (1996), El Korh et al. (2020), Faucher (2021), Lambert (1977), Reimold et al. (1983), and Reimold and Oskierski (1987). LGU – Lower Gneiss Unit, UGU – Upper Gneiss Unit.

CHAPTER 7

Synthesis and overall conclusions

7 SYNTHESIS AND OVERALL CONCLUSIONS

This study provides a detailed multi-disciplinary characterization of representative impactites and basement lithologies from the Rochechouart impact structure, France. The results allow a direct correlation between both groups of rocks in order to identify the most probable precursor lithologies for each impactite type. Moreover, the comprehensive analysis of U-Pb isotopes in zircon from different impactites was conducted with the objectives of: 1) evaluating the age of the impact event as well as potential post-impact events, 2) identifying the principal precursor rocks of the impactites through provenance analysis, and 3) understand the response of the isotopic system to varying degrees of shock metamorphism.

A total of 13 basement rocks, 15 impact melt rocks (IMRs), three suevites, and two monomict lithic breccias were studied. All samples were analyzed using petrography and whole-rock geochemistry, and Sr and Sm-Nd isotope data were obtained for all basement rocks and 13 impactites. Additionally, this investigation included the development of a comprehensive U-Pb zircon geochronology dataset with a total of 586 analyses on zircon from 9 basement samples obtained by LA-ICP-MS, and a total of 226 analyses on zircon from three IMRs and 327 analyses on zircon from two suevites obtained by LA-ICP-MS and SIMS methodologies. Furthermore, six zircons from two suevites and two zircons from an IMR were also analyzed for detailed textural characterization by EBSD.

The data were divided into three manuscripts: the first one, "Z*ircon U-Pb provenance analysis of impact melt and target rocks from the Rochechouart impact structure, France,*" was published in the journal Meteoritics & Planetary Science; the second one, "*Shock deformation and U-Pb isotope systematics in zircon from impactites of the Rochechouart impact structure: impact age and zircon provenance*." is to be submitted shortly to the journal Geochimica et Cosmochimica Acta; and the third one, *"What were the protoliths of the Rochechouart impactites? – A multiproxy provenance study",* is in process of writing and is intended to be submitted to the journal Geological Society of America Bulletin. The main points that this new information allows me to discuss are:

Provenance of the impactites

For the U-Pb zircon provenance analysis were studied zircons from IMRs from Recoudert and Montoume and a monzodiorite, a paragneiss, and two amphibolites analyzed by LA-ICP-MS in the first manuscript; zircons from suevites from Videix and Chassenon and an IMR from Babaudus analyzed by LA-ICP-MS and SIMS in the second paper; and zircons from eight more basement lithologies analyzed by LA-ICP-MS in the third paper.

It should be noted that significant challenges in this study were collecting zircons from samples with rather low concentrations of zirconium. In some cases, the small grain sizes of zircon relative to the analytical spot diameter of the LA-ICP-MS analyses did not allow for obtaining sufficient well-constrained results. These factors made data acquisition difficult and added complexity to obtaining a comprehensive geochronologic dataset. The Chéronnac granite and the Champagnac pegmatite and granite were the samples most affected by these problems, highlighting the need for further efforts to better represent their age distribution and complement the zircon provenance analysis.

In the impactites, colorless apparently unshocked zircons and reddish granular grains yielded highly heterogeneous age distributions. Pre-impact ages younger than the final phase of the evolution of the FMC basement (~272 Ma) were obtained in zircon from all impactites, representing a significant proportion of the geochronologic record of the IMR in comparison with the suevites. Moreover, in all samples, younger zircons are commonly associated with higher common Pb contents, and after correction, some analyses yielded relatively large errors on the $^{207}Pb/^{206}Pb$ ratios. This, combined with the small age difference between the impact event and the youngest basement lithologies, may have caused grains with partial resetting to plot close to or even on the concordia line in the Tera-Wasserburg plots.

In the provenance study, only the zircon ages of the suevites could be reasonably correlated to distinct basement rocks, to paragneisses for the Chassenon suevite, and a monzodiorite and leptynites for the Videix sample. In contrast, the proportion of ages younger than the latest stages of the FMC evolution in the zircons from the

IMRs generated a poor correlation between this impactite and the target lithologies. Some of the ages responsible for this discrepancy likely reflect incomplete resetting of the isotopic system. However, the possibility of other basement rocks undergoing post-Variscan events, not yet documented within the area of the impact structure, cannot be ruled out. Thus, to resolve these findings. It would be necessary to expand the geochronologic database of the basement rocks within the impact structure. Additionally, it is still possible that an unknown pre-impact material, no longer preserved in the impact structure, may have contributed to the formation of the impactites.

To better constrain the target rocks preferentially involved with the formation of the different types of impact breccia, we complemented the geochronologic results with petrographic, whole-rock geochemistry, Sr and Sm-Nd isotope characterization of the impactites and the basement rocks in the third paper. This study shows that although multiple basement lithologies share similar geochemical or isotopic signatures, impact breccias are best correlated with intermediate-silica target rocks, and suevite compositions commonly resemble the nearest target rock in outcrop and/or in the basal part of the drill-cores. Strontium and Sm-Nd isotope data indicate that the yellow IMRs are more comparable to paragneisses, whereas the red IMRs show a potentially higher contribution from granodiorite or monzodiorite from La Chassagne and La Martinie. It should be noted, however, that geochemical and isotopic data from some lithologies remain limited to a small number of samples.

These findings highlight that zircon provenance analysis can be complicated by the challenge of assessing the extent of the age resetting, especially in cases with a small difference between the age of the impact event and the ages of the target rocks. In this context, any interpretation of the ages obtained should be made with great caution, as the lack of correlation between the IMRs and the basement lithologies may not necessarily imply that the target rocks analyzed could not be the precursor rocks for the IMRs. Thus, alternative approaches that provide a better correlation with the basement, such as Sm-Nd isotopic analysis, are preferable for evaluating the most probable protoliths of these impactites. In this sense, expanding the database with additional data on major and trace immobile elements, Sm-Nd

isotopes, and samples from more localities is recommended to better characterize the compositional signatures of the basement rocks and impactites.

Meaning of impact and post-impact ages

Zircons from the impact melt rocks and the Videix suevite yielded ages of 204 ± 1, 206 ± 2 Ma, and 203 ± 4 Ma, consistent within error margins or very close to the currently favored $^{40}Ar/^{39}Ar$ age of the Rochechouart impact event at 206.92 + 0.20/ 0.32 Ma, after Cohen et al. (2017). However, grains yielding ages close to the impact event show an overall similar shocked granular texture associated with irregular, zoned, or homogeneous textures in the CL images, as well as a wide variation in U-Th contents, which makes it challenging to distinguish impact-related ages from potential post-impact events. Moreover, the range of obtained ages also highlights the complexity of obtaining reliable estimations of an impact age.

Furthermore, ages of 196 ± 2 and 191 ± 4 Ma were recorded for zircon from the Montoume and Babaudus IMRs and the Videix suevite. These zircons can either be granular or colorless and are similar to some ages previously reported by Rasmussen et al. (2020) and Horne (2016). These apparently post-impact ages are attributed to a thermal or hydrothermal event that is too young to be impact-related. Further analysis of other lithologies and better constraints on the age of hydrothermal alteration documented in the target rocks are recommended.

The resetting of the U-Pb system in zircon was seen to be controlled by shock intensity in the Chassenon suevite, and by shock intensity and the U and Th contents of the zircons in the Videix suevite. In the Babaudus IMR, similarities in age and U and Th contents between shocked zircons and some unshocked crystals suggest additional factors, like metamictization, could influence age resetting. This possibility was tested, but calculations of the radiation dose indicated that it was not the reason.

The study of the U-Pb systematics on zircon from the impactites of this investigation can be complemented with the analysis of more zircons by EBSD or other techniques, such as trace element characterization. This could provide a better understanding of the significance of the ages obtained and the behavior of the U-Pb isotopic system to different degrees of shock deformation.

Zircon shock metamorphism

The detailed zircon textural characterization by EBSD was conducted on the Videix suevite, a previously unexamined locality within the Rochechouart impact structure. This study led to the identification of reidite, granular grains corresponding to “former reidite in granular neoblastic” (FRIGN) zircon, and granular grains with granules lacking systematic orientation relationships. These findings show that these shock-related features are more widespread in the Rochechouart impact structure than previously reported. However, it is recommended that further extensive EBSD analysis of the reidite-bearing zircons be performed to understand better reidite proportions, reidite habits, and their implications for reidite formation and retention conditions.

Final conclusions

After the multidisciplinary characterization of 13 basement rocks and 20 impactites from the Rochechouart impact structure— including U-Pb geochronology with a total of 586 analyses on zircons from basement samples and 553 analyses on zircons from impactites—we conclude that (1) the age distribution of the Chassenon suevite closely correlates with paragneisses and the Videix suevite with monzodiorite and leptynites; (2) Sr and Sm-Nd data provide a more effective comparison between IMRs and the basement, with yellow IMRs resembling paragneisses and red IMRs suggesting a larger contribution from granodiorite or monzodiorite; (3) Our U-Pb zircon ages do not modify the previously most accepted impact age; and (4) the identification of diverse shock deformation features in the Videix suevite suggests that these textures are more widespread across the Rochechouart impact structure than previously recognized.

References

Abramov, O., and Kring, D. A. 2007. Numerical modeling of impact-induced hydrothermal activity at the Chicxulub crater. *Meteoritics and Planetary Science* 42: 93–112.

Alexandre, P. 2007. U-Pb zircon SIMS ages from the French Massif Central and implication for the pre-Variscan tectonic evolution in Western Europe. *Comptes Rendus. Géoscience* 339 (9): 613–621.

Alexandrov, P., Cheilletz, A., Deloule, É., and Cuney, M. 2000. 319 ± 7 Ma crystallization age for the Blond granite (northwest Limousin, French Massif Central) obtained by U/Pb ion-probe dating of zircons. *Comptes Rendus de l'Academie des Sciences, Sciences de La Terre et Des Planètes* 330: 617-622.

Anders, E., and Grevesse, N. 1989. Abundances of the elements: Meteoritic and solar. *Geochimica et Cosmochimica acta* 53(1): 197-214.

Andersen, T., and Elburg, M. A. 2021. Open-system behaviour of detrital zircon during weathering: an example from the Palaeoproterozoic Pretoria Group, South Africa. *Geological Magazine* 1–16.

Artemieva, N.A., and Shuvalov, V. V. 2016. From Tunguska to Chelyabinsk via Jupiter. *Annual Review of Earth and Planetary Sciences* 44: 37–56.

Bambier, A., Capdeville, J.-P., Cariou, E., Floc'h, J.P., Gabilly, P., and Hantzpergue, P. 1983. Notice explicative de la carte géologique de la France (1/50 000), Feuille La Rochefoucauld, France. Bureau de Recherches Géologiques et Minières, pp. 29.

Bellot, J.P., 2001. La structure de la croûte varisque du Sud-Limousin (Massif-Central français) et ses relations avec les minéralisations aurifères tardi-orogéniques: rapport des données géologiques, gitologiques, géophysiques et de la modélisation 3D. Ph. D. Thesis, Université de Montpellier II, Montpellier, France.

Bellot, J.P., and Roig, J.Y. 2007. Episodic exhumation of HP Rocks inferred from structural data and P-T paths from the southwestern Massif Central (Variscan Belt, France). *Journal of Structural Geology* 29 (9): 1538–1557.

Berger, J., Féménias, O., Ohnenstetter, D., Bruguier, O., Plissart, G., Mercier, J.C.C., and Demaiffe, D. 2010. New occurrence of UHP eclogites in Limousin (French Massif Central): Age, tectonic setting and fluid-rock interactions. *Lithos* 118 (3–4): 365–382.

Berthier, F., Duthou, J., and Roques, M. 1979. Datation géochronologique Rb/Sr sur roches totales du granite de Guéret (Massif Central). Age fini-Dévonien de mise en place de l'un de ses facies type. *Bulletin du Bureau de Recherches Géologiques et Minières* 1: 59–72.

Best, M.G. 2003. Igneous and Metamorphic Petrology, 2nd ed., xxi 729 pp. Oxford Blackwell Science. ISBN 1 405 10588 7.

Black, L. P., Kamo, S. L., Allen, M. C., Davis, D. W., Aleinikoff, J. N., Valley, J. W., Mundil, R., Campbell, I. H., Korsch, R. J., Williams, I. S., and Foudoulis, C. 2004. Improved $^{206}Pb/^{238}U$ microprobe geochronology by the monitoring of a trace-element-related matrix effect; SHRIMP, ID-TIMS, ELA-ICP-MS and oxygen isotope documentation for a series of zircon standards. *Chemical Geology* 205: 115–140.

Blichert-Toft, J. 2008. The Hf isotopic composition of zircon reference material 91500. *Chemical Geology* 253: 252–257.

Boutin, R., Edel, J.B., Montigny, R., and Westphal, M. 1991. Possible origin and age of late-Hercynian remagnetization occurring in amphibolite series from Plateau d'Aigurande, Massif Central, France. *Terra Abstracts* 3: 215.

Boutin, R., and Montigny, R. 1993. Datation $^{39}Ar/^{40}Ar$ des amphibolites du complexe leptyno-amphibolique du plateau d'Aigurande: collision Varisque à 390 Ma dans le Nord-Ouest du Massif Central français. *Comptes Rendus de l'Académie des Sciences. Série 2,* 316 : 1391–1398.

Carporzen, L., and Gilder, S.A. 2006. Evidence for coeval Late Triassic terrestrial impacts from the Rochechouart (France) meteorite crater. *Geophysical Research Letters* 33: L19308.

Cartannaz, C., Rolin, P., Cocherie, A., Marquer, D., Legendre, O., Fanning, C.M., Rossi, P. 2007. Characterization of wrench tectonics from dating of syn- to post-magmatism in the north-western French Massif Central. *International Journal of Earth Sciences* 96: 271–287.

Cathelineau, M., Boiron, M.C., Fourcade, S., Ruffet, G., Clauer, N., Belcourt, O., Coulibaly, Y., Banks, D.A., and Guillocheau, F. 2012. A major Late Jurassic fluid event at the basin/basement unconformity in western France: $^{40}Ar/^{39}Ar$ and K-Ar dating, fluid chemistry, and related geodynamic context. *Chemical Geology* 322: 99–120.

Cathelineau, M., Boiron, M.C., Holliger, P., and Poty, B. 1990. Metallogenesis of the French Part of the Variscan Orogen. Part II: Time-space relationships between U, Au and Sn-W ore deposition and geodynamic events - Mineralogical and U-Pb data. *Tectonophysics* 177 (1–3): 59–79.

Cavosie, A. J., Biren, M. B., Hodges, K. V., Wartho, J.-A., Horton, J. W., and Koeberl, C. 2021. Dendritic reidite from the Chesapeake Bay impact horizon, ocean drilling program site 1073 (offshore northeastern USA): a fingerprint of distal ejecta? *GEOLOGY* 49: 201–205.

Cavosie, A. J., Erickson, T. M., Timms, N. E., Reddy, S. M., Talavera, C., Montalvo, S. D., Pincus, M. R., Gibbon R. J., and Moser, D. 2015. A terrestrial perspective on using ex situ shocked zircons to date lunar impacts. *Geology* 43 : 999–1002.

Cavosie, A. J., Timms, N.E., Ferrière, L., and Rochette, P. 2018. FRIGN zircon - The only terrestrial mineral diagnostic of high-pressure and high-temperature shock deformation. *GEOLOGY* 46 (10): 891–894.

Chalier, M., Virlogeux, D., Duthou, J.-L. 1994. Les lamprophyres du district aurifère de Saint-Yrieix (Limousin, Massif central français). Âge Rb/Sr autunien et relations chronologiques avec le dépôt de l'or. *Comptes Rendus de l'Académie des Sciences* 319 (2): 1511-1518.

Chenevoy, M. 1958. Contribution à l'étude des schistes cristallins de la partie nord-ouest du Massif Central français. France Service de La Carte Geologique de La France. *Memoirs Pour Servir à l'Explication de la Carte Geologique Detaillée de La France*. Imprimerie Nationale, pp. 428.

Cherniak, D. J., and Watson, E. B. 2001. Pb diffusion in Zircon. *Chemical Geology* 172 (1–2): 5–24.

Chèvremont, P., Floc'h, J.P., Ménillet, F., Stussi, J. M., Delbos, R., Sauret, B., Blès, J. L., Courbe, C., Vuaillat, D., and Gravelat, C. 1996. Notice explicative de la

carte géologique de la France (1/50 000), Feuille Rochechouart (687): Orléans, France. Bureau de Recherches Géologiques et Minières, pp. 172.

Chew, D. M., Petrus, J. A., and Kamber, B. S. 2014. U–Pb LA–ICPMS dating using accessory mineral standards with variable common Pb. *Chemical Geology* 363: 185-199.

Clauer, N. 2020. The post-Variscan tectonic-thermal activity in the southeastern metalliferous province of the French Massif Central revisited with K-Ar ages of illite. *Ore Geology Reviews* 117 (November 2019): 103300.

Cocherie, A., Be Mezeme, E., Legendre, O., Fanning, M., Faure, M., and Rossi, P. 2005. Electron microprobe dating as a tool for understanding closure of U–Th–Pb system in monazite from migmatite. *American Mineralogist* 90: 607-618.

Cohen, B. E., Mark, D. F., Lee, M. R., and Simpson, S. L. 2017. A new high-precision $^{40}Ar/^{39}Ar$ age for the Rochechouart impact structure: At least 5 Ma older than the Triassic–Jurassic boundary. *Meteoritics and Planetary Science* 52 (8): 1600–1611.

Corfu, F., Hanchar, J. M., Hoskin, P. W.O., and Kinny, P. 2003. Atlas of zircon textures. Radiation effects in zircon. In: *Zircon - Reviews in Mineralogy and Geochemistry,* edited by J. M. Hanchar and P. W. O. Hoskin, vol. 53, 469-500. Washington, D.C.: Mineralogical Society of America.

Costa, S. 1992. East-west diachronism of the collisional stage in the French Massif Central: Implications for the european Variscan orogen. *Geodinamica Acta* 5 (1–2): 51–68.

Costa, S., and Maluski, H. 1988. Datations par la méthode ^{39}Ar-^{40}Ar de matériel magmatique et métamorphique paléozoique provenant du forage de Couy-Sancerre (Cher, France). Programme GPF. *Comptes Rendus de l'Académie des Sciences. Série 2,* 306 : 351–356.

Crósta, A.P., Reimold, W.U., Vasconcelos, M.A.R., Hauser, N., Oliveira, G.J.G., Maziviero, M.V., and Góes, A.M. 2019. Impact cratering: the South American record – Part I. *Chemie der Erde* 79: 1-61.

Crow, C. A., Mckeegan, K. D., and Moser, D. E. 2017. Coordinated U – Pb geochronology, trace element, Ti-in-zircon thermometry and microstructural analysis of Apollo zircons. *Geochimica et Cosmochimica Acta* 202: 264–284.

De Veslud, C. L. C., Alexandre, P., Ruffet, G., Cuney, M., and Cheilletz, A. 2013. A two-stage exhumation in western French Massif Central: New geochronological evidences of syn-collisional extension. *Lithos* 175: 1–15.

Deer, W. A., Howie, R. A., and Zussman, J. 1978. Framework silicates: Feldspar. In *Rock-forming Minerals,* vol 4A. Geological Society of London.

Do Couto, D., Faure, M., Augier, R., Cocherie, A., Rossi, P., Li, X. H., and Lin, W. 2016. Monazite U–Th–Pb EPMA and zircon U–Pb SIMS chronological constraints on the tectonic, metamorphic, and thermal events in the inner part of the Variscan orogen, example from the Sioule series, French Massif Central. *International Journal of Earth Sciences* 105: 557–579.

Duthou, J.-L. 1978. Les granitoides du Haut Limousin (Massif central francais). Chronologie Rb-Sr de leur mise en place. Le thermo métamorphisme carbonifère. *Bulletin de la Société Géologique de France* S7: 229–235.

Duthou, J. L., Cantagrel, J. M., Didier, J., and Vialette, Y. 1984. Palaeozoic granitoids from the French Massif Central: age and origin studied by $^{87}Rb/^{87}Sr$ system. *Physics of the Earth and Planetary Interiors* 35 (1–3): 131–144.

Duthou, J. L., Chenevoy, M., and Gay, M. 1994. Rb-Sr middle Devonian age of cordierite bearing migmatites from Lyonnais area (French Massif Central). *Comptes Rendus de l'Academie des Sciences, Serie 2, Sciences de la Terre et des Planetes* 319 (7): 791–796.

El Korh, A., Boiron, M. C., and Cividini, D. 2020. A multi-isotope study (Fe, Ge, O) of hydrothermal alteration in the Limousin ophiolite (French Massif Central). *Lithos* 378: 105876.

Erickson, T. M., Kirkland, C. L., Jourdan, F., Schmieder, M., Hartnady, M. I. H., Cox, M. A, and Timms, N. E. 2021. Resolving the age of the Haughton impact structure using coupled $^{40}Ar/^{39}Ar$ and U-Pb geochronology. *Geochimica et Cosmochimica Acta* 304: 68–82.

Erickson, T. M., Pearce, M. A., Reddy, S. M., Timms, N. E., Cavosie, A. J., Bourdet, J., Rickard, W. D. A., and Nemchin, A. A. 2017. Microstructural constraints on the mechanisms of the transformation to reidite in naturally shocked zircon. *Contributions to Mineralogy and Petrology* 172: 1- 26.

Eitel, M., Gilder, S. A., Kunzmann, T., and Pohl, J. 2014. Rochechouart impact crater melt breccias record no geomagnetic field reversal. *Earth and Planetary Science Letters* 387: 97–106.

Ewing, R. C., Meldrum, A., Wang, L.M., Weber, W. J., and Corrales, L. R. 2003. Radiation effects in zircon. In: *Zircon - Reviews in Mineralogy and Geochemistry,* edited by J. M. Hanchar and P. W. O. Hoskin, vol. 53, 387–425. Washington, D.C.: Mineralogical Society of America.

Faucher, J. 2021. Petrology and geochemistry of impact melt-rich lithologies of the Rochechouart impact structure (France). MSc thesis, Université de Lorraine (unpubl.), 31 pp.

Faure, M., Lardeaux, J.M., and Ledru, P. 2009. A review of the pre-Permian geology of the Variscan French Massif Central. *Comptes Rendus - Geoscience* 341: 202–213.

Faure, M., Leloix, C., and Roig, J-Y. 1997. L'evolution polycyclique de La chaine Hercynienne. *Bulletin de La Société Géologique de France* 168 (6): 695–705.

Faure, M., Mézème, B. E., Cocherie, A., Rossi, P., Chemenda, A., and Boutelier, D. 2008. Devonian geodynamic evolution the Variscan belt, insights from the French Massif Central and Massif Armoricain. *Tectonics* 27 (2): 1–19.

Faure, M., Mézème, B. E., Duguet, M., Cartier, C., and Talbot, J. Y. 2005. Paleozoic tectonic evolution of medio-Europa from the example of the French Massif Central and Massif Armoricain. *Journal of the Virtual Explorer* 19 (5): 1-25.

Faure, M., Thiéblemont, D., Beurrier, M., Lach, P., and Guerrot, C. 2024. Zircon, monazite and xenotime U/Pb isotopic analysis of the Chalencon septum in the Velay migmatites: Confirmation of Ediacaran-Lower Cambrian magmatism. New arguments supporting an Upper Permian hydrothermal episode. *Géologie de la France* 2: 13-27.

Ferrière, L., Koeberl, C., and Reimold, W. U. 2009. Characterisation of ballen quartz and cristobalite in impact breccias: New observations and constraints on ballen formation. *European Journal of Mineralogy* 21 (1): 203–217.

Franke, W., Cocks, L. R. M., and Torsvik, T. H. 2017. The Palaeozoic Variscan oceans revisited. *Gondwana Research* 48: 257–284.

French B. M. 1998. *Traces of Catastrophe: A Handbook of Shock-Metamorphic Effects in Terrestrial Meteorite Impact Structures.* LPI Contribution No. 954, Lunar and Planetary Institute, Houston, 120 pp.

Gebelin, A., 2004. Déformation et mise en place des granites (360-300 Ma) dans un segment de la chaîne Varisque (plateau de Millevaches, Massif Central). Ph. D. Thesis, Université de Montpellier II, Montpellier, France, p. 325. https://theses.fr/2004MON20151

Gébelin, A., Brunel, M., Monié, P., Faure, M., and Arnaud, N. 2007. Transpressional tectonics and Carboniferous magmatism in the Limousin, Massif Central, France: Structural and $^{40}Ar/^{39}Ar$ investigations. *Tectonics* 26: TC2008.

Gébelin, A., Roger, F., and Brunel, M. 2009. Syntectonic crustal melting and high-grade metamorphism in a transpressional regime, Variscan Massif Central, France. *Tectonophysics* 477: 229–243.

Geisler, T., Rashwan, A. A., Rahn, M. K. W., Poller, U., Zwingmann, H., Pidgeon, R. T., Schleicher, H., and Tomaschek, F. 2003. Low-temperature hydrothermal alteration of natural metamict zircons from the Eastern Desert, Egypt. *Mineralogical Magazine* 67(3): 485-508.

Ginster, U., Reiners, P. W., Nasdala, L., and Chanmuang, C. 2019. Annealing kinetics of radiation damage in zircon. *Geochimica et Cosmochimica Acta* 249: 225–246.

Gioia, S. M. C. L., and Pimentel, M. M. 2000. The Sm-Nd isotopic method in the geochronology laboratory of the University of Brasília. *Anais da Academia Brasileira de Ciências* 72: 219-245.

Gottwald, M., Kenkmann, T., and Reimold, W.U. 2020. Terrestrial impact structures: *The TanDEM-X Atlas*, Vol. 1 and 2. Munich, Germany: Verlag Dr. Friedrich Pfeil, 608 pp.

Guerrero, D., Reimold, W. U., Hauser, N., Kenny, G., Lambert, P. 2024. Zircon U-Pb provenance analysis applied to impactites from the Rochechouart impact structure, France. 2024. In: *Proceedings of the XIII South American Symposium on Isotope Geology, Búzios.* Campinas: Galoá. Abstract # 304228, pp. 133-134.

Guerrero, D., Reimold, W.U., Hauser, N., Figueiredo, I., Kenni, L., Lambert, P., 2024. Zircon U-Pb provenance analysis of impact melt and target rocks from the

Rochechouart impact structure, France. *Meteoritics and Planetary Science* 59(10): 2718-2743.

Hauser, N., Reimold, W. U., Cavosie, A.J., Crósta, A.P., Schwarz, W.H., Trieloff, M., Da Silva Maia de Souza, C., Pereira, L.A., Rodrigues, E.N., and Brown, M. 2019. Linking shock textures revealed by BSE, CL, and EBSD with U-Pb data (LA-ICP-MS and SIMS) from zircon from the Araguainha impact structure, Brazil. *Meteoritics and Planetary Science* 54 (10): 2286–2311.

Hawthorne, F. C., Oberti, R., Harlow, G. E., Maresch, W. V., Martin, R. F., Schumacher, J. C., and Welch, M. D. 2012. Nomenclature of the amphibole supergroup. *American Mineralogist* 97(11-12): 2031-2048.

Hazen, R. M., and Finger, L. W. 1979. Crystal structure and compressibility of zircon at high pressure. *American Mineralogist* 64: 196–201.

Herrmann, M., Kenny, G. G., Martell, J., and Alwmark, C. 2023. The first U – Pb age for shocked zircon from the Mien impact structure, Sweden, and implications for metamictization-induced zircon texture formed during impact events. *Meteoritics and Planetary Science* 59: 211-241.

Herrmann, M., Söderlund, U., Scherstén, A., Næraa, T., Holm-Alwmark, S., and Alwmark, C. 2021. The effect of low-temperature annealing on discordance of U–Pb zircon ages. *Scientific Reports* 11 (1): 7079.

Hey, M. H. 1954. A new review of the chlorites. *Mineralogical magazine and journal of the Mineralogical Society* 30(224): 277-292.

Hillebrandt, A. V., Krystyn, L., Kürschner, W. M., Bonis, N. R., Ruhl, M., Richoz, S., Schobben, M. A., et al. 2013. The Global Stratotype Sections and Point (GSSP) for the base of the Jurassic System at Kuhjoch (Karwendel Mountains, northern calcareous Alps, Tyrol, Austria). *Episodes* 36 (3): 162–198.

Holland, H. D., and Gottfried, D. 1955. The effect of nuclear radiation on the structure of zircon. *Acta Crystallographica* 8 (6): 291-300.

Holliger, P., Cuney, M., Friedrich, M., and Turpin, L. 1986. Age Carbonifère de l'unité de Brâme du complexe granitique peralumineux de Saint-Sylvestre (N.O. Massif Central) défini par les données isotopiques U-Pb sur zircon et monazite. *Comptes Rendus de l'Académie des Sciences* 303: 1309–1314.

Horne, A. 2016. (U-Th)/He, U/Pb, and radiation damage dating of the Rochechouart-Chassenon impact structure, France. MSc thesis, Arizona State University, pp. 47. https://keep.lib.asu.edu/items/154941.

Hoskin, P. W. O., and Schaltegger, U. 2003. The composition of zircon and igneous and metamorphic petrogenesis. In: *Zircon - Reviews in Mineralogy and Geochemistry,* edited by J. M. Hanchar and P. W. O. Hoskin, vol. 53, 27–62. Washington, D.C.: Mineralogical Society of America.

Howard, C. J., Hill, R. J., and Reichert, B. E. 1988. Structures of ZrO_2 polymorphs at room temperature by high-resolution neutron powder diffraction. *Acta Crystallographica Section B: Structural Science* 44: 116-120.

Jackson, S. E., Pearson, N. J., Griffin, W. L., and Belousova, E. A. 2004. The application of laser ablation-inductively coupled plasma-mass spectrometry to in situ U-Pb zircon geochronology. *Chemical Geology* 211 (1–2): 47–69.

Jarosewich, E., Nelen, J. A., and Norberg, J. A. 1980. Reference samples for electron microprobe analysis. *Geostandards Newsletter* 4(1): 43-47.

Jochum, K. P., Weis, U., Schwager, B., Stoll, B., Wilson, S. A., Haug, G. H., Andreae, M. O., and Enzweiler, J. 2016. Reference values following ISO guidelines for frequently requested rock reference materials. *Geostandards and Geoanalytical Research* 40(3): 333-350.

Jonckheere, R., Heinz, D., Hacker, B. R., Rafaja, D., Ratschbacher, L. 2019. A borehole investigation of zircon radiation damage annealing. *Terra Nova* 31: 263–270.

Jourdan, F., Reimold, W. U., and Deutsch, A. 2012. Dating terrestrial impact structures. *Elements* 8: 49–53.

Kamo, S.L., Reimold, W.U., Krogh, T.E., Colliston, W.P., 1996. A 2.023 Ga age for the Vredefort impact event and a first report of shock metamorphosed zircons in pseudotachylitic breccias and granophyre. *Earth and Planetary Science Letters* 144: 369–387.

Kelley, S. P., and Spray, J. G. 1997. A Late Triassic age for the Rochechouart impact structure, France. *Meteoritics and Planetary Science* 32 (5): 629–636.

Kenkmann, T. 2021. The terrestrial impact crater record: A statistical analysis of morphologies, structures, ages, lithologies, and more. *Meteoritics and Planetary Science* 56 (5): 1024–1070.

Kenkmann, T., Ivanov, B. A., and Stöffler, D. 2000. Identification of Ancient Impact Structures: Low-Angle Faults and Related Geological Features of Crater Basements. In *Impacts and the Early Earth. Lecture Notes in Earth Sciences,* edited by I. Gilmour, and C. Koeberl*,* vol 91, 279–307. Springer, Berlin, Heidelberg.

Kenny, G. G., Hyde, W. R., Storey, M., Garde, A. A., Whitehouse, M. J., Beck, P., Johansson, L., Søndergaard, A. S., Bjørk, A.A., MacGregor, J. A., Khan, S. A., Mouginot, J., Johnson, B. C., Silber, E. A., Wielandt, D. K. P., Kjær K. H., and Larsen, N. K. 2022. A Late Paleocene age for Greenland's Hiawatha impact structure. *Science Advances* 8: eabm2434.

Kenny, G.G., Morales, L. F., Whitehouse, M.J., Petrus, J. A., and Kamber, B. S. 2017. The formation of large neoblasts in shocked zircon and their utility in dating impacts. *Geology* 45: 1003–1006.

Kenny, G. G., Schmieder, M., Whitehouse, M. J., Nemchin, A. A., Morales, L. F. G., Buchner, E., Bellucci, J. J., and Snape, J. F. 2019. A new U-Pb age for shock-recrystallised zircon from the Lappajärvi impact crater, Finland, and implications for the accurate dating of impact events*. Geochimica et Cosmochimica Acta* 245: 479–494.

Kirkland, C. L., Smithies, R. H., Taylor, R. J. M., Evans, N., and McDonald, B. 2015. Zircon Th/U ratios in magmatic environs. *Lithos* 212: 397–414.

Kohn, M. J., Corrie, S. L., and Markley, C. 2015. The fall and rise of metamorphic zircon. *American Mineralogist* 100: 897–908.

Kovaleva, E. 2020. Textural identification of polycrystalline magmatic, tectonically-deformed, and shock-related zircon aggregates. *Minerals* 10 (5): 469.

Kovaleva, E., Kusiak, M. A., Kenny, G. G., Whitehouse, M. J., Habler, G., Schreiber, A., and Wirth, R. 2021. Nano-scale investigation of granular neoblastic zircon, Vredefort impact structure, South Africa: Evidence for complete shock melting. *Earth and Planetary Science Letters* 565: 116948.

Kraut, F., and French, B. M. 1971. The Rochechouart meteorite impact structure. *Journal of Geophysical Research* 76: 5407–5413.

Kraut, F., Short N. M., and French B. M. 1969. Preliminary report on a probable meteorite impact structure near Chassenon, France. *Meteoritics* 4:190-191.

Krogh, T.E., Kamo, S.L., Bohor, B.F., 1993. Fingerprinting the K/T impact site and determining the time of impact by U Pb dating of single shocked zircons from distal ejecta. *Earth and Planetary Science Letters* 119: 425–429.

Kroner, U., and Romer, R. L. 2013. Two plates - many subduction zones: The Variscan orogeny reconsidered. *Gondwana Research* 24 (1): 298–329.

Kunz, B. E., Regis, D., and Engi, M. 2018. Zircon ages in granulite facies rocks: Decoupling from geochemistry above 850 °C? *Contributions to Mineralogy and Petrology* 173 (3): 1–21.

Kusaba, K., Syono, Y., Kikuchi, M., and Fukuoka, K., 1985. Shock behavior of zircon: phase transition to scheelite structure and decomposition. *Earth and Planetary Science Letters* 72: 433–439.

Lafon, J.M. 1986. Géochronologie U-Pb appliquée à deux segments du massif central français, le Rouergue oriental et le Limousin central. Thèse d'État, Université Montpellier, France, pp. 152.

Lambert, P. 1974. La structure d'impact de Meteorite Géante de Rochechouart. Thèse de 3ème cycle, Université de Paris Sud, Orsay, France, pp. 148.

Lambert, P. 1977a. Les effets des ondes de choc naturelles et artificielles, et le cratère d'impact de Rochechouart (Limousin - France). Thèse d'État, Université de Paris Sud, Orsay, France, pp. 515.

Lambert, P. 1977b. Rochechouart impact crater: Statistical geochemical investigations and meteoritic contamination. In *Impact and Explosion Cratering,* edited by D.J. Roddy, R. O. Pepin, and R. B. Merill, 449–460. New York: Pergamon Press.

Lambert, P. 2010. Target and impact deposits at Rochechouart impact structure, France. *Special Paper of the Geological Society of America* 465 (25): 509–541.

Lambert, P., Alwmark, C., Baratoux, D., Bouley, S., Brack, A., Bruneton, P., Buchner, E., Claeys, P., Dence, M. R., Courtin Nomade, A., Duhamel Achin, I., Floch, J. P., French, B. M., Fudge, C., Gattacceca, J., Gibson, R. L., Goderis, S., Grieve,

R. A. F., Hauser, N., Hodges, K. V., Hörz, F., Humayun, M., Jourdan, F., Kelley, S. P., Kenkmann, T., Kring, D. A., Langenhorst, F., Lebreton, J. P., Lee, M. R., Lindgren, P., Lofi, J., Lorand, J. P., Luais, B., Masaitis, V., Meunier, A., Moore, C. B., Ormö, J., Osinski, G. R., Petit, S., Pezard, P. A., Poelchau, M., Pohl, J., Quesnel, Y., Ramboz, C., Reeves, H., Reimold, W. U., Rochette, P., Sapers, H. M., Schmieder, M., Schultz, P. H., Schwenzer, S. P., Sharp, T., Shoemaker, C. S., Simpson, S. L., Stöffler, D., Sturkell, E., Trumel, H., Walton, E., Westall, F., Wittmann, A., and Wünnemann K. 2019. The Rochechouart 2017-cores rescaled: Major features. *50th Lunar and Planetary Science Conference*, abstract # 2005, pp. 2.

Lambert, P. and CIRIR Consortium. 2020. Valorisation du géopatrimoine « Impacte de Rochechouart » - Résumé. *Géologues* No. 205, SGF, France, 23 pp.

Lambert, P., and Reimold, W. U. 2023. Terrestrial impact sites as field analogs for planetary exploration. *Frontiers in Astronomy and Space Sciences* 10: 1186173.

Lardeaux, J.-M. 2014. Deciphering orogeny: A metamorphic perspective Examples from European Alpine and Variscan belts: Part II: Variscan metamorphism in the French Massif Central – A review. *Bulletin de La Société Géologique de France* 185 (5): 281–310.

Leroux, H., Reimold, W.U., Koeberl, C., Hornemann, U., and Doukhan, J.C. 1999. Experimental shock deformation in zircon: a transmission electron microscopic study. *Earth and Planetary Science Letters* 169: 291–301.

Leroy, J., and Sonnet, J. 1976. Contribution à l'étude géochimique des filons de lamprophyres recoupant le granite à deux micas de Saint-Sylvestre (Massif central français). *Comptes Rendus de l'Académie des Sciences* 283: 1477-1480.

Lotout, C., Pitra, P., Poujol, M., Anczkiewicz, R., and Van Den Driessche, J. 2018. Timing and duration of Variscan high-pressure metamorphism in the French Massif Central: A multimethod geochronological study from the Najac Massif. *Lithos* 308: 381–394.

Ludwig, K., and Mundil, R. 2002. Extracting reliable U-Pb ages and errors from complex populations of zircons from Phanerozoic tuffs. *Geochimica et Cosmochimica Acta* 66 (15A): A463–A463.

Lugmair, G. W., and Marti, K. 1978. Lunar initial $^{143}Nd/^{144}Nd$: differential evolution of the lunar crust and mantle. *Earth and Planetary Science Letters* 39(3): 349-357.

Mader, D., and Koeberl, C. 2009. Using Instrumental Neutron Activation Analysis for geochemical analyses of terrestrial impact structures: Current analytical procedures at the University of Vienna Geochemistry Activation Analysis Laboratory. *Applied Radiation and Isotopes* 67(12): 2100-2103.

Martínez Catalán, J. R., Schulmann, K., and Ghienne, J.-F. 2021. The mid-Variscan allochthon: Keys from correlation, partial retrodeformation and plate-tectonic reconstruction to unlock the geometry of a non-cylindrical belt. *Earth-Science Reviews* 220 (September): 103700.

McGregor, M., McFarlane, C.R.M., and Spray, J.G. 2019. In situ multiphase U–Pb geochronology and shock analysis of apatite, titanite and zircon from the Lac La Moinerie impact structure, Canada. *Contributions to Mineralogy and Petrology* 174: 1-20.

McGregor, M., Timmons, M. E., Spray, J. G., and Whitehouse, M. J. 2021. High-resolution EBSD and SIMS U–Pb geochronology of zircon, titanite, and apatite: insights from the Lac La Moinerie impact structure, Canada. *Contributions to Mineralogy and Petrology* 176: 1–26.

Melleton, J., Cocherie, A., Faure, M., and Rossi, P. 2010. Precambrian protoliths and Early Paleozoic magmatism in the French Massif Central: U-Pb data and the north Gondwana connection in the west European Variscan belt. *Gondwana Research* 17 (1): 13–25.

Melleton, J., Faure, M., and Cocherie, A. 2009. Monazite U-Th/Pb chemical dating of the Early Carboniferous syn-kinematic MP/MT metamorphism in the Variscan French Massif Central. *Bulletin de La Societe Geologique de France* 180 (3): 283–292.

Melosh, H. J. 1989. *Impact Cratering: A Geologic Process*. New York: Oxford University Press, 258 pp.

Miranda, C. C., Milhomem Neto, J. M., and Evangelista Pinto, J. A. 2023. Metodologia U-Pb em zircão por LA-Q-ICP-MS no laboratório Pará-Iso/UFPA. *17º Simpósio de Geologia da Amazônia* Santarém-PA. 5 pp.

Montalvo, S.D., Reddy, S.M., Saxey, D.W., Rickard, W.D.A., Fougerouse, D., Quadir, Z., Johnson, T.E. 2019. Nanoscale constraints on the shock-induced transformation of zircon to reidite. *Chemical Geology* 507, 85-95.

Morel, M.L.A., Nebel, O., Nebel-Jacobsen, Y.J., Miller, J.S., and Vroon, P.Z. 2008. Hafnium isotope characterization of the GJ-1 zircon reference material by solution and laser-ablation MC-ICPMS. *Chemical Geology* 255: 231–235.

Moser, D.E. 1997. Dating the shock wave and thermal imprint of the giant Vredefort impact, South Africa. *Geology* 25: 7–10.

Moser, D. E., Cupelli, C. L., Barker, I. R., Flowers, R. M., Bowman, J. R., Wooden, J., and Hart, J. R. 2011. New zircon shock phenomena and their use for dating and reconstruction of large impact structures revealed by electron nanobeam (EBSD, CL, EDS) and isotopic U-Pb and (U-Th)/He analysis of the Vredefort Dome. *Canadian Journal of Earth Sciences* 48 (2): 117–139.

Moyen, J. F., Laurent, O., Chelle-Michou, C., Couzinié, S., Vanderhaeghe, O., Zeh, A., Villaros, A., and Gardien, V. 2017. Collision vs. subduction-related magmatism: two contrasting ways of granite formation and implications for crustal growth. *Lithos* 277: 154-177.

Murakami, T., Chakoumakos, B. C., Ewing, R. C., Lumpkin, G. R., and Weber, W. J. 1991. Alpha-decay event damage in zircon. *American Mineralogist* 76 (9-10): 1510-1532.

Nagl, P., and Mader, D. 2019. X-ray fluorescence (XRF) and instrumental neutron activation analysis (INAA) for the geochemical analysis of rocks, presented on in-house control samples (Abstract). *Mitteilungen der Österreichischen Mineralogischen Gesellschaft* 165: 67.

Nan, S., Wang, S., Zhang, F., Niu, J., Zhai, P., Liu, Y., Boatner, L., Qin, S., Liu, J., Maik, L., Ewing, R. C., and Li, W. 2024. Zircon-to-reidite phase transition enhanced by minor radiation damage: Implications for hypervelocity impacts. *Chemical Geology* 654: 122041.

Nasdala, L., Hofmeister, W., Norberg, N., Martinson, J.M., Corfu, F., Dörr, W., Kamo, S.L., Kennedy, A.K., Kronz, A., Reiners, P.W., Frei, D., Kosler, J., Wan, Y., Götze, J., Häger, T., Kröner, A., and Valley, J.W. 2008. Zircon M257 - a

Homogeneous Natural Reference Material for the Ion Microprobe U-Pb Analysis of Zircon. *Geostandards and Geoanalytical Research* 32: 247-265.

Nasdala, L., Wenzel, M., Vavra, G., Irmer, G., Wenzel, T., and Kober, B. 2001. Metamictisation of natural zircon: Accumulation versus thermal annealing of radioactivity-induced damage. *Contributions to Mineralogy and Petrology* 141 (2): 125–144.

Ormö, J., Sturkell, E., Lambert, P., Bourquin, S., and Cherfils, J-B. 2023. Oceanic resurge deposits at the Rochechouart impact structure (France) suggest a marine target environment. *Geological Magazine* 160: 794–802.

Osinski, G.R., Cockell, C.S., Pontefract, A., and Sapers, H.M. 2020. The role of meteorite impacts in the origin of life. *Astrobiology* 20: 1121–1149.

Osinski, G. R., and Ferrière, L. 2016. Shatter cones: (Mis)understood? *Science Advances* 2 (8): 1–10.

Osinski, G. R., Grieve, R.A.F., Ferrière, L., Losiak, A., Pickersgill, A.E., Cavosie, A.J., Hibbard, S.M., Hill, P.J.A., Bermudez, J.J., Marion, C.L., Newman, J.D., and Simpson, S.L. 2022. Impact earth: A review of the terrestrial impact record. *Earth-Science Reviews* 232: 104112.

Osinski, G. R., and Pierazzo, E. 2013. *Impact Cratering: Processes and Products*. Hoboken, NJ, Wiley-Blackwell, 316 pp.

Paton, C., Hellstrom, J., Paul, B., Woodhead, J., and Hergt, J. 2011. Iolite: Freeware for the visualisation and processing of mass spectrometric data. *Journal of Analytical Atomic Spectrometry* 26 (12): 2508-2518.

Petrus, J. A., and Kamber, B. S. 2012. VizualAge: A novel approach to laser ablation ICP-MS U-Pb geochronology data reduction. *Geostandards and Geoanalytical Research* 36(3): 247-270.

Petrus, J. A., Kenny, G. G., Ayer, J. A., Lightfoot, P. C., and Kamber, B. S. 2016. Uranium-lead zircon systematics in the Sudbury impact crater-fill: Implications for target lithologies and crater evolution. *Journal of the Geological Society* 173 (1): 59–75.

Piazolo, S., La Fontaine, A., Trimby, P., Harley, S., Yang, L., Armstrong, R., and Cairney, J.M. 2016. Deformation-induced trace element redistribution in zircon revealed using atom probe tomography. *Nature Communications* 7 (1): 10490.

Pin, C. 1989. Essai sur la chronologie et l'évolution géodynamique de la chaîne Hercynienne d'Europe. Ph. D. Thesis, Université Blaise Pascal - Clermont-Ferrand II. https://tel.archives-ouvertes.fr/tel-01001861.

Plan, A., Kenny, G. G., Erickson, T. M., Lindgren, P., Alwmark, C., Holm-Alwmark, S., Lambert, P., Scherstén, A., Söderlund, U., and Osinski, G. 2021. Exceptional preservation of reidite in the Rochechouart impact structure, France: New insights into shock deformation and phase transition of zircon. *Meteoritics and Planetary Science* 56 (10): 1795–1828.

Pohl, J., Ernstson, K., and Lambert, P. 1978. Gravity measurements in the Rochechouart impact structure (France). *Meteoritics* 13: 601–604.

Pohl, J., and Soffel, H. 1971. Paleomagnetic age determination of the Rochechouart impact structure (France). *Zeitschrift für Geophysik* 37: 857–866.

Quesnel, Y., Sailhac, P., Lofi, J., Lambert, P., Rochette, P., Uehara, M., and Camerlynck, C. 2021. Multiscale geoelectrical properties of the Rochechouart impact structure, France. *Geochemistry, Geophysics, Geosystems 22*: e2021GC010036.

Ramboz, C., Chèvremont, P., and Lambert, P. 2015. Continental-scale environmental and geochemical distal effects of the Rochechouart impact at the lower Hettangian. *13th SGA Biennal Meeting*, 6 p.

Rasmussen, C., Stockli, D. F., Erickson, T. M., and Schmieder, M. 2020. Spatial U-Pb Age Distribution in Shock-Recrystallized Zircon – A case study from the Rochechouart impact structure, France. *Geochimica et Cosmochimica Acta* 273: 313–330.

Rasmussen, C., Stockli, D. F., Ross, C. H., Pickersgill, A., Gulick, S. P., Schmieder, M., Christeson, G. L., Wittmann, A., Kring, D. A., and Morgan, J.V. 2019. U-Pb memory behavior in Chicxulub's peak ring — Applying U-Pb depth profiling to shocked zircon. *Chemical Geology* 525: 356–367.

Regorda, A., Lardeaux, J.-M., Roda, M., Marotta, A.M., and Spalla, M.I. 2020. How many subductions in the Variscan orogeny? Insights from numerical models. *Geoscience Frontiers* 11 (3): 1025–1052.

Reimold, W. U., Nieber-Reimold, J., Oskierski, W., and Rehfeldt, A. 1983. A Geochemical and chronological study of amphibolites & granitic rocks from the Haut-Limousin, Massif Central. *Fortschritte der Mineralogie*. 61: 178-180.

Reimold, W. U., and Oskierski, W. 1987. The Rb-Sr-Age of the Rochechouart impact structure, France, and geochemical constraints on impact melt-target rock-meteorite compositions. In *Research in Terrestrial Impact Structures*, edited by Jean Pohl, 94–114. Germany: Friedrich Vieweg & Sohn.

Reimold, W. U., Oskierski, W., and Huth, J. 1987. The pseudotachylite from Champagnac in the Rochechouart meteorite crater, France. *Journal of Geophysical Research* 92 (B4): E737–48.

Reimold, W. U., Schulz, T., König, S., Koeberl, C., Hauser, N., Wannek, D., and Schmitt, R. -T. 2021. Genesis of the Mafic Granophyre of the Vredefort Impact Structure (South Africa): Implications of New Geochemical and Se and Re-Os Isotope Data. In *Large Meteorite Impacts and Planetary Evolution VI*, edited by W. U. Reimold, and C. Koeberl. *Geological Society of America Special Paper* 550: 235–254.

Rieder, M., Cavazzini, G., D'yakonov, Y. S., Frank-Kamenetskii, V. A., Gottardi, G., Guggenheim, S., Koval, P., Müller, G., Neiva, A. M. R., Radoslovich, E. W., Robert, J-L., Sassi, F. P., Takeda, H., Weiss, Z., and Wones, D. R. 1998. Nomenclature of the micas. *Clays and Clay Minerals* 46(5): 586-595.

Rubatto, D. 2017. Zircon: The metamorphic mineral. *Reviews in Mineralogy and Geochemistry* 83 (1): 261-295.

Santallier, D., 1981. Les roches basiques dans la série métamorphique du Bas-Limousin, Massif Central (France). Ph. D. Thesis, Université Orléans, Orléans, France, pp. 350.

Santos, M. M., Lana, C., Scholz, R., Buick, I., Schmitz, M.D., Kamo, S.L., Gerdes, A., Corfu, F., Tapser, S., Lancaster, P., Storey, C. D., Basei, M. A. S., Tohver, E., Alkmim, A., Nalini, H., Krambrock, K., Fantini, C., and Wiedenbeck, M. 2017. A new appraisal of Sri Lankan BB zircon as a reference material for LA-ICP-MS U-Pb geochronology and Lu-Hf isotope tracing. *Geostandards and Geoanalytical Research* 41 (3): 335–358.

Sapers, H. M., Osinski, G. R., and Banerjee, N. 2009. Re-Evaluating the Rochechouart Impactites: Petrographic Classification, Hydrothermal Alteration and Evidence for Carbonate Bearing Target Rocks. *40th Annual Lunar and Planetary Science Conference*, abstract # 1284, pp. 2.

Sapers, H. M., Osinski, G. R., Banerjee, N. R., Ferrière, L., Lambert, P., and Izawa, M. R. M. 2014. Revisiting the Rochechouart impact structure, France. *Meteoritics and Planetary Science* 49 (12): 2152–2168.

Scaillet, S., Cuney, M., De Veslud, C. L. C., Cheilletz, A., and Royer, J.J. 1996. Cooling pattern and mineralization history of the Saint Sylvestre and western Marche leucogranite pluton, French Massif Central: II Thermal modelling and implications for the mechanisms of uranium mineralization. *Geochimica et Cosmochimica Acta* 60: 4673–4688.

Schmieder, M., Buchner, E., Schwarz, W.H., Trieloff, M., and Lambert, P. 2010. A Rhaetian $^{40}Ar/^{39}Ar$ Age for the Rochechouart impact structure (France) and implications for the latest Triassic sedimentary record. *Meteoritics and Planetary Science* 45 (8): 1225–1242.

Schmieder, M., and Kring, D. A. 2020. Earth's impact events through geologic time: a list of recommended ages for terrestrial impact structures and deposits. *Astrobiology* 20: 91–141.

Schmieder, M., Shaulis, B.J., Lapen, T.J., Buchner, E., and Kring, D.A. 2019. In situ U-Pb analysis of shocked zircon from the Charlevoix impact structure, Québec, Canada. *Meteoritics and Planetary Science* 54: 1808–1827.

Schmieder, M., Tohver, E., Jourdan, F., Denyszyn, S.W. and Haines, P.W. 2015. Zircons from the Acraman impact melt rock (South Australia): Shock metamorphism, U-Pb and $^{40}Ar/^{39}Ar$ systematics, and implications for the isotopic dating of impact events. *Geochimica et Cosmochimica Acta* 161: 71–100.

Schulmann, K., Martínez Catalán, J. R., Lardeaux, J. M., Janoušek, V., and Oggiano, G. 2014. The Variscan orogeny: Extent, timescale and the formation of the European crust. *Geological Society Special Publication* 405 (1): 1–6.

Schulte, P., Alegret, L., Arenillas, I., Arz, J.A., Barton, P.J., Brown, P.R., Bralower, P.J., Christeson, G.L., Claeys, P., Cockell, C.S., Collins, G.S., Deutsch, A., Goldin, T.J., Goto, K., Grajales-Nishimura, J.M., Grieve, R.A.F., Gulick, S.P.S.,

Johnson, K.R., Kiessling, W., Koeberl, C., Kring, D.A., MacLeod, K.G., Matsui, T., Melosh, H.J., Montanari, A., Morgan, J.V., Neal, C.R., Nichols, D.J., Norris, R.D., Pierazzo, E., Ravizza, G., Rebolledo-Vieyra, M., Reimold, W.U., Robin, E., Salge, T., Speijer, R.P., Sweet, A.R., Urrutia-Fucugauchi, J., Vajda, V., Whalen, M.T., and Willumsen, P.S. 2010. The Chicxulub impact and mass extinction at the Cretaceous-Paleogene boundary. *Science* 327, #5970, 1214-1218.

Schwarz, W. H., Hanel, M., and Trieloff, M. 2020. U-Pb dating of zircons from an impact melt of the Nördlinger Ries crater. *Meteoritics and Planetary Science* 55 (2): 312-325.

Sharman, G. R, Sharman, J. P., and Sylvester, Z. 2018. DetritalPy: A python-based toolset for visualizing and analysing detrital geo-thermochronologic data. *The Depositional Record* 4 (2): 202–215.

Shteynman, L., and Sharp, T.G. 2023. Does reidite formation reset U-Pb ages: direct measurements from Rochechouart impact structure. *54th Lunar and Planetary Science Conference,* Abstract # 2327, pp. 2.

Siégel, C., Bryan, S. E., Allen, C. M., and Gust., D. A. 2018. Use and abuse of zircon-based thermometers: A critical review and a recommended approach to identify antecrystic zircons. *Earth-Science Reviews* 176: 87–116.

Silva, J. P. A. D. 2020. Saturn – Uma nova ferramenta de correção de dados U-Pb para LA-ICP-MS. MS thesis, Escola de Minas, Universidade Federal de Ouro Preto, Ouro Preto. 51 pp.

Simpson, S. L., Boyce, A. J., Lambert, P., Lindgren, P., and Lee, M. R. 2017. Evidence for an impact-induced biosphere from the δ 34 S signature of sulphides in the Rochechouart impact structure, France. *Earth and Planetary Science Letters* 460: 192–200.

Sizaret, S., Marcoux, E., Jébrak, M., and Touray, J.C. 2004, The Rossignol fluorite vein, Chaillac, France: multiphase hydrothermal activity and intra-vein sedimentation. *Economic Geology* 99: 1107-1122.

Sláma, J., Košler, J., Condon, D.J., Crowley, J.L., Gerdes, A., Hanchar, J. M., Horstwood, M. S. A., Morris, G. A., Nasdala, L., Norberg, N., Schaltegger, U., Schoene, B., Tubrett, M. N., Whitehouse, M. J. 2008. Plešovice zircon - A new

natural reference material for U-Pb and Hf isotopic microanalysis. *Chemical Geology* 249 (1–2): 1–35.

Son, T. H., and Koeberl, C. 2005. Chemical variation within fragments of Australasian tektites. *Meteoritics and Planetary Science* 40(6): 805-815.

Spencer, C. J., Kirkland, C. L., and Taylor, R.J.M. 2016. Strategies towards Statistically robust interpretations of in situ U-Pb Zircon geochronology. *Geoscience Frontiers* 7 (4): 581–89.

Stacey, J.S., and Kramers, J.D. 1975. Approximation of terrestrial lead isotope evolution by a two-stage model. *Earth and Planetary Science Letters* 26: 207–221.

Steiger, R. H., and Jäger, E. 1977. Subcommission on geochronology: Convention on the use of decay constants in geo- and cosmochronology. *Earth and Planetary Science Letters* 36(3): 359-362.

Sun, S.S., and McDonough, W.F. 1989. Chemical and isotopic systematics of oceanic basalts: Implications for mantle composition and processes. *Geological Society, London, Special Publications* 42: 313–345

Szumila, I., Trail, D., Erickson, T., Simon, J.I., Wielicki, M.M., Lapen, T., Nakajima, M., Fries, M., and Bell, E.A. 2023. Microstructural changes and Pb mobility during the zircon to reidite transformation: implications for planetary impact chronology. *American Mineralogist* 108: 1516-1529.

Tagle, R., Schmitt, R.T., and Erzinger, J. 2009. Identification of the projectile component in the impact structures Rochechouart, France and Sääksjärvi, Finland: Implications for the impactor population for the earth. *Geochimica et Cosmochimica Acta* 73: 4891–4906.

Tartèse, R., Endley, S., and Joy, K. H. 2022. U-Pb Dating of zircon and monazite from the uplifted Variscan crystalline basement of the Ries impact crater. *Meteoritics and Planetary Science* 1–20.

Timms, N. E., Erickson, T.M., Pearce, M. A., Cavosie, A.J., Schmieder, M., Tohver, E., Reddy, S. M., Zanetti, M.R., Nemchin, A.A., and Wittmann, A. 2017. A pressure-temperature phase diagram for zircon at extreme conditions. *Earth-Science Reviews* 165: 185–202.

Tischendorf, G., Forster, H. J., Gottesmann, B., and Rieder, M. 2007. True and brittle micas: composition and solid-solution series. *Mineralogical Magazine* 71(3): 285-320.

Tolometti, G. D., Erickson, T. M., Osinski, G. R., Cayron, C., and Neish., C. D. 2022. Hot rocks: Constraining the thermal conditions of the Mistastin Lake impact melt deposits using zircon grain microstructures. *Earth and Planetary Science Letters* 584: 117523.

Vanderhaeghe, O., Laurent, O., Gardien, V., Moyen, J.F., Gébelin, A., Chelle-Michou, C., Couzinié, S., Villaros, A., and Bellanger, M. 2020. Flow of partially molten crust controlling construction, growth and collapse of the Variscan orogenic belt: The geologic record of the French Massif Central. *BSGF - Earth Sciences Bulletin* 191 (25): 2–56.

Vermeesch, P., Resentini, A., and Garzanti, E. 2016. An R package for statistical provenance analysis. *Sedimentary Geology* 336: 14–25.

Vermeesch, P. 2018a. Isoplot R: A free and open toolbox for geochronology. *Geoscience Frontiers* 9 (5): 1479–1493.

Vermeesch, P. 2018b. Dissimilarity measures in detrital geochronology. *Earth-Science Reviews* 178: 310–321.

Vermeesch, P. 2021. Maximum Depositional Age Estimation Revisited. *Geoscience Frontiers* 12 (2): 843–850.

Wagner, G. A., and Storzer, D. 1975. The age of the Rochechouart structure. *Meteoritics* 10: 503–504.

Wang, X., Griffin, W. L., Chen J., Huang, P., and Li, X. 2011. U and Th contents and Th/U ratios of zircon in felsic and mafic magmatic rocks: Improved zircon-melt distribution coefficients. *Acta Geologica Sinica* 85: 164-174.

Whitehouse, M. J., Ravindra Kumar, G. R., and Rimša, A. 2014. Behaviour of radiogenic Pb in zircon during ultrahigh-temperature metamorphism: an ion imaging and ion tomography case study from the Kerala Khondalite Belt, southern India. *Contributions to Mineralogy and Petrology* 168: 1–18.

Whitney, D. L., and Evans, B. W. 2010. Abbreviations for names of rock-forming minerals. *American Mineralogist* 95: 185–187.

Wiedenbeck, M., Allé, P., Corfu, F., Griffin, W. L., Meier, M., Oberli, F., Von Quadt, A., Roddick, J.C., and Spiegel, W. 1995. Three natural zircon standards for U-Th-Pb, Lu-Hf, trace element and REE analyses. *Geostandards Newsletter* 19 (1): 1-23.

Wittmann, A., Kenkmann, T., Schmitt, R. T., and Stöffler, D. 2006. Shock-metamorphosed zircon in terrestrial impact craters. *Meteoritics and Planetary Science* 41 (3): 433–454.

Woodhead, J., Hergt, J., Shelley, M., Eggins, S., and Kemp, R. 2004. Zircon Hf-isotope analysis with an excimer laser, depth profiling, ablation of complex geometries, and concomitant age estimation. *Chemical Geology* 209: 121–135.

Wright, S. I., Suzuki, S., and Nowell, M. M. 2016. In situ EBSD observations of the evolution in crystallographic orientation with deformation. *JOM* 68: 2730-2736.

Zhao, J., Xiao, L., Xiao, Z., Wu, X., He, Q., Hao, J., Li, R., and Lin, Y. 2025. Element Redistribution and Age Resetting in Shock-Deformed Zircon from the Chicxulub Impact Structure. *Geochimica et Cosmochimica Acta* (In Press).

Zhao, J., Zhang, X., Xiao, L., Cavosie, A. J., Timms, N. E., Nemchin, A., Xiao, Z., Hu, W., Chang, Y., Shu, J., He, Q., Zhao, S., Wang, J., Zhao, J., and the IODP 364 Science Party. 2024. Nanoscale constraints on the nucleation and evolution of granular zircon from reidite in impactites at the Chicxulub impact structure. *Earth and Planetary Science Letters* 626: 118507.

Zhou, Z., Zhao, J., Xiao, L., and Sun, J. 2024. Occurrences of complex ZrSiO4 variants from the Ries impact ejecta: Constraints for shock thermobarometer in zircon during impact processes. *Icarus* 420: 116205.